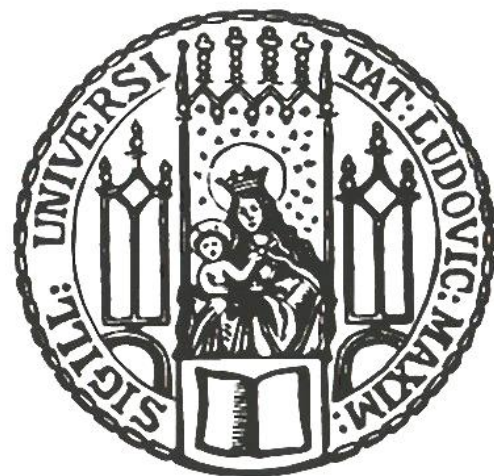


Studies of TS domain-mediated mechanisms regulating DNA methyltransferase 1

Patricia Wolf



München 2015

Erstgutachter: Prof. Dr. Heinrich Leonhardt
Zweitgutachter: Prof. Dr. Dirk Eick
Tag der Abgabe: 17.06.2015
Tag der mündlichen Prüfung: 29.07.2015

Studies of TS domain-mediated mechanisms regulating DNA methyltransferase 1

Dissertation
an der Fakultät für Biologie
der Ludwig-Maximilians-Universität München

vorgelegt von

Patricia Wolf aus Peißenberg
München, den 17.06.2015



Table of contents

Summary.....	V
Zusammenfassung.....	VII
1. Introduction.....	1
1.1 Epigenetic information	1
1.1.1 Histone post translational modifications	1
1.1.2 DNA modifications.....	6
1.2. Establishment and maintenance of DNA methylation	8
1.2.1 Establishment of DNA methylation.....	9
1.2.2 Maintenance of DNA methylation patterns by DNMT1.....	11
1.2.3 Cooperative readout of DNA and histone modifications by UHRF1 and UHRF2.....	15
1.2.4 Erasure of DNA methylation	17
1.3 Role of DNA modifications in neurogenesis and neurodegenerative diseases	21
1.3.1 DNA methylation in the developing and adult nervous system.....	21
1.3.2 DNA demethylation in the developing and adult nervous system.....	24
1.3.3 DNA methylation and neurodegenerative disease	26
1.4 Hereditary sensory and autonomic neuropathies (HSANs).....	28
1.4.1 HSAN-IE and ADCA-DN caused by mutations in <i>DNMT1</i>	28
1.4.2 Classification and genetic heterogeneity of HSANs	30
1.4.3 Disease modeling and treatment.....	34
1.4 Aims of this work	35
2. Results	37
2.1 Generation and characterization of rat and mouse monoclonal antibodies specific for MeCP2 and their use in X-inactivation studies.....	39
2.2 Versatile toolbox for high throughput biochemical and functional studies with fluorescent fusion proteins.....	55
2.3 Cooperative DNA and histone binding by Uhrf2 links the two major repressive epigenetic pathways.....	71
2.4 Dissection of cell cycle-dependent dynamics of Dnmt1 by FRAP and diffusion-coupled modeling	91
2.5 Poly(ADP-ribose) polymerase 1 (PARP1) associates with E3 ubiquitin-protein ligase UHRF1 and modulates UHRF1 biological functions.....	131
2.6 DNA methylation requires a DNMT1 ubiquitin interacting motif (UIM) and histone ubiquitination	151
2.7 Mutations of the DNMT1 TS domain found in HSAN-IE patients disrupt interaction with UHRF1, affect subnuclear targeting and lead to cell cycle-dependent destabilization	187

3. Discussion	221
3.1 Potential and limitations of the developed protein-protein interaction assay.....	221
3.2 Regulation and abundance of DNMT1 during the cell cycle.....	224
3.2.1 UHRF1-mediated mechanisms regulating DNMT1 chromatin targeting	224
3.2.2 Cell cycle-dependent modifications and interactions controlling DNMT1 abundance	231
3.3 Hereditary sensory and autonomic neuropathy type I with mutations in <i>DNMT1</i>	235
3.3.1 The TS domain as hotspot for HSAN-IE and ADAC-DN associated mutations in <i>DNMT1</i> ..	235
3.3.2 Functionally relevant regions within the TS domain	237
3.3.3 Unraveling HSAN disease mechanisms	238
4. Annex	243
4.1 References	243
4.2 Abbreviations	265
4.3 List of genes and corresponding proteins associated with HSAN-I to V.	269
4.4 Contributions	271
4.5 Declaration.....	273
4.6 Acknowledgements.....	275

Summary

In mammals, DNA methylation is crucial to regulate gene expression. After establishment during embryogenesis, DNA methylation patterns are faithfully propagated by the maintenance DNA methyltransferase 1 (DNMT1) during replication. Maintenance DNA methylation is subjected to complex regulation including protein interactions, cell cycle-dependent abundance and enzyme activation. Strikingly, DNMT1 enzymatic function requires both activation and regulation by its N-terminal domain (NTD). A key regulator and essential interaction partner of DNMT1 is the multi-domain protein UHRF1 (ubiquitin-like, containing PHD and RING finger domains 1). Regulatory mechanisms as well as the interplay between different UHRF1 domains in recruiting DNMT1 to its DNA target sites remain, however, elusive.

To functionally investigate the UHRF1 domain characteristics, we developed a versatile toolbox for semiquantitative and medium throughput analysis of protein-DNA, protein-histone tail peptide and protein-protein binding *in vitro*. Using this method we showed the specificity of UHRF1 for repressive histone marks and mapped a TS domain region in the NTD of DNMT1, which mediates the interaction with UHRF1. With complementation assays, we further demonstrated that interaction of DNMT1 with UHRF1 is necessary, but not sufficient for recruitment of DNMT1 to its substrate sites. In turn, none of the UHRF1 domains is dispensable for DNMT1 regulation suggesting a complex interplay of different UHRF1 functions. With defined mutations abolishing the E3 ubiquitin ligase activity of UHRF1, we demonstrated that the RING domain is crucial for the regulation of DNMT1. By mass spectrometry analysis we identified histone H3K18 as a novel ubiquitination target of UHRF1. We further showed that H3K18 ubiquitination by the RING domain is required for DNA methylation by DNMT1 *in vivo*. Moreover, PHD-mediated binding of UHRF1 to H3R2 is a prerequisite for subsequent histone ubiquitination. With bioinformatics and mutational analyses we identified and functionally characterized a ubiquitin interacting motif (UIM) in the TS domain of DNMT1. We used functional assays to illustrate that the UIM-mediated binding to ubiquitinated H3K18 and H2AK119 is essential for DNMT1 targeting and activity *in vivo*. These findings reveal an interdependent regulatory network controlling DNA methylation based on specific reading and writing of epigenetic marks by UHRF1. Our work uncovers UIM-dependent targeting of DNMT1 as a novel regulatory principle for DNA methylation beyond classic maintenance.

The identification of the UHRF1 interacting region and the UIM in the DNMT1 TS domain propose distinct non-redundant regulatory roles. Recently, medical studies reported several DNMT1 mutations associated with the human diseases hereditary sensory and autonomic neuropathy with dementia and hearing loss (HSAN-IE) and autosomal dominant cerebellar ataxia, deafness and narcolepsy (ADAC-DN). Interestingly, all mutations are located in the TS domain, but not within the UIM. As the underlying disease mechanisms are poorly understood, we set out to investigate functional defects of two HSAN-IE associated DNMT1 mutations (P496Y and Y500C). We found that mutant DNMT1 was not only deficient in UHRF1 and heterochromatin binding, but also led to DNMT1 destabilization. Our results provide an explanation for diminished activity of mutant DNMT1 accounting for the observed global DNA hypomethylation in HSAN-IE patients.

In conclusion, this work advances our understanding of how UHRF1 and two defined regions in the DNMT1 TS domain regulate DNA methylation and also suggests a new mechanism of DNMT1 dysfunction in the pathogenesis of human neurodegenerative diseases.

Zusammenfassung

DNA-Methylierung spielt eine fundamentale Rolle für die Regulierung der Genexpression in Säugern. Nach der Etablierung von DNA-Methylierungsmustern in der Embryonalentwicklung, überträgt die DNA-Methyltransferase 1 (DNMT1) diese epigenetischen Muster getreu an nachkommende Zellgenerationen. Erhaltungs-DNA-Methylierung ist einer Vielzahl von regulatorischen Mechanismen unterworfen, wie etwa Protein-Interaktionen, zellzyklusabhängigen Abundanzen und Enzymaktivierung. Die katalytische Aktivität von DNMT1 beruht auf ihrer C-terminale Domäne, die von der N-terminalen Domäne (NTD) reguliert und aktiviert wird. Eine wichtige regulatorische Rolle wird dem Protein "ubiquitin-like, containing PHD and RING finger domains 1" (UHRF1) zugeschrieben, das mit DNMT1 interagiert und essentiell für die DNA-Methylierung ist. Es ist jedoch unbekannt, welche regulatorischen Mechanismen DNMT1 zu ihrem Substrat rekrutieren und wie verschiedene UHRF1 Proteindomänen zusammenwirken.

Um die Eigenschaften der UHRF1 Domänen funktionell zu analysieren, haben wir einen molekularen Werkzeugkasten entwickelt, der es ermöglicht die Bindung von Proteinen an DNA, Histone und andere Proteine *in vitro* zu untersuchen. Mit dieser Methode konnten wir die Bindespezifität von UHRF1 für repressive Histon-Modifikationen zeigen und eine TS Domäne Region in der NTD von DNMT1 kartieren, die mit UHRF1 interagiert. Durch Komplementationsexperimente konnten wir nachweisen, dass die Interaktion von DNMT1 mit UHRF1 essentiell, jedoch nicht ausreichend für die Rekrutierung von DNMT1 zu ihren Substratstellen ist. Keine der UHRF1 Domänen ist wiederum für die Regulierung von DNMT1 verzichtbar, was auf eine Beteiligung verschiedener UHRF1 Funktionen in der Regulierung von DNA-Methylierung hindeutet. Durch gezielte Mutationen, die die E3 Ubiquitin Ligase Aktivität von UHRF1 beeinträchtigen, konnten wir klar zeigen, dass die RING Domäne von UHRF1 sehr wichtig für die DNA-Methylierung durch DNMT1 ist. Durch Massenspektrometrie haben wir H3K18 als neue Ubiquitinierungs-Zielstelle von UHRF1 identifiziert. H3K18 Ubiquitinierung und darauffolgende DNA-Methylierung erforderte auch die Bindung der PHD an H3R2. Mit bioinformatischen- und Mutations-Analysen haben wir ein Ubiquitin interagierendes Motif (UIM) in der TS Domäne von DNMT1 identifiziert, das an H3K18 und H2AK119 ubiquitinierte Histone bindet und sehr wichtig für die Funktionalität von DNMT1 *in vivo* ist. Diese Ergebnisse lassen ein regulatorisches Netzwerk zur Kontrolle der DNA-Methylierung erkennen, das spezifisches Lesen und Schreiben von epigenetischen Modifikationen durch UHRF1 erfordert. Unsere Forschungsarbeit hat den UIM abhängigen Rekrutierungsmechanismus als neues Regulierungsprinzip aufgedeckt, der DNMT1 über klassische Erhaltungsmethylierung hinaus an ihre Zielstellen bringt.

Die Identifizierung der UHRF1 interagierenden Region und des UIM deutet auf verschiedene, nicht redundante Rollen der TS Domäne von DNMT1 hin. Kürzlich haben einige medizinische Studien Mutationen in der TS Domäne von DNMT1 beschrieben, die mit der humanen Krankheit "hereditary sensory and autonomic neuropathy with dementia and hearing loss" (HSAN-IE) und "autosomal dominant cerebellar ataxia, deafness and narcolepsy" (ADAC-DN) in Verbindung gebracht werden. Alle Mutationen wurden in der TS Domäne gefunden, jedoch außerhalb des UIM. Da die zugrundeliegenden Krankheitsmechanismen kaum verstanden sind, haben wir funktionelle Defekte von zwei HSAN-IE assoziierten Mutationen (P496Y und Y500C) untersucht. HSAN-IE Mutationen führten dazu, dass DNMT1 nicht mehr mit UHRF1 interagierte. Weiterhin waren die DNMT1-Mutanten destabilisiert und zeigten schnellere Proteinkinetiken sowie eine schwächere Assoziation mit Heterochromatin. Unsere Ergebnisse liefern eine Erklärung für die herabgesetzte Aktivität der DNMT1 Mutanten, die zu globaler DNA-Hypomethylierung in HSAN-IE Patienten führt.

Zusammenfassend beleuchtet diese Forschungsarbeit nicht nur die Regulierung von DNA-Methylierung durch UHRF1 und zwei definierte Regionen in der TS Domäne, sondern beschreibt auch Mechanismen von DNMT1 Dysfunktionen, die an der Pathogenese neurodegenerativer Krankheiten beteiligt sein könnten.

1. Introduction

1.1 Epigenetic information

Epigenetic mechanisms are of central importance for the regulation of gene expression in mammalian genomes. Although each cell of the adult body carries the same primary genetic information identical to that of the zygote, it contains multiple cell types with diverse tissue functions (Bird 2002). To allow a complex and multifunctional organism to arise from a single cell, epigenetic patterns have to be dynamically changed during early embryonic development (Wu and Zhang 2010). Epigenetic patterns rely on heritable information found in the higher order chromatin structure governed by DNA and histone modifications, histone variants and histone remodeling as well as RNA-mediated gene silencing. Imprinting, X chromosome inactivation and cell differentiation are the most famous examples for processes that are substantially regulated by epigenetic mechanisms. Misregulation of these mechanisms leads to genomic instability and promotes tumorigenesis (Choi and Lee 2013). DNA and histone modifications are the most prominent epigenetic marks and will be introduced in the next two chapters.

1.1.1 Histone post translational modifications

Nucleosomes are composed of 147 base pairs superhelical DNA wrapped 1.65 times around a histone octamer formed by dimers of the four different core histones, H2A, H2B, H3 and H4 (Woodcock and Ghosh 2010). H1 is called linker histone and is localized near the DNA entry-exit sites of the core particle thereby stabilizing the nucleosome (Thoma et al. 1979). Histones possess a globular structure, but their N-terminal part protrudes from the core as a so called histone tail. Whereas post translational modifications (PTMs) on the histone core domains usually have a direct effect on the histone structure or on the interaction with surrounding DNA and neighboring nucleosomes, PTMs on the flexible histone tails have an indirect effect on chromatin compaction. Histone tail PTMs recruit specific reader modules that initiate further downstream pathways (Mersfelder and Parthun 2006; Kouzarides 2007). Euchromatic histone PTMs are usually found in less compacted active chromatin, while heterochromatic or also called repressive marks are enriched in densely compacted silent chromatin (Figure 1.1). Depending on the context and combination of histone PTMs, the functional output leading to activation or repression of the underlying gene can differ. Thus, histone PTMs are more complex than previously thought arguing against the original idea of a 'histone code'. Similar to the genetic code, the 'histone code' was proposed to have a definite and invariable outcome that only relies on the mark itself and on specific readers (Strahl and Allis 2000; Jenuwein and Allis 2001). Currently, histone PTMs tend to be summarized under the term 'chromatin signaling', which includes both, the DNA and histone context into the interpretation and underlines the dynamic interplay of different PTMs leading to the functional outcome (Sims and Reinberg 2008; Lee et al. 2010; Henikoff and Shilatifard 2011).

In general, histones are modified by so called writers that establish acetylation (ac), phosphorylation (ph), ubiquitination (ub), sumoylation (su), ADP ribosylation (ar), deimination, proline isomerization as well

as different degrees of methylation (me) (Kouzarides 2007). The most prevalent PTMs are set by three different groups of writers including histone acetyltransferases (HATs), kinases and histone methyltransferases (HMTs). Histones carrying certain PTMs are recognized by reader modules comprising specialized pockets to screen and bind their target (Kouzarides 2007; Taverna et al. 2007). In general, chromo-like domains of the Royal family and nonrelated PHD domains bind methylated histones, bromodomains recognize acetylated histones and a domain within 14-3-3 proteins recognizes phosphorylated histones. By reading the histone PTM, either the binding effector itself or associated complexes induce downstream functional pathways. Histone PTMs are not absolutely stable, but they can be removed by the action of erasers like histone deacetylases (HDACs), deubiquitinases and demethylases (Kouzarides 2007). In the following section, important histone PTMs together with their respective writers and biological functions are exemplified.

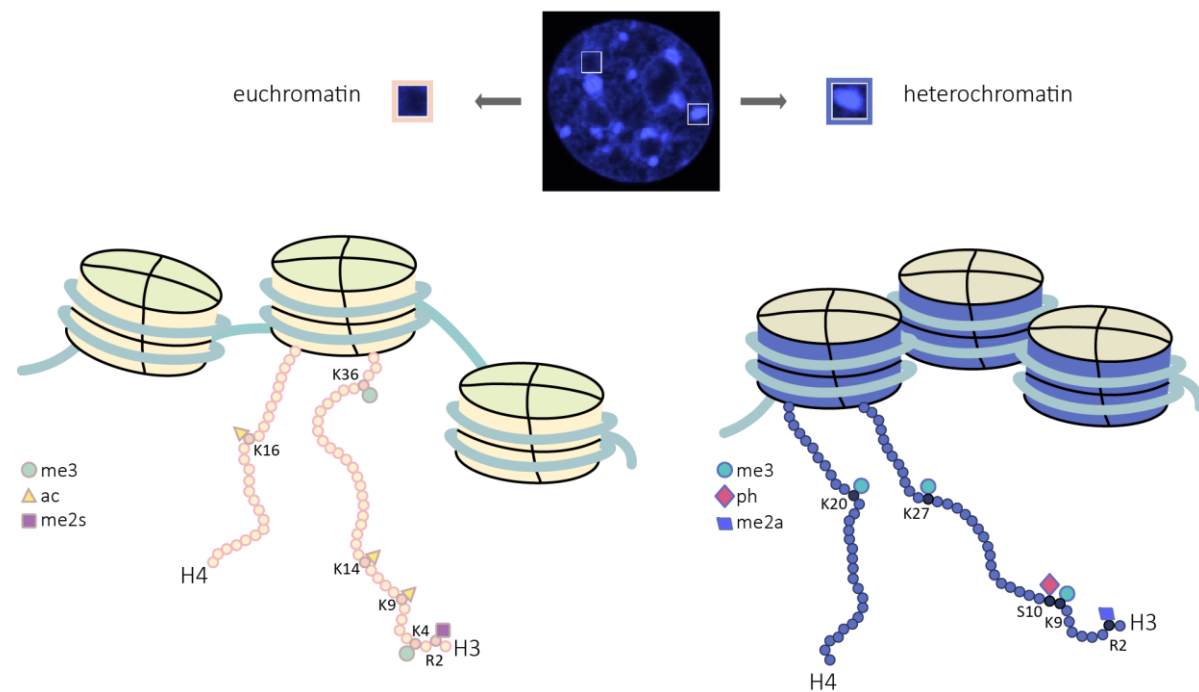


Figure 1.1: Histone post translational modifications in hetero- and euchromatic regions. In the upper panel DNA counterstaining of a mouse somatic nucleus is shown with intense DAPI signals in AT-rich heterochromatin. The illustrations in the lower panel exemplify characteristic eu- and heterochromatic histone post translational modifications (PTMs).

Euchromatic histone PTMs

Generally, euchromatin covers gene-rich chromatin regions that are located in the R-bands of mitotic Giemsa-stained chromosomes (Gilbert et al. 2004). Methylated histone N-terminal tails like H3R2me2s, H3K4me1, H3K4me3 and H3K36me3 as well as acetylated tails like H3K9ac, H3K14ac and H4K16ac are examples of activating histone PTMs that are prevalent in chromatin regions permissive to transcription.

One of the best characterized euchromatic histone PTMs is the methylation of lysine 4 on histone H3. Whereas H3K4me1 is enriched in active and poised enhancers, H3K4me3 is found in active and poised

promoters (Bernstein et al. 2005; Kouzarides 2007; Li et al. 2007a; Hon et al. 2009). H3K4me3 enables active transcription firstly by facilitating transcription initiation and secondly by inhibiting the writing of heterochromatic marks like H3K9me3. H3K4me3 is selectively bound by the PHD finger of the TATA box binding protein-associated factor TAF3, a subunit of the transcription factor TFIID that contributes to the initiation of transcription (Vermeulen et al. 2007).

To date, several writers for methylated H3K4 have been described: the lysine HMTs mixed lineage leukemia MLL1, MLL3 and MLL4 (Dou et al. 2005; Cho et al. 2007), SET domain containing 1A and 1B complex (SETD1A and SETD1B) (Lee and Skalnik 2005; Lee et al. 2007), histone lysine N-methyltransferase SET7 (Wang et al. 2001; Xiao et al. 2003) as well as SET and MYND domain-containing protein 2 (SMYD2) (Abu-Farha et al. 2008). The presence of H3K4 methylation closely correlates with H4K16 acetylation on active genes as MLL1, one of the writers of H3K4me, forms a stable complex with the H4K16-specific HAT MOF (Dou et al. 2005). Similarly, H3K4 methylation has a stimulating effect on subsequent histone H3 and H4 acetylation by p300 that is generally found in euchromatic regions (Wang et al. 2001). Furthermore, symmetrically dimethylated arginine 2 on H3 (H3R2me2s) is prevalent in active chromatin regions in combination with H3K4me3 (Guccione et al. 2007; Yuan et al. 2012).

Methylation of H3K9, a typical heterochromatic mark, prevents methylation of K4 by SET7 and vice versa (Wang et al. 2001; Binda et al. 2010). This indicates that these two histone PTMs linked to opposite states of chromatin compaction are mutually exclusive. Likewise, the H3K4 methylation activity of absent, small and homeotic discs 1-like protein (ASH1L), a subunit of the MLL complex, is also inhibited by preexisting K9 methylation (Gregory et al. 2007). Moreover, asymmetric dimethylation of arginine 2 on H3 (H3R2me2a), a mark enriched in silenced chromatin, hinders methylation of H3K4 (Guccione et al. 2007). Another crosstalk is observed between H3T3ph and H3K4me3. Phosphorylation of the neighboring position on the histone tail negatively regulates methylation of H3K4 (Southall et al. 2009).

Hyperacetylation of the N-terminal tails of all four core histones is a common feature of transcriptionally active regions in eukaryotic genomes (Vaquero et al. 2003). Genome-wide, the patterns of H3K4me3 overlap to a large extent with those of H3K9ac and H3K14ac (Gregory et al. 2007; Heintzman et al. 2007). Acetylation on H3K9 is established by the HAT elongator complex protein 3 (ELP3) and general control nonderepressible 5 (GCN5) as well as by the p300/CBP-associated factor (PCAF) (Kim et al. 2002; Jin et al. 2011). H3K9ac is prevalent at transcriptional start sites (TSSs) of active genes (Wang et al. 2008). H3K14 is preferentially acetylated by GCN5 in context of an H3 tail carrying the S10ph mark (Lo et al. 2000).

Interestingly, a direct impact of H4K16ac on chromatin compaction has been reported. The addition of an acetyl-group by CREB binding protein (CBP)/p300, GCN5 (Sterner and Berger 2000) or MOF neutralizes the basic charge of the lysine and prevents formation of compact 30-nm-like fibers *in vitro* (Shogren-Knaak et al. 2006). Consistently, H4K16ac is enriched in actively transcribed euchromatin and the HATs responsible for setting this mark also function as transcriptional coactivators (Carrozza et al. 2003; Vaquero et al. 2007).

Trimethylation of lysine 36 on H3 is enriched in transcribed regions of active genes (Hon et al. 2009). Mono- and dimethylation is established by different HMTs like nuclear receptor SET domain-containing protein 1, 2 and 3 (NSD1, NSD2 and NSD3), ASH1L, SET domain and mariner transposase fusion gene-containing protein (SETMAR), SMYD2 as well as SET domain-containing protein 3 (SETD3). Thereafter,

SETD2 introduces the trimethylated state of H3K36 (Wagner and Carpenter 2012). In a process conserved from yeast to human, SETD2 associates with the hyperphosphorylated form of RNA-Polymerase II thereby coupling H3K36 trimethylation to transcriptional elongation (Kizer et al. 2005).

Different degrees of H3K9 methylation can be associated with opposed chromatin states. Whereas mono- and dimethylated H3K9 is often found in silent euchromatic regions, the trimethylated counterpart is clearly enriched in silent heterochromatic regions.

Heterochromatic histone PTMs

In general, gene-poor heterochromatic regions found in the G- and C-bands of mitotic chromosomes defined by Giemsa staining are marked by low levels of histone acetylation, but high levels of histone methylation, especially on H3K9, H3K27 and H4K20 (Vaquero et al. 2003; Kouzarides 2007).

H3K9me3 is probably the best studied histone modification that contributes to heterochromatin formation. However, H3K9me3 might also have a function in euchromatic regions as it was recently unexpectedly found in actively transcribed genes like *STAT1* and *STAT3*. (Squazzo et al. 2006; Barski et al. 2007). Depending on the chromatin context, the methylation can be established by different writers that all share a conserved catalytically active SET domain.

The HMT SET domain, bifurcated 1 (SETDB1) targets unmodified H3K9 in euchromatic regions whereas the dimethylated or acetylated form and phosphorylation of the neighboring serine abolish the methylation activity *in vitro* (Schultz et al. 2002). SETDB1 alone is sufficient to achieve dimethylated H3K9, but the cofactor mAM, a murine ATFa-associated factor, is needed for the formation of the trimethylated form (Wang et al. 2003). *In vitro*, methylation of H3 tails by SETDB1 recruits the heterochromatin binding protein 1 (HP1) that contributes to the formation of densely packed chromatin (Schultz et al. 2002). The HMT G9a can also initiate the mono- and dimethylated form of H3K9 (Peters et al. 2003) and in addition methylates H3K27. Interestingly, G9a does not localize to heterochromatin supporting its role in silencing of euchromatic genes during early development (Tachibana et al. 2001; Tachibana et al. 2002).

Other H3K9-specific HMTs, suppressor of variegation 3-9 homolog 1 and 2 (SUV39H1 and SUV39H2) prefer the un- and monomethylated form of H3K9 as an initial substrate establish mainly the trimethylated state (Rea et al. 2000; Peters et al. 2003). One of the known SUV39H1/2 targets are the major satellite repeats located in the pericentromeric heterochromatin (PH) (Lehnertz et al. 2003; Peters et al. 2003). Notably, a feedback loop ensures establishment of stably compacted chromatin regions. HP1 specifically reads trimethylated H3K9 by binding of its chromodomain. Hereafter, HP1 recruits SUV39H1/2, which propagate the heterochromatic mark to neighboring nucleosomes thereby providing new binding sites for HP1 (Bannister et al. 2001; Lachner et al. 2001; Jacobs and Khorasanizadeh 2002; Nielsen et al. 2002). In contrast to the methylation activity of SETDB1 and G9a, which are not influenced by methylation of H3K4, the activity of SUV39H1 on histone tails carrying this euchromatic mark is severely inhibited *in vitro* (Nishioka et al. 2002a; Schultz et al. 2002).

Generally, di- and trimethylated H3K9 negatively correlates with methylated H3K4 (Wang et al. 2001). Moreover, trimethylation of H3K9 and the adjacent phosphorylation of S10 are interdependent. Pre-existing H3S10ph prevents methylation of K9 by SUV39H1 and dimethylation of H3K9 in turn reduces the activity of the Ipl1/aurora kinase (Yeast homolog to human Aurora B kinase) to phosphorylate H3S10 *in vitro* (Hsu et al. 2000; Rea et al. 2000). Consistently, double knockout *Suv39H1/2* mouse embryonic

fibroblasts display an elevated H3S10ph level (Rea et al. 2000). While the different writers of methylated H3K9 were long thought to act independently, a recent study describes the existence of a macromolecular complex including SETDB1, G9a and SUV39H1/2 (Fritsch et al. 2010).

Besides trimethylated H3K9, also trimethylated H3K27 is abundant in PH. Monomethylation of H3K27 is mainly set by the action of the histone-lysine N-methyltransferase enhancer of zeste homolog 2 (EZH2), a component of the Polycomb group repressor complex 2 (PRC2) that is involved in maintaining the silenced state of homeotic genes and the inactive X chromosome (Cao et al. 2002; Wutz 2011). In mammals, H3K27me3 is enriched in facultative heterochromatin of the female inactive X chromosome where it contributes to maintenance of the silent state essential for dosage compensation (Plath et al. 2003; Silva et al. 2003). Usually, di- and trimethylated forms of H3K27 catalyzed by EZH1 and EZH2 are prevalent at silent promoters. However, elevated levels of H3K27me1 were also found at active promoters of human genes (Barski et al. 2007).

A further lysine methylation site that is connected to transcriptional repression is trimethylation of lysine 20 on H4 (Kouzarides 2007). Monomethylation is preferentially written by the histone-lysine N-methyltransferase PR-SET7 (Xiao et al. 2005), whereas suppressor of variegation 4-20 homolog 1 and 2 (SUV4-20H1 and SUV4-20H2) enzymes prefer H4K20me1 as a substrate and establish the di- and potentially trimethylated state (Schotta et al. 2004; Yang et al. 2008). It has been proposed, that a sequential induction of trimethylated H3K9 and H4K20 takes place in PH. According to the model, HP1 binding to H3K9me3 leads to subsequent recruitment of SUV4-20H1/H2 (Schotta et al. 2004). However, there is growing evidence for SUV4-20H1/2 being solely dimethylases for H4K20 and that yet unknown proteins might be responsible for trimethylation (Wu et al. 2013; Southall et al. 2014). Interestingly, euchromatic acetylation of H4K16 and methylation of H4K20me have been described as antagonistic marks. By inhibiting the acetylation on K16, methylated H4K20 might ensure the silent state of underlying chromatin region (Nishioka et al. 2002b). Besides its implication in transcriptional regulation, methylation of H4K20 has been linked to DNA repair. Upon induction of double strand breaks, the DNA damage checkpoint component, p53 binding protein 1 (53BP1), is specifically recruited to H4K20me2 (Botuyan et al. 2006; Greeson et al. 2008). Moreover, H4K20 methylation is involved in DNA replication as H4K20me2 and me3 help to recruit the Orc complex to origins of replication (Jorgensen et al. 2013).

Cell cycle-dependent histone PTMs

A well studied example for a cell cycle-dependent and dynamic histone PTMs is the above mentioned phosphorylation of H3 on serine 10. Arising during late G2 phase in PH, H3S10ph is subsequently enriched along the chromosome during mitosis (Hendzel et al. 1997). It coordinates chromosome condensation and segregation (Wei et al. 1999). Notably, H3S10ph in G2 phase results in dissociation of HP1 proteins from heterochromatin (Fischle et al. 2005). It has been shown, that phosphorylation on S10 precludes the methylation of K9 by G9a, SETDB1 and SUV39H1/2 (Rea et al. 2000; Schultz et al. 2002; Duan et al. 2008).

Also H4K20me1 is accumulated on chromatin in dependence on the cell cycle stage (Rice et al. 2002). Whereas the level of this modification is very low in early S phase, it increases during S and G2 phase and reaches a peak in mitosis. The H4K20me1 levels directly correlate with the abundance of its writer, PR-SET7, showing the highest expression in G2 and M phase of the cell cycle (Jorgensen et al. 2013).

1.1.2 DNA modifications

DNA modifications have been first described in 1904 by Wheeler and Johnson who chemically synthesized 5-methylcytosine (5mC). A quantitative method to separate purines, pyrimidines and nucleosides from hydrolyzed DNA samples by paper chromatographie was established in 1948 (Hotchkiss 1948). By applying the method to a thymus DNA hydrolysate, Hotchkiss could separate the four bases adenine, guanine, thymidine and cytosine but also a 'fifth base' which migrated nearby cytosine and which he called 'Epi-cytosine', later named 5mC. Upon the discovery of ten-eleven translocation proteins (TETs) in 2009, the 'sixth base' and two additional DNA modifications were subsequently characterized, namely 5-hydroxymethylcytosine (5hmC), 5-formylcytosine (5fC) and 5-carboxycytosine (5caC) (Figure 1.2) (He et al. 2011; Ito et al. 2011; Pfaffeneder et al. 2011). Whereas 5mC is the most abundant modification in somatic cells covering 60-80% of all CpG dinucleotides in the adult human genome (Ehrlich et al. 1982; Smith and Meissner 2013), 5hmC is sparsely distributed (1-5% of 5mC) and is predominantly found in adult neurons (Kriaucionis and Heintz 2009; Globisch et al. 2010). The other two oxidized forms of cytosine are even less abundant covering 0.06 to 0.6% (5fC) or 0.01% (5caC) of all 5mC sites in mouse embryonic stem cells (ESCs) (Ito et al. 2011; Pfaffeneder et al. 2011).

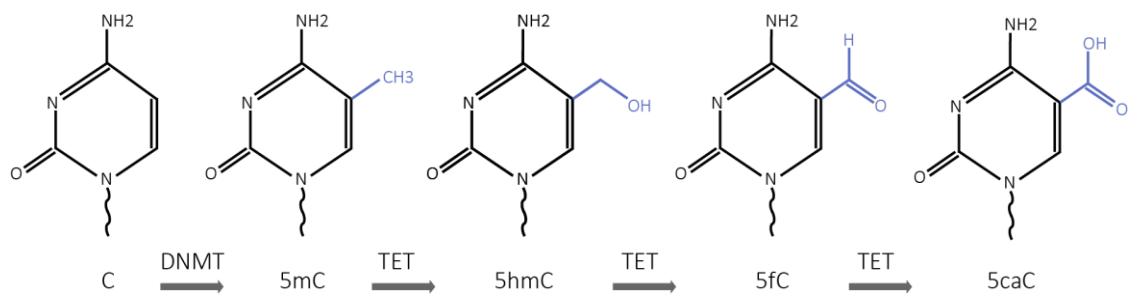


Figure 1.2: DNA modifications on cytosine in mammalian cells. Unmodified cytosine in a CpG context is methylated (5-methylcytosine (5mC)) by DNA methyltransferases (DNMTs) and can be further oxidized to 5-hydroxymethylcytosine (5hmC), 5-formylcytosine (5fC) and 5-carboxycytosine (5caC) by the ten-eleven translocation proteins (TETs).

In mammals, DNA methylation in promoter regions leads to transcriptional repression either directly by preventing transcription factor binding or indirectly by compacting of the chromatin structure. Whereas DNA methylation is mainly present in a CpG context in mammalian genomes, the modification is found in a CpT context in the insect *Drosophila melanogaster* (Bird 2002) and in a CpA, CpT and CpC context in plants (Law and Jacobsen 2010). Notably, in ESCs very low levels of CpA methylation were found, probably established by the DNA methyltransferase 3A (DNMT3A) being, however, no longer detectable in adult cells (Ramsahoye et al. 2000). Non CpG methylation is also prevalent in oocytes and mature neurons (Lister et al. 2009; Xie et al. 2012b; Lister et al. 2013; Shirane et al. 2013).

In vertebrates, CpG islands, which are regions with a high occurrence of CpG dinucleotides, are highly correlated with promoter regions as well as TSSs and are usually devoid of methylation (Bird et al. 1987). The transcriptionally permissive chromatin state of CpG islands makes them a common feature of housekeeping and many developmentally regulated genes (Deaton and Bird 2011). Several studies show that the methylation free state of CpG islands is dependent on transcription factor binding motifs and transcription factor recruitment (Brandeis et al. 1994; Macleod et al. 1994), but also on the euchromatic

histone mark H3K4me set by SETD1A (see 1.1.1) (Smith and Meissner 2013). Hypermethylation of CpG islands is linked to tumorigenesis and aberrant gene expression (Sproul and Meehan 2013).

Given that DNA methylation occurs as the second step in gene repression after histone PTMs on already silenced loci, it finalizes the epigenetic status of silent chromatin (Bird 2002). DNA methylation plays an important role, for instance in stabilizing the repressive status of transposable elements like the intracisternal A particle (IAP) elements (Walsh et al. 1998; Gaudet et al. 2004). Although DNA methylation is thought to be a relatively stable epigenetic mark in adult tissues, where the patterns only change as a consequence of specific cellular processes and needs, it is dynamically changed during early embryonic development (see 1.2.4) (Deaton and Bird 2011).

1.2. Establishment and maintenance of DNA methylation

Establishment, regulation and maintenance of DNA methylation is crucial for normal mammalian development. DNA methylation is catalyzed by the family of DNA methyltransferases (DNMTs) sharing several common features but diverging in their role and regulation.

Function of mammalian DNA methyltransferases

During early embryonic development the methyltransferases DNMT3A and DNMT3B set DNA methylation marks *de novo* on unmodified DNA. The maintenance methyltransferase DNMT1, by contrast, faithfully propagates the established DNA methylation patterns to successional cell generations after replication. According to their function, DNMT3A and DNMT3B are highly expressed during early development (Bird 2002).

The DNA methyltransferase 3 like protein (DNMT3L) does not comprise an intrinsic methyltransferase activity. Yet, it interacts with the *de novo* methyltransferases DNMT3A and DNMT3B and stimulates their activity during early development (Hata et al. 2002; Margot et al. 2003; Suetake et al. 2004). Upon differentiation, DNMT3L expression is downregulated (Hu et al. 2008). In the precursors of spermatogonial stem cells, DNMT3L is essential for the methylation of retrotransposons (Bourc'his and Bestor 2004). During gametogenesis, DNMT3L is crucial for the establishment of maternal imprints and *Dnmt3L* knockout results in midgestation lethality (Bourc'his et al. 2001).

DNMT2 is not required for DNA methylation in a CpG context in mammalian cells (Okano et al. 1998b). Instead it methylates the tRNA^{Asp} in a methyltransferase-like catalytic mechanism (Goll et al. 2006; Jurkowski et al. 2008). Moreover, DNMT2 was described to be responsible for DNA methylation in a CpA and CpT context in *Drosophila* embryos (Kunert et al. 2003). After *dnmt2* knockdown, differentiation defects were observed in zebrafish (Rai et al. 2007), whereas mouse ESCs lacking DNMT2 did not display any changes in global DNA methylation levels (Okano et al. 1998b).

Structure of mammalian DNA methyltransferases

All members of the DNMT family share a common C-terminal catalytic domain (CTD) harboring highly conserved sequence motifs (I-X) also found in the prokaryotic DNMTs (Figure 1.3) (Goll and Bestor 2005). Only in DNMT3L crucial catalytic motifs in the CTD are lacking, providing an explanation for its enzymatic inactivity (Hata et al. 2002). Except for DNMT2 that only comprises a CTD, all other DNMTs carry an additional N-terminal domain (NTD). In the *de novo* methyltransferases, this region is composed of a PWPP domain containing a highly conserved proline-tryptophan-tryptophan-proline motif. The PWPP domain is required for methylation of PH and mediates the targeting of the enzymes to chromatin in mitotic cells (Chen et al. 2004; Ge et al. 2004). Consistently, the PWPP domain of DNMT3A has been shown to bind H3K36me3, a histone mark prevalent in heterochromatic regions correlating with DNA methylation (Dhayalan et al. 2010). The plant homeodomain (PHD, also known as ATRX–DNMT3–DNMT3L (ADD) domain) in the NTD of DNMT3A and DNMT3L has been described as a reader module for unmodified H3K4. However, the binding to H3 tails is blocked by H3K4me3, a known euchromatic mark

(Ooi et al. 2007; Otani et al. 2009). The NTD of DNMT1 is composed of distinct domains important for protein-protein interactions and regulation of enzymatic activity (see 1.2.2).

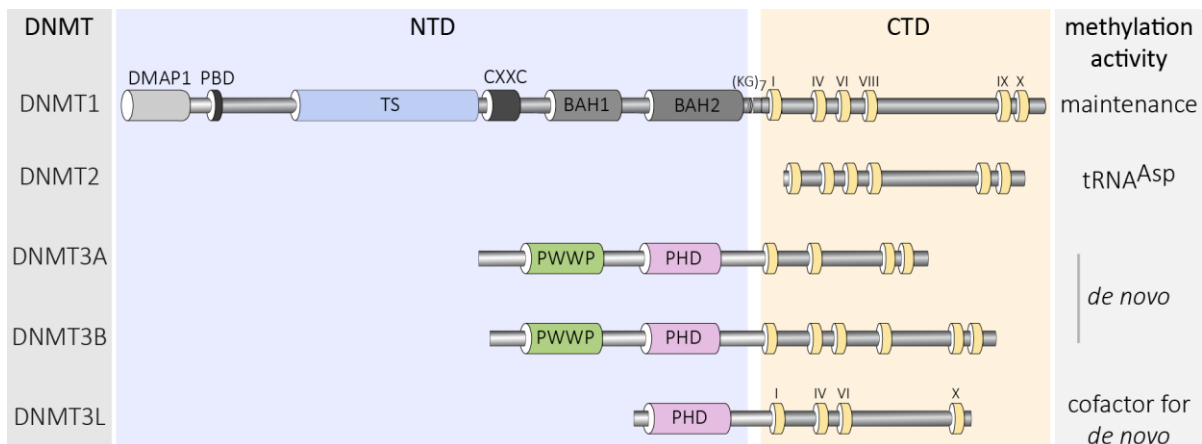


Figure 1.3: Domain structure and function of mammalian DNA methyltransferases. All members of the DNA methyltransferase (DNMT) family share a conserved C-terminal catalytic domain (CTD), whereas the N-terminal domain (NTD) differs in length and domain composition. The NTD of the maintenance methyltransferase DNMT1 harbors a DNA methyltransferase associated protein 1 (DMAP1) binding domain, a proliferating cell nuclear antigen (PCNA) binding domain (PBD), a targeting sequence (TS) domain, a zinc finger (CXXC) domain and two bromo-adjacent homology (BAH1 and BAH2) domains. The NTD of DNMT3A and DNMT3B comprises a proline-tryptophan-tryptophan-proline motif containing PWWP domain and a plant homeodomain (PHD) that is also found in DNMT3L. Modified from (Rottach et al. 2009).

1.2.1 Establishment of DNA methylation

DNA methylation patterns are established *de novo* during the blastocyst state by DNMT3A and DNMT3B (Okano et al. 1998a; Okano et al. 1999). As DNMT3B-deficient mice are embryonic lethal and DNMT3A-deficient mice die four weeks after birth, a pivotal role in development is attributed to the establishment of DNA methylation-mediated gene silencing (Okano et al., 1999; Li et al., 1992).

De novo DNA methylation might be the second step in the process of gene silencing. Retroviral transcription in ESCs is repressed before *de novo* methylation occurs (Gautsch and Wilson 1983; Niwa et al. 1983) arguing for a histone PTM-mediated gene silencing in this state. This idea is further supported by the methylation free character of CpG islands regardless of the gene expression status. Even if the corresponding gene of a CpG islands containing promoter is silent, for instance due to a tissue-restricted expression pattern of the human α -globin, the CpG island can remain unmethylated (Bird et al. 1987). Accordingly, short-term epigenetic memory is distinguishable from long-term memory depending on the stability of the epigenetic status. Short term epigenetic repression is often achieved by repressive histone PTMs like H3K27me3, which can be easily removed during subsequent cell generations (Wu and Zhang 2010). In contrast, the silent state of the inactive X chromosome in mammalian cells or of imprinted genes has to be stably propagated to the progeny (Wu and Zhang 2010). This so called constitutive heterochromatic state is further stabilized by DNA methylation in addition to repressive histone marks. When compared to histone PTMs, DNA methylation might be more stable, but it is not static as active DNA demethylation can reverse the repressive state (see 1.2.4).

One potential trigger ensuring *de novo* methylation at specific regions are repetitive sequences (Yates et al. 1999). In addition, *in vitro* studies showed that the PHD of DNMT3A recognizes unmodified H3K4 and that the enzymatic activity is blocked by heterochromatin, indicating that the chromatin structure has to be loosened up before the methylation reaction occurs (Hata et al. 2002; Takeshima et al. 2008; Otani et al. 2009).

Stable *oct4* promoter silencing

Stable silencing of promoters is controlled by coordinated establishment of repressive epigenetic marks on histone tails and DNA (Tsumura et al. 2006; Smith and Meissner 2013). This process takes place during differentiation, when pluripotency associated promoters, for instance promoters of *octamer binding transcription factor 4* (*oct4*), *nanog* and *sox2* as well as of germline-specific genes need to be stably silenced (Smith and Meissner 2013). OCT4 is an important regulator of stem cell renewal as well as pluripotency. The inactivation mechanism of its promoter during differentiation has been intensely studied (Figure 1.4). Initially, the repressor germ cell nuclear receptor (GCNF) binds to the RA receptor element (RARE) on the *oct4* promoter thereby transiently preventing transcription (Feldman et al. 2006). Next, the HMT G9a binds to the promoter region and recruits HDACs that remove the acetylation from H3K9 and K14 and pave the way for subsequent histone methylation (Hattori et al. 2004; Kimura et al. 2004; Feldman et al. 2006). After H3K9me3 is established by G9a and other HMTs like SUV39H1/2, HP1 binds to the histone tails and propagates the methylation to neighboring nucleosomes (Feldman et al. 2006). Moreover, G9a, SUV39H1/2 and HP1 recruit DNMT3A and DNMT3B leading to stable and irreversible local heterochromatinization by DNA methylation (Fuks et al. 2003). Notably, DNMT3A and DNMT3B have been shown to interact directly with each other leading to a mutual catalytic stimulation (Li et al. 2007b). This example clearly indicates that the interplay between the two major epigenetic modifications ensures stable gene silencing.

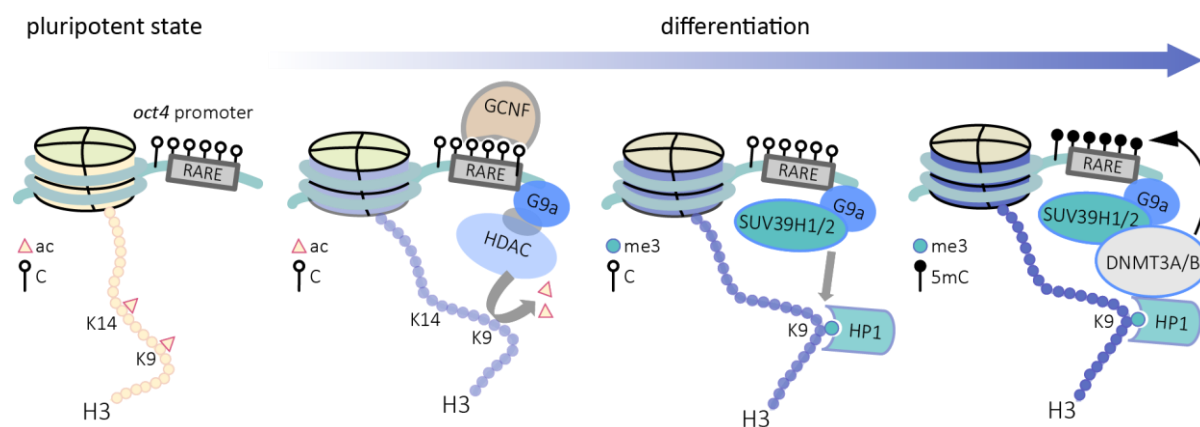


Figure 1.4: Stepwise silencing of the *oct4* promoter. Upon initiation of differentiation, the *octamer binding transcription factor 4* (*oct4*) promoter is transiently silenced by binding of the repressor germ cell nuclear receptor (GCNF) to the RA receptor element (RARE). Furthermore, G9a binds to the promoter and recruits histone deacetylases (HDACs) specific for deacetylation of H3K9 and H3K14. Together with suppressor of variegation 3-9 homolog 1 and 2 (SUV39H1/2), G9a methylates H3K9 that is subsequently bound by the heterochromatin binding protein (HP1). Stable and irreversible silencing is achieved by DNA methylation in the *oct4* promoter region mediated by the *de novo* methyltransferases 3A and B (DNMT3A/B) that are recruited by G9a, SUV39H1/2 and HP1. Inspired by (Feldman et al. 2006).

Further roles of DNMT3A and DNMT3B in DNA methylation-mediated gene silencing

In the postimplantation embryo, further epigenetic changes occur in primordial germ cells (PGCs). After erasure of parental DNA methylation imprints by DNA demethylation (see 1.2.4) (Yamaguchi et al. 2013), individual imprinted patterns and methylation at retrotransposons are re-established during gametogenesis by DNMT3A and DNMT3L (Bestor 2000; Hata et al. 2002; Bourc'his and Bestor 2004; Kaneda et al. 2004). Imprinting guarantees the expression of genes from only one chromosome, the maternal or the paternal, and is crucial for normal development and the prevention of parthenogenesis and tumor formation (Reik and Walter 2001). Furthermore, DNMT3B is required for silencing regions of the (peri)centromeric chromatin like minor satellite repeats and the inactive X chromosome (Minou et al. 1994; Okano et al. 1999; Xu et al. 1999; Hansen et al. 2000; Kondo et al. 2000). Besides acting as *de novo* methyltransferases, DNMT3A and DNMT3B contribute to the maintenance of the silent states of repetitive elements like long interspersed nuclear elements (LINEs) and minor satellites in pluripotent stem cells (Smith and Meissner 2013).

Additionally to direct blocking of transcription factor binding, DNA methylation-mediated transcriptional repression mainly relies on specific recruitment of 5mC binding proteins (MBPs) to methylated DNA. Three families of MBPs have been described: the methyl-CpG binding domain (MBD) family, the SRA family (also known as UHRF family, see 1.2.3) and the Kaiso protein family (Rottach et al. 2009; Buck-Koehntop and Defossez 2013). MBD1, MBD2, MBD3, MBD4, MBD5 and MBD6 as well as MeCP2 are members of the MBD family and except for MBD3, MBD5 and MBD6 have a preference for binding 5mC (Klose and Bird 2006; Buck-Koehntop and Defossez 2013). Interestingly, Kaiso, a well studied member of the Kaiso family, binds not only to two consecutive methylated CpG sites (Prokhorchuk et al. 2001; Prokhortchouk et al. 2001), but also to unmethylated DNA carrying TCCTGCNA as a recognition motif (Daniel et al. 2002; Buck-Koehntop et al. 2012). In general, MBPs translate DNA methylation into functional chromatin states by recruitment of HDACs, HMTs and histone remodeling complexes leading to chromatin compaction and transcriptional inactivation (Clouaire and Stancheva 2008).

1.2.2 Maintenance of DNA methylation patterns by DNMT1

Once the cell type-specific methylation pattern is established during differentiation mediated by the *de novo* methyltransferases DNMT3A and DNMT3B, it needs to be faithfully transmitted throughout all cell divisions by the maintenance methyltransferase DNMT1. Consistent with its important role during somatic DNA replication, DNMT1 is constitutively expressed in dividing cells with a peak in S phase of the cell cycle (Kishikawa et al. 2003). The fundamental importance of maintenance DNA methylation is underlined by the fact that disruption of the *Dnmt1* gene leads to embryonic lethality. Mouse embryos deficient for DNMT1 are characterized by severe developmental defects and pronounced cell death in brain and heart tissues, resulting in mortality prior to embryonic day 11. Albeit DNMT1-deficient ESCs show global DNA hypomethylation, cell morphology, viability and proliferation remain unaffected (Li et al. 1992).

Mechanism of methyl group transfer by DNMT1

The multi-step mechanism of methyl group transfer has been intensely studied and was proposed to be conserved from human to prokaryotic type II DNA cytosine methyltransferases (M.HhaI) (Figure 1.5) (Wu and Santi 1987; Bestor and Verdine 1994). In the first step, after binding and base flipping, DNMT1 forms a covalent complex with the C6 position of the target cytosine. In the second step, the methyl group is transferred from S-Adenosyl-L-Methionine (SAM) to the C5 position of the cytosine. Finally, the enzyme is released by β -elimination in the third step (Flynn et al. 1998; Pradhan et al. 1999).

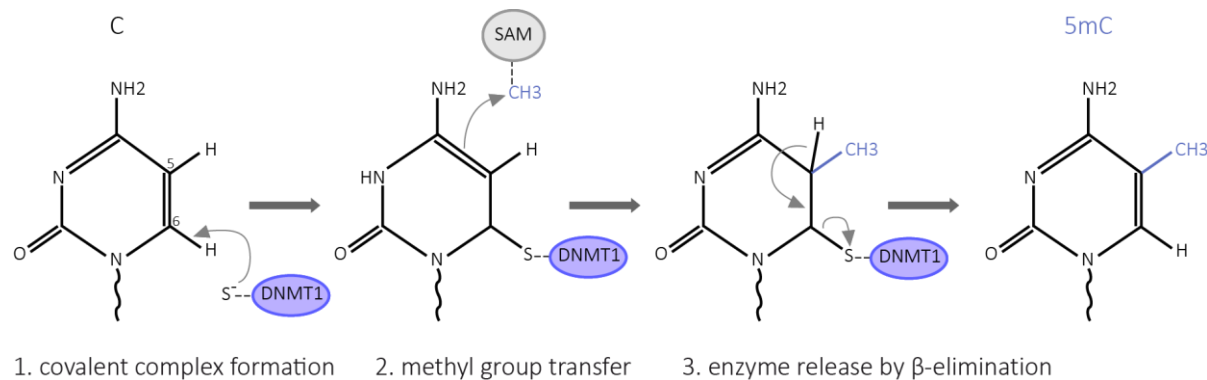


Figure 1.5: Mechanism of methyl group transfer by DNMT1. After the formation of a covalent complex of DNMT1 with the C6 position of the target cytosine, the methyl group is transferred from the donor S-Adenosyl-L-Methionine (SAM) to the C5 position of the cytosine. In the last step, DNMT1 is released by β -elimination.

Structure and regulation of DNMT1

A prerequisite for understanding the functionality and complex regulation of DNMT1 is the knowledge of its domains and its structure. Key features of different DNMT1 domains are summarized in Figure 1.6. DNMT1 is comprised of a CTD and a large regulatory NTD. The CTD is responsible for substrate binding and methyl group transfer, but it needs to be regulated by the NTD to allow for enzymatic activity of DNMT1 (Fatemi et al. 2001; Easwaran et al. 2004). The NTD of DNMT1 harbors distinct domains which mediate different regulatory processes such as protein-protein interaction, substrate specificity and cell cycle-dependent localization.

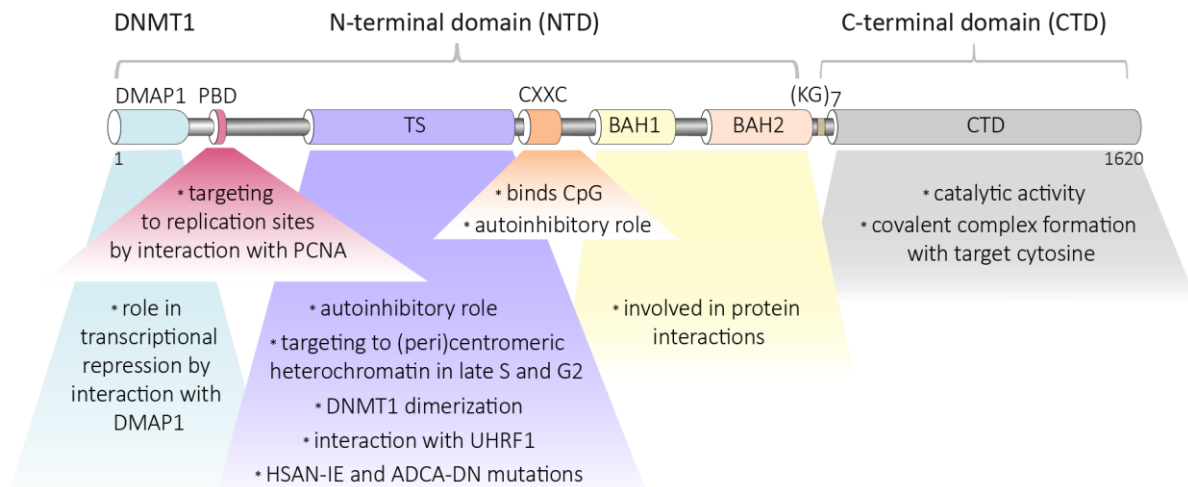


Figure 1.6: Domain structure and key features of DNMT1. DNMT1 (amino acid 1-1620) contains a catalytically active C-terminal domain (CTD) that is regulated by the large N-terminal domain (NTD) further subdivided into a DNA methyltransferase associated protein 1 (DMAP1) binding domain, a PCNA (proliferating cell nuclear antigen) binding domain (PBD), a targeting sequence (TS) domain, a zinc finger (CXXC) domain and two bromo-adjacent homology (BAH1 and BAH2) domains. Key features of the different domains are summarized. HSAN-IE: hereditary sensory and autonomic neuropathy with dementia and hearing loss; ADCA-DN: autosomal dominant cerebellar ataxia, deafness and narcolepsy.

The very N-terminal DNA methyltransferase associated protein 1 (DMAP1) domain mediates the interaction of DNMT1 with the transcriptional repressor DMAP1 (Rountree et al. 2000). DNMT1 has further been linked to the establishment of repressive histone marks. In late S phase, DNMT1 co-localizes and interacts with HDAC1 and HDAC2 thereby coupling histone deacetylation activity to DNA methylation at replicating heterochromatin (Fuks et al. 2000; Rountree et al. 2000).

The proliferating cell nuclear antigen (PCNA) binding domain (PBD) plays a fundamental role in cell cycle-dependent localization of the methyltransferase especially in early and mid S phase (Schermelleh et al. 2007; Schneider et al. 2013). By interaction with PCNA that forms a homotrimeric ring around the DNA at replication forks (Maga and Hubscher 2003), DNMT1 is targeted to sites of active DNA synthesis (Leonhardt et al. 1992; Chuang et al. 1997). Moreover, DNMT1 is also recruited to DNA damage sites through its interaction with PCNA (Mortusewicz et al. 2005).

In late S phase, the association with densely methylated heterochromatin might be regulated by combined action of the PBD and the large targeting sequence (TS) domain (Schneider et al. 2013). Remarkably, in G2 phase when DNA synthesis is already completed, DNMT1 still associates with chromocenters, which are intensely stained by DAPI and comprise chromatin of pericentromeric regions (Figure 1.7). This prolonged binding of DNMT1 to chromatin independently of replication may ensure complete methylation of remaining hemimethylated sites prior to M phase (Easwaran et al. 2004). Interestingly, in a crystallographic study of a large fragment of mouse DNMT1 (amino acid 291-1620) in complex with the cofactor SAM, but without DNA, the TS domain was found to be inserted into the DNA binding pocket of the CTD (Takeshita et al. 2011). In addition, another study indicates that the TS domain inhibits binding of DNMT1 to DNA in *trans* (Syeda et al. 2011). Consequently, the TS domain has an autoinhibitory role in the regulation of DNMT1 enzymatic activity that presupposes the occurrence of structural changes to allow for enzymatic activity. Besides its implication in mediating heterochromatin

binding and DNMT1 autoinhibition, the TS domain was found to be mutated in patients suffering from neurodegenerative diseases (see 1.4.1). Moreover, the TS domain has been described as a mediator of potential DNMT1 dimerization that has been proposed to facilitate the recognition of target sites on DNA (Fellinger et al. 2009). Importantly, the TS domain was found to be the interaction surface for ubiquitin-like, containing PHD and RING finger domains 1 (UHRF1), a cofactor and binding partner of DNMT1 (see 1.2.3) (Bostick et al. 2007; Achour et al. 2008; Felle et al. 2011).

In addition, DNMT1 features a CXXC type zinc finger domain (CXXC), which binds to unmethylated DNA (Frauer et al. 2011) and changes the structure of DNMT1 in a way that avoids *de novo* methylation activity (Song et al. 2011b). In complex with unmodified DNA the linker between the CXXC domain and the bromo adjacent homology domain 1 (BAH1) blocks the access of the catalytic center in the CTD to the target CpG site (Song et al. 2011b). The BAH domains are involved in several DNMT1-protein interactions including ubiquitin-specific processing protease 7 (USP7) that regulates DNMT1 stability (Du et al. 2010; Qin et al. 2011) and HP1 β (Fuks et al. 2003) as a binding partner. The linker between the NTD and the CTD contains seven lysine-glycine repeats ((KG)₇) thereby providing a flexible connection between the two domains of DNMT1.

Subcellular distribution of DNMT1 during the cell cycle

In mammalian cells, distinct patterns illustrate DNMT1 spatial distribution in different stages of the cell cycle (Figure 1.7) (Leonhardt et al. 2000).

In G1 phase, DNMT1 is distributed over the whole nucleus in a diffuse pattern similar to PCNA. Monomethylation of H3K56 by G9a provides a docking site for PCNA in this stage and facilitates DNA replication (Yu et al. 2012). When DNA synthesis is initiated in early S phase, PCNA serves as a stationary loading platform at the replication fork (Sporbert et al. 2005). In this cell cycle phase, PCNA co-localizes with DNMT1 at replication sites appearing as small spots correlated with gene dense active euchromatic regions (Gilbert et al. 2004; Woodfine et al. 2004). In mid S phase, when facultative heterochromatin like the inactive X chromosome in female cells and tissue-specific genes are replicated (Casas-Delucchi et al. 2011), PCNA and DNMT1 are found at replication sites in the periphery of the nucleus and nucleoli. In early and mid S phase the interaction with PCNA predominates the localization of DNMT1 as a mutant deficient in PCNA binding is diffusely distributed in the nucleus (Schermelleh et al. 2007). Upon replication of constitutive (peri)centromeric heterochromatin in late S phase, PCNA and DNMT1 are enriched at DNA replication sites clustering in typical horseshoe-like structures. These replication structures around chromocenters are characteristic for mouse cells harboring clusters of acrocentric chromosomes (Berezney et al. 2000; Leonhardt et al. 2000). The association of DNMT1 with these late S phase chromatin structures is dependent on the TS domain (Easwaran et al. 2004; Schneider et al. 2013). Remarkably, in G2 phase, DNMT1 shows a prolonged TS domain-mediated association with chromocenters independent of PCNA and replication (Easwaran et al. 2004).

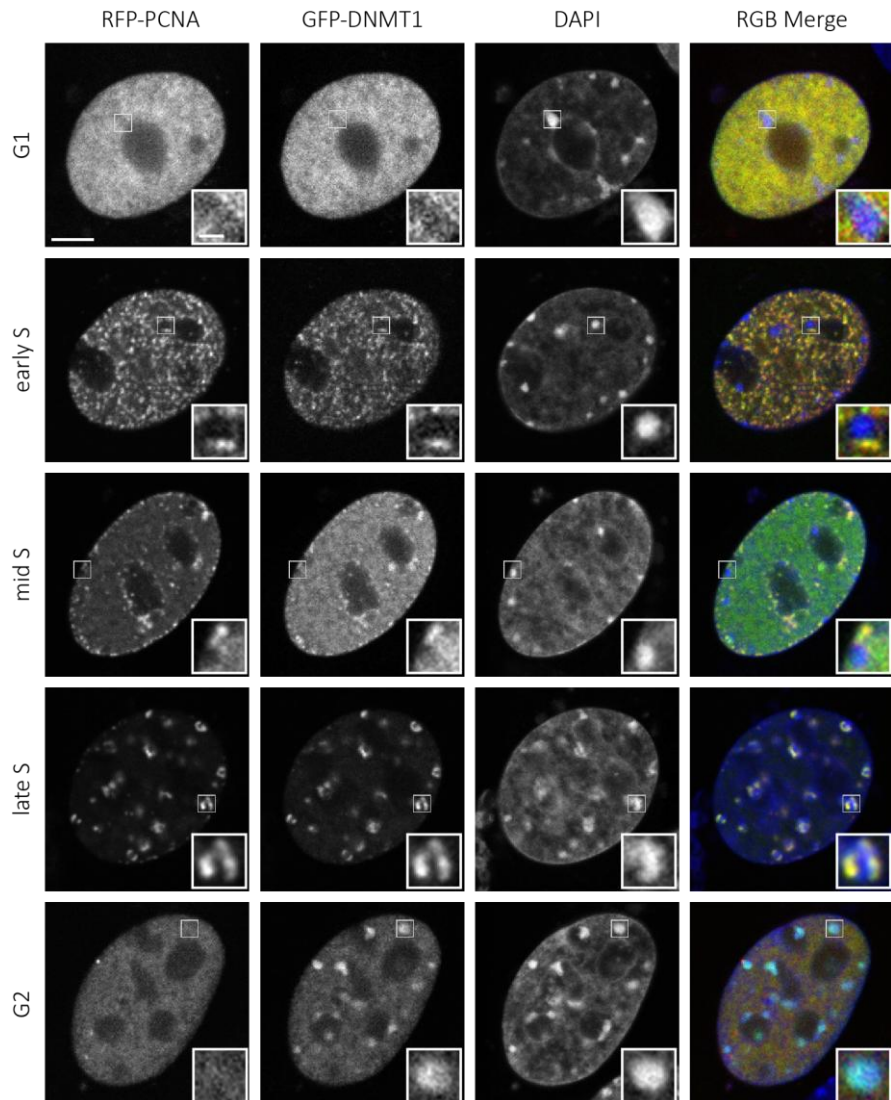


Figure 1.7: Spatial distribution of DNMT1 during the cell cycle. In mouse somatic cells (C2C12) GFP-DNMT1 co-localizes with RFP-PCNA in G1 and S phase, whereas in G2 phase only GFP-DNMT1 shows a prolonged association with heterochromatin. Scale bar 5 μ m. Enlargement display a three-times magnification of chromocenters intensely stained with DAPI. Scale bar 1 μ m.

1.2.3 Cooperative readout of DNA and histone modifications by UHRF1 and UHRF2

In 2007, UHRF1, also known as inverted CCAAT binding protein of 90 kDa in humans (ICBP90) or nuclear protein of 95 kDa in mice (NP95), was identified as an important cofactor of DNMT1-mediated maintenance DNA methylation. By recognition of hemimethylated DNA and by direct interaction with DNMT1, UHRF1 is thought to target DNMT1 to its substrate (Bostick et al. 2007; Sharif et al. 2007; Achour et al. 2008). Consistently, UHRF1-deficient ESCs have been shown to phenocopy the defects of DNMT1-deficient ESCs displaying a pronounced decrease in DNA methylation levels. Knockout of *Uhrf1* leads to embryonic lethality at mid-gestation (Muto et al. 2002).

UHRF1 was found to co-localize with PCNA during S phase (Uemura et al. 2000) and to play a role in cell cycle progression as well as DNA replication (Fujimori et al. 1998). In NIH3T3 cells, UHRF1 expression was described to be essential for S phase entry (Bonapace et al. 2002) and UHRF1-deficient ESCs were

found to be more sensitive towards treatment with the replication-inhibiting reagent hydroxyurea (Muto et al. 2002). Moreover, UHRF1 is involved in DNA repair and contributes to genome stability (Muto et al. 2002). Besides recruiting DNMT1 to newly replicated DNA, UHRF1 may also target DNMT1 to repair sites (Sharif et al. 2007; Achour et al. 2008; Hashimoto et al. 2009). UHRF1 has also been shown to interact with the *de novo* methyltransferases DNMT3A and DNMT3B and with histone modifying enzymes like HDAC1, G9a and Tat interacting protein of 60 kDa (TIP60) (Unoki et al. 2004; Achour et al. 2008; Kim et al. 2009; Meilinger et al. 2009). In agreement with its role in cell cycle progression, UHRF1 is prevalent in proliferating tissues like fetal and adult thymus, fetal liver as well as bone marrow. Furthermore, elevated expression of UHRF1 is found in primary tumors (Hopfner et al. 2000; Jenkins et al. 2005).

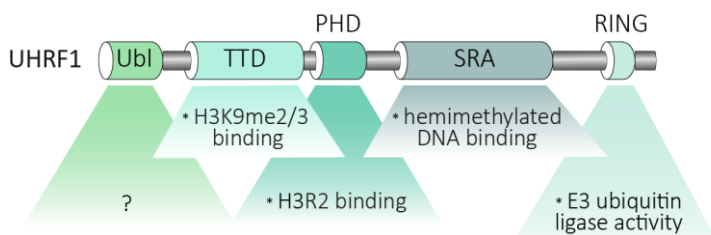


Figure 1.8: Domain structure and key features of UHRF1. UHRF1 is a multi-domain protein comprised of a ubiquitin-like (Ubl) domain followed by a tandem Tudor domain (TTD), a plant homeodomain (PHD), a SET and RING-associated (SRA) domain and a really interesting new gene (RING) domain. Binding preferences and properties are indicated.

The UHRF1 domain structure with indication of key features is summarized in Figure 1.8. Several studies illustrate the unique preference of the multi-domain protein UHRF1 for binding hemimethylated CpG sites via its SET and RING-associated (SRA) domain (Bostick et al. 2007; Sharif et al. 2007; Arita et al. 2008; Avvakumov et al. 2008; Hashimoto et al. 2008; Qian et al. 2008; Rottach et al. 2010) and for histone H3 tails, di- or trimethylated at K9, by the tandem Tudor domain (TTD) (Citterio et al. 2004; Karagianni et al. 2008; Rottach et al. 2010; Cheng et al. 2013). In addition to these two domains, also the plant homeodomain (PHD) contributes to the chromatin association of UHRF1 by binding to unmodified arginine 2 on histone H3 (Rajakumara et al. 2011; Wang et al. 2011) and acts together with the TTD for binding H3K9me2/3 (Arita et al. 2008; Arita et al. 2012; Cheng et al. 2013). Furthermore, the PHD was implicated in large-scale reorganization of PH (Papait et al. 2008). The really interesting new gene (RING) domain functions as a E3 ubiquitin ligase on histone H3 *in vitro* (Citterio et al. 2004; Karagianni et al. 2008), but also on non histone substrates like UHRF1 itself or DNMT1 (Jenkins et al. 2005; Du et al. 2010; Qin et al. 2011). In dependence on its E3 ubiquitin ligase activity, UHRF1 has been shown to increase the resistance of human tumor cells towards cytotoxic as well as genotoxic agents and thus is important for the regulation of human tumor cell proliferation (Jenkins et al. 2005). The function of the ubiquitin-like (Ubl) domain of UHRF1 remains largely unknown.

Studies on the crystal structure of the SRA domain in complex with hemimethylated DNA provide an explanation for the unique specificity of the domain for hemimethylated CpG sites. The methylated cytosine is flipped out of the DNA double helix stabilized by Watson-Crick polar hydrogen bonds and van der Waals interactions (Arita et al. 2008; Avvakumov et al. 2008; Hashimoto et al. 2008). By formation of a crescent moon-like structure with two loops, the SRA domain faces the minor and opposed major groove

of the DNA, the latter being positioned in close proximity to the backbone carbonyl oxygen of N494. Therefore, the addition of a methyl group to the unmodified cytosine would result in a steric clash (Hashimoto et al. 2008). Evidence for a coordinated readout of histone H3 tails carrying an unmodified R2 and a trimethylated K9 by UHRF1 is provided by the crystallographic study of the human TTD and PHD in complex with an H3K9me3 peptide (amino acid 1-17) (Cheng et al. 2013). The N-terminal part of the H3K9me3 peptide (amino acid 1-4) interacts with the PHD and the C-terminal part (amino acid 8-10) with the TTD thereby building a connection between the two domains. The PHD recognizes the unmodified H3 peptide independently of the TTD and the H3K9 trimethylation by formation of contacts to A1, R2 and K4. In contrast, binding of H3K9me3 by a hydrophobic pocket in the TTD and hydrogen bonds to R8 of the histone peptide is enhanced by the PHD (Cheng et al. 2013). Thus, UHRF1 specifically recognizes the K9 methylated H3 tail by coordinated binding of two reader modules (Arita et al. 2012). In summary, UHRF1 connects two major epigenetic modifications by recognition of methylated histones and methylated DNA, the latter being faithfully propagated after replication by recruitment of the maintenance DNA methyltransferase DNMT1.

The second member of the UHRF family, UHRF2 (also known as Np95/ICBP90-like RING finger protein (NIRF) or nuclear protein of 97 kDa (NP97)), harbors the same domains described for UHRF1 and shares a high primary sequence similarity with UHRF1. UHRF2 has been linked to intranuclear degradation of polyglutamine aggregates (Iwata et al. 2009) and to the regulation of the cell cycle (Mori et al. 2002; Li et al. 2004). It binds to the inactive cyclin-dependent kinase 2 (CDK2) and is also a phosphorylation target for CDK2. Given that CDK2 needs to be activated to allow for S phase entry, UHRF2 might participate in controlling G1/S phase transition (Li et al. 2004). Similar to UHRF1, UHRF2 has been shown to possess autoubiquitination activity and to ubiquitinate a PEST-containing nuclear protein (PCNP) (Mori et al. 2004). UHRF2 is also related to tumorigenesis. In colorectal cancer cell, UHRF2 is frequently upregulated and it was proposed to be involved in the development of breast cancer cells as well as gliomas (Wang et al. 2012; Wu et al. 2012a; Wu et al. 2012b). Hence, UHRF2 as well as UHRF1 both act as oncogenes and are promising targets for cancer therapy (Bronner et al. 2007). However, the detailed role and regulation of UHRF2 function remains elusive.

1.2.4 Erasure of DNA methylation

Although DNA methylation is thought to be relatively stable in somatic cells, dynamic changes of this important epigenetic mark can be observed during early development. A famous example for the erasure of DNA methylation is the active DNA demethylation which occurs in the sperm-derived paternal pronucleus four to eight hours after fertilization (Figure 1.9) (Mayer et al. 2000). Opposite to the maternal genome that is protected from epigenetic changes in this state, the paternal genome is subjected to genome-wide demethylation. Solely at specific sites including imprinting control regions like the H19 promoter (Olek and Walter 1997), IAP retrotransposons (Lane et al. 2003) and centromeric as well as pericentromeric regions (Rougier et al. 1998), active DNA demethylation is absent. During the following first cell divisions, the maternal genome starts to undergo passive demethylation. In this process, the 5mC mark is not propagated to the daughter strand after replication leading to progressive loss of DNA methylation (passive dilution). However, imprinted genes are excluded from passive dilution and are only

demethylated in primordial germ cells (Monk et al. 1987; Howlett and Reik 1991). Consistent with the absence of maintenance DNA methylation, the oocyte-specific isoform of DNMT1 (DNMT1o) is localized in the cytoplasm thereby retracting the enzyme from its substrate in the nucleus (Carlson et al. 1992; Cardoso and Leonhardt 1999).

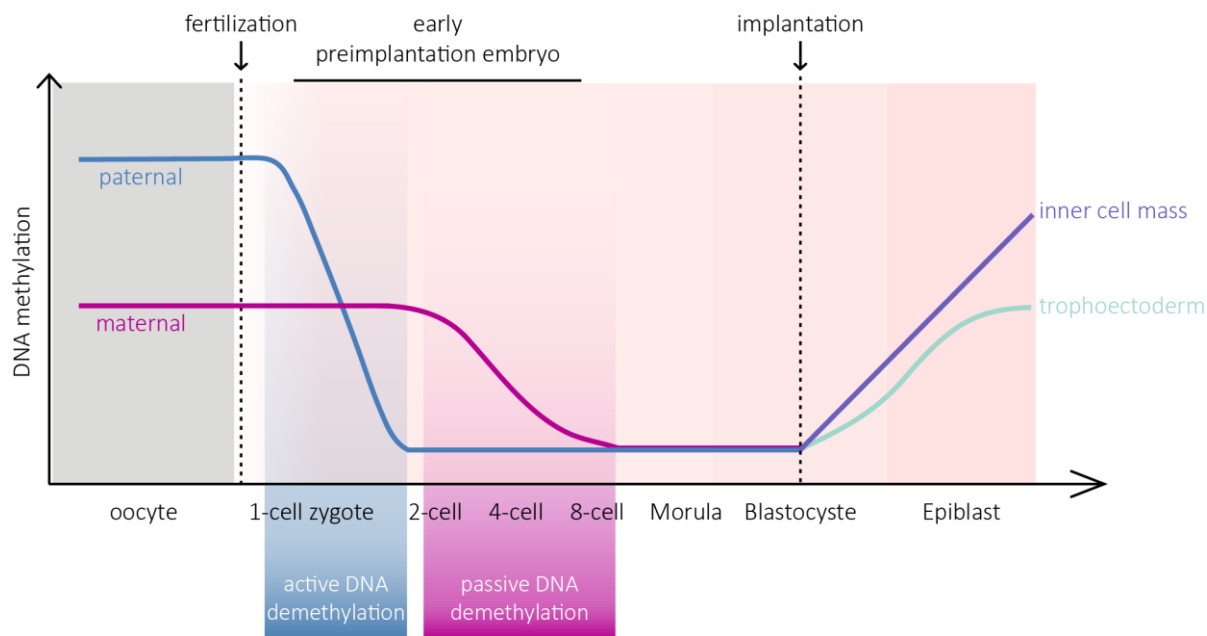


Figure 1.9: Dynamics of paternal and maternal DNA methylation in mouse pre- and postimplantation embryos. Shortly after fertilization, the paternal genome undergoes rapid genome-wide active demethylation, whereas the maternal genome stays at its methylated state. During the following first cell divisions, DNA methylation in the maternal genome is erased by passive demethylation in the absence of DNMT1 (passive dilution). Modified from (Wu and Zhang 2014).

Although active DNA demethylation was described for the first time in 1982 (Gjerset and Martin 1982), the underlying mechanism and the contributing proteins have not been identified until 2009 (Tahiliani et al. 2009). DNA demethylation is carried out by the family of TET proteins consisting of TET1, TET2 and TET3 that convert 5mC to 5hmC, 5fC and 5caC (see Figure 1.2) (Kriaucionis and Heintz 2009; Tahiliani et al. 2009). Expression levels of TET proteins differ among developmental stages and cell types pointing towards distinct functions of the different members (Szwagierczak et al. 2010; Wu and Zhang 2014).

The discovery of TET proteins and oxidized 5mC forms opens the possibility of a passive demethylation mechanism in the presence of an active maintenance methylation machinery that is distinct from the passive dilution. Interestingly, it has been shown that binding of MeCP2 and DNMT1 to chromatin is sensitive towards 5-hydroxymethylation and that the methylation efficiency of the latter on hemihydroxymethylated CpG sites is decreased *in vitro* by approximately 10-60 fold (Valinluck et al. 2004; Hashimoto et al. 2012). Moreover, it is known that other 5mC binding proteins like MBD1, MBD2 and MBD4 do not bind to 5hmC (Valinluck et al. 2004; Jin et al. 2010). Thus the 5hmC mark could represent an activating signal leading to passive demethylation by ineffective or missing propagation of DNA methylation. Indeed, this process was found to take place in erythropoiesis *in vivo* in dependence on rapid DNA replication (Shearstone et al. 2011). Given that DNMT1 is ineffective in methylating DNA in a hemihydroxymethylated context, the methylation pattern in tissues with high 5hmC levels might be

maintained by the action of DNMT3A and DNMT3B, which have a higher catalytic activity on the oxidized cytosine form (Hashimoto et al. 2012; Otani et al. 2013). The 5hmC-mediated passive demethylation process provides features for a higher flexibility enabling a dynamic cellular plasticity in dependence on external signals.

Apart from passive demethylation, TET proteins are mainly involved in the process of active demethylation, which occurs independently of replication. After the initial conversion of 5mC, several possible pathways can lead to demethylation of the 5hmC site. 5hmC might be directly removed by DNMT-dependent dehydroxymethylation (Liutkeviciute et al. 2009; Chen et al. 2012) or by decarboxylation of 5caC (Wu and Zhang 2010; Schiesser et al. 2012). Another possibility for active restoration of the unmodified C base is the excision of oxidized cytosine analogs by glycosylases leading to abasic sites that are recognized by the base excision repair (BER) machinery (Guo et al. 2011; He et al. 2011; Maiti and Drohat 2011). An emerging role in this pathway is assigned to the thymine DNA glycosylase (TDG), which has a preference for the excision of 5fC and 5caC in double stranded DNA (He et al. 2011; Kohli and Zhang 2013; Müller et al. 2014).

Active demethylation in the paternal pronucleus has been correlated with high TET3 expression levels and an increase in DNA hydroxymethylation (Inoue and Zhang 2011; Iqbal et al. 2011; Wossidlo et al. 2011), formylation as well as carboxylation (Inoue et al. 2011). Consistently, TET3 knockdown disturbs the decrease in 5mC and the simultaneous increase in 5hmC levels (Gu et al. 2011; Wossidlo et al. 2011). In line with the important role of TET3 in early embryonic development, *TET3* knockout mice die perinatally (Gu et al. 2011). In addition to TET proteins, a protein of the elongator complex, ELP3 has been described as an indispensable factor in active DNA demethylation of the paternal pronucleus (Okada et al. 2010). Similar to the decrease of 5mC in the maternal genome, the oxidized cytosines in the paternal pronucleus are erased by replication-dependent passive dilution after fusion with the maternal pronucleus (Inoue et al. 2011; Inoue and Zhang 2011). Furthermore, active restoration of unmodified C from a small proportion of 5fC and 5caC is achieved by TDG and the BER pathway (Hajkova et al. 2010; Inoue and Zhang 2011; Müller et al. 2014).

Another wave of global DNA demethylation takes place during the migration and specification of PGCs. Initially, DNA methylation is erased by a replication-dependent passive dilution of 5mC in absence of *de novo* and maintenance DNA methylation (Kagiwada et al. 2013; Seisenberger et al. 2013). Upon settling in the gonad, PGCs undergo a second complete demethylation process that is thought to be induced by TET-mediated oxidation of 5mC (Yamaguchi et al. 2012; Hackett et al. 2013). In the late stage of PGC reprogramming, erasure of paternal imprints in the female germline has been shown to rely on TET1 (Yamaguchi et al. 2013). In this second active demethylation step, promoters of germline-specific genes are transcriptionally activated in developing female PGCs (Yamaguchi et al. 2012). Therefore, TET proteins seem to be necessary for demethylation of imprinting control regions in late PGCs (Hackett et al. 2013).

In contrast to TET2 and TET3, knockdown of TET1 leads to defects in ESC self renewal, maintenance and inner cell mass specification prominently in the trophoectoderm (Ito et al. 2010) and *Tet1* knockout may result in embryonic lethality (Yamaguchi et al. 2013). TET1 is an important regulator of the pluripotency factor nanog by directly binding to its promoter and thereby protecting it from DNA methylation and silencing (Ito et al. 2010). Knockdown of TET2 has no obvious effect on early development, but a multitude of mutations in *TET2* were characterized in several human myeloid

malignancies including myelodysplastic syndromes (MDSs), myeloproliferative disorders (MPDs) and acute myeloid leukemias (AML) (Abdel-Wahab et al. 2009; Delhommeau et al. 2009; Jankowska et al. 2009; Kosmider et al. 2009; Langemeijer et al. 2009; Mohamedali et al. 2009; Saint-Martin et al. 2009; Tefferi et al. 2009; Konstandin et al. 2011). In MDS patients, methylation levels were found to be changed probably due to dysfunctions of the mutated protein in active DNA demethylation (Nolte and Hofmann 2008).

Unlike TET2 and TET3, which are expressed in several mouse adult tissues like kidney, liver and brain (Szwagierczak et al. 2010), TET1 is most abundant in the inner cell mass of blastocysts and in PGCs (Ito et al. 2010; Yamaguchi et al. 2012). Given that TET enzymes are expressed in somatic cells like brain tissues, DNA methylation might not be as stable as previously thought (Wu and Zhang 2014). Remarkably, 5hmC is not only an intermediate in the process of active demethylation, but there is also growing evidence for its function as an independent epigenetic mark. Interestingly, some 5hmC selective readers are expressed in specific cell types that might therefore initiate distinct regulatory processes (Spruijt et al. 2013). Furthermore, demethylation mediated by TET proteins might also be important to keep CpG islands in their unmethylated state permissive to transcriptional activation. In line with this, TET1 was found to be preferentially bound to CpG islands and abnormal CpG methylation occurred as a consequence of TET1 depletion (Ficz et al. 2011; Wu et al. 2011a; Wu et al. 2011b).

1.3 Role of DNA modifications in neurogenesis and neurodegenerative diseases

1.3.1 DNA methylation in the developing and adult nervous system

During neurogenesis, which starts at embryonic day 8 in mice and is most prominent at day 14, neuronal stem cells (NSCs) and progenitor cells (NPCs) give rise to functional neurons (Figure 1.10). Initially, neuroepithelial cells located in the ventricular and subventricular zone (VZ and SVZ) are transformed into radial glial cells (RGCs). RGCs directly generate nascent neurons or indirectly give rise to neurons via the stage of neuronal intermediate progenitor cells (nIPCs) and their symmetric division. Asymmetric division helps to retain the self renewing characteristics of RGCs and also creates oligodendrocyte and astrocyte intermediate progenitor cells (oIPCs and aIPCs). By migration of newborn neurons and RGCs, the neocortex is thickened and an interneuron network is formed. Finally, most RGCs detach from the VZ and migrate towards the cortical plate, where they are transformed to astrocytes. A few RGCs, also known as B cells, remain quiescent in the SVZ and serve as origin for adult neurogenesis (Yao and Jin 2014).

A characteristic of the mammalian brain is the generation of new neurons also in adulthood. Adult neurogenesis takes place in special zones of the mammalian brain, the SVZ and the subgranular zone (SGZ) of the hippocampal dentate gyrus (DG) and is important for certain forms of learning and memory (Braun and Jessberger 2014). In adulthood, quiescent B cells in the SVZ first generate transiently amplifying C cells. These nIPCs further differentiate into neuroblasts (also known as A cells) that migrate to the olfactory bulb and differentiate into various subtypes of local interneurons. In the DG, radial astrocytes generate B cells serving as nIPCs. After differentiation to neuroblasts in the inner granule cell layer, immature neurons arise and are further integrated into the existing circuitry (Yao and Jin 2014). As adult neurogenesis is restricted to two neurogenic niches, experience-driven regulation by proneurogenic signals and factors selectively guides neural differentiation and subsequent integration of functional neurons in the preexisting circuitry (Marr et al. 2010)

Thus integration of new experiences is not only based on the modulation of preexisting neuronal structures, but also on the generation and incorporation of new neurons in the network as a life-long phenomenon. Misregulation of adult neurogenesis was found to be involved in neurodegenerative disorders such as Alzheimer's disease and epilepsy as well as psychiatric disease like major depression (Braun and Jessberger 2014). As adult neurogenesis represents an endogenous regenerative system, it is a promising therapeutic target for neurodegenerative diseases (Marr et al. 2010).

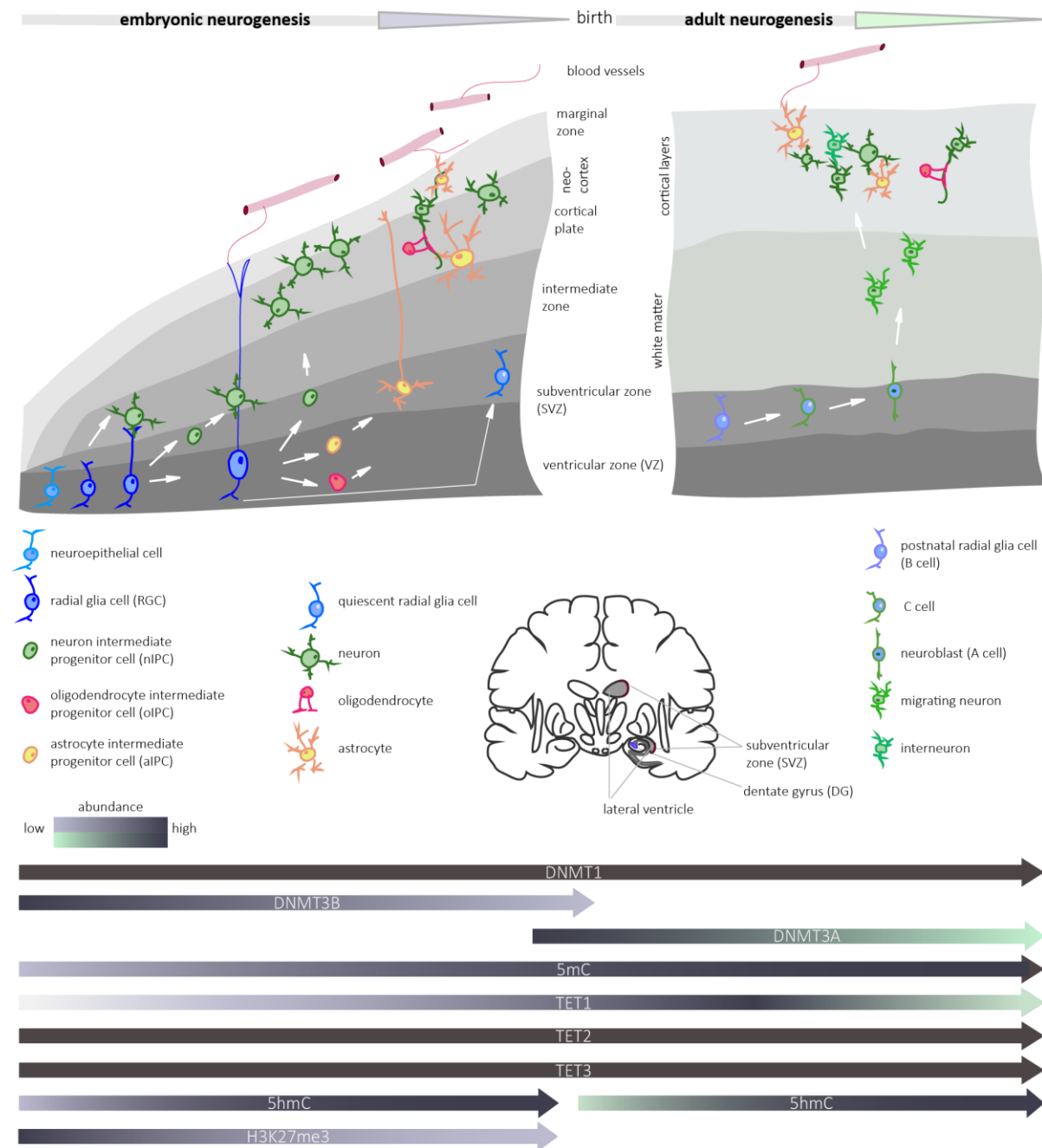


Figure 1.10: Embryonic and adult neurogenesis. Embryonic neurogenesis establishes cortical layers by generation and differentiation of neurons starting from radial glial cells (RGCs) and neuronal intermediate progenitor cells (nIPCs). Astrocytes and oligodendrocytes also arise from RGCs. Astrocytes have important functions in the CNS like supporting the blood-brain barrier, providing nutrients and maintaining the extracellular ion balance. Oligodendrocytes provide insulation of axons by creating a myelin sheath. Adult neurogenesis is restricted to two neurogenic niches in the mature brain, the subventricular zone (SVZ, exemplified in the right scheme) and the subgranular zone (SGZ) of the dentate gyrus (DG), both harboring quiescent NPCs that can give rise to functional neurons in an experience-driven process during adulthood. After the initial activating signal newborn neurons pass through three different stages: migration, maturation and integration into the preexisting network. Expression levels of DNMTs, TETs and epigenetic modifications during embryonic and adult neurogenesis are indicated below. Inspired by (Abcam 2014; Yao and Jin 2014).

In general, neurogenesis gives rise to various cell types all sharing the same primary genetic information, but performing different tasks, indicating a key role of epigenetic mechanisms in the

regulation of neural differentiation. The regulation of the CNS is fairly complex with a multitude of gene products interplaying in a spatially and temporally defined manner. In the nervous system more genes are expressed compared to any other tissue making its sensitivity towards minor alterations understandable (Mattson 2003; Santos-Reboucas and Pimentel 2007).

Surprisingly, in mammals, DNMT1 expression levels are high in the embryonic and adult brain especially in postmitotic neurons, but not in mitotic oligodendrocytes and astrocytes (Goto et al. 1994; Brooks et al. 1996; Trasler et al. 1996; Inano et al. 2000; Veldic et al. 2004). In contrast to nuclear localization in other cell types, DNMT1 is also located in the cytoplasm of neurons (Inano et al. 2000) opening the possibility that the protein might have functions other than DNA methylation in this cellular compartment. Consistent with its high expression level in the brain, DNA methylation by DNMT1 is essential for brain development and neuronal maturation (Fan et al. 2001). When compared to other tissues, like heart, liver and lung, brain tissue has a higher level of DNA methylation (Ehrlich et al. 1982). Treatment of undifferentiated NPCs with demethylating agents like 5-aza-dC leads to inductions of cholinergic, dopaminergic and noradrenergic neuronal differentiation characteristics (Okuse et al. 1993). Although replication-coupled maintenance DNA methylation is not required in postmitotic neurons, DNMT1 might restore DNA methylation patterns after base-excision repair of the G:T mismatches resulting from deamination of 5mC (Brooks et al. 1996).

DNMT3A expression levels are highest in the early postnatal period and decline with the progression to adulthood. DNMT3B is most abundant during early embryogenesis in NPCs (Feng et al. 2005; Watanabe et al. 2006). Thus, the *de novo* methyltransferases show a sequential expression profile with a transition from DNMT3B to DNMT3A expression during neuronal development. Whereas DNMT3B is thought to regulate early NPC differentiation and gene expression, DNMT3A might establish tissue-specific methylation patterns in postmitotic young neurons (Watanabe et al. 2002; Watanabe et al. 2004; Watanabe et al. 2006).

Conditional knockout of *Dnmt3a* in the nervous system leads to failures in motor coordination and premature death of mutant mice indicating an important role of DNMT3A in adult neuromuscular regulation (Nguyen et al. 2007). Furthermore, *in vitro* differentiation of *Dnmt3a*^{-/-} ESCs revealed a precipitate differentiation into the astrocyte and oligodendrocyte lineage accompanied by enhanced proliferation rate and mild global DNA hypomethylation. Thus, DNMT3A is involved in the timely and quantitatively regulation of embryonic NSC differentiation (Wu et al. 2012c). DNMT3A-dependent methylation of intergenic regions and gene bodies was found to promote adult neurogenesis by activating gene expression and concomitantly counteracting Polycomb-mediated repression of neurogenic regulators such as *Distal-less homeobox 2* (*Dlx2*). In conclusion, DNMT3A plays an important role in neurogenesis by limiting astrogial and oligodendroglial differentiation and enhancing neurogenic gene transcription (Wu et al. 2010). RNAi knockdown of *DNMT3B* in human ESCs resulted in accelerated maturation and expression of mature neural markers and neural crest specifiers suggesting a role of the *de novo* methyltransferase in regulating the timing of embryonic neural differentiation and maturation (Martins-Taylor et al. 2012). Induction of neuronal differentiation in pluripotent P19 stem cells caused upregulation of DNMT3B, but not DNMT3A or DNMT1. Likewise, neural differentiation was inhibited by knockdown of DNMT3B (Sheikh et al. 2013).

Already in 1969, the DNA modification hypothesis raised by Griffith and Mahler suggested that DNA modifications are stable enough to guarantee the persistence of memory (Griffith and Mahler 1969). In 1999, Francis Crick claimed that mechanisms of memory storage are regulated by gene loci-specific DNA methylation states (Crick 1984). Even though cell division is absent in terminally differentiated neurons, DNA methyltransferases have been found to be enzymatically active in these cells (Brooks et al. 1996). This finding has been linked to dynamic changes in CpG methylation patterns taking place after neuronal activity and behavioral changes due to external signals (Martinowich et al. 2003; Weaver 2007; Lubin et al. 2008; Nelson et al. 2008). Feelings of fear, for instance, are known to be shaped by early life experience in rodents. Behavioral differences were found to be based on DNA methylation changes of defined gene loci (Weaver et al. 2004; Miller and Sweatt 2007). Another study demonstrated that DNA methylation is an important regulator of memory formation and maintenance (Miller et al. 2010). Application of the DNA demethylating drug 5-aza-dC impaired contextual fear memory in rats proposing that DNA methylation contributes to memory maintenance. An influence of external conditions on neural plasticity related gene expression have been shown for the *brain derived neurotrophic factor (BDNF)*, *reelin*, *PP1* and *calcineurin* (Yu et al. 2011). These examples illustrate fundamental roles of the DNA methyltransferases in learning and memory formation that are different from *de novo* and maintenance functions during development and differentiation.

Synaptic plasticity is an important prerequisite for memory formation and learning. It refers to changes in the strength of a synapse caused by its own activity or other pathways. Synaptic plasticity has been found to rely on the enzymatic activity of DNA methyltransferases indicating that neuronal activity might induce DNA methylation-mediated changes in gene expression (Levenson et al. 2006; Miller and Sweatt 2007). As a neuron carries many synapses but only one nucleus, it is thought to be embedded in a complex network of numerous memories. Thus, the neuron-specific DNA methylation patterns might not simply influence the formation of individual memories, but they might rather integrate and maintain the entity of synaptic properties of the neuron (Yu et al. 2011).

In summary, DNA methylation patterns in the brain are not unchangeable during lifetime, but they can be modulated by external stimuli thereby allowing for behavioral plasticity, memory formation and maintenance (Yu et al. 2011).

1.3.2 DNA demethylation in the developing and adult nervous system

Reversion of DNA methylation has also been implicated in neurogenesis. The expression of growth arrest and DNA damage-inducible protein 45B (GADD45B), which is induced by neural activity, was reported to be required for adult neurogenesis. GADD45B is involved in demethylation of specific gene promoters in the DG leading to the expression of neurogenic factors like BDNF. *Gadd45b*^{-/-} mice exhibit not only deficits in activity-induced proliferation of adult neural progenitors in the DG, but also in the dendritic growth of newborn neurons in the adult brain (Ma et al. 2009).

Beside DNA methyltransferases, also TET enzymes are important for brain development. The content of the TET catalyzed product (5hmC) in ESCs and in the adult brain ranging from 0.3% to 0.7% (Kriaucionis and Heintz 2009; Yao and Jin 2014). Quantitative analyses in several regions of the mouse brain including the olfactory bulb, the cerebral cortex, the retina, the hippocampus, the cerebellum and the brainstem

revealed that the hypothalamus contains the highest 5hmC and the lowest 5mC levels (Munzel et al. 2010). In Purkinje neurons, 5hmC levels as high as 40% of the 5mC levels are reached (Kriaucionis and Heintz 2009). In general, 5hmC levels increase with the neuronal maturation providing an explanation for the rapid increase of 5hmC levels after birth (Figure 1.10) (Song et al. 2011a; Szulwach et al. 2011). Studies on the local distribution of 5hmC in the adult hippocampus and cerebellum of mice in three different stages of life revealed both an age-dependent dynamic regulation and a stable presence of 5hmC during neurodevelopment. On the one hand, dynamic acquisition of the 5hmC mark during neurodevelopment was observed at repetitive elements such as short interspersed nuclear elements (SINEs) and long terminal repeats (LTRs). In addition, 5hmC was enriched at gene bodies of developmentally activated genes with a concomitant loss of 5mC. On the other hand, 5hmC profiles of many tissue-specific differentially hydroxymethylated regions were stable in mice from six weeks after birth until one year of age emphasizing that 5hmC also serves as a stable and functional mark rather than only an intermediate product of demethylation in the brain. Surprisingly, 5hmC was depleted on female and male X chromosomes. Comparison of mouse 5hmC profiles with those of the human cerebellum, proposes conserved characteristics of 5hmC distribution in mammals (Szulwach et al. 2011). The important role of 5hmC in regulating cell type-specific gene expression in the brain was also underlined by a study showing that actively transcribed genes in the cerebellum harbor 5hmC-rich and 5mC-depleted gene bodies (Mellen et al. 2012).

All three members of the TET enzyme family are expressed in the brain with TET2 and TET3 showing the highest levels (Ito et al. 2010; Szwajerczak et al. 2010; Wen et al. 2014). TET1-mediated hydroxylation of 5mC and subsequent deamination by activation-induced deaminase (AID)/ apolipoprotein B mRNA-editing enzyme complex (APOBEC) is required for active demethylation in the DG. This base excision repair-mediated and replication-independent pathway promotes neural activity induced gene expression. Overexpression of both, TET1 or AID in the DG resulted in region-specific DNA demethylation at the *Bdnf* and brain-specific *fibroblast growth factor 1* (*Fgf1B*) promoter accompanied by elevated expression levels of these two genes known to be induced by neural activity. However, increased DNA demethylation was not observed at the non-neuronal *Fgf1G* promoter under the same experimental conditions. Therefore, dynamic changes of C modifications are thought to play an important role in differential gene expression during neurogenesis (Guo et al. 2011).

A recent study emphasizes the interdependence of DNA and histone modifications in regulating embryonic neurogenesis. Overexpression of TET2 and TET3 promoted neural differentiation, whereas overexpression of EZH2, a prominent writer of the repressive histone mark H3K27me3, prevented differentiation. Interestingly, increasing levels of 5hmC at gene bodies of neuronal function related genes were not concomitant with decreasing 5mC levels supporting the idea that 5hmC is a stable and independent DNA modification in the brain (Hahn et al. 2013).

Even though *Tet1* knockout mice are viable, they show deficits in spatial learning and memory. NSC in the SGZ of *Tet1* knockout mice are decreased by 45% when compared to the wildtype controls and many genes of NSCs isolated from the DG are hypermethylated and thus downregulated. Consequently, TET1 is an important regulator of NPC proliferation involved in adult neurogenesis (Zhang et al. 2013). Likewise, TET3 has been implicated in fear extinction learning as it triggers an increase in 5hmC levels required for rapid behavioral adaptation (Li et al. 2014).

In conclusion, embryonic and adult neurogenesis is tightly controlled by a variety of factors including epigenetic modifications on DNA and histones to guarantee the plasticity of the nervous system responding to external stimuli and signals.

1.3.3 DNA methylation and neurodegenerative disease

In the past decades, a great number of human diseases including cancer, syndromes associated with chromosomal instability, imprinting, arteriosclerosis and neurodegenerative disorders as well as mental retardation have been linked to alterations in epigenetic mechanisms. The reversibility of epigenetic marks in contrast to the primary genetic information makes them an attractive target for disease treatment (Santos-Reboucas and Pimentel 2007; Pogribny and Beland 2009).

Links between DNA methylation and neurodegeneration have been made in several studies. In general, alterations in DNA methylation have been reported in different neurological and neurodegenerative diseases.

Promoter hypermethylation has been implicated in Fragile X syndrome inherited in a X-linked dominant manner, Friedreich's ataxia and in spinal muscular atrophy (Urdinguio et al. 2009). Expanded CGG repeats in the *fragile X mental retardation-1 (FMR1)* promoter lead to a increased susceptibility for DNA methylation and subsequent gene silencing (Robertson and Wolffe 2000). The fact that treatment of Fragile X cells with 5-aza-dC could induce re-expression of the *FMR1* gene, whereas the HDAC inhibitor Trichostatin A (TSA) failed to do so, supports the idea that DNA methylation is the dominant gene silencing mechanism in neuronal cells compared to histone modifications (Coffee et al. 1999). In autosomal recessive Friedreich's ataxia, *frataxin (FXN)* gene transcription is impeded by DNA hypermethylation of specific CpG sites upstream of GAA repeat expansions in brain, cerebellum and heart tissues (Al-Mahdawi et al. 2008). In the autosomal recessively inherited spinal muscular atrophy disease, mutations in the *survival of motor neuron 1 (SMN1)* gene lead to decreased protein expression (Lunn and Wang 2008). Severity of this disease was found to depend on the degree of *SMN2* promoter methylation with gene silencing having a deteriorating effect (Hauke et al. 2009).

On the contrary, promoter hypomethylation has been found for instance at the *PAD12* gene in multiple sclerosis patients and at the *tumor necrosis factor alpha (TNF α)* gene leading to apoptosis of neuronal cells in the substantia nigra of Parkinson's disease patients (Pieper et al. 2008; Urdinguio et al. 2009). In Alzheimer's disease, *amyloid precursor protein (App)* and *presenilin 1 (Ps1)* gene promoter hypomethylation results in elevated levels of these proteins in the brain which contribute to the formation of amyloid plaques with intracellular tangles (Pogribny and Beland 2009).

Moreover, alterations in DNA methylation play a crucial role in X-linked dominant Rett syndrome caused by mutations in *MeCP2* and in autosomal recessive Immunodeficiency, Centromeric region instability, Facial anomalies (ICF) syndrome caused by mutations in *DNMT3B* (Robertson and Wolffe 2000). Like DNMT1, MeCP2 is most abundant in the brain when compared to any other tissue where it contributes to postnatal neuronal morphogenesis and function (Nan et al. 1997; Bienvenu and Chelly 2006). Rett mutations impair MeCP2 function as a transcriptional regulator (Bienvenu and Chelly 2006). Given the neuron restricted disease characteristics of Rett patients, the role of MeCP2 in reducing 'transcriptional noise' (Bird and Tweedie 1995) and controlling gene silencing by binding to promoter

regions might be especially important in brain cells (Robertson and Wolffe 2000). *DNMT3B* mutations identified in ICF patients are to a great extent located in the catalytic CTD. They lead to elongation of centromeric and juxtacentromeric heterochromatin and chromosomal abnormalities in phytohaemagglutinine stimulated lymphocytes (Franceschini et al. 1995). Affected chromosome regions contain satellite long-tandem-repeat arrays which are heavily methylated in healthy cells. In ICF patients, however, these regions become hypomethylated leading to chromosomal instability (Jeanpierre et al. 1993; Tagarro et al. 1994). Commonly, all disease phenotypes are characterized by a varying degree of mental impairment suggesting that DNA methylation makes an important contribution to shaping the epigenetic landscape during brain development (Robertson and Wolffe 2000).

Interestingly, DNMT3A has been described as an important regulator for motor neuron cell death. By overexpression of DNMT3A, but not DNMT1, spinal cord neurons enter the apoptotic pathway (Chestnut et al. 2011). The pro-apoptotic function of DNMT3A in motor neurons was dependent on its catalytic activity. Furthermore, DNMT3A and 5mC levels were found to be upregulated in human amyotrophic lateral sclerosis suggesting that DNA methylation plays a major role in the pathobiology. In contrast to that, reduced DNMT3A levels and genome hypomethylation in the whole spinal cord have been reported to accompany axonal degeneration (Iskandar et al. 2010).

In summary, besides its important role in cell differentiation and genomic stability, DNA methylation is also involved in neurogenesis, learning and memory formation. Neurodegenerative disorders have been associated with important epigenetic factors like MeCP2 and DNMT3B. The recent identification of several mutations in *DNMT1* suggests a previously underestimated importance of DNA methylation for the functionality and integrity of the nervous system.

1.4 Hereditary sensory and autonomic neuropathies (HSANs)

Among thirteen proteins affected in different forms of hereditary sensory and autonomic neuropathies (HSANs), DNMT1 was found to be mutated in hereditary sensory and autonomic neuropathy with dementia and hearing loss (HSAN-IE) and autosomal dominant cerebellar ataxia, deafness and narcolepsy (ADCA-DN) patients.

1.4.1 HSAN-IE and ADCA-DN caused by mutations in *DNMT1*

HSAN-IE and ADCA-DN are classified as subtypes of autosomal dominant HSANs. To date, 14 different missense mutations and one deletion mutation in *DNMT1* have been associated with HSAN-IE or ADCA-DN (Table 1.1). Notably, all reported mutations are located within the TS domain in the NTD of DNMT1 (see 3.3.1).

Table 1.1: Disease associated mutations in *DNMT1* with different phenotypes. 14 different point mutations and one deletion mutation found in the *DNMT1* TS domain of HSAN-IE and ADCA-DN patients with the corresponding phenotypes and clinical features are summarized. REM: rapid eye movement; CSF: cerebrospinal fluid; HLA-DQB1*06:02: major histocompatibility complex, class II, DQ beta 1 version with increased risk for developing narcolepsy; SOREMP: sleep-onset REM sleep periods; RSAW: REM sleep without atonia; MSLT: multiple sleep latency test.

HSAN type	Mutation	Locus	Phenotype	Clinical features	Case studies	Molecular studies	Reference
HSAN-IE	D490E + P491Y Y495C Y495H	Exon 20	Sensory neuropathy; sensorineural deafness; dementia; loss of sweating; gait unsteadiness; mutilating ulcer with amputations of distal extremities	Global atrophy in the brain; cerebellar atrophy; length-dependent progressive sensory axonal loss	4 unrelated families (USA, Japan)	Misfolding; premature degradation; reduced methyltransferase activity; impaired heterochromatin binding during G2; global hypomethylation; site-specific hypermethylation	(Klein et al. 2011; Klein et al. 2013)
	H569R	Exon 21	Loss of pain and vibration sense; chronic osteomyelitis, autonomic system dysfunctions; hearing loss, mild dementia	Absence of sensory nerve action potential; normal motor nerve conduction; mild diffuse cerebral and cerebellar atrophy	1 proband (Japan)	Not available	(Gosal 2013; Yuan et al. 2013)
	P507N K521Δ	Exon 20	Bilateral sensorineural deafness; severe axonal sensory polyneuropathy; severe somatic and autonomic small fibres and optic neuropathy	REM sleep behaviour disorder; mild cerebellar and cortical atrophy; HLA-DQB1*06:02 negative	3 probands from 2 unrelated families (Italy)	Not available	(Moghadam et al. 2014a)
	T481P P491L Y524D I531N C353F Y495C Y495H	Exon 20, 21	Hearing and sensory loss, behavior change, gait instability, cognitive decline, trophic ulcer, impaired balance, foot arthropathy, neuropathy, dementia, infections	Global, frontal or cerebellar atrophy, hypersomnia, SOREMP, narcolepsy, restless legs syndrome, REM-sleep behavior disorder, obstructive sleep apnoea syndrome, periodic limb movement disorder, RSAW, MSLT	45 probands (USA, Belgium, England, New Zealand, Germany)	Translocation of mutant protein to the cytoplasm, aggresome formation and autophagy, loss of heterochromatin binding ability during G2 phase, imbalanced protein homeostasis,	(Baets et al. 2015)
	A570V G605A V606F	Exon 21	Late onset cerebellar ataxia; sensorineural deafness; narcolepsy–cataplexy; dementia; late occurring hereditary sensory loss; moderate axonal sensory polyneuropathy; optic neuropathy; lower limbs oedema	Excessive daytime sleepiness; REM sleep behavior disorder; psychosis; HLA-DQB1*06:02 negative; low CSF hypocretin-1 level; global cerebral cortical atrophy	10 probands from 5 unrelated families, one sporadic case with <i>de novo</i> mutation (Italian, USA, UK, Swedish)	Mutations predicted (PolyPhen2, SIFT) to be damaging	(Winkelmann et al. 2012; Moghadam et al. 2014a)
	C596R	Exon 21	Late onset narcolepsy; cerebellar ataxia; deafness; gait instability; low CSF hypocretin-1 level	HLA-DQB1*06:02 positive; mild brain atrophy	1 pro-band with <i>de novo</i> mutation (Brazil)	Not available	(Pedroso et al. 2013)
ADCA-DN							

Disease characteristics and management

HSAN-IE is a late onset neurodegenerative disorder affecting the central nervous system (CNS) and peripheral nervous system (PNS). It is characterized by progressive loss of peripheral sensation and hearing as well as cognitive decline and dementia (Klein et al. 2011; Baets et al. 2015). ADCA-DN patients present with cerebellar ataxia, deafness and late onset dementia as well as narcolepsy (Winkelmann et al. 2012). These two subtypes of HSAN-I disease associated with mutations in *DNMT1* were previously thought to represent two distinct clinical entities. However, a recent study characterizing the phenotype of both, HSAN-IE and ADAC-DN patients, using the same set of neurophysiological and ophthalmological tests indicates the presence of some common features. Narcolepsy, absence of HLA-DQB1*06:02, deafness, optic neuropathy, small fibres polyneuropathy and lower limbs edema are clinical features of both subtypes (Moghadam et al. 2014a). Another recent study claims that mutations associated with HSAN-IE cluster within the N-terminal or central part of the *DNMT1* TS domain, whereas ADCA-DN associated mutations are found in the C-terminal part of the domain (Baets et al. 2015). These differences in the location of causative mutations might explain phenotypic variations.

Lately, potential markers of preclinical ADCA-DN patients have been reported (Moghadam et al. 2014e). The clinical picture of two asymptomatic daughters from an ADCA-DN patient was assessed by use of neurologic examination, sleep recordings, neurophysiologic neuroimaging and genetic tests. Both probands were carriers of a heterozygous mutation from the father. They presented with sleep-onset rapid eye movement periods (SOREMPs) and elevated cerebellar myoinositol (ml), a marker of glial cell activity and density characteristic for the early stage of neurodegenerative diseases. But abnormalities were neither found in the functionality of vision and hearing nor in structural brain magnetic resonance imaging (MRI) scans. Consequently, SOREMPs and increased levels of ml in the brain are two potential markers for preclinical ADCA-DN patients that might help to diagnose the disease at an early stage.

In symptomatic patients, if sensory impairment is a significant characteristic of the disease, prevention of injury is needed to avoid self-mutilating behavior. The skin of affected patients should be protected for instance by gloves, socks and shoes composed of a tissue that is suitable to resist against heat, cold and sharp objects. Hearing aids and assistive devices can be applied to enable communication in everyday life. Moreover, to counteract mental restlessness and delusions resulting from dementia, sedative or antipsychotic drugs may be administered (Klein 2012).

1.4.2 Classification and genetic heterogeneity of HSANs

The term HSANs has been introduced in 1975 for the first time and is classified in the group of inherited peripheral neuropathies (Dyck 1993). The other two groups of inherited peripheral neuropathies comprise hereditary motor neuropathies (HMN) and hereditary motor and sensory neuropathies (HMSN) (Figure 1.11). The categorization into these three groups is based on the involvement of motor, sensory or autonomic nerve fibers in the disease mechanism (Dyck 1993). Motor or also called efferent nerve fibers direct motor impulses from the CNS to the periphery. Sensory or also called afferent nerve fibers function in the opposite direction by conveying sensory impulses from the periphery of the body to the CNS. Autonomic nerve fibers stimulate and activate smooth muscle or glandular tissues (autonomic efferent nerve fibers) or receive sensory impulses from them (autonomic afferent nerve fibers).

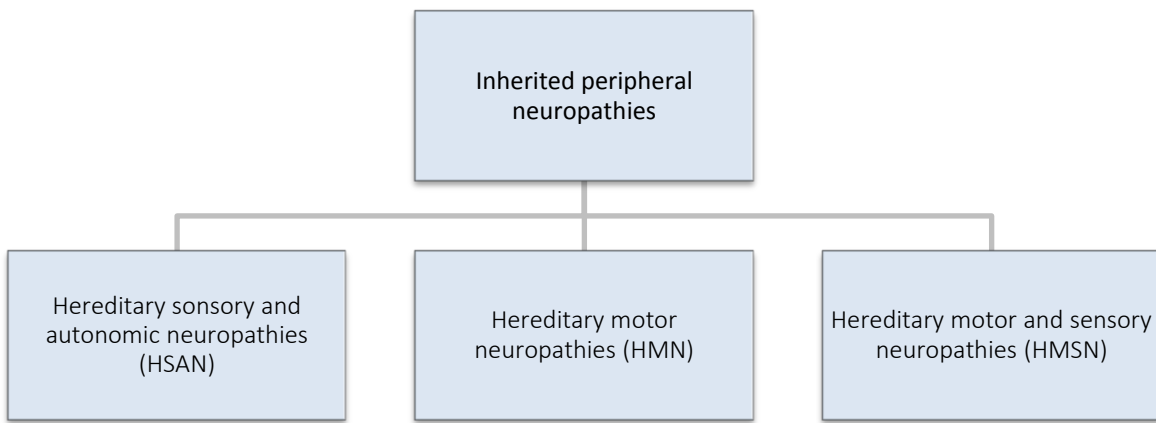


Figure 1.11: Categorization of inherited peripheral neuropathies. Depending on the involvement of motor, sensory or autonomic nerve fibers in the disease mechanism, three groups of inherited peripheral neuropathies are defined.

HSANs are a rare and diverse group of disorders of the PNS that manifest in progressive degeneration predominantly of sensory and autonomic neurons. Axonal damage is accompanied by demyelination in some cases. The disease pattern includes prominent distal sensory loss as well as different autonomic and motor disturbances. Patients with HSAN often lose sensation to pain, touch and temperature resulting in soft tissue infections, osteomyelitis or ulcerative mutilations of the limbs (Rotthier et al. 2012).

HSANs are clinically and genetically heterogeneous. Over the last 15 years, causative mutations in thirteen genes associated with different forms of HSANs have been identified (Figure 1.12). However, for at least two-thirds of the patients suffering from HSANs, the genetic cause has not yet been found, opening the possibility of an even broader spectrum of genes involved in this disease (Rotthier et al. 2009).

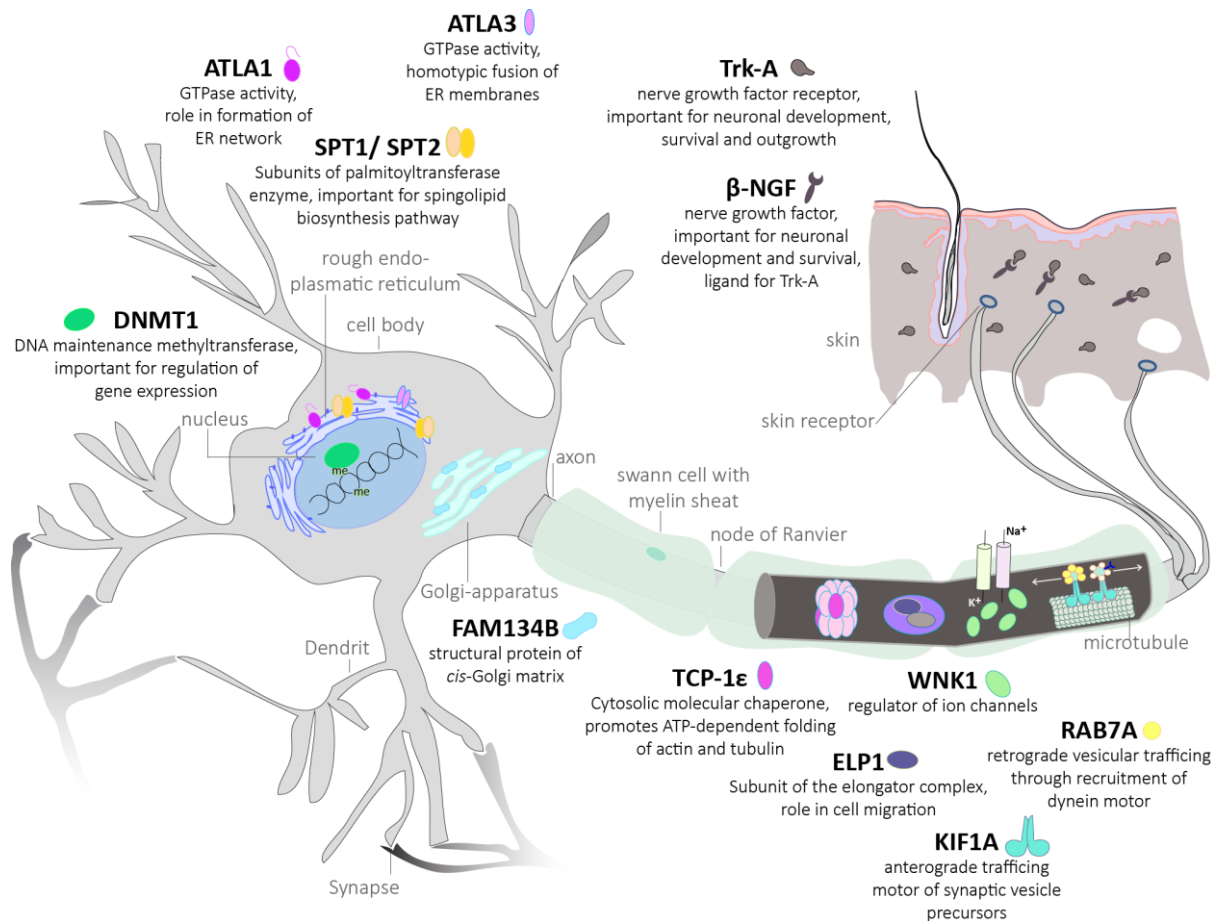


Figure 1.12: Protein functions of thirteen genes associated with HSANs. A mature peripheral sensory neuron in contact with the skin is represented schematically and protein functions that might be affected by HSAN mutations are indicated. Inspired by (Rotthier et al. 2012).

Depending on the age at onset, the mode of inheritance and on prevalent clinical features, HSANs are further subgrouped into type I to V (Dyck 1993). The autosomal dominant inherited type HSAN-I is characterized by a late onset between the second and fifth decade of life and a prominent sensory and usually minor motor involvement. HSAN-I can be further subdivided into HSAN-IE and ADCA-DN. Different from HSAN-I, HSAN-II to V and HSAN with spastic paraparesis are defined by profound autonomic disturbances, an autosomal recessive mode of inheritance and an early onset (congenital or in early childhood) (Rotthier et al. 2012). The proteins (WNK1, CCT5, FAM134B, KIF1A, NGF, NTRK1 and IKBKAP) corresponding to the genes mutated in HSAN-II to V are highly expressed in the PNS (Rotthier et al. 2012). The nervous system restricted expression pattern of the proteins causative for HSAN-II to V make the degenerations of the PNS as main disease characteristic and the linked disease mechanism fairly understandable (Rotthier et al. 2012). Interestingly, the protein encoded by the *kinesin family member 1A* gene (*KIF-1A*), one causative gene for HSAN-II, interacts with a domain of with-no-lysine(K)-1 (WNK1) that is encoded by the nervous-specific exon *HSN2* (Riviere et al. 2011). *HSN2*, in turn, is the only exon within *WNK1* that is affected by HSAN-II mutations (Lafreniere et al. 2004; Riviere et al. 2004; Roddier et al. 2005; Cho et al. 2006; Coen et al. 2006; Takagi et al. 2006). Furthermore, β -NGF, a protein mutated in HSAN-V patients is an important binding partner for Trk-A associated with HSAN-IV (Indo 2002). These two

examples illustrate the interconnection of genes affected by HSAN-II to V and allow for an estimation of the disease underlying mechanisms involving membrane excitability in the nociceptive system and axonal transport (Rotthier et al. 2012). In contrast, the HSAN-I etiology is far from being elucidated as the affected proteins (SPT1, SPT2, RAB7A, ATLA1, ATLA3 and DNMT1) are expressed in different tissues and participate in various biological pathways (Figure 1.12, see 4.3) (Rotthier et al. 2012). The heterogeneity and complexity of HSANs is also underlined by the fact, that affected proteins share only few common protein interaction partners (Figure 1.13). However, some factors bind to several HSAN associated proteins, like the transcription factor SP1, which interacts with DNMT1, Trk-A and KIF1A. Also direct interactions between two HSAN associated proteins can be found, like the interaction between DNMT1 and WNK1. Among the divergent biological pathways covered by HSAN associated proteins, endoplasmic reticulum stress and axonal transport are discussed as possible candidates for the disease mechanisms, but the specific role of affected protein and dysfunctions of the mutants have to be further clarified (Rotthier et al. 2012).

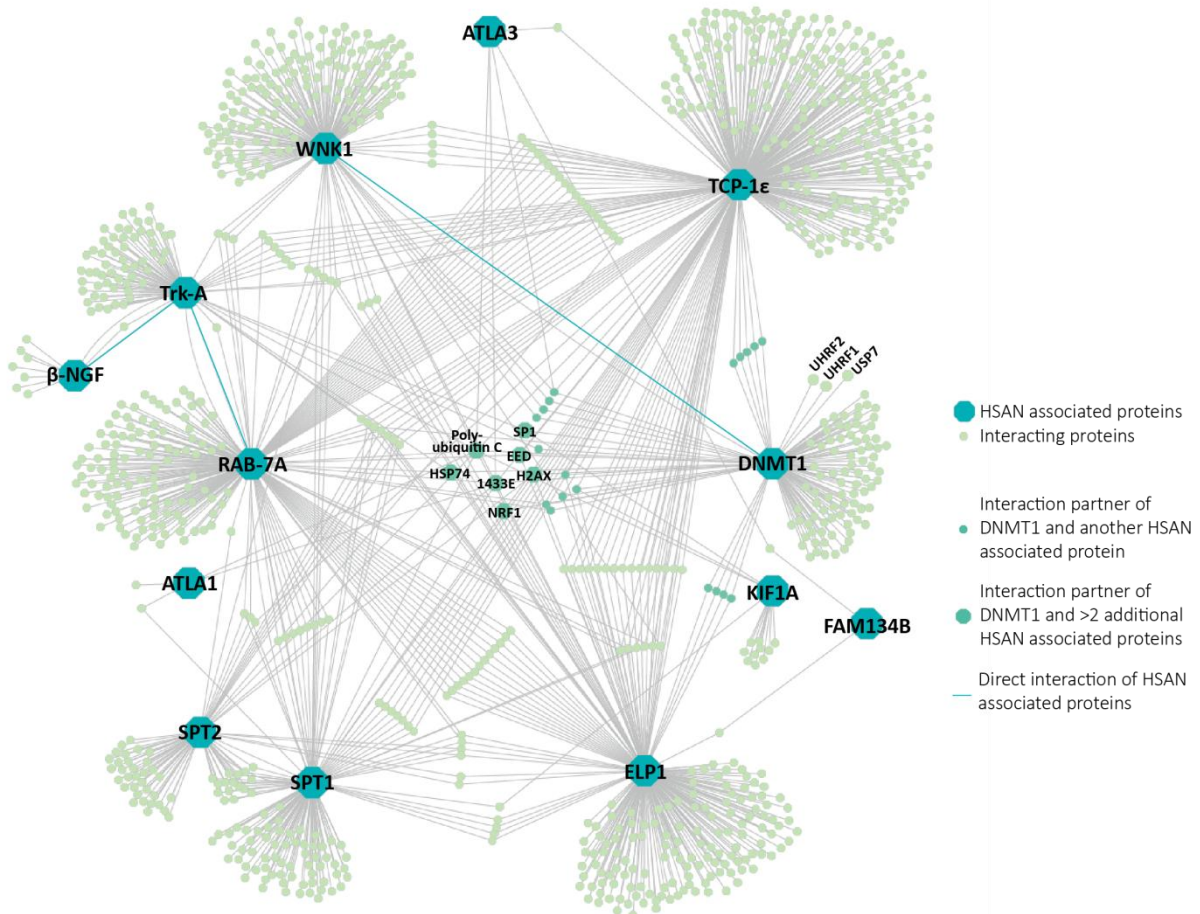


Figure 1.13: Protein-protein interaction network of HSAN associated proteins. Proteins associated with different types of HSAN share only few common interaction partners. The network was generated using the I2D database (Niu et al. 2010) and cytoscape.

1.4.3 Disease modeling and treatment

To date, possibilities for medical treatment of HSANs are fairly insufficient to abate the morbidity rate. Affected persons sustain ulcerative mutilations and osteomyelitis that often necessitate surgery or spontaneous amputations. Patients with severe early-onset HSAN (HSAN-III and HSAN-IV) even have reduced life expectancy due to chronic inflammations and pronounced autonomic disorders. However, in HSAN-II patients carrying a splice-site mutation of *ELP1* (Slaugenhaupt et al. 2001), tocotrienols, epigallocatechin gallate, kinetin and phosphatidylserine have been presented as promising therapeutic drugs (Anderson et al. 2003; Anderson and Rubin 2005; Gold-von Simson et al. 2009; Keren et al. 2010). These compounds increase the splicing efficiency at exon 20 of *IKBKAP* and antagonize aberrant splicing resulting in normal levels of full length *ELP1*. However, treatment of HSANs is fairly inadequate due to the lack of knowledge about the underlying molecular mechanisms and the unprofitability of developing drugs for this rarely occurring disease.

1.4 Aims of this work

DNA methylation of mammalian genomes represents a key epigenetic modification that is established during embryonic development and has to be faithfully transmitted to subsequent cell generations. During replication, the classic maintenance DNA methyltransferase DNMT1 is responsible for copying DNA methylation patterns from the mother cell to its progeny. Although the multi-domain protein UHRF1 has been described as an important DNMT1 binding partner that is essential for maintenance DNA methylation, defined regulatory roles of individual domains remained elusive. Therefore, the main objective of this work was to investigate UHRF1-dependent mechanisms regulating DNA methylation and study the function of the DNMT1 TS domain.

To get deeper insights into DNMT1 subnuclear distribution, protein abundance and interacting partners we generated rat monoclonal antibodies specific for DNMT1. In addition, our goal was to investigate UHRF1 binding specificities to DNA and histone modifications as well as to DNMT1. To this end, we developed a toolbox for semiquantitative and medium throughput analysis of protein-DNA, protein-histone tail peptide and protein-protein binding *in vitro*.

Besides chromatin binding domains, UHRF1 also harbors a RING domain that exerts E3 ubiquitin ligase activity on different substrates such as histones. To elucidate the interplay of UHRF1 epigenetic reader and writer functions, we aimed at determining novel H3 ubiquitination targets of the UHRF1 RING domain by mass spectrometry. A further aim was to systematically analyze the underlying regulatory processes by introduction of defined mutations in different UHRF1 domains. As UHRF1-dependent H3 ubiquitination was essential for DNMT1 targeting and function, our goal was to decipher regions in DNMT1 responsible for ubiquitinated histone binding. Furthermore, we wanted to investigate a potential link between DNMT1 recruitment and PRC-dependent H2A ubiquitination thereby challenging the historical view of DNMT1 as a simple copy machine.

Finally, we aimed at elucidating DNMT1 TS domain mutations associated with two neurodegenerative disease phenotypes named HSAN-IE and ADCA-DN. To get insights in the underlying disease mechanisms we wanted to characterize two disease associated DNMT1 mutants (P496Y and Y500C) with respect to their enzymatic activity, UHRF1 binding, subnuclear localization, protein dynamics and cell cycle-dependent abundances.

2. Results

2.1 Generation and characterization of rat and mouse monoclonal antibodies specific for MeCP2 and their use in X-inactivation studies

Generation and Characterization of Rat and Mouse Monoclonal Antibodies Specific for MeCP2 and Their Use in X-Inactivation Studies

K. Laurence Jost¹, Andrea Rottach^{2*}, Manuela Milden^{1,3}, Bianca Bertulat^{1,3}, Annette Becker^{1,3}, Patricia Wolf^{2,3}, Juan Sandoval³, Paolo Petazzi³, Dori Huertas³, Manel Esteller³, Elisabeth Kremmer⁴, Heinrich Leonhardt², M. Cristina Cardoso^{1*}

1 Department of Biology, Technische Universität Darmstadt, Darmstadt, Germany, **2** Department of Biology II, Ludwig Maximilians University Munich, Planegg-Martinsried, Germany, **3** Cancer Epigenetics and Biology Program, Bellvitge Biomedical Research Institute (IDIBELL), Barcelona, Spain, **4** Helmholtz Center Munich, German Research Center for Environmental Health, Institute of Molecular Immunology, Munich, Germany

Abstract

Methyl CpG binding protein 2 (MeCP2) binds DNA, and has a preference for methylated CpGs and, hence, in cells, it accumulates in heterochromatin. Even though it is expressed ubiquitously MeCP2 is particularly important during neuronal maturation. This is underscored by the fact that in Rett syndrome, a neurological disease, 80% of patients carry a mutation in the *MECP2* gene. Since the *MECP2* gene lies on the X chromosome and is subjected to X chromosome inactivation, affected patients are usually chimeric for wild type and mutant MeCP2. Here, we present the generation and characterization of the first rat monoclonal MeCP2 specific antibodies as well as mouse monoclonal antibodies and a rabbit polyclonal antibody. We demonstrate that our antibodies are suitable for immunoblotting, (chromatin) immunoprecipitation and immunofluorescence of endogenous and ectopically expressed MeCP2. Epitope mapping revealed that most of the MeCP2 monoclonal antibodies recognize the C-terminal domain and one the N-terminal domain of MeCP2. Using slot blot analysis, we determined a high sensitivity of all antibodies, detecting amounts as low as 1 ng of MeCP2 protein. Moreover, the antibodies recognize MeCP2 from different species, including human, mouse, rat and pig. Lastly, we have validated their use by analyzing and quantifying X chromosome inactivation skewing using brain tissue of MeCP2 heterozygous null female mice. The new MeCP2 specific monoclonal antibodies described here perform well in a large variety of immunological applications making them a very valuable set of tools for studies of MeCP2 pathophysiology *in situ* and *in vitro*.

Citation: Jost KL, Rottach A, Milden M, Bertulat B, Becker A, et al. (2011) Generation and Characterization of Rat and Mouse Monoclonal Antibodies Specific for MeCP2 and Their Use in X-Inactivation Studies. PLoS ONE 6(11): e26499. doi:10.1371/journal.pone.0026499

Editor: Frank Lyko, Deutsches Krebsforschungszentrum, Germany

Received August 3, 2011; **Accepted** September 28, 2011; **Published** November 28, 2011

Copyright: © 2011 Jost et al. This is an open-access article distributed under the terms of the Creative Commons Attribution License, which permits unrestricted use, distribution, and reproduction in any medium, provided the original author and source are credited.

Funding: This work was funded in part by grants of the Deutsche Forschungsgemeinschaft to H.L. and M.C.C. and the E-Rare EuroRETT network to M.C.C. P.P. has a fellowship from the FP7 DisChrom Project (PITN-GA-2009-238242), which is funded by the European Commission, and J.S. is a Juan de la Cierva researcher (JCI-2009-04490). The funders had no role in study design, data collection and analysis, decision to publish, or preparation of the manuscript.

Competing Interests: The authors have declared that no competing interests exist.

* E-mail: Cardoso@bio.tu-darmstadt.de

These authors contributed equally to this work.

Introduction

Methyl CpG binding protein 2 (MeCP2) was the second methyl CpG binding protein to be discovered [1] and the first to be cloned [2]. In interphase mouse nuclei, MeCP2 is prominently localized at heterochromatic foci [2]. In metaphase chromosomes, the association of MeCP2 with euchromatic arms is rather weak compared to a strong localization at pericentric heterochromatin [2], highly enriched in heavily methylated major satellite DNA repeats [3]. MeCP2 consists of a conserved methyl CpG binding domain (MBD) that binds to 5-methyl cytosine with high affinity and is shared with the other MBD protein family members. The transcriptional repression domain (TRD), which carries a nuclear localization sequence interacts with histone deacetylases and the transcriptional corepressor Sin3A [4,5,6]. Finally, the C-terminal domain binds nucleosomes (Figure 1).

Even though MeCP2 is ubiquitously expressed, it is genetically linked to a neurological disease called Rett syndrome (RTT, OMIM

312750). RTT was first described in 1966 by Andreas Rett [7] and affects one in every 10,000–15,000 female births [8,9,10]. Affected girls seem to develop normally until six to 18 months, subsequently they enter a developmental arrest, which is followed by strongly impaired motor skills, stereotypic hand movements, loss of speech, seizures, abnormal breathing, microcephaly, ataxia and other symptoms. Mutations within the *MECP2* gene located on chromosome Xq28 are found in approximately 80% of all classic RTT cases [8,11]. Since *MECP2* is located on the X chromosome it is subjected to random X chromosome inactivation. Thus, depending on which chromosome was inactivated, a mosaic pattern of healthy (wild type allele expressing) and affected (mutant allele expressing) cells is created [12]. A further important aspect is the stark discrepancy between MeCP2 mRNA expression levels compared to protein levels (e.g. [13]), which highlights the need for highly specific antibodies detecting MeCP2 on a protein level.

Up to now rabbit polyclonal and mouse monoclonal antibodies have been raised against MeCP2 but the available antibodies are

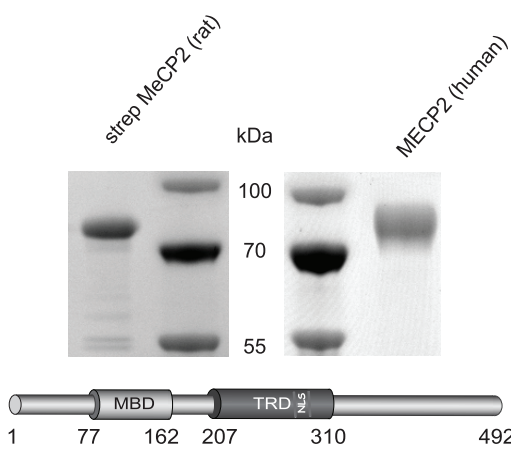


Figure 1. Antigen preparation. Purified strep-tagged MeCP2 (rat) and purified intein tagged MECP2 (human) were subjected to a SDS-PAGE and stained with Coomassie. The molecular weight markers are labeled in the middle. A schematic representation of the rat MeCP2 protein and its functional domains is shown below. MBD: methyl CpG binding domain; TRD: transcriptional repression domain; NLS: nuclear localization signal.

doi:10.1371/journal.pone.0026499.g001

limited in their application range. Here, we describe the generation of the first rat monoclonal antibodies against MeCP2 being capable of reacting specifically in most common immunological applications. To complete the collection, we generated two mouse monoclonal antibodies and a rabbit polyclonal antibody. We could demonstrate the suitability of these high affinity and specific antibodies for immunoblotting, (chromatin) immunoprecipitation, and immunofluorescence stainings of cells and tissues. Additionally, we used one of our anti-MeCP2 rat monoclonal

antibodies on MeCP2 heterozygous null mouse brain to analyze and quantify X chromosome inactivation skewing.

Materials and Methods

Plasmids

Mammalian expression constructs (Figure 3 and S1A) coding for GFP or YFP-tagged rat MeCP2 full length (MeCP2G) and domain constructs (MeCP2Y.3 and MeCP2Y.5) were previously described [14,15]. The mammalian expression constructs MeCP2G.9 and MeCP2G.8 were generated from the above plasmids by PCR amplification using the following primers:

pMeCP2G.9 ss ccgtcgagccatggggagccctccaggagagaaca
as cgccgatcctccgggtctgcgccttgcgtatggggagcac
pMeCP2G.8 ss ggaagatctccatggaaaccgtcagcattgaggtcaag
as ataagaatgcggcccttacttgtacagctgtccatgcc

The mammalian expression construct (Figure 6 and S1B) expressing GFP-tagged human MECP2 was described before [16] and was provided by S. Kudo (Hokkaido Institute of Public Health, Sapporo, Japan). For expression in Sf9 (Invitrogen Paisley PA4 9RF, UK) insect cells the Bac-to-Bac baculovirus expression system (Invitrogen Paisley PA4 9RF, UK) was used. To express MeCP2 with a N-terminal double strep-tag (Figure 1), a sequence encoding the strep-tactin target peptide strep tag III (MWSHPQFEKGGGSTGGGGWSHPQFEK) was synthesized (Entelechon, Bad Abbach, Germany) flanked by BamHI and NotI sites and subcloned into pFastBac1 (Invitrogen, Paisley PA4 9RF, UK) using the same sites. Rat MeCP2 full length was generated by PCR amplification from MeCP2G (described above) using the following primers:

MeCP2 ss: ggaagatctccatggaaaccgtcagcattgaggtcaag
as: ataagaatgcggcccttacttgtacagctgtccatgcc
with NotI and XhoI sites and subcloned in frame with the strep-tag in the pFastBac1 vector. For expression of rat MeCP2-GFP in Sf9 insect cells (Figure 2) the mammalian expression construct

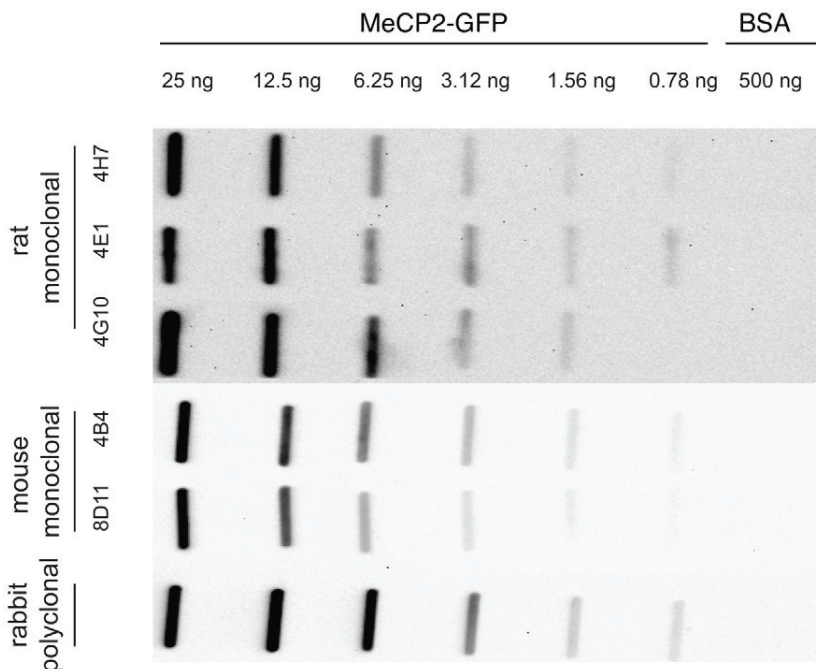


Figure 2. Antibody sensitivity. The detection limit of the MeCP2 antibodies was tested on native rat MeCP2-GFP by slot blotting analysis and lies between 1.58 and 0.78 ng of recombinant purified rat MeCP2.

doi:10.1371/journal.pone.0026499.g002

coding for MeCP2G full length (described above) was cut using NotI and XhoI and cloned in frame in the pFastBac1 vector.

A prokaryotic expression construct coding for intein tagged human MECP2 (Figure 1) [17] was obtained from C.L. Woodcock (University of Massachusetts, Amherst, USA).

Tissues

Male mouse MeCP2 hemizygous brains (Figures 5 and 6) [18] were kindly provided by the group of P. Huppke (Georg August University, Göttingen, Germany). Female mouse MeCP2 null heterozygous brains (Figure 7) [18] were kindly provided by the group of L. Villard (Faculte de Medecine La Timone, Marseille, France). Wild type mouse brains (C57BL/6N; Charles River Laboratories International, Inc., Wilmington, MA 01887, USA) were used as control. Mice were over 10 months old.

Cell culture and transfection

For immunofluorescence (IF) experiments mouse C2C12 myoblasts [19] were cultured using standard conditions described previously [20]. For subsequent IF experiments (Figure 6 and S1B), C2C12 cells were transiently transfected with human GFP-MECP2 expression construct [16] using Transfectin (Bio Rad, München, Germany) according to manufacturer's advice.

For the epitope mapping (Figure 3 and S1A), human embryonic kidney (HEK) 293T [21] cells were cultured in DMEM supplemented with 10% fetal calf serum and 50 µg/ml gentamicin and transfected with full length rat MeCP2 and domain constructs (described above) using polyethylenimine (Sigma, St. Louis, MO, USA).

MeCP2 antigens for immunization (Figure 1) and slot blot applications (Figure 2) were produced using the baculovirus system in Sf9 insect cells. Sf9 cells were maintained in EX-CELL 420 Insect Serum Free (SAFC) medium supplemented with 10% fetal bovine serum shaking at 100 rpm and 28°C. Transfection of Sf9

cells to produce recombinant baculovirus, was performed using Cellfectin (Invitrogen, Paisley PA4 9RF, UK) according to the manufacturer's instructions.

Antigen purification

Sf9 insect cells were infected with the recombinant baculovirus (coding for MeCP2 with N-terminal double strep-tag; [22]) and incubated at 28°C with shaking for 5 days. The cells were pelleted by centrifugation (200× g, 5 min, 4°C) and resuspended in a buffer containing 25 mM Tris-HCl, pH 8.0; 1 M NaCl; 50 mM glucose; 10 mM EDTA; 0.2% Tween-20; 0.2% NP40. The buffer was supplemented with protease inhibitors (Complete mini; Roche, Mannheim, Germany). After incubation on ice for 10 min, cells were disrupted with a high-pressure homogenizer (EmulsiFlex-C5, Avestin) followed by centrifugation at 14,000× g for 30 min.

Strep-tagged recombinant rat MeCP2 protein was purified by incubating the supernatant with 500 µl of strep-tactin sepharose beads (IBA, Göttingen, Germany) for 4 h at 4°C on a rotary shaker. To elute strep-tagged proteins, the beads were incubated with D-Desthiobiotin (0.5 mg/ml; IBA, Göttingen, Germany), dissolved in 1× PBS, for 30 min at 4°C. After centrifugation (200× g, 2 min), beads were separated from the eluate containing the purified proteins. The elution step was performed three successive times.

Intein tagged human MECP2 protein was purified as previously described resulting in untagged MECP2 through protein splicing [23].

Immunizations, generation of hybridomas and ELISA screening

Monoclonal antibodies specific for MeCP2 were generated via the hybridoma technology as described by Rottach et al. [24]. 80 µg of a N-terminal, strep-tagged full length rat MeCP2 were

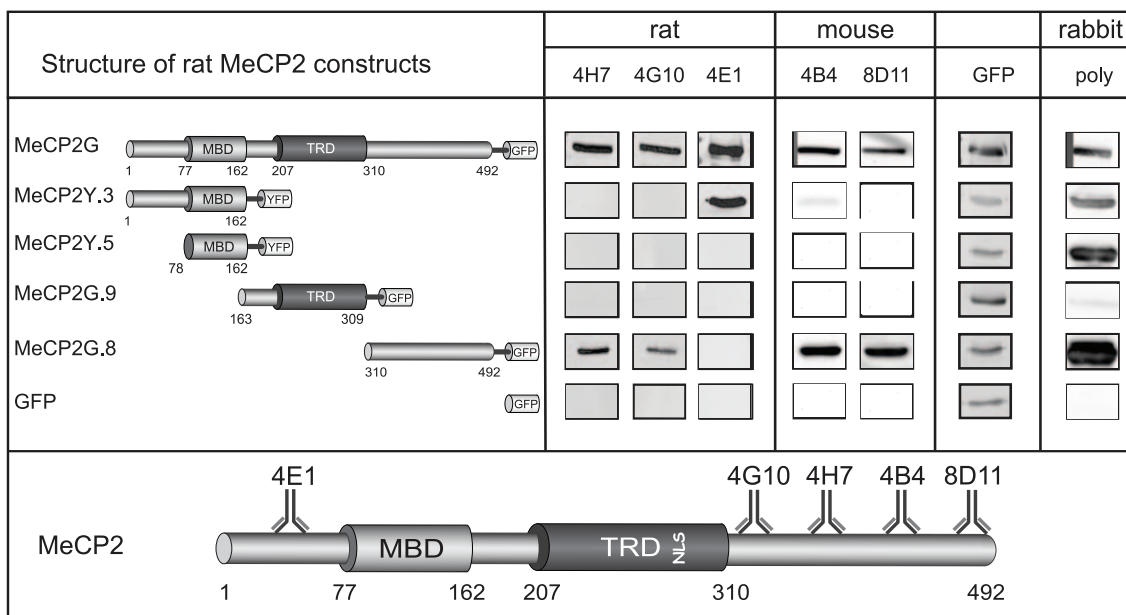


Figure 3. Epitope mapping. To determine the binding site of the new monoclonal antibodies within the MeCP2 protein, we probed extracts of mammalian cells expressing different MeCP2 constructs fused to GFP/YFP as indicated. To control for the level of the fusion proteins, the membranes were reprobed with anti GFP mouse monoclonal antibody. A summary of the epitope mapping results for the different antibodies is shown below. MeCP2 functional domains are as in Figure 1.

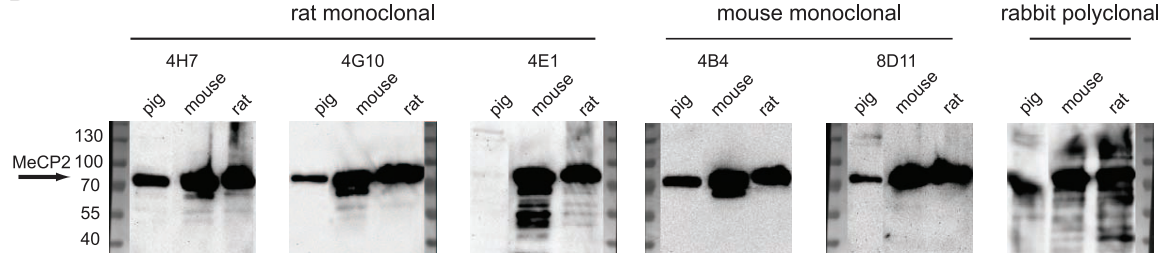
doi:10.1371/journal.pone.0026499.g003



A

M. musculus	MVAGMLGLREEKSEDQDLQGLRDKPLFKKKAKDKKKEDKEGKHEPLQPSAHHSAEPAEAGKAETSESSGSAPAVPEASASPKQRSSIIRDRGPMYDDPTL	100
R. norvegicus	MVAGMLGLRKEKSEDQDLQGLKEKPLKFKKVKKDKKEDKEGKHEPLQPSAHHSAEPAEAGKAETSESSGSAPAVPEASASPKQRSSIIRDRGPMYDDPTL	100
H. sapiens	MVAGMLGLREEKSEDQDLQGLKDKPLKFKKVKKDKKEKEGKHEPVQPSAHHSAEPAEAGKAETSESSGSAPAVPEASASPKQRSSIIRDRGPMYDDPTL	100
S. scrofa	MVAGMLGLREEKSEEQDLQGLKDKPLKFKKVKKDKKDDREGKHEPLQPAAHHSAPAEAGKAETSESSGSAPAVPEASASPKQRSSIIRDRGPMYDDPTL	100
M. musculus	PEGWTRKLKQRKSGRSAGKYDVLINPQGKAFRSKVELIAYFEKVGDTSLDPNDFDFTVTRGRGSPSRREQKPKPKSPKAPGTGRGRGRPKGSGTGRPK	200
R. norvegicus	PEGWTRKLKQRKSGRSAGKYDVLINPQGKAFRSKVELIAYFEKVGDTSLDPNDFDFTVTRGRGSPSRREQKPKPKSPKAPGTGRGRGRPKGSGTGRPK	200
H. sapiens	PEGWTRKLKQRKSGRSAGKYDVLINPQGKAFRSKVELIAYFEKVGDTSLDPNDFDFTVTRGRGSPSRREQKPKPKSPKAPGTGRGRGRPKGSGTGRPK	200
S. scrofa	PEGWTRKLKQRKSGRSAGKYDVLINPQGKAFRSKVELIAYFEKVGDTSLDPNDFDFTVTRGRGSPSRREQKPKPKSPKAPGTGRGRGRPKGSGTGRPK	200
M. musculus	AAASEGVQVQKRVLEKSPGKLVKMFPQASPGKGEGGGATTSAQVMVIKRPGRKRKAEDPQAIPKKRGRKPGSVAAAAAAEAKKKAVKESSIRSVHETV	300
R. norvegicus	AAASEGVQVQKRVLEKSPGKLVKMFPQASPGKGEGGGATTSAQVMVIKRPGRKRKAEDPQAIPKKRGRKPGSVAAAAAAEAKKKAVKESSIRSVQETV	300
H. sapiens	AAATSEGVQVQKRVLEKSPGKLVKMFPQTSPGGKAEGGGATTSTQVMVIKRPGRKRKAEDPQAIPKKRGRKPGSVAAAAAAEAKKKAVKESSIRSVQETV	300
S. scrofa	AAASEGVQVQKRVLEKSPGKLVKMFPQASPGKSAEGGGATTSAQVMVIKRPGRKRKAEDPQAIPKKRGRKPGSVAAAAAAEAKKKAVKESSIRSVQETV	300
M. musculus	LPIKKRKTRETVSIEVKEVVKPLLVSTLGEKGSKGLKTCSPGRKSKESSPKGRSSASSPPKKEHHHHHHHSESTKAPMPLP--SPPPPEPESSEDPI	398
R. norvegicus	LPIKKRKTRETVSIEVKEVVKPLLVSTLGEKGSKGLKTCSPGRKSKESSPKGRSSASSPPKKEHHHHHHHAEESPKAIPMPLP--PPPPPEPQSSEDPI	398
H. sapiens	LPIKKRKTRETVSIEVKEVVKPLLVSTLGEKGSKGLKTCSPGRKSKESSPKGRSSASSPPKKEHHHHHHHSESPKAIPVPLPPPLPPPEPESSEDPT	400
S. scrofa	LPIKKRKTRETVSIEVKEVVKPLLVSTLGEKGSKGLKTCSPGRKSKESSPKGRSSASSPPKKEHHHHHHHSESPKAIPVPLPPPLPPPEPESSEDPT	393
M. musculus	SPPEPQDLSSSICKEEKMPRGGSLESQDGPCKEPAKTQPMVA-----TTTTVAEKYKHRGEGERKDIVSSSMPPRNREEPVDSRTPVTERVS	484
R. norvegicus	SPPEPQDLSSSICKEEKMPRGGSLESQDGPCKEPAKTQPMVA-----TTTTVAEKYKHRGEGERKDIVSSSMPPRNREEPVDSRTPVTERVS	492
H. sapiens	SPPEPQDLSSVCKEEKMPRGGSLESQDGPCKEPAKTQPAVA-----TAATAAEKYKHRGEGERKDIVSSSMPPRNREEPVDSRTPVTERVS	486
S. scrofa	SPPEPQDLSSNVCREEKMPRGGSLESQDGPCKEPAKTQPAVA-----TAATAAEKYKHRGEGERKDIVSSSMPPRNREEPVDSRTPVTERVS	479

B



C

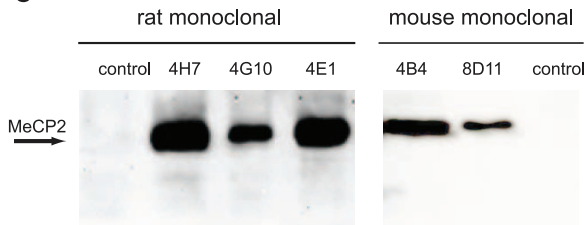


Figure 4. Antibody specificity. **A)** Sequence alignment of MeCP2 from different species. Identical residues are shaded in gray. The identities range from 93% (human-mouse) to 97% (rat-mouse). **B)** For a multi-species immunoblot nuclear extracts from pig, mouse and rat brain (10^6 nuclei) were loaded and probed with the antibodies as indicated. **C)** For immunoprecipitation analysis, mouse brain whole cell (for rat antibodies) and nuclei (for mouse antibodies) extracts were incubated with the monoclonal antibodies as indicated followed by western blot analysis.

doi:10.1371/journal.pone.0026499.g004

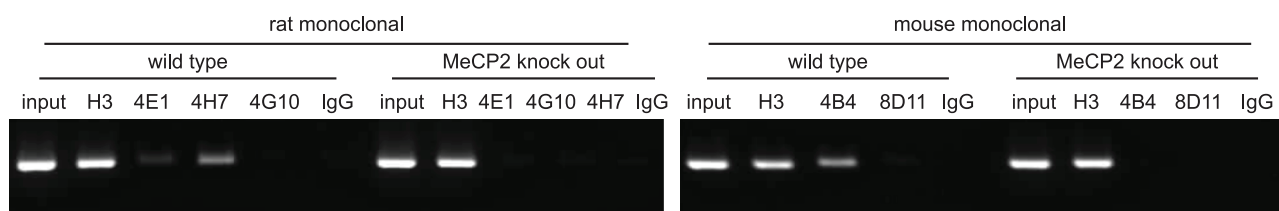
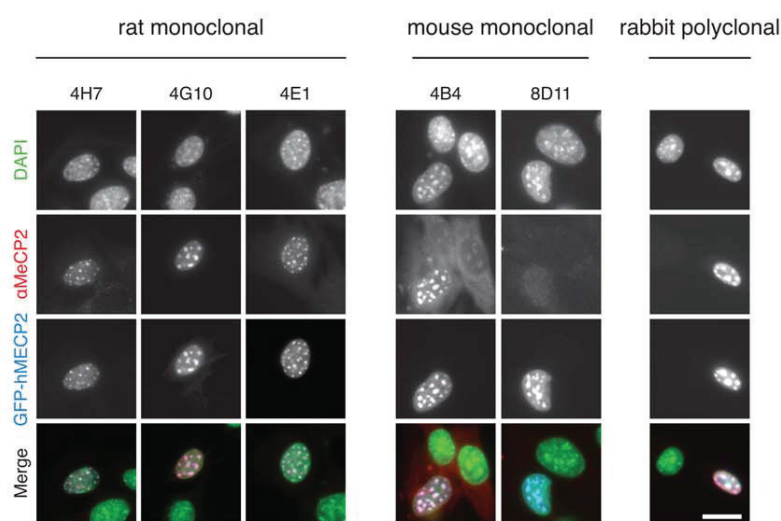


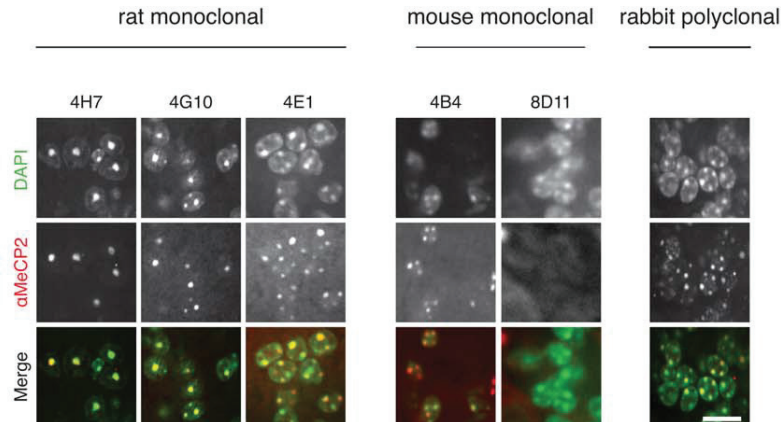
Figure 5. Chromatin immunoprecipitation. Chromatin immunoprecipitation assays were performed using mouse brain nuclear extracts obtained from wild type mice and MeCP2 knock out (KO) mice as negative control. The anti histone H3 antibody was used as a positive control of chromatin immunoprecipitation assay efficiency. IgG was used as a negative control of chromatin immunoprecipitation.

doi:10.1371/journal.pone.0026499.g005

A



B



C

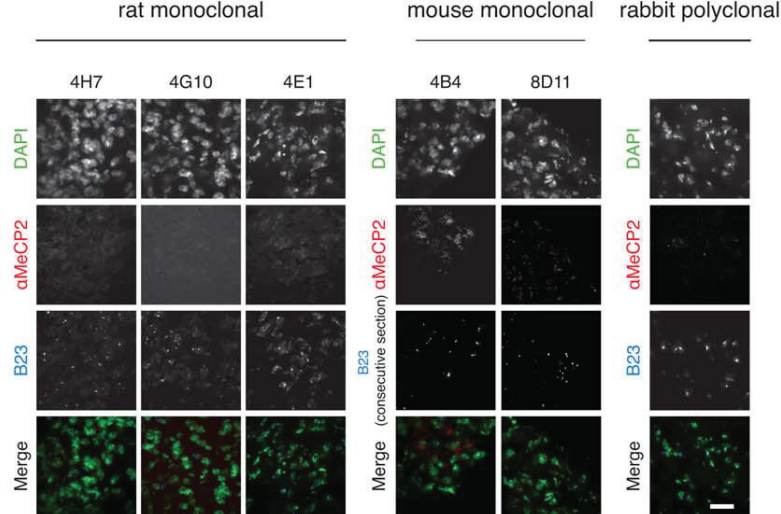


Figure 6. In situ analysis of MeCP2 in cells and tissue. **A**) Mouse myoblasts (C2C12 cells) were transiently transfected with GFP-MECP2 (human) and fixed using formaldehyde. MeCP2 was then detected with our monoclonal antibodies (undiluted) and our rabbit polyclonal antibody (1:500). The first row shows the DNA counterstain (DAPI) of transfected and untransfected cells (green). The row underneath shows the signal obtained by our antibody staining (red). The third row shows the localization of the transfected GFP-MECP2 (blue). The merge contains an overlay of the antibody staining, the fluorescent signal of GFP-MECP2 and the DNA counterstain. Scale bar 20 μ m. **B**) Mouse wild type brain sections (25 μ m) were stained using our antibodies. The first row shows the DNA counterstain with DAPI highlighting heterochromatic regions. The central row shows the signal obtained by immunofluorescence with our antibodies. The last row shows an overlay of DAPI and MeCP2. Scale bar 20 μ m. **C**) Mouse MeCP2 hemizygous null brain sections (25 μ m) were stained as described above as a negative control. Mouse anti B23 antibody was used as a positive control (consecutive section when testing mouse monoclonal anti MeCP2). Scale bar 40 μ m.

doi:10.1371/journal.pone.0026499.g006

injected both intraperitoneally and subcutaneously into Lou/C rats and CBL mice using CpG2006 (TIB MOLBIOL, Berlin, Germany) as adjuvant. 8 weeks later and 3 days before fusion a boost was given intraperitoneally and subcutaneously. Spleen cells were isolated and fused to the myeloma cell line P3X63-Ag8.653 (ATCC, Rockville, MD, USA) using polyethylene glycol 1500 (PEG 1500, Roche, Mannheim, Germany). After fusion, cells were cultured in 96-well plates using RPMI 1640 with 20% fetal calf serum, penicillin/streptomycin, glutamine, pyruvate, and non-essential amino acids (PAA, Cölbe, Germany) supplemented by aminopterin (Sigma, St. Louis, MO, USA). The hybridoma supernatants were tested in a solid-phase enzyme linked immunosorbent assay (ELISA). Microtiter plates were coated over night with strep-tagged rat MeCP2 at a concentration of 3–5 g/ml in 0.1 M sodium carbonate buffer (pH 9.6) and blocked with non-fat milk (Frema, Neuform, Zarrentin, Germany). The hybridoma supernatants were added and the bound monoclonal antibodies were detected using a cocktail of biotinylated mouse monoclonal antibodies against the rat IgG heavy chains, thus avoiding the detection of IgM mouse monoclonal antibodies (anti IgG1, anti IgG2a, anti IgG2b [ATCC, Manassas, VA], anti IgG2c [Ascension, Munich, Germany]). For visualization, peroxidase-labeled avidin (Alexis, San Diego, CA) antibodies were applied and o-phenylenediamine was used as chromogen in the peroxidase reaction. The clones 4H7, 4G10 and 4E1 (rat monoclonal) as well as 4B4 and 8D11 (mouse monoclonal) were stably subcloned and used for further characterization.

The rabbit polyclonal antibody was generated using the untagged human MECP2 according to the Express rabbit protocol from PickCell (PickCell, Amsterdam, Netherlands) and used in form of antiserum.

All monoclonal antibodies are available upon request.

Ethics statement

Immunizations of mice and rats for the purpose of generating monoclonal antibodies were approved by the Government of Upper Bavaria, according to the animal experimentation law § 8a, permit number 209.1/211-2531.6-4/99.

Sensitivity assay via slot blot analysis

Purification of MeCP2-GFP. SF9 insect cells were infected with the recombinant baculovirus (coding for rat MeCP2-GFP) and incubated at 28°C with shaking for 5 days. The cells were pelleted and resuspended as explained above for strep-tag MeCP2 and disrupted by sonication (three times each for 25 seconds, 70% power; Bandelin Sonopuls GM70, Sonontrude HD70, Berlin, Germany) on ice. Lysates were cleared by centrifugation at 15,000 \times g for 30 min at 4°C.

Recombinant rat MeCP2-GFP protein was purified by incubating 200 ml whole cell lysate with 1 ml (1.5 mg/ml) GBP nanotrap according to the manufacturer's advice (Chromotek, Planegg-Martinsried, Germany). After transfer of the GBP nanotrap beads containing lysate to a Bio-Rad Poly-Prep chromatog-

raphy column (Cat: 731-1550, Bio-Rad Laboratories, Hercules CA 94547, USA) the column was washed three times with 10 ml PBS. To elute the MeCP2-GFP protein, the beads were incubated with 5 ml of a high salt buffer. Buffer exchange was done with PBS using Amicon ultra centrifugal filters (Ultracel 10 kDa molecular weight cutoff; Millipore, Ireland). Eluted protein was quantified with Pierce the 660 nm protein assay (Thermo Scientific; Pro: #1861426, Schwerte, Germany) and checked by SDS-PAGE analysis (data not shown).

Slot blotting analysis. Native MeCP2-GFP was spotted directly onto a nitrocellulose membrane (GE Healthcare, München, Germany). Membranes were incubated in blocking buffer, 5% (w/v) non-fat dry milk in PBS (PBSM), for 20 min at room temperature. Primary antibodies were used undiluted and incubated for 2 h at room temperature, followed by three washes in PBS/0.1% Tween-20. Subsequently, membranes were incubated for 1 h at room temperature with horseradish peroxidase conjugated anti-rabbit IgG (Sigma, St. Louis, MO, USA) diluted 1:10,000 or anti-mouse (GE Healthcare, München, Germany) and rat IgG (Sigma, St. Louis, MO, USA) 1:5,000 in 5% (w/v) PBSM. After three washing steps in PBS/0.1% Tween-20, signals were detected with ECL (GE Healthcare, München, Germany).

Epitope mapping

For epitope mapping, different constructs of rat MeCP2 with C-terminal GFP or YFP tag were used for transient transfection of HEK 293T cells. After cell lysis (20 mM Tris-HCl pH 7.5, 150 mM NaCl, 0.5%NP40, 2 mM PMSF, 0.5 mM EDTA, 1 \times mammalian protease inhibitor mix, 1 mg/ml DNase, 2 mM MgCl₂) the concentration of the GFP fusion proteins was calculated using a fluorescent read out of GFP and YFP (Infinite® M1000, TECAN), respectively (GFP: excitation wavelength: 490 nm, emission wavelength: 511 nm, YFP: excitation wavelength: 525 nm, emission wavelength: 538 nm). The protein concentration was normalized to the construct with the lowest expression rate and lysates were diluted accordingly (228 nM GFP or YFP). The samples were boiled in Laemmli sample buffer at 95°C for 10 min and loaded on a 10% SDS-PAGE. Western blot analysis was performed as described above. In addition to the polyclonal and monoclonal anti MeCP2 antibodies, anti GFP mouse monoclonal antibody (Cat: 11814460001, Roche Diagnostics GmbH, Mannheim, Germany) was used to control for expression level of the different deletion proteins.

Cross-species reactivity assay via western blot analysis

For western blot analysis brain cell nuclei were extracted from pig (obtained fresh from the local slaughterhouse), mouse and rat (Charles River Laboratories International, Inc., Wilmington, MA 01887, USA) as described [25] and lysed in RIPA buffer (50 mM Tris/HCl pH 8, 150 mM NaCl, 1% Tween, 0.5% Doc, 0.1% SDS). For each gel lane, lysates from 10⁶ nuclei were loaded.

Samples were separated on a 10% SDS-PAGE and transferred to a nitrocellulose membrane (GE Healthcare, München, Germany). The following primary antibodies were used for western blot analysis: rabbit polyclonal anti MeCP2 (1:500), mouse monoclonal and rat monoclonal anti MeCP2 (undiluted). Secondary antibodies were as above for slot blot analysis.

Immunoprecipitation

Mechanically disrupted mouse brain tissue (3–4 brains) was dissolved in buffer A (20 mM Tris pH 7.9, 0.6 M NaCl, 1.5 mM MgCl₂, 0.2 mM EDTA, 0.4% NP-40), and then diluted with buffer B (20 mM Tris pH 7.9, 1.5 mM MgCl₂, 0.2 mM EDTA, 0.4% NP-40) to obtain an NaCl concentration of 200 mM. Mouse brain extracts were incubated with 400 µl of the rat monoclonal MeCP2 antibody indicated, at 4°C for 2 h with shaking. As negative control, anti RFP mix rat monoclonal antibody [26] of equal amount was used. 100 µl protein G agarose beads, that were equilibrated with buffer B, were added and incubated with the extract for 1 h at 4°C with shaking. After three washes with buffer B immuno complexes were dissolved in 60 µl 1× Laemmli sample buffer.

For successful immunoprecipitation using the mouse monoclonal antibodies nuclei had to be isolated first, followed by a modified protocol. Mechanically disrupted mouse brain tissue was resuspended and washed with ice-cold PBS supplemented with protease inhibitor cocktail (Roche, Mannheim, Germany). Cell pellets were resuspended in cell lysis buffer (HEPES 5 mM, KCl 85 mM, NP40 0.5% pH 8.0) supplemented with protease inhibitor cocktail and subsequently homogenized with a douncer. The nuclear pellet obtained was resuspended in nuclei lysis buffer (Tris-HCl 50 mM, EDTA 10 mM, SDS 1% pH 8.1) and sonicated with a Bioruptor (Diagenode) for 5 minutes (30 sec ON, 30 sec OFF cycles) to get a homogeneous extract.

The extract was diluted with immunoprecipitation buffer (SDS 0.1%, Triton X-100 1.1%, EDTA 1.2 mM, NaCl 165 mM, Tris-HCl 16.7 mM pH 8.1) and followed by a pre-clearing overnight at 4°C with magnetic beads (Invitrogen, Paisley PA4 9RF, UK). Non-related mouse IgG antibody was used as a negative control. The amount of extract that was used for each immunoprecipitation varied from 10–500 µg. Antibody-Dynabeads M-280 sheep anti-mouse IgG (Invitrogen, Paisley PA4 9RF, UK) were added to pre-cleared chromatin and incubated with shaking for 2 h at 4°C. 10 µg of nuclear extract were loaded as input. After three washes with immunoprecipitation buffer immuno complexes were eluted from the beads with 25 µl 2× Laemmli sample buffer.

Samples were analyzed by western blot as described above.

Chromatin immunoprecipitation

Nuclei were obtained from wild type and MeCP2 knock out male brain as described above with an additional cross-linking step, after mechanical disruption, with 1% formaldehyde for 10 min. Adding glycine to a final concentration of 0.125 M stopped the cross-linking reaction. The lysed nuclear pellet was sonicated with a Bioruptor (Diagenode) for 15 minutes (30 sec ON, 30 sec OFF cycles). The average chromatin size of the fragments obtained was ~300 bp. Magnetic beads were used for pre-clearing of diluted chromatin (over night at 4°C) and for incubation (2 h at 4°C with shaking) with H3 (ab1791, Abcam), our rat monoclonal antibodies: 4E1, 4H7, and 4G10 or our mouse monoclonal antibodies: 4B4 and 8D11. Non-related mouse IgG antibody was used as a negative control. The input was obtained from the nuclear extract and represents 5% of the chromatin that is used for the chromatin immunoprecipitation

with each antibody. The immuno-complexes were washed: twice with low salt buffer (Tris-HCl 50 mM pH 8.0, NaCl 150 mM, SDS 0.1%, NP-40 1%, EDTA 1 mM, deoxicolate Na 0.5%), twice with high salt buffer (Tris-HCl 50 mM pH 8.0, NaCl 500 mM, SDS 0.1%, NP-40 1%, EDTA 1 mM, Na deoxicolate 0.5%), twice with LiCl buffer (Tris-HCl 50 mM pH 8.0, LiCl 250 mM, SDS 0.1%, NP-40 1%, EDTA 1 mM, Na deoxicolate 0.5%) and twice with TE buffer (Tris-HCl 10 mM pH 8.0, EDTA 0.25 mM). Cross-linked chromatin was then eluted from the magnetic beads (Dynabeads M-280 sheep anti-mouse IgG for mouse monoclonal antibodies and protein G for rat monoclonal antibodies) by adding elution buffer (NaHCO₃ 100 mM, SDS 1%). Samples were reverse cross-linked over night at 65°C and incubated with proteinase K at 50 µg/ml final concentration for 1 h. DNA was purified with the PCR purification kit (Qiagen) and used for PCR analysis, which was carried out with the following primers:

Xist (promoter) 5'-CCTGTACGACCTAAATGTCC-3'
5'-GTATTAGTGTGCGGTGTTGC-3'.

In the case of our rat monoclonal antibodies 38 PCR cycles were used and in the case of our mouse monoclonal antibodies 35 cycles.

Immunofluorescence analysis

Cells. For immunofluorescence staining, C2C12 cells were seeded on glass coverslips and transiently transfected with GFP tagged MECP2 (human). Cells were fixed with 3.7% formaldehyde in PBS and incubated with the undiluted rat/mouse anti MeCP2 antibodies for 1 h at room temperature. After incubation with the secondary Alexa 647 conjugated goat anti rat/mouse IgG antibody (Invitrogen Paisley PA4 9RF, UK) diluted 1:400 in PBS containing 2% BSA, the cells were counterstained with DAPI (2 µg/ml) and mounted in Vectashield medium (Vector Labs, Burlingame, CA, USA).

Tissues. Mouse brains were fixed by overnight immersion in PBS-buffered 4% paraformaldehyde. The brains were embedded in Tissue Tek (Sakura, Zoeterwoude, Netherlands) and cryosectioned (25 µm) using a cryostat HM 560 (Microm, Walldorf, Germany).

Sections were air dried at room temperature for 30 min, rehydrated in 10 mM sodium citrate buffer (pH 6.0) for 5 min, pulse-heated (80°C) for 30 min in the microwave. The slides were equilibrated in PBS after heating and incubated with the following antibodies: anti MeCP2 mouse monoclonal (undiluted), rat monoclonal (undiluted), rabbit polyclonal (1:500), anti B23 mouse monoclonal (Sigma, St. Louis, MO, USA, 1:1,000) and anti tyrosine hydroxylase rabbit antibody (AB152, Millipore, Billerica, MA, USA) Both, primary and secondary antibodies were complemented with 0.1% Triton X-100 and 1% BSA. No additional blocking step was performed. Incubation was done under a glass chamber (made of coverslips) in a humid box for 12–24 h at room temperature [27]. Washings between antibody incubations and after incubation with secondary antibodies were performed with PBS with 0.05% Triton X-100 at 37°C, 3×20 min. In order to stabilize preparations, immunostained sections were post-fixed with 2% paraformaldehyde for 10 min before counterstaining with DAPI (2 µg/ml) for 1 h and mounted in Vectashield medium (Vector Labs, Burlingame, CA, USA).

Microscopy

Epifluorescence images were obtained on a Zeiss Axiovert 200 microscope equipped with Plan-Apochromat ×63/1.4 numerical aperture (NA) oil immersion objective lenses and a Sensicam (PCO) CCD camera. Confocal images were collected using an

UltraVIEW VoX spinning disc system (Perkin Elmer) on a Nikon Ti microscope equipped with an oil immersion Plan-Apochromat $\times 40/1.3$ NA objective lens (pixel size in XY = 186 nm, Z-step = 0.3 μ m).

Scoring of tyrosine hydroxylase and MeCP2 positive cells was done by eye in z-stacks.

Results and Discussion

Generation of rat/mouse monoclonal antibodies against MeCP2

To generate new rat and mouse antibodies potentially detecting different domains of MeCP2, we generated a baculovirus expression plasmid coding for the full length rat MeCP2 with a double strep-tag and transfected/infected Sf9 insect cells with this construct. The recombinant protein was purified using strep-tactin sepharose leading to a single band in SDS-PAGE analysis (Figure 1). The protein was used to immunize Lou/C rats and CBL mice, leading to the generation of a panel of clonal hybridomas by fusion of lymphocytes from immunized animals with the myeloma cell line P3X63-Ag8.653. All antibodies generated by the hybridomas were initially screened in a solid-phase enzyme linked immunosorbent assay (ELISA, data not shown). Positive hybridoma supernatants from clones 4H7, 4G10 and 4E1 (rat monoclonal) as well as 4B4 and 8D11 (mouse monoclonal) were stably subcloned and used for further characterization. In parallel, we immunized rabbits with untagged human MECP2 protein to generate polyclonal antibodies and used the resulting antiserum directly.

Sensitivity of the rat and mouse antibodies

To test the sensitivity of the antibodies we performed slot blot analysis with native rat MeCP2-GFP protein. The protein was applied in decreasing amounts ranging from 25 ng down to 0.78 ng. All monoclonal antibodies showed clear signals down to 1.56 ng of native protein and the rat monoclonal antibody 4E1 was still able to detect 0.78 ng of MeCP2 protein (Figure 2). The rabbit anti MeCP2 polyclonal antiserum was also able to detect down to 0.78 ng of native protein (Figure 2). The last column contained 500 ng BSA as negative control and none of the antibodies reacted with it.

Epitope mapping

To determine the binding domain of the new monoclonal antibodies within the MeCP2 protein, we used different constructs of GFP/YFP tagged MeCP2 expressed in mammalian cells. The cell lysates were analyzed by SDS-PAGE, blotted on a nitrocellulose membrane and incubated with the different antibodies. All fusions were expressed as controlled by incubation of the membranes with anti GFP mouse monoclonal antibody. The results (Figure 3 and S1A) show that the rat monoclonal antibodies 4G10 and 4H7 reacted against the C-terminus of MeCP2 and 4E1 against the N-terminus. Both mouse monoclonal antibodies 4B4 and 8D11 showed specific binding to the C-terminus. Since none of the antibodies detected the MBD domain, which is highly conserved in all MBD proteins no cross-reaction with these proteins is expected. Additionally, the polyclonal rabbit antibody detected all fragments except the TRD.

Specificity and cross species reactivity

MeCP2 is highly conserved throughout different species (Figure 4A). To test for cross species reactivity, nuclei from pig, mouse and rat brain tissue were isolated and extracts analyzed by western blot. As shown in Figure 4B all antibodies detected

endogenous MeCP2 in mouse and rat. Remarkably, the rat monoclonal antibody 4E1 was the only one that did not detect MeCP2 in nuclear extracts from pig brain. This coincides with the fact that it is the only antibody in our tests to react with the N-terminal part (amino acids 1–78) of MeCP2 (see below). Only five amino acids are not identical in this domain of MeCP2 in the pig compared to mouse and rat. We, thus, conclude that the epitope recognized by rat monoclonal antibody 4E1 must include one or more of these residues (Figure 4A, highlighted in red).

An important and commonly used method for studying protein interaction partners is immunoprecipitation. Thus, we tested next the ability of the monoclonal antibodies to specifically immunoprecipitate MeCP2 from mouse brains. We could show that our three rat antibodies were able to specifically pull down MeCP2 from whole brain extract (Figure 4C). Additional unspecific bands at 35 kDa were also detected in the negative control (rat anti RFP antibody mix) [26] and are most probably due to unspecific binding to the beads (data not shown). To successfully use our two mouse monoclonal antibodies for immunoprecipitation we needed to isolate nuclei from mouse brain first. We could then show that our mouse antibodies were also capable of specifically pulling down MeCP2 from mouse brain nuclei extracts (Figure 4C).

To next determine if our monoclonal MeCP2 antibodies are competent for chromatin immunoprecipitation analysis using purified nuclei from mouse brain. We analyzed the occupancy of MeCP2 in the promoter of *Xist* in the X chromosome, which is known to bind MeCP2 in mouse and is used as a standard positive control for MeCP2 binding. Two of our rat monoclonal antibodies were able to immunoprecipitate chromatin (4E1 and 4H7, Figure 5) with 4H7 producing a stronger signal than 4E1 and 4G10 not yielding a detectable signal. The latter might be due to technical limitations, or to the epitope recognized by the 4G10 mAb being masked when the MeCP2 protein is bound to chromatin. From our mouse antibodies only 4B4 was able to clearly chromatin immunoprecipitation (Figure 5). The three antibodies (rat 4E1 and 4H7 and mouse 4B4) suitable for chromatin immunoprecipitation show no band in the knockout brain whereas H3, which is used as positive control for chromatin immunoprecipitation, shows a band in wild type and knock out brain. Our polyclonal rabbit anti MeCP2 antibody was previously shown to be suitable for chromatin immunoprecipitation analysis [28]. Our antibodies therefore cover the whole range of important biochemical assays commonly performed.

In situ analysis of MeCP2 in cells and in tissue

Western blot techniques usually deal with denatured protein and do not give information about the localization of the protein in the cell. It is therefore important to test whether the new antibodies correctly detect MeCP2 localization *in situ*. MeCP2 is predominantly localized at pericentric heterochromatic regions in mouse cells, which are highly enriched in strongly methylated major satellite DNA repeats and tend to form clusters known as chromocenters [14]. Immunostainings were thus performed on mouse myoblasts expressing GFP tagged human MECP2 using formaldehyde and methanol as fixation reagents (Figure 6A and S1B). Our three rat monoclonal antibodies revealed strong signals co-localizing with the ectopically expressed GFP-MECP2 and worked in both fixation conditions. Untransfected cells did not give a signal, consistent with undetectable endogenous levels of MeCP2 in those cells [14]. Using the mouse monoclonals, only 4B4 gave a signal for ectopically expressed protein. 8D11 exhibited high background noise and no specific binding in both fixation conditions. Our polyclonal rabbit antiserum showed

strong and specific binding even when used at a dilution of 1:500. DAPI was used as a counterstain and additional control in all cells since DAPI's preference for AT rich regions strongly highlights chromocenters.

Since MeCP2 plays a crucial role in RTT syndrome one of the most important goals for us was to test whether the antibodies work on brain tissue detecting MeCP2 in its native conformation. We, therefore, prepared cryosections of wild type mouse brain and also MeCP2 hemizygous null male mouse brain as negative control. The 25 μ m-thick wild type brain sections were stained with the anti MeCP2 antibodies and counterstained with DAPI as marker for chromocenters. As demonstrated in Figure 6B our rat monoclonal antibodies show a strong and specific staining of chromocenters colocalizing with DAPI. Our mouse monoclonal antibody 4B4 shows a less intense but still specific staining of MeCP2. Unfortunately, the antibody 8D11 was not able to detect endogenous MeCP2 in brain, as it had failed to do with ectopic MeCP2 expression in cells, and is therefore not suitable for immunofluorescence. The strongest signals were achieved with our polyclonal rabbit antiserum, which was used as a positive control (Figure 6B). To verify the specificity to MeCP2 we performed the same stainings in MeCP2 null mouse brain sections. We added anti B23 nucleoli marker antibody as a positive staining control. As shown in Figure 6C none of the anti MeCP2 antibodies showed any significant signal in the knock out

brain sections whereas B23 showed a clear and specific signal. The double staining with anti-B23 mouse monoclonal antibody was facilitated by the combination with our rat monoclonals, whereas, in the case of the mouse monoclonals, we had to perform the anti B23 staining using an adjacent tissue section. Additionally, using rat monoclonal antibodies obviated the cross reaction with endogenous mouse immunoglobulins present in the tissue, whereas these were readily detected when using the mouse monoclonal antibodies.

X chromosome inactivation skewing in MeCP2 heterozygous mouse brain

Since MeCP2 lies on the X chromosome it is subjected to random X chromosome inactivation in early development. In RTT, X chromosome inactivation leads to a mosaic pattern of all the cells, theoretically in a 50:50 ratio of healthy (active X containing wild type *MeCP2* allele) and affected (active X containing mutant *MeCP2* allele) cells. Deviations from this ratio indicate skewed inactivation of the X chromosome and affect the severity of RTT symptoms. Our antibodies should be highly suitable for studies concerning X chromosome inactivation as well as other studies on RTT affected brain and other tissues.

To test this, we evaluated X chromosome inactivation skewing in female MeCP2 heterozygous brain. We performed a double

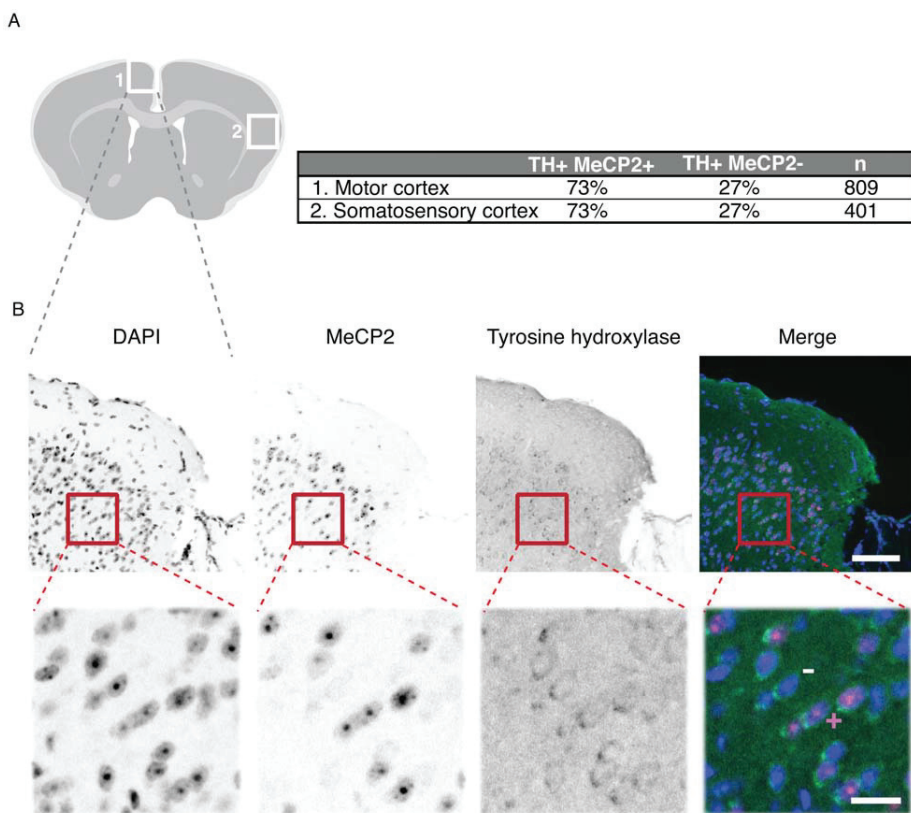


Figure 7. X chromosome inactivation skewing in brain from heterozygous MeCP2 null mouse. **A)** Schematic overview of a cryosection of a (female) heterozygous MeCP2 null brain with regions analyzed for X chromosome inactivation skewing marked with white squares. The results of the quantification of tyrosine hydroxylase positive, MeCP2 positive or negative cells are shown. N indicates the number of tyrosine hydroxylase positive neurons scored. **B)** Representative images of a section co stained with DAPI (DNA), anti MeCP2 (4H7) and anti tyrosine hydroxylase antibodies. The motor cortex region is depicted in an overview (upper panels; scale bar 80 μ m). A magnification corresponding to the red square is shown in the lower panels (scale bar 20 μ m). To illustrate the scoring strategy, an example of tyrosine hydroxylase and MeCP2 positive neuron is marked by + and of tyrosine hydroxylase positive and MeCP2 negative neuron is marked by -.

doi:10.1371/journal.pone.0026499.g007

Subtype	rat monoclonal			mouse monoclonal		rabbit polyclonal
	4H7	4G10	4E1	4B4	8D11	
Native immuno (slot blot)	✓	✓	✓	✓	✓	✓
Immunoprecipitation	✓	✓	✓	✓	✓	✓
Chromatin immunoprecipitation	✓	+/-	✓	✓	—	✓
Western blot	✓	✓	✓	✓	✓	✓
Immunofluorescence (cells) ¹	✓	✓	✓	✓	—	✓
Immunofluorescence (tissue)	✓	✓	✓	✓	—	✓
Epitope	C	C	N	C	C	
Species reactivity ²	H, P, R, M	H, P, R, M	H, R, M	H, P, R, M	P, R, M	H, P, R, M

¹Methanol and formaldehyde fixation ²Not all species were tested in all methods listed above H = Human; P = Pig; R = Rat; M = Mouse

Figure 8. Summary of the characterization of the rabbit, rat and mouse anti MeCP2 antibodies.
doi:10.1371/journal.pone.0026499.g008

staining with rabbit anti tyrosine hydroxylase (TH) and our rat MeCP2 antibody (4H7). TH is the first enzyme in the biosynthesis of dopamine and norepinephrine from tyrosine and is, therefore, a marker for dopaminergic and noradrenergic neurons. Roux et al. [29] showed that TH positive cells always co-expressed MeCP2 and, hence, X chromosome inactivation skewing can be obtained by counting TH positive cells with and without MeCP2 signal. We focused on two areas of the cortex, the motor cortex and the somatosensory cortex (Figure 7). In both cases we could observe a pronounced X chromosome inactivation skewing favoring wild type MeCP2 expression (73%). Previously published mouse data suggest that X chromosome inactivation skewing in brain is the reason for very different phenotypes in RTT [30]. The degree of skewing is controversial and might dependent on the tissue analyzed or the method applied [30,31]. Our antibodies could help to elucidate the state of X chromosome inactivation in RTT tissue in particular also with respect to truncated versus full length MeCP2 by a combination of the N and C-terminal specific antibodies.

Figure 8 summarizes the characterization of the novel anti MeCP2 antibodies. The antibodies recognize MeCP2 from different species, including human, mouse, rat and pig. Whereas the two new mouse antibodies are suitable for western blot, immunoprecipitation and to a lesser extend for immunofluorescence, the rabbit polyclonal as well as the rat monoclonal antibodies performed very well in immunoblotting, immunoprecipitation, and immunofluorescence analysis of ectopic and endogenous MeCP2. In addition, one mouse and two rat monoclonal antibodies as well as the rabbit polyclonal antiserum perform well in chromatin immunoprecipitation making them a

very valuable set of tools for studies of MeCP2 pathophysiology *in situ* and *in vitro*.

Supporting Information

Figure S1 A) Epitope mapping. Complete blots of the epitope mapping presented in Figure 3 together with a schematic representation of the constructs. **B) *In situ* analysis of MeCP2 in cells.** Mouse myoblasts (C2C12 cells) were transiently transfected with GFP-MECP2 (human) and fixed with methanol. MECP2 was then detected with our monoclonal antibodies (undiluted) and our rabbit polyclonal antibody (1:500). The first row shows the DNA counterstain (DAPI) of transfected and untransfected cells (green). The row underneath shows the signal obtained by our antibody staining (red). The third row shows the localization of the transfected GFP-MECP2 (blue). The merge contains an overlay of the antibody staining, the fluorescent signal of GFP-MECP2 and the DNA counterstain. Scale bar 20 μ m. (PDF)

Acknowledgments

We would like to thank P. Huppke and C. Brendel (Georg August University, Göttingen, Germany) for the generous gift of MeCP2 knock out mouse brain and L. Villard and J-C. Roux (Faculte de Medecine La Timone, Marseille, France) for the generous gift of heterozygous MeCP2 knock out brain. We would also like to thank C. L. Woodcock (University of Massachusetts, Amherst, USA) for the generous gift of the plasmid expressing intein tagged human MECP2 and S. Kudo (Hokkaido Institute of Public Health, Sapporo, Japan) for providing the GFP-tagged human MECP2 mammalian expression construct. Last but not least, we would like to thank A. Lemkuhl, M. Hofstaetter and D. Nowak for technical expertise as well as I. Solovei and B. Joffe for help and discussions.

Author Contributions

Conceived and designed the experiments: HL MCC. Performed the experiments: AB EK MM AR PW KLJ BB PP JS DH ME. Analyzed the data: KLJ BB. Wrote the paper: KLJ MCC.

References

- Meehan RR, Lewis JD, Bird AP (1992) Characterization of MeCP2, a vertebrate DNA binding protein with affinity for methylated DNA. *Nucleic Acids Res* 20: 5085–5092.
- Lewis JD, Meehan RR, Henzel WJ, Maurer-Fogy I, Jeppesen P, et al. (1992) Purification, sequence, and cellular localization of a novel chromosomal protein that binds to methylated DNA. *Cell* 69: 905–914.
- Jones KW (1970) Chromosomal and nuclear location of mouse satellite DNA in individual cells. *Nature* 225: 912–915.
- Jones PL, Veenstra GJ, Wade PA, Vermaak D, Kass SU, et al. (1998) Methylated DNA and MeCP2 recruit histone deacetylase to repress transcription. *Nat Genet* 19: 187–191.
- Nan X, Campoy FJ, Bird A (1997) MeCP2 is a transcriptional repressor with abundant binding sites in genomic chromatin. *Cell* 88: 471–481.
- Nan X, Ng HH, Johnson CA, Laherty CD, Turner BM, et al. (1998) Transcriptional repression by the methyl-CpG-binding protein MeCP2 involves a histone deacetylase complex. *Nature* 393: 386–389.
- Rett A (1966) [On an unusual brain atrophy syndrome in hyperammonemia in childhood]. *Wien Med Wochenschr* 116: 723–726.
- Amir RE, Van den Veyver IB, Wan M, Tran CQ, Francke U, et al. (1999) Rett syndrome is caused by mutations in X-linked MECP2, encoding methyl-CpG-binding protein 2. *Nat Genet* 23: 185–188.
- Hagberg B (1985) Rett's syndrome: prevalence and impact on progressive severe mental retardation in girls. *Acta Paediatr Scand* 74: 405–408.
- Hagberg B, Aicardi J, Dias K, Ramos O (1983) A Progressive Syndrome of Autism, Dementia, Ataxia, and Loss of Purposeful Hand Use in Girls - Rett's Syndrome - Report of 35 Cases. *Annals Neurol* 14: 471–479.
- Amir RE, Zoghbi HY (2000) Rett syndrome: methyl-CpG-binding protein 2 mutations and phenotype-genotype correlations. *Am J Med Genet* 97: 147–152.
- Chahrour M, Zoghbi HY (2007) The story of Rett syndrome: from clinic to neurobiology. *Neuron* 56: 422–437.
- Shahbazian MD, Antalffy B, Armstrong DL, Zoghbi HY (2002) Insight into Rett syndrome: MeCP2 levels display tissue- and cell-specific differences and correlate with neuronal maturation. *Hum Mol Genet* 11: 115–124.
- Brero A, Easwaran HP, Nowak D, Grunewald I, Cremer T, et al. (2005) Methyl CpG-binding proteins induce large-scale chromatin reorganization during terminal differentiation. *J Cell Biol* 169: 733–743.
- Agarwal N, Hardt T, Brero A, Nowak D, Rothbauer U, et al. (2007) MeCP2 interacts with HPI and modulates its heterochromatin association during myogenic differentiation. *Nucleic Acids Res* 35: 5402–5408.
- Kudo S, Nomura Y, Segawa M, Fujita N, Nakao M, et al. (2003) Heterogeneity in residual function of MeCP2 carrying missense mutations in the methyl CpG binding domain. *J Med Genet* 40: 487–493.
- Yusufzai TM, Wolffe AP (2000) Functional consequences of Rett syndrome mutations on human MeCP2. *Nucleic Acids Res* 28: 4172–4179.
- Guy J, Hendrich B, Holmes M, Martin JE, Bird A (2001) A mouse Mecp2-null mutation causes neurological symptoms that mimic Rett syndrome. *Nat Genet* 27: 322–326.
- Yaffe D, Saxel O (1977) Serial passaging and differentiation of myogenic cells isolated from dystrophic mouse muscle. *Nature* 270: 725–727.
- Cardoso MC, Leonhardt H, Nadal-Ginard B (1993) Reversal of terminal differentiation and control of DNA replication: cyclin A and Cdk2 specifically localize at subnuclear sites of DNA replication. *Cell* 74: 979–992.
- Suetake I, Mishima Y, Kimura H, Lee YH, Goto Y, et al. (2011) Characterization of DNA-binding activity in the N-terminal domain of the DNA methyltransferase Dnmt3a. *Biochem J* 437: 141–148.
- Gloeckner CJ, Boldt K, Schumacher A, Roepman R, Ueffing M (2007) A novel tandem affinity purification strategy for the efficient isolation and characterisation of native protein complexes. *Proteomics* 7: 4228–4234.
- Georgel PT, Horowitz-Scherer RA, Adkins N, Woodcock CL, Wade PA, et al. (2003) Chromatin compaction by human MeCP2. Assembly of novel secondary chromatin structures in the absence of DNA methylation. *J Biol Chem* 278: 32181–32188.
- Rottach A, Kremmer E, Nowak D, Boisguerin P, Volkmer R, et al. (2008) Generation and characterization of a rat monoclonal antibody specific for PCNA. *Hybridoma* 27: 91–U99.
- Prusov AN, Zatsepina OV (2002) Isolation of the chromocenter fraction from mouse liver nuclei. *Biochemistry* 67: 423–431.
- Rottach A, Kremmer E, Nowak D, Leonhardt H, Cardoso MC (2008) Generation and Characterization of a Rat Monoclonal Antibody Specific for Multiple Red Fluorescent Proteins. *Hybridoma* 27: 337–343.
- Solovei I, Kreysing M, Lanctot C, Kosem S, Peichl L, et al. (2009) Nuclear architecture of rod photoreceptor cells adapts to vision in mammalian evolution. *Cell* 137: 356–368.
- Vasiliou SA, Ali FR, Haddley K, Cardoso MC, Bubb VJ, et al. (2011) The SLC6A4 VNTR genotype determines transcription factor binding and epigenetic variation of this gene in response to cocaine in vitro. *Addict Biol*. doi: 10.1111/j.1369-1600.2010.00288.x.
- Roux JC, Dura E, Villard L (2008) Tyrosine hydroxylase deficit in the chemoafferent and the sympatheticoadrenergic pathways of the Mecp2 deficient mouse. *Neurosci Lett* 447: 82–86.
- Young JI, Zoghbi HY (2004) X-chromosome inactivation patterns are unbalanced and affect the phenotypic outcome in a mouse model of rett syndrome. *Am J Hum Genet* 74: 511–520.
- Gibson JH, Williamson SL, Arbuckle S, Christodoulou J (2005) X chromosome inactivation patterns in brain in Rett syndrome: implications for the disease phenotype. *Brain Dev* 27: 266–270.



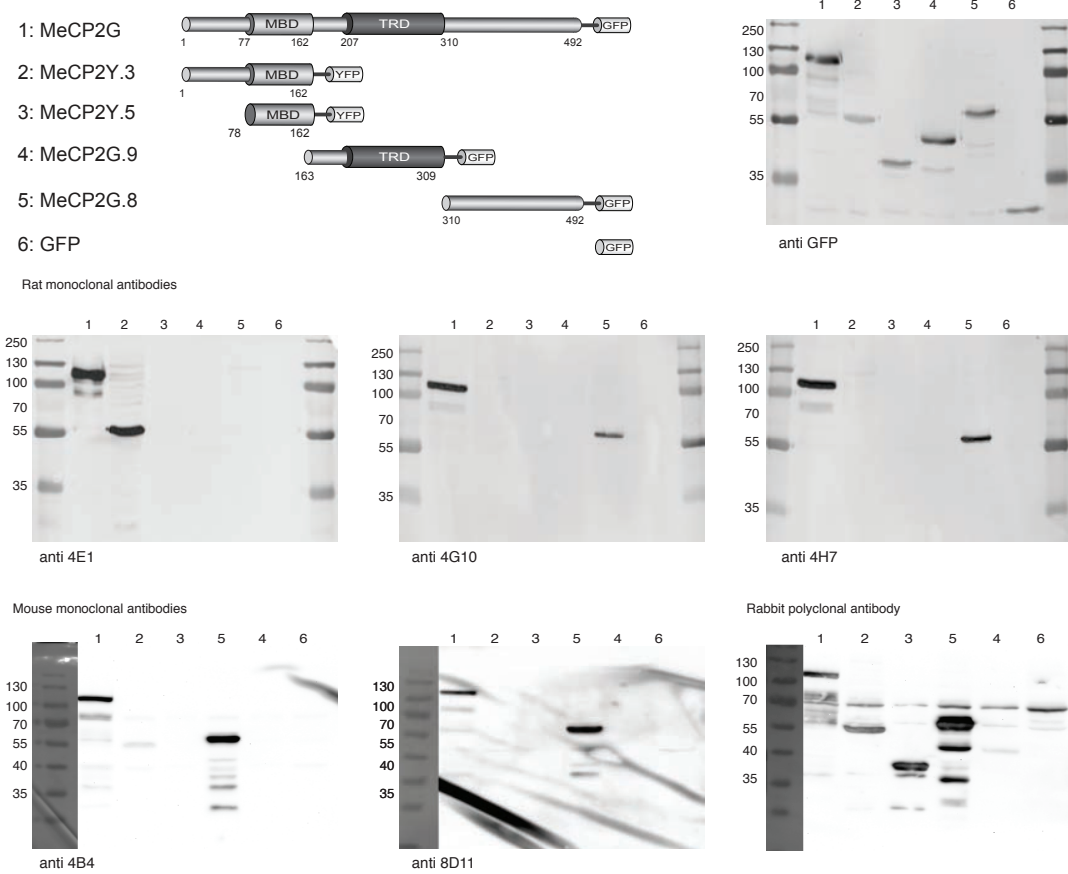
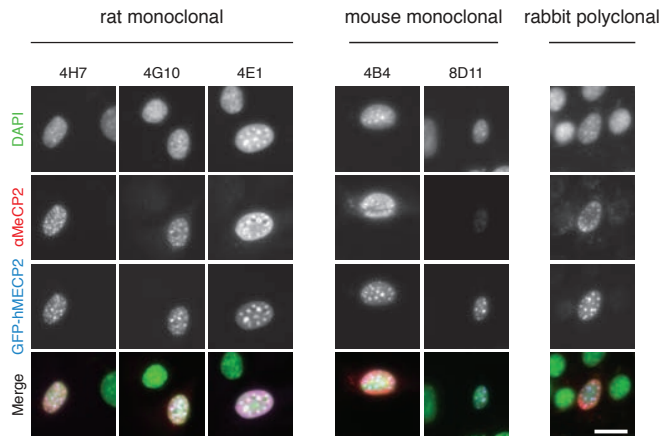
A**B**

Figure S1. A) Epitope mapping. Complete blots of the epitope mapping presented in Figure 3 together with a schematic representation of the constructs. **B) *In situ* analysis of MeCP2 in cells.** Mouse myoblasts (C2C12 cells) were transiently transfected with GFP-MECP2 (human) and fixed with methanol. MECP2 was then detected with our monoclonal antibodies (undiluted) and our rabbit polyclonal antibody (1:500). The first row shows the DNA counterstain (DAPI) of transfected and untransfected cells (green). The row underneath shows the signal obtained by our antibody staining (red). The third row shows the localization of the transfected GFP-MECP2 (blue). The merge contains an overlay of the antibody staining, the fluorescent signal of GFP-MECP2 and the DNA counterstain. Scale bar 20 μ m.

2.2 Versatile toolbox for high throughput biochemical and functional studies with fluorescent fusion proteins

Versatile Toolbox for High Throughput Biochemical and Functional Studies with Fluorescent Fusion Proteins

Garwin Pichler^{1*}, Antonia Jack², Patricia Wolf¹, Sandra B. Hake²

1 Department of Biology II and Center for Integrated Protein Science Munich (CIPSM), Ludwig Maximilians University Munich, Planegg-Martinsried, Munich, Germany

2 Center for Integrated Protein Science Munich at the Adolf-Butenandt Institute, Department of Molecular Biology, Ludwig Maximilians University of Munich, Munich, Germany

Abstract

Fluorescent fusion proteins are widely used to study protein localization and interaction dynamics in living cells. However, to fully characterize proteins and to understand their function it is crucial to determine biochemical characteristics such as enzymatic activity and binding specificity. Here we demonstrate an easy, reliable and versatile medium/high-throughput method to study biochemical and functional characteristics of fluorescent fusion proteins. Using a new system based on 96-well micro plates comprising an immobilized GFP-binding protein (GFP-mulitTrap), we performed fast and efficient one-step purification of different GFP- and YFP-fusion proteins from crude cell lysate. After immobilization we determined highly reproducible binding ratios of cellular expressed GFP-fusion proteins to histone-tail peptides, DNA or selected RFP-fusion proteins. In particular, we found Cbx1 preferentially binding to di- and trimethylated H3K9 that is abolished by phosphorylation of the adjacent serine. DNA binding assays showed, that the MBD domain of MeCP2 discriminates between fully methylated over unmethylated DNA and protein-protein interactions studies demonstrate, that the PBD domain of Dnmt1 is essential for binding to PCNA. Moreover, using an ELISA-based approach, we detected endogenous PCNA and histone H3 bound at GFP-fusions. In addition, we quantified the level of H3K4me2 on nucleosomes containing different histone variants. In summary, we present an innovative medium/high-throughput approach to analyse binding specificities of fluorescently labeled fusion proteins and to detect endogenous interacting factors in a fast and reliable manner *in vitro*.

Citation: Pichler G, Jack A, Wolf P, Hake SB (2012) Versatile Toolbox for High Throughput Biochemical and Functional Studies with Fluorescent Fusion Proteins. PLoS ONE 7(5): e36967. doi:10.1371/journal.pone.0036967

Editor: Pierre-Antoine Defossez, Université Paris-Diderot, France

Received January 12, 2012; **Accepted** April 10, 2012; **Published** May 11, 2012

Copyright: © 2012 Pichler et al. This is an open-access article distributed under the terms of the Creative Commons Attribution License, which permits unrestricted use, distribution, and reproduction in any medium, provided the original author and source are credited.

Funding: GP was supported by the International Doctorate Program NanoBioTechnology (IDK-NBT, <http://www.cens.de/doctorate-program/>) and GP and AJ by the International Max Planck Research School for Molecular and Cellular Life Sciences (IMPRS-LS, <https://www.imprs-ls.de/>). PW is a fellow of the Graduate School Life Science Munich (LSM, <http://www.lsm.bio.lmu.de/>). SBH was supported by CIPSM (<http://www.cipsm.de/en/index.html>) and the DFG (<http://www.dfg.de/index.jsp>). The funders had no role in study design, data collection and analysis, decision to publish, or preparation of the manuscript.

Competing Interests: The authors have declared that no competing interests exist.

* E-mail: pichler@bio.lmu.de

Introduction

Over the past decade a variety of proteomic approaches have been used to identify cellular components in order to understand the mechanism and inner workings of cells [1]. For example, mass spectrometry-based proteomics uncovered the proteome of many different organisms as well as cell-type specific differences in protein expression. However, to understand and characterize the function of single proteins, as well as the interplay between different factors, it is essential to gain further insights into their abundance, localization, dynamic interactions and substrate specificities.

Fluorescent proteins like the green fluorescent proteins (GFP) [2] and spectral variants have become popular tools to study the localization and dynamic interactions of proteins *in vivo*. Despite, the availability of a variety of commercial mono- and polyclonal antibodies against GFP and other fluorescent proteins [3,4] (e.g. Abcam, UK; Sigma, USA; Roche, Germany, ChromoTek, Germany), proteins are mostly fused to a small epitope tag such as FLAG or c-Myc to analyze biochemical characteristics like enzymatic activities and/or binding specificities. Thus, integration of such *in vitro* data with *in vivo* data obtained with fluorescently labeled proteins has, in part, been impeded by the simple fact that

different protein tags are used for different applications. The gold standard to examine binding affinities is surface plasmon resonance (SPR) [5]. One drawback of this method is the need of large amount of proteins. Such proteins have to be expressed and purified from bacterial systems (e.g. *E.coli*) or lower eukaryotes such as yeast (e.g. *S. cerevisiae*). Thus, the recombinant proteins lack essential post-translational modifications or are not folded properly possibly leading to different binding properties and inaccurate results. In addition with SPR measurements one can only determine the binding affinity to one substrate. This does not reflect the *in vivo* situation where most proteins have the choice between many different binding substrates in parallel.

Protein microarrays are an alternative to study protein-protein interactions in high-throughput manner [6]. Once more the drawback of this *in vitro* method is the laborious and time-consuming preparation of recombinant proteins or protein domains. Therefore protein microarrays are limited to domains that can be produced as soluble, well-folded proteins [6].

Recently, specific GFP binding proteins based on single domain antibodies derived from *Lama alpaca* have been described [7] (GFP-Trap ChromoTek, Germany). The GFP-Trap exclusively binds to wtGFP, eGFP and GFP^{S65T} as well as to YFP and eYFP. Coupling to matrices including agarose beads or magnetic

particles the GFP-Trap allows for one-step purification of GFP-fusion proteins. Previous studies made use of the GFP-Trap to perform a broad range of different methods including mass spectrometry analysis [8], DNA binding, DNA methyltransferase activity assays [9], as-well-as histone-tail peptide binding assays [10]. One major disadvantage of the GFP-Trap is, that batch purification of GFP-fusions is very laborious and time-consuming and one cannot test different GFP-fusion and/or assay conditions in parallel. Here, we present an innovative and versatile high-throughput method to quantitatively measure binding specificities and to detect endogenous interacting factors in a fast and reliable manner *in vitro*: 96-well micro plates coated with immobilized GFP-Trap (GFP-multiTrap). To demonstrate the general suitability of our assays, we choose already known binding partners and compared our results with previous publications. Using this method, we could confirm that Cbx1 preferentially binds to di- and trimethylated histone H3 lysine 9 and that this binding is abolished by phosphorylation of the adjacent serine 10 [11–13]. In addition, we determined a 4-fold preference of the MBD domain of MeCP2 for fully over unmethylated DNA in accordance to [14–16]. Furthermore, we performed protein-protein interaction assays and found that the Dnmt1 binds to PCNA in a PBD domain-dependent manner consistent to [17,18]. In contrast, LigaseIII binds Xrc1 but does not interact with PCNA [19,20]. Using an ELISA-based assay, we were able to detect endogenous PCNA bound to immunoprecipitated Dnmt1, Fen1 and PCNA itself. In accordance with our protein-protein interaction data, Dnmt1 lacking the PBD domain (Dnmt1 Δ PBD) could not co-immunoprecipitate with PCNA. Consistent with our histone-tail peptide binding data, we could detect endogenous histone H3 bound to Cbx1. Finally, we quantified specific histone modifications on nucleosomes comprising different histone variants. All of these data clearly demonstrate the versatility and easy handling of this high-throughput approach and its immense benefit to many researchers.

Results

One-step Purification of GFP-fusion Proteins

In a first step, we tested the efficiency of the GFP-multiTrap to purify GFP-fusion proteins from cellular extracts. First, we examined the pull-down efficiency of a GFP-tagged protein and chose GFP-Cbx1 as a model protein. Cbx1 is a chromodomain-containing protein related to the Drosophila HP1 β , a well-studied heterochromatin-associated protein [11]. We used cell extracts from HEK293T cells transiently expressing GFP-Cbx1 or GFP, purified the GFP-fusions using the GFP-multiTrap, eluted the bound fractions, separated them by SDS-PAGE and visualized the bound proteins by coomassie staining. The bound fractions displayed mainly GFP as well as GFP-Cbx1 with only minor impurities (Figure 1A), providing therefore a reliable tool for downstream biochemical analyses. Notably, the washing conditions can be varied according to the downstream applications. In addition to these qualitative results, we performed experiments to quantify the pull-down efficiency. For this purpose we quantified the amount of bound GFP with varying concentrations of input GFP from cellular extracts. After binding, the single wells were subjected to several washing steps and bound GFP was analyzed by fluorescent read-out using a micro plate reader. Notably, the input amount of protein/substrate was measured in solution, whereas the bound fraction represents one value on the 96-well surface. We measured the fluorescence intensities of bound GFP and plotted the amount of bound GFP as a function of total GFP (Figure 1B). The amount of bound GFP increased linearly from 10

to 130 nM of total input and saturated between 130 and 400 nM. Next, we quantified the amount of bound GFP by immunoblotting. Therefore, we eluted the bound GFP fractions, separated them by SDS-PAGE, visualized the bound proteins by immunoblot analysis (Figure 1C) and quantified the GFP signal by measuring the mean intensity via Image J (Figure 1D). Similar to the quantification by fluorescent read out using a micro plate reader, the amount of bound GFP increases linearly from 10 to 130 nM of total input and saturates between 130 and 400 nM.

In summary, we demonstrated that the GFP-multiTrap allows for fast and efficient one-step purification of GFP-fusion proteins directly from crude cell lysates in a high-throughput manner. The method works well for both qualitative and quantitative measurements and the immunoprecipitated GFP-fusions can then be further tested in biochemical assays.

In vitro Histone-tail Peptide and DNA Binding Assay

In the next assay we determined whether this approach is also feasible to quantify binding affinities between GFP-proteins and peptides or DNA. First, we analyzed histone-tail peptide binding specificities of the chromobox homolog 1, Cbx1, fused with a N-terminal GFP-tag using the GFP-multiTrap. GFP-Cbx1 was purified from mammalian cell lysate, as described above, and the bound protein was incubated with TAMRA-labeled histone-tail peptides. A set of 20 different histone-tail peptides (Table 1) was used in technical triplicates in parallel and GFP served as negative control (GFP data is not shown). After removal of unbound substrate the amounts of protein and histone-tail peptide were determined by fluorescence intensity measurements using a micro plate reader. Binding ratios were calculated by dividing the concentration of bound histone-tail peptide by the concentration of GFP fusion (Figure 2A). GFP-Cbx1 preferentially binds H3K9me3 and H3K9me2 histone-tail peptides consistent with previous studies [11,12]. As expected, the phosphorylation of serine 10 (S10p) next to the trimethylated lysine 9 leads prevents binding of Cbx1, which is in accordance with previous reports [13]. In addition to fluorescent quantification via a micro plate reader, we scanned the TAMRA signals using a Typhoon scanner (Figure 2B). Here, we detected TAMRA signals in the wells corresponding to di- and trimethylated H3K9. Notably, we did not detect differences in binding towards di- and trimethylated H3K9 using a micro plate reader. However, we could detect a preference for tri- over dimethylated H3K9 using a fluorescence scanner. These differences could result from different sensitivities of both methods. Furthermore, we performed a competition assay to demonstrate the specificity of the histone-tail peptide-binding assay. We incubated GFP-Cbx1 with TAMRA-labeled H3K9me3 in parallel with either biotinylated H3K9me3 or H3K9ac histone-tail peptides. As expected, the addition of biotinylated H3K9me3 histone-tail peptide significantly decreased the binding of Cbx1 to TAMRA-labeled H3K9me3, whereas the addition of biotinylated H3K9ac did not alter the binding ratios (Figure 2C). In previous studies [11,12], the binding affinities of the HP1 β chromo domain, the Drosophila homolog of mammalian Cbx1, for both di- and trimethylated H3K9 peptides have been found to be 7 and 2.5 μ M, respectively. In contrast, we could not detect a significant difference in binding ratios between di- and trimethylated H3K9 histone tail peptides using a micro plate reader (Figure 2A). One explanation could be the use of different expression systems. While the binding ratios for the HP1 β chromo domain were determined using bacterially expressed protein we used a fluorescent fusion protein derived from mammalian cells. In this context a recent study revealed that recombinant HP1 α prepared from mammalian cultured cells exhibited a stronger binding affinity for K9-

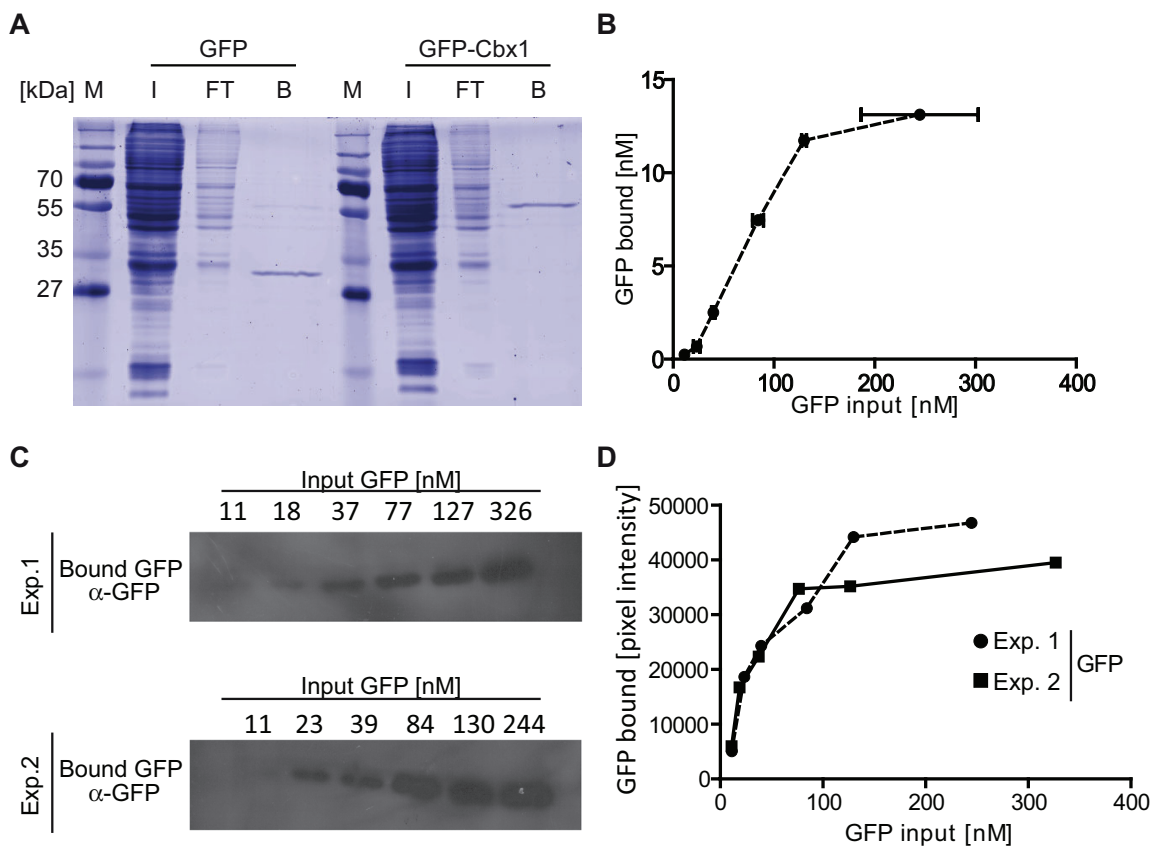


Figure 1. One-step purification of GFP and GFP-fusion proteins. Purification of GFP and GFP-Cbx1 expressed in HEK293T cells. All GFP concentrations were quantified via plate reader. (A) Purification of GFP and GFP-Cbx1 from HEK293T cell extracts, transiently transfected with the GFP-fusions. Input (I), flow-through (FT) and bound (B) fractions were separated by SDS-PAGE and visualized by coomassie staining. (B) Different amounts of GFP cell lysate were added into wells of a 96-well plate immobilized with the GFP-Trap (GFP-multiTrap). Shown are means \pm SD from two independent experiments. (C) Bound GFP fractions from both independent experiments (B) were eluted, separated by SDS-PAGE and visualized by immunoblot analysis using an anti-GFP mouse antibody (Roche, Germany). (D) Quantification of bound GFP fractions by immunoblotting. The mean intensities of the GFP signals were measured using Image J.

doi:10.1371/journal.pone.0036967.g001

methylated histone H3 (H3K9me) in comparison to protein produced in *Escherichia coli* [21]. Biochemical analyses revealed that HP1 α was multiply phosphorylated at N-terminal serine residues (S11–14) in human and mouse cells and that this phosphorylation enhanced the affinity of HP1 α for H3K9me, displaying the importance of post-translational modifications for binding affinities [21]. To determine the binding affinity of GFP-Cbx1 to H3K9me3, we varied the input amount of histone-tail peptide. We plotted the amount of bound histone-tail peptide as a function of total peptide and fitted the values using GraphPad Prism and nonlinear regression (Figure 2D). The amount of bound H3K9me3 histone-tail peptide increases linearly and saturates at approximately 500 nM of input peptide. In contrast to H3K9me3, we could not detect any binding of Cbx1 to H3 histone-tail peptides. Notably, the exact determination of binding affinities was not possible due to differences in the technical measurement of input versus bound fractions. Here, the input amount of protein/substrate was measured in solution, whereas the bound fraction represents one value on the 96-well surface.

In addition to histone-tail peptide binding assays, we performed DNA-binding assays. We purified the methyl-binding domain (MBD) of MeCP2, fused with a C-terminal YFP tag, from cell extracts as described and performed competition binding analysis by incubating immobilized MBD-YFP with fluorescently labeled

un- and fully methylated DNA (Table 1). As a result we observed a five-fold preference of MBD for fully methylated DNA over unmethylated DNA (Figure 2E). In addition, we measured the amount of bound DNA to MBD-YFP by varying the input amount of DNA. We plotted the amount of bound un- and fully methylated DNA as a function of total un- and fully methylated DNA and fitted the values using GraphPad Prism and nonlinear regression (Figure 2F). Similar to the relative binding ratios, MBD binds preferentially to fully methylated DNA. These results are in accordance with previous studies describing that MeCP2 interacts specifically with methylated DNA mediated by the MBD domain. In these studies, electrophoretic mobility shift assays (EMSA) using the isolated MBD domain expressed in *E. coli* were performed and dissociation constants of 14,7 and 1000 nM were calculated for symmetrically methylated and unmethylated DNA, respectively [14–16].

To assess the suitability of the *in vitro* histone-tail peptide and DNA binding assay for high-throughput applications, the Z-factor was calculated. For histone-tail peptide binding assays, we calculated the Z-factor using the relative binding ratios of H3K9me3 to GFP-Cbx1 as positive state and of H3K9me0 to GFP-Cbx1 as negative state. For the DNA binding assay, we calculated the Z-factor using the relative binding ratios of fully methylated DNA to MBD-YFP as positive state and of

Table 1. Sequences of DNA oligonucleotides and histone-tail peptides.

DNA oligos				
DNA substrate	DNA sequence			DNA labeling
CG-up	5'- CTCACAACTAACTACCATCCGGACCAGAAGAGTCATCATGG -3'			No
MG-up	5'- CTCACAACTAACTACCATCMGGACCAGAAGAGTCATCATGG -3'			No
um550	5'- CCATGATGACTCTTCTGGTCCGGATGGTAGTTAGTTGAG -3'			ATTO550 at 5'end
um700	5'- CCATGATGACTCTTCTGGTCCGGATGGTAGTTAGTTGAG -3'			ATTO700 at 5'end
mC700	5'- CCATGATGACTCTCTGGTCMGGATGGTAGTTAGTTGAG -3'			ATTO700 at 5'end
DNA substrates				
DNA substrate	CpG site	Label	Oligo I	Oligo II
UMB-550	unmethylated	550	CG-up	um550
UMB-700	unmethylated	700	CG-up	um700
FMB-700	Fully methylated	700	MG-up	mC700
DNA sets				
Binding set	Control set			
UMB-550	UMB-550			
FMB-700	UMB-700			
Histone-tail peptides				
H3 (1–20)	ART K QTARKSTGGKAPRKQLK		TAMRA at C-terminus	
H3K4me1	ART X1 QTARKSTGGKAPRKQLK			
H3K4me2	ART X2 QTARKSTGGKAPRKQLK			
H3K4me3	ART X3 QTARKSTGGKAPRKQLK			
H3K4ac	ART Z QTARKSTGGKAPRKQLK			
H3K9me1	ARTKQTAR X1 S TGGKAPRKQLK			
H3K9me2	ARTKQTAR X2 S TGGKAPRKQLK			
H3K9me3	ARTKQTAR X3 S TGGKAPRKQLK			
H3K9me3S10p	ARTKQTAR X3 Z2 TGGKAPRKQLK			
H3K9ac	ARTKQTAR Z S TGGKAPRKQLK			
H3 (17–36)	RKQLATKAAR K SAPATGGVK		TAMRA at N-terminus	
H3K27me1	RKQLATKAAR X1 SAPATGGVK			
H3K27me2	RKQLATKAAR X2 SAPATGGVK			
H3K27me3	RKQLATKAAR X3 SAPATGGVK			
H3K27ac	RKQLATKAAR Z SAPATGGVK			
H4 (10–29)	LGKGGAKRHR K VL RDNIQGI			
H4K20me1	LGKGGAKRHR X1 VL RDNIQGI			
H4K20me2	LGKGGAKRHR X2 VL RDNIQGI			
H4K20me3	LGKGGAKRHR X3 VL RDNIQGI			
H4K20ac	LGKGGAKRHR Z VL RDNIQGI			

X1: monomethylated Lysine; X2: dimethylated Lysine; X3: trimethylated Lysine; Z: acetylated Lysine; Z2: phosphorylated Serine.
doi:10.1371/journal.pone.0036967.t001

unmethylated DNA to MBD-YFP as negative state (Table 2). The Z-factors of 0.766 for the histone-tail peptide binding assay and 0.756 for the DNA binding assay strongly indicate that both assays are robust, reproducible and suitable for high-throughput applications.

In vitro Protein-protein Binding Assay

In addition to the detection of substrate specificity (e.g. histone-tail peptide) and DNA binding, analysis of the interaction with other cellular components and factors is essential to understand the function of proteins.

The use of fluorescence intensity read-out systems for the quantification of protein-protein interactions *in vitro* provides a new



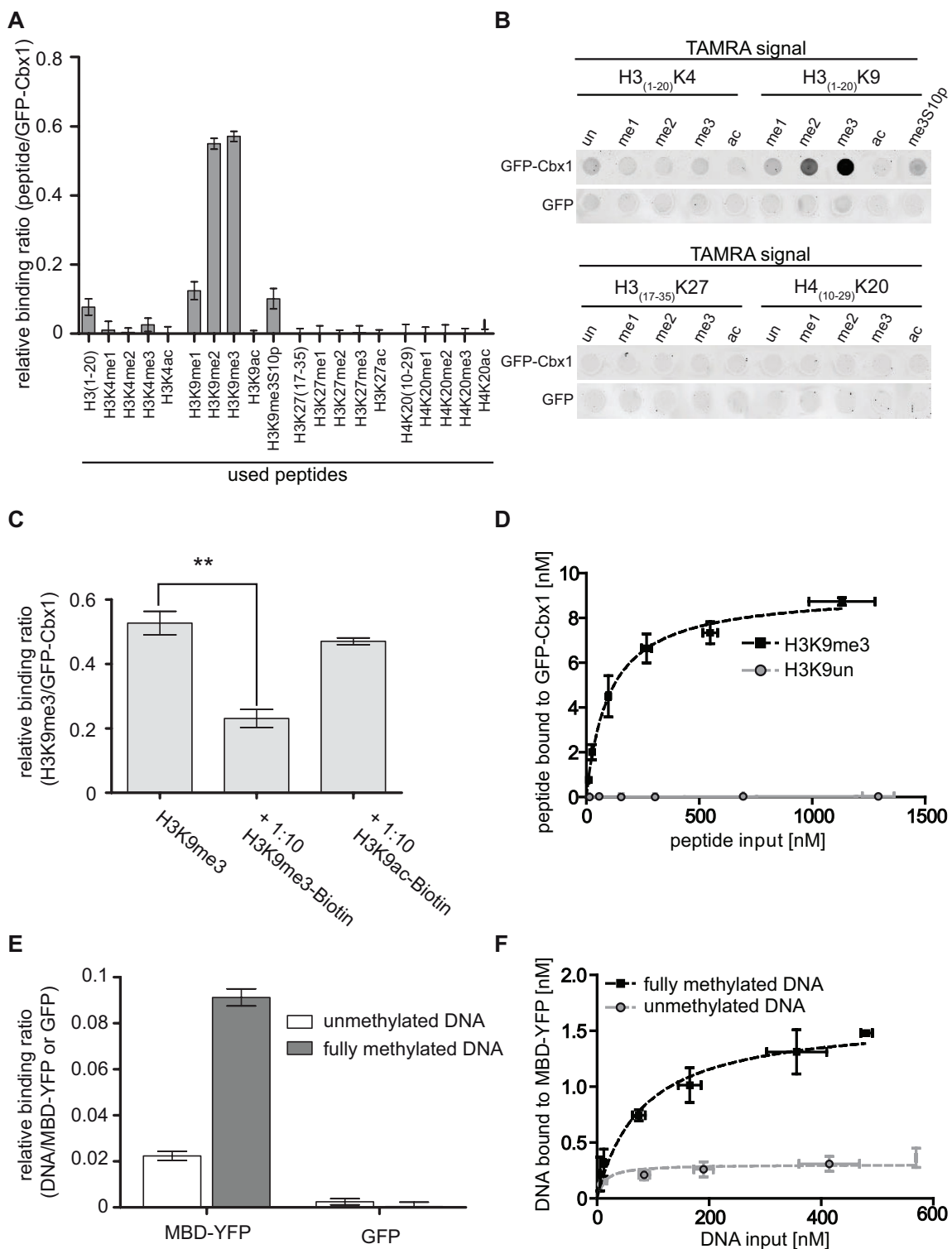


Figure 2. In vitro histone-tail peptide and DNA binding assay. *In vitro* binding ratios of fluorescently labeled substrates over bound GFP fusion proteins were determined. (A)–(D) *In vitro* histone-tail peptide binding assay with GFP-Cbx1. (A) Histone H3- and H4-tail binding specificities of Cbx1. A final concentration of 0.15 μ M TAMRA-labeled histone-tail peptide was added per well. Fluorescent signals of bound TAMRA-labeled histone-tail peptides and GFP-fusion protein were quantified via plate reader. Shown are means \pm SD from three independent experiments (B) Fluorescent signals of bound TAMRA-labeled histone-tail peptides visualized by fluorescent scanner. (C) Competition assay between TAMRA-labeled H3K9me3 and biotinylated histone-tail peptides with GFP-Cbx1. Shown are means \pm SD from three independent experiments. Statistical significance between the binding ratios is indicated; ** $P < 0.003$. (D) Different amounts of TAMRA-labeled H3K9me3 and H3 histone-tail peptides were added to GFP-Cbx1. Three or two independent experiments for H3K9me3 or H3 histone-tail peptides were performed, respectively. Shown are means \pm SD and the amount of bound histone-tail peptide was plotted as a function of total histone-tail peptide. The curve was fitted using GraphPad Prism and

nonlinear regression. All input and bound fractions were quantified via a plate reader. (E) DNA binding specificities of the MBD domain of MeCP2 to un- and fully methylated DNA in direct competition. Shown are means \pm SD from three independent experiments. (F) Different amounts of Atto550-labeled unmethylated and Atto700-labeled fully methylated DNA in direct competition were added to purified MBD-YFP. Shown are means \pm SD from three independent experiments. The amount of bound DNA peptide was plotted as a function of total DNA. The curve was fitted using GraphPad Prism and nonlinear regression. All input and bound fractions were quantified via a plate reader.
doi:10.1371/journal.pone.0036967.g002

and simple method avoiding laborious and inaccurate protein detection using conventional immunoblotting systems.

To address the question if such interaction analysis can be performed in a multi-well format we analyzed the interaction of single GFP-fusions with RFP-fusion proteins expressed in mammalian cells. More precisely, we determined quantitative binding ratios between nuclear located proteins involved in DNA-replication (PCNA) [17,18], DNA-methylation (Dnmt1) [22] as well as in DNA-repair (Xrccl) [23]. As described, we immobilized GFP-fusions on the GFP-multiTrap and incubated them with cell lysate containing RFP-fusion proteins. After binding, we removed unbound material, measured the concentrations of RFP and GFP and calculated the molar binding ratios. Firstly, we determined the binding ratios of the green fluorescent PCNA-binding domain of Dnmt1 (GFP-PBD) to RFP-PCNA and used Dnmt1 Δ PBD as a negative control. By measuring the fluorescent signal intensities we detected that RFP-PCNA binds to GFP-PBD in a molar ratio of 1.42 ± 0.31 but not to Dnmt1 Δ PBD (Figure 3A).

For a direct comparison we eluted the bound fractions, separated them by SDS-PAGE and visualized the proteins by immunoblotting (Figure 3B). Both, GFP-PBD and RFP-PCNA are detected in the input and bound fractions whereas RFP is not visible in the bound fraction of GFP-PBD (Figure 3B).

In addition, we measured the amount of bound RFP-fusion to GFP-PBD with varying the input amount of RFP-fusion. We plotted the amount of bound RFP-fusion as a function of total RFP-fusion and fitted the values using GraphPad Prism and nonlinear regression (Figure 3C). Similar to the relative binding ratios, GFP-PBD binds to RFP-PCNA but not to RFP.

These results are in accordance with previous findings that Dnmt1 associates with the replication machinery by directly binding to PCNA, a homotrimeric ring which serves as loading platform for replication factors, and that this binding depends on the PCNA-binding domain in the very N-terminus of Dnmt1 [17,18]. In addition by determining the quantitative binding ratio between both partner proteins our approach provides a more detailed insight in the binding events occurring at the central loading platform of the DNA replication.

Secondly, we determined the molar binding ratio of GFP-Ligase III to RFP-Xrccl. Xrccl binds in a molar ratio of 0.61 ± 0.14 to Ligase III but did not bind to other proteins such as GFP-PBD,

GFP-Dnmt1 Δ PBD or GFP. Previous studies demonstrated that DNA Ligase III was recruited to DNA repair sites via its BRCT domain mediated interaction with Xrccl [19,20].

For the protein-protein binding assays, we calculated the Z-factor using the molar binding ratios of RFP-PCNA to GFP-PBD as positive state and RFP to GFP-PBD as negative state (Table 2). The Z-factor of 0.56 indicated that the protein-protein binding assay is robust and reproducible.

In summary, we demonstrate a new quantitative and reliable high-throughput method to analyze protein-protein interactions using GFP- and RFP-fusion proteins.

Enzyme-linked Immunosorbent Assay (ELISA)

Next we examined endogenous protein-protein interactions using an ELISA assay. For this purpose, we precipitated GFP-fusion proteins in the 96 well format on the GFP-multiTrap and cross-linked bound fractions with formaldehyde (CH_2O) and/or treated the bound fractions with methanol (MeOH). Using specific antibodies against PCNA, we determined the binding of endogenous PCNA to GFP fusions of Dnmt1, Dnmt1 Δ PBD, PCNA, Fen1, which is a flap endonuclease and an essential DNA replication protein [24]. We could detect endogenous PCNA binding to Dnmt1 but not to Dnmt1 Δ PBD similar to the results obtained with the protein-protein interaction assay using RFP-PCNA (Figure 4A). In addition, we detected binding of endogenous PCNA to Fen1 but also to PCNA itself. These results fit well to former studies showing that Fen1 or maturation factor 1 associates with PCNA in a stoichiometric complex of three Fen1 molecules per PCNA trimer [25,26]. In addition to 100 described interacting partners, it is known that PCNA also interacts with itself and forms a trimeric ring, which is confirmed by our ELISA assay by giving a signal for endogenous PCNA binding to GFP-PCNA (Figure 4A).

Next, we determined the binding of Cbx1 to endogenous histone H3. Similar to PCNA, we precipitated GFP-Cbx1 and GFP and detected endogenous H3 via an H3-antibody coupled to HRP. In accordance with the experiments using TAMRA labeled histone 3 peptides, we observed an H3 ELISA signal for binding to Cbx1 but not to GFP. Using an H3K9me3-specific antibody, we could not detect an ELISA signal (data not shown), due to the fact that the tight binding of Cbx1 (Figure 2) to H3K9me3 most likely

Table 2. Overview of relative binding ratios and Z-factor values.

Relative binding ratios of Substrate/GFP- or YFP-fusion						
Fusion protein	Histone-tail peptide binding		DNA binding		Protein-protein binding	
	GFP-Cbx1		MBD-YFP		GFP-PBD	
Substrate	H3K9me3	H3K9un	Fully methylated DNA	Unmethylated DNA	RFP-PCNA	RFP
Average ratio	0,5715	0,0772	0,0912	0,0223	1,487	0,005
Standard deviation	0,0150	0,0236	0,0037	0,0019	0,2111	0,006
Z-factor	0,766		0,756		0,560	

Based on the average relative binding ratios and the standard deviations we calculated the Z-factor.
doi:10.1371/journal.pone.0036967.t002



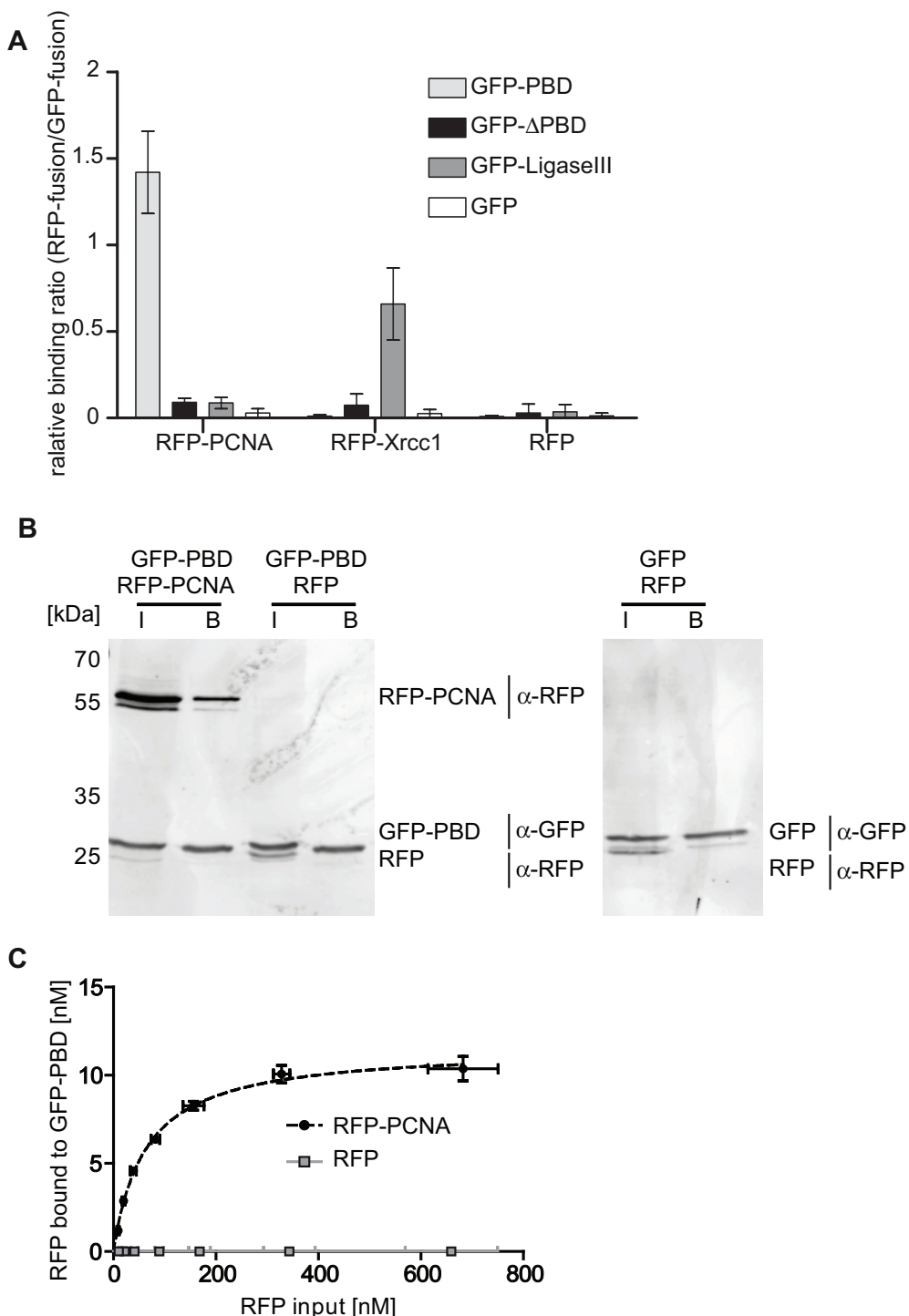


Figure 3. In vitro Protein-Protein binding assay. (A) *In vitro* binding ratios of RFP-fusion proteins over GFP-fusion proteins. Shown are means \pm SD from six independent experiments. (B) After immunoprecipitation input (I) and bound (B) fractions were separated by SDS-PAGE and visualized by immunoblot analysis using the anti-GFP rat monoclonal antibody, 3H9, and the anti-RFP rat monoclonal antibody, 5F8 (both ChromoTek, Germany). GFP-PBD: 30 kDa; RFP-PCNA: 56 kDa; GFP: 28 kDa, RFP: 26 kDa. (C) Different amounts of RFP-fusion protein were added to purified GFP-PBD. Shown are means \pm SD from two independent experiments. The amount of bound RFP was plotted as a function of total RFP. The curve was fitted using GraphPad Prism and nonlinear regression. All input and bound fractions were quantified via a plate reader.
doi:10.1371/journal.pone.0036967.g003

occludes the antibody epitope, as has been proposed for HP1 binding to H3K9me3. In this study, the histone H3 trimethyl-lysine epitope is embedded in an aromatic cage blocking thereby

most likely the binding of any antibodies [27]. To further analyze the bound fractions, we eluted GFP-Cbx1 and GFP, separated them on an SDS-PAGE gel and visualized GFP and H3 by

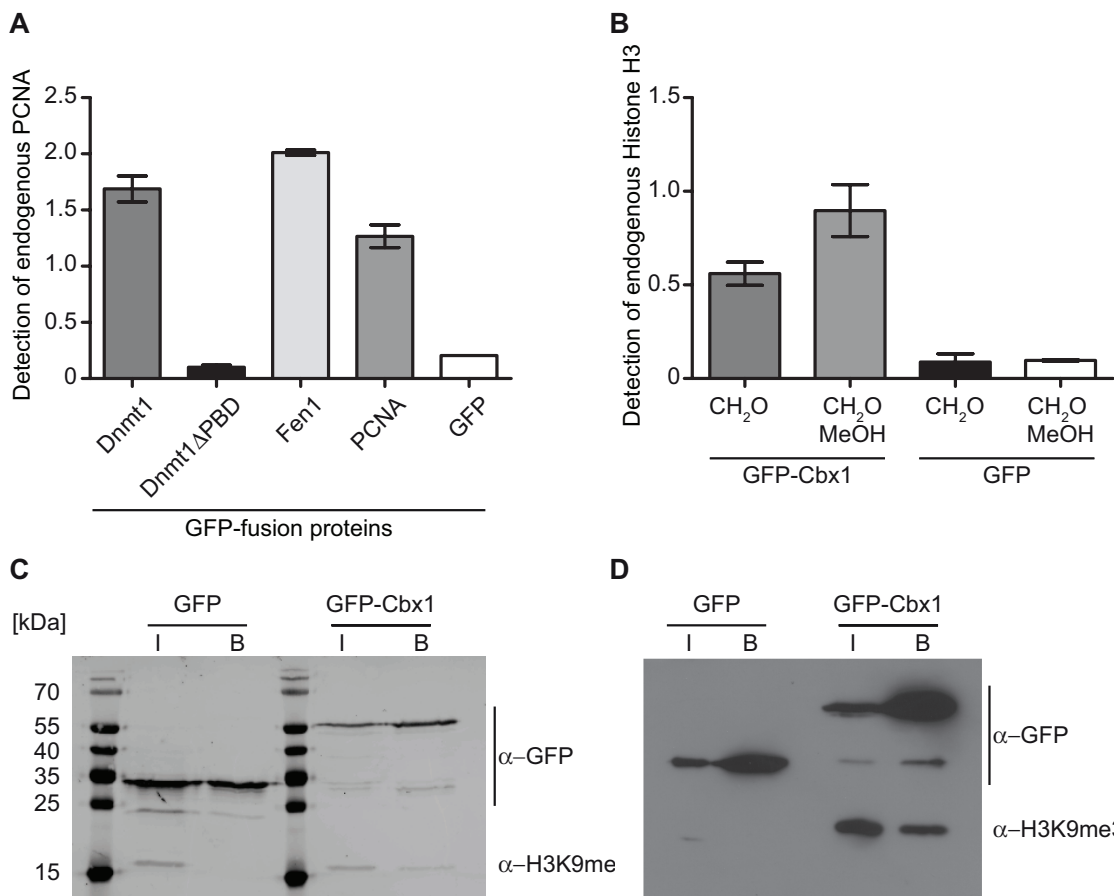


Figure 4. Pulldown of endogenous interaction partners. GFP-fusions were immunoprecipitated and endogenous interacting proteins were detected either by ELISA or immunoblot analysis. (A) ELISA signal (Absorbance at 450 nm) of bound endogenous PCNA detected by a PCNA antibody to purified GFP-fusion proteins. Shown are means \pm SD from three independent experiments. (B) ELISA signal (Absorbance at 450 nm) of bound endogenous Histone H3 detected by an H3 antibody to purified GFP-fusion proteins. Bound fractions were either cross-linked with 2% formaldehyde (CH₂O) and/or additionally permeabilized with MeOH. Shown are means \pm SD from two independent experiments. (C) and (D) After immunoprecipitation input (I) and bound (B) fractions were separated by SDS-PAGE and visualized by immunoblot analysis. (C) The total protein concentration of the input fractions were adjusted. (D) The GFP concentrations of the input fractions were adjusted. doi:10.1371/journal.pone.0036967.g004

immunoblotting. Histone H3 was detectable in the input fractions of both GFP and GFP-Cbx1 but as expected, only in the bound fraction of GFP-Cbx1.

Comparative Analysis of Posttranslational Histone Modifications

Histone posttranslational modifications play an important role in the structural organization of chromatin and often correlate to transcriptional activation or repression depending on their type and location. Recently, it has been shown that nucleosomal incorporation of histone variants can lead to alterations in modification patterning and that such changes may complement the properties brought by the variant itself [28].

In order to investigate the suitability of the GFP-multiTrap in comparing such histone posttranslational modifications, we isolated nucleosomes from HeLa cells expressing either GFP-H2A or GFP-H2A.Z and precipitated them with the 96 well micro plate. GFP levels were then recorded (data not shown) to ensure equal loading of substrate per well. In addition, as a negative control, the cytoplasmic supernatant fraction was also incubated with the GFP-multiTrap. An ELISA approach was then used to

quantify differences in histone H3K4me2 levels between the two different nucleosome compositions. Following cross-linking and permeabilization, bound nucleosomes were incubated with either anti-H3, directly conjugated to HRP or anti-H3K4me2 (both antibodies Abcam, UK). Histone H3K4me2 levels were then normalized to the histone H3 signal. In accordance with published data, H2A containing nucleosomes were depleted in H3K4me2 where as those containing H2A.Z showed a large enrichment for this modification (Figure 5) [28].

Discussion

One challenge of the proteomic era is the effective integration of proteomic, cell biological and biochemical data. Ideally, proteomic data on tissue and cell cycle-specific expression of specific proteins should be combined with subcellular localization and binding dynamics of fluorescent proteins. Additionally, it is crucial to determine cell biological and biochemical characteristics such as interacting factors, enzymatic activity and substrate binding specificities. The integration of all these different data has, in part, been impeded by the simple fact that different protein tags

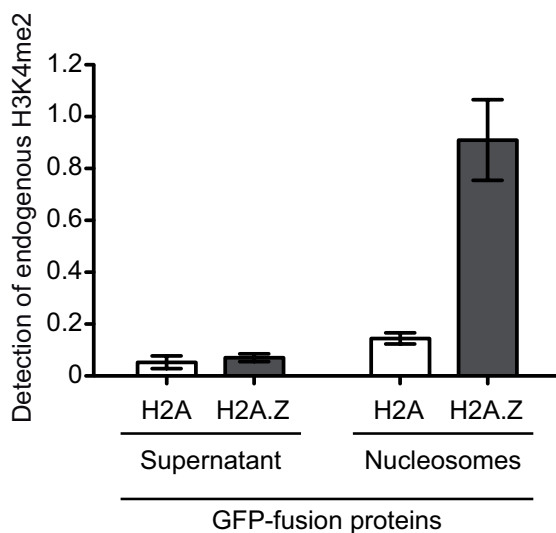


Figure 5. Comparative analysis of posttranslational histone modifications. Cytoplasmic supernatant (SN) or mononucleosome (MN) fractions prepared from HeLa cells expressing GFP-H2A or GFP-H2A.Z were precipitated and the levels of H3 and H3K4me2 were detected by ELISA (Absorbance at 450 nm). Shown are the H3K4me2 levels normalized to H3 and means \pm SD from two independent experiments.

doi:10.1371/journal.pone.0036967.g005

are used for different applications. Here, we present a new versatile, high-throughput method to determine *in vitro* binding specificities and to detect endogenous interacting factors of GFP-fusion proteins. We use 96-well micro plates with immobilized GFP-Trap (GFP-multiTrap) for fast and efficient purification of GFP-fusion proteins. We demonstrate the efficiency and purity of the GFP immunoprecipitation (Figure 1), a prerequisite to obtain reliable biochemical data on e.g. binding specificities. Moreover, we measured histone-tail binding, DNA and protein-protein binding ratios underlying the versatility of our approach (Figure 2 and 3 and Table 2). The suitability of the demonstrated assays for high-throughput biochemical and functional studies was assessed by calculating the Z-factors (Table 2). Therefore, our assay is suitable to examine an initial high-throughput screening for potential binding partners. Moreover, the assay can be used for compound screening. Additionally, our method allows for detection of endogenous interaction factors based on an ELISA assay (Figure 4 and 5).

In contrast to other high-throughput techniques like conventional microarrays, it does not require time-consuming recombinant protein expression and purification but allows for the direct biochemical analyses of GFP-fusion proteins expressed in mammalian cells. The versatile GFP-multiTrap combined with the widespread use of fluorescent fusion proteins now enables a fast and direct quantitative correlation of microscopic data concerning the subcellular localization and mobility of fluorescent fusion proteins with their enzymatic activity, interacting factors, and DNA binding properties combining cell biology and biochemistry with mutual benefits.

Materials and Methods

Expression Constructs, Cell Culture and Transfection

Mammalian expression constructs encoding GFP-Dnmt1, GFP-Dnmt1 Δ PBD, GFP-PBD, GFP-PCNA, RFP-PCNA, GFP-Ligase

III, mRFP, GFP, MBD-YFP, GFP-Fen1 and RFP-Xrcc1 were described previously [7,20,29–37]. Note that all constructs encode fusion proteins of GFP, RFP or yellow fluorescent protein (YFP). The Cbx1 expression construct was derived by PCR from mouse cDNA, cloned into pEGFP-C1 (Clontech, USA) and verified by DNA sequencing. Throughout this study enhanced GFP (eGFP) constructs were used and for simplicity referred to as GFP-fusions. HEK293T cells [30] and HeLa Kyoto [29] were cultured in DMEM supplemented with either 50 μ g/ml gentamicin (HEK293T) or 1% penicillin/streptomycin (HeLa Kyoto) and 10% fetal calf serum. For expression of GFP/RFP/YFP fusion proteins, HEK293T cells were transfected with the corresponding expression constructs using polyethylenimine (Sigma, USA). 2. HeLa Kyoto cells were transfected using FuGene HD (Roche, Germany) according to the manufacturer's instructions. The plasmid coding for GFP-H2A (H2A type 1, NP_003501.1) was kindly provided by Emily Bernstein (Mount Sinai Hospital) and the plasmid coding for GFP-Z-1 was a gift from Sachihiro Matsunaga (University of Tokyo). Stable cell lines were selected with 600 μ g/ml G418 (PAA, Austria) and individual cell clones sorted by using a FACSaria machine (Becton Dickinson, Germany).

Histone-tail Peptides and DNA Substrate Preparation

Fluorescently labeled DNA substrates were prepared by mixing two HPLC-purified DNA oligonucleotides (IBA GmbH, Germany Table 1) in equimolar amounts, denaturation for 30 sec at 92°C and slow cool-down to 25°C allowing hybridization. Histone-tail peptides were purchased as TAMRA conjugates and/or biotinylated (PSL, Germany) and are listed in Table 1.

Preparation of Protein Extracts

HEK293T cells were cultured and transfected as described [38]. For extract preparation 1 mg/ml DNaseI, 1 mM PMSF and Protease Inhibitor cocktail (Roche, Germany) were included in the lysis buffer (20 mM Tris-HCl pH 7.5, 150 mM NaCl, 2 mM MgCl₂, 0.5% NP40) or nuclear extract buffer (10 mM HEPES pH 7.9, 10 mM KCl, 1.5 mM MgCl₂, 0.34 M Sucrose, 10% Glycerol, 1 mM β -mercapto-ethanol). Cells were lysed for 30 minutes on ice followed by a centrifugation step (15/12000 rpm/4°C). Extracts from transfected 10 cm plates were diluted to 500 μ L with immunoprecipitation buffer (IP buffer; 20 mM Tris-HCl pH 7.5, 150 mM NaCl, 0.5 mM EDTA) or dilution buffer (20 mM HEPES pH 7.9, 150 mM KCl). An aliquot of 10 μ L (2%) were added to SDS-containing sample buffer (referred to as Input (I)).

Purification and Elution of GFP/YFP/RFP- Fusions

For purification, 100 μ L or 50 μ L precleared cellular lysate for full-area plates or half-area plates, respectively, was added per well and incubated for 2 hours at 4°C on a GFP-multiTrap plate by continuous shaking. After removing the supernatant, wells were washed twice with 100 μ L of washing buffer (WB; 20 mM Tris-HCl pH 7.5, 100–300 mM NaCl, 0.5 mM EDTA) and 100 μ L of IP or dilution buffer was added for measurement. The amounts of bound protein were determined by fluorescence intensity measurements with a Tecan Infinite M1000 plate reader (Tecan, Austria). Wavelengths for excitation and emission of GFP are 490 \pm 10 nm and 511 \pm 10 nm, for RFP are 586 \pm 5 nm and 608 \pm 10 nm and for YFP 525 \pm 5 nm and 538 \pm 5 nm, respectively. The concentration of proteins was calculated using calibration curves that were determined by measuring the fluorescence signal of known concentrations of purified GFP, RFP and YFP. Notably, factors interfering with

fluorescence intensity measurements such as absorption of excitation light by cell lysates, auto fluorescence of the samples and/or scattering of the excitation/emission light by cell debris are negligible (Figure S1). Bound proteins were eluted with 300 mM Glycin pH 2.5 and subsequently buffered with 1 M Tris pH 7.5. Elution fractions were added to SDS-containing sample buffer (referred to as Bound (B)). Bound proteins were visualized by immunoblotting using the anti-GFP mouse monoclonal antibody (Roche, Germany).

In vitro Histone-tail Peptide Binding Assay

The *in vitro* histone-tail binding assay was performed as described previously [10]. After one-step purification of GFP fusion proteins the wells were blocked with 100 μ L 3% milk solved in TBS-T (0.075% Tween) for 30 minutes at 4°C on a plate vortex, shaking gently. After blocking, the wells were equilibrated in 50 μ L IP buffer supplemented with 0.05% Tween. TAMRA-labeled histone-tail peptides were added either to a final concentration of 0.15 μ M or of the indicated concentrations and the binding reaction was performed at RT for 20 min on a plate vortex, shaking gently. After removal of unbound substrate the amounts of protein and histone-tail peptide were determined by fluorescence intensity measurements. The concentrations of bound TAMRA-labeled histone-tail peptides were calculated using calibration curves that were determined by measuring a serial dilution of TAMRA-labeled peptides with known concentrations.

Binding ratios were calculated dividing the concentration of bound histone-tail peptide by the concentration of GFP fusion. Wavelengths for excitation and emission of TAMRA were 560 \pm 5 nm and 586 \pm 5 nm, respectively.

In vitro DNA Binding Assay

In vitro DNA binding assay was performed as described previously [9,10] with the following modifications. GFP/YFP fusions were purified from HEK293T extracts using the 96-well GFP-binder plates and incubated with two differentially labeled DNA substrates at a final concentration of either 100 nM or of the indicated concentration for 60 min at RT in IP buffer supplemented with 2 mM DTT and 100 ng/ μ L BSA. After removal of unbound substrate the amounts of protein and DNA were determined by fluorescence intensity measurements. The concentration of bound ATTO-labeled DNA substrates was calculated using calibration curves that were determined by measuring a serial dilution of DNA-coupled fluorophores with known concentrations. Binding ratios were calculated dividing the concentration of bound DNA substrate by the concentration of GFP/YFP fusion, corrected by values from a control experiment using DNA substrates of the same sequence but with different fluorescent label, and normalized by the total amount of bound DNA. Wavelengths for excitation and emission of ATTO550 were 545 \pm 5 nm and 575 \pm 5 nm and for ATTO700 700 \pm 10 nm and 720 \pm 10, respectively.

Protein-Protein Interaction

GFP fusions were purified from HEK293T extracts using the 96-well GFP multiTrap plates, blocked with 3% milk and incubated with cellular extracts comprising the RFP fusions with the indicated concentrations for 30 min at RT. After removal of unbound RFP fusion (washing buffer) the amounts of proteins were determined by fluorescence intensity measurements. Binding ratios were calculated dividing the concentration of bound RFP fusion by the concentration of GFP fusion. Wavelengths for excitation and emission of RFP were 586 \pm 5 nm and 608 \pm 10 nm,

respectively. Bound proteins were eluted and separated by SDS-PAGE and visualized by immunoblotting using the anti-GFP rat monoclonal antibody; 3H9, and the anti-red rat monoclonal antibody, 5F8 (both ChromoTek, Germany).

Enzyme-linked Immunosorbent Assay (ELISA)

GFP fusions were purified (from HEK293T extracts) using the 96-well GFP-multiTrap plates and were washed twice with dilution buffer (for nucleosome experiments salt concentration was adjusted to 300 mM). After washing bound fractions were either cross-linked with 2% formaldehyde and/or additionally permeabilized with 100% MeOH. After blocking with 3% milk solved in TBS-T (0.075% Tween) the wells were incubated with primary antibody (monoclonal rat anti-H3-HRP (Abcam, UK), polyclonal rabbit anti-H3K4me2 (Abcam, UK) or monoclonal rat anti-PCNA, 16D10 (ChromoTek, Germany) overnight at 4°C on a plate vortex, shaking gently. The wells were washed three times with 200 μ L TBS-T and horseradish peroxidase-conjugated secondary antibody (Sigma, USA) was incubated for 1 h at RT for the detection of PCNA or H3K4me2. The wells were washed again as described above. For PCNA experiments detection was carried out by incubating each well with 100 μ L TMB (3,3',5,5'-tetramethylbenzidine) for 10 minutes at RT. The reactions were stopped with the addition of 100 μ L 1 M H₂SO₄. For nucleosome experiments, detection was carried out using OPD (Sigma, USA) according to the manufacturers instructions. Bound histone H3, PCNA or H3K4me2 levels were quantified by determination of the absorbance at 450 nm using a Tecan Infinite M1000 plate reader (Tecan, Austria).

Preparation of Mononucleosomes

2 \times 10⁷–10 \times 10⁷ HeLa cells, expressing either GFP-H2A or GFP-H2A.Z, were incubated in PBS, 0.3% Triton X-100 and Protease Inhibitor Cocktail (Roche, Germany) for 10 min at 4°C. Nuclei were pelleted and supernatant (SN) transferred and retained. The pellet was washed once in PBS, resuspended in EX100 buffer (10 mM Hepes pH 7.6, 100 mM NaCl, 1.5 mM MgCl₂, 0.5 mM EGTA, 10% (v/v) glycerol, 10 mM β -glycerol phosphate 1 mM DTT, Protease Inhibitor Cocktail (Roche, Germany) and CaCl₂ concentration adjusted to 2 mM. Resuspended nuclei were digested with 1.5 U MNase (Sigma, USA) for 20 min at 26°C. The reaction was stopped by addition of EGTA to a final concentration of 10 mM followed by centrifugation for 10 min at 1000 rcf, 4°C. Mononucleosome containing supernatant (MN) was retained.

Calculation of the Z-factors

To assess the suitability of the assay for high-throughput biochemical and functional studies, the Z-factor was calculated using the equation $Z = 1 - \frac{3 \times (\sigma_p + \sigma_n)}{|\mu_p - \mu_n|}$ [39]. In this equation, σ is the standard deviation of the positive (p) and the negative (n) control; μ is the mean value for the molar binding ratio (for positive (μ_p) and negative (μ_n) controls). The values of three independent experiments were used to calculate the Z-factor and all values are listed in Table 2.

Supporting Information

Figure S1 Factors interfering the measured fluorescence intensities. (A) The concentrations of GFP and RFP expressed in HEK293T cells were measured in serial dilutions of crude cell extracts. Shown are means \pm SD from two independent experiments. Fluorescence intensities were measured via a plate reader and the GFP and RFP concentrations were determined as described in the Material and Methods part. (B) Background GFP

and RFP signals in cell lysates of untransfected HEK293T cells. The fluorescence intensities (FI) were measured via a plate reader and the concentrations were determined as described in the Material and Methods part.

(DOC)

Acknowledgments

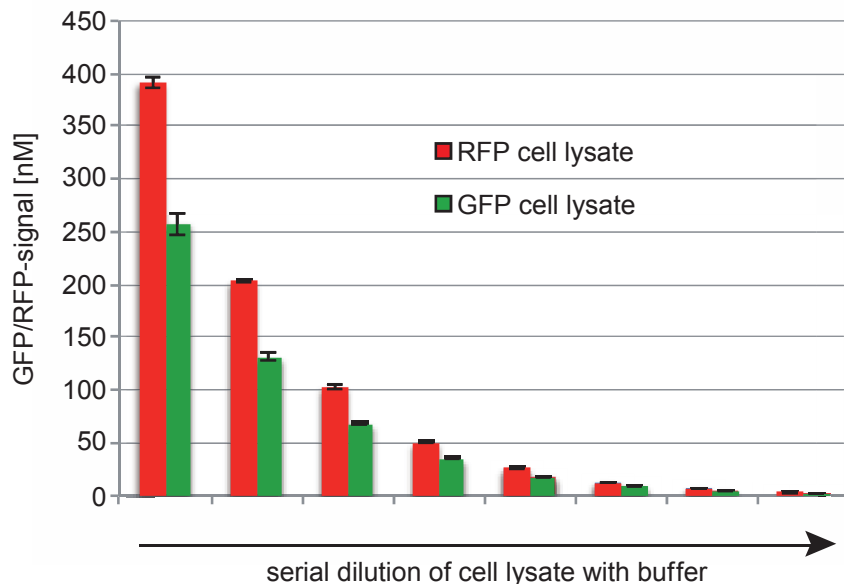
We thank Heinrich Leonhardt and Ulrich Rothbauer for comments on the manuscripts and discussion. We also thank ChromoTek for the supply of GFP-multiTrap.

References

- Walther TC, Mann M (2010) Mass spectrometry-based proteomics in cell biology. *J Cell Biol* 190: 491–500. doi:10.1083/jcb.201004052.
- Chalfie M, Tu Y, Euskirchen G, Ward WW, Prasher DC (1994) Green fluorescent protein as a marker for gene expression. *Science* 263: 802–805.
- Cristea IM, Williams R, Chait BT, Rout MP (2005) Fluorescent proteins as proteomic probes. *Mol Cell Proteomics* 4: 1933–1941. doi:10.1074/mcp.M500227-MCP200.
- Rottach A, Kremmer E, Nowak D, Leonhardt H, Cardoso MC (2008) Generation and characterization of a rat monoclonal antibody specific for multiple red fluorescent proteins. *Hybridoma* 27: 337–343. doi:10.1089/hyb.2008.0031.
- Aslan K, Lakowicz JR, Geddes CD (2005) Plasmon light scattering in biology and medicine: new sensing approaches, visions and perspectives. *Curr Opin Chem Biol* 9: 538–544. doi:10.1016/j.cbpa.2005.08.021.
- Kaushansky A, Allen JE, Gordus A, Stiffler MA, Karp ES, et al. (2010) Quantifying protein-protein interactions in high throughput using protein domain microarrays. *Nat Protoc* 5: 773–790. doi:10.1038/nprot.2010.36.
- Rothbauer U, Zolghadr K, Muyldermans S, Schepers A, Cardoso MC, et al. (2008) A versatile nanotrap for biochemical and functional studies with fluorescent fusion proteins. *Mol Cell Proteomics* 7: 282–289. doi:10.1074/mcp.M700342-MCP200.
- Trinkle-Mulcahy L, Boulon S, Lam YW, Urcia R, Boisvert FM, et al. (2008) Identifying specific protein interaction partners using quantitative mass spectrometry and bead proteomes. *J Cell Biol* 183: 223–239. doi:10.1083/jcb.200805092.
- Frauer C, Leonhardt H (2009) A versatile non-radioactive assay for DNA methyltransferase activity and DNA binding. *Nucleic Acids Research* 37: e22–e22. doi:10.1093/nar/gkn1029.
- Pichler G, Wolf P, Schmidt CS, Meilinger D, Schneider K, et al. (2011) Cooperative DNA and histone binding by Uhrf2 links the two major repressive epigenetic pathways. *J Cell Biochem* doi:10.1002/jcb.23185.
- Kaustov L, Quyang H, Amaya M, Lemak A, Nady N, et al. (2010) Recognition and specificity determinants of the human Cbx chromodomains. *J Biol Chem* doi:10.1074/jbc.M110.191411.
- Jacobs SA, Taverna SD, Zhang Y, Briggs SD, Li J, et al. (2001) Specificity of the HP1 chromo domain for the methylated N-terminus of histone H3. *EMBO J* 20: 5232–5241. doi:10.1093/emboj/20.18.5232.
- Fischle W, Tseng BS, Dommel HL, Ueberheide BM, Garcia BA, et al. (2005) Regulation of HP1-chromatin binding by histone H3 methylation and phosphorylation. *Nature* 438: 1116–1122. doi:10.1038/nature04219.
- Valinluck V, Tsai H-H, Rogstad DK, Burdzy A, Bird A, et al. (2004) Oxidative damage to methyl-CpG sequences inhibits the binding of the methyl-CpG binding domain (MBD) of methyl-CpG binding protein 2 (MeCP2). *Nucleic Acids Research* 32: 4100–4108. doi:10.1093/nar/gkh739.
- Nan X, Meehan RR, Bird A (1993) Dissection of the methyl-CpG binding domain from the chromosomal protein MeCP2. *Nucleic Acids Research* 21: 4886–4892.
- Free A, Wakefield RI, Smith BO, Dryden DT, Barlow PN, et al. (2001) DNA recognition by the methyl-CpG binding domain of MeCP2. *J Biol Chem* 276: 3353–3360. doi:10.1074/jbc.M007224200.
- Leonhardt H, Page AW, Weier HU, Bestor TH (1992) A targeting sequence directs DNA methyltransferase to sites of DNA replication in mammalian nuclei. *Cell* 71: 865–873.
- Chuang LS, Ian HI, Koh TW, Ng HH, Xu G, et al. (1997) Human DNA-(cytosine-5) methyltransferase-PCNA complex as a target for p21WAF1. *Science* 277: 1996–2000.
- Mortusewicz O, Leonhardt H (2007) XRCC1 and PCNA are loading platforms with distinct kinetic properties and different capacities to respond to multiple DNA lesions. *BMC Mol Biol* 8: 81. doi:10.1186/1471-2199-8-81.
- Mortusewicz O, Rothbauer U, Cardoso MC, Leonhardt H (2006) Differential recruitment of DNA Ligase I and III to DNA repair sites. *Nucleic Acids Research* 34: 3523–3532. doi:10.1093/nar/gkl492.
- Hiragami-Hamada K, Shimmyoza K, Hamada D, Tatsu Y, Uegaki K, et al. (2011) N-terminal phosphorylation of HP1{alpha} promotes its chromatin binding. *Mol Cell Biol* 31: 1186–1200. doi:10.1128/MCB.01012–10.
- Bestor TH (2000) The DNA methyltransferases of mammals. *Human Molecular Genetics* 9: 2395–2402. doi:10.1093/hmg/9.16.2395.
- Caldecott KW (2003) XRCC1 and DNA strand break repair. *DNA repair* 2: 955–969.
- Tom S, Henriksen LA, Bambara RA (2000) Mechanism whereby proliferating cell nuclear antigen stimulates flap endonuclease 1. *J Biol Chem* 275: 10498–10505.
- Chen U, Chen S, Saha P, Dutta A (1996) p21Cip1/Waf1 disrupts the recruitment of human Fen1 by proliferating-cell nuclear antigen into the DNA replication complex. *Proc Natl Acad Sci USA* 93: 11597–11602.
- Jönsson ZO, Hindges R, Hübchen U (1998) Regulation of DNA replication and repair proteins through interaction with the front side of proliferating cell nuclear antigen. *EMBO J* 17: 2412–2425. doi:10.1093/emboj/17.8.2412.
- Jacobs SA, Khorasanizadeh S (2002) Structure of HP1 chromodomains bound to a lysine 9-methylated histone H3 tail. *Science* 295: 2080–2083. doi:10.1126/science.1069473.
- Viens A, Mechold U, Brouillard F, Gilbert C, Leclerc P, et al. (2006) Analysis of human histone H2AZ deposition in vivo argues against its direct role in epigenetic templating mechanisms. *Molecular and Cellular Biology* 26: 5325–5335. doi:10.1128/MCB.00584–06.
- Neumann B, Held M, Liebel U, Erflé H, Rogers P, et al. (2006) High-throughput RNAi screening by time-lapse imaging of live human cells. *Nat Methods* 3: 385–390. doi:10.1038/nmeth876.
- DuBridge RB, Tang P, Hsia HC, Leong PM, Miller JH, et al. (1987) Analysis of mutation in human cells by using an Epstein-Barr virus shuttle system. *Molecular and Cellular Biology* 7: 379–387.
- Brero A (2005) Methyl CpG-binding proteins induce large-scale chromatin reorganization during terminal differentiation. *J Cell Biol* 169: 733–743. doi:10.1083/jcb.200502062.
- Sporbert A, Domaing P, Leonhardt H, Cardoso MC (2005) PCNA acts as a stationary loading platform for transiently interacting Okazaki fragment maturation proteins. *Nucleic Acids Research* 33: 3521–3528. doi:10.1093/nar/gki665.
- Leonhardt H, Rahn HP, Weinzierl P, Sporbert A, Cremer T, et al. (2000) Dynamics of DNA replication factories in living cells. *J Cell Biol* 149: 271–280.
- Schermelleh L, Spada F, Easwaran HP, Zolghadr K, Margot JB, et al. (2005) Trapped in action: direct visualization of DNA methyltransferase activity in living cells. *Nat Methods* 2: 751–756. doi:10.1038/nmeth794.
- Easwaran HP, Schermelleh L, Leonhardt H, Cardoso MC (2004) Replication-independent chromatin loading of Dnmt1 during G2 and M phases. *EMBO Rep* 5: 1181–1186. doi:10.1038/sj.embor.7400295.
- Mortusewicz O, Schermelleh L, Walter J, Cardoso MC, Leonhardt H (2005) Recruitment of DNA methyltransferase I to DNA repair sites. *Proc Natl Acad Sci USA* 102: 8905–8909. doi:10.1073/pnas.0501034102.
- Campbell RE, Tour O, Palmer AE, Steinbach PA, Baird GS, et al. (2002) A monomeric red fluorescent protein. *Proc Natl Acad Sci USA* 99: 7877–7882. doi:10.1073/pnas.082243699.
- Schermelleh L, Haemmer A, Spada F, Rosing N, Meilinger D, et al. (2007) Dynamics of Dnmt1 interaction with the replication machinery and its role in postreplicative maintenance of DNA methylation. *Nucleic Acids Research* 35: 4301–4312. doi:10.1093/nar/gkm432.
- Zhang J, Chung T, Oldenburg K (1999) A Simple Statistical Parameter for Use in Evaluation and Validation of High Throughput Screening Assays. *J Biomol Screen* 4: 67–73.

Supporting material

A



B

	GFP channel		RFP channel	
	cell lysate untransfected	blank	cell lysate untransfected	blank
Fl	33	14.5	206	228
Fl - blank	18.5	0	0	0
[nM]	0.78	0	0	0

Figure S1: Factors interfering the measured fluorescence intensities. (A) The concentrations of GFP and RFP expressed in HEK293T cells were measured in serial dilutions of crude cell extracts. Shown are means \pm SD from two independent experiments. Fluorescence intensities were measured via a plate reader and the GFP and RFP concentrations were determined as described in the Material and Methods part. **(B)** Background GFP and RFP signals in cell lysates of untransfected HEK293T cells. The fluorescence intensities (Fl) were measured via a plate reader and the concentrations were determined as described in the Material and Methods part.

2.3 Cooperative DNA and histone binding by Uhrf2 links the two major repressive epigenetic pathways

Cooperative DNA and Histone Binding by Uhrf2 Links the Two Major Repressive Epigenetic Pathways

Garwin Pichler, Patricia Wolf, Christine S. Schmidt, Daniela Meilinger, Katrin Schneider, Carina Frauer, Karin Fellinger, Andrea Rottach, and Heinrich Leonhardt*

Ludwig Maximilians University Munich, Department of Biology II and Center for Integrated Protein Science Munich (CIPS^M), Großhaderner Str. 2, 82152 Planegg-Martinsried, Germany

ABSTRACT

Gene expression is regulated by DNA as well as histone modifications but the crosstalk and mechanistic link between these epigenetic signals are still poorly understood. Here we investigate the multi-domain protein Uhrf2 that is similar to Uhrf1, an essential cofactor of maintenance DNA methylation. Binding assays demonstrate a cooperative interplay of Uhrf2 domains that induces preference for hemimethylated DNA, the substrate of maintenance methylation, and enhances binding to H3K9me3 heterochromatin marks. FRAP analyses revealed that localization and binding dynamics of Uhrf2 *in vivo* require an intact tandem Tudor domain and depend on H3K9 trimethylation but not on DNA methylation. Besides the cooperative DNA and histone binding that is characteristic for Uhrf2, we also found an opposite expression pattern of *uhrf1* and *uhrf2* during differentiation. While *uhrf1* is mainly expressed in pluripotent stem cells, *uhrf2* is upregulated during differentiation and highly expressed in differentiated mouse tissues. Ectopic expression of Uhrf2 in *uhrf1*^{−/−} embryonic stem cells did not restore DNA methylation at major satellites indicating functional differences. We propose that the cooperative interplay of Uhrf2 domains may contribute to a tighter epigenetic control of gene expression in differentiated cells. *J. Cell. Biochem.* 112: 2585–2593, 2011. © 2011 Wiley-Liss, Inc.

KEY WORDS: UHRF1; UHRF2; DNA METHYLATION; HISTONE MODIFICATIONS; EPIGENETICS

DNA methylation and histone modifications are major epigenetic marks involved in the regulation of gene expression, inheritance of chromatin states, genome stability, and cellular differentiation [Bird, 2002; Kouzarides, 2007; Reik, 2007]. Misregulation of epigenetic pathways, like erroneous DNA methylation, may lead to cancer and other diseases [Jones and Baylin, 2007]. Open questions concern the crosstalk and mechanistic link between different epigenetic signals.

Genome-scale DNA methylation studies revealed a connection between DNA methylation and histone modifications. Specifically, DNA methylation correlates with the absence of H3K4 methylation and presence of H3K9 methylation [Meissner et al., 2008]. This correlation may in part be caused by DNA methyltransferases specifically recognizing histone modifications. For instance, the de novo DNA methyltransferase Dnmt3a and its cofactor Dnmt3L specifically recognize unmethylated H3K4 mediated by the ATRX-Dnmt3-Dnmt3L (ADD) domain [Ooi et al., 2007; Otani et al., 2009]. Dnmt1, which is involved in maintenance methylation during DNA

replication and DNA repair [Leonhardt et al., 1992; Mortusewicz et al., 2005], specifically methylates hemimethylated DNA [Bestor and Ingram, 1983; Pradhan et al., 1997] and associates with constitutive heterochromatin via its targeting sequence (TS) domain [Eswaran et al., 2004].

Recently, Uhrf1 (also known as Np95 or ICBP90) has been shown to link DNA and histone modifications and has emerged as an essential cofactor for the maintenance of genomic DNA methylation. Genetic ablation of *uhrf1* leads to remarkable genomic hypomethylation, a phenotype similar to *dnmt1*^{−/−} embryonic stem cells (ESCs) [Bostick et al., 2007; Sharif et al., 2007]. Uhrf1 binds hemimethylated DNA via a SET and RING associated domain (SRA) domain and targets Dnmt1 to its substrate of maintenance DNA methylation [Bostick et al., 2007; Sharif et al., 2007; Arita et al., 2008; Avvakumov et al., 2008; Hashimoto et al., 2008; Qian et al., 2008; Rottach et al., 2010]. This targeting activity of Uhrf1 is based on specific binding to the heterochromatin mark H3K9me3 via a tandem Tudor domain (TTD) [Karagianni et al., 2008; Rottach et al.,

Additional supporting information may be found in the online version of this article.

Grant sponsor: Deutsche Forschungsgemeinschaft (DFG).

Karin Fellinger's present address is Intervet International GmbH, Unterschleissheim, Germany.

*Correspondence to: Dr. Heinrich Leonhardt, Department of Biology II, Ludwig Maximilians University Munich, 82152 Planegg-Martinsried, Germany. E-mail: h.leonhardt@lmu.de

Received 1 April 2011; Accepted 11 May 2011 • DOI 10.1002/jcb.23185 • © 2011 Wiley-Liss, Inc.

Published online 19 May 2011 in Wiley Online Library (wileyonlinelibrary.com).

2010]. In addition, Uhrf1 interacts with Dnmt3a and Dnmt3b and with histone modifying enzymes like HDAC1, G9a, and Tip60 [Unoki et al., 2004; Achour et al., 2009; Kim et al., 2009; Meilinger et al., 2009]. Finally, Uhrf1 displays E3 ubiquitin ligase activity for histone H3 [Citterio et al., 2004] and is involved in large scale reorganization of chromocenters [Papait et al., 2008].

Interestingly, a second member of the Uhrf family, Uhrf2, harbors similar domains [Bronner et al., 2007]. Until now, the only known function of Uhrf2 is a role in intranuclear degradation of polyglutamine aggregates [Iwata et al., 2009]. In this study, we systematically investigated the function and interplay of distinct Uhrf2 domains in DNA and histone tail substrate recognition and report first hints on cell-type specific functions of Uhrf1 and Uhrf2.

MATERIALS AND METHODS

EXPRESSION CONSTRUCTS

Expression constructs for GFP, RFP-PCNA, Uhrf1-GFP, and GFP constructs of Dnmt1 were described previously [Sporbert et al., 2005; Fellinger et al., 2009; Meilinger et al., 2009]. All Uhrf2 expression constructs were derived by PCR from mouse *uhrf2*-myc cDNA (MR210744, ORIGENE). To obtain GFP fusion constructs, the *uhrf1* cDNA [Rottach et al., 2010] was replaced by *uhrf2* encoding PCR fragments in the pCAG-*uhrf1*-GFP vector. The deletion and point mutant expression constructs were derived from the corresponding wild-type constructs by overlap extension PCR [Ho et al., 1989] and PCR-based mutagenesis. The following start and end amino acids were chosen: Uhrf2 tandem Tudor domain, amino acids 118–312; Uhrf2 PHD domain, amino acids 325–395; Uhrf2 tandem Tudor-PHD domain, amino acids 118–395; Uhrf1 tandem Tudor-PHD domain, amino acids 121–370. The linker exchange constructs were derived by PCR using overlapping primers that contained the partial linker sequence. Amino acid sequences of the linkers: Uhrf1: KERRPLIASPSQPPA; Uhrf2: GAHPISFADGKF. All constructs were verified by DNA sequencing. Throughout this study enhanced GFP constructs were used and for simplicity referred to as GFP fusions.

CELL CULTURE, TRANSFECTION, CELL SORTING, AND DIFFERENTIATION

HEK293T cells, MEFs, and ESCs were cultured and transfected as described [Schermelleh et al., 2007; Rottach et al., 2010] with the exception that Lipofectamin (Invitrogen) was used for transfection of MEFs. E14 *uhrf1*^{−/−} ESCs were transfected with Uhrf1-GFP and Uhrf2-GFP expression constructs using FuGENE HD (Roche) according to the manufacturer's instructions. ESCs were sorted for GFP positive cells 48 h after transfection with a FACS Aria II instrument (Becton Dickinson). ESC strains wt E14, wt J1, and E14 *uhrf1*^{−/−} were cultured and differentiated to embryoid bodies as described [Szwagierczak et al., 2010]. The ESC strain wt JM8A3.N1 (EUCOMM, Germany) was cultured in Knockout D-MEM (Gibco-BRL, Grand-Island, NY) medium containing 10% fetal bovine serum (PAA Laboratories GmbH, Austria), 0.1 mM β-mercaptoethanol (Gibco-BRL), 2 mM L-glutamine, 100 U/ml penicillin, 100 µg/ml streptomycin (PAA Laboratories GmbH). The medium was supple-

mented with 1,000 U/ml recombinant mouse LIF (Millipore, Temecula, CA).

RNA ISOLATION, cDNA SYNTHESIS, AND QUANTITATIVE REAL-TIME PCR

RNA isolation and cDNA synthesis were performed as described [Szwagierczak et al., 2010]. Equal amounts of cDNA were used for Real-time PCR with TaqMan Gene Expression Master Mix (Applied Biosystems) on the 7500 Fast Real-time PCR System (Applied Biosystems) according to the manufacturer's instructions. The following TaqMan Gene expression assays were used: Gapdh (Assay ID: Mm99999915_g1), *uhrf1* (Assay ID: Mm00477865_m1) and *uhrf2* (Assay ID: Mm00520043_m1). Gene expression levels were normalized to Gapdh and calculated using the comparative C_T Method (ΔΔC_T Method).

IN VITRO DNA BINDING AND HISTONE-TAIL PEPTIDE BINDING ASSAY

The in vitro binding assays were performed as described previously [Frauer and Leonhardt, 2009; Rottach et al., 2010]. NoCpG DNA substrates were produced in a primer extension reaction [Frauer and Leonhardt, 2009] others by hybridization of two DNA oligos (Supplementary Fig. S7B–D). Histone-tail peptides were purchased as TAMRA conjugates (PSL, Germany; Supplementary Fig. S7A). Peptides were added in a molar ratio 1.5:1 (peptide/GFP fusion) and the binding reaction was performed at RT for 15 min with constant mixing. For combined assays, samples were additionally incubated with either H3K9me3 or H3K9ac histone-tail peptides in a molar ratio 1.5:1 (peptide/GFP fusion) or increasing amount of DNA substrate as indicated. The binding reaction was performed at RT for 60 min with constant mixing.

IMMUNOFLUORESCENCE STAINING AND ANTIBODIES

For immunostaining, MEF cells and ESCs were grown on cover slips and transiently transfected with Uhrf2-GFP (MEF cells), or co-transfected with Uhrf2-GFP and RFP-PCNA (ESCs). Cells were fixed with 2.0% or 3.7% formaldehyde in PBS and permeabilized in PBS containing 0.2% Triton X-100. The post-translational histone modification H3K9me3 was detected via a rabbit primary antibody (Active Motif) and a secondary anti-rabbit antibody conjugated to Alexa Fluor 594 (Molecular Probes, Eugene, OR). The antibodies were diluted 1:1,000 or 1:500, respectively, in PBS containing 0.02% Tween-20 and 2% BSA. GFP-Binder (ChromoTek, Germany) was used to boost GFP signals and was labeled with Alexa Fluor 488. Cells were counterstained with DAPI and mounted in Vectashield (Vector Laboratories, Burlingame, CA). Images of the cells were obtained using a TCS SP5 AOBS confocal laser scanning microscope (Leica, Wetzlar, Germany) with a 63x/1.4 NA Plan-Apochromat oil immersion objective. GFP, Alexa Fluor 488, RFP, and Alexa Fluor 594 were excited with a 488-nm argon laser and a 561-nm diode laser, respectively. Image series were recorded with a frame size of 512 × 512 pixels, a pixel size of 100 nm and with a detection pinhole size of 1 Airy Unit.

LIVE CELL MICROSCOPY AND FLUORESCENCE RECOVERY AFTER PHOTOBLEACHING (FRAP) ANALYSIS

Live cell imaging and FRAP analyses were performed as described [Schermelleh et al., 2007] with the exception that imported images were intensity normalized, converted to 8-bit and Gauss-filtered (2 pixel radius). Data sets showing lateral movement were corrected by image registration using the StackReg plug-in of ImageJ [Abramoff et al., 2004] starting with a frame when approximately half recovery was reached. Within the first 30 s after bleaching, images were taken every 150 ms and then in intervals of 1 s.

DNA METHYLATION ANALYSIS

Genomic DNA was isolated with the QIAamp DNA Mini Kit (Qiagen) and 1.5 μ g were bisulfite converted using the EZ DNA Methylation-Gold Kit (Zymo research) according to the manufacturer's instructions. Primer sequences for major satellites were AAAAT-GAGAAACATCCACTTG (forward primer) and CCATGATTTCAGTTTCTT (reverse primer). For amplification we used Qiagen Hot Start Polymerase in 1 \times Qiagen Hot Start Polymerase buffer supplemented with 0.2 mM dNTPs, 0.2 μ M forward primer, 0.2 μ M reverse primer, 1.3 mM betaine (Sigma) and 60 mM tetramethylammonium-chloride (TMAC, Sigma). Major satellites were amplified in a single amplification and pyrosequencing reactions were carried out by Varionostic GmbH (Ulm, Germany).

STATISTICAL ANALYSIS

Results were expressed as means \pm SD or means \pm SEM. The difference between two mean values was analyzed by Student's *t*-test and was considered as statistically significant in case of $P < 0.05$ (*) and highly significant for $P < 0.001$ (**).

RESULTS

OPPOSITE EXPRESSION PATTERN OF *UHRF1* AND *UHRF2* DURING DIFFERENTIATION

Recently, Uhrf1 has emerged as an essential factor for the maintenance of DNA methylation. Sequence analyses revealed that Uhrf2 harbors five recognizable domains similar to Uhrf1 (Fig. 1A), but its role in the regulation of DNA methylation is still unclear. We compared the expression pattern of *uhrf1* and *uhrf2* in ESCs and somatic cells, during differentiation and in differentiated mouse tissues (Fig. 1B-D and Supplementary Fig. S1). Interestingly, both genes show opposite expression patterns; while *uhrf1* is expressed in ESCs and down regulated during differentiation, which is consistent with previous reports [Muto et al., 1995; Fujimori et al., 1998; Hopfner et al., 2000], *uhrf2* is upregulated and highly expressed in differentiated mouse tissues. The switch in the expression pattern argues against a functional redundancy of both genes and is consistent with the drastic loss of DNA methylation in *uhrf1*^{-/-} ESCs despite the presence of intact *uhrf2* alleles. Therefore, the opposite expression pattern of both genes suggests different functional roles of *uhrf1* and *uhrf2* in development.

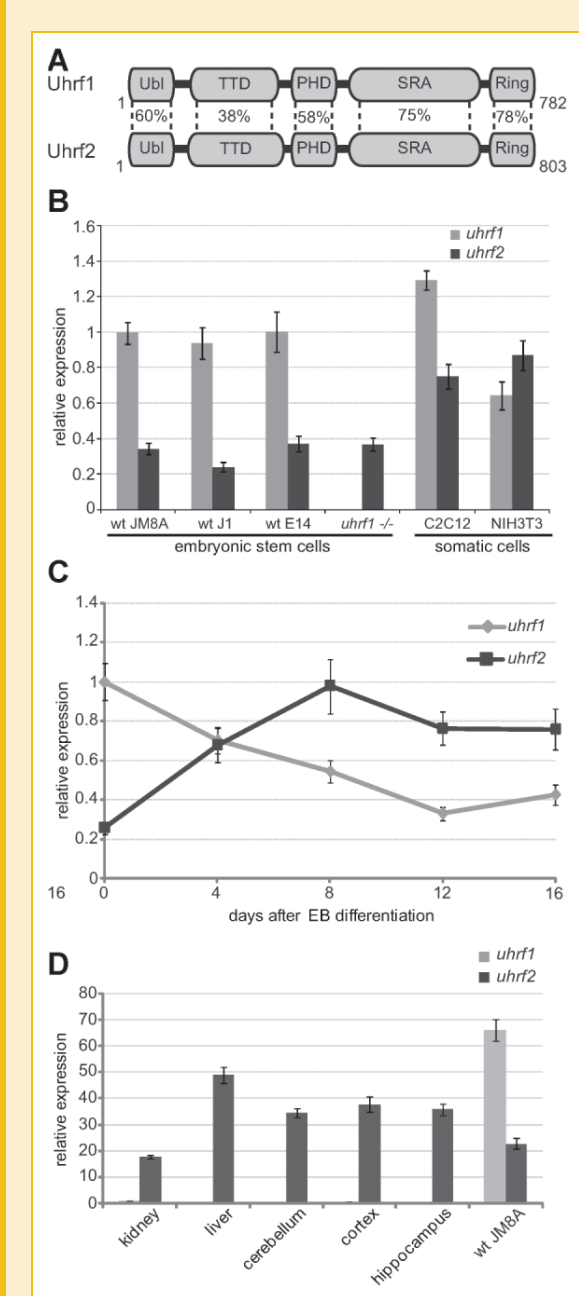


Fig. 1. Opposite expression pattern of *uhrlf1* and *uhrlf2* during differentiation. A: Schematic outline of the multi-domain architecture of Uhrf1 in comparison to Uhrf2. An N-terminal ubiquitin-like domain (Ub) is followed by a tandem Tudor domain (TTD), a plant homeodomain (PHD), a SET and RING associated (SRA) domain and a C-terminal really interesting new gene (RING) domain. Numbers indicate primary sequence similarities of single domains determined by BlastP search [Altschul, 1991]. Expression analysis of *uhrlf1* and *uhrlf2* by Real-time PCR in ESCs and somatic cells (B), during differentiation of wt J1 ESCs (C) and in various adult mouse tissues in comparison to the expression data in ESCs (D). Expression levels are relative to *uhrlf1* in wtJM8A (B), day 0 of differentiation (C) and to kidney (D) (*uhrlf1* set to 1). Shown are means \pm SD of at least two independent experiments.

COOPERATIVE BINDING OF REPRESSIVE EPIGENETIC MARKS BY UHRF2

To investigate DNA and histone-tail binding preferences of Uhrf2 in vitro, we used a versatile binding assay developed for GFP fusion proteins [Rothbauer et al., 2008; Frauer and Leonhardt, 2009;

Rottach et al., 2010]. Similar to Uhrf1, histone-tail peptide binding assays revealed that Uhrf2 preferentially binds to H3(1–20) and H3K9me3 peptides (Fig. 2A). This binding activity of Uhrf2 is mediated by the TTD but not the PHD domain (Fig. 2B). Consistently, acetylation of H3K9, underrepresented in heterochromatin,

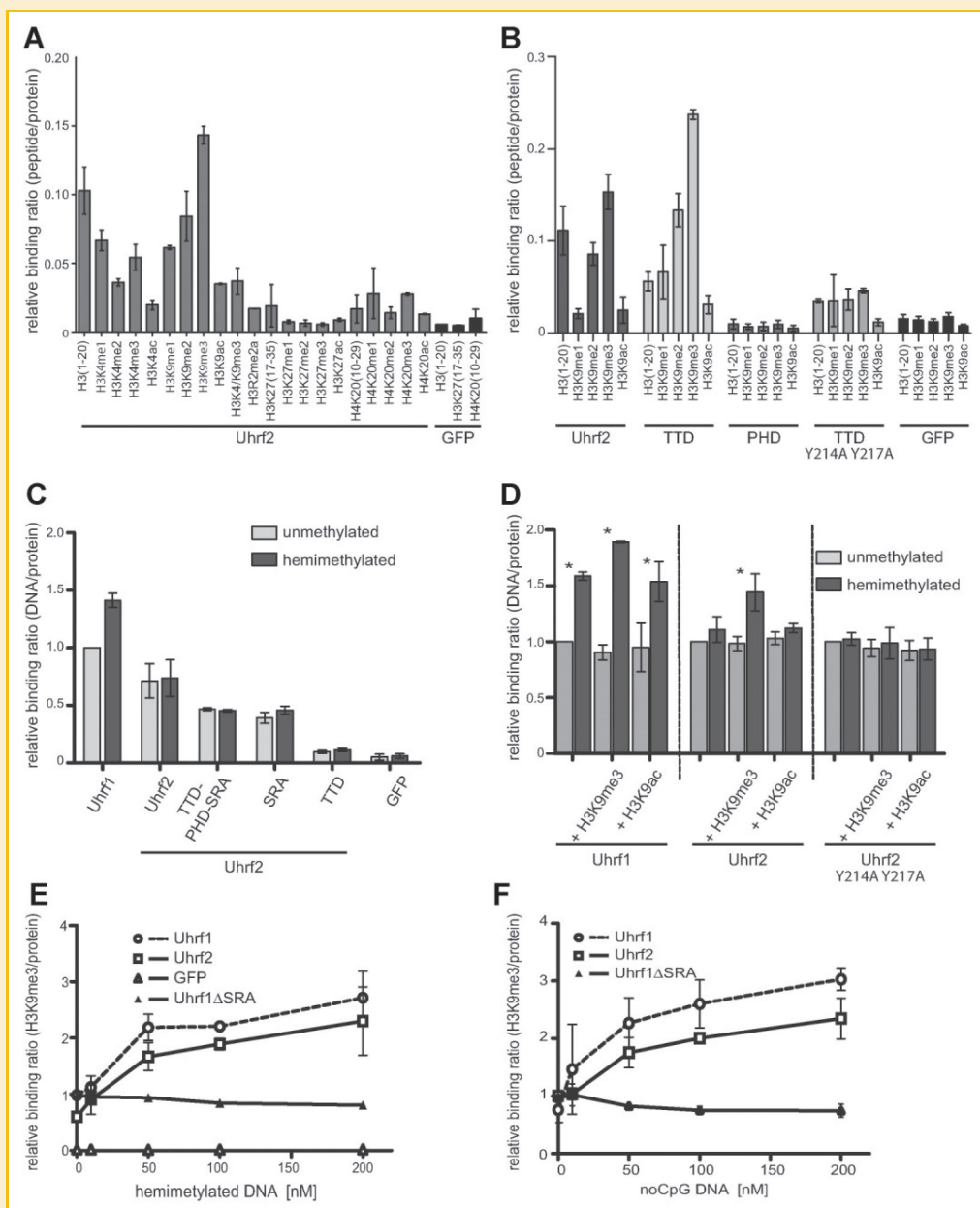


Fig. 2. Cooperative binding of repressive epigenetic marks by Uhrf2. In vitro binding ratios of fluorescently labeled substrate over bound GFP fusion proteins were determined. A: Histone H3- and H4-tail binding specificities of Uhrf2. Shown are means \pm SD of biological duplicates. B: Histone H3 tail binding specificity of Uhrf2, its tandem Tudor domain (TTD), its PHD domain and its TTD mutant (Y214A Y217A). Shown are means \pm SEM of at least three independent experiments. C: DNA binding properties of Uhrf1, Uhrf2 and of single (SRA, TTD) and combined Uhrf2 domains (TTD-PHD-SRA). Shown are means \pm SEM of three independent experiments. D: DNA binding properties of Uhrf1, Uhrf2 and Uhrf2 Y214A Y217A in combination with histone-tail peptide binding. Shown are means \pm SD of three independent experiments (Uhrf1, Uhrf2) and of two independent experiments (Uhrf2 Y214A Y217A). Values were normalized to the binding ratio of each GFP fusion for unmethylated DNA without histone-tail peptide. Statistical significance of differences between the binding ratios with un- and hemimethylated DNA is indicated: * $P < 0.05$. E + F: H3K9me3 peptide binding by Uhrf1, Uhrf2, and Uhrf1ΔSRA with increasing concentrations of DNA substrate containing either one central hemimethylated (E) or noCpG site (F). Shown are means \pm SD of biological duplicates. Values were normalized to the binding ratio of Uhrf1ΔSRA without DNA.

prevented the binding of Uhrf2 and its TTD. The binding of Uhrf1 to H3K9me3 is mediated by an aromatic cage in the TTD [Rottach et al., 2010]. Site-directed mutagenesis of Uhrf2 changing the two conserved tyrosine residues to alanine (Y214A Y217A) (Supplementary Fig. S2) abolished specific peptide binding (Fig. 2B) and supports a function of the aromatic cage in H3K9me3 recognition.

Whereas Uhrf1 preferentially binds to hemimethylated DNA, Uhrf2 failed to show a preference for hemi-over unmethylated DNA (Fig. 2C). These differences in DNA binding preferences between Uhrf1 and Uhrf2 were confirmed by electrophoretic mobility shifts (Supplementary Fig. S3). To further investigate the functional interplay between DNA and histone binding we performed combined binding assays (Fig. 2D). Interestingly, binding to heterochromatin-specific H3K9me3 peptides induced a significant preference of Uhrf2 for hemi-over unmethylated DNA. Uhrf1 already on its own showed preference for hemimethylated DNA that was further enhanced by binding to H3K9me3 peptides. To test the specificity of this cooperativity we mutated the aromatic cage in Uhrf2 that is necessary for H3K9me3 histone-tail peptide binding. The mutated Uhrf2 (Y214A Y217A) showed comparable DNA binding activity as the wild-type Uhrf2 but addition of heterochromatin-specific H3K9me3 peptides did not induce preference for hemi-over unmethylated DNA (Fig. 2D).

In the reverse experiment, addition of DNA enhanced binding of Uhrf1 and Uhrf2 to the H3K9me3 peptide (Fig. 2E,F). This was not observed for the DNA binding mutant of Uhrf1 (Uhrf1 Δ SRA) which showed constant peptide binding with increasing DNA concentrations. These findings suggest that single binding events of distinct Uhrf2 domains lead to multivalent engagement of different repressive epigenetic marks. In fact, multivalent engagement of DNA and histone tail peptides via the SRA domain and the TTD, respectively, results in affinity enhancement and additional specificity for hemimethylated DNA, the substrate of maintenance methylation.

CELLULAR LOCALIZATION AND DYNAMICS OF UHRF2 DEPEND ON HISTONE H3K9 METHYLATION

To monitor the subcellular localization of Uhrf2, we expressed Uhrf2-GFP constructs in cells with different genetic backgrounds. In wild type (wt) ESCs, Uhrf2 is localized in the nucleus and is enriched at pericentric heterochromatin (PH) (Fig. 3A,B and Supplementary Fig. S4A–C). To investigate which epigenetic marks at PH are recognized by Uhrf2 we determined the localization of Uhrf2 in genetically modified ESCs either lacking all three major DNA methyltransferases Dnmt1, Dnmt3a, and Dnmt3b (TKO) [Tsumura et al., 2006] or ESCs lacking the two major H3K9 methyltransferases Suv39H1/H2 (*Suv39h dn*) [Lehnertz et al., 2003]. TKO cells are practically devoid of genomic DNA methylation and *Suv39h dn* ESCs show substantially reduced H3K9me3 levels. We found Uhrf2 localized at PH in TKO but not in *Suv39h dn* ESCs, indicating that localization of Uhrf2 is dependent on H3K9 but not on DNA methylation (Fig. 3A). Consistently, immunostaining of wt mouse embryonic fibroblasts (MEFs) showed co-localization of Uhrf2 and H3K9me3 marks at PH, which was not observed in *Suv39h dn* MEFs [Peters et al., 2001] (Fig. 3B). Also, mutations in the TTD (Uhrf2 Y214A Y217A) that abolished binding to H3K9me3 peptides in vitro

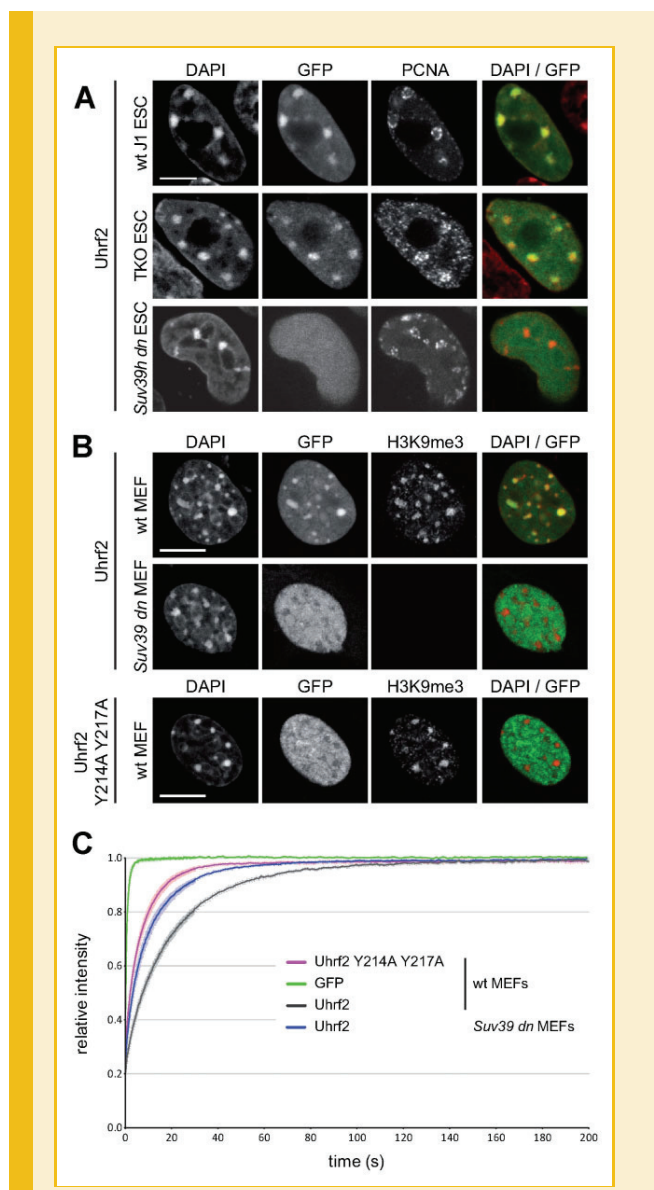


Fig. 3. Cellular localization and dynamics of Uhrf2 depend on histone H3K9 methylation. **A:** Confocal mid sections of fixed wt J1, TKO and *Suv39h dn* ESCs transiently expressing Uhrf2-GFP and RFP-PCNA and counterstained with DAPI, which preferentially highlights PH. Merged images are displayed on the right side (GFP: green; DAPI: red). Scale bar 5 μ m. **B:** Confocal mid sections of fixed wt MEFs and *Suv39h dn* MEFs transiently expressing Uhrf2-GFP or Uhrf2 Y214A Y217A-GFP were immunostained for H3K9me3 and counterstained with DAPI. Merged images are displayed on the right side (GFP: green; DAPI: red). Scale bar 5 μ m. **C:** Dynamics of Uhrf2-GFP and Uhrf2 Y214A Y217A-GFP in living MEFs determined by half nucleus FRAP analysis. GFP is shown as reference. Curves represent means \pm SEM from at least 8 nuclei.

disrupted enrichment at PH in wt MEFs (Fig. 3B). The dependence of Uhrf2 localization on H3K9me3 was also confirmed by quantitative correlation analysis (Supplementary Fig. S4D,E).

To investigate the effect of H3K9me3 on the dynamics of Uhrf2 in living cells we performed quantitative fluorescence recovery after photobleaching (FRAP) analyses in wt and *Suv39h dn* MEFs. We chose to bleach half nuclei to include a representative number of

interactions from different nuclear domains and structures in the bleached area [Rottach et al., 2010]. Recovery of Uhrf2-GFP fluorescence in *Suv39h dn* MEFs [half-time $t_{1/2} = 5.9 \pm 0.6$ s] and of the TTD mutant in wt MEFs ($t_{1/2} = 3.2 \pm 0.4$ s) was considerably faster than the recovery of Uhrf2-GFP in wt MEFs ($t_{1/2} = 11.8 \pm 0.6$ s) pointing to a crucial role of H3K9me3 in Uhrf2 dynamics in living cells (Fig. 3C). Taken together, these results clearly demonstrate that the interaction of Uhrf2 with the heterochromatin mark H3K9me3 is required for the localization at PH and affects binding dynamics in living cells.

COOPERATIVE BINDING OF THE COMBINED UHRF2 TTD-PHD DOMAIN

Recently, several studies showed multivalent binding to histone-tail peptides [Ruthenburg et al., 2007]. In case of Uhrf1 and Uhrf2, the TTD is followed by a second histone-tail binding domain, a PHD domain (Fig. 1A). As the isolated PHD domains of Uhrf1 and Uhrf2 did not show binding to H3 histone-tail peptides (Fig. 2B) [Rottach et al., 2010], we tested whether the combination of the PHD and the TTD results in cooperative histone-tail binding. Surprisingly, the combined TTD-PHD domain of Uhrf2 displayed a fourfold increased binding to H3K9me2/me3 in comparison to the single TTD, which was not observed for the corresponding construct of Uhrf1 (Figs. 2B and 4A).

Sequence alignments of the combined domains revealed two striking differences between Uhrf1 and Uhrf2. Firstly, Uhrf2 harbors an additional stretch of 33 highly conserved amino acids present in the TTD (Supplementary Fig. S5A). Secondly, the linker region between the TTD and PHD domain of Uhrf2 is highly conserved, whereas this region is highly diverse in Uhrf1 (Supplementary Fig. S5A). To test which sequence is responsible for the observed cooperative interplay between PHD and TTD, we generated and tested different hybrid and deletion constructs (Supplementary Fig. S5B). Notably, replacement of the native linker in the Uhrf2 TTD-PHD construct by the Uhrf1 linker caused decreased relative binding ratios to H3K9me2/3 comparable to the single Uhrf2 TTD (Fig. 4B). Transferring the Uhrf2 linker to the Uhrf1 TTD-PHD construct as well as deletion of the Uhrf2 stretch region did not affect the binding to H3K9me3 peptides (Fig. 4B).

These results suggest that the cooperative interplay of different Uhrf2 domains, which is responsible for the increased binding to heterochromatin marks, is dependent on the highly conserved linker region connecting the TTD and PHD domains. A similar functional importance of linker sequences has been described for BPTF and histone lysine demethylases [Li et al., 2006; Horton et al., 2010].

UHRF1 AND UHRF2 ARE NOT FUNCTIONALLY REDUNDANT IN ESCS

To investigate whether Uhrf1 and Uhrf2 are functionally redundant we performed interaction and rescue assays. Like Uhrf1, also Uhrf2 interacts with Dnmts (Supplementary Fig. S6) suggesting a similar function in DNA methylation. To test for such a functional role, we ectopically expressed Uhrf2-GFP or Uhrf1-GFP in *uhrf1*^{-/-} ESCs and determined DNA methylation levels at major satellites by pyrosequencing. While ectopic expression of Uhrf1-GFP led to significant increase of DNA methylation levels at CpG sites of major satellite DNA in *uhrf1*^{-/-} ESCs, Uhrf2-GFP did not restore DNA

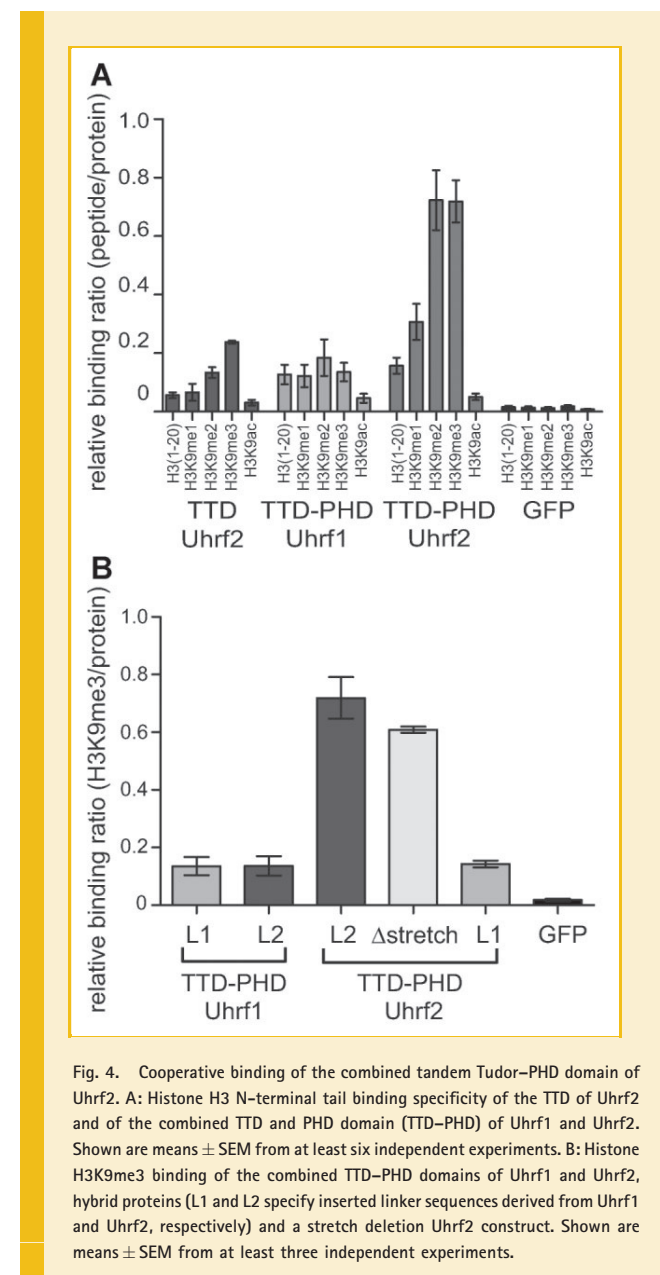


Fig. 4. Cooperative binding of the combined tandem Tudor-PHD domain of Uhrf2. A: Histone H3 N-terminal tail binding specificity of the TTD of Uhrf2 and of the combined TTD and PHD domain (TTD-PHD) of Uhrf1 and Uhrf2. Shown are means \pm SEM from at least six independent experiments. B: Histone H3K9me3 binding of the combined TTD-PHD domains of Uhrf1 and Uhrf2, hybrid proteins (L1 and L2 specify inserted linker sequences derived from Uhrf1 and Uhrf2, respectively) and a stretch deletion Uhrf2 construct. Shown are means \pm SEM from at least three independent experiments.

methylation at these sites (Fig. 5). These results point to functional differences between Uhrf1 and Uhrf2 in vivo.

DISCUSSION

Over the past decades many different histone modifications were discovered that are involved in epigenetic gene regulation. A key question is how these histone marks are linked to DNA methylation pattern and how this complex epigenetic information is integrated and translated into defined chromatin structures and gene expression levels. Epigenetic regulators that bind DNA and histone marks are ideally suited to link these pathways and intramolecular interactions between different binding domains may contribute to

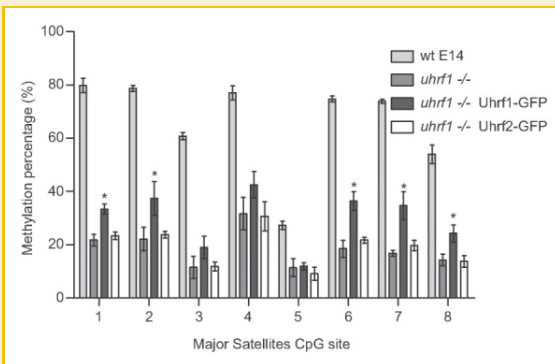


Fig. 5. Uhrf1 and Uhrf2 are not functionally redundant in ESCs. DNA methylation analysis of wt E14 ESCs, *uhrf1*^{-/-} ESCs and of *uhrf1*^{-/-} ESCs ectopically expressing Uhrf1-GFP or Uhrf2-GFP. ESCs transiently expressing Uhrf1-GFP and Uhrf2-GFP were isolated by FACS sorting 48 h after transfection and CpG methylation levels of major satellites repeats were analysed by bisulfite treatment, PCR amplification and direct pyrosequencing. Statistical significance of differences in DNA methylation levels between *uhrf1*^{-/-} ESCs and *uhrf1*^{-/-} ESCs with ectopically expressed Uhrf1-GFP or Uhrf2-GFP are indicated; **P* < 0.05. Shown are means \pm SD from three independent experiments.

substrate specificity and epigenetic regulation [Hashimoto et al., 2009].

Recently, Uhrf1, an essential factor for the maintenance of DNA methylation, has been shown to bind to repressive DNA and histone modifications via an SRA and a tandem Tudor domain, respectively. Here we provide the first systematic characterization of the second member of the Uhrf family, Uhrf2, and demonstrate that Uhrf2 binds to the H3K9me3 heterochromatin mark via an aromatic cage of a tandem Tudor domain (TTD). Mutations in the aromatic cage abolished binding to H3K9me3 histone-tail peptides in vitro and prevented enrichment of Uhrf2 at pericentric heterochromatin in vivo. Interestingly, similar mutations in the aromatic cage of Uhrf1 prevented repression of *p16^{INK4A}* [Nady et al., 2011] suggesting a link between H3K9me3 binding and a function of Uhrf proteins in gene repression.

Our results point to a complex regulation of substrate recognition by Uhrf2 involving cooperative binding domains and critical linker sequences. In contrast to Uhrf1, preferential binding of Uhrf2 to hemimethylated DNA, the substrate of DNA maintenance methylation, was only induced upon simultaneous binding to H3K9me3 histone-tail peptides. Binding of Uhrf1 and Uhrf2 to DNA in turn enhanced binding to H3K9me3 histone-tail peptides. Consistently, SILAC-based proteomic analysis identified enrichment of UHRF1 at nucleosomes containing repressive DNA and H3K9 methylation marks [Bartke et al., 2010]. Together, these data demonstrate a cooperative interplay between DNA and histone tail binding domains of Uhrf1 and Uhrf2. A similar effect was reported for MSL3 that specifically binds to H4K20me1 via a chromodomain only in the presence of DNA [Kim et al., 2010].

An additional level of complexity was added by recent studies showing multivalent binding of histone-tail peptides by mixed two-effector modules [Ruthenburg et al., 2007]. Notably, the combined TTD-PHD domain of Uhrf2, but not of Uhrf1, showed enhanced

binding to H3K9me3 histone-tail peptides. This cooperativity was dependent on the highly conserved linker region connecting the TTD and PHD domains. Similarly, an important role was attributed to the linker sequence between the histone binding domain (PHD) and the histone modifying domain of jumanji histone lysine demethylases [Horton et al., 2010].

The dramatic loss of DNA methylation in *uhrf1*^{-/-} ESCs [Bostick et al., 2007; Sharif et al., 2007] is remarkable, especially considering the presence of the *uhrf2* gene, which encodes a highly similar protein as demonstrated in this study. As one possible explanation for this lack of functional redundancy we found, in contrast to *uhrf1*, relatively low *uhrf2* mRNA levels in ESCs, which were not affected by genetic *uhrf1* ablation. Moreover, both genes also show opposite expression patterns during differentiation. The failure of ectopically expressed Uhrf2 to restore DNA methylation in *uhrf1* deficient cells clearly points to functional differences between both proteins in vivo. However, more definitive insights into the specific function(s) of Uhrf2 will require targeted mutations and subsequent analyses of pluripotent as well as differentiated cells. Based on the cooperative binding of Uhrf2 domains to repressive DNA and histone marks we propose that Uhrf2 might contribute to a tighter control of gene repression in differentiated cells as compared to a less stringent control by Uhrf1 in pluripotent ESCs.

ACKNOWLEDGMENTS

The authors are grateful to En Li (Novartis Institutes for Biomedical Research, Boston, MA) for J1 ESCs, to Masaki Okano (RIKEN Center for Developmental Biology, Kobe, Japan) for TKO ESCs, to Thomas Jenuwein (Max-Planck Institute of Immunobiology and Epigenetics, Freiburg, Germany) for the *Suv39h dn* MEFs and to Gunnar Schotta (Adolf-Butenandt-Institute, Faculty of Medicine, Ludwig Maximilians University Munich, Germany) for the *Suv39h dn* ESCs. This work was supported by the Nanosystems Initiative Munich (NIM) and by grants from the Deutsche Forschungsgemeinschaft (DFG) SFB646 and SFB684 to H.L. G.P., C.S.S., K.S., and C.F. were supported by the International Doctorate Program NanoBioTechnology (IDK-NBT) and the International Max Planck Research School for Molecular and Cellular Life Sciences (IMPRS-LS). PW is a fellow of the Graduate School Life Science Munich (LSM).

REFERENCES

- Abramoff MD, Magelhaes PJ, Ram SJ. 2004. Image processing with ImageJ. *Biophotonics Int* 11:36–42.
- Achour M, Fuhrmann G, Alhosin M, Ronde P, Chataigneau T, Mousli M, Schini-Kerth VB, Bronner C. 2009. UHRF1 recruits the histone acetyltransferase Tip60 and controls its expression and activity. *Biochem Biophys Res Commun* 390:523–528.
- Altschul SF. 1991. Amino acid substitution matrices from an information theoretic perspective. *J Mol Biol* 219:555–565.
- Arita K, Ariyoshi M, Tochio H, Nakamura Y, Shirakawa M. 2008. Recognition of hemi-methylated DNA by the SRA protein UHRF1 by a base-flipping mechanism. *Nature* 455:818–821.
- Avvakumov GV, Walker JR, Xue S, Li Y, Duan S, Bronner C, Arrowsmith CH, Dhe-Paganon S. 2008. Structural basis for recognition of hemi-methylated DNA by the SRA domain of human UHRF1. *Nature* 455:822–825.

Bartke T, Vermeulen M, Xhemalce B, Robson SC, Mann M, Kouzarides T. 2010. Nucleosome-interacting proteins regulated by DNA and histone methylation. *Cell* 143:470–484.

Bestor TH, Ingram VM. 1983. Two DNA methyltransferases from murine erythroleukemia cells: Purification, sequence specificity, and mode of interaction with DNA. *Proc Natl Acad Sci USA* 80:5559–5563.

Bird A. 2002. DNA methylation patterns and epigenetic memory. *Genes Dev* 16:6–21.

Bostick M, Kim JK, Esteve PO, Clark A, Pradhan S, Jacobsen SE. 2007. UHRF1 plays a role in maintaining DNA methylation in mammalian cells. *Science* 317:1760–1764.

Bronner C, Achour M, Arima Y, Chataigneau T, Saya H, Schini-Kerth VB. 2007. The UHRF family: Oncogenes that are druggable targets for cancer therapy in the near future? *Pharmacol Ther* 115:419–434.

Citterio E, Papait R, Nicassio F, Vecchi M, Gomiero P, Mantovani R, Di Fiore PP, Bonapace IM. 2004. Np95 is a histone-binding protein endowed with ubiquitin ligase activity. *Mol Cell Biol* 24:2526–2535.

Easwaran HP, Schermelleh L, Leonhardt H, Cardoso MC. 2004. Replication-independent chromatin loading of Dnmt1 during G2 and M phases. *EMBO Rep* 5:1181–1186.

Fellinger K, Rothbauer U, Felle M, Langst G, Leonhardt H. 2009. Dimerization of DNA methyltransferase 1 is mediated by its regulatory domain. *J Cell Biochem* 106:521–528.

Frauer C, Leonhardt H. 2009. A versatile non-radioactive assay for DNA methyltransferase activity and DNA binding. *Nucleic Acids Res* 37:e22.

Fujimori A, Matsuda Y, Takemoto Y, Hashimoto Y, Kubo E, Araki R, Fukumura R, Mita K, Tatsumi K, Muto M. 1998. Cloning and mapping of Np95 gene which encodes a novel nuclear protein associated with cell proliferation. *Mamm Genome* 9:1032–1035.

Hashimoto H, Horton JR, Zhang X, Bostick M, Jacobsen SE, Cheng X. 2008. The SRA domain of UHRF1 flips 5-methylcytosine out of the DNA helix. *Nature* 455:826–829.

Hashimoto H, Horton JR, Zhang X, Cheng X. 2009. UHRF1, a modular multi-domain protein, regulates replication-coupled crosstalk between DNA methylation and histone modifications. *Epigenetics* 4:8–14.

Ho SN, Hunt HD, Horton RM, Pullen JK, Pease LR. 1989. Site-directed mutagenesis by overlap extension using the polymerase chain reaction. *Gene* 77:51–59.

Hopfner R, Mousli M, Jeltsch JM, Voulgaris A, Lutz Y, Marin C, Bellocq JP, Oudet P, Bronner C. 2000. ICBP90, a novel human CCAAT binding protein, involved in the regulation of topoisomerase IIalpha expression. *Cancer Res* 60:121–128.

Horton JR, Upadhyay AK, Qi HH, Zhang X, Shi Y, Cheng X. 2010. Enzymatic and structural insights for substrate specificity of a family of jumonji histone lysine demethylases. *Nat Struct Mol Biol* 17:38–43.

Iwata A, Nagashima Y, Matsumoto L, Suzuki T, Yamanaka T, Date H, Deoka K, Nukina N, Tsuji S. 2009. Intracellular degradation of polyglutamine aggregates by the ubiquitin-proteasome system. *J Biol Chem* 284:9796–9803.

Jones PA, Baylin SB. 2007. The epigenomics of cancer. *Cell* 128:683–692.

Karagianni P, Amazit L, Qin J, Wong J. 2008. ICBP90, a novel methyl K9 H3 binding protein linking protein ubiquitination with heterochromatin formation. *Mol Cell Biol* 28:705–717.

Kim JK, Esteve PO, Jacobsen SE, Pradhan S. 2009. UHRF1 binds G9a and participates in p21 transcriptional regulation in mammalian cells. *Nucleic Acids Res* 37:493–505.

Kim D, Blus BJ, Chandra V, Huang P, Rastinejad F, Khorasanizadeh S. 2010. Corecognition of DNA and a methylated histone tail by the MSL3 chromo-domain. *Nat Struct Mol Biol* 17:1027–1029.

Kouzarides T. 2007. Chromatin modifications and their function. *Cell* 128:693–705.

Lehnertz B, Ueda Y, Derijck AA, Braunschweig U, Perez-Burgos L, Kubicek S, Chen T, Li E, Jenuwein T, Peters AH. 2003. Suv39h-mediated histone H3 lysine 9 methylation directs DNA methylation to major satellite repeats at pericentric heterochromatin. *Curr Biol* 13:1192–1200.

Leonhardt H, Page AW, Weier HU, Bestor TH. 1992. A targeting sequence directs DNA methyltransferase to sites of DNA replication in mammalian nuclei. *Cell* 71:865–873.

Li H, Ilin S, Wang W, Duncan EM, Wysocka J, Allis CD, Patel DJ. 2006. Molecular basis for site-specific read-out of histone H3K4me3 by the BPTF PHD finger of NURF. *Nature* 442:91–95.

Meilinger D, Fellinger K, Bultmann S, Rothbauer U, Bonapace IM, Klinkert WE, Spada F, Leonhardt H. 2009. Np95 interacts with de novo DNA methyltransferases, Dnmt3a and Dnmt3b, and mediates epigenetic silencing of the viral CMV promoter in embryonic stem cells. *EMBO Rep* 10:1259–1264.

Meissner A, Mikkelsen TS, Gu H, Wernig M, Hanna J, Sivachenko A, Zhang X, Bernstein BE, Nusbaum C, Jaffe DB, Gnirke A, Jaenisch R, Lander ES. 2008. Genome-scale DNA methylation maps of pluripotent and differentiated cells. *Nature* 454:766–770.

Mortusewicz O, Schermelleh L, Walter J, Cardoso MC, Leonhardt H. 2005. Recruitment of DNA methyltransferase I to DNA repair sites. *Proc Natl Acad Sci USA* 102:8905–8909.

Muto M, Utsuyama M, Horiguchi T, Kubo E, Sado T, Hirokawa K. 1995. The characterization of the monoclonal antibody Th-10a, specific for a nuclear protein appearing in the S phase of the cell cycle in normal thymocytes and its unregulated expression in lymphoma cell lines. *Cell Prolif* 28:645–657.

Nady N, Lemak A, Walker JR, Avvakumov GV, Karetzky MS, Achour M, Xue S, Duan S, Allali-Hassani A, Zuo X, Wang YX, Bronner C, Chedin F, Arrowsmith CH, Dhe-Paganon S. 2011. Recognition of multivalent histone states associated with heterochromatin by UHRF1. *J Biol Chem*. [Epub ahead of print].

Ooi SK, Qiu C, Bernstein E, Li K, Jia D, Yang Z, Erdjument-Bromage H, Tempst P, Lin SP, Allis CD, Cheng X, Bestor TH. 2007. DNMT3L connects unmethylated lysine 4 of histone H3 to de novo methylation of DNA. *Nature* 448:714–717.

Otani J, Nankumo T, Arita K, Inamoto S, Ariyoshi M, Shirakawa M. 2009. Structural basis for recognition of H3K4 methylation status by the DNA methyltransferase 3A ATRX-DNMT3-DNMT3L domain. *EMBO Rep* 10:1235–1241.

Papait R, Pistore C, Grazini U, Babbio F, Cogliati S, Pecoraro D, Brino L, Morand AL, Dechampesme AM, Spada F, Leonhardt H, McBlane F, Oudet P, Bonapace IM. 2008. The PHD domain of Np95 (mUHRF1) is involved in large-scale reorganization of pericentromeric heterochromatin. *Mol Biol Cell* 19:3554–3563.

Peters AH, O'Carroll D, Scherthan H, Mechtler K, Sauer S, Schofer C, Weipoltshammer K, Pagani M, Lachner M, Kohlmaier A, Opravil S, Doyle M, Sibilia M, Jenuwein T. 2001. Loss of the Suv39h histone methyltransferases impairs mammalian heterochromatin and genome stability. *Cell* 107:323–337.

Pradhan S, Talbot D, Sha M, Benner J, Hornstra L, Li E, Jaenisch R, Roberts RJ. 1997. Baculovirus-mediated expression and characterization of the full-length murine DNA methyltransferase. *Nucleic Acids Res* 25:4666–4673.

Qian C, Li S, Jakoncic J, Zeng L, Walsh MJ, Zhou MM. 2008. Structure and hemimethylated CpG binding of the SRA domain from human UHRF1. *J Biol Chem* 283(50):34490–34494.

Reik W. 2007. Stability and flexibility of epigenetic gene regulation in mammalian development. *Nature* 447:425–432.

Rothbauer U, Zolghadr K, Muyllyders S, Schepers A, Cardoso MC, Leonhardt H. 2008. A versatile nanotrap for biochemical and functional studies with fluorescent fusion proteins. *Mol Cell Proteomics* 7:282–289.

Rottach A, Frauer C, Pichler G, Bonapace IM, Spada F, Leonhardt H. 2010. The multi-domain protein Np95 connects DNA methylation and histone modification. *Nucleic Acids Res* 38:1796–1804.

Ruthenburg AJ, Li H, Patel DJ, Allis CD. 2007. Multivalent engagement of chromatin modifications by linked binding modules. *Nat Rev Mol Cell Biol* 8:983–994.

Schermelleh L, Haemmer A, Spada F, Rosing N, Meilinger D, Rothbauer U, Cardoso MC, Leonhardt H. 2007. Dynamics of Dnmt1 interaction with the replication machinery and its role in postreplicative maintenance of DNA methylation. *Nucleic Acids Res* 35:4301–4312.

Sharif J, Muto M, Takebayashi S, Suetake I, Iwamatsu A, Endo TA, Shinga J, Mizutani-Koseki Y, Toyoda T, Okamura K, Tajima S, Mitsuya K, Okano M, Koseki H. 2007. The SRA protein Np95 mediates epigenetic inheritance by recruiting Dnmt1 to methylated DNA. *Nature* 450:908–912.

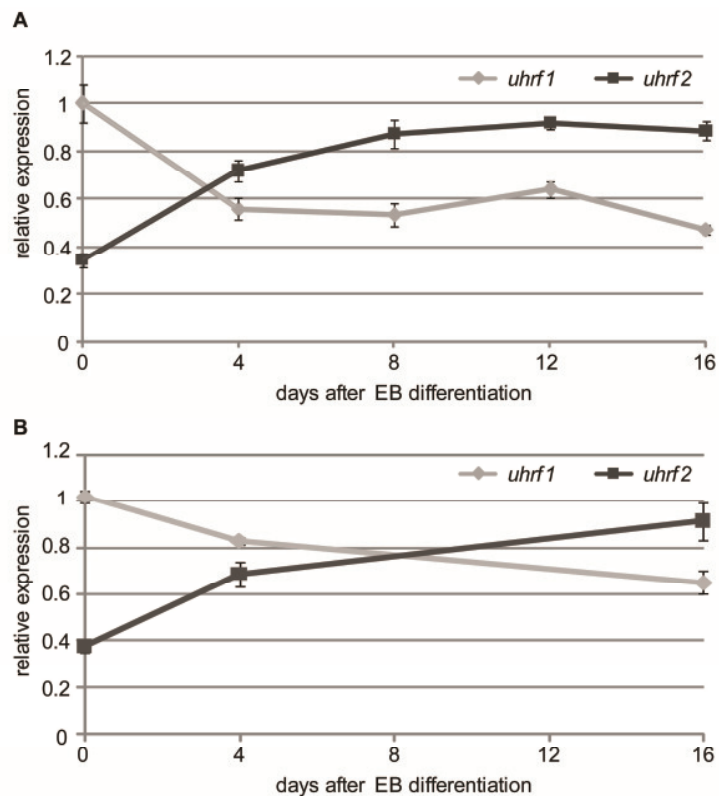
Sporbert A, Domaing P, Leonhardt H, Cardoso MC. 2005. PCNA acts as a stationary loading platform for transiently interacting Okazaki fragment maturation proteins. *Nucleic Acids Res* 33:3521–3528.

Szwagierczak A, Bultmann S, Schmidt CS, Spada F, Leonhardt H. 2010. Sensitive enzymatic quantification of 5-hydroxymethylcytosine in genomic DNA. *Nucleic Acids Res* 38:e181.

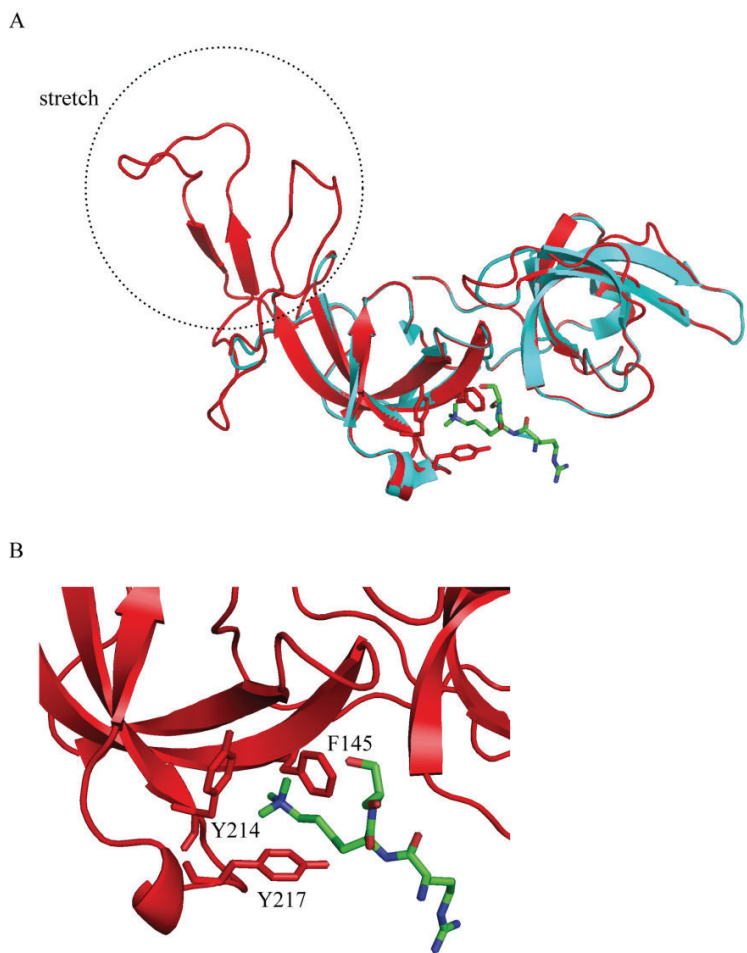
Tsumura A, Hayakawa T, Kumaki Y, Takebayashi S, Sakaue M, Matsuoka C, Shimotohno K, Ishikawa F, Li E, Ueda HR, Nakayama J, Okano M. 2006. Maintenance of self-renewal ability of mouse embryonic stem cells in the absence of DNA methyltransferases Dnmt1, Dnmt3a and Dnmt3b. *Genes Cells* 11:805–814.

Unoki M, Nishidate T, Nakamura Y. 2004. ICBP90, an E2F-1 target, recruits HDAC1 and binds to methyl-CpG through its SRA domain. *Oncogene* 23: 7601–7610.

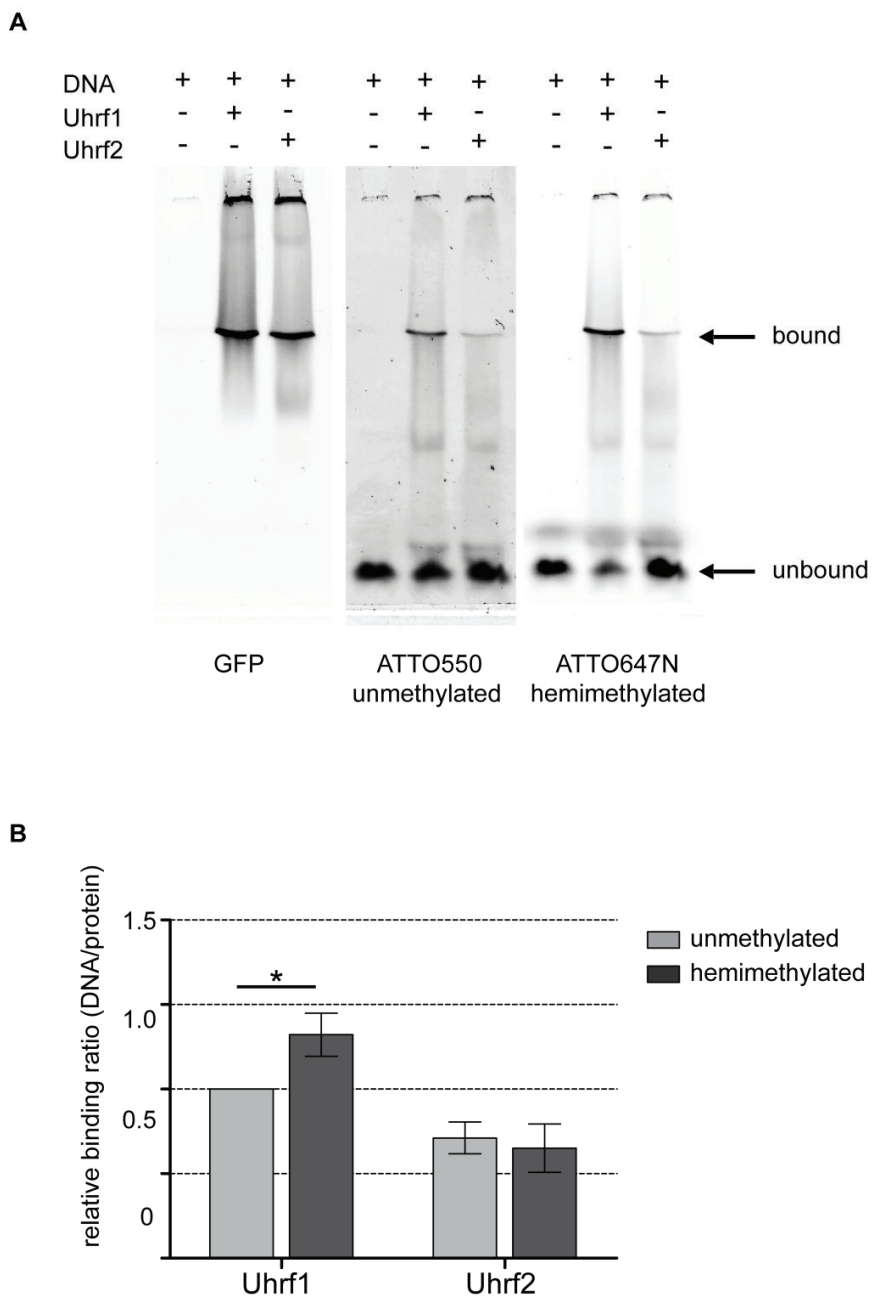
Supplementary Information



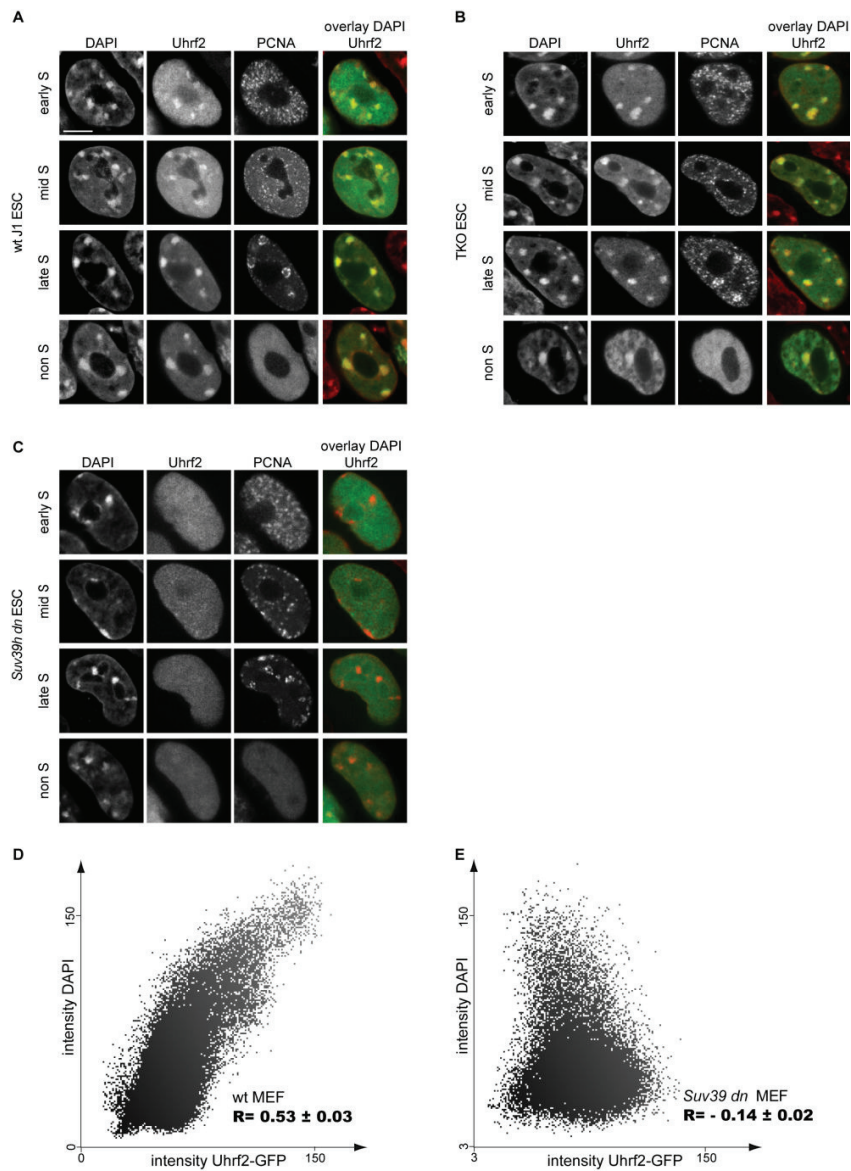
Supplementary Figure S1. Opposite expression pattern of *uhrf1* and *uhrf2*. Expression analyses of *uhrf1* and *uhrf2* by Real-time PCR during differentiation of ESCs with two different genetic backgrounds (wt E14 (**A**) and wt JM8A (**B**)). Transcript levels of *uhrf1* at day 0 of EB formation are used as reference point (set to 1). Shown are means \pm SD from three technical replicates of one biological experiment.



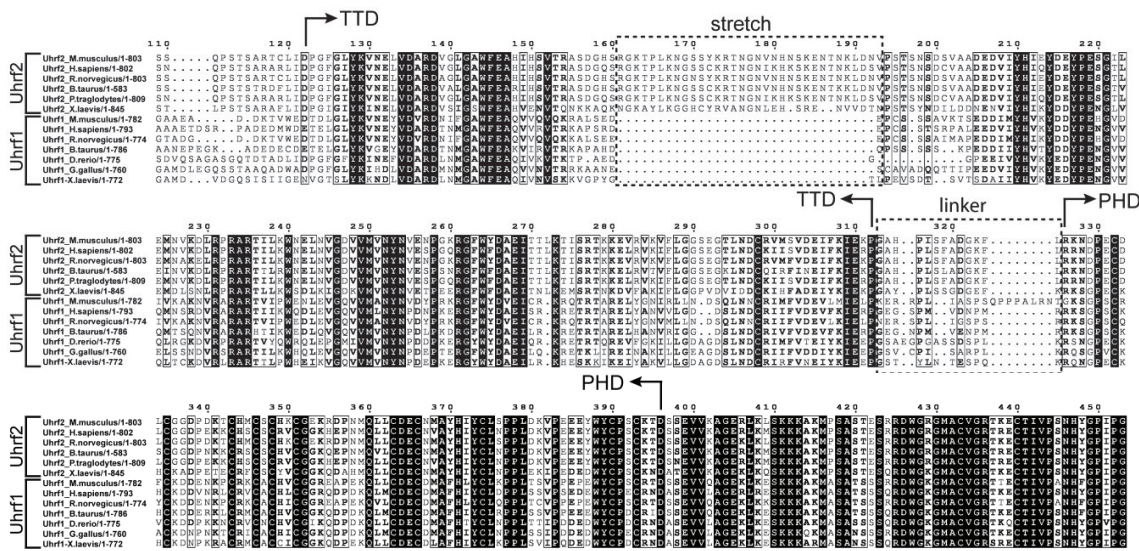
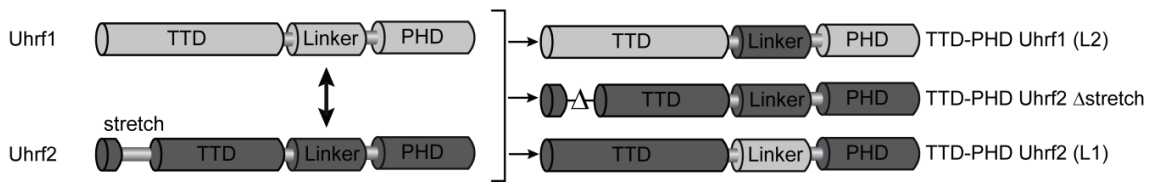
Supplementary Figure S2. Model of the tandem Tudor domain (TTD) of Uhrf2. **(A)** A model of the TTD of Uhrf2 was generated using SWISS Model [Arnold et al., 2006; Guex and Peitsch, 1997] with the solved structure of the TTD of Uhrf1 (PDB: 3DB3) as template. Both structures, the Uhrf2 model in red and the Uhrf1 template in cyan, are superimposed in PyMOL [Schrodinger, 2010]. **(B)** H3K9me3 is embedded in an aromatic cage formed by three aromatic residues of Uhrf2.



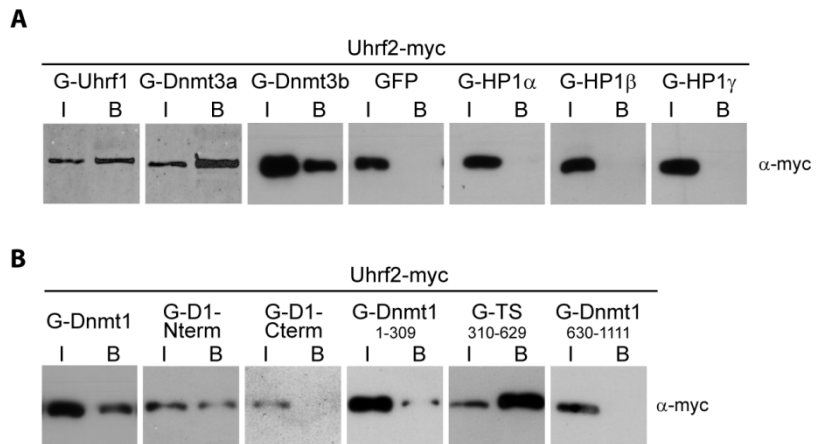
Supplementary Figure S3. Electrophoretic mobility shift of Uhrf1 and Uhrf2. **(A)** Un- and hemimethylated DNA substrates (1 pmol each in direct competition) were incubated with 0.63 pmol purified Uhrf1-GFP or Uhrf2-GFP. Samples were subjected to 3.5% non-denaturing PAGE and analyzed with a fluorescence scanner (Typhoon TRIO scanner, GE Healthcare) to detect ATTO550 (unmethylated substrate), ATTO647N (hemimethylated substrate) and GFP. **(B)** Band intensities were quantified with ImageJ [Abramoff, 2004]. To quantify bound DNA/protein ratios, grey values of unbound DNA bands were subtracted from the corresponding DNA input bands and subsequently normalized by the grey values of the GFP bands. All values were normalized to the relative binding ratio of Uhrf1 to unmethylated substrate. Shown are means \pm SD from three independent experiments. Statistical significance between the binding ratios of un- and hemimethylated DNA is indicated; *P < 0.05.



Supplementary Figure S4. Cell-cycle dependent localization of Uhrf2 in cells with different genetic backgrounds. Confocal mid sections of fixed wt J1 (A), TKO (B) and *Suv39h dn* ESCs (C), transiently expressing Uhrf2-GFP. Cells were co-transfected with a RFP-PCNA expression vector to distinguish S phase stages [Sporbert et al., 2005] and counterstained with DAPI. Merged images are displayed on the right. Scale bar 5 μ m. In wt J1 and TKO ESCs the Uhrf2 fusion protein accumulates at pericentric heterochromatin independent of the cell-cycle stage and methylation levels (A) (B). In contrast, Uhrf2-GFP shows a fully dispersed nuclear distribution in *Suv39h dn* cells indicating the dependency on H3K9me3 methylation for localization at PH *in vivo* (C). (D) and (E) Scatter blot of GFP-Uhrf2 and DAPI signals in wt MEFs and *Suv39h dn* MEFs. The corresponding Pearson correlation coefficients $R \pm SEM$ are calculated from ten analysed cells. The software Volocity (Perkin Elmer) was used for analysis, selecting the cell nucleus as region of interest. Note that Pearson correlation coefficients range from +1 to -1 for perfect to no co-localization.

A**B**

Supplementary Figure S5. Alignment and recombination of Uhrf1 and Uhrf2 domains. (A) Alignment of the tandem Tudor domain (TTD) and PHD domains from vertebrate Uhrf2 and Uhrf1 orthologs. Accession numbers for Uhrf2: *Homo sapiens* CAH74119.1; *Bos taurus* AAI48950.1; *Mus musculus* Q7TMI3; *Rattus norvegicus* NP_001101055.1; *Pan troglodytes* XP_528534.2; *Xenopus laevis* AAI28674.1. Accession numbers for Uhrf1: *Homo sapiens* Q96T88.1; *Bos taurus* AAI51672.1; *Mus musculus* Q8VDF2.2; *Rattus norvegicus* Q7TPK1.2; *Dario rerio* NP_998242.1; *Xenopus laevis* AAI28674.1, *Gallus gallus* XP_418269.2. Arrows show the start and end positions of the TTD and PHD domains. Absolutely conserved residues are black shaded, while positions showing conservative substitutions are boxed with residues in bold face. The additional stretch region found in the TTD of Uhrf2 and the linker region between TTD and PHD finger are boxed with dotted black lines. (B) Schematic outline of engineered constructs including the deletion of the stretch region and the swapping of linker sequences.



Supplementary Figure S6. Uhrf2 interacts with Uhrf1, Dnmt1 and Dnmt3a/b. **(A)** Co-immunoprecipitation of Uhrf2-myc and GFP-Uhrf1, GFP-Dnmt3a, GFP-Dnmt3b, GFP-HP1 α , GFP-HP1 β , GFP-HP1 γ or GFP transiently co-expressed in HEK293T cells. Note that Uhrf2 interacts with Uhrf1, Dnmt3a and Dnmt3b. **(B)** Co-immunoprecipitation of Uhrf2-myc and GFP-Dnmt1 constructs transiently co-expressed in HEK293T cells: GFP-Dnmt1 (G-Dnmt1), GFP-fusions of the N-terminal and C-terminal part of Dnmt1 (G-D1-Nterm, G-D1-Cterm) and truncated Dnmt1 constructs (G-Dnmt1 1-309, G-TS 310-629, G-Dnmt1 630-1111). Note that Uhrf2 interacts with full-length Dnmt1, the N-terminal part and the targeting sequence (G-TS 310-629). One percent of input (I) relative to bound fractions (B) was loaded. Co-immunoprecipitation was performed using the GFP trap [Rothbauer et al., 2008]. Co-precipitated myc-tagged proteins were detected using a mouse monoclonal primary anti-myc antibody (Invitrogen, Germany) and an HRP- or Cy5-conjugated secondary anti-mouse antibody (Sigma, Germany, or Jackson ImmunoResearch Laboratories, USA, respectively).

A

Peptide name	Peptide sequence	Peptide labelling
H3K4me1	ART X1 QTARKSTGGKAPRKQLK	
H3K4me2	ART X2 QTARKSTGGKAPRKQLK	
H3K4me3	ART X3 QTARKSTGGKAPRKQLK	
H3K4ac	ART Z QTARKSTGGKAPRKQLK	
H3K4/9un	ARTKOTARKSTGGKAPRKQLK	
H3K9me1	ARTKOTAR X1 STGGKAPRKQLK	TAMRA at C-terminus
H3K9me2	ARTKOTAR X2 STGGKAPRKQLK	
H3K9me3	ARTKOTAR X3 STGGKAPRKQLK	
H3K9ac	ARTKOTAR Z STGGKAPRKQLK	
H3R2me2a	A X4 TKQTATARSTGGKAPRKQLK	
H3K4me3K9me3	ART X3 QTAR X3 STGGKAPRKQLK	
H3K27un	RKQLATKAARKSAPATGGVK	
H3K27me1	RKQLATKAAR X1 SAPATGGVK	
H3K27me2	RKQLATKAAR X2 SAPATGGVK	
H3K27me3	RKOLATKAAR X3 SAPATGGVK	
H3K27ac	RKOLATKAAR Z SAPATGGVK	
H4K20un	LGKGGAKRHRKVLRDNIQGI	
H4K20me1	LGKGGAKRHR X1 VL RDNIQGI	TAMRA at N-terminus
H4K20me2	LGKGGAKRHR X2 VL RDNIQGI	
H4K20me3	LGKGGAKRHR X3 VL RDNIQGI	
H4K20ac	LGKGGAKRHR Z VL RDNIQGI	

X1: Lysine(me1); X2: Lysine(me2); X3: Lysine(me3); X4: Arginine(me2 asymmetric) Z: Lysine(ac)

B

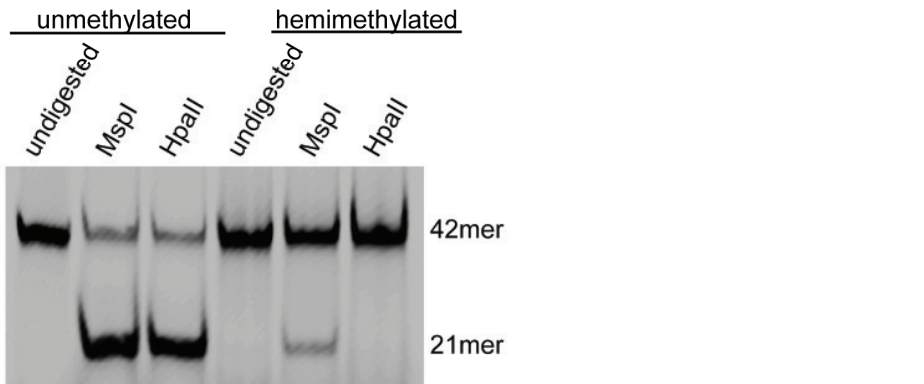
DNA substrate	DNA sequence	DNA labelling
CGup	CTCAACAACTAACTACCAT CCG GACCAGAAGAGTCATCATGG	no
MGup	CTCAACAACTAACTACCAT CGG GACCAGAAGAGTCATCATGG	no
noCpG	CTCAACAACTAACTACCAT CGG CGG GACCAGAAGAGTCATCATGG	no
um647N	CCATGATGACTCTCTGGT CCG GATGGTAGTTAGTTAGTGTGAG	ATTO647N at 5'end
um700	CCATGATGACTCTCTGGT CCG GATGGTAGTTAGTTAGTGTGAG	ATTO700 at 5'end
Fill-In-550	CCATGATGACTCTCTGGTC	ATTO550 at 5'end
Fill-In-590	CCATGATGACTCTCTGGTC	ATTO590 at 5'end
Fill-In-647N	CCATGATGACTCTCTGGTC	ATTO647N at 5'end
Fill-In-700	CCATGATGACTCTCTGGTC	ATTO700 at 5'end

C

Mspl
HpaII

CTCAACAACTAACTACCAT**CCGG**ACCAGAAAGAGTCATCATGG
GAGTTGTTGATTGATGGTA**GGCC**CTGGTCTTCTCAGTAGTACC ★ 42mer

CGGACCAGAAAGAGTCATCATGG
CTGGTCTTCTCAGTAGTACC ★ 21mer



Supplementary Figure S7. Histone-tail peptide and DNA sequences and quality control of DNA substrates. **(A)** Amino acid sequence of TAMRA-labelled peptides for *in vitro* histone-tail peptide binding assays. Histone-tail peptides were purchased as TAMRA conjugates (PSL, Germany). **(B)** DNA oligos used for preparation of double-stranded probes for *in vitro*

DNA binding assays. M: 5-methyl-cytosine. For hybridization, DNA oligos were mixed in equimolar amounts, heated to 92°C and cooled down to room temperature. DNA substrates for Figure 2F were completed in a primer extension reaction. By using a control set of DNA probes with identical sequence but different fluorescent labels we observed effects due to probe preparation and/or unspecific binding of ATTO dyes (data not shown). The values obtained from the control set were used to normalize every probe/protein pair. **(C)** Quality control of DNA substrates. Un- and hemimethylated DNA substrates (2 pmol; Atto647N labelled) were digested with 1 unit Mspl or Hpall and analyzed by 15% non-denaturing PAGE for CpG methylation. Note that unmethylated DNA substrate is digested by both enzymes, whereas hemimethylated substrate is only cut by Mspl. Enzyme recognition motifs are boxed and asterisks represent ATTO labels.

Supplementary References

Abramoff MD, Magelhaes, P.J., Ram, S.J. 2004. Image Processing with ImageJ. *Biophotonics International* 11:36-42.

Arnold K, Bordoli L, Kopp J, Schwede T. 2006. The SWISS-MODEL workspace: a web-based environment for protein structure homology modelling. *Bioinformatics* 22:195-201.

Guex N, Peitsch MC. 1997. SWISS-MODEL and the Swiss-PdbViewer: an environment for comparative protein modeling. *Electrophoresis* 18:2714-23.

Rothbauer U, Zolghadr K, Muyllydermans S, Schepers A, Cardoso MC, Leonhardt H. 2008. A versatile nanotrap for biochemical and functional studies with fluorescent fusion proteins. *Mol Cell Proteomics* 7:282-9.

Schrodinger, LLC. 2010. The PyMOL Molecular Graphics System, Version 1.3editor^editors.

Sporbert A, Domaing P, Leonhardt H, Cardoso MC. 2005. PCNA acts as a stationary loading platform for transiently interacting Okazaki fragment maturation proteins. *Nucleic Acids Res* 33:3521-8.

2.4 Dissection of cell cycle-dependent dynamics of Dnmt1 by FRAP and diffusion-coupled modeling

Dissection of cell cycle-dependent dynamics of Dnmt1 by FRAP and diffusion-coupled modeling

Katrin Schneider¹, Christiane Fuchs², Akos Dobay¹, Andrea Rottach¹, Weihua Qin¹, Patricia Wolf¹, José M. Álvarez-Castro¹, Marcus M. Nalaskowski³, Elisabeth Kremmer⁴, Volker Schmid⁵, Heinrich Leonhardt¹ and Lothar Schermelleh^{1,*}

¹Department of Biology and Center for Integrated Protein Science, Ludwig Maximilians University Munich (LMU), 82152 Planegg-Martinsried, Germany, ²Institute for Bioinformatics and Systems Biology, Helmholtz Zentrum München, German Research Center for Environmental Health, 85764 Neuherberg, Germany,

³Department of Biochemistry and Signal Transduction, University Medical Center Hamburg-Eppendorf, 20246 Hamburg, Germany, ⁴Institute of Molecular Immunology, Helmholtz Zentrum München, German Research Center for Environmental Health, 81377 Munich, Germany and ⁵Department of Statistics, Ludwig Maximilians University Munich (LMU), 80539 Munich, Germany

Received November 15, 2012; Revised February 26, 2013; Accepted February 27, 2013

ABSTRACT

DNA methyltransferase 1 (Dnmt1) reestablishes methylation of hemimethylated CpG sites generated during DNA replication in mammalian cells. Two subdomains, the proliferating cell nuclear antigen (PCNA)-binding domain (PBD) and the targeting sequence (TS) domain, target Dnmt1 to the replication sites in S phase. We aimed to dissect the details of the cell cycle-dependent coordinated activity of both domains. To that end, we combined super-resolution 3D-structured illumination microscopy and fluorescence recovery after photobleaching (FRAP) experiments of GFP-Dnmt1 wild type and mutant constructs in somatic mouse cells. To interpret the differences in FRAP kinetics, we refined existing data analysis and modeling approaches to (i) account for the heterogeneous and variable distribution of Dnmt1-binding sites in different cell cycle stages; (ii) allow diffusion-coupled dynamics; (iii) accommodate multiple binding classes. We find that transient PBD-dependent interaction directly at replication sites is the predominant specific interaction in early S phase (residence time $T_{res} \leq 10$ s). In late S phase, this binding class is taken over by a substantially stronger ($T_{res} \sim 22$ s) TS domain-dependent interaction at PCNA-enriched replication sites and

at nearby pericentromeric heterochromatin subregions. We propose a two-loading-platform-model of additional PCNA-independent loading at post-replicative, heterochromatic Dnmt1 target sites to ensure faithful maintenance of densely methylated genomic regions.

INTRODUCTION

DNA methylation is an essential epigenetic mechanism in mammals involved in gene regulation, genomic imprinting, X inactivation and carcinogenesis (1–3). Once established *de novo* during cell differentiation, the genomic methylation pattern is maintained by the DNA methyltransferase 1 (Dnmt1), a 183 kDa-sized enzyme that transfers methyl groups to hemimethylated substrate CpG sites generated during DNA synthesis in S phase (2,4,5). Hence, it seems obvious that the regulation of Dnmt1 is tightly coupled to DNA replication. In fact, using fluorescence recovery after photobleaching (FRAP), we have previously reported that Dnmt1 associates with replication foci (RF) by a highly transient interaction with the replication clamp proliferating cell nuclear antigen (PCNA) in early S phase via the PCNA-binding domain (PBD) of Dnmt1, enhancing the efficiency of covalent complex formation at its substrate sites (6,7). PCNA forms a homotrimeric ring around the DNA at replication forks and operates as a quasi-immobile

*To whom correspondence should be addressed. Tel: +44 1865 613264; Fax: +44 1865 613340; Email: lothar.schermelleh@bioch.ox.ac.uk
Present address: Lothar Schermelleh, Department of Biochemistry, University of Oxford, Oxford OX1 3QU, United Kingdom.

Akos Dobay, Institute of Evolutionary Biology and Environmental Studies, University of Zurich, 8057 Zurich, Switzerland.

José M. Álvarez-Castro, Department of Genetics, University of Santiago de Compostela, 27002 Lugo, Spain.

Lothar Schermelleh, Department of Biochemistry, University of Oxford, Oxford OX1 3QU, United Kingdom.

The authors wish it to be known that, in their opinion, the first two authors should be regarded as joint First Authors.

© The Author(s) 2013. Published by Oxford University Press.

This is an Open Access article distributed under the terms of the Creative Commons Attribution Non-Commercial License (<http://creativecommons.org/licenses/by-nc/3.0/>), which permits unrestricted non-commercial use, distribution, and reproduction in any medium, provided the original work is properly cited.

loading platform for various replication-associated factors (8,9). Furthermore, the targeting sequence (TS) domain has been found to mediate association of Dnmt1 to constitutive heterochromatin from late S phase into G2 (10,11), the latter finding challenging the strict coupling to the replication process. In addition, the TS domain was implicated in the interaction with Uhrf1 (12). Uhrf1 is an essential cofactor in the DNA methylation process and it has been proposed that Uhrf1 targets Dnmt1 to hemimethylated sites (13–17). Although the role and regulation of Dnmt1 has been a popular field of research for many years, the details and functional implications of the cell cycle-dependent coordinated binding activity of the PBD and the TS domain still remain elusive.

FRAP techniques offer an effective tool to study *in vivo* the mobility of cellular proteins and to gain a better understanding of molecular interactions that drive or limit the mobility of fluorescent fusions expressed in cells (18–21). By bleaching a subpopulation of fluorescent proteins and by analyzing the redistribution of fluorescence over time, one can obtain measures of the half-time of recovery and the size of mobile fractions. To furthermore extract kinetic parameters from fluorescence recovery curves, one can describe the underlying dynamics of the proteins by a set of differential equations and apply a fitting procedure. Such kinetic modeling approaches can be useful to detect and quantify distinct dynamic populations [mobility classes (MCs)] and have been successfully used to quantitatively characterize diffusion and to some extent interactions inside living cells (22–24). Within the nucleus, the mobility of protein factors can be limited by binding to rather immobile structures, most prominently to chromatin, or to stationary enzyme complexes, such as the replication machinery, transcription domains or splicing speckles (25–27). The majority of these interactions are surprisingly transient to accommodate dynamic exchange, which is pivotal to provide cellular plasticity and efficient responses to external signals (28–30).

We aimed to extract quantitative measures of the binding properties of Dnmt1 *in vivo*. Unlike for many other nuclear factors, Dnmt1-binding sites are non-homogeneously distributed with association sites constantly changing their location throughout the cell cycle. To characterize the contribution of the PBD and TS domain on these changing interactions, we analyzed the mobility of wild type and mutants of GFP-tagged Dnmt1. In particular, we interpreted the differences between the mutants by modeling FRAP experiments where half of the nucleus is bleached. As the spatial distribution of the different binding sites is unknown *a priori*, we modified classical reaction-diffusion models in a way that diffusion is simplified into a two-compartment exchange model and binding events are averaged over the entire half-nucleus. This model also takes into account potential multiple binding partners of proteins with different binding affinities.

Our results provide evidence that the collective integrity of the PBD and TS domain is necessary and sufficient for the entire S phase-dependent targeting of Dnmt1 to its localization sites. Transient PBD-mediated interaction at

RF is the predominant specific interaction in early S phase, while in late S phase, this binding class is relegated by an ~2-fold stronger TS domain-dependent binding. Supported by super-resolution imaging with 3D-structured illumination microscopy (3D-SIM) (31,32) we show that TS binding is not restricted to replication sites but also occurs PCNA/PBD-independently at postreplicative constitutive heterochromatin. We propose a two-loading-platform-model in which the increasing density of hemimethylated CpG sites in conjunction with increased level of heterochromatin marks at postreplicative heterochromatin in late S phase provides high-affinity binding sites for TS-mediated binding of Dnmt1. PCNA-independent loading downstream of replication thus provides a mechanism to ensure maintenance of densely methylated heterochromatic DNA sequences.

MATERIALS AND METHODS

Expression constructs and cell culture

The expression constructs, 1xGFP, 2xGFP, 4xGFP, GFP-Dnmt1^{WT}, GFP-Dnmt1^{Q162E} and GFP-Dnmt1^{ΔTS} have been described previously (6,33,34). GFP-Dnmt1^{Q162E/ΔTS} was derived from GFP-Dnmt1^{ΔTS} by overlap extension PCR. Mouse C2C12 myoblast cells were cultured in DMEM supplemented with 20% fetal bovine serum and 50 µg/ml gentamycin. For live cell experiments, cells were seeded in Lab-Tek chamber slides (Nunc) or µ-slides (Ibidi), using either pools of stably expressing cells or transiently transfected cells.

Creation of stably expressing cells has been described before (6). For transient transfections, cells were grown up to 30–40% confluence and transfected with TransFectin transfection reagent (Bio-Rad) or FuGENE HD (Roche) according to the manufacturer's instructions. Cells were then incubated overnight (TransFectin) or ~40 h (FuGENE HD) before performing FRAP experiments (6).

Only moderately expressing cells with unsuspicious morphology were chosen for further analysis. The overall Dnmt1 level of endogenous and ectopically expressed protein was determined for all analyzed constructs and cell lines by immunofluorescence labeling using a novel Dnmt1-specific rat monoclonal antibody 5A10. Quantitative analysis of labeling intensities revealed on average 2-fold increased protein levels compared with non-transfected control cells confirming no major overexpression of the GFP-Dnmt1 fusion constructs (see Supplementary Methods and Supplementary Figure S1 for details on the antibody characterization and the immunofluorescence assay).

EdU pulse labeling, immunofluorescence staining and structured illumination microscopy

Cells, stably expressing GFP-Dnmt1 fusions were seeded on No. 1.5H precision coverslips (Marienfeld Superior), formaldehyde fixed and permeabilized with ice-cold methanol. For labeling of postreplicative DNA, 5 µM 5-ethyl-2'-deoxyuridine (EdU) was added to the growth medium 60 min before fixation. Endogenous PCNA was fluorescently labeled either with a rat monoclonal

antibody 16D10 (35) or a mouse monoclonal antibody PC10 (Abcam) and secondary antibodies conjugated to Alexa Fluor 594 (Invitrogen) or CF405S (Biotium). GFP was postlabeled with ATTO488 conjugated GFP-Booster (ChromoTek). Edu was detected by Cu (I) catalyzed cycloaddition ('click-chemistry') of 20 μ M Alexa Fluor 594 Azide (Invitrogen) diluted in 0.1 M Tris/HCl (pH 8.6) containing 4 mM CuSO₄ and 50 mM Na-ascorbate. Cells were counterstained with 1 μ g/ml 4',6-diamidino-2-phenylindole and embedded in Vectashield (Vector Laboratories).

3D-SIM was performed on a DeltaVision OMX V3 (Applied Precision) system equipped with a 100 \times /1.40 NA PlanApo oil immersion objective (Olympus), Cascade II:512 EMCCD cameras (Photometrics) and 405, 488 and 593 nm diode lasers. Structured illumination (SI) image stacks were acquired with a z-distance of 125 nm and with 15 raw SI images per plane (5 phases, 3 angles). The SI raw data were then computationally reconstructed with channel specifically measured optical transfer functions using the softWoRX 4.0 software package (Applied Precision) to obtain a super-resolution image stack with a lateral (x,y) resolution of \sim 120 nm and an axial (z) resolution of \sim 300 nm (31). Images from the different color channels were registered with alignment parameter obtained from calibration measurements with 0.2 μ m diameter TetraSpeck beads (Invitrogen).

Live cell microscopy and quantitative FRAP analysis

Live cell imaging and FRAP experiments were typically performed on an UltraVIEW VoX spinning disc microscope with integrated FRAP PhotoKinesis accessory (PerkinElmer) assembled to an Axio Observer D1 inverted stand (Zeiss) and using a 63 \times /1.4 NA Plan-Apochromat oil immersion objective. The microscope was equipped with a heated environmental chamber set to 37°C. Fluorophores were excited with 488 nm or 561 nm solid-state diode laser lines. Confocal image series were typically recorded with 14-bit image depth, a frame size of 256 \times 256 pixels, a pixel size of 110 nm and with time intervals of 154 ms. For photo-bleaching experiments, the bleach regions, typically with a length of 8–10 μ m, were chosen to cover the anterior half of the oval-shaped nucleus. Photobleaching was performed using two iterations with the acousto-optical tunable filter (AOTF) of the 488 nm and the 514 nm laser line set to 100% transmission. Typically, 20 prebleach and 780 postbleach frames were recorded for each series. In some cases, FRAP experiments were performed on a TCS SP5 AOBS confocal laser scanning microscope (Leica) using comparable settings as previously described (6).

Data correction, normalization and quantitative evaluations were performed by automated processing with ImageJ (<http://rsb.info.nih.gov/ij/>) using a set of self-developed macros followed by calculations in Excel. Details are provided in the Supplementary Methods and in Supplementary Figure S4.

Mathematical model

The mathematical models used to statistically infer the kinetic parameters from corrected and normalized FRAP datasets are based on a compartmental approach and biochemical kinetic principles. The model for diffusion-uncoupled FRAP, i.e. for molecules that diffuse much more rapidly than they bind or unbind, has previously been described (22,36). A model for diffusion-coupled FRAP is developed in this work and illustrated in Figure 4A; a similar approach has been taken in (37). The model considers transitions between the bound and the free state of a protein with *association rate constant* k_{on} and *dissociation rate constant* k_{off} . As substantiated in the Supplementary Methods, the association and dissociation dynamics can be expressed in terms of linear ordinary differential equations (ODEs) when replacing k_{on} by an *effective association rate constant* k_{on}^* . The ODEs are given below. While bound proteins remain fixed at the respective binding sites, free proteins diffuse through the nucleus, thus changing their locations. Movements between the bleached and the unbleached section are modeled with a *diffusion rate constant* k_{diff} . Its value depends on the geometry of the cell and is not immediately eligible for interpretation purposes. See the Supplementary Methods for details on the modeling of the movement of proteins.

Bleached and unbleached molecules are assumed to behave identically, and therefore it suffices to focus on one type only. Hence, let P_{bl}^{free} , P_{unbl}^{free} , P_{bl}^{bound} and P_{unbl}^{bound} denote the fractions of unbleached free and bound proteins in the bleached and unbleached sections, measured with respect to all unbleached proteins in the nucleus. These four parameters sum up to one such that one of them can be left out. Define $P^{free} = P_{bl}^{free} + P_{unbl}^{free}$ and $P^{bound} = P_{bl}^{bound} + P_{unbl}^{bound}$. The overall dynamics of unbleached proteins is described by

$$\frac{dP_{bl}^{free}}{dt} = -k_{on}^* P_{bl}^{free} + k_{off} P_{bl}^{bound} + k_{diff} (f_{bl} P_{unbl}^{free} - (1 - f_{bl}) P_{bl}^{free}), \quad (1)$$

$$\frac{dP_{unbl}^{free}}{dt} = -k_{on}^* P_{unbl}^{free} + k_{off} (1 - P_{bl}^{free} - P_{unbl}^{free} - P_{bl}^{bound}) - k_{diff} (f_{bl} P_{unbl}^{free} - (1 - f_{bl}) P_{bl}^{free}), \quad (2)$$

$$\frac{dP_{bl}^{bound}}{dt} = k_{on}^* P_{bl}^{free} - k_{off} P_{bl}^{bound}. \quad (3)$$

The recovery curve equals $F = (P_{bl}^{free} + P_{bl}^{bound})/f_{bl}$. This term was adjusted to the data normalization procedure described in the Supplementary Methods and approaches the value one as time progresses.

There is possibly more than one type of binding partner for Dnmt1, i.e. the protein may sometimes associate to a partner of one type and sometimes to a partner of another type. These partners may differ with respect to the affinity of Dnmt1 to enter the bound state and the mean residence times in this state. All binding partners with identical or similar kinetic properties are gathered in one MC.

This term seems more appropriate than *classes of binding sites* (22) because different sites with identical kinetic properties cannot be distinguished using FRAP data. The number of MCs could hence be smaller than the number of different binding partners. Furthermore binding-unrelated processes like anomalous diffusion can fall into an MC.

Suppose there are M classes of kinetically different binding partners for the protein of interest, labeled with numbers $i \in \{1, \dots, M\}$. For all i , define $P_{bl}^{bound,i}$ and $P_{unbl}^{bound,i}$ as the fractions of type- i bound proteins in the bleached and unbleached sections, respectively, with $P_{bound,i} = P_{bl}^{bound,i} + P_{unbl}^{bound,i}$. Let $f_i = P_{bound,i} / P_{bound}$ be the fraction of type- i bound proteins with respect to all bound proteins. Furthermore, denote by $k_{on,i}^*$ and $k_{off,i}$ the association and dissociation rate constants corresponding to the i th MC. Then, the recovery is described by

$$\frac{dP_{bl}^{free}}{dt} = -P_{bl}^{free} \sum_{i=1}^M k_{on,i}^* + \sum_{i=1}^M k_{off,i} P_{bl}^{bound,i} + k_{diff} (f_{bl} P_{unbl}^{free} - (1 - f_{bl}) P_{bl}^{free}), \quad (4)$$

$$\frac{dP_{unbl}^{free}}{dt} = -P_{unbl}^{free} \sum_{i=1}^M k_{on,i}^* + \sum_{i=1}^M k_{off,i} P_{unbl}^{bound,i} - k_{diff} (f_{bl} P_{unbl}^{free} - (1 - f_{bl}) P_{bl}^{free}), \quad (5)$$

$$\frac{dP_{bl}^{bound,i}}{dt} = k_{on,i}^* P_{bl}^{free} - k_{off,i} P_{bl}^{bound,i}, \quad (6)$$

$$\frac{dP_{unbl}^{bound,i}}{dt} = k_{on,i}^* P_{unbl}^{free} - k_{off,i} P_{unbl}^{bound,i}, \quad (7)$$

where $i = 1, \dots, M$. The fluorescence intensity is $F = (P_{bl}^{free} + \sum_{i=1}^M P_{bl}^{bound,i}) / f_{bl}$.

Parameter estimation

The mathematical model contains several unknowns: The model parameters $k_{on,i}^*$, $k_{off,i}$ and k_{diff} , the initial values F_0 , $P_{bl,0}^{free}$, $P_{bl,0}^{bound}$ for the components F , P_{bl}^{free} , P_{bl}^{bound} , etc. and the fractions f_{bl} , f_i of bleached proteins, bound proteins of type i , etc. Due to computational effort, parameter redundancies and strong correlation between some parameters, it is not meaningful to statistically infer all these unknowns simultaneously. Instead, some values were fixed as follows: k_{diff} and f_{bl} were experimentally determined (see Supplementary Table S3, Figure 4B and the data normalization description above). The smallest k_{off} value was set to 0.005 (see the Results section). F_0 was chosen equal to the first value of the FRAP curve. $P_{bl,0}^{free}$ was set equal to $f_{bl} F_0$. The association rates result from the other estimates as $k_{on,i}^* = k_{off,i} f_i (1 - P_{bl}^{free}) / P_{bl}^{free}$. Statistical inference of all remaining variables was carried out by least squares estimation. The ODEs (1)–(3) and (4)–(7) were numerically solved with the Euler scheme with step length 0.03, which corresponded to one-fifth of the observation interval. All software was written in R (R Development Core Team, 2011, R Foundation for Statistical Computing, Vienna, Austria).

We estimated the model parameters for each FRAP curve separately and compared the estimates for curves from the same cell cycle phase and Dnmt1 construct afterwards. For more details about the numerics, see the Supplementary Methods.

Model choice

In our analysis, we estimate models with different numbers of MCs. Because the models are nested, the inclusion of more MCs always leads to a better or at least equally good fit. However, one may ask whether the additional computational effort for multiple MCs is worth the improved matching of the data. At first glance, model choice criteria like the Akaike information criterion (AIC) (38) seem appropriate. In our application, however, the difference in the mean squared residuals for different models is typically small owing to parameter redundancies. Because of the large number of model parameters, the AIC will often favor less MCs although the curvature of the recovery curves is better described by more complex models. For that reason, we developed a model selection criterion that penalizes complexity less rigorously and is specific to our application. Due to the relatively small noise in the FRAP curves (Figure 3B and Supplementary Figure S6), we do not expect to overfit the data. The criterion reads as follows.

As explained in the Results section, the up to three MCs are further distinguished into one or two distinctive mobility classes (DMCs) and up to one catalytic mobility class (CMC). These have to fulfill three rules:

- (1) If a DMC or CMC is present, the fraction P_{bound} of bound proteins should be above a certain threshold:

$$P_{bound} \geq \varepsilon_{bound}.$$

Otherwise the DMCs and CMC are discarded, and we assume no MCs for this FRAP curve.

- (2) Two distinct MCs should differ substantially in their dissociation rates. In the model with two DMCs that means that one should have

$$\frac{k_{off,DMC1} - k_{off,DMC2}}{k_{off,DMC2}} \geq \delta_{DMC}$$

or

$$\frac{k_{off,DMC2} - k_{off,CMC}}{k_{off,CMC}} \geq \delta_{CMC}.$$

Otherwise we assume the effective number of DMCs to be one.

- (3) An MC only truly contributes to the model if it reaches a certain size:

$$f_{DMC1} P_{bound} \geq \varepsilon_{DMC} \text{ and } f_{DMC2} P_{bound} \geq \varepsilon_{DMC}$$

and

$$f_{CMC} P_{bound} \geq \varepsilon_{CMC}.$$

Otherwise we assume the effective number of DMCs to be one.

We derive appropriate values for the above thresholds by cluster analysis; see the Supplementary Methods for details and results. For each measured curve, we now

select the model that yields the best fit. This is typically the model with two DMCs and one CMC, but in many cases, the fit of the model with one DMC and one CMC is equally good and hence preferred. For the chosen model, the original number of DMCs is replaced by the effective number of DMCs as determined by the above rules (Supplementary Figure S9). Then, for each cell cycle phase and protein construct, the primarily chosen effective number of DMCs is determined. The model with the according number of DMCs is chosen for this phase and construct. Supplementary Table S3 displays the mean estimates for the selected model for all FRAP curves. These results always assume the original number of DMCs and do not further reduce it to an effective number.

RESULTS

Necessity and sufficiency of the PBD and TS domain for S phase-specific targeting of Dnmt1

Our aim was to analyze the S phase-dependent regulation of the Dnmt1-binding behavior. To that end, we investigated four GFP fusions: wild type Dnmt1 (GFP-Dnmt1^{WT}), the full-length Dnmt1 carrying a point mutation (GFP-Dnmt1^{Q162E}) within the PBD (6), a Dnmt1 mutant carrying a deletion of a highly conserved part of the TS domain comprising the amino acids 459–501 (GFP-Dnmt1^{ΔTS}) and a Dnmt1 double mutant containing both mutations (GFP-Dnmt1^{Q162E/ΔTS}) (Figure 1A). To identify different cell cycle stages, we first co-expressed GFP-Dnmt1 constructs with PCNA fused to monomeric red fluorescent protein (RFP-PCNA) in mouse C2C12 myoblast cells and acquired confocal mid sections of the living cells (Figure 1B). As previously described (6), GFP-Dnmt1^{WT} co-localized with RFP-PCNA at RF in early S phase. Co-localization with RF was also apparent in late S phase, when DNA of pericentromeric heterochromatin (pHC) is replicated. In contrast, the double mutant GFP-Dnmt1^{Q162E/ΔTS} was diffusely distributed within nuclei throughout interphase, suggesting a deficiency to target RF during S phase. GFP-Dnmt1^{ΔTS} still accumulated at RF in early and late S phase, but showed a slightly weaker association compared with GFP-Dnmt1^{WT}, indicating the activity of PBD-mediated targeting in all S phase stages, independent of the presence of the TS domain (Figure 1B and Supplementary Figure S2). As previously reported, GFP-Dnmt1^{Q162E} showed a diffuse nuclear distribution in early S phase but notable association to pHC replicating in late S phase (6). Together, this suggests that the PBD-mediated interaction with PCNA is necessary for the Dnmt1 localization in early S phase, but evidently not for the association at pHC in late S phase.

For a more detailed view on the spatial relationships of wild-type and mutant Dnmt1 and PCNA at RF, we used super-resolution 3D-SIM (31,32). Owing to the ~8-fold improved volumetric resolution of 3D-SIM (39), we could clearly notice subtle variations in the Dnmt1 localization that escaped detection with conventional imaging

(Figure 2 and Supplementary Figure S3). In late S phase, GFP-Dnmt1^{WT} coincides to a large extent with immunofluorescently labeled endogenous PCNA foci in locally decondensed parts of otherwise homogenously compacted chromocenters with some Dnmt1 signal extending slightly (by a few 100 nm) beyond the PCNA signal. Interestingly, RF outside of chromocenters showed almost no enrichment of Dnmt1 (Figure 2A). In contrast, early S phase cells showed a more balanced co-localization at RF (Supplementary Figure S3A). Co-immunostaining of non-transfected cells with the Dnmt1-specific monoclonal antibody 5A10 confirmed the same localization characteristics for the endogenous Dnmt1, hence excluding potential artifacts by the GFP-tagging or overexpression (Supplementary Figure S3B). As opposed to this, GFP-Dnmt1^{ΔTS} precisely co-localized with all PCNA marked RF inside and outside of chromocenters (Figure 2B). GFP-Dnmt1^{Q162E}, similar to the wild type, displayed an enrichment at chromocenter-associated RF but also in the nearby regions of the chromocenters that were more compacted. We further noted these regions to become larger toward the end of late S phase, indicating that TS-mediated binding primarily occurs at postreplicative pHC (Supplementary Figure S3C). Pulse replication labeling with 5-ethenyl-2'-deoxyuridine and co-staining with PCNA confirmed the association of both, wild type and the PBD mutant Dnmt1 to postreplicative pHC (Figure 2D). Hence, we conclude a strict co-localization of the ΔTS mutant with PCNA at replication sites in late S phase, whereas both TS domain-containing constructs (GFP-Dnmt1^{Q162E} stronger than GFP-Dnmt1^{WT}) show a non-strict co-localization and a tendency to bind adjacent postreplicative pHC.

To gain further knowledge about the cell cycle-dependent dynamics of Dnmt1, we compared FRAP kinetics of mutant proteins with those of GFP-Dnmt1^{WT} in early S phase, late S phase and non-S phase cells with diffuse localization. The latter comprises mostly G1 cells but may also contain a smaller subset of late G2 phase cells, according to the different lengths of both stages. The comparison was done by half-nucleus FRAP analyses to quantify the strength and contribution of the PBD- and TS domain-mediated interactions in the distinct stages (Figure 3A). For a thorough quantitative evaluation of half-nucleus FRAP data, which preceded the application of the mathematical model, we developed an improved protocol for image registration, nuclear segmentation and data normalization (details described in Supplementary Methods and Supplementary Figure S4).

Initial controls revealed that the additional expression of RFP-PCNA influenced the kinetics of GFP-Dnmt1^{WT} (Supplementary Figure S5). Hence, to avoid any biasing effects, we decided not to co-express RFP-PCNA, but instead to collectively analyze all nuclei with diffuse nuclear distribution of the respective GFP fusion protein. Control measurements of diffusely localized GFP-Dnmt1^{Q162E} in RFP-PCNA co-expressing cells revealed no difference between the 'early S phase' and 'G1/late G2' group (data not shown). We quantitatively analyzed half-nucleus FRAP experiments of 10–20

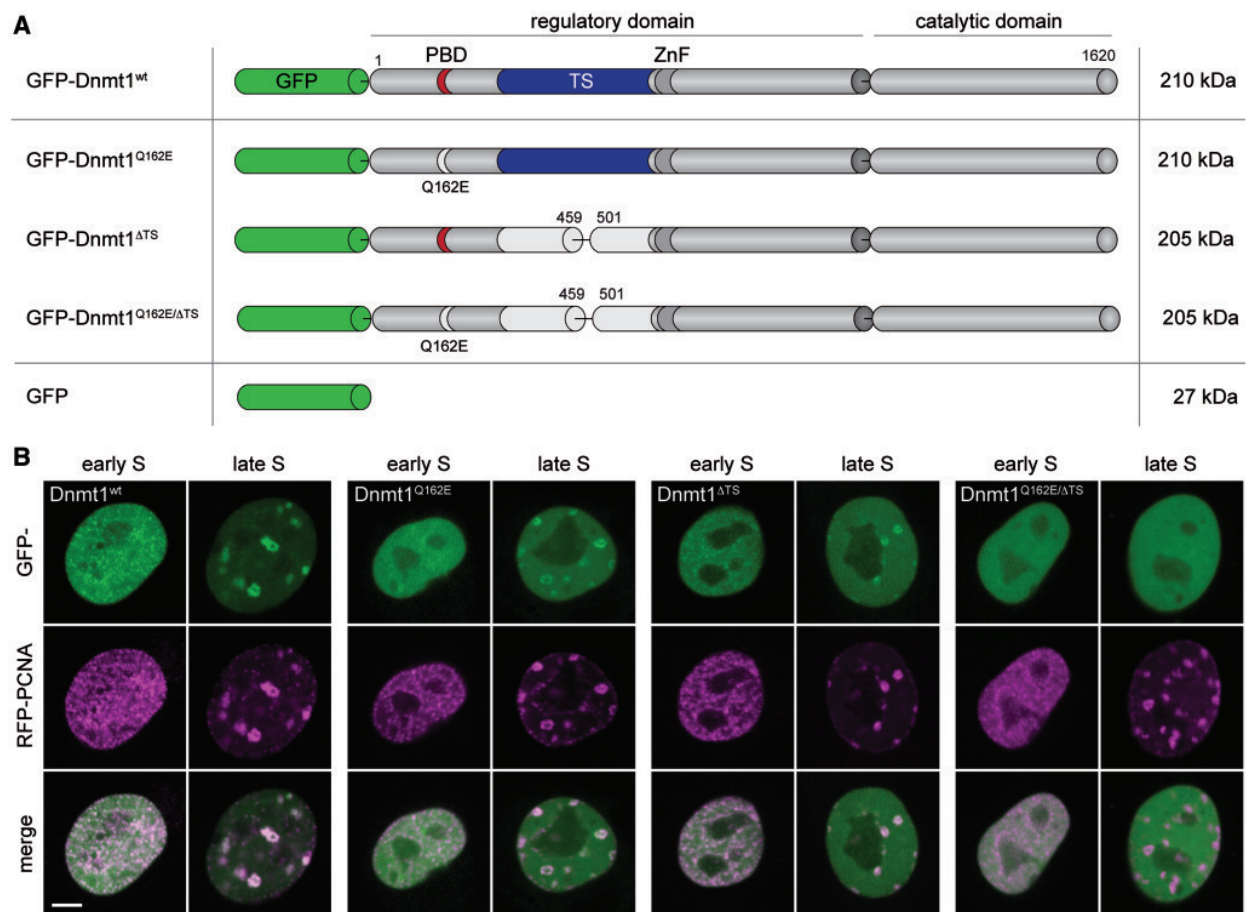


Figure 1. Domain structure and subnuclear localization of GFP-Dnmt1 constructs. (A) Dnmt1 consists of a large N-terminal regulatory domain containing PBD, TS domain and a CXXC zinc finger (ZnF) domain, and a conserved C-terminal catalytic domain. The point mutation of a highly conserved glutamine to glutamic acid introduced within the PBD eliminates interaction with the replication machinery (GFP-Dnmt1^{Q162E}). A deletion in the central part of the TS domain (GFP-Dnmt1^{ΔTS}) was introduced to abolish interaction with constitutive heterochromatin. Furthermore a construct containing both mutations was generated (GFP-Dnmt1^{Q162E/ΔTS}). GFP alone is used as a control for a non-binding protein. (B) Spinning disk confocal mid sections of GFP-Dnmt1 wild type (wt) and mutant constructs in live mouse C2C12 cells co-expressing RFP-PCNA to mark RF. In early S phase, GFP-Dnmt1^{wt} accumulates at RF, whereas PCNA-binding deficient GFP-Dnmt1^{Q162E} is diffusely distributed throughout the nucleus. GFP-Dnmt1^{ΔTS} is still associated with RF, but not as prominently as GFP-Dnmt1^{wt}. In late S phase GFP-Dnmt1^{wt}, GFP-Dnmt1^{Q162E} and GFP-Dnmt1^{ΔTS} accumulate at larger RF of late replicating pHC, although with slightly less strong enrichment observed for both mutants. GFP-Dnmt1^{Q162E/ΔTS} is distributed diffusely in the nucleus throughout interphase. Scale bar: 5 μm.

datasets for each construct and categorized cell cycle stage(s) (Figure 3B and Supplementary Figure S6) and determined half-times of the recovery ($t_{1/2}$) and mobile fractions (MF) (Supplementary Table S1)

In accordance with our previous observations (6), GFP-Dnmt1^{wt} showed a moderately reduced mobility in early S phase ($t_{1/2} 6.3 \pm 0.3$ s) compared with G1/late G2 phase ($t_{1/2} 3.3 \pm 0.1$ s) (Figure 3B and C). In late S phase, the recovery was even more reduced ($t_{1/2} 8.3 \pm 0.6$ s). Recovery kinetics of the GFP-Dnmt1^{Q162E/ΔTS} double mutant comprising all interphase stages revealed the same fast recovery kinetics ($t_{1/2} 3.6 \pm 0.3$ s) as observed for GFP-Dnmt1^{wt} in G1/late G2 phase, suggesting the complete loss of any S phase-specific interaction. The result implies that the collective integrity of PBD and the TS domain is necessary and sufficient for the entire S phase-dependent targeting of Dnmt1 to its localization sites.

Next, we analyzed both single mutants, GFP-Dnmt1^{Q162E} and GFP-Dnmt1^{ΔTS}, to dissect the specific role of both domains in early S phase and late S phase. In agreement with our previous analyses of GFP-Dnmt1^{Q162E}, the kinetics measured for the pooled G1/late G2 and early S phase cells showing a diffuse distribution, was almost identical to that of GFP-Dnmt1^{wt} diffusely distributed only in G1/late G2 phase ($t_{1/2} 3.1 \pm 0.2$ s versus 3.3 ± 0.1 s) consistent with the loss of PCNA interaction in early S phase. In late S phase, despite localizing similar to GFP-Dnmt1^{wt}, the kinetics was slightly faster ($t_{1/2} 5.4 \pm 0.4$ s), indicating a contribution of the PBD to the binding behavior of Dnmt1^{wt} also in late S phase. However, the recovery was still slower as compared with the cells with diffuse localization, pointing toward an additional TS domain interaction. Comparing the wild-type construct with GFP-Dnmt1^{ΔTS}, the mutant

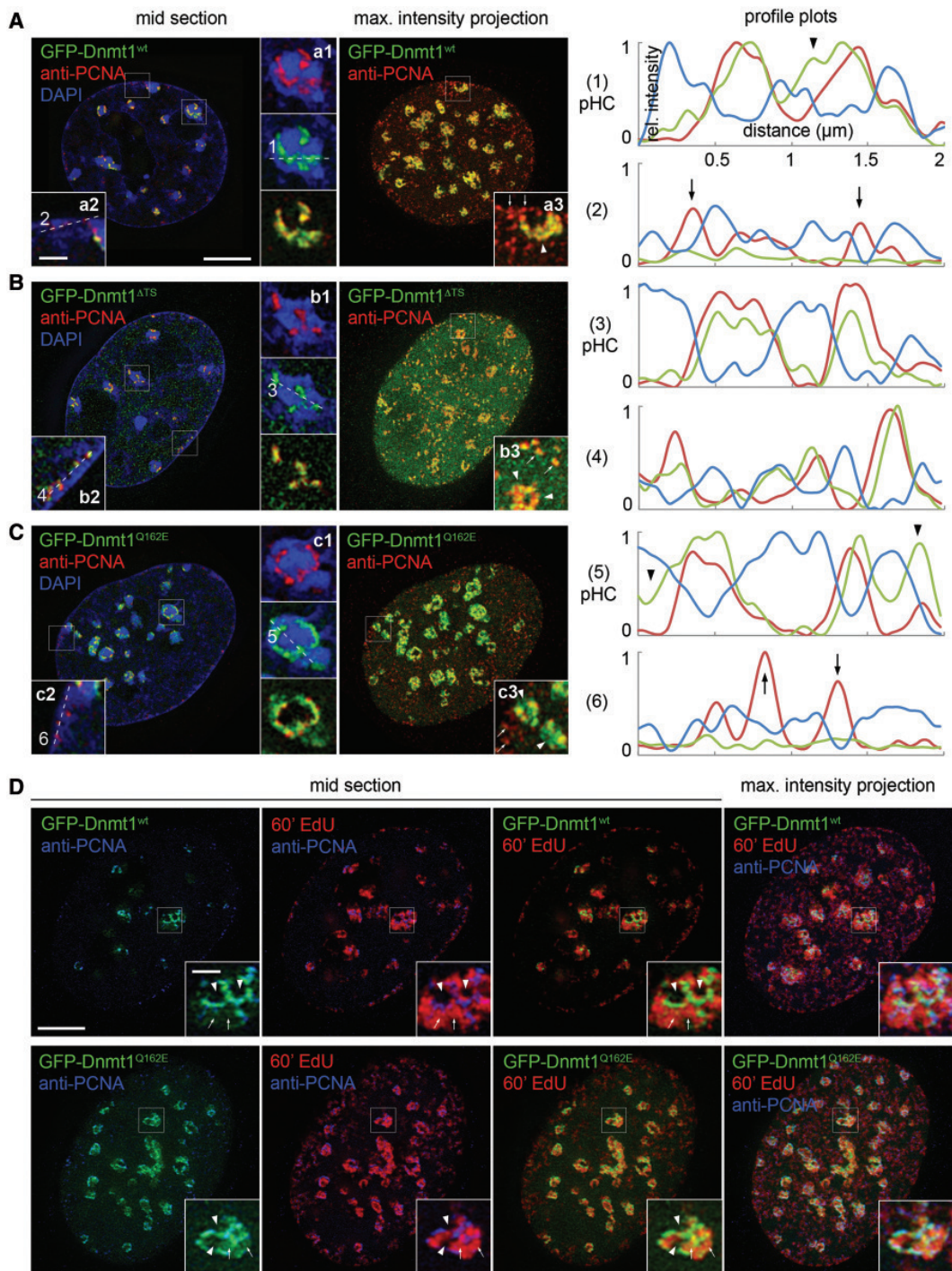


Figure 2. Super-resolution imaging of heterochromatin association of GFP-Dnmt1 constructs in late S phase. (A–C) 3D-SIM optical mid sections and z-projections from C2C12 cells expressing GFP-Dnmt1 wild type and mutant constructs immunostained with antibodies against endogenous PCNA. Profile plots were scaled between minimum and maximum intensity values for each nucleus. (A) GFP-Dnmt1^{wt} co-localizes largely but not strictly with PCNA inside ~200 nm wide lacunas within otherwise densely packed DAPI-intense chromocenters of clustered pHC (inset a1, arrowheads in profile plot 1 and inset a3). Anti-PCNA-labeled RF outside of chromocenters show only minor or no association of Dnmt1 (inset a2, arrows in profile plot 2 and inset a3). (B) GFP-Dnmt1^{ΔTS} strictly co-localizes with PCNA at RF inside and outside chromocenters (insets b1+b2 and profile plots 3+4). An increased diffuse fraction is visible as small grainy evenly distributed nucleoplasmic background. (C) GFP-Dnmt1^{Q162E} does not strictly co-localize with PCNA, but also associates with adjacent regions of pHC (arrowheads, inset c3 and profile plot 5). No association is detected in RF outside chromocenters (arrows, inset c3 and profile plot 6). (D) Additional replication labeling with a 60-min EdU pulse prior fixation. Association of GFP-Dnmt1^{wt} and GFP-Dnmt1^{Q162E} to chromocenter regions outside of PCNA foci is restricted to the bulk of EdU-labeled postreplicative chromatin (insets, arrows), while unlabeled, presumably not yet replicated chromocenter regions are still void of GFP-Dnmt1 (insets, arrowheads). Scale bars: 5 μm and 1 μm (insets).

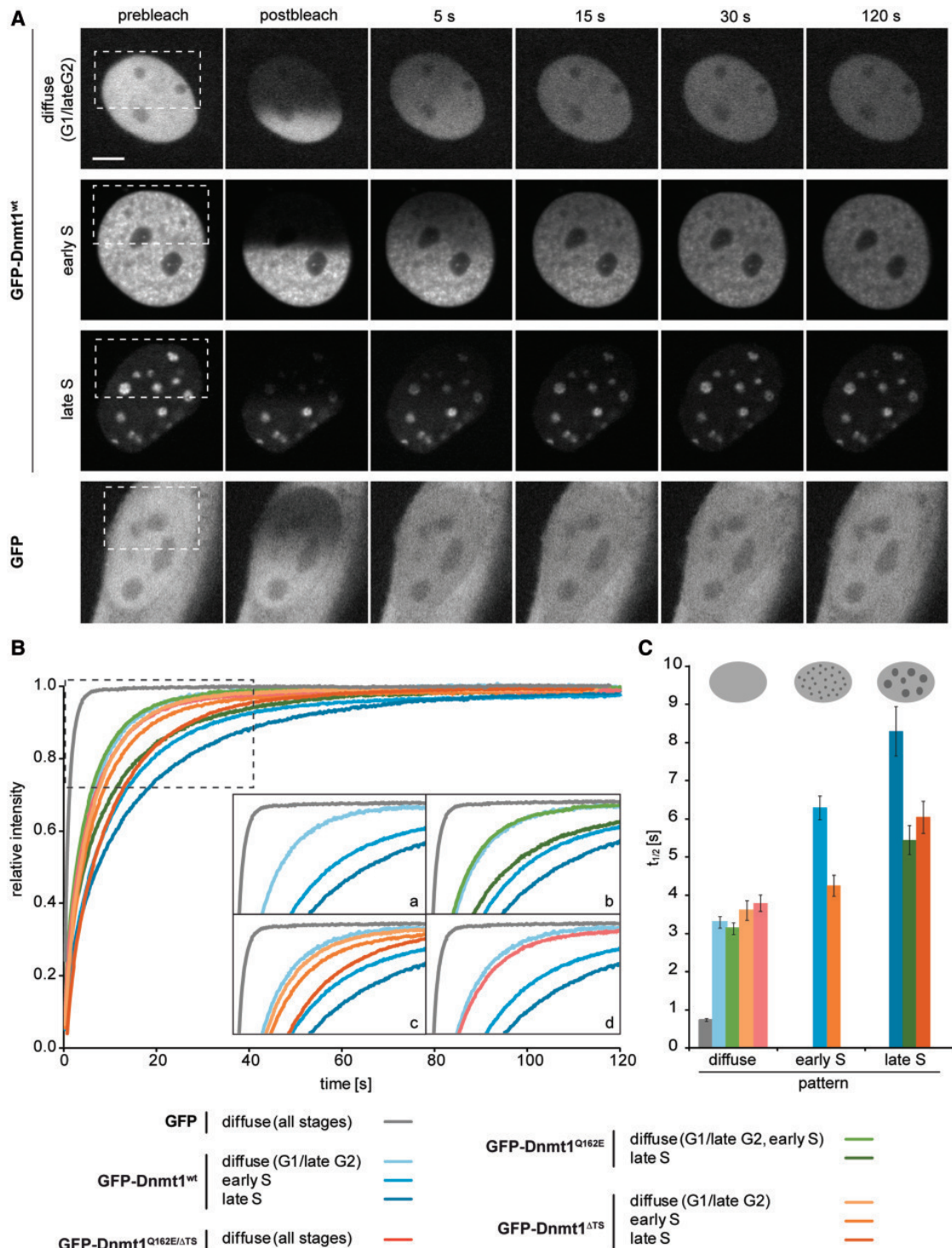


Figure 3. Quantitative FRAP evaluation of GFP and GFP-Dnmt1 constructs. **(A)** Representative time frames of exemplary half-nucleus FRAP series recorded with spinning disk confocal microscopy. Scale bar: 5 μ m. **(B)** Mean recovery curves displayed for all measured constructs and cell cycle stages. The inset illustrates cycle-dependent kinetics of GFP and GFP-Dnmt1^{wt} alone (a), and in comparison with GFP-Dnmt1^{Q162E} (b), GFP-Dnmt1^{ΔTS} (c) and GFP-Dnmt1^{Q162E/ΔTS} (d). GFP-Dnmt1^{wt} in cells with diffuse localization shows a decreased mobility compared with GFP. The GFP-Dnmt1^{wt} mobility decreases stepwise in early S phase and in late S phase. The mobility of GFP-Dnmt1^{Q162E} in G1 (late G2) and early S cells (diffuse nuclear localization, pooled) is almost identical to GFP-Dnmt1^{wt} G1 (late G2) cells. In late S phase, a moderately increased mobility is observed for both, GFP-Dnmt1^{Q162E} and GFP-Dnmt1^{ΔTS} mutants compared with GFP-Dnmt1^{wt}. Of note, despite comparable overall kinetics, both curves (dark green, dark orange) are clearly different in their shape. In early S phase, the $t_{1/2}$ of GFP-Dnmt1^{ΔTS} is reduced compared to GFP-Dnmt1^{wt}. GFP-Dnmt1^{Q162E/ΔTS} (all interphase stages, pooled) displays kinetics almost identical to GFP-Dnmt1^{wt} in cells with diffuse localization. For clarity, error bars are omitted here, but shown in Supplementary Figure S6. **(C)** Half-times of recovery ($t_{1/2}$) determined for each construct and distribution pattern. Error bars represent SEM.

showed also faster kinetics in late S phase ($t_{1/2} 6.0 \pm 0.4$ s), suggesting that the TS domain together with the PBD are necessary for the wild-type kinetics in late S phase. Besides the role of the TS domain in late S phase, this mutation also enhanced the mobility in early S phase ($t_{1/2} 4.2 \pm 0.3$ s) in accordance with the fact that the early S phase pattern of RF association was less prominent (Figure 1B). This result indicates that the binding by the PBD domain to RF is necessary, but not sufficient for the early S phase-specific localization of Dnmt1.

We also noted that the mobile fractions (MF) of the wild-type construct within the observation time of 2 min dropped from around 100% in non-S phase to $\sim 98\%$ in early and late S phase. This directs to a small immobile fraction of covalently bound Dnmt1 involved in the covalent complex formation during the enzymatic reaction (Supplementary Table S1). This observation is consistent with a rather slow speed of the enzyme reaction measured *in vitro* with hemimethylated substrate (40–43). A small immobile fraction ($\sim 1\%$) was also noted for the Dnmt1 mutant construct.

To test the general ability as well as differences in the efficiency of the investigated regulatory Dnmt1 mutants to undergo covalent complex formation *in vivo*, we measured the time-dependent immobilization by FRAP on incubation with the mechanism-based inhibitor 5-aza-2'-deoxycytidine (44) (see Supplementary Methods for details on the trapping assay). In agreement with the observed small immobile fractions, all mutants became immobilized albeit with variable efficiencies, with GFP-Dnmt1^{WT} being already fully immobilized within 30–45 min (corresponding to a trapping rate of $\sim 3\% \text{ min}^{-1}$), followed by GFP-Dnmt1^{Q162E}, GFP-Dnmt1^{ΔTS} and GFP-Dnmt1^{Q162E/ΔTS} (only $\sim 10\% \text{ h}^{-1}$) (Supplementary Figure S7).

We conclude that the PBD and the TS domain are the only domains directly involved in S phase-specific targeting of Dnmt1 with respect to localization and kinetics and that both domains contribute to enhance the efficiency to initiate the catalytic reaction *in vivo*. To decipher the exact relationship of PBD- and TS domain-mediated binding in early and late S phase, however, a more sophisticated analysis is needed.

Kinetic modeling of half-nucleus FRAP with multiple binding classes and diffusion-coupled dynamics

We next sought to characterize the contribution of the PBD- and TS domain-mediated interactions in different stages of the cell cycle in a more precise quantitative manner. Hence, we utilized mathematical modeling to estimate the fraction of protein bound by these domains and the binding strength in the different cell cycle stages.

The choice of the model was based on several considerations. First, to take account for the heterogeneous spatial distribution of binding sites that strongly varies in different cell cycle stages. Second, to correct for diffusion-related effects. Third, to deal with multiple potentially superimposing interactions, or binding classes, respectively, including a small fraction of protein covalently bound during the catalytic reaction (Figure 4A). Such a

level of complexity goes beyond the assumptions of FRAP analysis based on present reaction-diffusion models (45–48). Therefore, we decided to use a compartmental approach with size-calibrated diffusion correction, suitable for experiments with half-nucleus bleaching, which ensure representative distribution of binding sites in all cell cycle stages. Each of the two halves was then considered as a well-mixed homogeneous interaction system where proteins can bind to different binding partners (22,36).

Taking diffusion into account is especially important for assessing nuclear proteins as most of them undergo transient interactions in a diffusion-coupled behavior (18,46). This is also true for Dnmt1 (Supplementary Figure S8). To approximate the diffusion of the protein, we introduced a size-dependent correction factor (k_{diff}) as a measure for the exchange of free molecules between the bleached and unbleached half to approximate the diffusion of the protein as similarly performed in (37) (Figure 4A; see Materials and Methods). To estimate this exchange parameter, we performed FRAP calibration measurements of GFP monomers, dimers and trimers, as they have known sizes and are presumably inert in cells (Figure 4B). The k_{diff} value corresponding to the size of GFP-Dnmt1 was extrapolated from the k_{diff} values experimentally determined for the other three constructs in the same cell line using an exponential regression curve (Figure 4B and Supplementary Table S2).

We noted that the normalized FRAP curves of GFP-Dnmt1 constructs, in particular those from S phase cells, typically did not reach a straight plateau after 2-min observation time. Instead, they still followed a slight incline. As outlined above, this might be attributed to a small fraction of molecules actively involved in covalent complex formation during methyl group transfer. *In vitro* measurements have previously demonstrated a rather slow catalytic reaction of human DNMT1 on hemimethylated DNA in the range of 1–22 min per CpG (40–43). To account for this possibility, we added a class with variable fraction size but a small fixed dissociation rate (k_{off}). This class is referred to as CMC. As opposed to that, classes with free k_{off} values will be referred to as DMC. The k_{off} value for the CMC was chosen to be 0.005 s^{-1} , which is equivalent to a mean residence time of 200 s (40). By fixing it, we avoided an additional free parameter in our fitting procedure. To further decrease the number of free parameters in our model, we also fixed the bleached fraction f_{bl} to an experimentally determined value for each FRAP experiment (see Materials and Methods). Altogether we estimated the k_{off} values of up to two DMCs, the fraction sizes of bound proteins (one CMC and two DMCs), and the remaining pool of free molecules (f_{free}).

Although this modeling approach does not cover the whole details of our experimental system, it concentrates on the characterization of the interactions while still integrating some essential information on the diffusion process and therefore provides a way to interpret the differences between the different forms of Dnmt1 during the different phases of the cell cycle. In conclusion, our compartmental model uses an experimentally

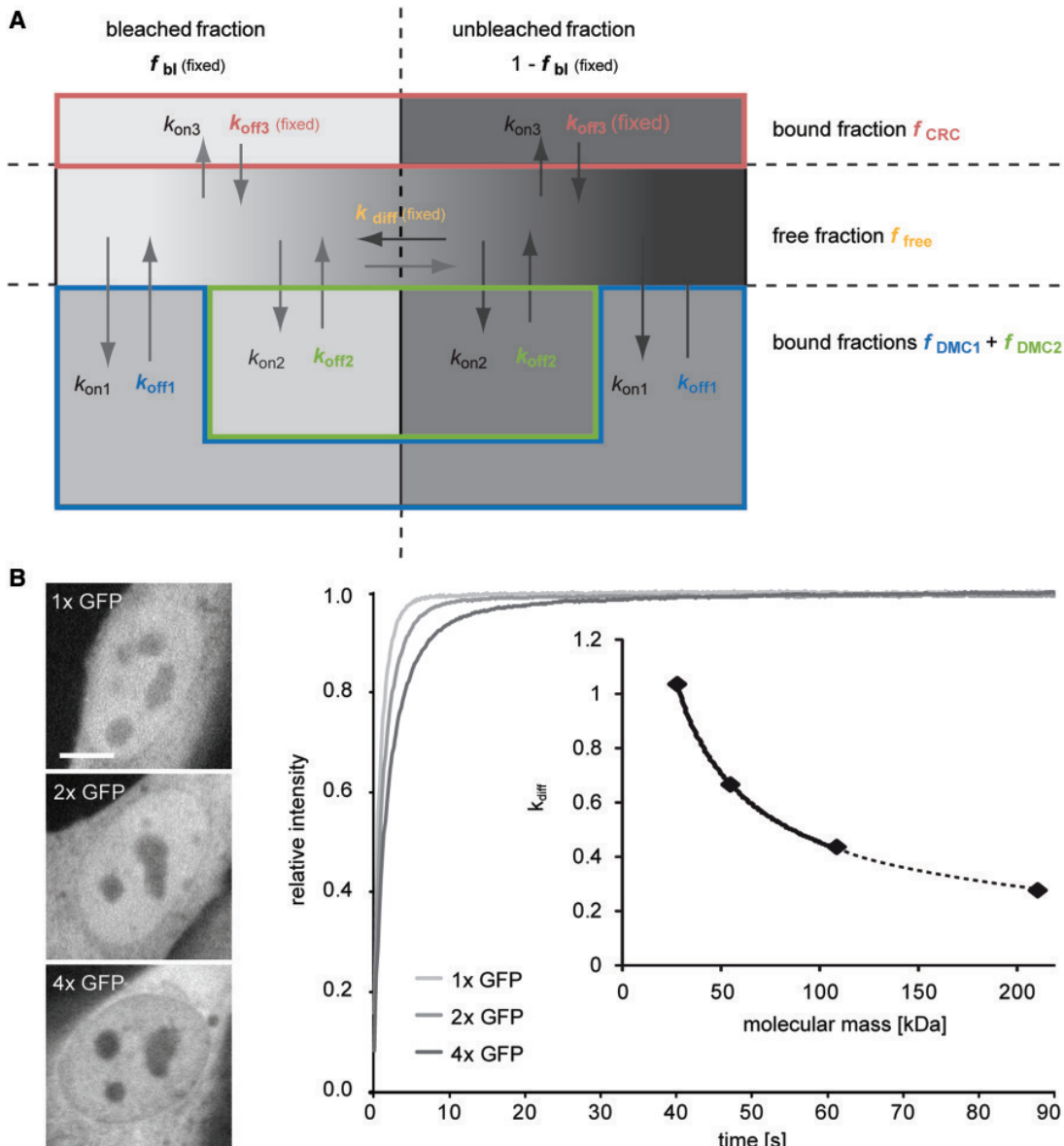


Figure 4. Refined diffusion-coupled compartmental model for three MCs and determination of k_{diff} from GFP multimer measurements. (A) The nuclear compartment is divided into four main compartments: bleached and unbleached molecules in the bound or free state, respectively. The bound state can be subdivided into three compartments with specific properties. For Dnmt1, we choose two DMCs (DMC1 and DMC2, blue and green frame, respectively) and one CMC (red frame) with a fixed k_{off} . Molecules bind and unbind with association and dissociation rates given by $k_{on,i}$ and $k_{off,i}$, respectively. In our refined modeling approach, the parameter f_{BL} is experimentally determined for each individual FRAP series. Migration of molecules is implemented in the model by introducing a new diffusion rate constant k_{diff} . This parameter corrects for the size-dependent exchange of the free molecules between the bleached and unbleached compartment. Parameter and variables entering the sets of differential equations are written in bold; predetermined/fixed values are indicated. (B) Quantitative FRAP evaluation of GFP multimers. The GFP mobility of the dimer and the tetramer decreases stepwise as compared with the monomer. The k_{diff} factor for the GFP constructs is estimated from the model with no DMC/CMC. From these values, the corresponding k_{diff} factor for the size of GFP-Dnmt1 is estimated using an exponential regression curve (inset diagram).

determined cell type-specific correction for size-dependent diffusion effects and can extract up to three dissociation rates and the sizes of all bound pools and the remaining free pool. This way we took into account several interaction partners, diffusion-coupled dynamics and the irregular distribution of binding sites of the protein.

Quantifying the properties of the PBD- and TS domain-mediated binding by FRAP modeling

We applied the enhanced kinetic model to our FRAP data of GFP-Dnmt1^{WT} and mutants. For each FRAP curve, the parameters of three differential equation models were determined using least squares estimation. These models

accounted for (i) no DMC/CMC, i.e. free proteins only, (ii) one DMC plus CMC or (iii) two DMCs plus CMC. The k_{diff} values were chosen according to the respective protein sizes (Supplementary Table S2). For each individual FRAP curve, the most appropriate model was determined based on the mean squared residuals and certain restrictions on the fraction sizes and magnitudes of the dissociation rates (see Materials and Methods). Then, for each construct and cell cycle phase, we identified the model that was preferentially chosen for the majority of datasets (Supplementary Figure S9). This model was then used to determine the final mean k_{off} values, the reciprocal mean residence times $T_{res} = 1/k_{off}$ as well as the corresponding fraction sizes for all measured constructs and cell cycle stages (Figure 5 and Supplementary Table S3).

Model estimation for our reference FRAP measurements with GFP monomers and dimers provided a clear tendency of having no DMC (100% free fraction), whereas most FRAP curves of GFP-tetramers were best explained by a large free fraction (>91%) plus a smaller fraction of reduced mobility (<8%). Notably, the T_{res} determined for this fraction was rather high and showed a large variation indicating a GFP-multimer-specific effect. Analyzing the GFP-Dnmt1 constructs, we observed that a small fraction (f_{CMC} 1–4%) was always assigned to the class of molecules potentially involved in the catalytic process (CMC). Estimation of the size of the CMC is numerically difficult owing to the small fraction size. We hence do not interpret those estimates here.

For GFP-Dnmt1^{wt} expressing cells in G1/late G2, our model likewise estimated a large free fraction of ~80% and a population of ~19% with a relatively low mean residence time ($T_{res} \sim 8$ s). In early S phase, the bound fraction doubled to ~40% owing to binding to immobilized PCNA trimeric rings at replication forks (6, 49). The mean residence time measured for this class was with $T_{res} \sim 10$ s slightly higher. The largest fraction of 56% was still assigned to the free pool. In late S phase cells, the bound fraction remained in a similar range with 48%. Importantly, concomitant with binding to pHc at chromocenters, the model identified two distinct DMCs: 18% of the proteins were still bound with an intermediate strength (DMC1: $T_{res} \sim 10$ s), and an additional 28% with a substantially higher strength (DMC2: $T_{res} \sim 22$ s).

An 18–22% fraction with consistent kinetics was constitutively present in all cell cycle stages of the investigated GFP-Dnmt1 constructs. The nature of this constitutive MC remains unclear. In addition to the mutants described here, we performed FRAP analyses of a series of mutant constructs with deletions of potential interacting regions within the regulatory domain of Dnmt1, which included N-terminal truncations of various length (data not shown) and deletion within the ZnF domain (50). None of these mutants showed faster kinetics than GFP-Dnmt1^{wt} in diffuse cells. We therefore attribute this constitutive class to an anomalous diffusive behavior (see discussion) and not to particular DNA/chromatin binding mediated by a specific domain.

The modeling of FRAP data of the GFP-Dnmt1^{Q162E} mutant revealed a modest reduction of the DMC1 fraction

size as compared with the level of GFP-Dnmt1^{wt} in all measured phases (diffuse, late S) (DMC1: 10–14%; $T_{res} \sim 9$ s). In late S phase cells, a second slower DMC with similar strength was still retained (DMC2: 23%; $T_{res} \sim 19$ s). From these results, we conclude that Dnmt1 binds PCNA at replication sites of early S phase cells with a mean residence time of ~10 s and with no more than 20–25% of the nuclear Dnmt1 pool being involved in this reaction. The binding of the Dnmt1 constructs with intact PBD to PCNA, as well as complete loss of the interaction by introduction of the Q162E point mutation was confirmed biochemically by co-immunoprecipitation (Supplementary Figure S10). In late S phase, only a minor decrease in the mean residence times of the first and second DMC was observable for GFP-Dnmt1^{Q162E} as compared with the wild type, indicating that the PBD does contribute, if only to a small extent, to the binding strength in late S phase. However, the overall bound fraction of molecules decreased compared with GFP-Dnmt1^{wt} in late S phase (66% versus 52%) causing an overall faster FRAP kinetics. The double mutant GFP-Dnmt1^{Q162E/ΔTS} did not establish any association pattern throughout interphase. In accordance, the extracted kinetic properties were almost identical to those of GFP-Dnmt1^{wt} in G1/late G2 (19%; $T_{res} \sim 8$ s).

Modeling of GFP-Dnmt1^{ΔTS} in early S phase revealed a modest reduction of the fraction size and binding strength (DMC1: 30%; $T_{res} \sim 8.5$ s compared with 39%; $T_{res} \sim 10$ s in the wild type). This could argue for either a stabilization of the PCNA complex at the replication sites by the TS domain or may hint to the presence of a minor fraction of strong binding sites, which is too small to be identified as a distinct class. In late S phase, still only one DMC was identified for GFP-Dnmt1^{ΔTS} (DMC1: 40%, $T_{res} \sim 9$ s), similar to GFP-Dnmt1^{wt} in early S phase. This suggests a prevalence of TS domain-mediated binding over PBD mediated, provided that the conditions for TS binding are complied (i.e. high density of hemimethylated CpG sites in conjunction with heterochromatic marks; see discussion below). In this case, binding to PCNA does only seem to play a supportive role. This view is also in accordance with the finding that in late S phase, the Q162E mutation alone does not change the DMC1 or DMC2 substantially, but only leads to a moderate increase in free protein.

DISCUSSION

We addressed the complex problem of dissecting the cell cycle-dependent regulation of Dnmt1 by super-resolution 3D imaging, FRAP and kinetic modeling. Two main factors add to the complexity of the analysis. First, Dnmt1 is a large enzyme with multiple regulatory subdomains, interaction partners and cell cycle-dependent regulation. Second, the distribution pattern of Dnmt1 is highly variable throughout the cell cycle. Hence, we chose a global approach using half-nucleus FRAP to capture in all cases representative fractions of bound molecules and binding sites. Previous studies often used spot bleaching with a defined geometry that allowed the extraction of diffusion coefficients (24,51,52). However, such models

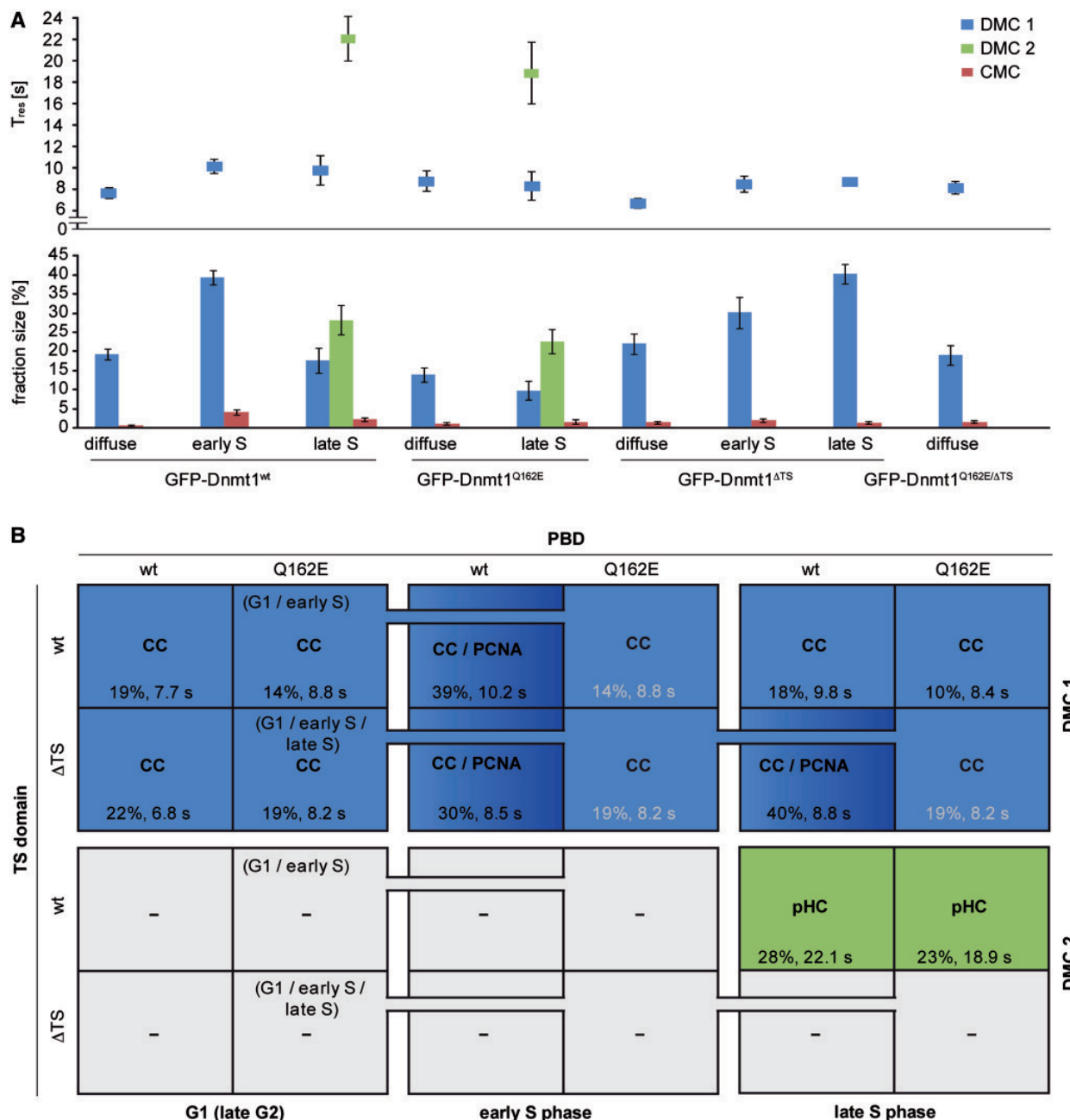


Figure 5. Parameters extracted from the kinetic modeling of GFP-Dnmt1 constructs. (A) Mean residence times (T_{res} , upper panel) and fractions of bound molecules (f_{bound} , lower panel) in three different classes (DMC1, DMC2, CMC) are displayed (not displayed free fractions add to 100% total amount). In all analyzed GFP-Dnmt1 constructs, a fast population of molecules was identified with mean residence times between 6 s and 10 s (DMC1). The fraction of this fast population (DMC1) typically varies between 10% and 22%, but rises for GFP-Dnmt1^{WT} in early S phase (40%) and for GFP-Dnmt1^{ΔTS} in early and late S phase (30 and 40%, respectively) due to the interaction with PCNA. A second, slower class (DMC2) was determined for both constructs with intact TS domain in late S phase with residence times varying from 19 to 22 s (DMC2) and an average size between 23 and 28%, respectively. The size of the CMC with a fixed T_{res} of 200 s varies between 0 and 4.1%. Bars indicate SEM. (B) Parameters are sorted according to their targets PCNA and pHC and the constitutively present unspecified MC (constitutive class, CC).

typically only included no more than one additional binding class, while we expected multiple interactions. Therefore, none of the previous models was immediately applicable to our case, which prompted us to devise a customized model.

To eliminate a weak point of diffusion-uncoupled approaches, we further corrected for size-dependent diffusion using a calibration factor that was experimentally determined from measurements of GFP multimer proteins. Anomalous diffusion behavior has previously

been shown for GFP and dextran in the nucleus (53–55). This indicates that calculation of size-dependent diffusion differences according to the Stokes-Einstein relation might lead to wrong parameter estimates for proteins in the nucleus (56), especially when large size differences like between GFP and Dnmt1 are taken into account.

FRAP measurements are sensitive to experimental conditions and set-ups (57). We tried to correct for most conceivable external influences during image evaluation by using a tailored workflow of postprocessing steps (see Supplementary Materials and Methods). This involved image registration, constrained automated nuclear segmentation and three-step normalization/correction. Altogether, this allows us to compensate for lateral cell movement, nuclear import and export, bleaching due to image acquisition and variations in bleaching depth, which otherwise potentially affect the raw data and subsequent modeling results. Moreover, we modeled a slow CMC using a low fixed k_{off} value, taking into account that a small fraction of molecules is likely to be involved in catalysis and thereby transiently immobilized by a covalent complex formation (40,43). Finally, we also reduced the number of free parameters by fixing the size of the bleached fraction to a value experimentally determined for each FRAP series. The number of DMCs was determined by model choice rules, which are oriented toward the numerical properties of the model.

Although our model allows for three distinct MC, we possibly cannot estimate their number and properties beyond all doubt, mostly because two or more distinct interactions may fall into one MC (see Materials and Methods). If interaction strengths of multiple interactions are relatively close to each other, they may not be detected as separate classes but be captured as one with an intermediate mixed k_{off} . The appearance of such parameter redundancies depends on the model and the values of the underlying parameters (e.g. 58). However, different dynamics can still be distinguished indirectly by a changed fraction size. An example for mixed interactions in one class is the similar kinetics of the non-specified *constitutive class* and of GFP-Dnmt1^{wt} binding to PCNA. This rather small constitutive fraction may be attributed to one or more residual transient interactions. So far, we could not detect any specific subdomain of Dnmt1 that would be responsible for a transient interaction throughout the cell cycle (data not shown). Thus, we tend to attribute this to an anomalous diffusive behavior within the nucleus that is identified as a pseudo-binding class. This may be caused by restrained accessibility of dense chromatin domains and transient trapping inside of small chromatin lacunas ('corralling') generating a 'pseudo' binding effect and/or by unspecific transient binding with a broad distribution of binding affinities (53,54,59). Dnmt1 could also be constitutively present in a free diffusing complex including interacting proteins like PCNA or Uhrf1. In fact, Dnmt1 interactions have been described for a variety of proteins including other DNA methyltransferases, chromatin modifiers and transcriptional regulators (60). Interactions with high molecular weight complexes could potentially slow down diffusion

of GFP-Dnmt1 and thus contribute to the observed dynamics.

Another limitation of our method is the precision limit imposed by a still large cell-to-cell variability due to (i) technical reasons like residual uncorrected cell motion or z-drift, irradiation/transfection-induced DNA damage or cell cycle arrest or (ii) biological reasons such as variations in endogenous expression and methylation levels or local environment. Therefore, for example, the quantification of the apparently small CMC gives no robust results. However, by estimating the kinetic parameters for each FRAP curve separately, we take into account this extrinsic noise and quantify it through standard errors. Finally, using experimental FRAP data, it can never be ruled out that the kinetics are influenced by variations in k_{on} rates. However, the method does not allow assessing changes in the accessibility of the binding sites. These technical limitations could only be solved using large-scale simulations and even more complex models.

Despite these potential shortcomings, by application of our method, one can still obtain a detailed picture of the distinct cell cycle-dependent dynamics of proteins. We have shown that the PBD and the TS domain are the only domains involved in direct S phase-dependent targeting of Dnmt1 and responsible for delaying its mobility. Furthermore, we discriminated two different MCs that could be matched to these two different domains of Dnmt1. In this study, we quantified the time they bind on average and found the binding via the TS domain to be >2-fold stronger than via the PBD, whereas the corresponding fractions of bound protein were in a similar size range between 20 and 30%.

In accordance with previous studies, we show that the more transient interaction with PCNA increases the concentration of Dnmt1 at replication sites to enhance the efficiency of maintenance DNA methylation (7). In addition, we have characterized the stronger binding properties of the TS domain. The related MC was only present in late S phase, when pericentric heterochromatin (pHC) clustered in DAPI dense chromocenters is replicated, suggesting a switch between PBD-mediated binding in early S phase to the TS domain-mediated binding in late S phase. The analysis of the single mutants, however, hinted at a somewhat more complex situation, as the deletion within the TS domain also influenced GFP-Dnmt1 kinetics in early S phase and the mutation in the PBD influenced the GFP-Dnmt1 localization in late S phase. This rather argues for a more subtle continuous change in binding balance instead of a simple on/off switching. Hence, association via the TS domain might occur also in early S phase, but at much lower abundance. Indeed a substantial minority (8/21) of early S phase cells could be better fitted with two respective distinct MCs, indicating some cell-to-cell variability, possibly in transition to mid S phase. On the other hand, PBD-mediated co-localization with PCNA is also observed in late S phase. However, as the fraction size with the respective faster off-rate is reduced to non-S phase level, this Dnmt1 fraction may be handed over to form a late S phase-specific, more stable complex, such that the TS domain-specific off-rate becomes

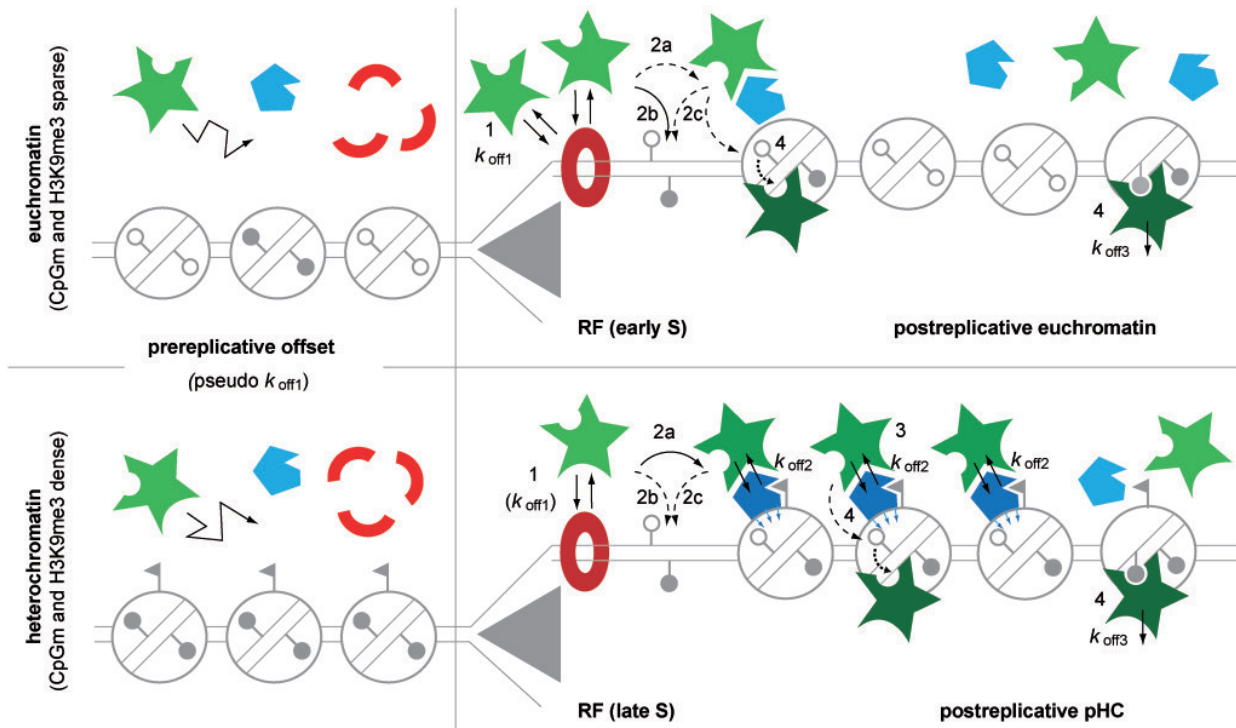


Figure 6. Two-loading-platform-model for the cell cycle-dependent targeting of Dnmt1 to RF and pHC. Schematic representation not drawn to scale. Closed and open lollipops indicate methylated and non-methylated CpG sites, respectively; flags indicate heterochromatin specific marker (e.g. H3K9me3). Dnmt1 is depicted in green. The model postulates two auxiliary factors that act as immobilizing platforms under certain conditions: PCNA (red) that assembles as trimeric ring at the replication fork throughout S phase, and a second unspecified factor (e.g. Uhrf1, blue) that binds strongly to hemimethylated postreplicative heterochromatin. Independent of replication, most Dnmt1 molecules (~80% in G1, >50% in S phase) are freely roaming the nucleoplasm (left column). In addition, a non-specified MC with a pseudo $k_{off,1}$ is constitutively present throughout interphase, which may be attributed to either non-specific binding to chromatin or transient trapping ('corralling') of the large enzyme in the nucleoplasmic environment. When replicating euchromatic sequences in early S phase (upper row) an additional ~20% fraction of the Dnmt1 pool transiently binds via the PBD to immobilized PCNA rings (red donut) with a mean residence time ($1/k_{off,1}$) of ~10 s (1). Targeting to PCNA at RF enhances the efficiency of a small fraction of Dnmt1 to form metastable covalent complexes ($k_{off,1}$) with hemimethylated CpG substrate sites in close vicinity. This may occur on already assembled nucleosomes, likely involving complex formation with one or several auxiliary factors (2a), or directly on the naked DNA substrate adjacent to PCNA (2b) or to nucleosomes (2c). In late S phase, replication through chromatin with now abundant heterochromatic marks in conjunction with dense CpG methylation triggers the generation of high-affinity binding sites for an auxiliary protein. These may then act as second loading platform (dark blue pentagons) for TS-mediated binding with mean residence time ($1/k_{off,2}$) of ~22 s involving ~25% of the Dnmt1 pool. Formation of this transient complex with subsequent substrate binding of a small subset of molecules occurs either directly at the replication fork promoted by PBD-mediated targeting, or PCNA independently at already displaced postreplicative heterochromatin chromatin that may have escaped loading in the first instance (3). This second PCNA-independent loading complex may be assembled well into G2 phase, until all hemimethylated Dnmt1 target sites are fully methylated, which finally triggers disassembly of the loading complex and dissociation of Dnmt1 (4). Of note, this conceptual model is based on the differential availability of binding sites and the free interplay of forces. While higher affinity binding sites are occasionally generated also in early S phase, they may be too sparse to constitute a separate MC.

predominant. In this stage, PCNA binding would thus be an auxiliary factor for TS-mediated binding of a Dnmt1 subfraction. Besides, supported by super-resolution microscopy, we provide evidence for additional PCNA/PBD-independent binding to pHC. The latter seems to be dependent not only on the heterochromatic context alone, but also on the presence of hemimethylated postreplicative DNA as precondition. Accordingly we did not observe any pHC association in early S phase. It is tempting to speculate that the observed kinetics reflect the binding of the TS domain to Uhrf1, an essential epigenetic factor that has previously been shown to target Dnmt1 to hemimethylated CpG sites and to bind trimethylated H3K9 (13–17). However, we cannot rule out other/additional modes of binding of the TS domain

to pHC. In support of a role of Uhrf1 as a docking platform for Dnmt1, a previous FRAP study demonstrated a much slower recovery of GFP-Uhrf1 compared to GFP-Dnmt1^{wt} in mouse embryonic stem cells (61).

In light of our data we propose a conceptual two-loading-platform model (outlined in Figure 6). According to this, the kinetic balance would shift from predominant PCNA/PBD binding in early S phase, toward TS-mediated binding in later S phase stages when replicating densely methylated heterochromatic sequences. This shift would be triggered by the strongly increased appearance of hemimethylated CpG sites in conjunction with heterochromatin marks (e.g., H3K9me3). These would then offer the target for the formation of a

stable complex (involving e.g. Uhrf1) that acts as a second Dnmt1 loading platform on postreplicative chromatin sites. PCNA-independent loading complexes may persist also beyond S phase, until all hemimethylated Dnmt1 target sites are fully methylated, which in turn triggers complex disassembly and gradual loss of TS-mediated binding in G2 phase. Such a mechanism would thus safeguard faithful maintenance of dense methylation at constitutive heterochromatin important for genome stability (3), against the backdrop of a rather slow and inefficient catalytic reaction (40).

While we favor a model of free interplay of forces in conjunction with a cell cycle dependent varying abundance of high affinity binding sites, we cannot rule out an effect by an induced conformational change of the Dnmt1 protein to expose the TS domain at the onset of late S phase. In this context, several modifications have been reported like acetylation, ubiquitination, phosphorylation, methylation and sumoylation, resulting in a change in activity and/or abundance of Dnmt1 (60,62–64). For example, it has been shown that Uhrf1 ubiquitinates Dnmt1 at the C-terminal part of the TS domain (33). Further studies will have to address the exact interplay of Uhrf1 and Dnmt1 as a function of variable (hemi)methylation density and the role of posttranslational modifications of Dnmt1.

In the present study, we have reached substantial improvements on the experimental conditions and workflow for the quantitative and qualitative evaluation of half-nucleus FRAP experiments. Still, extracting definite answers from modeling of such FRAP data remains difficult and to some extent limited. Of note, our analysis involved multiple decisions on the data normalization, fixation of parameters, model choice, etc. Although all steps have been carried out with greatest care, this deterministic approach will still fall to some extent short. New stochastic modeling approaches may be able to realistically take into account random events and may hence better explain intrinsic variability of the FRAP curves. Nonetheless, this article provides a framework for the global assessment and quantitative measurement of diffusion-coupled nuclear protein dynamics with heterogeneous and variable distribution of binding sites, e.g. during cell cycle and development.

Our approach provided new insights into the complex cell cycle dependent regulation of the multi-domain protein Dnmt1 in the epigenetic network. We arrived at a probabilistic two-loading-platform model that provides a possible explanation how PBD and TS domain act cooperatively to faithfully maintain genomic methylation patterns through cell cycle and cell divisions. Further studies will address the mechanistic nature of the complex formation involving the TS domain and the targeting of Dnmt1 to hemimethylated sites.

SUPPLEMENTARY DATA

Supplementary Data are available at NAR Online: Supplementary Tables 1–3, Supplementary Figures 1–10,

Supplementary Methods and Supplementary References [65–68].

ACKNOWLEDGMENTS

We thank Joachim Hermisson and Julia Sommer for helpful discussions. We are grateful to Florian Rieß, Susanne Giehler, Andreas Mäiser, Anna Ullraum, Carina Frauer and Thomas Pyttel for technical help. We further thank Nikola Müller and Garwin Pichler for critical comments on the manuscript.

FUNDING

Deutsche Forschungsgemeinschaft [DFG SFB TR5 and SFB 684 to H.L and L.S.]; Nanosystems Initiative Munich [NIM to H.L.]; Bundesministerium für Bildung und Forschung (BMBF) Episys program [to H.L.]. K.S. was supported by the International Doctorate Program NanoBioTechnology (IDK-NBT) and the International Max Planck Research School for Molecular and Cellular Life Sciences (IMPRS-LS). P.W. is a fellow of the Graduate School Life Science Munich (LSM). CF was supported by the European Union within the European Research Council (ERC) grant LatentCauses. Funding for open access charge: Deutsche Forschungsgemeinschaft [SFB TR5 to L.S.].

Conflict of interest statement. None declared.

REFERENCES

1. Reik,W. (2007) Stability and flexibility of epigenetic gene regulation in mammalian development. *Nature*, **447**, 425–432.
2. Bird,A. (2002) DNA methylation patterns and epigenetic memory. *Genes Dev.*, **16**, 6–21.
3. Gaudet,F., Hodgson,J.G., Eden,A., Jackson-Grusby,L., Dausman,J., Gray,J.W., Leonhardt,H. and Jaenisch,R. (2003) Induction of tumors in mice by genomic hypomethylation. *Science*, **300**, 489–492.
4. Bestor,T.H. (2000) The DNA methyltransferases of mammals. *Hum. Mol. Genet.*, **9**, 2395–2402.
5. Prokhortchouk,E. and Dufossez,P.A. (2008) The cell biology of DNA methylation in mammals. *Biochim. Biophys. Acta.*, **1783**, 2167–2173.
6. Schermelleh,L., Haemmer,A., Spada,F., Rosing,N., Meilinger,D., Rothbauer,U., Cardoso,M.C. and Leonhardt,H. (2007) Dynamics of Dnmt1 interaction with the replication machinery and its role in postreplicative maintenance of DNA methylation. *Nucleic Acids Res.*, **35**, 4301–4312.
7. Spada,F., Haemmer,A., Kuch,D., Rothbauer,U., Schermelleh,L., Kremmer,E., Carell,T., Langst,G. and Leonhardt,H. (2007) DNMT1 but not its interaction with the replication machinery is required for maintenance of DNA methylation in human cells. *J. Cell Biol.*, **176**, 565–571.
8. Chuang,L.S., Ian,H.I., Koh,T.W., Ng,H.H., Xu,G. and Li,B.F. (1997) Human DNA-(Cytosine-5) Methyltransferase-PCNA Complex as a Target for p21WAF1. *Science*, **277**, 1996–2000.
9. Moldovan,G.L., Pfander,B. and Jentsch,S. (2007) PCNA, the maestro of the replication fork. *Cell*, **129**, 665–679.
10. Leonhardt,H., Page,A.W., Weier,H.U. and Bestor,T.H. (1992) A targeting sequence directs DNA methyltransferase to sites of DNA replication in mammalian nuclei. *Cell*, **71**, 865–873.
11. Eswaran,H.P., Schermelleh,L., Leonhardt,H. and Cardoso,M.C. (2004) Replication-independent chromatin loading of Dnmt1 during G2 and M phases. *EMBO Rep.*, **5**, 1181–1186.

12. Frauer,C. and Leonhardt,H. (2011) Twists and turns of DNA methylation. *Proc. Natl Acad. Sci. USA*, **108**, 8919–8920.
13. Sharif,J., Muto,M., Takebayashi,S., Suetake,I., Iwamatsu,A., Endo,T.A., Shinga,J., Mizutani-Koseki,Y., Toyoda,T., Okamura,K. *et al.* (2007) The SRA protein Np95 mediates epigenetic inheritance by recruiting Dnmt1 to methylated DNA. *Nature*, **450**, 908–912.
14. Arita,K., Ariyoshi,M., Tochio,H., Nakamura,Y. and Shirakawa,M. (2008) Recognition of hemi-methylated DNA by the SRA protein UHRF1 by a base-flipping mechanism. *Nature*, **455**, 818–821.
15. Avvakumov,G.V., Walker,J.R., Xue,S., Li,Y., Duan,S., Bronner,C., Arrowsmith,C.H. and Dhe-Paganon,S. (2008) Structural basis for recognition of hemi-methylated DNA by the SRA domain of human UHRF1. *Nature*, **455**, 822–825.
16. Hashimoto,H., Horton,J.R., Zhang,X., Bostick,M., Jacobsen,S.E. and Cheng,X. (2008) The SRA domain of UHRF1 flips 5-methylcytosine out of the DNA helix. *Nature*, **455**, 826–829.
17. Bostick,M., Kim,J.K., Esteve,P.O., Clark,A., Pradhan,S. and Jacobsen,S.E. (2007) UHRF1 plays a role in maintaining DNA methylation in mammalian cells. *Science*, **317**, 1760–1764.
18. Sprague,B.L. and McNally,J.G. (2005) FRAP analysis of binding proper and fitting. *Trends Cell Biol.*, **15**, 84–91.
19. Reits,E.A. and Neefjes,J.J. (2001) From fixed to FRAP: measuring protein mobility and activity in living cells. *Nat. Cell Biol.*, **3**, E145–E147.
20. Phair,R.D. and Misteli,T. (2001) Kinetic modelling approaches to *in vivo* imaging. *Nat. Rev. Mol. Cell Biol.*, **2**, 898–907.
21. Lippincott-Schwartz,J. and Patterson,G.H. (2003) Development and use of fluorescent protein markers in living cells. *Science*, **300**, 87–91.
22. Phair,R.D., Scaffidi,P., Elbi,C., Vecerova,J., Dey,A., Ozato,K., Brown,D.T., Hager,G., Bustin,M. and Misteli,T. (2004) Global nature of dynamic protein-chromatin interactions *in vivo*: three-dimensional genome scanning and dynamic interaction networks of chromatin proteins. *Mol. Cell Biol.*, **24**, 6393–6402.
23. Axelrod,D., Koppel,D.E., Schlessinger,J., Elson,E. and Webb,W.W. (1976) Mobility measurement by analysis of fluorescence photobleaching recovery kinetics. *Biophys. J.*, **16**, 1055–1069.
24. Stasevich,T.J., Mueller,F., Brown,D.T. and McNally,J.G. (2010) Dissecting the binding mechanism of the linker histone in live cells: an integrated FRAP analysis. *EMBO J.*, **29**, 1225–1234.
25. Houtsmuller,A.B. and Vermeulen,W. (2001) Macromolecular dynamics in living cell nuclei revealed by fluorescence redistribution after photobleaching. *Histochem. Cell Biol.*, **115**, 13–21.
26. Dundr,M. and Misteli,T. (2001) Functional architecture in the cell nucleus. *Biochem. J.*, **356**, 297–310.
27. Cardoso,M.C., Schneider,K., Martin,R.M. and Leonhardt,H. (2012) Structure, function and dynamics of nuclear subcompartments. *Curr. Opin. Cell Biol.*, **24**, 79–85.
28. Gorski,S.A., Dundr,M. and Misteli,T. (2006) The road much traveled: trafficking in the cell nucleus. *Curr. Opin. Cell Biol.*, **18**, 284–290.
29. Misteli,T. (2001) Protein dynamics: implications for nuclear architecture and gene expression. *Science*, **291**, 843–847.
30. Meshorer,E. and Misteli,T. (2006) Chromatin in pluripotent embryonic stem cells and differentiation. *Nat. Rev. Mol. Cell Biol.*, **7**, 540–546.
31. Schermelleh,L., Carlton,P.M., Haase,S., Shao,L., Winoto,L., Kner,P., Burke,B., Cardoso,M.C., Agard,D.A., Gustafsson,M.G. *et al.* (2008) Subdiffraction multicolor imaging of the nuclear periphery with 3D structured illumination microscopy. *Science*, **320**, 1332–1336.
32. Gustafsson,M.G., Shao,L., Carlton,P.M., Wang,C.J., Golubovskaya,I.N., Cande,W.Z., Agard,D.A. and Sedat,J.W. (2008) Three-dimensional resolution doubling in wide-field fluorescence microscopy by structured illumination. *Biophys. J.*, **94**, 4957–4970.
33. Qin,W., Leonhardt,H. and Spada,F. (2011) Usp7 and Uhrf1 control ubiquitination and stability of the maintenance DNA methyltransferase Dnmt1. *J. Cell Biochem.*, **112**, 439–444.
34. Seibel,N.M., Eljouni,J., Nalaskowski,M.M. and Hampe,W. (2007) Nuclear localization of enhanced green fluorescent protein homomultimers. *Anal. Biochem.*, **368**, 95–99.
35. Rottach,A., Kremmer,E., Nowak,D., Boisguerin,P., Volkmer,R., Cardoso,M.C., Leonhardt,H. and Rothbauer,U. (2008) Generation and characterization of a rat monoclonal antibody specific for PCNA. *Hybridoma*, **27**, 91–98.
36. Phair,R.D., Gorski,S.A. and Misteli,T. (2004) Measurement of dynamic protein binding to chromatin *in vivo*, using photobleaching microscopy. *Methods Enzymol.*, **375**, 393–414.
37. Carrero,G., Crawford,E., Hendzel,M.J. and de Vries,G. (2004) Characterizing fluorescence recovery curves for nuclear proteins undergoing binding events. *Bull. Math. Biol.*, **66**, 1515–1545.
38. Akaike,H. (1973) Information theory and an extension of the maximum likelihood principle. In: Petrov,B.N. and Csaki,F. (eds), *2nd International Symposium on Information Theory*. Akademiai Kiado, Budapest, pp. 267–281.
39. Schermelleh,L., Heintzmann,R. and Leonhardt,H. (2010) A guide to super-resolution fluorescence microscopy. *J. Cell Biol.*, **190**, 165–175.
40. Song,J., Rechkoblit,O., Bestor,T.H. and Patel,D.J. (2011) Structure of DNMT1-DNA complex reveals a role for autoinhibition in maintenance DNA methylation. *Science*, **331**, 1036–1040.
41. Bacolla,A., Pradhan,S., Roberts,R.J. and Wells,R.D. (1999) Recombinant human DNA (cytosine-5) methyltransferase. II. Steady-state kinetics reveal allosteric activation by methylated dna. *J. Biol. Chem.*, **274**, 33011–33019.
42. Wood,R.J., McKelvie,J.C., Maynard-Smith,M.D. and Roach,P.L. (2010) A real-time assay for CpG-specific cytosine-C5 methyltransferase activity. *Nucleic Acids Res.*, **38**, e107.
43. Pradhan,S., Bacolla,A., Wells,R.D. and Roberts,R.J. (1999) Recombinant human DNA (cytosine-5) methyltransferase. I. Expression, purification, and comparison of de novo and maintenance methylation. *J. Biol. Chem.*, **274**, 33002–33010.
44. Schermelleh,L., Spada,F., Easwaran,H.P., Zolghadr,K., Margot,J.B., Cardoso,M.C. and Leonhardt,H. (2005) Trapped in action: direct visualization of DNA methyltransferase activity in living cells. *Nat. Methods*, **2**, 751–756.
45. Braga,J., McNally,J.G. and Carmo-Fonseca,M. (2007) A reaction-diffusion model to study RNA motion by quantitative fluorescence recovery after photobleaching. *Biophys. J.*, **92**, 2694–2703.
46. Beaudouin,J., Mora-Bermudez,F., Klee,T., Daigle,N. and Ellenberg,J. (2006) Dissecting the contribution of diffusion and interactions to the mobility of nuclear proteins. *Biophys. J.*, **90**, 1878–1894.
47. Sprague,B.L., Pego,R.L., Stavreva,D.A. and McNally,J.G. (2004) Analysis of binding reactions by fluorescence recovery after photobleaching. *Biophys. J.*, **86**, 3473–3495.
48. Mai,J., Trump,S., Ali,R., Schultz,R.L., Hager,G., Hanke,T., Lehmann,I. and Attinger,S. (2011) Are assumptions about the model type necessary in reaction-diffusion modeling? A FRAP application. *Biophys. J.*, **100**, 1178–1188.
49. Sporbert,A., Domaing,P., Leonhardt,H. and Cardoso,M.C. (2005) PCNA acts as a stationary loading platform for transiently interacting Okazaki fragment maturation proteins. *Nucleic Acids Res.*, **33**, 3521–3528.
50. Frauer,C., Rottach,A., Meilinger,D., Bultmann,S., Fellinger,K., Hasenoder,S., Wang,M., Qin,W., Soding,J., Spada,F. *et al.* (2011) Different binding properties and function of CXXC zinc finger domains in Dnmt1 and Tet1. *PLoS One*, **6**, e16627.
51. Erdel,F., Schubert,T., Marth,C., Langst,G. and Rippe,K. (2010) Human ISWI chromatin-remodeling complexes sample nucleosomes via transient binding reactions and become immobilized at active sites. *Proc. Natl Acad. Sci. USA*, **107**, 19873–19878.
52. Xouri,G., Squire,A., Dimaki,M., Geverts,B., Verveer,P.J., Taraviras,S., Nishitani,H., Houtsmuller,A.B., Bastiaens,P.I. and Lygerou,Z. (2007) Cdt1 associates dynamically with chromatin throughout G1 and recruits Geminin onto chromatin. *EMBO J.*, **26**, 1303–1314.
53. Wachsmuth,M., Waldeck,W. and Langowski,J. (2000) Anomalous diffusion of fluorescent probes inside living cell nuclei investigated

by spatially-resolved fluorescence correlation spectroscopy. *J. Mol. Biol.*, **298**, 677–689.

54. Bancaud,A., Huet,S., Daigle,N., Mozziconacci,J., Beaudouin,J. and Ellenberg,J. (2009) Molecular crowding affects diffusion and binding of nuclear proteins in heterochromatin and reveals the fractal organization of chromatin. *EMBO J.*, **28**, 3785–3798.

55. Banks,D.S. and Fradin,C. (2005) Anomalous diffusion of proteins due to molecular crowding. *Biophys. J.*, **89**, 2960–2971.

56. Dross,N., Spriet,C., Zwerger,M., Muller,G., Waldeck,W. and Langowski,J. (2009) Mapping eGFP oligomer mobility in living cell nuclei. *PLoS One*, **4**, e5041.

57. Trembecka,D.O., Kuzak,M. and Dobrucki,J.W. (2010) Conditions for using FRAP as a quantitative technique—fluence of the bleaching protocol. *Cytometry A*, **77**, 366–370.

58. Seber,G.A.F. and Wild,C.J. (1989) *Nonlinear Regression*. John Wiley, New York.

59. Weiss,M., Elsner,M., Kartberg,F. and Nilsson,T. (2004) Anomalous subdiffusion is a measure for cytoplasmic crowding in living cells. *Biophys. J.*, **87**, 3518–3524.

60. Qin,W., Leonhardt,H. and Pichler,G. (2011) Regulation of DNA methyltransferase 1 by interactions and modifications. *Nucleus*, **2**, 392–402.

61. Rottach,A., Frauer,C., Pichler,G., Bonapace,I.M., Spada,F. and Leonhardt,H. (2010) The multi-domain protein Np95 connects DNA methylation and histone modification. *Nucleic Acids Res.*, **38**, 1796–1804.

62. Lee,B. and Muller,M.T. (2009) SUMOylation enhances DNA methyltransferase 1 activity. *Biochem. J.*, **421**, 449–461.

63. Esteve,P.O., Chang,Y., Samaranayake,M., Upadhyay,A.K., Horton,J.R., Feehery,G.R., Cheng,X. and Pradhan,S. (2011) A methylation and phosphorylation switch between an adjacent lysine and serine determines human DNMT1 stability. *Nat. Struct. Mol. Biol.*, **18**, 42–48.

64. Du,Z., Song,J., Wang,Y., Zhao,Y., Guda,K., Yang,S., Kao,H.Y., Xu,Y., Willis,J., Markowitz,S.D. et al. (2010) DNMT1 stability is regulated by proteins coordinating deubiquitination and acetylation-driven ubiquitination. *Sci. Signal.*, **3**, ra80.

65. Nelder,J.A. and Mead,R. (1965) A simplex method for function minimization. *Comput. J.*, **7**, 308–313.

66. Fuchs,C. (2013) *Inference for Diffusion Processes*. Springer, Heidelberg.

67. Lei,H., Oh,S.P., Okano,M., Juttermann,R., Goss,K.A., Jaenisch,R. and Li,E. (1996) De novo DNA cytosine methyltransferase activities in mouse embryonic stem cells. *Development*, **122**, 3195–3205.

68. Meilinger,D., Fellinger,K., Bultmann,S., Rothbauer,U., Bonapace,I.M., Klinkert,W.E., Spada,F. and Leonhardt,H. (2009) Np95 interacts with de novo DNA methyltransferases, Dnmt3a and Dnmt3b, and mediates epigenetic silencing of the viral CMV promoter in embryonic stem cells. *EMBO Rep.*, **10**, 1259–1264.

SUPPLEMENTARY METHODS

Expression constructs and cell culture

The expression construct GFP-Dnmt1^{C1229W} has been previously described (1). *Dnmt1*^{-/-} and wild type J1 mouse embryonic stem cells (C/C) (2), either non-transfected or stably transfected with GFP-Dnmt1^{wt}, GFP-Dnmt1^{Q162E} and GFP-Dnmt1^{ΔTS} were cultured without feeder cells in gelatinized flasks. Culture conditions and creation of stably expressing cells has been described before (3).

In vivo Dnmt1 trapping assay

The trapping assay to measure postreplicative methylation efficiency in living cells was previously described (1). 5-Aza-2'-deoxycytidine (Sigma) was added at a final concentration of 30 µM and cells were incubated for the indicated periods before performing FRAP experiments. Microscope settings and quantitative FRAP analysis are described in Material and Methods (live cell microscopy and quantitative FRAP analysis).

Dnmt1 immunostaining and evaluation of relative expression levels

Non-transfected and transiently or stably transfected cells expressing GFP-Dnmt1 fusions were seeded on No. 1.5H precision coverslips (Marienfeld Superior), formaldehyde fixed and permeabilized with 0.5% Triton-X-100 or ice-cold methanol, if PCNA was detected. Endogenous PCNA was fluorescently labeled with the mouse monoclonal antibody PC10 (Abcam) and a secondary anti-mouse antibody conjugated to Alexa Fluor 594 (Invitrogen). The rat IgG1 monoclonal antibody 5A10 was raised against murine Dnmt1 with an N-terminal His₆-tag. The protein was purified from Sf9 insect cells via recombinant baculoviruses. Immunization, generation of hybridomas and ELISA screening was performed as previously described (4). Secondary antibodies were conjugated to Alexa Fluor 488 or Alexa Fluor 594 (Invitrogen). Cells were counterstained with 1 µg/ml 4',6-diamidino-2-phenylindole and embedded in Vectashield (Vector Laboratories).

Mean intensity levels of Dnmt1 (endogenous and exogenous) in the nucleus were measured on 2 µm image stacks (0.5 µm z-distance) in Volocity 6.1 (PerkinElmer) using the SD based automatic threshold function on the DAPI staining. Objects below 200 µm³ were excluded and objects separated with an object size guide of 1200 µm³. For evaluation of the transfected cells, only low to moderate expressing cells with a mean nuclear GFP intensity between 500 and 2000 grey values were considered (analogous to FRAP experiments). For the calculation of the anti-Dnmt1 fluorescence intensities, background subtracted mean intensities of at least 20 cells (transiently transfected) or 70 cells (non-transfected and stably transfected cells), respectively, were averaged. Finally relative ratios of transfected over non-transfected cells were calculated and the standard deviations were determined.

Co-immunoprecipitation and western blot analysis

Co-immunoprecipitation and western blot analysis was performed as previously described (5) with the following changes. For extract preparation 150 mM NaCl, 1 mg/ml DNaseI (AppliChem), 2 mM MgCl₂

and 1x protease inhibitor mix (Serva) were included in the lysis buffer. For dilution of lysates and for washing steps an immunoprecipitation buffer was used (20 mM Tris-HCl pH 7.5, 150 mM NaCl, 0.5 mM EDTA).

The following primary monoclonal antibodies were used for immunoblotting: rat anti-Dnmt1 5A10 (see Dnmt1 immunostaining and evaluation of relative expression levels), rat anti-PCNA 16D10 (4), mouse anti-GFP (Roche) and mouse anti- β -Actin (Sigma-Aldrich). Secondary anti-rat and anti-mouse antibodies were either conjugated to HRP (Dianova) or Alexa Fluor 594/647 (Invitrogen).

Data correction and normalization

Imported image series were intensity normalized, converted to 8-bit and Gauss-filtered (2 pixel radius). Datasets showing lateral movement of cells were corrected by image registration using the *StackReg* plug-in of ImageJ starting with a frame where approximately half recovery was reached. Mean intensities over time were extracted from four regions of interest (ROIs): The total nuclear area (T) was defined manually or by applying the *Autothreshold* function of ImageJ on the prebleach frame and on the last frame. The overlapping region of both threshold-defined areas was used to create the minimal ROI. This ROI was then divided into a bleached (B) and an unbleached area, where the coordinates of the bleached ROI were used to determine the bleaching border (the last line perpendicular to the major axis of the nucleus, Supplementary Figure 4 A). Finally, a background ROI (BG) outside of the cell was defined manually or with the *Autothreshold* function. The mean gray values over time were measured and pasted to an MS Excel worksheet.

Raw data (Supplementary Figure 4 B) from T and B regions were background subtracted resulting in T' and B' with T'_t representing the data according to the respective time point t . A reference value $T'_{\text{postbleach}}$ was defined as the average of the resulting postbleach values from time points 10-20 after bleaching, and $T'_{\text{prebleach}}$ as the average of the last five prebleach values. Additional gain or loss of total fluorescence during postbleach acquisition may potentially be caused by nuclear import, bleaching-by-acquisition and flux of unbleached molecules from above and below the recorded optical plane. In order to correct for such effects, the postbleach values were corrected by multiplication with $T'_{\text{postbleach}}/T'_t$. Accordingly, prebleach values were multiplied with $T'_{\text{prebleach}}/T'_t$ leading to T''_t and B''_t . To correct for cell-to-cell differences in bleaching depth, we subtracted a value Φ from all mean fluorescence values T''_t and B''_t . The value Φ was determined from the mean fluorescence in the distal part (50%) of the bleached region at the first postbleach time point as follows: To measure the bleaching depth, we determined fluorescence intensity profiles of the total nuclear region along the major axis of the nucleus and determined the number of pixels in the nucleus (T region) for each line along the axis at the first postbleach time point (Supplementary Figure 4 C). The bleaching depth Φ was then determined with the following Equation (S 1), where P stands for the number of pixels of each line in the T region $i \in \{1, \dots, 256\}$ along the axis as $P_{\text{postbleach},i}$ and the mean fluorescence intensity of the lines as $I_{\text{postbleach},i}$, respectively, until 50% of the bleached lines indicated by h :

$$\Phi = \frac{\sum_{i=1}^h (P_{\text{postbleach},i} \times (I_{\text{postbleach},i} - BG_{\text{postbleach}}))}{\sum_{i=1}^h P_{\text{postbleach},i}}. \quad (\text{S 1})$$

The corrected values for T_t''' and B_t''' were divided by the respective means of the last five prebleach values $T_{\text{prebleach}}'''$ to account for intensity differences in the bleached and unbleached regions before bleaching. The corrected relative intensity values in the bleached region were finally corrected for the loss of fluorescence due to half nucleus bleaching. This was achieved by dividing each value B_t''' through the corresponding total nuclear value T_t''' resulting in $B_t^{''''}$. After complete recovery, the resulting fluorescence intensities will level off around the value 1, subject to stochastic fluctuations (Supplementary Figure 4 D). The bleached fraction was given by $f_{\text{bl}} = 1 - T_{\text{postbleach}}'''/T_{\text{prebleach}}'''$ using the Φ corrected values. Calculation of the mobile fraction (MF) was performed by

$MF = (B_{\text{plateau}}''' - B_{\text{postbleach}}''')/(1 - B_{\text{postbleach}}''')$. B_{plateau} was defined as the average intensity of the last 20 frames. For the half time recovery ($t_{1/2}$) the according time to $F_{1/2}$ was chosen from the results with

$$F_{1/2} = (B_{\text{plateau}}'''' - B_{\text{postbleach}}''')/2 + B_{\text{postbleach}}'''.$$

Mathematical model

The mathematical models used for the statistical analysis of the recovery curves are based on a compartmental approach and biochemical kinetic principles. The model for diffusion-uncoupled FRAP, i.e. for molecules that diffuse much more rapidly than they bind or unbind, has previously been described (6-7). A model for diffusion-coupled FRAP is developed in this work; a similar approach has been taken in (8). The compartmental description of the diffusion-coupled model is illustrated in Figure 4 A; the diffusion-uncoupled model is a simplification thereof. Both models consider transitions between the bound and the free state of a protein with *association rate constant* k_{on} and *dissociation rate constant* k_{off} . Dissociation follows a linear process, while association is originally of second order. However, the product of k_{on} and the concentration [BS] of available binding sites can be assumed constant (9), resulting in an *effective association rate constant* $k_{\text{on}}^* = k_{\text{on}}[\text{BS}]$. This simplification allows the conversion of the second order association process to a pseudo-first order process. Hence, the association and dissociation dynamics can be expressed in terms of linear ordinary differential equations (ODEs), which are given below. While bound proteins remain fixed at the respective binding sites, free proteins diffuse through the nucleus, thus changing their locations among the bleached and the unbleached sections. In diffusion-uncoupled FRAP, diffusion of free molecules happens so rapidly that their concentration is identical in the bleached and in the unbleached section. Hence, it is not necessary to model the location of a free molecule. In a diffusion-coupled situation, on the other hand, movements between the bleached and the unbleached section are modeled with a *diffusion rate constant* k_{diff} . Every two molecules that are located at the same distance from the bleaching border are supposed to cross this border within a certain time interval with the same probability, no matter whether the direction of diffusion is from the bleached to the unbleached area or the other way round. If, however, the bleached fraction f_{bl} is not equal to one half, the sizes of the bleached and unbleached sections differ. Then, due to the geometry of the bleached area, several of the proteins in the larger

section are located further away from the bleaching border than the proteins in the smaller area. In order to account for this imbalance, the probabilities for diffusion events in the two possible directions are weighted with factors f_{bl} and $1 - f_{bl}$, respectively. The value of k_{diff} depends on the geometry of the cell and is not immediately eligible for interpretation purposes.

Bleached and unbleached molecules are assumed to behave identically, and therefore it suffices to focus on one type only. The following considerations model the dynamics of the unbleached molecules as these are visible through their fluorescence. Let P_{bl}^{free} , P_{unbl}^{free} , P_{bl}^{bound} and P_{unbl}^{bound} denote the fractions of unbleached free and bound proteins in the bleached and unbleached sections, measured with respect to all unbleached proteins in the nucleus. These four parameters sum up to one such that one of them can be left out. Define $P^{free} = P_{bl}^{free} + P_{unbl}^{free}$ and $P^{bound} = P_{bl}^{bound} + P_{unbl}^{bound}$. In diffusion-uncoupled FRAP, one has $P_{bl}^{free} = f_{bl}P^{free}$ and $P_{unbl}^{free} = (1 - f_{bl})P^{free}$. The overall dynamics of unbleached proteins in diffusion-uncoupled FRAP is described by

$$\frac{dP_{bl}^{free}}{dt} = -(k_{on}^* + k_{off})P^{free} + k_{off}, \quad (S2)$$

$$\frac{dP_{bl}^{bound}}{dt} = k_{on}^* f_{bl} P^{free} - k_{off} P_{bl}^{bound}. \quad (S3)$$

In case of diffusion-coupled FRAP, one has

$$\frac{dP_{bl}^{free}}{dt} = -k_{on}^* P_{bl}^{free} + k_{off} P_{bl}^{bound} + k_{diff}(f_{bl}P_{unbl}^{free} - (1 - f_{bl})P_{bl}^{free}), \quad (S4)$$

$$\frac{dP_{unbl}^{free}}{dt} = -k_{on}^* P_{unbl}^{free} + k_{off}(1 - P_{bl}^{free} - P_{unbl}^{free} - P_{bl}^{bound}) - k_{diff}(f_{bl}P_{unbl}^{free} - (1 - f_{bl})P_{bl}^{free}), \quad (S5)$$

$$\frac{dP_{bl}^{bound}}{dt} = k_{on}^* P_{bl}^{free} - k_{off} P_{bl}^{bound}. \quad (S6)$$

In case of $k_{diff} \gg k_{on}^*, k_{off}$, i.e. for diffusion-uncoupled FRAP, Equations (S4)-(S6) are dominated by the diffusion rather than binding dynamics until $P_{bl}^{free} \approx f_{bl}P^{free}$, which is the basic assumption of diffusion-uncoupled recovery. Hence, the two models are consistent. In both setups, the recovery curve equals

$$F = \frac{P_{bl}^{free} + P_{bl}^{bound}}{f_{bl}}.$$

This term was adjusted to the data normalization procedure described above and approaches the value one as time progresses. From (S2)-(S3) and (S4)-(S6) above, one arrives at differential equations for the fluorescence F . Interestingly, in case of diffusion-uncoupled recovery, the ODE for F is independent of P^{free} and P_{bl}^{bound} . Its explicit solution reads

$$F(t) = 1 + (F_0 - 1)\exp(-k_{off}(t - t_0)),$$

where F_0 is the initial value at time t_0 . This equation does not contain k_{on}^* , and hence this parameter cannot be estimated directly from the recovery curve. However, we assume the nucleus to be in chemical equilibrium. Therefore the fraction P^{free} is presumed to be constant, i.e. $dP^{free}/dt = 0$. From this, one obtains

$$P^{free} = \frac{k_{off}}{k_{on}^* + k_{off}}.$$

Hence, approximation of k_{on}^* is possible if estimates are available for k_{off} and P^{free} .

There is possibly more than one type of binding partner for Dnmt1, i.e. the protein may sometimes associate to a partner of one type and sometimes to a partner of another type. These partners may

differ with respect to the affinity of Dnmt1 to enter the bound state and the mean residence times in this state. All binding partners with identical or similar kinetic properties are gathered in one *mobility class* (MC). This term seems more appropriate than *classes of binding sites* (6), because different sites with identical kinetic properties cannot be distinguished using FRAP data. The number of MCs could hence be smaller than the number of different binding partners. Furthermore binding-unrelated processes like anomalous diffusion can fall into an MC.

Suppose there are M classes of kinetically different binding partners for the protein of interest, labeled with numbers $i \in \{1, \dots, M\}$. For all i , define $P_{\text{bl}}^{\text{bound},i}$ and $P_{\text{unbl}}^{\text{bound},i}$ as the fractions of type- i bound proteins in the bleached and unbleached sections, respectively, with $P^{\text{bound},i} = P_{\text{bl}}^{\text{bound},i} + P_{\text{unbl}}^{\text{bound},i}$. Let $f_i = P^{\text{bound},i} / P^{\text{bound}}$ be the fraction of type- i bound proteins with respect to all bound proteins. Furthermore, denote by $k_{\text{on},i}^*$ and $k_{\text{off},i}$ the association and dissociation rate constants corresponding to the i th MC. Then, the diffusion-uncoupled recovery is described by

$$\begin{aligned}\frac{dP^{\text{free}}}{dt} &= -(k_{\text{off},M} + \sum_{i=1}^M k_{\text{on},i}^*)P^{\text{free}} + k_{\text{off},M} + \sum_{i=1}^{M-1} (k_{\text{off},i} - k_{\text{off},M})P^{\text{bound},i}, \\ \frac{dP_{\text{bl}}^{\text{bound},i}}{dt} &= k_{\text{on},i}^* f_{\text{bl}} P^{\text{free}} - k_{\text{off},i} P_{\text{bl}}^{\text{bound},i}, \\ \frac{dP_{\text{unbl}}^{\text{bound},i}}{dt} &= k_{\text{on},i}^* (1 - f_{\text{bl}}) P^{\text{free}} - k_{\text{off},i} P_{\text{unbl}}^{\text{bound},i},\end{aligned}$$

where $i = 1, \dots, M$. For diffusion-coupled FRAP, one has

$$\frac{dP_{\text{bl}}^{\text{free}}}{dt} = -P_{\text{bl}}^{\text{free}} \sum_{i=1}^M k_{\text{on},i}^* + \sum_{i=1}^M k_{\text{off},i} P_{\text{bl}}^{\text{bound},i} + k_{\text{diff}} (f_{\text{bl}} P_{\text{unbl}}^{\text{free}} - (1 - f_{\text{bl}}) P_{\text{bl}}^{\text{free}}), \quad (\text{S 7})$$

$$\frac{dP_{\text{unbl}}^{\text{free}}}{dt} = -P_{\text{unbl}}^{\text{free}} \sum_{i=1}^M k_{\text{on},i}^* + \sum_{i=1}^M k_{\text{off},i} P_{\text{unbl}}^{\text{bound},i} - k_{\text{diff}} (f_{\text{bl}} P_{\text{unbl}}^{\text{free}} - (1 - f_{\text{bl}}) P_{\text{bl}}^{\text{free}}), \quad (\text{S 8})$$

$$\frac{dP_{\text{bl}}^{\text{bound},i}}{dt} = k_{\text{on},i}^* P_{\text{bl}}^{\text{free}} - k_{\text{off},i} P_{\text{bl}}^{\text{bound},i}, \quad (\text{S 9})$$

$$\frac{dP_{\text{unbl}}^{\text{bound},i}}{dt} = k_{\text{on},i}^* P_{\text{unbl}}^{\text{free}} - k_{\text{off},i} P_{\text{unbl}}^{\text{bound},i}. \quad (\text{S 10})$$

In both cases, the observed fluorescence intensity is

$$F = \frac{P_{\text{bl}}^{\text{free}} + \sum_{i=1}^M P_{\text{bl}}^{\text{bound},i}}{f_{\text{bl}}}.$$

Parameter estimation

The mathematical model contains several unknowns: The model parameters $k_{\text{on},i}^*$, $k_{\text{off},i}$ and k_{diff} , the initial values F_0 , $P_{\text{bl},0}^{\text{free}}$, $P_{\text{bl},0}^{\text{bound}}$ for the components F , $P_{\text{bl}}^{\text{free}}$, $P_{\text{bl}}^{\text{bound}}$ etc., and the fractions f_{bl} , f_i of bleached proteins, bound proteins of type i etc. Due to computational effort, parameter redundancies and strong correlation between some parameters, it is not meaningful to statistically infer all these unknowns simultaneously. Instead, some values were fixed as follows: k_{diff} and f_{bl} were experimentally determined (see Supplementary Table 1, Figure 4 B and the data normalization description above). The smallest k_{off} value was set to 0.005 (see the Results section). F_0 was chosen equal to the first value of the FRAP curve. $P_{\text{bl},0}^{\text{free}}$ was set equal to $f_{\text{bl}} F_0$. The association rates result from the other estimates as $k_{\text{on},i}^* = k_{\text{off},i} f_i (1 - P^{\text{free}}) / P^{\text{free}}$ as explained below. Statistical inference of all remaining variables was carried out by least squares estimation. To that end, the Nelder-Mead algorithm (10)

was applied to find combinations of parameter values which minimize the sum of squared residuals between the observed FRAP curve and its simulated counterpart. In most cases, the output of the optimization procedure depended on the initial guesses of all unknown variables. Hence, several initial guesses were randomly drawn and passed to the Nelder-Mead algorithm. The overall best fit was then chosen from the set of return values. This procedure was continued until the global optimum did not change anymore. In case of diffusion-uncoupled FRAP, the modeled recovery curves can be calculated by means of explicit functions as described in detail below. For diffusion-coupled FRAP, the ODEs (S 4)-(S 6) and (S 7)-(S 10) were numerically solved with the Euler scheme with step length 0.03, which corresponded to one fifth of the observation interval. All software was written in R (R Development Core Team, 2011, R Foundation for Statistical Computing, Vienna, Austria).

We estimated the model parameters for each FRAP curve separately and compared the estimates for curves from the same cell cycle phase and Dnmt1 construct afterwards. An alternative would have been to simply consider the average curve for each phase and construct and to derive parameters for this mean course. In our opinion, however, the second procedure would cause a loss of information. Averaging did not seem appropriate to us as there is undoubtedly extrinsic noise. Our analysis additionally yields insight about uncertainties caused by cell-to-cell variability.

Numerics

In our analyses, we always assume the system to be in chemical equilibrium. For both diffusion-coupled and diffusion-uncoupled FRAP, the system of ODEs is linear, and hence there is an explicit solution of the above ODEs available. For diffusion-coupled FRAP, however, this involves the (typically approximate) computation of a matrix exponential. For that reason, we prefer to numerically solve the ODEs of the diffusion-coupled model. For diffusion-uncoupled FRAP, an exact computation of the solution of the ODEs is easily possible, see (11).

For diffusion-coupled FRAP, we proceed as follows: Assume

$$F_0, P_{\text{bl},0}^{\text{free}}, P_{\text{unbl},0}^{\text{free}}, f_1, \dots, f_{M-1}, k_{\text{off},1}, \dots, k_{\text{off},M}, k_{\text{diff}}$$

to be given. In practice, we determine F_0 , $P_{\text{bl},0}^{\text{free}}$ and k_{diff} experimentally as described above. The remaining $2M$ variables are estimated statistically, i.e. they are optimized using the Nelder-Mead algorithm. In order to avoid non-identifiabilities, we require $k_{\text{off},1} \geq k_{\text{off},2} \geq \dots \geq k_{\text{off},M}$. From the above parameters, we compute

- $f_M = 1 - f_1 - \dots - f_{M-1}$
- $P_{\text{unbl},0}^{\text{free}} = P^{\text{free}} - P_{\text{bl},0}^{\text{free}}$
- $P_{\text{bl},0}^{\text{bound}} = f_{\text{bl}} F_0 - P_{\text{bl},0}^{\text{free}}$
- $P^{\text{bound}} = 1 - P^{\text{free}}$
- $P_{\text{unbl},0}^{\text{bound}} = P^{\text{bound}} - P_{\text{bl},0}^{\text{bound}}$
- $P_{\text{bl},0}^{\text{bound},i} = f_i P_{\text{bl},0}^{\text{bound}}$ for $i = 1, \dots, M$
- $P_{\text{unbl},0}^{\text{bound},i} = f_i P_{\text{unbl},0}^{\text{bound}}$ for $i = 1, \dots, M$
- $k_{\text{on},i}^* = k_{\text{off},i} f_i^{\frac{1-P^{\text{free}}}{P^{\text{free}}}}$ for $i = 1, \dots, M$

These values are now used to numerically solve the diffusion-coupled ODE model.

Model choice

In our analysis, we estimate models with different numbers of MCs. Since the models are nested, the inclusion of more MCs always leads to a better or at least equally good fit. However, one may ask whether the additional computational effort for multiple MCs is worth the improved matching of the data. At first glance, model choice criteria like the Akaike information criterion (AIC) (12) seem appropriate. In our application, however, the difference in the mean squared residuals for different models is typically small due to the already mentioned parameter redundancies. Because of the large number of model parameters, the AIC will often favor less MCs although the curvature of the recovery curves is better described by more complex models. For that reason, we developed a model selection criterion which penalizes complexity less rigorously and is specific to our application. Due to the relatively small noise in the FRAP curves (Figure 3 B and Supplementary Figure 6), we do not expect to overfit the data. The criterion reads as follows: As explained in the Results section, the up to three MCs are further distinguished into one or two distinctive mobility classes (DMCs) and up to one catalytic mobility class (CMC). These have to fulfill three rules:

(1) If a DMC or CMC is present, the fraction P^{bound} of bound proteins should be above a certain threshold:

$$P^{\text{bound}} \geq \varepsilon_{\text{bound}}.$$

Otherwise the DMCs and CMC are discarded, and we assume no MCs for this FRAP curve.

(2) Two distinct MCs should differ substantially in their dissociation rates. In the model with two DMCs that means that one should have

$$\frac{k_{\text{off},\text{DMC}1} - k_{\text{off},\text{DMC}2}}{k_{\text{off},\text{DMC}2}} \geq \delta_{\text{DMC}} \quad \text{or} \quad \frac{k_{\text{off},\text{DMC}2} - k_{\text{off},\text{CMC}}}{k_{\text{off},\text{CMC}}} \geq \delta_{\text{CMC}}.$$

Otherwise we assume the effective number of DMCs to be one.

(3) An MC only truly contributes to the model if it reaches a certain size:

$$f_{\text{DMC}1} P^{\text{bound}} \geq \varepsilon_{\text{DMC}} \quad \text{and} \quad f_{\text{DMC}2} P^{\text{bound}} \geq \varepsilon_{\text{DMC}} \quad \text{and} \quad f_{\text{CMC}} P^{\text{bound}} \geq \varepsilon_{\text{CMC}}.$$

Otherwise we assume the effective number of DMCs to be one.

We derive appropriate values for the above thresholds by cluster analysis. To that end, we consider the best fits for all FRAP curves and all models. From these, we select the corresponding marginal estimates which are in a critical region. For example, we consider the set of all P^{bound} estimates that are between 0% and 10%. These sets are separately divided into two clusters such that the sum of variances within the clusters is minimized. The resulting thresholds are $\varepsilon_{\text{bound}} = 3.5\%$, $\varepsilon_{\text{DMC}} = 5\%$, $\varepsilon_{\text{CMC}} = 2 \cdot 10^{-7}\%$, $\delta_{\text{DMC}} = 10^{-4}$ and $\delta_{\text{CMC}} = 3.77$.

For each measured curve, we now select the model which yielded the best fit. This is typically the model with two DMCs and one CMC, but in many cases the fit of the model with one DMC and one CMC is equally good and hence preferred. For the chosen model, the original number of DMCs is replaced by the effective number of DMCs as determined by the above rules. This effective number enters Supplementary Figure 9. Then, for each cell cycle phase and protein construct, the primarily chosen effective number of DMCs is determined. The model with the according number of DMCs is

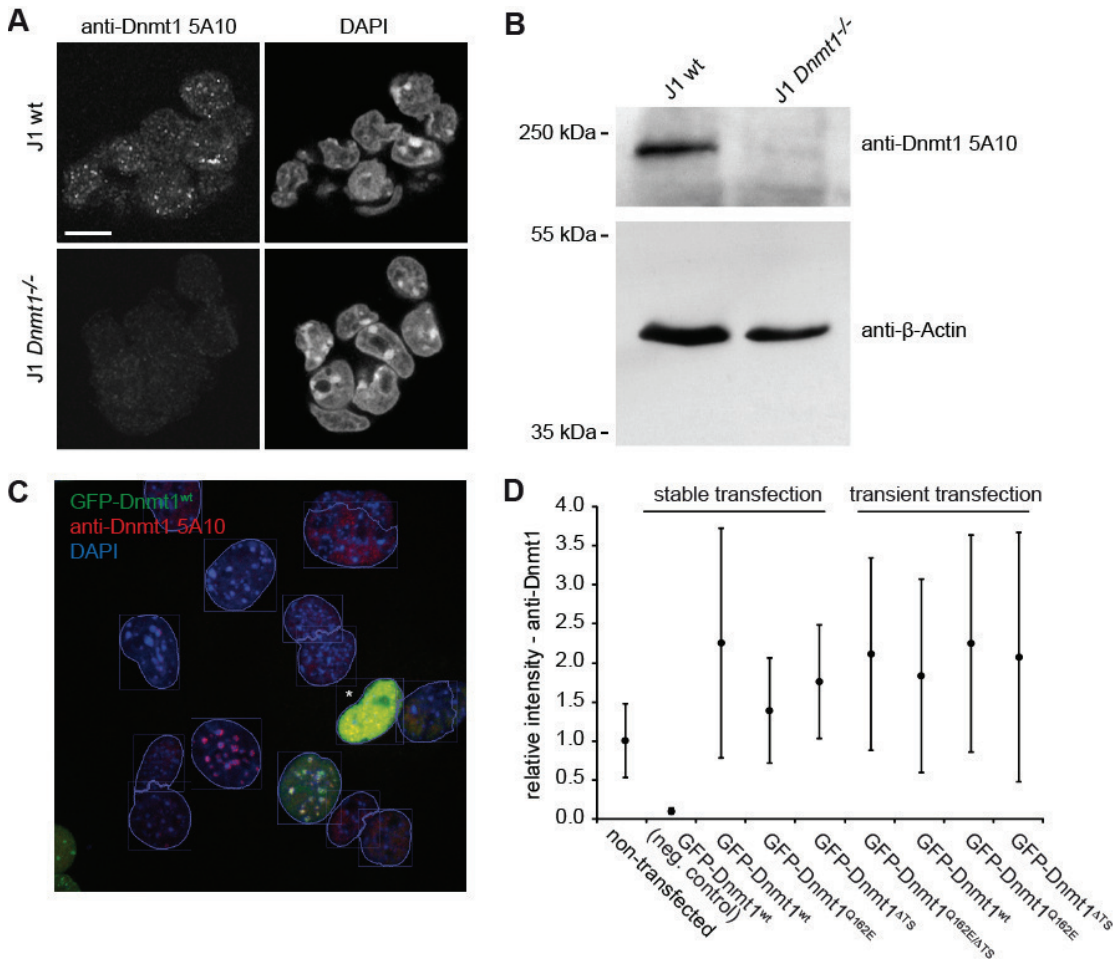
chosen for this phase and construct. Supplementary Table 2 displays the mean estimates for the so chosen model for all FRAP curves. These results always assume the original number of DMCs and do not further reduce it to an effective number.

SUPPLEMENTARY REFERENCES

1. Schermelleh, L., Spada, F., Easwaran, H.P., Zolghadr, K., Margot, J.B., Cardoso, M.C. and Leonhardt, H. (2005) Trapped in action: direct visualization of DNA methyltransferase activity in living cells. *Nat Methods*, **2**, 751-756.
2. Lei, H., Oh, S.P., Okano, M., Juttermann, R., Goss, K.A., Jaenisch, R. and Li, E. (1996) De novo DNA cytosine methyltransferase activities in mouse embryonic stem cells. *Development*, **122**, 3195-3205.
3. Schermelleh, L., Haemmer, A., Spada, F., Rosing, N., Meilinger, D., Rothbauer, U., Cardoso, M.C. and Leonhardt, H. (2007) Dynamics of Dnmt1 interaction with the replication machinery and its role in postreplicative maintenance of DNA methylation. *Nucleic Acids Res*, **35**, 4301-4312.
4. Rottach, A., Kremmer, E., Nowak, D., Boisguerin, P., Volkmer, R., Cardoso, M.C., Leonhardt, H. and Rothbauer, U. (2008) Generation and characterization of a rat monoclonal antibody specific for PCNA. *Hybridoma (Larchmt)*, **27**, 91-98.
5. Meilinger, D., Fellinger, K., Bultmann, S., Rothbauer, U., Bonapace, I.M., Klinkert, W.E., Spada, F. and Leonhardt, H. (2009) Np95 interacts with de novo DNA methyltransferases, Dnmt3a and Dnmt3b, and mediates epigenetic silencing of the viral CMV promoter in embryonic stem cells. *EMBO Rep*, **10**, 1259-1264.
6. Phair, R.D., Scaffidi, P., Elbi, C., Vecerova, J., Dey, A., Ozato, K., Brown, D.T., Hager, G., Bustin, M. and Misteli, T. (2004) Global nature of dynamic protein-chromatin interactions in vivo: three-dimensional genome scanning and dynamic interaction networks of chromatin proteins. *Mol Cell Biol*, **24**, 6393-6402.
7. Phair, R.D., Gorski, S.A. and Misteli, T. (2004) Measurement of dynamic protein binding to chromatin in vivo, using photobleaching microscopy. *Methods Enzymol*, **375**, 393-414.
8. Carrero, G., Crawford, E., Hendzel, M.J. and de Vries, G. (2004) Characterizing fluorescence recovery curves for nuclear proteins undergoing binding events. *Bull Math Biol*, **66**, 1515-1545.
9. Sprague, B.L. and McNally, J.G. (2005) FRAP analysis of binding: proper and fitting. *Trends Cell Biol*, **15**, 84-91.
10. Nelder, J.A. and Mead, R. (1965) A Simplex Method for Function Minimization. *Comput J*, **7**, 308-313.
11. Fuchs, C. (2013) *Inference for Diffusion Processes*. Springer, Heidelberg.
12. Akaike, H. (1973) In Petrov, B. N. and Csaki, F. (eds.), *2nd International Symposium on Information Theory*, Budapest: Akademiai Kiado, pp. 267-281.

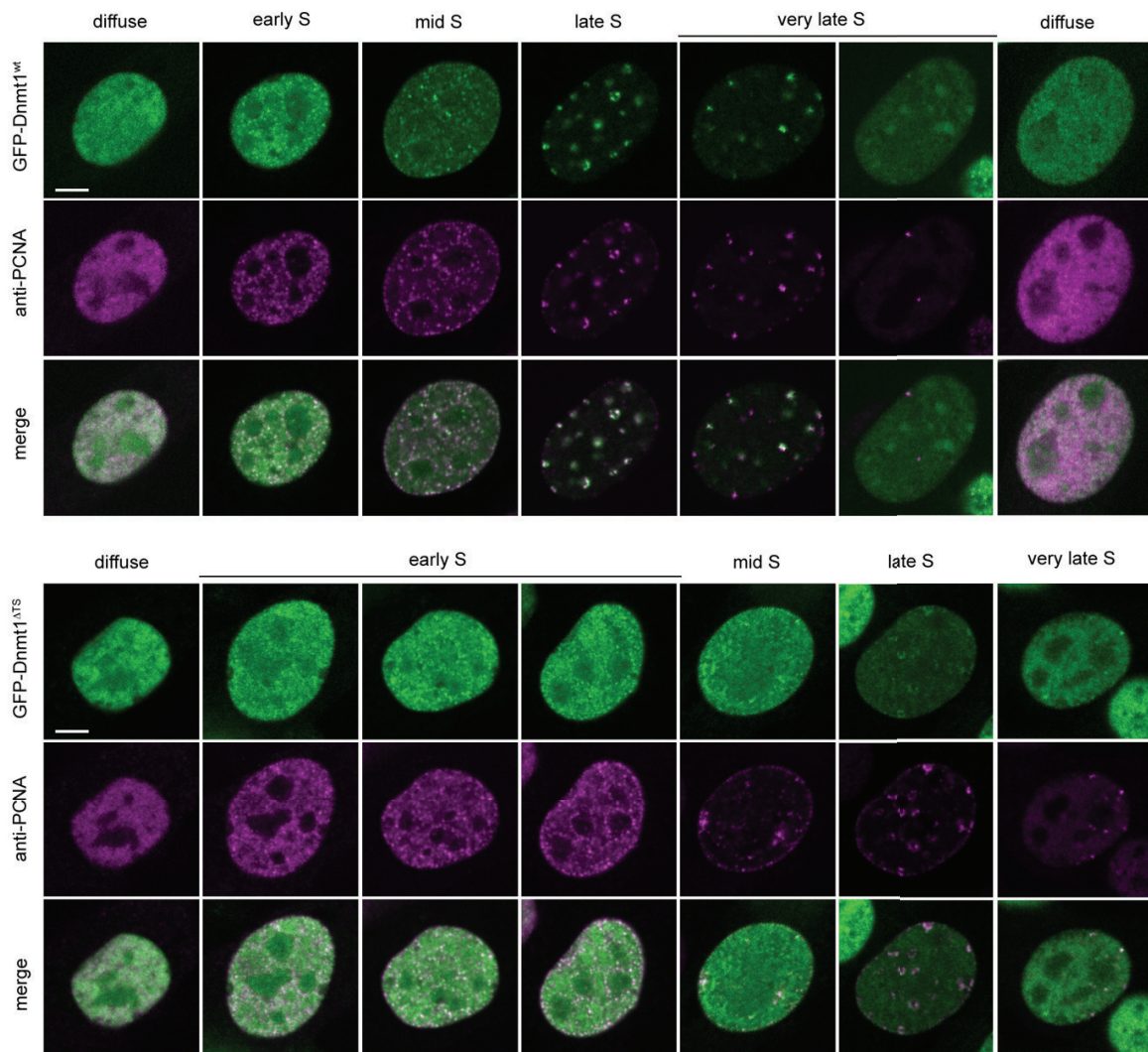
SUPPLEMENTARY FIGURES

S1



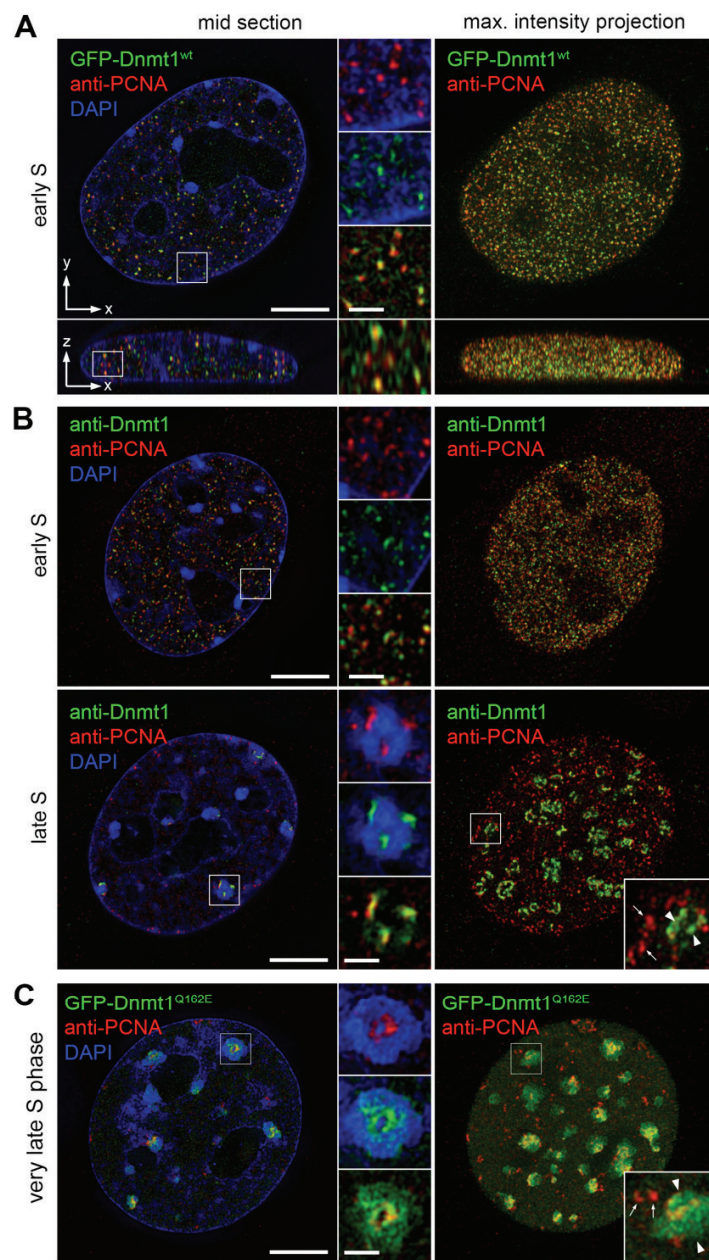
Supplementary Figure 1. Specificity test of the anti-Dnmt1 antibody 5A10 and levels of ectopic and endogenous Dnmt1 expression. (A) Immunostaining of J1 wt and *Dnmt1*^{-/-} embryonic stem cells (C/C) shows a typical Dnmt1 staining pattern in the wt cells, but no nuclear enrichment in the *Dnmt1*^{-/-} cells. Scale bar: 10 μ m. (B) Western blot analysis gives no signal of the anti-Dnmt1 5A10 antibody in J1 *Dnmt1*^{-/-} cells (C/C), but a clear band of 183 kDa in the J1 wt cells. β -Actin (42 kDa) was used as a loading control. (C) Automated quantification of Dnmt1 expression levels using Volocity software (PerkinElmer). The screenshot shows a representative extended focus image used for the evaluation. Nuclei were segmented according to their DAPI signal and the mean nuclear intensities of the Dnmt1 antibody signal and of the GFP signal determined. Highly overexpressing cells (example marked by asterisk) were excluded from the analysis (analogue to the FRAP experiments below). (D) Quantitative evaluation of anti-Dnmt1 5A10 antibody signal intensity in GFP-Dnmt1 expressing cells (representing the endogenous and ectopically expressed Dnmt1) relative to non-transfected C2C12 cells (endogenous only). For the negative control no primary antibody was used. Error bars indicate standard deviations.

S2



Supplementary Figure 2. Localization of GFP-Dnmt1^{wt} and GFP-Dnmt1^{ΔTS} in relation to endogenous PCNA. GFP-Dnmt1^{wt} and GFP-Dnmt1^{ΔTS} are depicted in green and PCNA is depicted in magenta. From early S phase until the beginning of late S phase GFP-Dnmt1^{wt} is associated with replication foci, highlighted by spots of immobilized PCNA. GFP-Dnmt1^{wt} remains to some extent enriched at heterochromatic regions in very late S phase and in transition to G2. GFP-Dnmt1^{ΔTS} shows less prominent association with replication foci throughout all S phase stages. In contrast to the wild type, no enrichment at heterochromatic regions is apparent in very late S phase. Scale bars: 5 μ m.

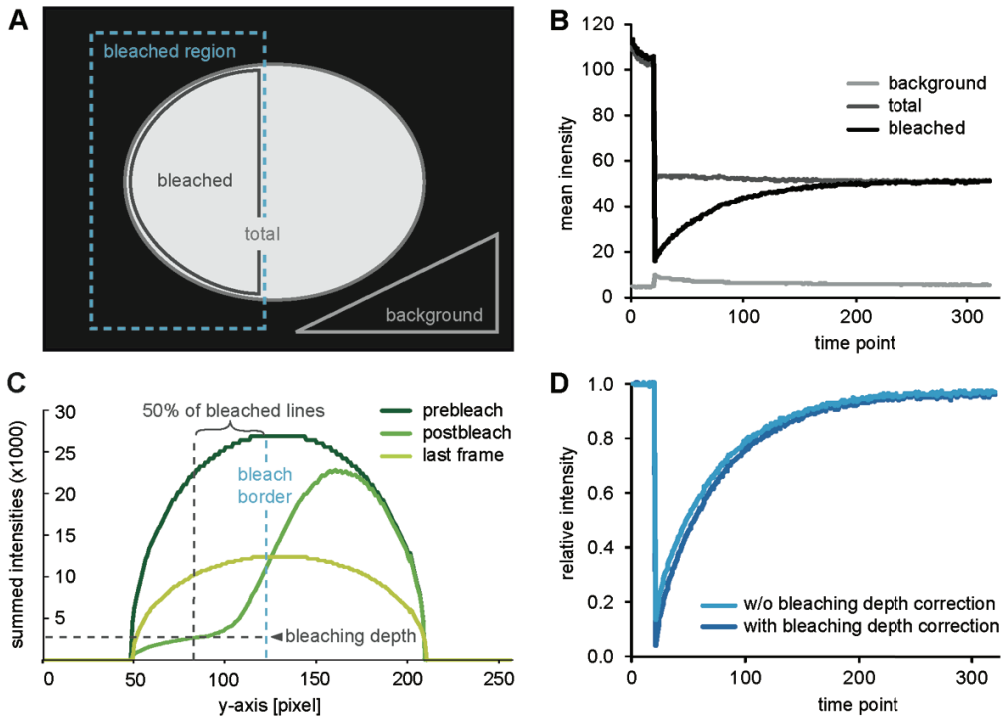
S3



Supplementary Figure 3. Super-resolution imaging of GFP-Dnmt1 constructs and endogenous Dnmt1. (A) C2C12 cell in early S-phase expressing GFP-Dnmt1^{wt} and immunostained with antibodies against endogenous PCNA (complementary to Fig 2 A) demonstrates a high degree of co-localization but variable amount of GFP-Dnmt1 associated with early S-phase replication foci (RF). Lateral and orthogonal cross section and z-projection of a 3D-SIM image stack is shown. (B) Co-staining of endogenous Dnmt1 using the 5A10 antibody together with PCNA reveal the same characteristic distribution pattern in early and late S phase as observed for GFP-Dnmt1^{wt} in C2C12 cells (compare panel A and Fig 2 A). (C) C2C12 cell expressing GFP-Dnmt1^{Q162E} in a very late S-phase stage as identified by only a few remaining PCNA labeled replication sites (complementary to Fig 2 C). In this

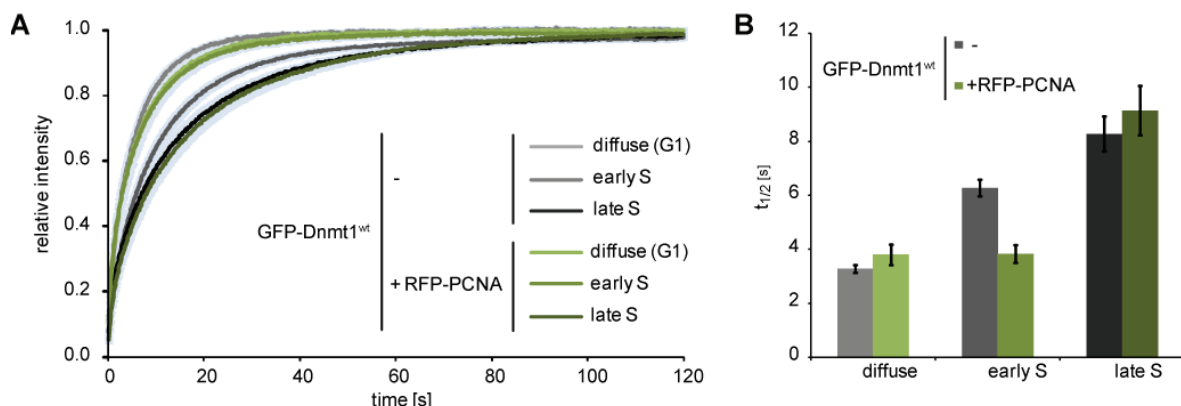
stage the region of pHC association extends over almost the entire chromocenter volume indicating binding to postreplicative pHC only. Scale bars: 5 μ m and 1 μ m (insets).

S4



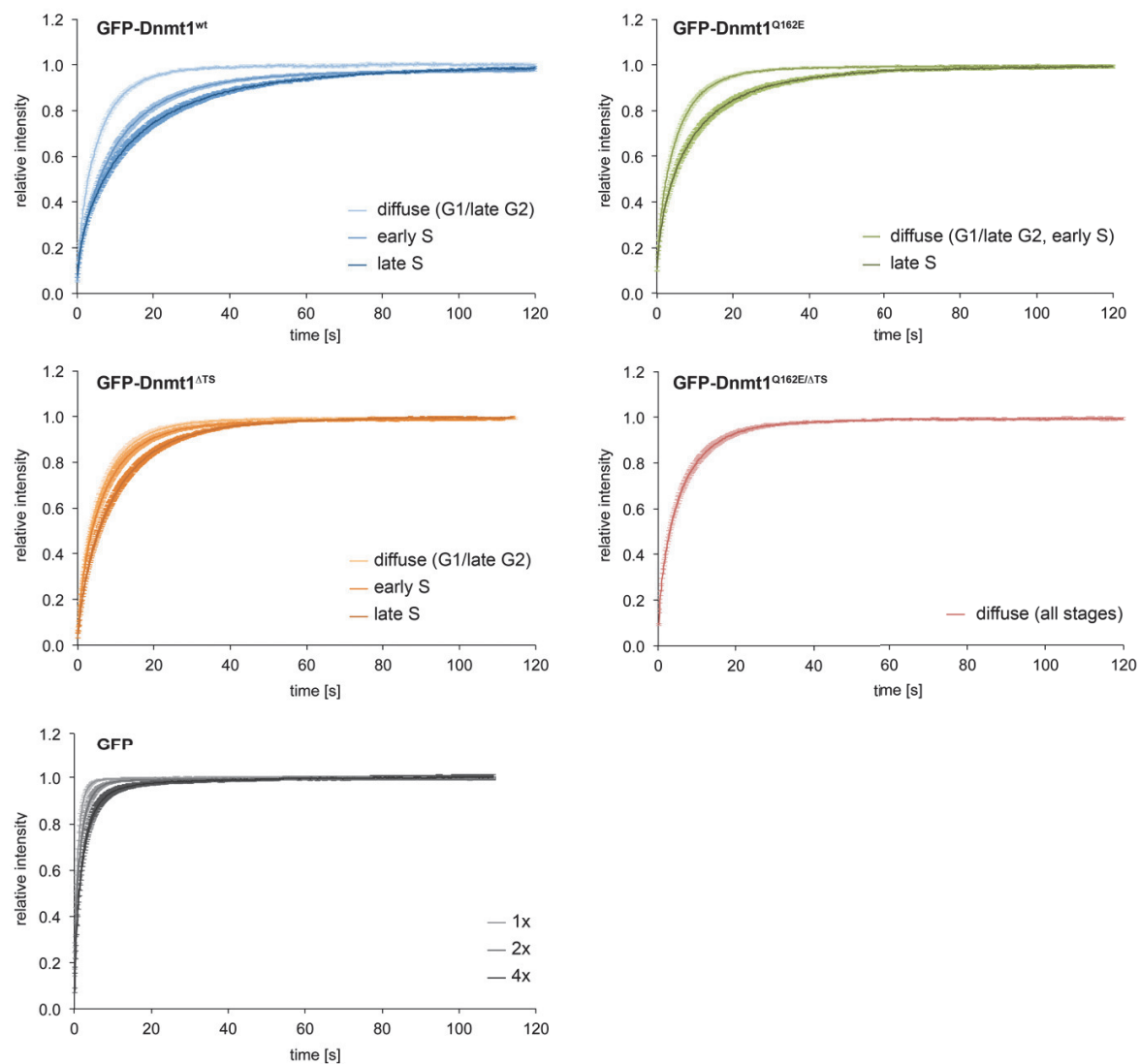
Supplementary Figure 4. Quantitative evaluation of FRAP experiments. (A) The three evaluation ROIs (bleached, total, background) are represented schematically. (B) Mean intensity over time in the ROIs depicted in A for an example FRAP experiment (GFP-Dnmt1^{WT} with diffuse localization). (C) Determination of the bleaching depth in the distal part of the schematic nucleus. The mean fluorescence intensity of each line along the nucleus from the bleached to unbleached region is illustrated for the prebleach, the postbleach and the last frame. The bleaching depth is determined by the average intensity in the region containing 50% of the bleached lines distal to the bleach border. (D) Comparison of the corrected and normalized data depicted in B without and with bleaching depth correction.

S5



Supplementary Figure 5. Quantitative FRAP evaluation of GFP-Dnmt1^{wt} with and without RFP-PCNA coexpression. (A) Mean recovery curves and (B) half times of recovery ($t_{1/2}$) are displayed. Coexpression of RFP-PCNA causes an enhanced mobility of GFP-Dnmt1^{wt} in early S.

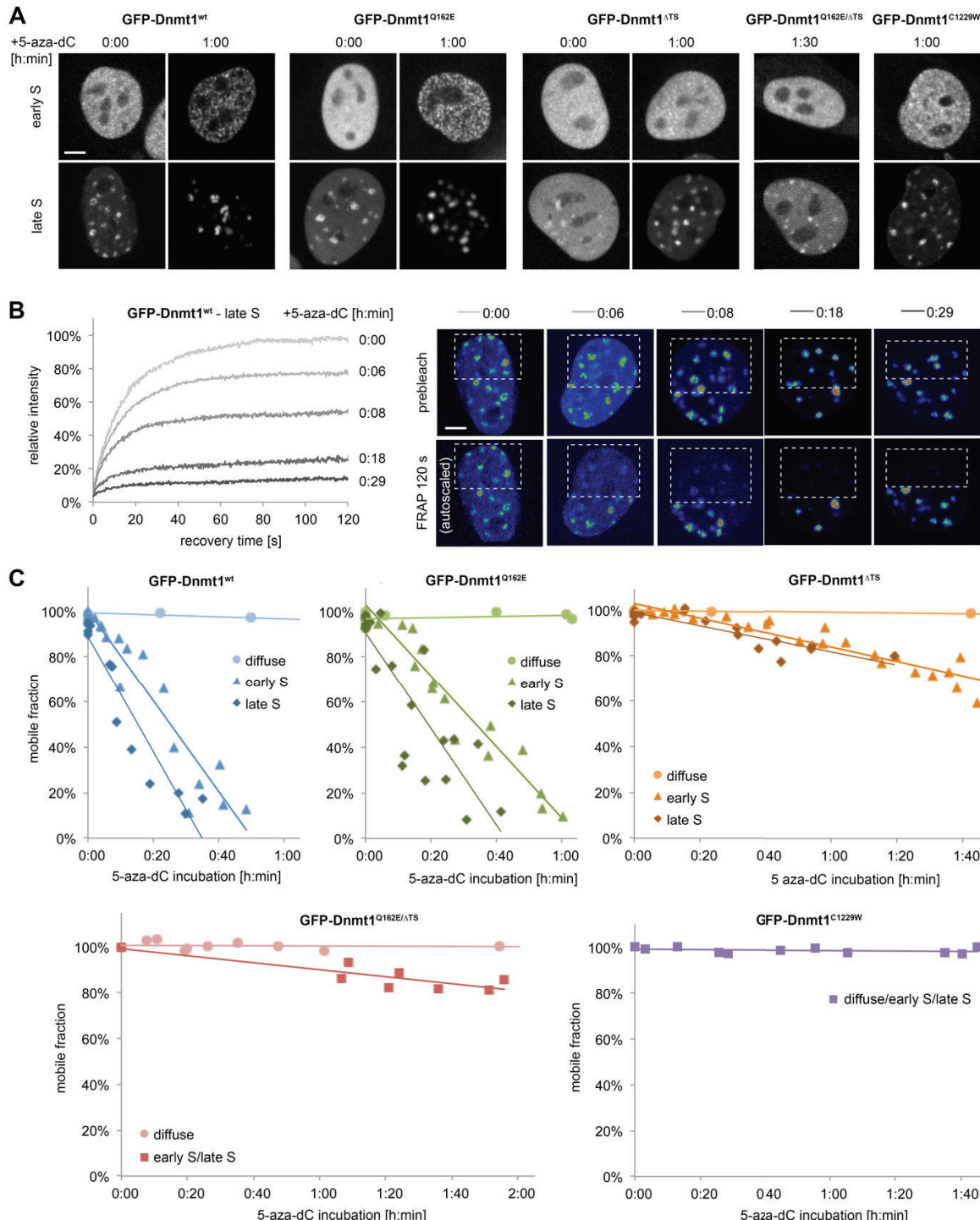
S6



Supplementary Figure 6. Quantitative FRAP evaluation of GFP and GFP-Dnmt1 constructs.

Averaged recovery curves displayed for all measured constructs and cell cycle stage including error bars representing the standard error of the mean for every time point (complementary to Fig 3 B).

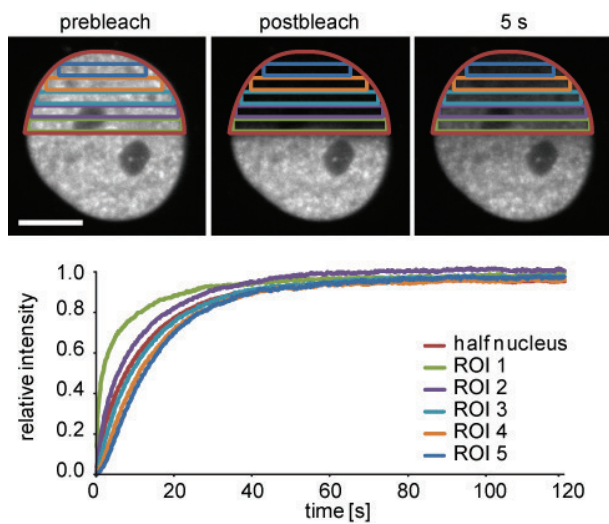
S7



Supplementary Figure 7. Covalent complex formation of GFP constructs analyzed by *in vivo* trapping assay (A) Confocal mid sections of representative cells are displayed before (time point 0:00) and after treatment with the mechanism-based inhibitor 5-aza-dC for 60 min (1:00) or 90 min (1:30), respectively. Upon treatment GFP-Dnmt1^{wt} shows a much stronger focal aggregation at RF

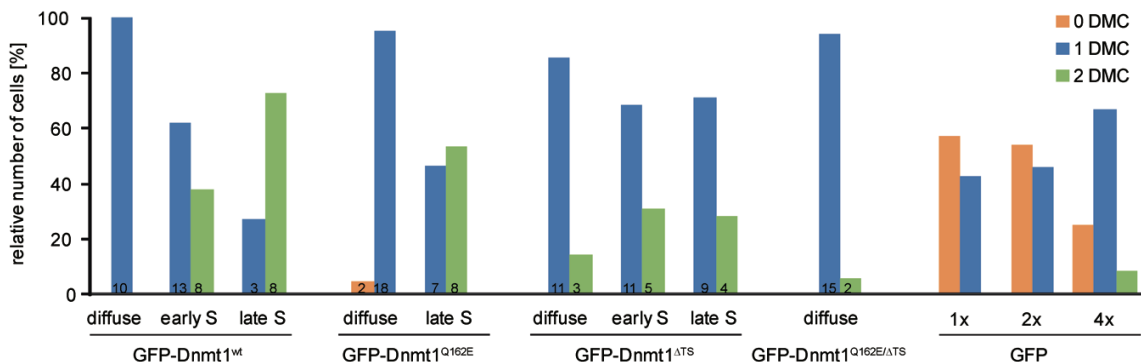
and complete depletion of the diffuse fraction. This indicates the immobilization of the mobile enzyme pool due to irreversible covalent complex formation at 5-aza-dC substituted hemi-methylated substrate sites continuously generated during replication progression. GFP-Dnmt1^{Q162E} shows a similar strong enrichment at RF and depletion of the diffuse fraction after 60 min of treatment. The degree of 5-aza-dC-induced RF-association is less prominent for GFP- Dnmt1^{ΔTS} and the least prominent for the GFP-Dnmt1^{Q162E/ΔTS}. In contrast, a catalytic mutant construct GFP-Dnmt1^{C1229W}, that is unable to form the transient covalent enzyme-substrate complex required for the methyl group transfer, shows no apparent enriched aggregation at RF upon 5-aza-dC treatment. **(B)** Quantitative measurement of the 5-aza-dC-induced immobilization by time-dependent FRAP analysis. Example FRAP measurements of late S phase cells at different 5-aza-dC incubation times (left panel) and the corresponding confocal mid sections of the prebleach time point and 120 s after bleaching (right panel) are shown. The mobile fraction as determined from the recovery plateau reached after 120 s decreases with incubation time. **(C)** Time-dependent decrease of the mobile fractions of GFP-Dnmt1^{wt}, the regulatory mutants GFP-Dnmt1^{Q162E}, GFP- Dnmt1^{ΔTS}, GFP- Dnmt1^{Q162E/ΔTS} and catalytically inactive mutant GFP-Dnmt1^{C1229W} in early and late S phase upon 5-aza-dC treatment. The results highlight the general ability of all analyzed regulatory mutants, but not the catalytic mutant, to undergo covalent complex formation that initiates the enzymatic reaction. Moreover, clear differences in the efficiency of immobilization become apparent between the analyzed constructs, with the fastest trapping rate observed for GFP-Dnmt1^{wt} followed by GFP-Dnmt1^{Q162E}, GFP- Dnmt1^{ΔTS} and GFP- Dnmt1^{Q162E/ΔTS}. Linear trend lines are depicted for every construct and cell cycle stage.

S8



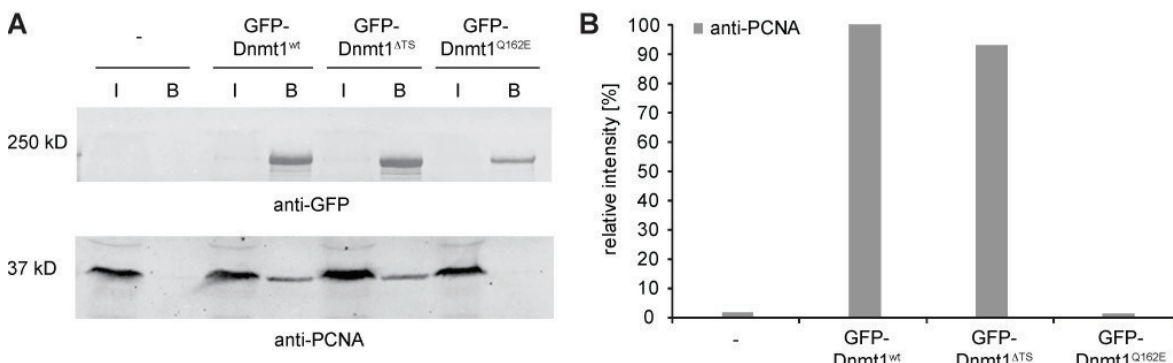
Supplementary Figure 8. Kinetic dependence of GFP-Dnmt1^{wt} on the distance to the bleach border – diffusion-coupled kinetics. Representative images from a FRAP time series and the corresponding recovery curves after half nucleus FRAP (red line) from different evaluation regions of interest (ROIs) as indicated. A stepwise decreased initial mobility is detectable for ROIs that are distant to the bleach border indicating diffusion-coupled kinetics.

S9



Supplementary Figure 9. Relative number of FRAP experiments with zero, one or two distinctive mobility classes. The dominating number of FRAP experiments with the GFP multimers are fitted with 100% free fraction (0 DMC), except for the GFP tetramer (1 DMC). Using our model a preference for one DMC is found for all GFP-Dnmt1 constructs with diffuse localization and in early S phase cells. A preference for two DMCs is found in late S phase independently of the construct. The dominant DMC classification was chosen for further quantifications.

S10



Supplementary Figure 10. Interaction between Dnmt1 and PCNA is abolished by Q162E mutation, but not TS deletion. (A) PCNA is co-precipitated with GFP-Dnmt1 from *Dnmt1*^{-/-} mouse embryonic stem (C/C) cells. Protein extracts of C/C cells without or with stably expressing GFP-Dnmt1^{wt}, GFP-Dnmt1^{Q162E} or GFP-Dnmt1^{ΔTS} were immunoprecipitated with the GFP-Trap (ChromoTek). The immunoprecipitated proteins were separated by SDS-PAGE and detected by GFP or PCNA specific antibodies. (B) Quantification of co-precipitated PCNA relative to the amount co-precipitated with GFP-Dnmt1^{wt}.

SUPPLEMENTARY TABLES

S1

Constructs	stage	N	MF [%]	$t_{1/2}$ [s]
GFP-Dnmt1 ^{wt}	diffuse	10	99.7±0.3	3.3±0.1
	early S	21	97.5±0.5	6.3±0.3
	late S	11	98.3±0.5	8.3±0.6
GFP-Dnmt1 ^{Q162E}	diffuse	20	99.4±0.4	3.1±0.2
	late S	15	99.1±0.5	5.4±0.4
GFP-Dmmt1 ^{ΔTS}	diffuse	14	99.2±0.5	3.8±0.2
	early S	16	98.9±0.5	4.2±0.3
	late S	14	99.4±0.3	6.0±0.4
GFP-Dmmt1 ^{Q162E/ΔTS}	diffuse	17	98.9±0.6	3.6±0.3
GFP multimers	1x	14	100.2±0.4	0.7±0.03
	2x	13	99.2±0.4	1.0±0.1
	4x	12	100.2±1.4	1.5±0.2

Supplementary Table 1. Cell cycle dependent kinetic properties of GFP and GFP-Dnmt1

constructs analyzed by FRAP. N indicates the number of analyzed cells, MF the mobile fraction and $t_{1/2}$ the half time of recovery. Values larger than 100% are due to technical deviations. Mean values \pm SEM are listed.

S2

Constructs	size [kDa]	k_{diff}
1x GFP	27	1.04
2x GFP	54	0.67
4x GFP	108	0.44
GFP-Dnmt1 ^{wt}	210	0.28

Supplementary Table 1. Size-dependent k_{diff} values of GFP-Dnmt1^{wt} and GFP multimers. k_{diff} values are extracted by kinetic modeling of the GFP multimer FRAP data except for GFP-Dnmt1^{wt}, which was extrapolated from the other k_{diff} values.

S3

Constructs	stage	N	f_{free} [%]	DMC	f_{DMC1} [%]	$T_{\text{res, DMC1}}$ [s]	$k_{\text{off, DMC1}}$ [1/s]	f_{DMC2} [%]	$T_{\text{res, DMC2}}$ [s]	$k_{\text{off, DMC2}}$ [1/s]	f_{CMC} [%]
GFP-Dnmt1 ^{WT}	diffuse	10	80.2±1.4	1	19.2±1.4	7.7±0.5	0.14±0.01	-	-	-	0.6±0.3
	early S	21	56.5±2.1	1	39.3±1.8	10.2±0.7	0.11±0.01	-	-	-	4.1±0.6
	late S	11	51.9±2.6	2	17.6±3.2	9.8±1.4	0.25±0.11	28.2±3.8	22.1±2.1	0.05±0.00	2.3±0.6
GFP-Dnmt1 ^{Q162E}	diffuse	20	84.8±1.9	1	13.9±1.9	8.8±1.0	0.18±0.06	-	-	-	1.2±0.3
	late S	15	65.9±2.5	2	9.8±2.5	8.5±1.3	0.59±0.27	22.6±2.3	18.9±2.9	0.07±0.01	1.6±0.6
GFP-Dmmt1 ^{ΔTS}	diffuse	14	76.5±2.8	1	22.0±2.6	6.8±0.5	0.16±0.01	-	-	-	1.5±0.4
	early S	16	67.9±4.2	1	30.1±4.1	8.5±0.8	0.13±0.01	-	-	-	2.0±0.5
	late S	14	58.3±2.5	1	40.3±2.6	8.8±0.2	0.12±0.00	-	-	-	1.4±0.3
GFP-Dmmt1 ^{Q162E/ΔTS}	diffuse	17	79.2±2.6	1	19.1±2.6	8.2±0.6	0.13±0.01	-	-	-	1.7±0.4
GFP multimers	1x	14	100.0	0	-	-	-	-	-	-	-
	2x	13	100.0	0	-	-	-	-	-	-	-
	4x	12	91.1±2.8	1	8.0±2.7	14.9±5.6	0.39±0.014	-	-	-	0.9±0.5

Supplementary Table 3. Cell cycle dependent properties of GFP and GFP-Dnmt1 constructs extracted by kinetic modeling. N indicates the number of analyzed cells and DMC the number of distinctive mobility classes determined by the kinetic modeling. The fraction of bound proteins is subdivided into f_{DMC1} , f_{DMC2} and f_{CMC} representing the fractions of proteins bound with the kinetics of DMC1, DMC2 or CMC, respectively. The fraction of unbound proteins is denoted as f_{free} . k_{off} indicates the dissociation rate, T_{res} the mean residence time given by $1/k_{\text{off}}$ for DMC1 and DMC2, if present. All listed values are mean values ± SEM. Note that $\text{mean}(T_{\text{res}})$ is computed as $\text{mean}(1/k_{\text{off}})$ and deviates from $1/\text{mean}(k_{\text{off}})$.

2.5 Poly(ADP-ribose) polymerase 1 (PARP1) associates with E3 ubiquitin-protein ligase UHRF1 and modulates UHRF1 biological functions

Poly(ADP-ribose) Polymerase 1 (PARP1) Associates with E3 Ubiquitin-Protein Ligase UHRF1 and Modulates UHRF1 Biological Functions*

Received for publication, February 21, 2014, and in revised form, April 29, 2014. Published, JBC Papers in Press, April 29, 2014, DOI 10.1074/jbc.M113.527424

Mike De Vos^{†1}, Rosy El Ramy[‡], Delphine Quénet^{‡2}, Patricia Wolf[§], Fabio Spada^{§3}, Najat Magroun[‡], Federica Babbio[¶], Valérie Schreiber[‡], Heinrich Leonhardt^{§4}, Ian Marc Bonapace[¶], and Françoise Dantzer^{‡5}

From the [‡]Poly(ADP-ribosylation and Genome Integrity Group, Equipe Labellisée Ligue Nationale Contre le Cancer, Laboratoire d'Excellence Medalis, Institut de Recherche de l'Ecole de Biotechnologie de Strasbourg, UMR7242, Centre Nationale de la Recherche Scientifique/Université de Strasbourg, Boulevard Sébastien Brant, BP10413, 67412 Illkirch, France, the [§]Department of Biology II, Center for Integrated Protein Science Munich, Ludwig Maximilians University Munich, 82152 Planegg-Martinsried, Germany, and the [¶]Department of Structural and Functional Biology, University of Insubria, Via Alberto da Giussano 12, 21052 Busto Arsizio, Italy

Background: PARP1 and UHRF1 participate in heterochromatin dynamics and the maintenance of DNA methylation, raising the question of whether both proteins cooperate in these events.

Results: We reveal a physical and functional poly(ADP-ribose)-mediated interaction of PARP1 with UHRF1 that helps to adjust UHRF1-regulated biological activities.

Conclusion: PARP1 is a regulator of UHRF1-controlled H4K20me3 accumulation and DNMT1 expression.

Significance: PARP1 associates and cooperates with UHRF1 to regulate heterochromatin-associated events.

Poly(ADP-ribose) polymerase 1 (PARP1, also known as ARTD1) is an abundant nuclear enzyme that plays important roles in DNA repair, gene transcription, and differentiation through the modulation of chromatin structure and function. In this work we identify a physical and functional poly(ADP-ribose)-mediated interaction of PARP1 with the E3 ubiquitin ligase UHRF1 (also known as NP95, ICBP90) that influences two UHRF1-regulated cellular processes. On the one hand, we uncovered a cooperative interplay between PARP1 and UHRF1 in the accumulation of the heterochromatin repressive mark H4K20me3. The absence of PARP1 led to reduced accumulation of H4K20me3 onto pericentric heterochromatin that coincided with abnormally enhanced transcription. The loss of H4K20me3 was rescued by the additional depletion of UHRF1. In contrast, although PARP1 also seemed to facilitate the association of UHRF1 with DNMT1, its absence did not impair the loading of DNMT1 onto heterochromatin or the methylation of pericentric regions, possibly owing to a compensating interaction of DNMT1 with PCNA. On the other hand, we showed that PARP1 controls the UHRF1-mediated ubiquitination of DNMT1 to timely regulate its abundance during S and G₂ phase. Together, this report identifies PARP1 as a novel modulator of two UHRF1-regulated heterochromatin-associated

events: the accumulation of H4K20me3 and the clearance of DNMT1.

Post-translational modifications of histones and CpG methylation into DNA are defined as fundamental epigenetic mechanisms that elicit specific effects on various chromatin-associated biological events including gene expression, chromatin structure, and integrity or differentiation. Among the chromatin-associated proteins that catalyze or modulate these processes, an explosion of recent findings has introduced poly(ADP-ribose) polymerase 1 (PARP1,⁶ also known as ARTD1) and its activity as a major actor with both structural and regulatory roles (1–3). After binding to specific DNA structures or nucleosomes, PARP1 catalyzes an NAD⁺-dependent polymerization of negatively charged ADP-ribose units to form a ramified polymer called poly(ADP-ribose) (PAR) onto a variety of relevant chromatin-associated targets such as histones, histone-binding proteins, chromatin modulators, and PARP1 itself. The process by which PARP1 introduces covalently bound PAR onto target proteins is known as PARylation. Like other post-translational modifications, PARylation regulates the biochemical and functional properties of the modified target. Furthermore, PAR, either protein-free or covalently linked on proteins, is capable of noncovalent binding with specific proteins owing to the presence of a PAR-binding motif (4).

Interestingly, PARP1 has been particularly studied for its implication in the structure and function of heterochromatin sometimes in redundancy with PARP2. PARP1 binds to and

* This work was supported by the Association pour le Recherche Contre le Cancer (ARC), the CNRS, and the Université de Strasbourg. This work has also been published within the LABEX ANR-10-LABX-0034_Medalis and received financial support from the French government via the Agence Nationale de la Recherche under the Programme d'Investissement d'Avenir.

¹ Supported by the Fonds National de la Recherche (Luxembourg).

² Present address: Laboratory of Receptor Biology and Gene Expression, National Institutes of Health, NCI, Bethesda, MD 20892.

³ Present address: Dept. of Chemistry, Ludwig Maximilians University Munich, 81377 Munich, Germany.

⁴ Supported by Deutsche Forschungsgemeinschaft (DFG) Grant SFB 684.

⁵ To whom correspondence should be addressed. Tel.: 33-3-68854707; Fax: 33-3-68854683; E-mail: francoise.dantzer@unistra.fr.

⁶ The abbreviations used are: PARP, poly(ADP-ribose) polymerase; PAR, poly(ADP-ribose); DNMT, DNA methyltransferase; SRA, SET and RING-associated; TTD, tandem Tudor domain; PHD, plant homeodomain; WB, Western blot; IP, immunoprecipitation; IF, immunofluorescence; RIP, radioimmune precipitation assay; Ubl, ubiquitin-like; PCNA, proliferating cell nuclear antigen.

Interaction and Cooperation of PARP1 with UHRF1

interacts with specific components of constitutive heterochromatin such as telomeres (5, 6), centromeres (7, 8), and pericentromeres (9–11) or silent ribosomal RNA repeats (12, 13). The $\text{PARP1}^{+/+};\text{PARP2}^{-/-}$ background displays specific female embryonic lethality associated with X chromosome instability, suggesting a role in the maintenance of facultative heterochromatin as well (14). Recent reports imply a particular contribution of PARP1 to the propagation of the repressive heterochromatin marks after the passage of the replication fork. This has been suggested first by its interaction with the SWI/SNF-like chromatin remodeler SMARCAD1 (SWI/SNF-related matrix-associated actin-dependent regulator of chromatin subfamily A containing DEAD/H box 1) involved in the inheritance of the silenced pericentric heterochromatin (11) and has been next exemplified by its association with the nucleolar remodeling complex NoRC, where it serves to perpetuate silent ribosomal DNA heterochromatin (12).

It is also becoming increasingly clear that PARP1-catalyzed PARylation participates in the DNA methyltransferase-1 (DNMT1)-mediated establishment and maintenance of DNA methylation patterns (15). A series of cellular studies shows that the blockage of PARylation causes anomalous DNA hypermethylation on genomic DNA and in particular on CpG islands (16–19), whereas increased PARylation is associated with widespread DNA hypomethylation (20). Furthermore, PARP1 and DNMT1 were found in a complex also containing PAR (21). The current working model proposes that PARylated-PARP1 binds to the DNMT1 promoter, attracts DNMT1 through its PAR-binding motif, and inhibits its catalytic activity, thereby protecting the DNMT1 promoter from methylation (15, 22). In this model, PARP1 automodification is promoted by the chromatin insulator CTCF (CCCTC-binding factor) (20).

Recently, UHRF1 (ubiquitin-like, with PHD and RING finger domains 1, also known as NP95 or ICBP90) has also emerged as a central mediator in the faithful inheritance of DNA methylation in mammals. Deletion of UHRF1 in mice is embryonic lethal, and the derived embryonic stem cells display loss of DNA methylation, altered chromatin structure, and enhanced transcription of repetitive elements (23). The initial model was that UHRF1 binds to hemi-methylated DNA via its SET and RING-associated (SRA) domain and acts as a recruitment factor for DNMT1 to copy the methylation pattern onto the newly synthesized daughter strand during DNA replication (24, 25). Subsequent reports have identified an additional binding of UHRF1 to di/trimethylated histone H3 on lysine 9 (H3K9me2 and H3K9me3) involving its tandem Tudor domain (TTD) and its plant homeodomain (PHD), which may contribute to its localization to pericentric heterochromatin (26–29). A recent study highlights the significant contribution of TTD-mediated binding to H3K9me3 in DNA methylation maintenance, likely by regulating DNMT1 stability during mitosis (30). Together, these studies suggest that UHRF1 mediates cross-talk between histone modifications and DNA methylation maintenance.

Interestingly, UHRF1 also contains a Ring domain endowed with E3 ubiquitin ligase activity and has been shown to ubiquitinate itself, histone H3, and DNMT1 but with different outcomes (31, 32). Although the UHRF1-dependent ubiquitylation

of H3 has been reported to act as a platform for the recruitment of DNMT1 to DNA replication sites, the ubiquitination of DNMT1 along with its deubiquitination by Usp7 (also known as HAUSP) represents a major process for the tight regulation of DNMT1 levels (33–36).

In addition to its association with DNMT1, UHRF1 interacts with many other chromatin modulators such as the *de novo* methyltransferases DNMT3a and DNMT3b, the histone deacetylase HDAC1, the histone methyltransferase G9a, or the histone acetyltransferase Tip60 (37–40). Most of these associations involve the SRA domain. Therefore, beyond its critical role in DNA methylation maintenance, UHRF1 functions in several other chromatin-related pathways including DNA repair, silencing of viral promoters, and replication and silencing of pericentric heterochromatin (37, 41, 42).

As both PARP1 and UHRF1 were found to act in common chromatin-related pathways and share DNMT1 as a protein partner, we anticipated a possible physical and functional cooperation between the two proteins. We identified PARP1 as a novel interacting partner of UHRF1 that modulates two of its biological properties. First, we identify a related contribution of PARP1 and UHRF1 in the maintenance of the repressive mark H4K20me3 at pericentric heterochromatin, which possibly helps to control overall transcriptional silencing. We also show that PARP1 helps to maintain the association of UHRF1 with DNMT1 although with no consequence on the loading of DNMT1 to heterochromatic sites or the DNMT1-mediated methylation of major satellite repeats. Second, we describe PARP1 as a negative regulator of the ubiquitin ligase activity of UHRF1 onto DNMT1, thereby introducing PARP1 as an additional modulator of DNMT1 abundance during S and G₂ phases. This can represent an additional way to maintain DNA methylation and transcriptional silencing, more specifically during the replication of pericentric heterochromatin and onward.

EXPERIMENTAL PROCEDURES

Plasmids and Antibodies—Plasmids encoding GST-fused full-length or truncated versions of human PARP1 were described elsewhere (13). Plasmids encoding Myc-tagged full-length and deleted versions of UHRF1 or GFP-DNMT1 also were described elsewhere (27, 31). The GFP-UHRF1 single domain constructs for Ubl and Ring domain expression constructs were generated by PCR using the corresponding wild-type full-length GFP-UHRF1 construct (27). The GFP-PHD, TTD, and SRA expression constructs have been described previously (27, 43). Details on individual plasmid constructs, which were verified by sequencing, are available upon request. Mouse monoclonal anti-Myc antibody (9E10: WB, 1/250; IP, 3 $\mu\text{g}/\text{sample}$) and rabbit anti-DNMT1 antibody (H-300: WB, 1/200; IF, 1/100) were from Santa Cruz Biotechnology. Rabbit polyclonal anti-GST (G7781: WB, 1/10000), the mouse monoclonal anti-actin antibody (A2066: WB, 1/500) and rabbit polyclonal anti-GAPDH antibody (G9545: WB, 1/10000) were from Sigma. The rabbit polyclonal anti-poly(ADP-ribose) antibody (4335-MC-100: WB, 1/1000) was from Trevigen. The mouse monoclonal anti-PCNA antibody (PC-10: WB, 1/2000; IP, 4 $\mu\text{g}/\text{sample}$) was from Dako-Cytomation. The mouse monoclo-

Interaction and Cooperation of PARP1 with UHRF1

nal anti-GFP antibody (11814460001: WB, 1/10000) was from Roche. The mouse monoclonal anti-HA.11 antibody (16B12: WB, 1/10000) was from Covance. The rabbit anti-H3K4me3 (pAB-003-050: IF, 1/200) was from Diagenode. The rabbit anti-H3K9me3 (ab8898: IF, 1/2000), mouse anti-H4K16ac (ab23352: IF, 1/100), and rabbit polyclonal anti-H4K20me3 (ab9053: IF, 1/500; WB, 1/1000) were from Abcam. The mouse monoclonal anti-H4 was from Millipore (07-108: WB, 1/10000) was from Millipore. The mouse monoclonal anti-UHRF1 (IF, 1/1000) has been described elsewhere (44). The mouse monoclonal anti-PARP1 antibody (EGT-69: WB, 1/10000) and rabbit polyclonal anti-UHRF1 antibody (WB, 1/2000; IP, 5 μ l/sample; IF, 1/1000) are described in Refs. 45 and 31, respectively. The rabbit polyclonal anti-PARP1 (2869-70: IP, 15 μ l/sample) was produced in-house. The Alexa-conjugated antibodies for IF (Alexa Fluor 568 goat anti-rabbit IgG, Alexa Fluor 568 goat anti-mouse IgG, and Alexa Fluor 488 goat anti-mouse IgG: IF, 1/1500) were from Molecular Probes.

Cell Culture, Synchronization, and siRNA Knockdown—COS-1 and PARP1^{+/+} and PARP1^{-/-} 3T3 cells were grown in DMEM (1 g/liter D-glucose, Invitrogen) supplemented with 10% FBS (PanBiotech) and 0.1% gentamicin (Invitrogen) at 37 °C in 5% CO₂.

Synchronization of 3T3 cells was performed by serum starvation (DMEM (1 g/liter), 0.1% FBS, and 0.1% gentamicin) for 48 h. After release in fresh medium, cells were collected at different time points as determined by preliminary flow cytometry experiments (T14 h for G₁, T22 h for S, and T24 h for G₂) for protein detection by Western blotting. To inhibit protein synthesis, cells were treated with cycloheximide (Sigma) at 20 μ g/ml for 24 h (including release time) before collecting the cells.

For UHRF1 knockdown in 3T3 cells, gene-specific ON-TARGETplus SMARTpool siRNAs (pool of four sequences) for UHRF1 (L-055507-01-0010) and the control ON-TARGET nontargeting pool siRNA (D-001810-10-20) were from Dharmacon. Cells in suspension were electroporated with 50 nm siRNA pools using the Neon transfection system (Invitrogen) according to the manufacturer's instructions. A second electroporation with 50 nm siRNA pools was performed 48 h later. The transfected cells were collected 96 h after the first electroporation and processed for RNA extraction, protein extraction, or immunofluorescence staining.

Western Blot Analysis, GST Pulldown, GFP-Trap Capture, and Immunoprecipitation—For Western blotting and immunoprecipitation of endogenous proteins, cells were lysed in RIPA-like buffer (50 mM Tris, pH 8, 0.5% Triton, 0.25% sodium deoxycholate, 150 mM NaCl, 1 mM EDTA, 50 mM sodium fluoride, 20 mM sodium pyrophosphate, pH 7.2, 1 mM sodium orthovanadate, 1 mM Pefabloc, and one tablet of protease inhibitor complex/10 ml (Complete Mini, Roche Diagnostics)) and incubated on ice for 20 min. After centrifugation at 10,000 rpm at 4 °C for 20 min, cleared suspensions were quantified by Bradford protein assay, and 50 μ g of protein was analyzed by SDS-PAGE electrophoresis and immunoblotting using the appropriate antibodies.

Histones were acid extracted from a total of 1 \times 10⁶ PARP1^{+/+} and PARP1^{-/-} 3T3 cells following the Abcam his-

tone extraction protocol. The protein content was determined using the Bradford assay, and 30 μ g of protein was analyzed by SDS-PAGE electrophoresis and immunoblotting using the appropriate anti-histone antibodies.

For pulldown experiments, 1 \times 10⁶ COS-1 cells were transfected by jetPEI (Polyplus transfection) with 8 μ g of total recombinant DNA. Forty-eight hours later, cells were lysed by three cycles of freeze/thaw in 50 mM Tris-HCl, pH 8, 150 mM NaCl, 0.1% Nonidet P-40, 0.5 mM Pefabloc, and one tablet of protease inhibitor complex/10 ml. Cleared lysates were incubated with glutathione-Sepharose beads (GE Healthcare) for purification of GST-tagged proteins for 2 h at 4 °C. Beads were subsequently washed twice with washing buffer (10 mM Tris-HCl, pH 8, 0.1% Nonidet P-40, 0.5 mM Pefabloc, and protease inhibitor complex) containing 500 mM NaCl and twice with washing buffer containing 150 mM NaCl. For the experiment shown in Fig. 2C, beads were washed twice with washing buffer containing 750 mM NaCl, once with washing buffer containing 500 mM NaCl, and twice with washing buffer containing 150 mM NaCl. The final pellets were resuspended in Laemmli buffer and subjected to 10% SDS-PAGE.

For GFP-Trap capture, 1 \times 10⁶ COS-1 cells were transfected by JetPEI with 8 μ g of total recombinant DNA. Forty-eight hours later, cells were lysed in RIPA-like buffer as described above and incubated with the GFP-Trap® A (Chromotek, Planegg-Martinsried, Germany) overnight at 4 °C for affinity purification of the GFP-tagged protein. Beads were subsequently washed twice with washing buffer (10 mM Tris-HCl, pH 8, 0.1% Nonidet P-40, 0.5 mM Pefabloc, and protease inhibitor complex) containing 500 mM NaCl and twice with washing buffer containing 150 mM NaCl. The final pellets were resuspended in Laemmli buffer and subjected to 4–20% SDS-PAGE for protein analysis or processed for *in vitro* PARylation as detailed below.

For the *in vitro* binding assays, 4 \times 10⁶ COS-1 cells were transfected by JetPEI with 8 μ g of Myc-SRA. Forty-eight hours later, cells were lysed in RIPA-like buffer as described above, incubated with the anti-Myc antibody overnight at 4 °C followed by a 2-h incubation at 4 °C with protein A/G-Sepharose (GE Healthcare). Next, beads were resuspended in 100 μ l of dilution buffer (20 mM Tris-HCl pH 7.5, 0.1% Nonidet P-40, 0.5 mM Pefabloc) and incubated together with 300 ng of purified recombinant PARP1 for 20 min at 30 °C. Beads were then washed twice with dilution buffer containing 750 mM NaCl, twice with dilution buffer containing 400 mM NaCl, and twice with dilution buffer containing 150 mM NaCl. The final pellets were resuspended in Laemmli buffer and subjected to 10% SDS-PAGE.

For immunoprecipitation experiments of endogenous proteins, RIPA-like cell extracts were precleared by incubation on protein A/G-Sepharose beads for 1 h at 4 °C before incubation with the indicated antibodies overnight at 4 °C followed by a 2-h incubation at 4 °C with protein A/G-Sepharose (GE Healthcare). Beads were washed four times with 20 mM Tris-HCl, pH 7.5, 150–750 mM NaCl, 0.1% Nonidet P-40, and 0.5 mM Pefabloc, resuspended in Laemmli buffer, and analyzed by SDS-PAGE and immunoblotting. Blots were incubated with the appropriate antibodies as indicated. When indicated, 100 nm

Interaction and Cooperation of PARP1 with UHRF1

PARP inhibitor Ku-0058948 was added to the culture medium 2 h before lysis and maintained throughout the experiment.

In Vitro PARylation—For poly(ADP-ribosylation) of immunopurified proteins, purified PARP1 (1 μ g) was incubated with immunopurified Myc-tagged UHRF1, Myc-TRF2 as a positive control, GFP, or GFP-tagged single domains of UHRF1 for 10 min at 25 °C in 480 μ l of activity buffer (50 mM Tris-HCl, pH 8, 0.2 mM dithiothreitol, 4 mM MgCl₂, 0.1 μ g/ μ l BSA, and 100 nM NAD⁺ (for PARP1) or 1 μ M NAD⁺ (for PARP2)) containing 2 μ Ci of [α -³²P]NAD⁺ (800 Ci/mmol, PerkinElmer Life Sciences) and 900 ng of DNase I-activated calf thymus DNA. The reaction was stopped by the addition of 500 μ l of cold washing buffer (50 mM Tris-HCl, pH 8, 400 mM NaCl, 0.1% Nonidet P-40, and 0.5 mM PMSF) on ice, and beads were washed five times with washing buffer and resuspended in 20 μ l of Laemmli buffer. Reaction products were analyzed by gel electrophoresis on 10% SDS-PAGE and autoradiography. For PARylation of purified recombinant UHRF1 tested in ubiquitination assays, purified PARP1 (100 ng) was incubated alone or together with purified UHRF1 (100 ng) for 20 min at 25 °C in 15 μ l of activity buffer (25 mM Tris-HCl, pH 7.6, 5 mM MgCl₂, 1 mM dithiothreitol, 0.1 μ g/ μ l BSA, 5 ng/ μ l DNA, and 10 μ M NAD⁺).

Immunofluorescence Studies—Immunofluorescence was performed essentially as described previously (13). Briefly, cells grown on glass coverslips were washed twice with PBS and fixed for 15 min with PBS, 3.7% formaldehyde, followed by three washes in blocking buffer (PBS, 0.1% Triton X-100, and 0.1% milk). Cells were then incubated overnight at 4 °C with the primary antibodies diluted in blocking buffer. After three washes with PBS, 0.1% Triton X-100, and 0.1% milk, cells were incubated for 3 h at room temperature with the appropriate conjugated secondary antibodies diluted in blocking buffer. DNA was counterstained with 4',6'-diamidino-2-phenylindole (DAPI, 25 ng/ml in PBS). Slides were mounted using Mowiol 4-88 (Hoechst), and immunofluorescence microscopy was performed using a Leica microscope (Leica Microsystems, Heidelberg, Germany) and the capture software (Improvision, PerkinElmer Life Sciences).

DNA Methylation Analysis—Methylation of mouse major and minor satellite repeats was determined by pyrosequencing of bisulfite-treated, PCR-amplified, genomic DNA as described (46).

RT-PCR Analysis—Total RNA was extracted from \sim 3 \times 10⁶ PARP1^{+/+} and PARP1^{-/-} cells with TRIzol (Invitrogen) according to the manufacturer's instructions. The remaining DNA was digested by incubation with RNase-free DNase I (Promega) (1 unit/ μ g RNA), and isolated RNA was purified using the RNA Clean-up XS kit (Machery-Nagel). Reverse transcription (RT) was done on 800 ng of purified RNA using oligo(dT) primers (Sigma) and the AMV reverse transcriptase (Finnzyme). PCR reactions were performed on 5% of the RT volume using the Phusion polymerase (Finnzyme) and the following primer pairs: major satellite repeat forward, 5'- GAC-GACTTGAAAAATGACGAAATC-3'; major satellite repeat reverse, 5'-CATATTCCAGGTCCCTTCAGTGTGC-3'; GAPDH forward, 5'- TTCTGAGTGGCAGTGATGGC-3'; and GAPDH reverse, 5'- AACAAACCCTTCATTGACCTC-3'. Transcripts

were analyzed on ethidium bromide-stained agarose gels using the Typhoon instrument and quantified by ImageJ.

In Vivo Ubiquitination Assay—PARP1^{+/+} and PARP1^{-/-} cells were co-transfected with 5 μ g of GFP, GFP-DNMT1, or Myc-UHRF1 and 5 μ g of HA-Ub using the jetPEI method. Thirty-six hours later, the cells were treated with 5 μ M MG-132 (Enzo) for another 12 h and lysed with RIPA-like buffer as described above. After GFP quantification by Western blotting, equivalent amounts of GFP-DNMT1 were immunopurified using GFP-Trap[®] A (Chromotek) as described above. Myc-UHRF1 was immunoprecipitated using an anti- Myc antibody as described above. Beads were washed twice with washing buffer A (20 mM Tris-HCl, pH 7.5, 0.1% Nonidet P-40, 400 mM NaCl, and 0.5 mM Pefabloc), twice with washing buffer B (20 mM Tris-HCl, pH 7.5, 0.1% Nonidet P-40, 150 mM NaCl, and 0.5 mM Pefabloc), resuspended in Laemmli buffer, and processed for Western blotting. Twenty-five % of the sample was loaded for detecting GFP-DNMT1 or Myc-UHRF1, and 75% of the sample was loaded for detecting GFP-Dnmt-1^{Ub} or Myc-UHRF1^{Ub} using the anti-HA antibody.

In Vitro Ubiquitination Assay—Purified recombinant UHRF1 (100 ng (31)) was first incubated alone or together with purified recombinant PARP1 (100 ng) in a PARP activity buffer with or without NAD⁺ as described above. After 20 min at 25 °C, PARylated or non-PARylated (PARP assay performed without NAD⁺) UHRF1 was subsequently incubated alone or together with purified recombinant GST-DNMT1 (300 ng, BPS Bioscience) as indicated in a standard ubiquitination reaction mixture (15 μ l) containing 100 ng of human recombinant ubiquitin-activating enzyme (Boston Biochem), 300 ng of human recombinant UbcH5b (Boston Biochem), and 10 μ g of HA-tagged human recombinant ubiquitin (Boston Biochem) in 25 mM Tris-HCl, pH 7.6, 5 mM MgCl₂, 1 mM DTT, 2 mM ATP, and 100 mM NaCl. During ubiquitination, PARP activity was inhibited by adding 330 nM Ku-0058948. The reaction was incubated at 37 °C for 1 h and stopped by adding 1,25 \times final Laemmli buffer. Ubiquitinated proteins were analyzed by Western blot analysis; one-half of the final volume was used for HA-ubiquitin detection and one-eighth of the volume was used for poly(ADP-ribose) polymer detection.

RESULTS

PARP1 Interacts with the E3 Ubiquitin Ligase UHRF1 in a PAR-dependent Manner—Previous studies have identified PARP1 together with DNMT1 in a proteomic analysis of anti-UHRF1 immunoprecipitates, thus making PARP1 a possible candidate for modulating UHRF1-DNMT1 functional interplay (24).

To expand on these findings, we decided to investigate the comparative association of PARP1 and PARP2 with UHRF1 (Fig. 1A). COS-1 cells were transfected with Myc-tagged UHRF1 together with GST, GST-fused PARP1, or GST-fused PARP2. After glutathione-Sepharose beads were trapped, copurified Myc-UHRF1 was assessed by Western blot analysis using an anti-Myc antibody. To test the role of PARylation in the interaction, pulldown assays were performed in the presence of the potent PARP inhibitor Ku-0058948. As shown in Fig. 1A, UHRF1 was clearly coprecipitated with GST-PARP1

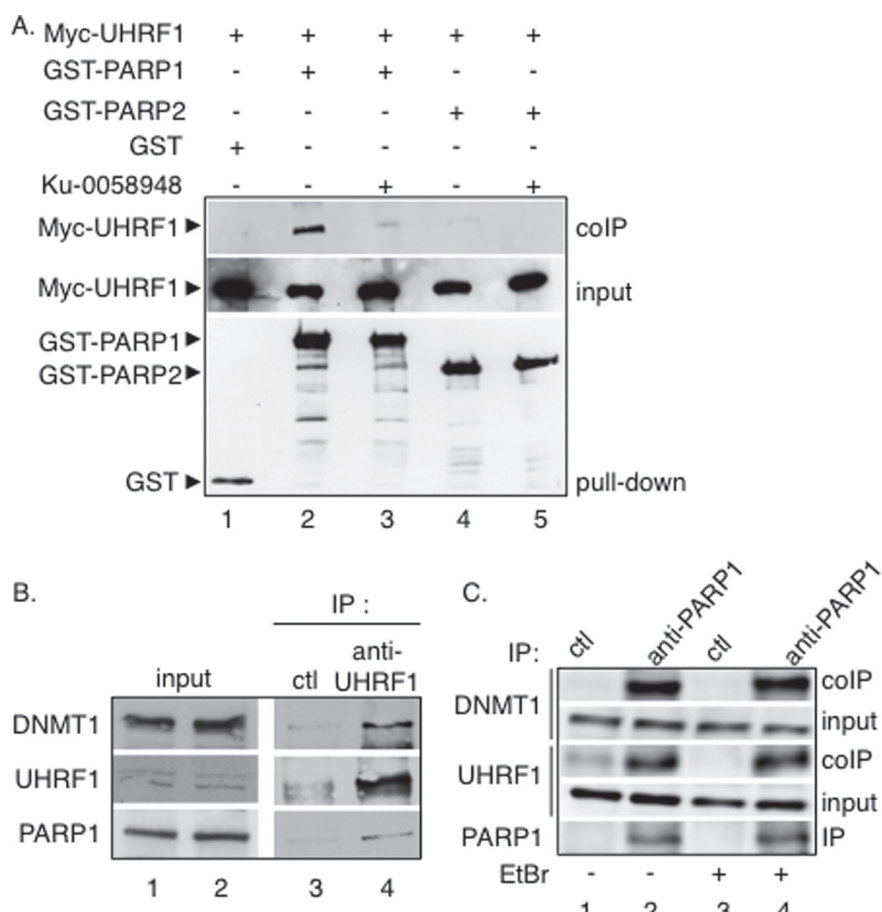


FIGURE 1. Selective PAR-dependent association of UHRF1 with PARP1 in mammalian cells. *A*, selective coprecipitation of Myc-UHRF1 with GST-PARP1. GST (lane 1), GST-PARP1 (lanes 2 and 3), and GST-PARP2 (lanes 4 and 5) were expressed in COS-1 cells together with Myc-tagged UHRF1 (lanes 1–5). Interacting proteins were analyzed by GST pulldown and Western blotting with subsequent anti-Myc and anti-GST antibodies. *Input* corresponds to 1/60th the amount of cell extract used for GST pulldown. In lanes 3 and 5, the PARP inhibitor Ku-0058948 was added throughout the experiment. *B*, coimmunoprecipitation of PARP1 and DNMT1 with UHRF1 in mouse 3T3 cells. Wild-type mouse cell extracts were immunoprecipitated with an anti-UHRF1 antibody (lane 4) or a control antibody (Ctl, lane 3) and analyzed by Western blotting. *Input* (lanes 1 and 2) corresponds to 1/30th the amount of cell extract used for immunoprecipitation. *C*, coimmunoprecipitation of UHRF1 and DNMT1 with PARP1 in mouse 3T3 cells. Wild-type mouse cell extracts were immunoprecipitated with an anti-PARP1 antibody (lanes 2 and 4) or a control antibody (lanes 1 and 3) and analyzed by Western blotting. To prevent any coprecipitation of either partner through DNA, EtBr (10 µg/ml) was added throughout the immunoprecipitation when indicated (lanes 3 and 4). *Input* corresponds to 1/30th the amount of cell extract used for immunoprecipitation. The association of PARP1 with UHRF1 is not mediated by DNA.

(lane 2) but not efficiently with GST-PARP2 (lanes 4–5) and not with GST alone (lane 1), defining a preferential association of UHRF1 with PARP1 compared with PARP2. Furthermore, a significantly weaker copurification of UHRF1 with GST-PARP1 was observed in the presence of Ku-0058948 (Fig. 1A, lane 3), revealing a critical role of PARylation in their association. The UHRF1-PARP1 interaction and the association with DNMT1 was next verified by coimmunoprecipitation experiments with the endogenous proteins (Fig. 1, *B* and *C*). Using an anti-UHRF1 antibody, we efficiently coimmunoprecipitated both PARP1 and DNMT1 from 3T3 mouse extracts (Fig. 1B, lane 4), whereas no coprecipitation was detected using a control antibody (Fig. 1B, lane 3). In a reciprocal experiment (Fig. 1C), when 3T3 cell extracts were immunoprecipitated with an anti-PARP1 antibody, significant fractions of UHRF1 and DNMT1 were detected in the PARP1 immunoprecipitate (lane 2) but not in the control immunoprecipitate (lane 1). To further prevent any coprecipitation of either of the proteins through DNA, we performed the coprecipitation experiments in the

presence of ethidium bromide, which intercalates into DNA and thereby competes for interacting proteins (Fig. 1C, lanes 3 and 4). The addition of ethidium bromide did not abolish the DNMT1-UHRF1-PARP1 interaction, suggesting that DNA was not involved (Fig. 1C, compare lanes 4 and 2). Together these results describe the existence of a protein complex containing PARP1, UHRF1, and DNMT1 in mammalian cells.

To further characterize the UHRF1-PARP1 association, we aimed to identify the region of PARP1 to which UHRF1 binds (Fig. 2A). GST fusion proteins expressing truncated versions of PARP1 (amino acids 1–385 (DNA-binding domain), amino acids 384–524 (automodification domain), and amino acids 572–1014 (catalytic domain)) were tested for their interaction with Myc-UHRF1. Myc-UHRF1 coprecipitated efficiently with full-length PARP1 and its DNA-binding domain (Fig. 2A, lanes 2 and 3) and less efficiently with the automodification domain, defined as the site of autoPARylation (lane 4). No coprecipitation was detected with GST alone or the PARP catalytic domain (Fig. 2A, lanes 1 and 5). As noted above, the association of Myc-

Interaction and Cooperation of PARP1 with UHRF1

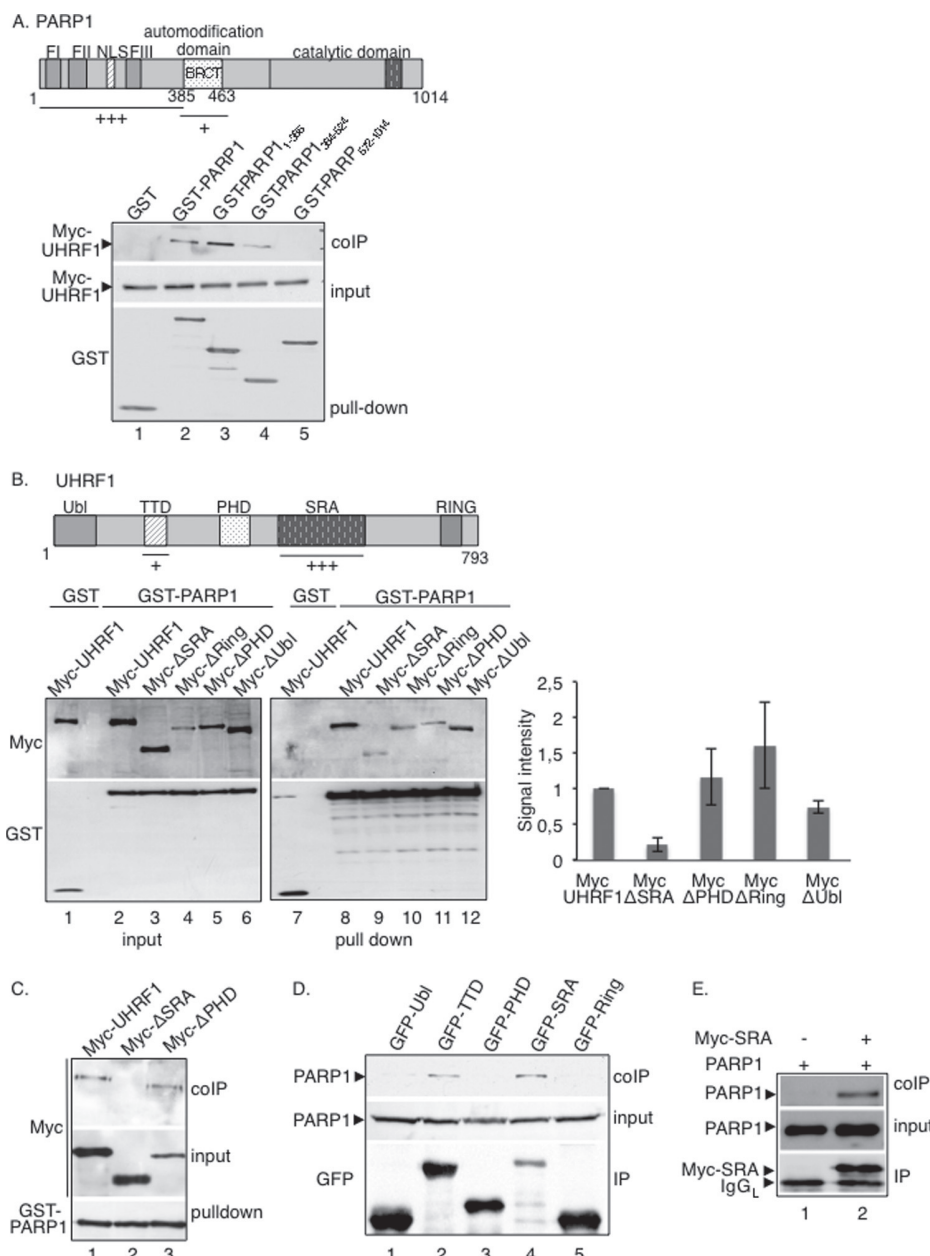


FIGURE 2. The UHRF1-PARP1 interaction preferentially involves the DNA-binding domain of PARP1 and the SRA domain of UHRF1. *A*, UHRF1 interacts preferentially with the DNA-binding domain and weakly with the automodification domain of PARP1. *Top*, schematic representation of PARP1 indicating the interacting domains identified. *Bottom*, GST (lane 1), GST-PARP1 (lane 2), GST-PARP1-(1–385) expressing the DNA-binding domain (lane 3), GST-PARP1-(384–524) expressing the automodification domain (BRCT) (lane 4), and GST-PARP1-(572–1014) expressing the catalytic domain (lane 5) were expressed in COS-1 cells together with Myc-UHRF1 (lanes 1–5). Interacting proteins were analyzed by GST pulldown and Western blotting with subsequent anti-Myc and anti-GST antibodies. *Input* corresponds to one-tenth the amount of cell extract used for GST pulldown. *B*, the absence of the SRA domain impairs the interaction of UHRF1 with PARP1. *Top*, schematic representation of UHRF1 indicating the interacting domains identified. *Bottom left*, Myc-UHRF1 (lanes 1, 2, 7, and 8) or Myc-tagged deletion mutants of UHRF1 (lanes 3–6 and 9–12) were expressed in COS-1 cells together with either GST (lanes 1 and 7) or GST-PARP1 (lanes 2–6 and 8–12). Interacting proteins were analyzed as described in *A* (lanes 7–12). *Input* corresponds to 1/60th the amount of cell extract used for GST pulldown (lanes 1–6). *Bottom right*, the signal intensities of the coprecipitating Myc-tagged proteins relative to their expression and GST-PARP1 pulldown were measured in three independent experiments using ImageJ. The coprecipitation of Myc-UHRF1 was set to 1. Mean values \pm S.D. are indicated. *C*, at higher stringency conditions of the washing buffer, the association of Myc-ΔSRA with GST-PARP1 is lost (lane 2), whereas the association of Myc-UHRF1 (lane 1) or Myc-ΔPHD (lane 3) with GST-PARP1 is maintained. The experiment was done as described in *B* except that the stringency conditions of the washing buffers were increased (beads were washed twice with washing buffer containing 750 mM NaCl, once with washing buffer containing 500 mM NaCl, and twice with washing buffer containing 150 mM NaCl). *D*, PARP1 interacts preferentially with the SRA domain of UHRF1 and to a lesser extent with the TTD. GFP fusion proteins expressing different domains of UHRF1 (GFP-Ubl, ubiquitin-like domain (lane 1); GFP-TTD, Tudor domain (lane 2); GFP-PHD, plant homeodomain (lane 3); GFP-SRA, SET- and Ring-associated domain (lane 4); GFP-Ring, Ring domain (lane 5)) were expressed in COS-1 cells. GFP immunoprecipitates were blotted successively with an anti-PARP1 antibody to detect coprecipitating PARP1 and an anti-GFP antibody to detect the GFP immunoprecipitates. *E*, *in vitro* interaction of PARP1 with immunopurified Myc-SRA. Purified recombinant PARP1 was incubated in a batch assay together with immunopurified Myc-SRA (lane 2) or a control anti-Myc immunoprecipitate (lane 1). Bound PARP1 was analyzed by Western blotting using, successively, anti-PARP1 and anti-Myc antibodies.

UHRF1 with the DNA-binding domain of PARP1 was not impaired by the presence of ethidium bromide (not shown).

In reciprocal experiments intended to identify the PARP1 interaction domain within UHRF1, Myc fusion proteins expressing various UHRF1 deletion domains were tested for their interaction with GST-PARP1 (Fig. 2B). When compared with the expression profile of each fusion protein (Fig. 2B, lanes 1–6) and the efficient binding of the full-length Myc-UHRF1 (lane 8), only the internal deletion of the SRA domain significantly reduced UHRF1 binding to GST-PARP1 (lane 9). No unspecific binding to GST was detected (Fig. 2B, lane 1). As an additional experiment, we then compared the binding of Myc-UHRF1, Myc-ΔSRA (UHRF1 deleted for the SRA domain), and Myc-ΔPHD (UHRF1 deleted for the PHD domain) to GST-PARP1 as above but under higher stringency conditions of the washing buffer (Fig. 2C). Although the association of Myc-ΔSRA with GST-PARP1 was lost (Fig. 2C, lane 2), the association of Myc-UHRF1 and Myc-ΔPHD with GST-PARP1 was maintained (lanes 1 and 3). To further ascertain the selective interaction with the SRA domain and exclude a possible misfolding of the deleted constructs, GFP fusion proteins expressing the different domains (Ubl, TTD, PHD, and SRA) were tested for their interaction with endogenous PARP1 (Fig. 2D). When compared with the expression profile of each fusion protein, we confirmed that PARP1 coprecipitated efficiently with GFP-SRA despite its weakest expression (Fig. 2D, lane 4), and we identified a coprecipitation of PARP1 with the TTD domain (lane 2). No coprecipitation of PARP1 was detected with the Ubl, PHD, or Ring domain (Fig. 2D, lanes 1, 3, and 5). To verify the preferential interaction with the SRA *in vitro*, Myc-SRA was expressed in COS-1 cells, immunopurified using an anti-Myc antibody, and incubated together with purified recombinant PARP1. After Myc immunoprecipitation followed by stringent washes, copurification of purified PARP1 was analyzed by Western blotting. As shown in Fig. 2E, PARP1 efficiently copurified with Myc-SRA (lane 2), whereas no PARP1 was detected in the control anti-Myc immunoprecipitate (lane 1). Taken together, these data identified a selective and PAR-dependent physical interaction between PARP1 and UHRF1 that requires the DNA-binding domain and, to a lesser extent, the BRCT domain of PARP1 and preferentially the SRA domain, but also the TTD, of UHRF1.

UHRF1 Is PARylated by PARP1 Preferentially onto Its SRA Domain and to a Lesser Extent onto Its TTD—To investigate the functional relevance of the PARP1-UHRF1 interaction, we next evaluated the ability of PARP1 to PARylate UHRF1 *in vitro*. To this end, Myc-tagged full-length UHRF1 and Myc-tagged TRF2 used as a positive PARylated control were expressed in COS-1 cells, purified by anti-Myc immunoprecipitation followed by stringent washes, and incubated with PARP1 or no protein in the presence of [α -³²P]NAD⁺ and DNase-I treated calf thymus DNA (Fig. 3A). When compared with the expression profile of each fusion protein (Fig. 3A, lanes 5–8), autoradiography revealed PARylation of the positive control TRF2 as described previously (lane 3 (5)) and a significant PARylation of full-length UHRF1 (lane 1). No PARylation was observed in the absence of PARP1 (Fig. 3A, lanes 2 and 4). We next aimed to map the PARylated domain within UHRF1 (Fig. 3B). To this

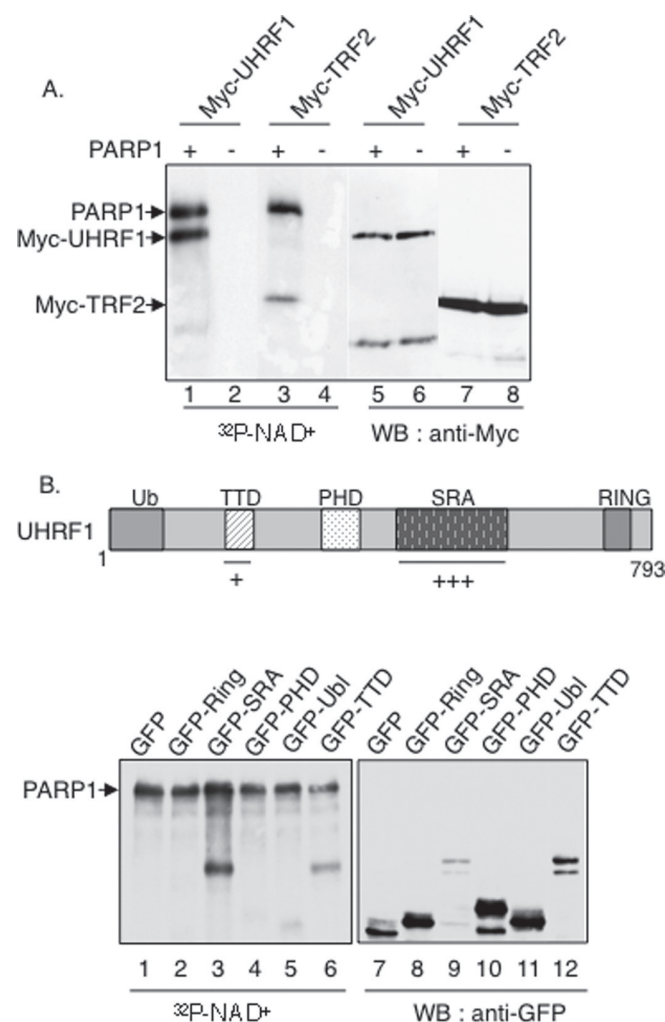


FIGURE 3. UHRF1 is PARylated preferentially onto its SRA domain but also onto its TTD. *A*, PARylation of full-length UHRF1 by PARP1. Myc-UHRF1 (lanes 1, 2, 5, and 6) or Myc-TRF2 (lanes 3, 4, 7, and 8) was expressed in COS-1 cells, immunopurified with an anti-Myc antibody, and incubated together with either PARP1 or without PARPs in activity buffer containing [α -³²P]NAD⁺ and fragmented DNA. *Right panel*, autoradiography. *Left panel*, analysis of the fusion proteins with an anti-Myc antibody by Western blotting. *B*, *upper panel*, schematic representation of UHRF1 indicating the PARylated TTD and SRA domain. *Lower panel*, GFP fusion proteins expressing GFP alone (lanes 1 and 7) or different domains of UHRF1 (GFP-Ring (lanes 2 and 8), GFP-SRA (lanes 3 and 9), GFP-PHD (lanes 4 and 10), GFP-Ubl (lanes 5 and 11), and GFP-TTD (lanes 6 and 12)) were expressed in COS-1 cells, immunopurified by GFP trapping, and incubated together with PARP1 in the activity buffer containing [α -³²P]NAD⁺ and fragmented DNA as in *A*. *Left*, analysis of the PARylated domains by autoradiography. The *upper band* represents PARylated PARP1. *Right*, analysis of the fusion proteins with an anti-GFP antibody by Western blotting.

end, a PARylation assay was performed as described above using immunopurified GFP (Fig. 3B, lanes 1 and 7) or GFP fusion proteins expressing the different Ring (lanes 2 and 8), SRA (lanes 3 and 9), PHD (lanes 4 and 10) Ubl (lanes 5 and 11), and TTD (lanes 6 and 12) single domains of UHRF1. Autoradiography revealed a significant PARylation of the SRA domain (Fig. 3B, lane 3) despite its weakest expression (lane 9) and to a lesser extent the TTD (lanes 6 and 12), whereas no PARylation was detected for the other domains or GFP alone (lanes 1, 2, 4, and 5). An efficient PARylation was also detected on the immunopurified Myc-tagged SRA, whereas a reduced PARylation

Interaction and Cooperation of PARP1 with UHRF1

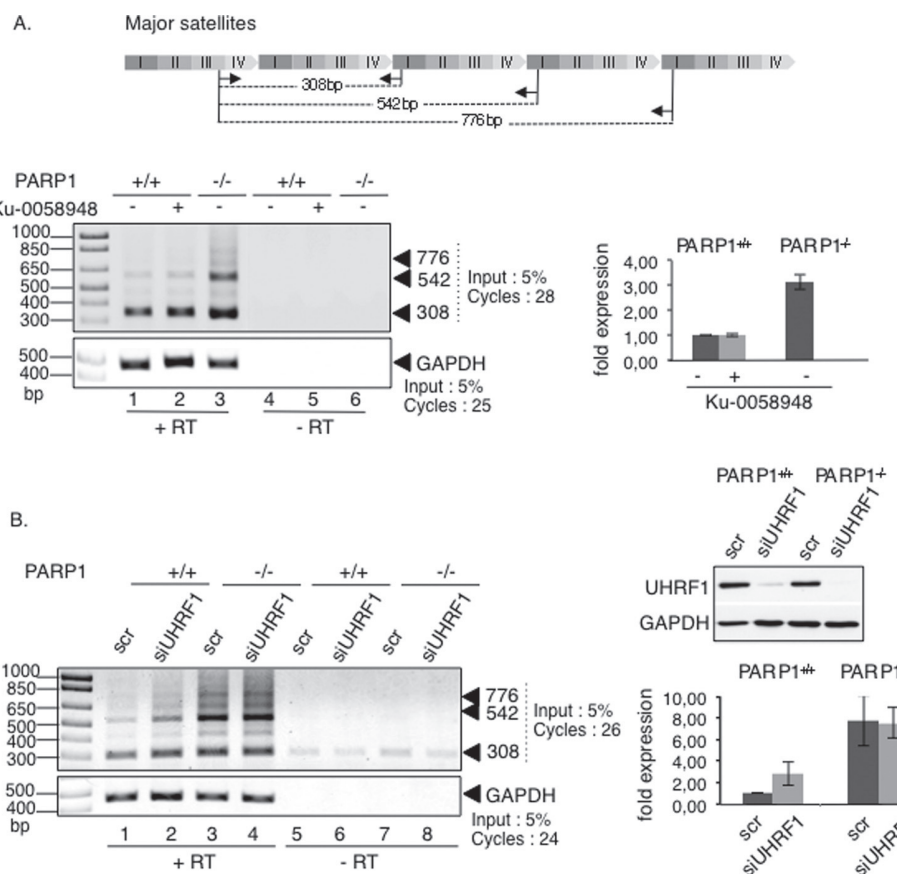


FIGURE 4. The absence of PARP1 causes derepression of major satellite transcripts. Enhanced transcriptions of major satellite repeats in PARP1 $^{-/-}$ cells are shown. *A*, top, schematic representation of major satellite repeats (pericentric heterochromatin) showing the repeat distribution (I–IV) and the primers (arrows) used for PCR analysis. Lower left, representative RT-PCR analysis using total RNA extracted from PARP1 $^{+/+}$ (lanes 1, 2, 4, and 5) or PARP1 $^{-/-}$ cells (lanes 3 and 6), mock-treated cells (lanes 1, 3, 4, and 6), or cells treated with Ku-0058948 (lanes 2 and 5) for 48 h. As a control, reactions were performed with mock-transcribed cDNAs (–RT, lanes 4–6). The relative amounts of input and PCR amplification cycles are indicated. Lower right, the fold expression (histogram) represents the major satellite transcript levels (normalized against GAPDH) relative to control PARP1 $^{+/+}$ set to 1 for three independent experiments. Mean data \pm S.D. are indicated. *B*, left, representative RT-PCR analysis using total RNA extracted from PARP1 $^{+/+}$ (lanes 1, 2, 5, and 6) or PARP1 $^{-/-}$ cells (lanes 3, 4, 7, and 8) transfected with a scrambled siRNA (scr, lanes 1, 3, 5, and 7) or with siUHRF1 (lanes 2, 4, 6, and 8) for 96 h. As a control, reactions were performed with mock-transcribed cDNAs (–RT, lanes 5–8). Right, the fold expression (histogram) represents the major satellite transcript levels (normalized against GAPDH) relative to control PARP1 $^{+/+}$ set to 1 for three independent experiments. Mean data \pm S.D. are indicated.

was detected for the Myc-tagged SRA-deleted mutant of UHRF1 (not shown). Together, these results identified the SRA domain as a preferential site of PARylation, in agreement with the recent report by Zhang *et al.* (47), who identified two site-specific ADP-ribosylated residues within the SRA domain of UHRF1 by boronate affinity chromatography used to isolate ADP-ribosylated peptides. To a lesser extent, the TTD is also PARylated.

PARP1 and UHRF1 Favor the Silencing of Major Satellite Repeats—UHRF1 was described previously as contributing to the silencing of major satellites sequences, partly by targeting DNMT1 for DNA maintenance methylation during pericentric heterochromatin replication (23, 24, 42). In addition, PARP1 was found associated with the major satellite elements of pericentric heterochromatin (12). To get insights into the biological meaning of the UHRF1-PARP1 association, we first sought to determine whether PARP1 was also involved in the transcriptional silencing of major satellite repeats. To this aim, we analyzed the transcriptional activity across these elements by semi-quantitative RT-PCR using RNA extracts from the PARP1 $^{+/+}$ and PARP1 $^{-/-}$ cells (Fig. 4A). Our data revealed a significant

increase of the satellite transcripts from pericentric regions in PARP1 $^{-/-}$ cells compared with the PARP1 $^{+/+}$ cells (Fig. 4A, *lane 3 versus 1*). In contrast the inhibition of PARP activity in PARP1 $^{+/+}$ cells did not alter the overall transcription of these regions (Fig. 4A, *lane 2 versus 1*). To explore the contribution of UHRF1 in the transcriptional reactivation of major satellites observed in PARP1 $^{-/-}$ cells, we examined the effect of an additional siRNA-mediated knockdown of UHRF1 (Fig. 4B). In agreement with previous data (42), the depletion of UHRF1 by siRNA in PARP1 $^{+/+}$ cells induced pericentric transcription, although to a significant lower extent than the absence of PARP1 (Fig. 4B, *lanes 2 and 3 versus 1*). In contrast, the depletion of UHRF1 in PARP1 $^{-/-}$ cells did not significantly impair the enhanced transcriptional activity induced by the absence of PARP1, thus suggesting that both enzymes likely act in the same pathway (Fig. 4B, *lane 4 versus 3*). In a comparative experiment, we also analyzed the transcriptional activity of minor satellites. In agreement with the previously described association of PARP1 with centromeric regions (12), we also detected an important increase in the transcripts of centric regions, indicating a role of PARP1 in the silencing of these

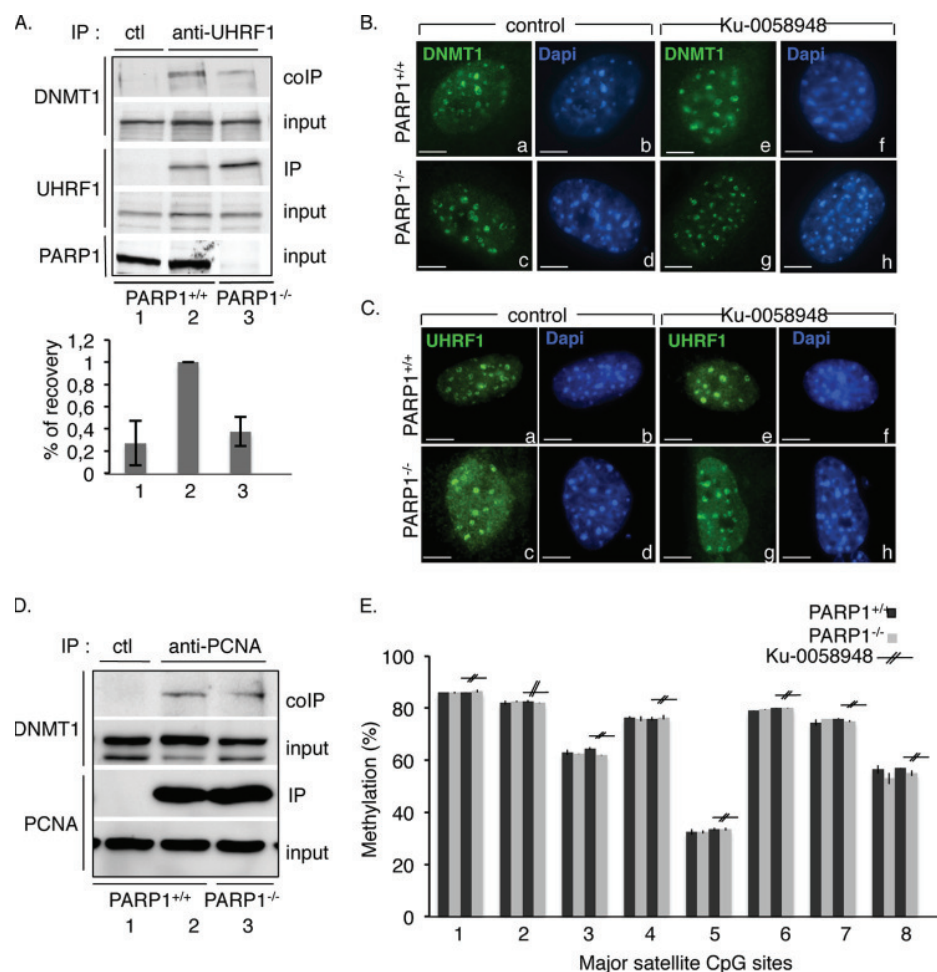


FIGURE 5. The absence of PARP1 affects the association of UHRF1 with DNMT1 but not their targeting to replicating heterochromatin or the methylation of CpG repeats. *A*, the interaction of DNMT1 with UHRF1 is reduced in PARP1^{-/-} cells. *Left*, equivalent amounts of total protein cell lysates from PARP1^{+/+} (lane 2) and PARP1^{-/-} cells (lane 3) were immunoprecipitated using an anti-UHRF1 antibody (lanes 2 and 3) or a control antibody (ctl, lane 1) and analyzed for the coimmunoprecipitation of DNMT1 by Western blotting. Inputs correspond to 1/30th of the amount of total cell extract used for immunoprecipitation. *Right*, the signal intensities of the coprecipitating DNMT1 relative to DNMT1 expression and UHRF1 immunoprecipitation were measured in three independent experiments using ImageJ. The colP in PARP1^{+/+} cells (lane 2) was set to 1. Mean values \pm S.D. are indicated. *B*, the absence of PARP1 does not perturb the accumulation of DNMT1 onto pericentric heterochromatin. Shown are representative images of DNMT1 (*a*, *c*, *e*, and *g* (green)) immunostaining of the typical ring-shaped pericentric duplication bodies from PARP1^{+/+} (*a*, *b*, *e*, and *f*) or PARP1^{-/-} (*c*, *d*, *g*, and *h*) cells either mock-treated (*a*–*d*) or treated with the PARP inhibitor Ku-0058948 (*e*–*h*). DNA was counterstained with DAPI (*b*, *d*, *f*, and *h* (blue)). Scale bars: 7 μ m. *C*, the absence of PARP1 does not perturb the accumulation of UHRF1 onto pericentric heterochromatin. Shown are representative images of UHRF1 (*a*, *c*, *e*, and *g* (green)) immunostaining of the typical ring-shaped pericentric duplication bodies from PARP1^{+/+} (*a*, *b*, *e*, and *f*) or PARP1^{-/-} (*c*, *d*, *g*, and *h*) cells either mock-treated (*a*–*d*) or treated with the PARP inhibitor Ku-0058948 (*e*–*h*). DNA was counterstained with DAPI (*b*, *d*, *f*, and *h* (blue)). Scale bars: 7 μ m. *D*, the interaction of DNMT1 with PCNA is maintained in PARP1^{-/-} cells. Equivalent amounts of total protein cell lysates from PARP1^{+/+} (lanes 1 and 2) and PARP1^{-/-} cells (lane 3) were immunoprecipitated using an anti-PCNA antibody (lanes 2 and 3) or a control antibody (lane 1) and analyzed for the coimmunoprecipitation of DNMT1 by Western blotting. Input corresponds to 1/25th of the amount of total cell extract used for immunoprecipitation. *E*, the methylation profile of pericentric repeats is normal in PARP1^{-/-} cells. Total DNA was isolated from PARP1^{+/+} or PARP1^{-/-} cells either mock-treated or treated with Ku-0058948 for 24 h and then bisulfite-treated. Histograms show the methylation percentage at individual CpG sites as measured by pyrosequencing.

regions (not shown). However, the mechanism involved is likely unrelated to UHRF1, as suggested by the previously reported normal transcription of these regions in the absence of UHRF1 (42).

The Absence of PARP1 Alters the Interaction of UHRF1 with DNMT1 but with No Consequences for the Methylation of Pericentric Regions—Enhanced transcriptional activity at pericentric regions could be caused by defective DNMT1-catalyzed CpG methylation. Among the UHRF1 functional domains that facilitate the loading of DNMT1 to replicating heterochromatic regions, the SRA domain mediates the recognition and preferential binding to hemi-methylated CpG sites and facilitates the

interaction of UHRF1 with DNMT1 (24, 29, 30). Because we identified SRA as the preferential interaction domain (Fig. 2C) and PARylation site for PARP1 (Fig. 3B), we went on to test whether PARP1 is involved in the association of UHRF1 with DNMT1 (Fig. 5A). To address this question, whole extracts from PARP1^{+/+} or PARP1^{-/-} 3T3 cells were immunoprecipitated with an anti-UHRF1 antibody and probed for the coimmunoprecipitation of DNMT1 by Western blotting. We observed a significantly reduced coimmunoprecipitation of DNMT1 with UHRF1 in PARP1^{-/-} cells (Fig. 5A, lane 3) compared with PARP1^{+/+} (lane 2) cells, indicating that PARP1 is required for the efficient association of DNMT1 with UHRF1.

Interaction and Cooperation of PARP1 with UHRF1

No unspecific coprecipitation was observed with the control antibody (Fig. 5A, *lane 1*).

Consequently, we went on to examine by immunofluorescence analysis whether the reduced DNMT1-UHRF1 association affects the focal localization of DNMT1 to replicating heterochromatin (Fig. 5B). Because both the TTD and SRA domain of UHRF1 mediate its targeting to pericentric heterochromatin, we also verified the accumulation of UHRF1 onto these regions (Fig. 5C). Notwithstanding, we found a normal accumulation of both proteins onto the characteristic horse-shoe-like replication factories in the PARP1^{-/-} cells (Fig. 5C, compare *panels c* and *d*, with *a* and *b*) as well as after PARP inhibition (compare *panels e–h* with *a* and *b*) suggesting that PARP1 and PARP activity is not absolutely required for the mid-S phase-specific targeting of UHRF1 and DNMT1 to pericentric heterochromatin.

Because loading of DNMT1 onto replication foci was also shown to be promoted by PCNA (48), we explored the role of PARP1 in the association of DNMT1 with PCNA. We compared the coimmunoprecipitation of DNMT1 using an anti-PCNA antibody in PARP1^{+/+} *versus* PARP1^{-/-} cells (Fig. 5D). We observed a similarly efficient interaction of DNMT1 with PCNA (Fig. 5D, *lane 2* *versus* *3*) in both cell lines, indicating that the association between these proteins is maintained in the absence of PARP1. No precipitation of DNMT1 was detected using the control antibody (Fig. 5D, *lane 1*).

Finally we verified whether the reduced DNMT1-UHRF1 association perturbs DNMT1 catalytic activity. We analyzed the methylation status of pericentric repeats by genomic bisulfite sequencing of DNA extracted from PARP1^{+/+} and PARP1^{-/-} cells treated or not with the PARP inhibitor Ku-0058948 (Fig. 5E). Consistent with the normal recruitment of DNMT1 and UHRF1 onto heterochromatic foci, no apparent difference in the methylation profile of these repetitive regions was detected between both cell lines and after PARP inhibition. Similarly, the absence of PARP1 did not affect the methylation profile of minor satellites at centromeres (not shown).

Taken together, these results identified a role of PARP1 in stabilizing the interaction of UHRF1 with DNMT1. Despite the reduced interaction between DNMT1 and UHRF1 in the absence of PARP1, the recruitment of DNMT1 to heterochromatic regions and its activity are maintained owing to its efficient interaction with PCNA. Moreover, these data indicate that the derepression of the major satellites detected in the absence of PARP1 might not simply be caused by impaired DNA methylation but likely involves another defect that we aimed to identify next.

PARP1 and UHRF1 Cooperate to Regulate the Repressive Mark H4K20me3—To further decipher how PARP1 regulates the silencing of pericentric regions, given the link of UHRF1 with repressive chromatin marks (24, 27, 30) we then asked whether the transcriptional activation was accompanied by modifications of the chromatin signatures of pericentric heterochromatin. We looked for H3K9 and H4K20 trimethylation, which is linked with silencing, and H4K16 acetylation or H3K4 trimethylation, which is required for gene activation (Fig. 6). The staining of H3K9m3 remained unchanged, and no detect-

able acetylation of H4K16 or trimethylation of H3K4 could be detected at DAPI-dense heterochromatic regions of PARP1^{-/-} cells (Fig. 6A, compare *panels d, h*, and *l* with *b, f*, and *j*, respectively). In contrast, the absence of PARP1 led to a specific loss of the local repressive H4K20me3 mark at heterochromatic foci in most of the cells (>80%), thus indicating a less compact heterochromatin structure that could contribute to up-regulation of the heterochromatin transcripts described above (Fig. 6B, compare *panel g* with *a* and *vertical bar 3* with *1*). Remarkably, the additional depletion of UHRF1 rescued the localization of H4K20me3 to heterochromatin regions in the PARP1^{-/-} cells (Fig. 6B, compare *panel j* with *g* and *vertical bar 4* with *3*), whereas it did not perturb H4K20me3 staining in the PARP1^{+/+} cells (compare *panel d* with *a* and *vertical bar 2* with *1*). To ascertain that the absence of H4K20me3 heterochromatic staining was not due simply to an overall reduction in H4K20me3, we evaluated the global expression of H4K20me3 by Western blot analysis of acid-extracted histones from PARP1^{+/+} and PARP1^{-/-} cells (Fig. 6C). We found rather an increase in the overall expression of H4K20me3 in the PARP1^{-/-} cells. Taken together, these findings highlight a related contribution of PARP1 and UHRF1 in the transcriptional repression of pericentric heterochromatin through a mechanism that at least partly involves a specific regulation of the repressive mark H4K20me3 at heterochromatin.

PARP1 Restrains UHRF1-mediated Ubiquitination of DNMT1 and Modulates Its Stability during the Cell Cycle—Among the various UHRF1-regulated processes, recent reports have identified an UHRF1-mediated ubiquitination of DNMT1 that coordinately regulates its stability with the completion of DNA replication (34, 35). Because PARylation has also recently been connected with ubiquitination and proteasomal degradation (4, 49, 50), we decided also to explore a possible involvement of PARP1 in this pathway. We compared the level of Myc-UHRF1-mediated ubiquitination of immunopurified GFP-DNMT1 in PARP1^{+/+} *versus* PARP1^{-/-} 3T3 cells (Fig. 7A). Strikingly, the absence of PARP1 led to an apparent increase in the ubiquitination levels of GFP-DNMT1 (Fig. 7A, *left panel*, *lane 8* *versus* *7*), whereas the autoubiquitination levels of Myc-UHRF1 were weaker and remained rather unchanged in similar experimental conditions (*right panel*, *lane 2* *versus* *1*). No unspecific ubiquitination of GFP was detected (Fig. 7A, *left panel*, *lanes 3* and *4*). Thus, these results introduced PARP1 as a negative regulator of UHRF1-ubiquitin ligase activity onto DNMT1. To confirm and examine this hypothesis further, we performed *in vitro* ubiquitination assays using purified recombinant PARP1, UHRF1, and GST-DNMT1 in the presence of the ubiquitin-activating enzyme E1, the ubiquitin-conjugating enzyme E2, and ubiquitin (Fig. 7B). To discriminate between a structural and enzymatic role for PARP1, UHRF1 was first preincubated together with PARP1 in the absence (inactive PARP1) or presence of NAD⁺ (active PARP1) and subsequently tested in the ubiquitination assays (Fig. 7B, *diagram*). The addition of inactive PARP1 did not significantly impact the autoubiquitination of UHRF1 (Fig. 7B, *lane 3* *versus* *2*) or the ubiquitination of GST-DNMT1 (*lane 6* *versus* *5*). However, when UHRF1 was first PARylated with active PARP1 in the presence of NAD⁺, its ubiquitination activity onto DNMT1 was signifi-

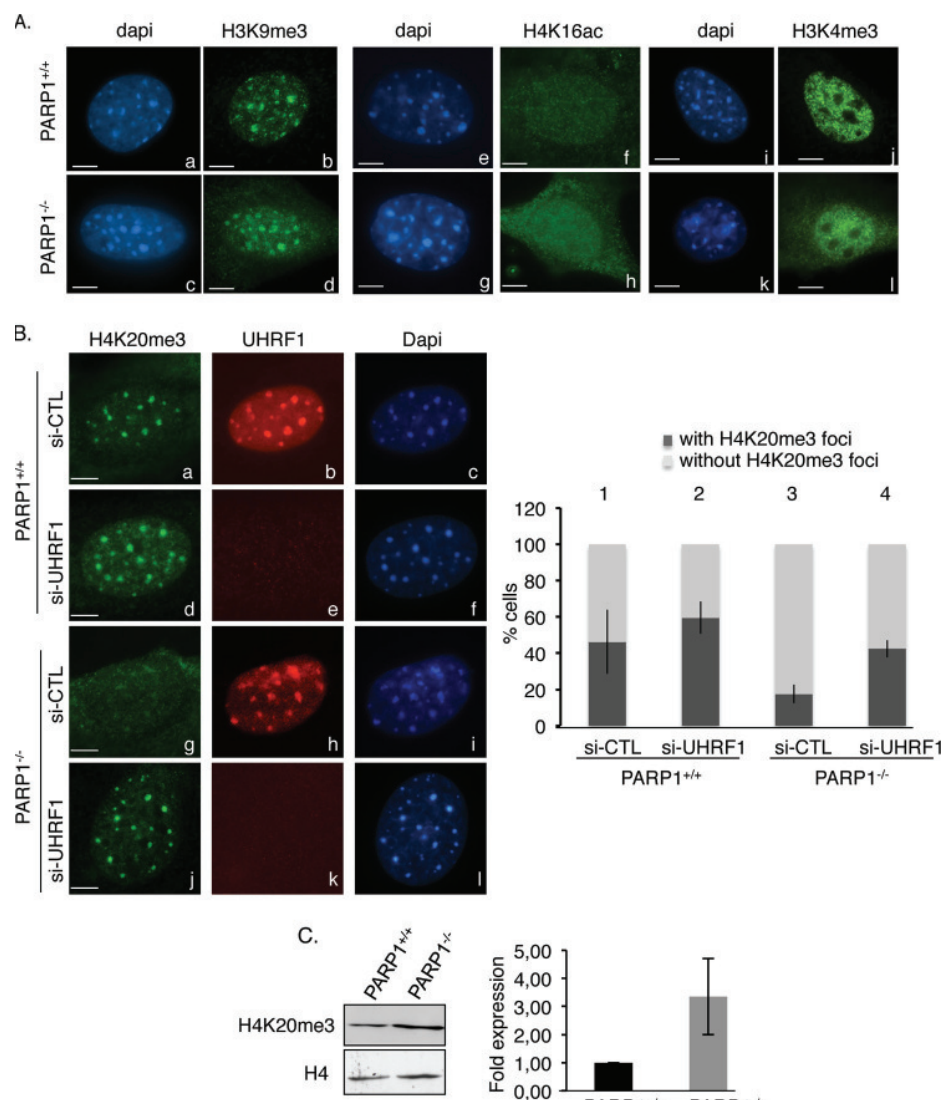


FIGURE 6. The absence of PARP1 causes reduced staining of the repressive mark H4K20me3 at pericentric regions, which is rescued by the additional depletion of UHRF1. *A*, PARP1^{-/-} cells display normal H3K9me3, H4K16ac, and H3K4me3 staining onto DAPI-dense heterochromatic regions. Shown are representative immunofluorescence images for the comparative distribution of H3K9me3 (*b* and *d* (green)), H4K16ac (*f* and *h* (green)), and H3K4me3 (*j* and *l*) in PARP1^{+/+} and PARP1^{-/-} interphase cells. DNA and heterochromatic foci are counterstained with DAPI (*a*, *c*, *e*, *g*, *i*, and *k*). Scale bars: 7 μm. *B*, left, representative images for the loss of H4K20me3 staining at HC regions in PARP1^{-/-} cells rescued by the additional depletion of UHRF1. Shown is immunofluorescence analysis of H4K20me3 (*a*, *d*, *g*, and *j* (green)) and UHRF1 (*b*, *e*, *h*, and *k* (red)) in PARP1^{+/+} and PARP1^{-/-} cells transfected with either control siRNA (*si-CTL*) or si-UHRF1. DNA and heterochromatic foci are counterstained with DAPI (*c*, *f*, *i*, and *l*). Right, the histogram depicts the percentage of cells with or without H4K20me3 staining. An average of 500 cells/cell line were scored in >20 randomly selected fields. Results are averages from three independent experiments. Mean values ± S.D. are indicated. *C*, the overall expression of H4K20me3 is weakly increased in the PARP1^{-/-} cells. Left, equivalent amounts of acid-extracted histones from PARP1^{+/+} and PARP1^{-/-} cells were analyzed by Western blotting using an anti-H4K20me3 antibody and an anti-H4 antibody as loading control. Right, the signal intensities of H4K20me3 relative to H4 were measured in three independent experiments using ImageJ. Mean values ± S.D. are indicated.

cantly reduced (Fig. 7*B*, *lane 7* versus *5*), whereas the autoubiquitination of UHRF1 was only weakly if significantly modified (*lane 4* versus *2*). Under similar experimental conditions, the ubiquitination of GST used as control was never observed (Fig. 7*B*, *lanes 8* and *9*). Interestingly, the addition of PARP1, when automodified previously, had no significant impact on UHRF1 activity (not shown). Altogether, these data reveal that the PARP1-catalyzed PARylation of UHRF1 inhibits its ubiquitin ligase activity essentially toward DNMT1.

The UHRF1 triggered ubiquitination of DNMT1 was described previously as targeting DNMT1 for proteasomal degradation, thereby regulating its protein stability (35). Therefore,

we followed the protein expression profile of DNMT1 in PARP1^{+/+} and PARP1^{-/-} 3T3 cells throughout the cell cycle after release from serum starvation (Fig. 8). To carefully address DNMT1 protein stability as opposed to its steady state levels, cells were treated with the protein synthesis inhibitor cycloheximide. We observed a similar abundance of DNMT1 in whole cell extracts from nonsynchronized and G₁-synchronized PARP1^{+/+} and PARP1^{-/-} cells (Fig. 8, *lanes 1–4*). In contrast, we detected a reduced level of DNMT1 in the S and G₂ PARP1^{-/-} cells compared with the PARP1^{+/+} cells (Fig. 8, compare *lane 6* with *5* and *8* with *7*). Therefore, consistent with the ubiquitination data, these results suggest that PARP1 likely

Interaction and Cooperation of PARP1 with UHRF1

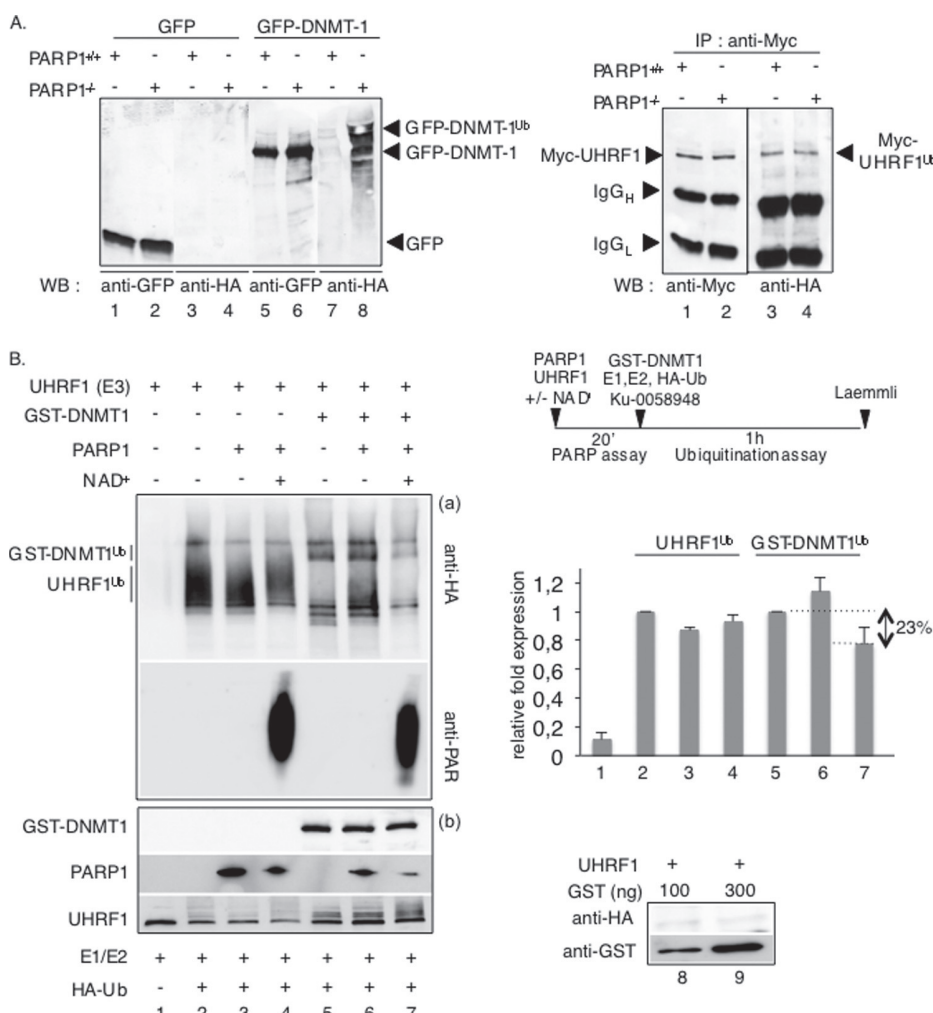


FIGURE 7. PARP1 selectively inhibits the UHRF1-driven ubiquitination of DNMT1 *in vivo* and *in vitro*. **A**, *in vivo* ubiquitination assays. The absence of PARP1 enhances the UHRF1-mediated ubiquitination of DNMT1 but not the autoubiquitination of UHRF1 *in vivo*. *Left*, PARP1^{+/+} and PARP1^{-/-} cells were transfected with either GFP-DNMT1 (lanes 5–8) or GFP (lanes 1–4) together with HA-ubiquitin and treated with 5 μ M MG-132 for 12 h to inhibit proteasomal degradation. GFP immunoprecipitates were blotted successively with an anti-HA antibody to detect ubiquitinated proteins (lanes 3, 4, 7, and 8) and an anti-GFP antibody (lanes 1, 2, 5, and 6) to detect immunopurified proteins. *Right*, PARP1^{+/+} (lanes 1 and 3) and PARP1^{-/-} (lanes 2 and 4) cells were transfected with Myc-UHRF1 together with HA-ubiquitin and treated as described above. Myc immunoprecipitates were blotted successively with an anti-HA antibody to detect ubiquitinated UHRF1 (lanes 3 and 4) and an anti-Myc antibody to detect immunopurified UHRF1 (lanes 1 and 2). **B**, *in vitro* ubiquitination assays. *Left*, PARP1-catalyzed poly(ADP-ribosylation) of UHRF1 selectively inhibits its ubiquitination activity onto DNMT1. Purified UHRF1 was first preincubated alone (lanes 1, 2, and 5) or together with purified PARP1 (lanes 3, 4, 6, and 7) as indicated in the PARP activity buffer. PARP activity is induced by the addition of NAD⁺. The proteins were subsequently assayed for UHRF1 ubiquitination activity onto itself (lanes 1–4) or onto GST-DNMT1 (lanes 5–7). *a*, ubiquitinated proteins (UHRF1^{ub} and GST-DNMT1^{ub}) were detected by immunoblotting using an anti-HA antibody, and the PARP activity was verified by immunoblotting using an anti-PAR antibody. *b*, the purified recombinant proteins mixed in the experiment were detected by Western blotting using anti-GST, anti-PARP1, and anti-UHRF1 antibodies. The lower amount of PARP1 detected in lanes 4 and 7 is explained by its automodification, which limits its detection by the monoclonal anti-PARP1 antibody used. As a control, reactions were performed with GST (lanes 8 and 9). *Lower right*, a representative experiment of three is shown. *Upper right*, a schematic diagram of the experiment is shown. *Lower right*, the relative-fold expression (histogram) represents the ImageJ-quantified ubiquitinated protein levels of the samples containing PARP1 relative to the samples without PARP1 (lanes 1, 3, and 4 versus 2; lanes 6 and 7 versus 5). The values represent the mean \pm S.D. of three independent experiments.

helps to maintain DNMT1 protein stability throughout the progression of the cell cycle.

DISCUSSION

In this study we identified a PAR-dependent physical and functional interaction of PARP1 with UHRF1 involving DNMT1 in which PARP1 helps to modulate two different UHRF1-regulated processes: the accumulation of the repressive mark H4K20me3 on one hand and the abundance of DNMT1 on the other hand. Both events possibly contribute to the silencing of pericentric heterochromatin.

We revealed enhanced transcriptional activity in PARP1^{-/-} cells in both the centric and pericentric regions, thus implying a key role of PARP1 in their silencing. Accordingly, recent chromatin immunoprecipitation experiments have identified an association of PARP1 with minor and major satellites in NIH3T3 cells (12). Furthermore, PARP1 has been described as a key element in the repression of rRNA transcription and inheritance of silent rDNA chromatin (12). UHRF1 was shown previously to exert a selective transcriptional control on the DNA satellites of pericentric heterochromatin but not centromeric heterochromatin (42). That the additional depletion of

Interaction and Cooperation of PARP1 with UHRF1

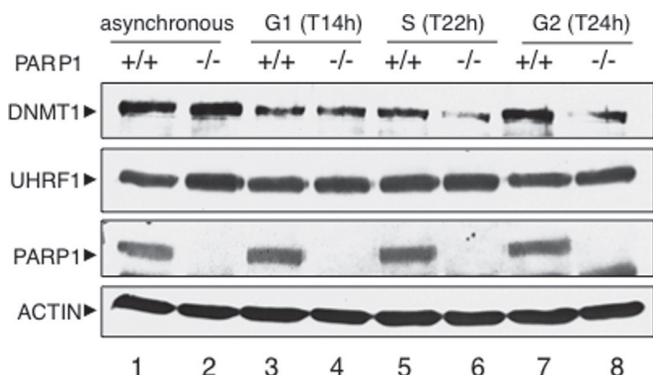


FIGURE 8. DNMT1 abundance is reduced in PARP1^{-/-} cells. Protein expression from nonsynchronized (lanes 1 and 2) and synchronized (lanes 3–8) PARP1^{+/+} and PARP1^{-/-} cells was analyzed by SDS-PAGE and Western blotting with the appropriate antibodies. To evaluate protein stability, cells were treated with cycloheximide before lysis. Progression of serum-starved cells released into fresh medium through the cell cycle was monitored by flow cytometry analysis (not shown). The time points of release as determined by FACS are indicated in parentheses.

UHRF1 in PARP1^{-/-} cells has no additive impact on the transcription of pericentric repeats implies that both proteins likely act in the same molecular process. In addition, based on the physical and functional interaction of UHRF1 and PARP1, it is tempting to speculate on a selective coordinated interplay between both enzymes for the silencing of major satellite sequences. What would be the molecular mechanism involved?

UHRF1 has been shown to bind hemi-methylated CpG dinucleotides specifically and to associate with DNMT1 through the same SRA domain. In addition, UHRF1 is described as binding methylated H3K9 through its TTD (26, 29). Together these activities cooperate for the loading of DNMT1 to pericentric heterochromatic sites to guarantee the maintenance of DNA methylation (24, 29). The PARylation of both the SRA domain and the TTD of UHRF1 reported here and the previously described functional interaction between PARP1 and DNMT1 (15) prompted us to investigate a possible role of PARP1 in one or the other of these properties. The conserved accumulation of UHRF1 onto the DAPI-dense replicating heterochromatic regions of PARP1^{-/-} cells or after PARP inhibition suggests that PARP1 might not be absolutely required for the binding of UHRF1 to hemi-methylated CpG sites. In contrast, we found a reduced interaction of UHRF1 with DNMT1 in the PARP1^{-/-} cells, thus rather indicating a contribution of PARP1 to the formation or the stability of the UHRF1-DNMT1 complex. In line with this hypothesis, DNMT1 contains a PAR-binding domain and was shown to interact noncovalently with PAR (21). These observations led to the hypothesis that the PARylation of UHRF1 can serve to construct a robust interaction network among PARP1, UHRF1, and DNMT1 and to favor the association among the members of this complex by noncovalent interactions. In addition, we also found a PARP1-catalyzed poly(ADP-ribosylation) of DNMT1 that can contribute to its interaction with UHRF1 (not shown). Notwithstanding, the reduced UHRF1-DNMT1 association observed in the absence of PARP1 did not significantly perturb the loading or the catalytic activity of DNMT1 as revealed by its normal enrichment at heterochromatic regions

of PARP1^{-/-} or PARP-inhibited cells and by the wild type-like methylation status detected at the major satellite repeats. Based on our findings, we propose that this is at least partly explained by a compensating activity of PCNA in promoting the localization of DNMT1 onto replication foci as supported by the PCNA-DNMT1 interaction that is maintained in the absence of PARP1. Alternatively, a compensating DNA methylation activity by DNMT3 proteins, recruited via the Suv39h-mediated H3K9me3 (51), a modification not impaired in PARP1^{-/-} cells, is an appealing hypothesis. In any case, the overall derepression of the major satellites detected in the absence of PARP1 in the asynchronous cells cannot simply be caused by impaired DNA methylation, suggesting the involvement of another mechanism that we aimed to identify.

UHRF1 has also been reported to have key functions in sensing and controlling chromatin features other than just the CpG methylation status of pericentric heterochromatin. Therefore, a conceivable hypothesis is that PARP1 participates in the UHRF1-mediated chromatin modifications required for its silencing. UHRF1, through its SRA domain, recruits HDAC1, which deacetylates histone H4, thereby controlling the transcription of major satellites (38). However, in contrast to findings in UHRF1-depleted cells, we did not detect hyperacetylation of H4K16 at heterochromatic sites in the PARP1^{-/-} cells, indicating that PARP1 might not be required for this mechanism. The TTD and SRA domain of UHRF1 have also been suggested to mediate the binding activity and specificity of UHRF1 onto H3K9me3 sites and regulate the organization of this epigenetic mark onto pericentric heterochromatin (26, 29, 30, 32). Furthermore, a perturbed H3K9me3 profile as reported in Suv39h^{-/-} cells, is associated with enhanced transcription of major satellite repeats owing to defective recruitment of DNMT3b (51, 52). Again, the normal staining of H3K9me3 observed in the PARP1^{-/-} cells suggests that PARP1 might not be involved in its accumulation onto heterochromatic regions. In contrast, our findings reveal a selective cross-talk between PARP1 and UHRF1 in the regulation of the repressive mark H4K20me3 that characterizes the correct condensation and thereby the silencing of pericentric heterochromatin. The results suggest that UHRF1 negatively regulates the accumulation of H4K20me3 onto HC foci and that PARP1 serves to control this activity. Future work will be required to further dissect the molecular link between both proteins and their activities and to identify the targets among the proteins that orchestrate the sequential methylation of H4K20 at pericentric regions, including SET8/PR-Set7, SUV4-H20.1, and SUV4-H20.2, or those that catalyze demethylation, such as PHF2 and PHF8 (53). That the depletion of UHRF1 alone is not sufficient to decrease the enhanced transcription of the major satellites observed in the PARP1^{-/-} cells and restore their repression might simply be explained by a broader role of PARP1 at pericentric heterochromatin. In support of this view, PARP1 was found to interact with the SWI/SNF-like factor SMARCA1, involved in the maintenance of epigenetic marks throughout pericentric heterochromatin replication (11), to cooperate with the histone deacetylase SirT1 for the maintenance of pericentric heterochromatin integrity (9) and to mediate the inheritance of silent rDNA chromatin (12). In addition, the repressive mark

Interaction and Cooperation of PARP1 with UHRF1

H4K20me3 is probably not the only requirement for the transcriptional silencing of pericentric heterochromatin. Alternatively, given the emerging function of H4K20 methylation in genome maintenance, whether derepression of satellite repeats might be partially elicited by perturbed pericentric and centromeric heterochromatin integrity as reported for BRCA-deficient cells (54) cannot be excluded. In support of this idea, both UHRF1-deficient and PARP1^{-/-} cell lines were found to display higher genome instability and defects in chromosome segregation (14, 55).

Given the recently uncovered role of UHRF1 in the clearance of DNMT1 through its ubiquitination and proteasomal degradation (33–35), our results imply an additional possible contribution of PARP1 and its activity to this process. Much recent evidence exists to support a broad role of PARPs in ubiquitin-mediated protein degradation. A first example is the association of PARP1 with the E3 ubiquitin ligase CHFR (checkpoint with Forkhead and Ring finger domains), which was shown to induce the polyubiquitination of PARP1 and its degradation in response to mitotic stress (56). PARP1 and PARylation have also been implicated in the ubiquitination of repair proteins catalyzed by the E3 ligase RNF146/Iduna in response to genotoxic stress, and Tankyrase (PARP5a)-catalyzed PARylation has been associated with the RNF146/Iduna-triggered ubiquitination of targets from the Wnt/β-catenin signaling pathway (49, 50). In our study we define PARP1 as a negative regulator of the E3 ubiquitin ligase activity of UHRF1 onto DNMT1. *In vivo* this is exemplified by an enhanced ubiquitination of DNMT1 in PARP1^{-/-} cells, whereas the autoubiquitination of UHRF1 remains rather unaffected. This regulation may preserve DNMT1 from early proteasomal degradation and consequently facilitate its accumulation throughout the cell cycle. In support of this assumption, we detected decreased DNMT1 stability in the S and G₂ phases of the cell cycle in PARP1^{-/-} cells. Recent reports have identified an additional role of Usp7 (HAUSP) in promoting DNMT1 stability both by deubiquitinating DNMT1 and by inhibiting UHRF1 activity (34, 35). Whether PARP1 also controls the deubiquitinating activity of Usp7 onto DNMT1 represents a possibility, although we have observed that the interaction of Usp7 with UHRF1 and DNMT1 is not perturbed by the absence of PARP1 (not shown).

Based on our results, we propose PARP1 as a novel player in the UHRF1-mediated fine-tuned regulation of DNMT1 abundance throughout the cell cycle. Does this cellular process also contribute to the repression of major satellites in addition to the accumulation of H4K20me3? The possibility exists. The repression of mouse pericentric HC is tightly coupled to the cell cycle. Although two bursts of transcription have been detected in late G₁ to early S phase just before the replication of chromocenters and during mitosis to generate transcripts that drive the reassembly of heterochromatin, major satellites are silenced in a large part of G₁ and when cells are engaged in replicating chromocenters from mid-late S phase to G₂ (57). It is conceivable that the enhanced UHRF1-catalyzed degradation of DNMT1 that we detected in the PARP1^{-/-} cells from S to G₂ perturbs DNA methylation at pericentric regions and participates together with the loss of H4K20me3 in the abnormal derepression of satellite repeats, specifically during the replication of

these regions and onward. As a consequence, reduced pericentric heterochromatin silencing can be associated with the delay of mid-to-late S phase replication that we detected in the PARP1^{-/-} cells (not shown). Similarly, UHRF1 and BRCA1 have been proposed to control the silencing of major satellites repeats and the replication of pericentric heterochromatin (42, 54, 58).

In summary, our findings define PARP1 as part of a protein complex containing UHRF1 and DNMT1 in which PARP1 regulates two UHRF1-associated biological activities. Accumulating reports in the literature show that the functional role of the UHRF1-DNMT1 association is dual. (i) On one hand, it helps to recruit DNMT1 to replicating heterochromatic regions for DNA methylation maintenance; (ii) on the other, it mediates the ubiquitination of DNMT1 to regulate DNMT1 stability. Similarly, our data suggest that the biological outcome of the PARP1-UHRF1 association is also dual. (i) Both proteins cooperate in the maintenance of the repressive mark H4K20me3 at pericentric heterochromatin to favor transcriptional silencing, and (ii) PARP1 seems to negatively regulate the UHRF1-catalyzed ubiquitination of DNMT1 to maintain the abundance of DNMT1 from S to G₂ phase. This can be an additional way to control transcriptional repression, specifically during the replication of pericentric heterochromatin and onward.

Acknowledgment—We thank S. Link (Ludwig Maximilians University) for technical help with the GFP-UHRF1 plasmid constructs.

REFERENCES

1. Krishnakumar, R., and Kraus, W. L. (2010) The PARP side of the nucleus: molecular actions, physiological outcomes, and clinical targets. *Mol. Cell* **39**, 8–24
2. Quénét, D., El Ramy, R., Schreiber, V., and Dantzer, F. (2009) The role of poly(ADP-ribosylation) in epigenetic events. *Int. J. Biochem. Cell Biol.* **41**, 60–65
3. Kraus, W. L., and Hottiger, M. O. (2013) PARP-1 and gene regulation: progress and puzzles. *Mol. Aspects Med.* **34**, 1109–1123
4. Kalisch, T., Amé, J. C., Dantzer, F., and Schreiber, V. (2012) New readers and interpretations of poly(ADP-ribosylation). *Trends Biochem. Sci.* **37**, 381–390
5. Dantzer, F., Giraud-Panis, M. J., Jaco, I., Amé, J. C., Schultz, I., Blasco, M., Koering, C. E., Gilson, E., Ménissier-de Murcia, J., de Murcia, G., and Schreiber, V. (2004) Functional interaction between poly(ADP-Ribose) polymerase 2 (PARP-2) and TRF2: PARP activity negatively regulates TRF2. *Mol. Cell. Biol.* **24**, 1595–1607
6. Gomez, M., Wu, J., Schreiber, V., Dunlap, J., Dantzer, F., Wang, Y., and Liu, Y. (2006) PARP1 Is a TRF2-associated poly(ADP-ribose)polymerase and protects eroded telomeres. *Mol. Biol. Cell* **17**, 1686–1696
7. Saxena, A., Saffery, R., Wong, L. H., Kalitsis, P., and Choo, K. H. (2002) Centromere proteins Cenpa, Cenpb, and Bub3 interact with poly(ADP-ribose) polymerase-1 protein and are poly(ADP-ribosylated). *J. Biol. Chem.* **277**, 26921–26926
8. Saxena, A., Wong, L. H., Kalitsis, P., Earle, E., Shaffer, L. G., and Choo, K. H. (2002) Poly(ADP-ribose) polymerase 2 localizes to mammalian active centromeres and interacts with PARP-1, Cenpa, Cenpb and Bub3, but not Cenpc. *Hum. Mol. Genet.* **11**, 2319–2329
9. El Ramy, R., Magroun, N., Messadecq, N., Gauthier, L. R., Boussin, F. D., Kolthur-Seetharam, U., Schreiber, V., McBurney, M. W., Sassone-Corsi, P., and Dantzer, F. (2009) Functional interplay between Parp-1 and SirT1 in genome integrity and chromatin-based processes. *Cell. Mol. Life Sci.* **66**, 3219–3234
10. Quénét, D., Gasser, V., Fouillen, L., Cammas, F., Sanglier-Cianferani, S.,

Interaction and Cooperation of PARP1 with UHRF1

Lossen, R., and Dantzer, F. (2008) The histone subcode: poly(ADP-ribose) polymerase-1 (Parp-1) and Parp-2 control cell differentiation by regulating the transcriptional intermediary factor TIF1beta and the heterochromatin protein HP1 α . *FASEB J.* **22**, 3853–3865

- Rowbotham, S. P., Barki, L., Neves-Costa, A., Santos, F., Dean, W., Hawkes, N., Choudhary, P., Will, W. R., Webster, J., Oxley, D., Green, C. M., Varga-Weisz, P., and Mermoud, J. E. (2011) Maintenance of silent chromatin through replication requires SWI/SNF-like chromatin remodeler SMARCAD1. *Mol. Cell* **42**, 285–296
- Guett, C., Scheifele, F., Rosenthal, F., Hottiger, M. O., and Santoro, R. (2012) Inheritance of silent rDNA chromatin is mediated by PARP1 via noncoding RNA. *Mol. Cell* **45**, 790–800
- Meder, V. S., Boeglin, M., de Murcia, G., and Schreiber, V. (2005) PARP-1 and PARP-2 interact with nucleophosmin/B23 and accumulate in transcriptionally active nucleoli. *J. Cell Sci.* **118**, 211–222
- Ménissier de Murcia, J., Ricoul, M., Tartier, L., Niedergang, C., Huber, A., Dantzer, F., Schreiber, V., Amé, J. C., Dierich, A., LeMeur, M., and Sabatier, L., Chambon, P., and de Murcia, G. (2003) Functional interaction between PARP-1 and PARP-2 in chromosome stability and embryonic development in mouse. *EMBO J.* **22**, 2255–2263
- Caiafa, P., Guastafierro, T., and Zampieri, M. (2009) Epigenetics: poly(ADP-ribosylation) of PARP-1 regulates genomic methylation patterns. *FASEB J.* **23**, 672–678
- de Capoa, A., Febbo, F. R., Giovannelli, F., Niveleau, A., Zardo, G., Marenzi, S., and Caiafa, P. (1999) Reduced levels of poly(ADP-ribosylation) result in chromatin compaction and hypermethylation as shown by cell-by-cell computer-assisted quantitative analysis. *FASEB J.* **13**, 89–93
- Zardo, G., D'Erme, M., Reale, A., Strom, R., Perilli, M., and Caiafa, P. (1997) Does poly(ADP-ribosylation) regulate the DNA methylation pattern? *Biochemistry* **36**, 7937–7943
- Zardo, G., and Caiafa, P. (1998) The unmethylated state of CpG islands in mouse fibroblasts depends on the poly(ADP-ribosylation) process. *J. Biol. Chem.* **273**, 16517–16520
- Zardo, G., Reale, A., Passananti, C., Pradhan, S., Buontempo, S., De Matteis, G., Adams, R. L., and Caiafa, P. (2002) Inhibition of poly(ADP-ribosylation) induces DNA hypermethylation: a possible molecular mechanism. *FASEB J.* **16**, 1319–1321
- Guastafierro, T., Cecchinelli, B., Zampieri, M., Reale, A., Riggio, G., Sthandler, O., Zupi, G., Calabrese, L., and Caiafa, P. (2008) CTCF activates PARP-1 affecting DNA methylation machinery. *J. Biol. Chem.* **283**, 21873–21880
- Reale, A., Matteis, G. D., Galleazzi, G., Zampieri, M., and Caiafa, P. (2005) Modulation of DNMT1 activity by ADP-ribose polymers. *Oncogene* **24**, 13–19
- Zampieri, M., Passananti, C., Calabrese, R., Perilli, M., Corbi, N., De Cave, F., Guastafierro, T., Bacalini, M. G., Reale, A., Amicosante, G., and Calabrese, L., Zlatanova, J., and Caiafa, P. (2009) Parp1 localizes within the Dnmt1 promoter and protects its unmethylated state by its enzymatic activity. *PLoS One* **4**, e4717
- Bostick, M., Kim, J. K., Estève, P. O., Clark, A., Pradhan, S., and Jacobsen, S. E. (2007) UHRF1 plays a role in maintaining DNA methylation in mammalian cells. *Science* **317**, 1760–1764
- Sharif, J., Muto, M., Takebayashi, S., Suetake, I., Iwamatsu, A., Endo, T. A., Shinga, J., Mizutani-Koseki, Y., Toyoda, T., Okamura, K., and Tajima, S., Mitsuya, K., Okano, M., Koseki, H. (2007) The SRA protein Np95 mediates epigenetic inheritance by recruiting Dnmt1 to methylated DNA. *Nature* **450**, 908–912
- Arita, K., Ariyoshi, M., Tochio, H., Nakamura, Y., and Shirakawa, M. (2008) Recognition of hemi-methylated DNA by the SRA protein UHRF1 by a base-flipping mechanism. *Nature* **455**, 818–821
- Nady, N., Lemak, A., Walker, J. R., Avvakumov, G. V., Karet, M. S., Achour, M., Xue, S., Duan, S., Allali-Hassani, A., Zuo, X., Wang, Y. X., Bronner, C., Chédin, F., Arrowsmith, C. H., and Dhe-Paganon, S. (2011) Recognition of multivalent histone states associated with heterochromatin by UHRF1 protein. *J. Biol. Chem.* **286**, 24300–24311
- Rottach, A., Frauer, C., Pichler, G., Bonapace, I. M., Spada, F., and Leonhardt, H. (2010) The multi-domain protein Np95 connects DNA methylation and histone modification. *Nucleic Acids Res.* **38**, 1796–1804
- Cheng, J., Yang, Y., Fang, J., Xiao, J., Zhu, T., Chen, F., Wang, P., Li, Z., Yang, H., and Xu, Y. (2013) Structural insight into coordinated recognition of H3K9me3 by the plant homeodomain (PHD) and tandem tudor domain (TTD) of the ubiquitin-like, containing PHD and RING finger domains, 1 (UHRF1). *J. Biol. Chem.* **288**, 1329–1339
- Liu, X., Gao, Q., Li, P., Zhao, Q., Zhang, J., Li, J., Koseki, H., and Wong, J. (2013) UHRF1 targets DNMT1 for DNA methylation through cooperative binding of hemi-methylated DNA and methylated H3K9. *Nat. Commun.* **4**, 1563
- Rothbart, S. B., Krajewski, K., Nady, N., Tempel, W., Xue, S., Badeaux, A. I., Barsyte-Lovejoy, D., Martinez, J. Y., Bedford, M. T., Fuchs, S. M., Arrowsmith, C. H., and Strahl, B. D. (2012) Association of UHRF1 with methylated H3K9 directs the maintenance of DNA methylation. *Nat. Struct. Mol. Biol.* **19**, 1155–1160
- Citterio, E., Papait, R., Nicassio, F., Vecchi, M., Gomiero, P., Mantovani, R., Di Fiore, P. P., and Bonapace, I. M. (2004) Np95 is a histone-binding protein endowed with ubiquitin ligase activity. *Mol. Cell. Biol.* **24**, 2526–2535
- Karagianni, P., Amazit, L., Qin, J., and Wong, J. (2008) ICBP90, a novel methyl K9 H3-binding protein linking protein ubiquitination with heterochromatin formation. *Mol. Cell. Biol.* **28**, 705–717
- Felle, M., Joppien, S., Németh, A., Diermeier, S., Thalhammer, V., Dobner, T., Kremmer, E., Kappler, R., and Längst, G. (2011) The USP7/Dnmt1 complex stimulates the DNA methylation activity of Dnmt1 and regulates the stability of UHRF1. *Nucleic Acids Res.* **39**, 8355–8365
- Qin, W., Leonhardt, H., and Spada, F. (2011) Usp7 and Uhrf1 control ubiquitination and stability of the maintenance DNA methyltransferase Dnmt1. *J. Cell. Biochem.* **112**, 439–444
- Du, Z., Song, J., Wang, Y., Zhao, Y., Guda, K., Yang, S., Kao, H. Y., Xu, Y., Willis, J., Markowitz, S. D., Sedwick, D., Ewing, R. M., and Wang, Z. (2010) DNMT1 stability is regulated by proteins coordinating deubiquitination and acetylation-driven ubiquitination. *Sci. Signal.* **3**, ra80
- Nishiyama, A., Yamaguchi, L., Sharif, J., Johmura, Y., Kawamura, T., Nakanishi, K., Shimamura, S., Arita, K., Kodama, T., Ishikawa, F., Koseki, H., and Nakanishi, M. (2013) Uhrf1-dependent H3K23 ubiquitylation couples maintenance DNA methylation and replication. *Nature* **502**, 249–253
- Meilinger, D., Fellinger, K., Bultmann, S., Rothbauer, U., Bonapace, I. M., Klinkert, W. E., Spada, F., and Leonhardt, H. (2009) Np95 interacts with *de novo* DNA methyltransferases, Dnmt3a, and Dnmt3b and mediates epigenetic silencing of the viral CMV promoter in embryonic stem cells. *EMBO Rep.* **10**, 1259–1264
- Unoki, M., Nishidate, T., and Nakamura, Y. (2004) ICBP90, an E2F-1 target, recruits HDAC1 and binds to methyl-CpG through its SRA domain. *Oncogene* **23**, 7601–7610
- Achour, M., Fuhrmann, G., Alhosin, M., Rondé, P., Chataigneau, T., Moussi, M., Schini-Kerth, V. B., and Bronner, C. (2009) UHRF1 recruits the histone acetyltransferase Tip60 and controls its expression and activity. *Biochem. Biophys. Res. Commun.* **390**, 523–528
- Kim, J. K., Estève, P. O., Jacobsen, S. E., and Pradhan, S. (2009) UHRF1 binds G9a and participates in p21 transcriptional regulation in mammalian cells. *Nucleic Acids Res.* **37**, 493–505
- Mistry, H., Tamblyn, L., Butt, H., Sisigoreo, D., Gracias, A., Larin, M., Gopalakrishnan, K., Hande, M. P., and McPherson, J. P. (2010) UHRF1 is a genome caretaker that facilitates the DNA damage response to γ -irradiation. *Genome Integr.* **1**, 7
- Papait, R., Pistore, C., Negri, D., Pecoraro, D., Cantarini, L., and Bonapace, I. M. (2007) Np95 is implicated in pericentromeric heterochromatin replication and in major satellite silencing. *Mol. Biol. Cell* **18**, 1098–1106
- Pichler, G., Wolf, P., Schmidt, C. S., Meilinger, D., Schneider, K., Frauer, C., Fellinger, K., Rottach, A., and Leonhardt, H. (2011) Cooperative DNA and histone binding by Uhrf2 links the two major repressive epigenetic pathways. *J. Cell. Biochem.* **112**, 2585–2593
- Hopfner, R., Mousli, M., Jeltsch, J. M., Voulgaris, A., Lutz, Y., Marin, C., Bellocq, J. P., Oudet, P., and Bronner, C. (2000) ICBP90, a novel human CCAAT-binding protein, involved in the regulation of topoisomerase II α expression. *Cancer Res.* **60**, 121–128
- Boehler, C., Gauthier, L. R., Mortusewicz, O., Biard, D. S., Saliou, J. M., Bresson, A., Sanglier-Cianferani, S., Smith, S., Schreiber, V., Boussin, F.,

Interaction and Cooperation of PARP1 with UHRF1

and Dantzer, F. (2011) Poly(ADP-ribose) polymerase 3 (PARP3), a newcomer in cellular response to DNA damage and mitotic progression. *Proc. Natl. Acad. Sci. U.S.A.* **108**, 2783–2788

46. Frauer, C., Rottach, A., Meilinger, D., Bultmann, S., Fellinger, K., Hassenöder, S., Wang, M., Qin, W., Söding, J., Spada, F., and Leonhardt, H. (2011) Different binding properties and function of CXXC zinc finger domains in Dnmt1 and Tet1. *PLoS One* **6**, e16627
47. Zhang, Y., Wang, J., Ding, M., and Yu, Y. (2013) Site-specific characterization of the Asp- and Glu-ADP-ribosylated proteome. *Nat. Methods* **10**, 981–984
48. Chuang, L. S., Ian, H. I., Koh, T. W., Ng, H. H., Xu, G., and Li, B. F. (1997) Human DNA-(cytosine-5) methyltransferase-PCNA complex as a target for p21WAF1. *Science* **277**, 1996–2000
49. Zhang, Y., Liu, S., Mickanin, C., Feng, Y., Charlott, O., Michaud, G. A., Schirle, M., Shi, X., Hild, M., Bauer, A., Myer, V. E., Finan, P. M., Porter, J. A., Huang, S. M., and Cong, F. (2011) RNF146 is a poly(ADP-ribose)-directed E3 ligase that regulates axin degradation and Wnt signalling. *Nat. Cell Biol.* **13**, 623–629
50. Kang, H. C., Lee, Y. I., Shin, J. H., Andrabi, S. A., Chi, Z., Gagné, J. P., Lee, Y., Ko, H. S., Lee, B. D., Poirier, G. G., Dawson, V. L., and Dawson, T. M. (2011) Iduna is a poly(ADP-ribose) (PAR)-dependent E3 ubiquitin ligase that regulates DNA damage. *Proc. Natl. Acad. Sci. U.S.A.* **108**, 14103–14108
51. Lehnertz, B., Ueda, Y., Derijck, A. A., Braunschweig, U., Perez-Burgos, L., Kubicek, S., Chen, T., Li, E., Jenuwein, T., and Peters, A. H. (2003) Suv39h-mediated histone H3 lysine 9 methylation directs DNA methylation to major satellite repeats at pericentric heterochromatin. *Curr. Biol.* **13**, 1192–1200
52. Peters, A. H., O'Carroll, D., Scherthan, H., Mechtler, K., Sauer, S., Schöfer, C., Weipoltshammer, K., Pagani, M., Lachner, M., Kohlmaier, A., Opravil, S., Doyle, M., Sibilia, M., and Jenuwein, T. (2001) Loss of the Suv39h histone methyltransferases impairs mammalian heterochromatin and genome stability. *Cell* **107**, 323–337
53. Jørgensen, S., Schotta, G., and Sørensen, C. S. (2013) Histone H4 Lysine 20 methylation: key player in epigenetic regulation of genomic integrity. *Nucleic Acids Res.* **41**, 2797–2806
54. Zhu, Q., Pao, G. M., Huynh, A. M., Suh, H., Tonnu, N., Nederlof, P. M., Gage, F. H., and Verma, I. M. (2011) BRCA1 tumour suppression occurs via heterochromatin-mediated silencing. *Nature* **477**, 179–184
55. Muto, M., Kanari, Y., Kubo, E., Takabe, T., Kurihara, T., Fujimori, A., and Tatsumi, K. (2002) Targeted disruption of Np95 gene renders murine embryonic stem cells hypersensitive to DNA damaging agents and DNA replication blocks. *J. Biol. Chem.* **277**, 34549–34555
56. Kashima, L., Idogawa, M., Mita, H., Shitashige, M., Yamada, T., Ogi, K., Suzuki, H., Toyota, M., Ariga, H., Sasaki, Y., and Tokino, T. (2012) CHFR protein regulates mitotic checkpoint by targeting PARP-1 protein for ubiquitination and degradation. *J. Biol. Chem.* **287**, 12975–12984
57. Lu, J., and Gilbert, D. M. (2007) Proliferation-dependent and cell cycle-regulated transcription of mouse pericentric heterochromatin. *J. Cell Biol.* **179**, 411–421
58. Pageau, G. J., and Lawrence, J. B. (2006) BRCA1 foci in normal S-phase nuclei are linked to interphase centromeres and replication of pericentric heterochromatin. *J. Cell Biol.* **175**, 693–701

2.6 DNA methylation requires a DNMT1 ubiquitin interacting motif (UIM) and histone ubiquitination

DNA methylation requires a DNMT1 ubiquitin interacting motif (UIM) and histone ubiquitination

Weihua Qin^{1, 3, 4, *}, Patricia Wolf^{1, 3, 4, *}, Nan Liu^{1, 3, 4}, Stephanie Link^{1, 3, 4}, Martha Smets^{1, 3, 4}, Federica La Mastra^{1, 3, 5}, Ignasi Forné^{2, 3}, Garwin Pichler^{1, 3, 6}, David Hörl^{1, 3, 4}, Karin Fellinger^{1, 3, 7}, Fabio Spada^{1, 3, 8}, Ian Marc Bonapace⁵, Axel Imhof^{2, 3}, Hartmann Harz^{1, 3, 4}, Heinrich Leonhardt^{1, 3, 4}

¹Department of Biology II, Ludwig Maximilians University Munich, Großhaderner Str. 2, 82152 Planegg-Martinsried, Germany;

²Adolf-Baenert Institute, Ludwig Maximilians University Munich, Schillerstr. 44, 80336 Munich, Germany; ³Center for Integrated Protein Science Munich (CIPSM), ⁴Nanosystems Initiative Munich (NIM), ⁵Department of Theoretical and Applied Sciences, University of Insubria, Via Manara 7, 21052 Busto Arsizio (VA), Italy

DNMT1 is recruited by PCNA and UHRF1 to maintain DNA methylation after replication. UHRF1 recognizes hemimethylated DNA substrates via the SRA domain, but also repressive H3K9me3 histone marks with its TTD. With systematic mutagenesis and functional assays, we could show that chromatin binding further involved UHRF1 PHD binding to unmodified H3R2. These complementation assays clearly demonstrated that the ubiquitin ligase activity of the UHRF1 RING domain is required for maintenance DNA methylation. Mass spectrometry of UHRF1-deficient cells revealed H3K18 as a novel ubiquitination target of UHRF1 in mammalian cells. With bioinformatics and mutational analyses, we identified a ubiquitin interacting motif (UIM) in the N-terminal regulatory domain of DNMT1 that binds to ubiquitinated H3 tails and is essential for DNA methylation *in vivo*. H3 ubiquitination and subsequent DNA methylation required UHRF1 PHD binding to H3R2. These results show the manifold regulatory mechanisms controlling DNMT1 activity that require the reading and writing of epigenetic marks by UHRF1 and illustrate the multifaceted interplay between DNA and histone modifications. The identification and functional characterization of the DNMT1 UIM suggests a novel regulatory principle and we speculate that histone H2AK119 ubiquitination might also lead to UIM-dependent recruitment of DNMT1 and DNA methylation beyond classic maintenance.

Keywords: UHRF1; histone ubiquitination; DNMT1; DNA methylation

Cell Research advance online publication 12 June 2015; doi:10.1038/cr.2015.72

Introduction

Epigenetic mechanisms including DNA and histone modifications are crucial for the regulation of gene expression during development. DNA methylation occurs

at the C5 position of cytosine residues, mostly within cytosine-guanine dinucleotides (CpG), and is involved in imprinting, X-chromosome inactivation, stable transcriptional repression, genome stability and tumorigenesis [1]. DNA methylation patterns are established by the *de novo* methyltransferases DNMT3A and DNMT3B during gametogenesis and early development, and are propagated by the maintenance methyltransferase DNMT1 after DNA replication in somatic cells.

DNMT1 comprises a regulatory N-terminal domain (NTD), which covers two-thirds of the molecule, and a C-terminal catalytic domain (CD), which contains all essential motifs of active C5 DNA methyltransferases. The NTD controls the subcellular distribution of DNMT1 during the cell cycle and its enzymatic activity. A sub-domain in the NTD was initially described as a targeting sequence (TS) as it was found to mediate the associa-

*These two authors contributed equally to this work.

Correspondence: Heinrich Leonhardt

E-mail: h.leonhardt@lmu.de

Tel: +49 89 2180 74232; Fax: +49 89 2180 74236

¹Current address: Department of Proteomics and Signal Transduction, Max Planck Institute of Biochemistry, Martinsried, Germany

²Current address: Intervet International GmbH, Unterschleißheim, Germany

³Current address: Department of Chemistry, Ludwig Maximilians University Munich, Germany

Received 21 November 14; Revised 27 March 15; Accepted 7 May 2015

tion of DNMT1 with late replicating pericentromeric heterochromatin [2]. Subsequent studies defined a distinct proliferating cell nuclear antigen (PCNA) binding domain (PBD) responsible for the interaction with the replication machinery [3]. The subnuclear localization of DNMT1 undergoes characteristic changes throughout the cell cycle reflecting PBD-mediated PCNA binding during S phase and TS domain-mediated heterochromatin association during late S and G2 phase [4, 5]. The association of DNMT1 with the replication machinery enhances methylation efficiency, but is not strictly required for postreplicative maintenance DNA methylation [6, 7]. In contrast, the TS domain was found to be required for DNMT1 enzymatic activity [8, 9]. However, the molecular mechanism of TS domain function in the regulation of maintenance DNA methylation remains elusive.

Besides its role in replication-independent heterochromatin binding, the TS domain mediates DNMT1 homodimerization [9] and autoinhibition [10, 11]. A recent crystal structure shows that the TS domain inserts into the DNA binding pocket of the CD, indicating a role of intramolecular interactions in the regulation of DNMT1 activity [10, 11]. Moreover, the TS domain interacts with the SET- and RING-associated (SRA) domain of ubiquitin like, containing PHD and RING finger domains 1 (UHRF1) [12-14]. In contrast to UHRF2, the interaction of UHRF1 with DNMT1 was found to be S phase-dependent [15].

UHRF1, also known as NP95 (mouse) or ICBP90 (human), has been reported as a crucial cofactor for maintenance DNA methylation. Mice lacking UHRF1 show a similar phenotype as *Dnmt1* null (*Dnmt1*^{-/-}) mice that manifests in genomic DNA hypomethylation and developmental arrest at embryonic day 9.5 [16-18]. The SRA domain of UHRF1 preferentially binds to hemimethylated DNA resulting from semiconservative DNA replication and is, therefore, thought to play an important role in loading DNMT1 onto newly synthesized DNA substrates [16, 17, 19-22]. The heterochromatin association of UHRF1 is also mediated by the tandem Tudor domain (TTD), which forms an aromatic cage for specific binding of histone H3 tails containing a trimethylated lysine 9 (H3K9me3) residue [22-25]. The plant homeodomain (PHD) was reported to act in combination with the TTD to read the H3K9me3 mark [26] and to contribute to large-scale reorganization of pericentromeric heterochromatin [27]. In addition, UHRF1 harbors a really interesting new gene (RING) domain endowed with ubiquitin E3 ligase activity *in vitro*, which is required for growth regulation of tumor cells [24, 28]. The ubiquitination state and stability of DNMT1 is controlled by UHRF1 and the ubiquitin-specific protease USP7 [29, 30]. UHRF1 over-

expression leads to DNA hypomethylation by the destabilization and delocalization of DNMT1 [31]. Besides its role in marking DNMT1 for proteasomal degradation, UHRF1 also exerts its ubiquitin E3 ligase activity on histone substrates [24, 25].

A recent study describes replication-dependent H3K23 ubiquitination by UHRF1 in *Xenopus* extracts [32]. Knockdown and rescue experiments in HeLa cells showed that SRA domain-mediated DNA binding as well as RING domain-dependent E3 ubiquitin ligase activity of UHRF1 are required for H3 ubiquitination. Expression of the SRA and RING domain mutants in *Uhrf1*^{-/-} mouse cells could neither restore DNMT1 replication targeting nor DNA methylation levels. A deletion of large parts of the DNMT1 TS domain abolished binding to ubiquitinated H3K23 *in vitro*, but effects on enzymatic activity were not investigated. In particular, the structure and function of the rather large TS domain with its multiple roles and interactions remain to be clarified.

In this study, we elucidate the complex interplay between UHRF1 and DNMT1. While we could confirm the general role of UHRF1 in recruiting DNMT1 to substrate sites by direct interaction, we found that DNMT1 targeting and activities are essentially controlled by specific binding to histone tails ubiquitinated by UHRF1. We generated defined mutations in different UHRF1 domains that retained SRA domain-mediated binding to hemimethylated DNA substrate sites, TTD-mediated recognition of H3K9me3 and binding of DNMT1, but did not allow maintenance DNA methylation. We could show that binding to unmodified H3R2 via the PHD and ubiquitination of H3K18 via the RING domain are required for UHRF1 to mediate maintenance DNA methylation. In turn, we identified a ubiquitin interacting motif (UIM) in the TS domain of DNMT1 that reads this ubiquitin mark and is strictly required for maintenance DNA methylation *in vivo*. These results show the manifold regulatory mechanisms controlling DNMT1 activity and illustrate the multifaceted interplay between DNA and histone modifications.

Results

The interaction of DNMT1 with UHRF1 is required for maintenance DNA methylation

To test whether the interaction of DNMT1 with UHRF1 is indeed required for maintenance DNA methylation, we generated stable cell lines based on *Dnmt1*^{-/-} ESCs expressing green fluorescent protein (GFP) fusions of either DNMT1 wild-type (GFP-DNMT1 wt) or a truncated TS domain deletion mutant (GFP-DNMT1 Δ458-500) that is defective in binding to UHRF1 (Figure

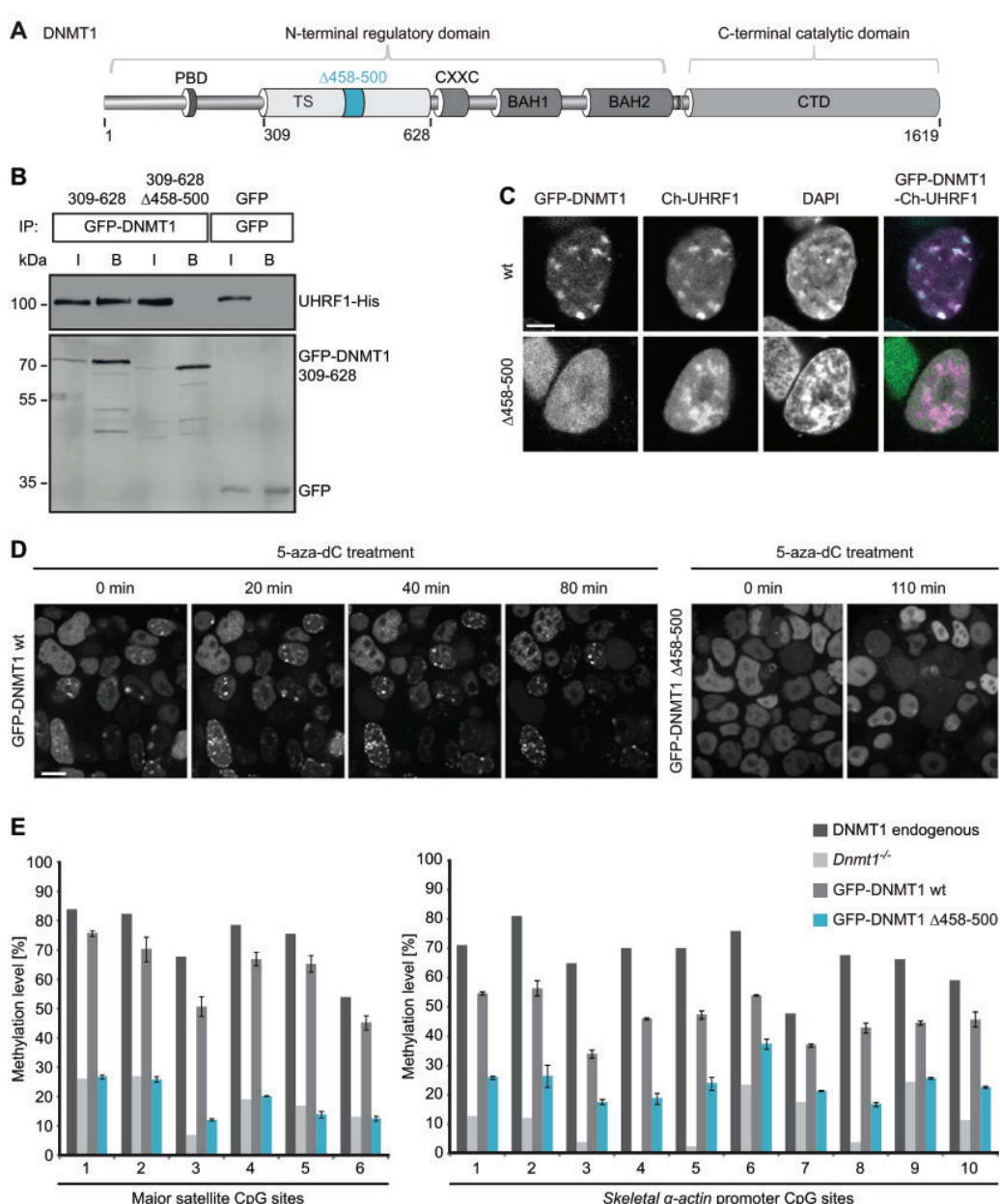


Figure 1 The DNMT1 TS domain is required for UHRF1 interaction, heterochromatin targeting and maintenance DNA methylation. **(A)** Schematic outline of DNMT1 domains and the TS domain deletion ($\Delta 458-500$). DNMT1 comprises a large N-terminal domain (NTD) harboring the PCNA binding domain (PBD), the targeting sequence (TS) domain and two bromo adjacent homology (BAH) domains. The active catalytic center of DNMT1 resides within its C-terminal domain (CD). **(B)** Co-immunoprecipitation of UHRF1-His and the GFP-DNMT1 TS domain (309-628) wild-type (wt) or $\Delta 458-500$ constructs. Both constructs were co-expressed in HEK 293T cells and after immunoprecipitation of GFP fusions, bound proteins were detected by western blot with an anti-UHRF1 and an anti-GFP antibody. GFP was used as negative control. I, input; B, bound. **(C)** Confocal mid sections of fixed ESCs stably expressing GFP-DNMT1 wt or $\Delta 458-500$ mutant constructs. Ch-UHRF1 was transiently co-expressed to illustrate heterochromatic regions, DAPI was used for counterstaining. Scale bar, 5 μ m. **(D)** Covalent complex formation of GFP-DNMT1 wt and GFP-DNMT1 $\Delta 458-500$ mutant were analyzed by an *in vivo* trapping assay. Confocal mid-sections of ESCs stably expressing GFP-DNMT1 wt and deletion mutant constructs before and after treatment with the mechanism-based inhibitor 5-aza-dC are displayed. Scale bar, 10 μ m. **(E)** Local DNA methylation analyses at the major satellite repeats and the skeletal α -actin promoter. CpG methylation levels of mouse *Dnmt1*^{-/-} ESCs stably expressing GFP-DNMT1 wt or GFP-DNMT1 $\Delta 458-500$ mutant constructs were analyzed by bisulfite treatment of genomic DNA, PCR amplification and direct pyrosequencing. The methylation level of the J1 wt cell line (endogenous DNMT1) and untransfected *Dnmt1*^{-/-} cells are shown for comparison. Mean values \pm SD from two different clones were calculated, respectively.

1A and 1B). The deleted region was determined by a sequence alignment of TS domains from higher eukaryotes and a conserved core region of the domain was chosen for mutational analysis (Supplementary information, Figure S1A). In contrast to GFP-DNMT1 wt, GFP-DNMT1 Δ458-500 did not co-localize with cherry (Ch)-UHRF1 and showed a dispersed distribution in the nucleus (Figure 1C), suggesting that the interaction with UHRF1 is essential for subnuclear localization of DNMT1.

Next, we investigated the role of UHRF1 interaction for the catalytic function of DNMT1. Notably, GFP-DNMT1 Δ458-500 that did not interact with UHRF1 was able to fully methylate hemimethylated DNA substrates *in vitro* (Supplementary information, Figure S1C). To test the DNA methylation activity of this deletion mutant *in vivo*, we made use of a trapping assay. In this assay, the cytosine analogue 5-aza-2'-deoxycytidine (5-aza-dC) forms an irreversible covalent complex with the methyltransferase at the C6 position of the cytosine residue when incorporated into DNA during replication thereby trapping the enzyme at DNA replication foci. Trapped DNMT1 fractions increase over time and allow monitoring the activity-dependent accumulation of DNMT1 at its target sites [33]. In ESCs stably expressing GFP-DNMT1 wt, foci of immobilized protein emerged already within 20 min (Figure 1D, left panel). In contrast, GFP-DNMT1 Δ458-500 was not enriched at replication foci even after 110 min, indicating that the deletion mutant is unable to methylate newly replicated DNA in living cells (Figure 1D, right panel). To pursue this idea, we further analyzed site-specific DNA methylation levels of stable GFP-DNMT1 wt and Δ458-500 ESC lines (Supplementary information, Figure S1B). GFP-DNMT1 could restore local DNA methylation at the major satellite repeats in *Dnmt1*^{-/-} ESCs leading to an average methylation level of 62% that is comparable to the level of the wt cell line expressing the endogenous protein (74%, Figure 1E, left panel). In contrast, the DNMT1 mutant deficient in UHRF1 binding was unable to reestablish local DNA methylation patterns resulting in decreased levels at the major satellite repeats (average 19%) similar to the *Dnmt1*^{-/-} control cell line (average 18%). Consistently, a similar defect of GFP-DNMT1 Δ458-500 in DNA methylation activity was observed at the single-copy sequence of the *skeletal α-actin* promoter (Figure 1E, right panel). Furthermore, similar results were obtained from DNA methylation analyses at the minor satellite repeats and the *Dnmt1o* promoter confirming that stable expression of GFP-DNMT1 Δ458-500 could not restore DNA methylation in a *Dnmt1*^{-/-} cell line (Supplementary information, Figure S1D).

In summary, we provide strong evidence that the

GFP-DNMT1 Δ458-500 mutant deficient in UHRF1 binding, even though able to methylate DNA substrates *in vitro*, cannot restore DNA methylation patterns in *Dnmt1*^{-/-} ESCs. These findings suggest that the interaction of DNMT1 with UHRF1 is required to maintain DNA methylation *in vivo*.

The PHD and RING domain of UHRF1 are essential for maintenance DNA methylation

Cooperative binding of the UHRF1 TTD to di- and trimethylated histone H3K9 and of the SRA domain to hemimethylated DNA was described as a prerequisite for targeting DNMT1 to its substrate and for subsequent DNA methylation [34]. Given the regulatory impact of these two domains, we were interested in how the PHD and RING domain of UHRF1 may functionally contribute to maintenance DNA methylation by DNMT1. To this end, we introduced point mutations in the PHD and RING domain (UHRF1-GFP H346G and UHRF1-GFP H730A, respectively) that are expected to prevent coordination of zinc ions by zinc-finger motifs (Figure 2A and Supplementary information, Figure S2A). Consequently, the mutation in the RING domain significantly reduced the E3 ubiquitin ligase activity of UHRF1 *in vivo* (Supplementary information, Figure S2C and S2D). Notably, the preference of UHRF1-GFP for hemimethylated DNA was not impaired by the PHD and RING domain mutations (Supplementary information, Figure S2B).

First, we tested whether the point mutations in the PHD and RING domain influence the interaction of UHRF1 with DNMT1. UHRF1-GFP wt as well as UHRF1-GFP H346G and UHRF1-GFP H730A still co-precipitated with red fluorescent protein (RFP)-DNMT1, indicating that the mutations do not affect the interaction with DNMT1 directly (Figure 2B). In addition, the unaltered interactions were confirmed by a fluorescent three-hybrid assay [35, 36]. In this assay, UHRF1-GFP fusion constructs were used as baits by tethering them to a *lac* operator (*lacO*) array present in baby hamster kidney (BHK) cells that simultaneously express RFP-DNMT1 as a prey. Accumulation of RFP-DNMT1 at the *lacO* spot enriched for UHRF1-GFP wt, UHRF1-GFP H346G or UHRF1-GFP H730A clearly demonstrates that the mutant proteins were still able to interact with DNMT1 *in vivo* (Figure 2C).

In order to perform functional studies on the PHD and RING domain mutants, we stably expressed GFP-tagged UHRF1 wt, UHRF1 H346G or UHRF1 H730A in *Uhrf1*^{-/-} ESCs. Similar to wt, also UHRF1-GFP H346G and UHRF1-GFP H730A showed focal enrichment at heterochromatin (Figure 2D, first panel and Supplementary information, Figure S2E). Thus, the mutations

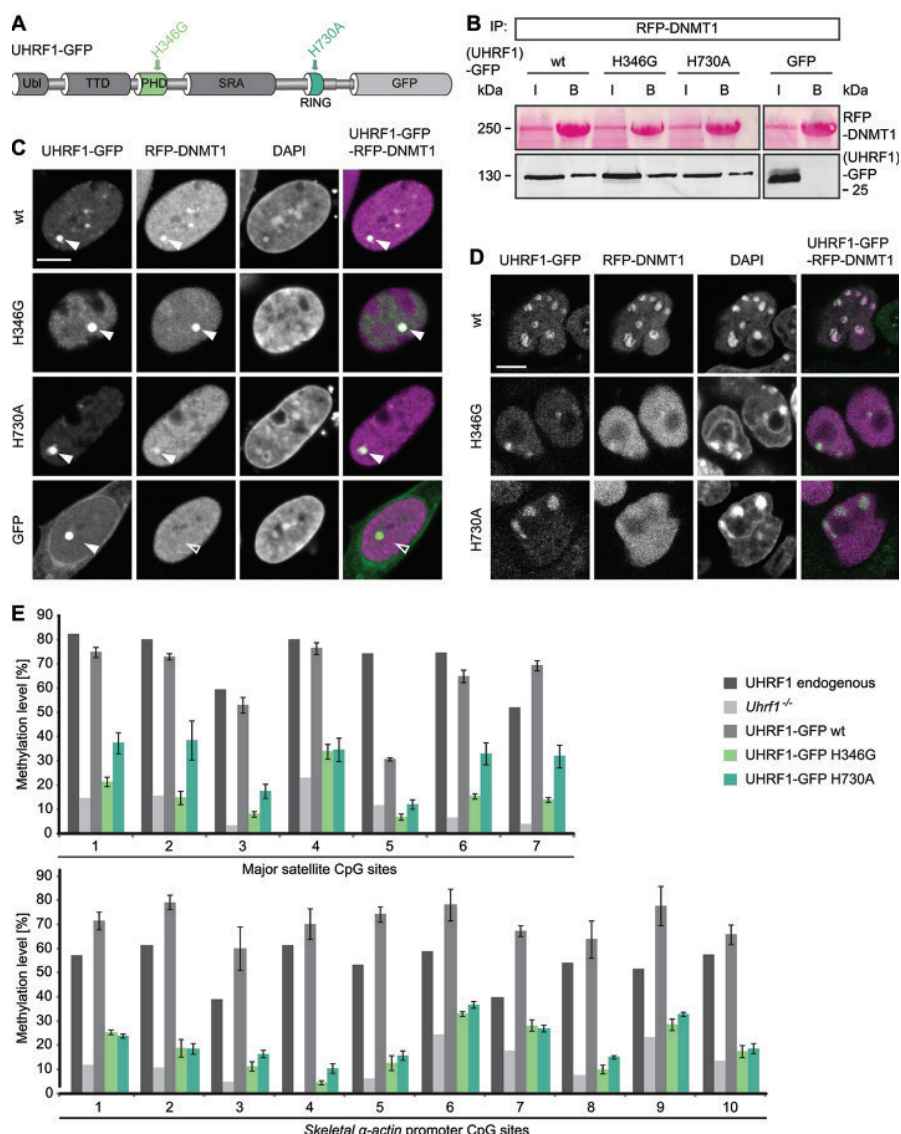


Figure 2 Mutations in the PHD and RING domain of UHFR1 affect DNMT1 targeting and maintenance DNA methylation, but not the interaction with DNMT1. **(A)** Schematic outline of the multidomain protein UHFR1. UHFR1 harbors a ubiquitin-like (UbI) domain, a plant homeodomain (PHD) and a tandem Tudor domain (TTD) followed by a SET and RING-associated (SRA) domain and a really interesting new gene (RING) domain. UHFR1-GFP expression constructs carrying point mutations in the PHD (H346G) and RING domain (H730A) are illustrated. **(B)** Co-immunoprecipitation of UHFR1-GFP wt or PHD and RING domain mutants co-expressed with RFP-DNMT1 in HEK 293T cells. RFP-DNMT1 was immunoprecipitated using the RFP-Trap and bound UHFR1-GFP was detected by western blot with an anti-GFP antibody. GFP was used as negative control. Immunoprecipitated RFP-DNMT1 is shown by Ponceau staining. I, input; B, bound. **(C)** Fluorescence three-hybrid assay for visualization of the interaction RFP-DNMT1 with UHFR1-GFP wt or PHD and RING domain mutants. Displayed are confocal mid sections of BHK cells carrying a stably integrated Lac-operator array that were triple transfected with LacI fused to the GFP-binder, UHFR1-GFP constructs and RFP-DNMT1. DAPI was used for chromatin counterstaining. Closed arrows indicate the co-localization of both proteins at the *lacO* spot, open arrows indicate no co-localization. GFP was used as negative control. Scale bar, 5 μ m. **(D)** Confocal mid sections of fixed *Uhrf1*^{-/-} ESCs stably expressing UHFR1-GFP wt or PHD and RING domain mutant constructs. RFP-DNMT1 was transiently co-expressed and DNA was counterstained by DAPI. Scale bar, 5 μ m. **(E)** Local DNA methylation analyses at major satellite repeats and the *skeletal α -actin* promoter. CpG site methylation levels of mouse E14 *Uhrf1*^{-/-} ESCs stably expressing UHFR1-GFP wt or PHD and RING domain mutant constructs were analyzed by bisulfite treatment of genomic DNA, PCR amplification and direct pyrosequencing. The methylation level of E14 wt ESCs (endogenous UHFR1) and untransfected E14 *Uhrf1*^{-/-} cells are shown for comparison. Mean values \pm SD from two different clones were calculated, respectively.

do not affect localization of UHRF1. In contrast to its chromatin association in the UHRF1-GFP wt cell line, transiently co-expressed RFP-DNMT1 did not co-localize with UHRF1-GFP H346G and UHRF1-GFP H730A, but showed a dispersed distribution in the nucleus (Figure 2D, second panel). This observation is consistent with the result of a staining for endogenous DNMT1 (Supplementary information, Figure S2F). Only in the UHRF1-GFP wt cell line, endogenous DNMT1 was enriched at S phase-specific replication sites, whereas it was diffusely distributed in the nucleus of the mutant cell lines pointing towards a defective DNMT1 targeting mechanism. To examine if DNMT1 methylation activity depends on the PHD and RING domain of UHRF1, we performed site-specific methylation analyses at heterochromatic regions. Consistent with defects in targeting DNMT1 to replication sites, DNA methylation levels at the major satellite repeats and the *skeletal α-actin* promoter revealed that both UHRF1-GFP H346G and UHRF1-GFP H730A were not able to mediate DNA remethylation by DNMT1 in *Uhrf1*^{-/-} ESCs in contrast to UHRF1-GFP wt (Figure 2E). Especially at the major satellite repeats, the average DNA methylation in the PHD mutant cell lines remained nearly unchanged (16%) from the *Uhrf1*^{-/-} control cell line (11%). Also, the average methylation levels in the RING domain mutant cell lines (29%) did not reach the wt DNA methylation level (62%) at the major satellite repeats. Similar results were obtained for the minor satellite repeats and the *Dnmt1o* promoter (Supplementary information, Figure S3A). Consistent with this site-specific DNA hypomethylation, the stable UHRF1 mutant cell lines also showed decreased global DNA methylation levels as compared with the wt (Supplementary information, Figure S3B and S3C). Partial rescue of global DNA methylation in the RING domain mutant cell lines could be due to residual E3 ubiquitin ligase activity of UHRF1-GFP H730A (Figure 3B, Supplementary information, Figure S2C and S2D).

To exclude the possibility that DNA hypomethylation might result from lower expression of the PHD and RING domain mutant (Figure 3A), we performed a transient rescue assay in *Uhrf1*^{-/-} ESCs. Even though expression levels of the mutant constructs exceeded those of the UHRF1-GFP wt, the PHD and RING domain mutants could not mediate remethylation at the major satellite repeats (Supplementary information, Figure S3D and S3E) arguing for functional rather than expression defects.

In summary, the PHD and RING domain mutants, although not affecting UHRF1 heterochromatin localization or the direct interaction with DNMT1, cannot mediate either targeting of DNMT1 to replication foci nor maintenance DNA methylation. These findings suggest

that these UHRF1 domains contribute to the recruitment of DNMT1 by indirect mechanisms.

The PHD and RING domain of UHRF1 are required for ubiquitination of histone H3

Histone H3 has been reported as a UHRF1-dependent ubiquitination target in *Xenopus* egg extracts [32], providing a potential mechanism for the recruitment of DNMT1 to chromatin. Thus, we set out to investigate whether H3 ubiquitination required PHD-mediated histone binding and RING domain-mediated ubiquitin E3 ligase activity of UHRF1 in mammalian cells. To this end, we extracted histones from wt or *Uhrf1*^{-/-} ESCs and detected modified H3. As expected, histone H3 was less ubiquitinated in the absence of UHRF1 (Figure 3A and 3B), indicating that UHRF1 serves as a ubiquitin E3 ligase for H3 in mammalian cells. We also found that ubiquitination levels of histone H3 in *Uhrf1*^{-/-} ESCs stably expressing the RING domain mutant UHRF1-GFP H730A were not rescued to the level of wt cells. Surprisingly, the PHD mutant UHRF1-GFP H346G also could not restore ubiquitination of histone H3 (Figure 3A and 3B).

Since the PHD has been reported to bind to unmodified H3R2 [26, 37-39], we investigated the role of this histone residue in H3 ubiquitination by mutational analyses. Compared with GFP-H3 wt, ubiquitination of a GFP-H3 R2A mutant expressed in human embryonic kidney (HEK) 293T cells was clearly reduced (Figure 3C) pointing towards an important role of the R2 residue for UHRF1-dependent H3 ubiquitination.

To further test the histone binding properties of the PHD mutant *in vitro*, we performed a peptide pull-down assay with wt or PHD and RING domain mutant UHRF1-GFP using H3 peptides with an unmodified, trimethylated or acetylated K9 residue. The mutation in the RING domain did not alter the histone binding of UHRF1-GFP showing a preference for unmodified and K9 trimethylated H3 peptides similar to the wt protein (Figure 3D). The mutation in the PHD, however, decreased the binding to both, the unmodified and the K9 trimethylated peptide. We further examined the histone binding preferences of UHRF1-GFP with an *in vitro* histone tail binding assay. The results revealed the binding of UHRF1-GFP to unmodified but not R2 dimethylated H3 histone tails (Supplementary information, Figure S4), consistent with prior K_d measurements [39]. As the PHD of UHRF1 has been shown to bind unmethylated H3R2 residues and to contribute to the K9 methylated H3 histone binding of the TTD [26, 37-39], we propose that PHD-dependent histone binding is required for UHRF1-mediated ubiquitination of histone H3.

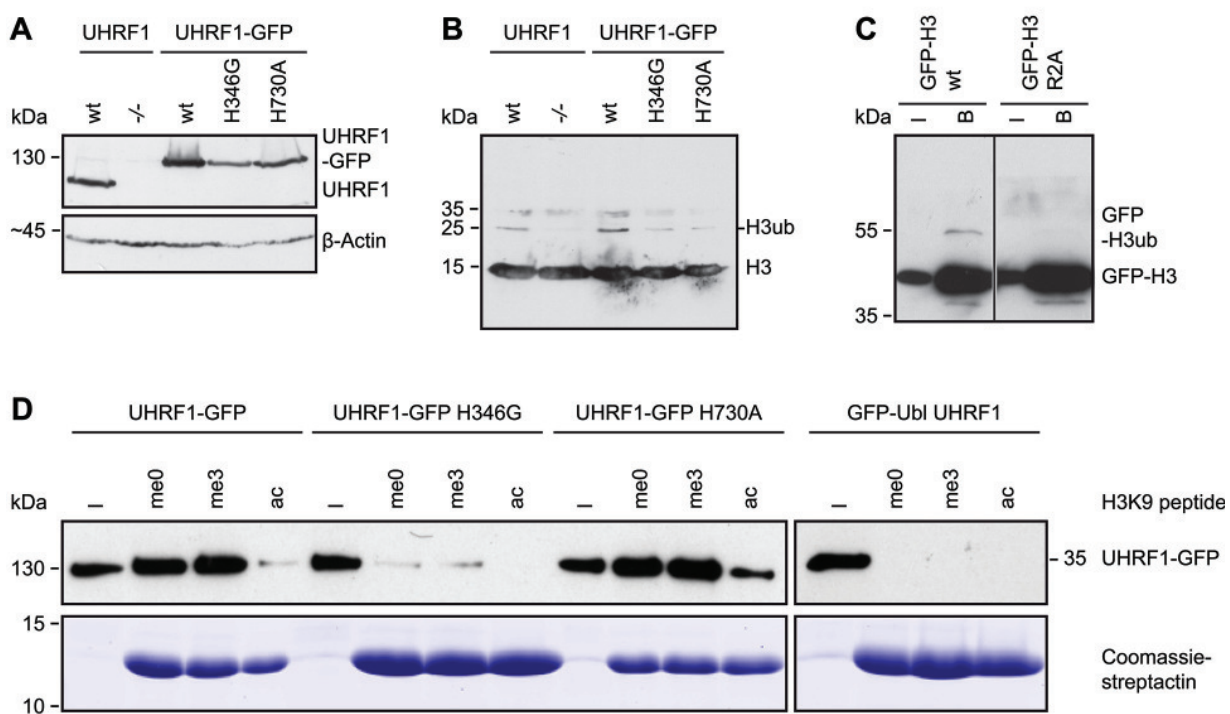


Figure 3 Histone H3 ubiquitination requires the UHRF1 PHD and RING domain. **(A)** Western blot analyses of endogenous UHRF1 or stably expressed UHRF1-GFP wt or H346G and H730A mutants in E14 *Uhrf1*^{-/-} ESCs with an anti-UHRF1 antibody. Equal loading is shown by an anti-β-Actin antibody. **(B)** Analyses of H3 ubiquitination from acid extracted histones derived from the different cell lines in (A). A specific anti-H3 antibody was used for detection. **(C)** Ubiquitination of GFP-H3 in dependence on R2. GFP-H3 wt and the arginine to alanine mutant (R2A) were co-expressed with UHRF1-His in HEK 293T cells, respectively, and after immunoprecipitation with the GFP-Trap, the bound fraction was detected by western blotting with a specific anti-H3 antibody. I, input; B, bound. **(D)** *In vitro* peptide pull-down assay of UHRF1-GFP wt or the PHD and RING domain mutants from crude cells extracts of HEK 293T cells using H3 peptides (amino acid 1-20) that were either unmodified (me0), K9 trimethylated (me3) or K9 acetylated (ac) and functionalized on streptactin beads. The GFP-Ubl domain of UHRF1 was used as negative control. Coomassie-streptactin is shown as loading control. I, input.

UHRF1 ubiquitinates histone H3 on K18 in mammalian cells

Using *Xenopus* extracts immunodepleted for DNMT1, H3 was shown to be ubiquitinated at the K23 residue [32]. To map ubiquitination sites on histone H3 tails in mammalian cells, we performed mass spectrometry using human and mouse cells. In contrast to the results from *Xenopus* extracts, the K18 residue of histone H3 was identified as novel ubiquitination site in mouse ESCs, while the K23 residue was unmodified or acetylated (Figure 4A and 4B). Relative quantification of H3 peptides containing ubiquitinated K18 and an unmodified or acetylated K23 residue showed a reduction of K18 ubiquitination in ESCs lacking UHRF1 (Figure 4C and 4D). Similarly, immunoprecipitation of GFP-UHRF1 from HEK 293T cells and subsequent mass spectrometry also revealed ubiquitination at K18 but not at K23 (Supplementary information, Figure S5A). Comparison of ubiquitination levels of overexpressed GFP-H3 carrying R2A, K18A or

K23A mutations suggests that in this constellation K23 could also be modified (Supplementary information, Figure S5B). Interestingly, the GFP-H3 R2A construct showed reduced ubiquitination levels indicating that the R2 residue plays a role in regulating H3 ubiquitination.

DNMT1 harbors a UIM that mediates binding to ubiquitinated H3 and is essential for DNA methylation activity in vivo

To unravel how H3 ubiquitination may contribute to maintenance DNA methylation, we screened DNMT1 for potential binding motifs. With bioinformatics analyses, we identified a ubiquitin interacting motif (UIM) in the N-terminal regulatory domain of DNMT1. This motif is located in a region spanning from amino acid 380 to 399 of mouse DNMT1 and shows striking similarity to UIMs of known ubiquitin interacting proteins (Figure 5A). Comparison of the ubiquitin binding properties between GFP-DNMT1 wt and mutants either lacking

the UIM (Δ 356-404) or containing substitutions of the relevant and conserved amino acids in the motif to alanine (D381A-E382A-S392A, D381A-E382A-M385A-S392A-D395A, Figure 5A and Supplementary information, Figure S6A) showed a defect in the association with ubiquitinated histone H3 and ubiquitinated H2AK119 (Figure 5B, 5C and Supplementary information, Figure S6B-S6D). To further elucidate UIM-dependent ubiquitinated histone binding, we quantified modified H318-26 peptides bound by GFP-DNMT1 wt or the UIM mutants by mass spectrometry. Whereas H3 histone peptides ubiquitinated at K18 and acetylated or unmodified at K23 co-immunoprecipitated with GFP-DNMT1 wt, only little to no ubiquitinated peptide signals were detected for the UIM mutants (Figure 6A, 6B). GFP-DNMT1 Δ 458-500 defective in UHRF1 interaction (Figure 1B) showed reduced (Figure 6B) or undetectable (Figure 5B, 5C) binding to ubiquitinated H3 and H2A. This deletion located in a TS domain region C-terminal of the UIM might affect the integrity and functionality of the motif responsible for ubiquitin binding. Therefore, we cannot rule out that apart from disrupted UHRF1 binding also defects in the association with ubiquitinated histones contributed to the observed changes in subnuclear distribution and protein function of GFP-DNMT1 Δ 458-500 (Figure 1C-1E).

Besides a decreased binding to ubiquitinated H3, the TS domain point and deletion mutants exhibited an increased binding to H3 or core histones compared with GFP-DNMT1 wt (Figure 5B). Therefore, specific binding of DNMT1 to ubiquitinated H3 via its UIM might prevent the enzyme from stable chromatin association and thereby facilitate DNA methylation.

To clarify the functional role of the UIM in maintenance DNA methylation *in vivo*, we performed a functional complementation assay in *Dnmt1*^{-/-} ESC lines transiently expressing GFP-DNMT1 wt, GFP-DNMT1 Δ 356-404, GFP-DNMT1 D381A-E382A-S392A or GFP-DNMT1 D381A-E382A-M385A-S392A-D395A. Local DNA methylation analyses at the major satellite repeats and the *skeletal α-actin* promoter showed that the UIM mutants were not able to reestablish DNA methylation patterns (Figure 6C). GFP-DNMT1 wt restored DNA methylation at the major satellite repeats to 48%. By comparison, the UIM deletion and point mutants were not able to rescue resulting in low average methylation levels of 20% to 23% comparable to untransfected *Dnmt1*^{-/-} ESCs (15%). Similar results were also observed at the minor satellite repeats and the *Dnmt1* promoter (Supplementary information, Figure S7A).

Given that the GFP-DNMT1 TS UIM deletion and point mutants were able to interact with Ch-UHRF1 (Supplementary information, Figure S7B), we were in-

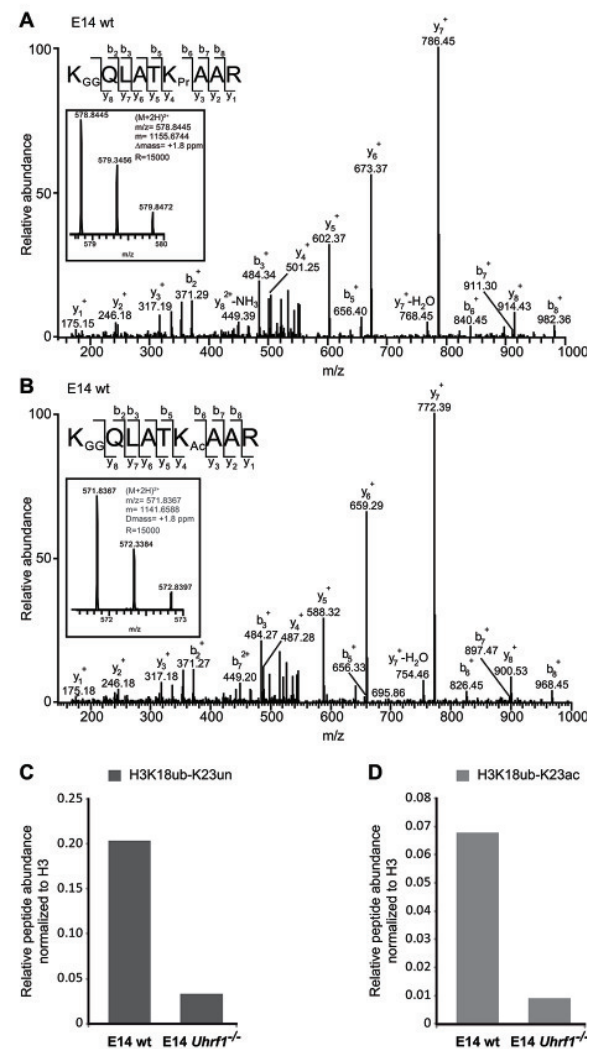


Figure 4 UHRF1 ubiquitinates histone H3 at K18 in mammalian cells. **(A)** Identification of H3 18-26 peptides carrying ubiquitination (GG) at K18 and no modification (Pr) at K23 by LC-MS/MS. MS2 fragmentation spectrum of the precursor ion is shown in the inset. An almost complete series of b and full y product ions generated by CID fragmentation were detectable providing a high confidence in its correct identification and localization of the ubiquitin modification. Inset: mass, charge and measurement error determination of the H3 18-26 peptides K18GGK23Pr in the E14 wt sample. Displayed is the isotopic distribution of the H3 peptide from which the mass to charge ratio (m/z), the charge (2 $+$) and the monoisotopic mass value (m) were derived. Δm : difference between the expected and the measured masses; R : resolution of the MS measurement. **(B)** Identification of H3 18-26 peptides carrying ubiquitination (GG) at K18 and acetylation (Ac) at K23 by LC-MS/MS as in (A). **(C, D)** Quantification of H3 18-26 peptides carrying ubiquitination (ub) at K18 and an unmodified (un) or acetylated (ac) K23 residue from E14 wt and E14 *Uhrf1*^{-/-} samples. Extracted ion chromatograms of the ions corresponding to the peptides of interest were used for the quantification. The signals were normalized against the total amount of analyzed H3 proteins.

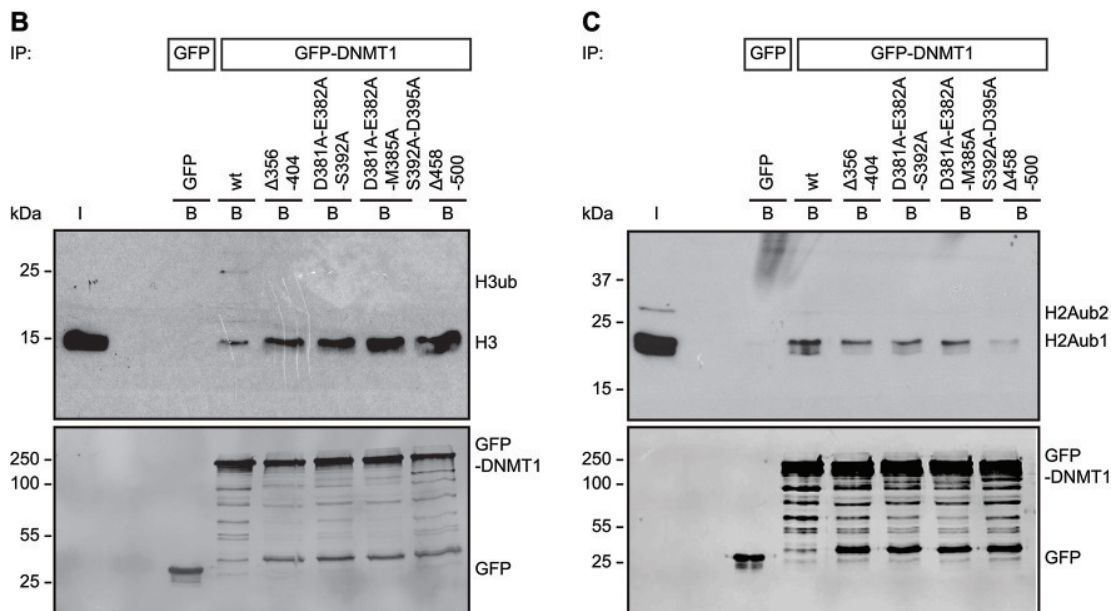
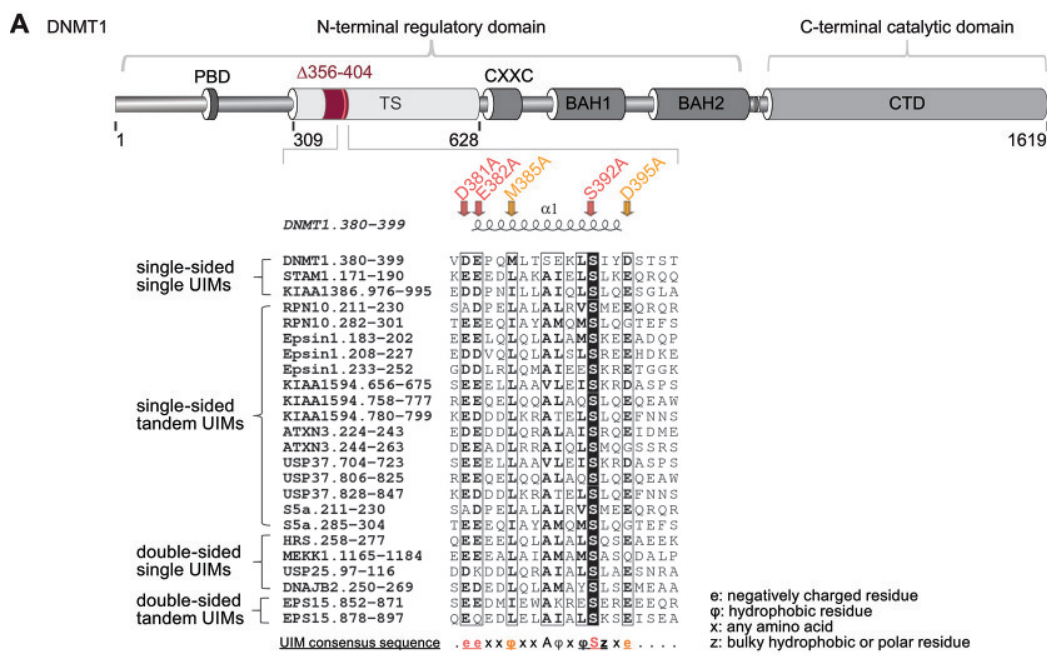


Figure 5 The TS domain of DNMT1 harbors a ubiquitin interacting motif (UIM) that is essential for binding to ubiquitinated H3 and H2A. **(A)** Schematic outline of the UIM in the TS domain of DNMT1 and indication of the UIM deletion (Δ 356-404) and the point mutations (D381A-E382A-S392A and D381A-E382A-M385A-S392A-D395A). A peptide sequence of DNMT1 encompassing amino acid 380-399 was aligned with peptide sequences of proteins previously known to contain UIMs. Identical amino acids are highlighted in black, highly similar amino acids are framed in black. The secondary structure of the DNMT1 region (pdb: 3EPZ [10]) harboring the UIM is displayed on top of the sequence alignment generated using ESPript [78]. The consensus sequence for single-sided UIMs [58] is shown below. The UIMs were found by scanning the protein primary sequences against a collection of motifs in ExPASy Prosite. Putative subgroups of UIMs are indicated on the left. **(B)** Ubiquitinated histone H3 binding assay. After extraction of histones from HEK 293T cells, the extracts were incubated with GFP-DNMT1 wt or mutants immobilized on the GFP-Trap and the bound fractions were analyzed by western blotting with specific anti-H3 and anti-GFP antibodies. GFP was used as negative control. I, input; B, bound. **(C)** Ubiquitinated histone H2A binding assay as in (B). Bound fractions were analyzed by western blotting with specific anti-H2AK119ub and anti-GFP antibodies. Analyses of the anti-H2AK119ub antibody specificity and of peptides isolated from the corresponding band are shown in Supplementary information, Figure S6C and S6D. H2Aub1, monoubiquitinated H2A; H2Aub2, diubiquitinated H2A.

terested in how the UIM in DNMT1 has an influence on the subnuclear localization of the protein. Immunostaining of replicating DNA with a specific anti-PCNA antibody indicated that GFP-DNMT1 wt was enriched at S phase-specific replication foci, while GFP-DNMT1 Δ 356-404, GFP-DNMT1 D381A-E382A-S392A and GFP-DNMT1 D381A-E382A-M385A-S392A-D395A showed only weak association with the PCNA-stained replication sites especially in late S phase (Supplementary information, Figure S8). To analyze the UIM-dependent enrichment of DNMT1 at late-replicating heterochromatin, we quantified mean fluorescence intensities at chromocenters compared with the nucleoplasmic region (Figure 7A). In late S phase ES and mouse embryonic fibroblasts (MEF) cells, GFP-DNMT1 wt localized at chromocenters, whereas the UIM mutations abolished heterochromatin enrichment (Figure 7B and 7C). These results clearly demonstrate the key role of the UIM in DNMT1 targeting via ubiquitinated histone H3 binding and for maintenance DNA methylation in mammalian cells.

Discussion

DNA methylation is an important epigenetic modification regulating gene expression in development and disease. A key question is how methylation marks are set, maintained and removed. According to previous models, DNA methylation marks are set by the *de novo* methyltransferases DNMT3A and DNMT3B during development and maintained by the maintenance DNA methyltransferase DNMT1 that specifically recognizes and modifies hemimethylated DNA substrates. However, the preference of DNMT1 for hemimethylated DNA measured *in vitro* [40-43] is not sufficient to explain efficient maintenance of DNA methylation patterns over many cell division cycles *in vivo*. The interaction of DNMT1 with the replication protein PCNA was shown to enhance maintenance DNA methylation by a factor of two, but not to be essential [6, 7]. In contrast, the interacting factor UHRF1 recruiting and allosterically activating DNMT1 is essential for DNA methylation [14, 16, 17, 44]. In this study, we have now dissected the distinct role of different UHRF1 and DNMT1 domains in directing DNA methylation.

In line with previous studies, we show that, albeit being weak, the TS domain-mediated interaction of DNMT1 with the SRA domain of UHRF1 is required for targeting and function of DNMT1 *in vivo*. Accordingly, truncated DNMT1 (Δ 458-500) deficient in UHRF1 binding showed weaker association with chromocenters in late S phase mouse fibroblasts [4] and failed to maintain DNA methylation in ESC (Figure 1).

Heterochromatin binding of UHRF1 is mediated by

the TTD, PHD and SRA domain and defects in any of these three domains lead to decreased DNA methylation by DNMT1 [34, 45, 46]. Accordingly, it was postulated that UHRF1 reads and binds repressive histone marks and hemimethylated DNA and via direct protein-protein interaction recruits DNMT1 for maintenance DNA methylation.

Defects of a RING domain mutant (C713A, C515A and C716A) in restoring ubiquitinated H3 in HeLa cells after knockdown of human DNMT1 and UHRF1 have previously been reported [32]. We found that the RING domain, though not directly involved in UHRF1 chromatin binding or interaction with DNMT1, is indispensable for DNA methylation by DNMT1. Remarkably, a UHRF1 RING domain mutant (H730A) with diminished ubiquitin E3 ligase activity (Supplementary information, Figure S2C and S2D) that could still bind DNMT1 (Figure 2B), hemimethylated DNA and K9 trimethylated H3 peptides *in vitro* (Figure 3D and Supplementary information, Figure S2B) and chromocenters *in vivo* (Supplementary information, Figure S2E), nonetheless failed in recruiting DNMT1 to replication sites (Figure 2D and Supplementary information, Figure S2F). These findings suggest that DNMT1 recruitment to replication forks is not based on direct interaction with UHRF1, but on the catalytic activity of the RING domain. Previously, the RING domain of UHRF1 has been reported to have an autoubiquitination activity [28] and, in addition, to ubiquitinate DNMT1 [29, 30] and histone substrates [24, 25]. A recent study describes that ubiquitination of H3 by UHRF1 provides docking sites for DNMT1 on chromatin and thus couples maintenance DNA methylation and replication [32]. While we could confirm the essential role of UHRF1, we obtained new insights into the complex functional interplay of UHRF1 and DNMT1 domains.

First, in contrast to ubiquitination at K23 in *Xenopus* egg extracts [32], our mass spectrometry results identified H3K18 as ubiquitination target of UHRF1 in mammalian cells (Figure 4A, 4B and Supplementary information, Figure S5A). By mutational analysis in HEK 293T cells, we found that in absence of K18, the mutated GFP-tagged H3 might be ubiquitinated at K23 (Supplementary information, Figure S5B). However, by semiquantitative analysis of endogenous ubiquitinated H3 peptides in wt versus *Uhrf1*^{-/-} mouse ESCs using mass spectrometry, we clearly show the specificity of K18 ubiquitination by UHRF1 and its reduction by UHRF1 depletion (Figure 4C, 4D). Second, in the previous study, a deletion of 100 amino acids within the DNMT1 TS domain (Δ 325-425) caused a loss of histone binding *in vitro* [32]. The TS domain is, however, involved in multiple interactions and required for proper folding, stability and activity of DNMT1. The incomplete structural information indicates

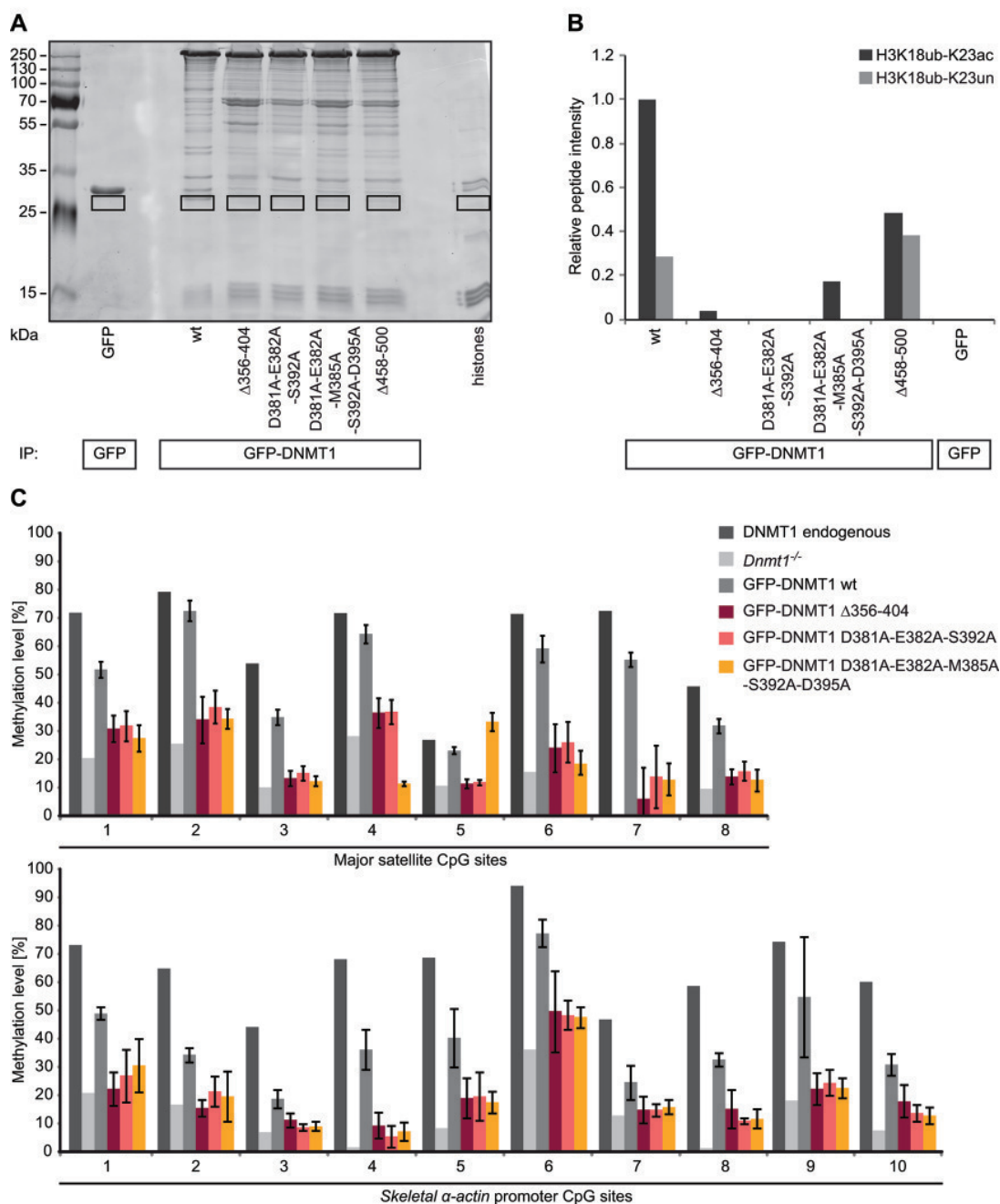


Figure 6 The DNMT1 UIM is required for ubiquitinated H3K18 binding and for DNA methylation. **(A)** Ubiquitinated histone binding experiments using GFP-DNMT1 wt or UIM mutants as well as the Δ 458-500 mutant deficient in binding to UHRF1. Equal amounts of GFP fusions were immobilized on the GFP-Trap and incubated with acid extracted histones. Bound proteins were visualized by Coomassie staining and the fractions highlighted by black rectangles were analyzed by mass spectrometry. GFP was used as negative control. **(B)** Quantification of H3 18-26 peptides carrying ubiquitination (ub) at K18 and an acetylated (ac) or unmodified (un) K23 residue from histone binding experiment shown in (A). Extracted ion chromatograms of the ions corresponding to the peptides of interest were used for quantification (H3K18ubK23ac: $m/z = 571.8353 \pm 10$ ppm; H3K18ubK23un: $m/z = 578.8441 \pm 10$ ppm). **(C)** Local DNA methylation analyses of J1 *Dnmt1*^{-/-} ESCs expressing GFP-DNMT1 wt or Δ 356-404 and UIM point mutants. CpG methylation levels at the major satellite repeats and the skeletal α -actin promoter were analyzed by bisulfite treatment of genomic DNA, PCR amplification and direct pyrosequencing. Methylation levels of untransfected J1 *Dnmt1*^{-/-} cells are shown for comparison. Mean values \pm SD from three to four biological replicates were calculated, respectively.

different TS domain conformations and a role in autoinhibition of the CD, but does not provide any further mechanistic insights [10, 11, 47]. With bioinformatics and mutational analyses, we identified a conserved UIM located in the TS domain of DNMT1 (amino acids 381–395) that mediates the recognition of ubiquitinated H3 *in vitro* (Figure 5, 6A, 6B and Supplementary information, Figure S6B). Localization and activity analyses with specific mutants *in vivo* clearly indicated that the UIM is required for DNMT1 subnuclear distribution and maintenance DNA methylation (Figures 6C, 7 and Supplementary information, Figure S7A and S8).

Last, we could show that besides hemimethylated DNA binding by the SRA domain [32], UHRF1 PHD binding to H3R2 is also required for H3 ubiquitination and subsequent DNA methylation (Figure 2E and 3B). Therefore, we propose that cooperative chromatin binding of the TTD, the PHD and the SRA domain constitutes a prerequisite for H3K18 ubiquitination. These ubiquitinated histone tails are recognized by the UIM and thus mediate DNMT1 chromatin binding. Thereby, UHRF1 acts as a reader and writer of histone marks and via recruitment of DNMT1 dynamically links DNA and histone modification pathways. Based on these results, we propose a ubiquitination-dependent chromatin targeting mechanism for DNMT1 that is essential for maintenance DNA methylation after replication (Figure 8A). The identification and functional characterization of a UIM in DNMT1 not only changes our view of maintenance DNA methylation, but also opens new perspectives for the involvement of DNMT1 in other repressive epigenetic pathways (Figure 8B).

Besides association with ubiquitinated H3, we found that DNMT1 also binds ubiquitinated H2AK119 (Figure 5C and Supplementary information, Figure S6C, S6D). Consistently, DNMT1 was recently detected among proteins binding to H2A ubiquitinated at K119 in *Drosophila*, corresponding to K119 in mammals [48]. H2AK119 ubiquitination is catalyzed by RING1A/1B, two components of the Polycomb repressive complex 1 (PRC1), and plays an important role in regulating gene expression [49]. Similar to UHRF1-dependent H3 ubiquitination, H2A ubiquitination by RING1A/1B might also contribute to DNA methylation. We speculate that UIM-mediated binding of DNMT1 to ubiquitinated H2AK119 might direct DNMT1 to un- or hemimethylated sites dependent on PRC1 ubiquitination activity (Figure 8B, left half).

PRC1-dependent H2A ubiquitination further leads to PRC2 recruitment and subsequent H3K27 methylation [50]. Enhancer of Zeste homolog 2 (EZH2), a component of PRC2, writes methylated H3K27 and interacts with DNMTs. This interaction was shown to be required for DNA methylation of EZH2 target promoters [51].

DNMT1 depletion in differentiated cells affects H2A ubiquitination-dependent PRC2 recruitment at pericentromeric heterochromatin [52]. Thus, UIM binding to ubiquitinated H2A is likely DNA replication independent and DNMT1 might function as adaptor protein mediating PRC2 recruitment and repressive Polycomb domain formation.

Besides recruiting DNMT1 to specific sites on chromatin, the UIM could also play a role in the allosteric activation of the enzyme. The UIM is located within the TS domain of DNMT1 that had been shown to bind the CD and thereby inhibit catalytic activity [10, 11]. It is tempting to speculate that competitive UIM binding to ubiquitinated histone tails displaces the TS domain from the DNA binding pocket and abolishes autoinhibition of DNMT1.

Given the emerging role of ubiquitination in DNA methylation, it is interesting to notice that ubiquitination is a highly dynamic post-translational modification that can be reversed by ubiquitin-specific proteases (USPs). The UHRF1-DNMT1 complex has been reported to contain USP7 that deubiquitinates and stabilizes DNMT1 [29, 30]. Thus, USP7 might in addition modulate the ubiquitination status of histone H3 and thereby regulate DNMT1 association with chromatin. An alternative pathway controlling DNMT1 chromatin association could involve the recently described chromatin acetylation of H3K18 and K23 [53, 54]. Acetylated H3K18 is enriched at the transcriptional start sites of active and poised genes [55]. Thus, H3K18 acetylation might counteract ubiquitination and thereby prevent binding and silencing of active genes by DNMT1. The dynamic interplay of ubiquitination and acetylation of H3K18 likely controls DNMT1 chromatin binding and thereby directs methylation activity. Studies of UHRF1 and DNMT1 complex composition in different cell cycle phases and cell types should provide further insights into the fine-tuning of DNMT1 activity *in vivo*.

Given the complex role of the large TS domain on the one hand and the scarce structural and mechanistic data on the other hand, our identification of a well defined UIM provides a concrete basis for functional insights. Ubiquitin binding proteins with defined UIMs have been described in various cellular processes like, e.g., sorting of ubiquitinated membrane proteins for lysosomal degradation. The crystal structure of the signal transducing adaptor molecule 1 (STAM1) [56] suggests that three central amino acids in the UIM, L176, A179 and S183 form a hydrophobic interface for ubiquitin binding [57]. Similar to the UIM in STAM1, the UIM in DNMT1 also harbors a conserved hydrophobic amino acid M385 and S392 flanked by negatively charged amino acids (D381, E382 and D395), which we found to be essential in our analyses (Figures 5, 6 and 7). Different from other UIMs,

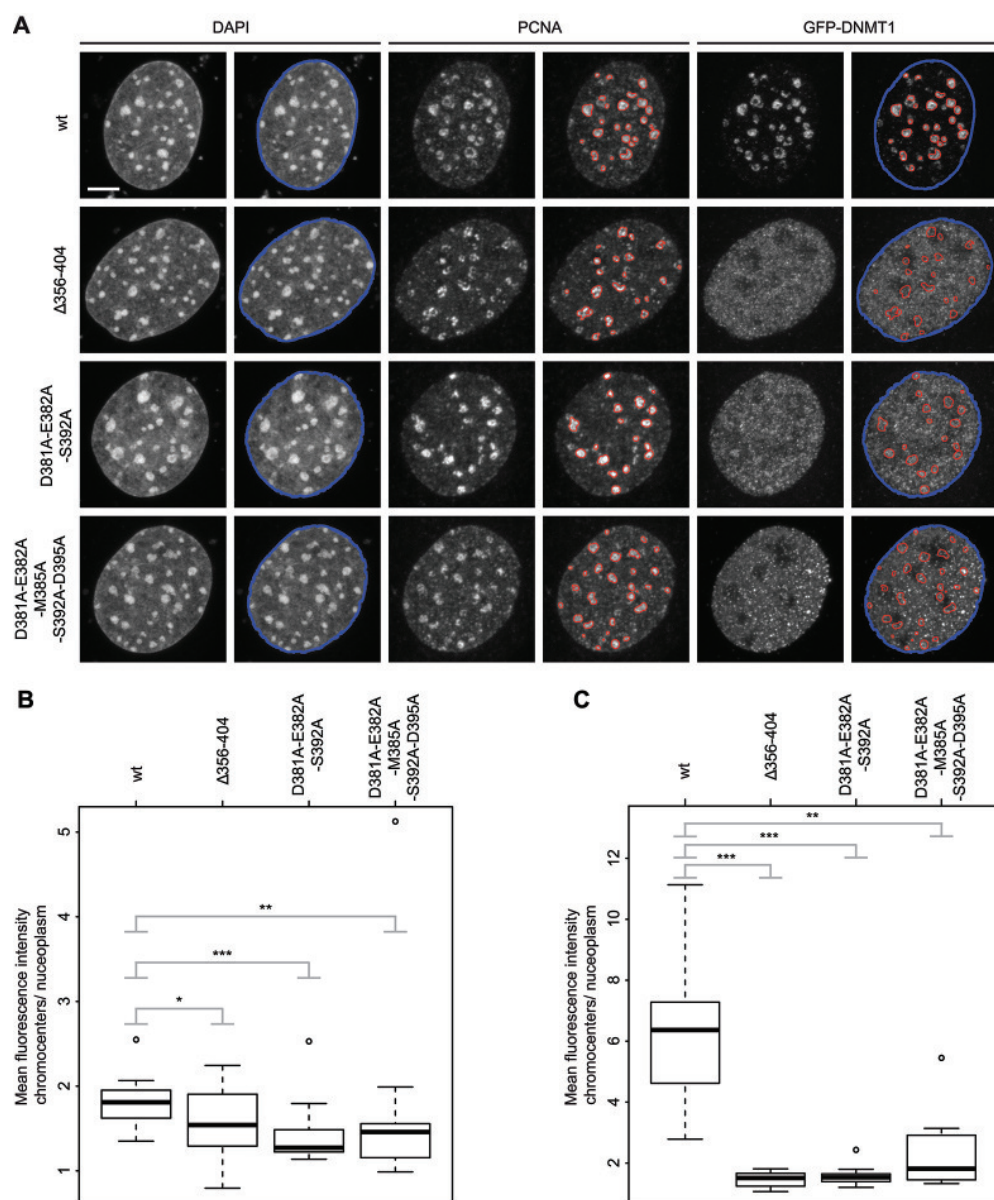


Figure 7 GFP-DNMT1 UIM mutants show a decreased association with PCNA-stained replication sites in late S phase compared with the wt. **(A)** Maximum intensity projections of MEF cells transiently expressing GFP-DNMT1 wt or UIM mutants. Replicating DNA was stained with a specific anti-PCNA antibody and chromatin was counterstained with DAPI. Replication foci masks (red) match the enrichment of GFP-DNMT1 wt in late S phase, whereas the UIM mutants do not show a focal enrichment. Segmentations were generated in an automated fashion using a machine learning algorithm (WEKA). The nuclear mask outlined in blue was based on the DAPI staining, whereas the replication foci masks outlined in red were based on the PCNA staining. Both masks were superimposed on the GFP channels. The GFP-DNMT1 signal inside the red masks (chromocenters) relative to the remainder of the nucleus (nucleoplasm) was quantified. Scale bar, 5 μ m. **(B)** Quantification of chromocenter association of GFP-DNMT1 wt or UIM mutants in late S phase J1 *Dnmt1*^{-/-} ESCs. The ratio of the mean GFP fluorescence intensity at chromocenters over the mean intensity in the nucleoplasm is shown in the box plot from 15 (wt), 16 (Δ 356-404), 12 (D381A-E382A-S392A) or 18 (D381A-E382A-M385A-S392A-D395A) cells. The results were further analyzed in R using a Wilcoxon test and considered as statistical significant for $P < 0.05$ (*) and $P < 0.01$ (**) or highly significant for $P < 0.001$ (***). The following P values were calculated: Δ 356-404: $P = 0.049$, D381A-E382A-S392A: $P = 0.0016$ and D381A-E382A-M385A-S392A-D395A: $P = 0.0056$. **(C)** Quantification of chromocenter association of GFP-DNMT1 wt or UIM mutants in late S phase MEF cells as in (B). Eleven (wt), 12 (Δ 356-404, D381A-E382A-S392A) or 10 (D381A-E382A-M385A-S392A-D395A) cells were analyzed. The following P values were calculated in R using a Wilcoxon test: Δ 356-404: $P = 0.00000148$, D381A-E382A-S392A: $P = 0.00000148$ and D381A-E382A-M385A-S392A-D395A: $P = 0.0012$.

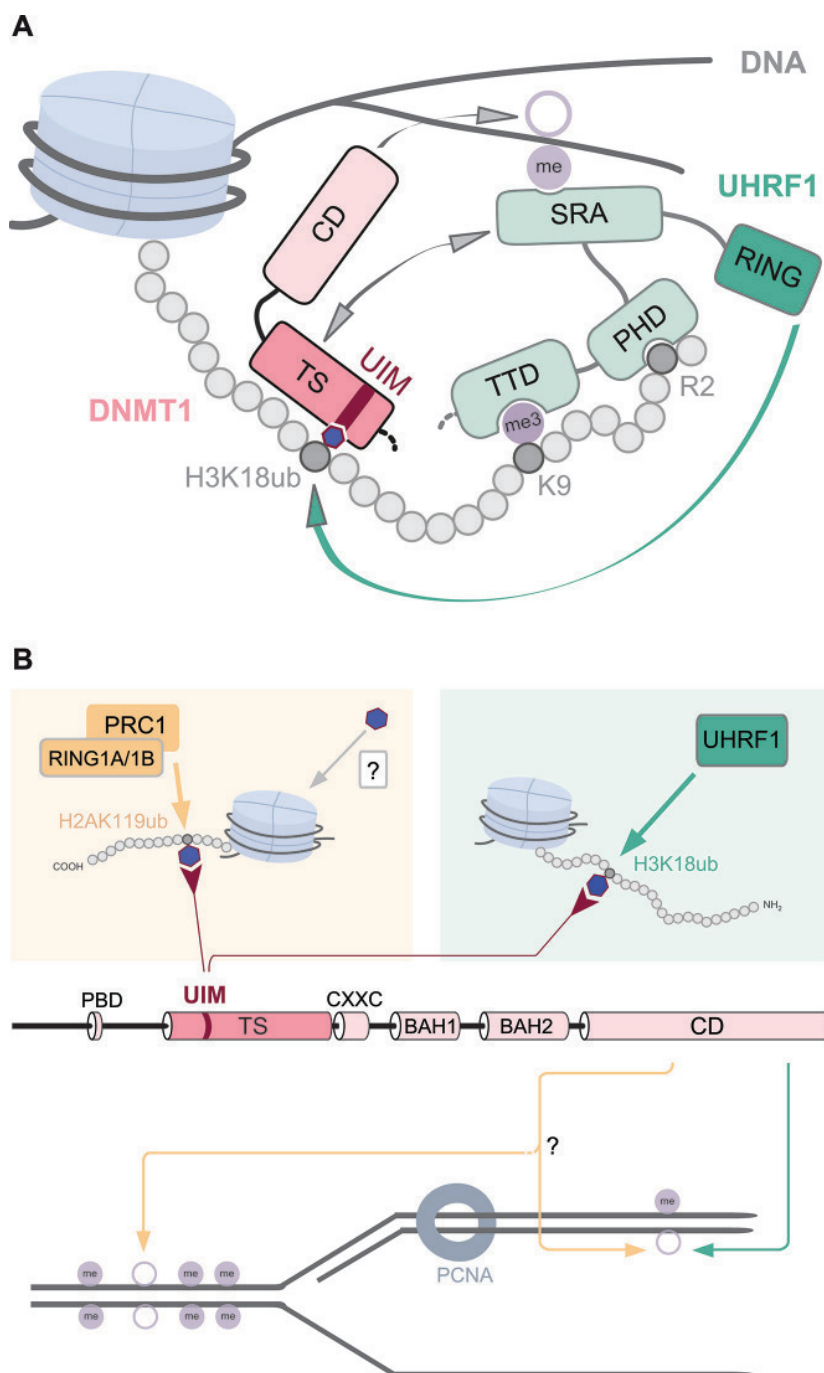


Figure 8 Overview of interactions and modifications controlling DNMT1 activity. **(A)** UHRF1 is enriched at H3 tails as a result of the PHD-mediated binding to H3R2, the TTD-mediated binding to methylated H3K9 and recognition of hemimethylated CpG sites via the SRA domain. By interaction of the SRA domain with the TS domain, DNMT1 is directly recruited to its target sites. UHRF1 chromatin binding via its TTD, PHD and SRA domain is a prerequisite for subsequent H3 ubiquitination by the RING domain. The UIM of DNMT1 binds to H3 tails ubiquitinated at K18 by UHRF1 and is essential for DNMT1 targeting and DNA methylation *in vivo*. **(B)** The previously described direct interaction of DNMT1 with UHRF1 and PCNA is not sufficient for maintenance DNA methylation. Besides the UHRF1-dependent H3K18 ubiquitination recruiting DNMT1 via its UIM for maintenance DNA methylation (right half), we propose an alternative pathway that involves H2AK119 ubiquitination by RING1A/1B of PRC1 (left part). The identification of the DNMT1 UIM now opens the possibility that ubiquitination of histone tail residues by ubiquitin E3 ligases might constitute alternative pathways for DNA methylation by DNMT1 CD beyond classic maintenance. Blue hexagons represent a ubiquitin moiety.

the central conserved A residue is not present in DNMT1 (Supplementary information, Figure S6A). Based on sequence alignments and structural information, UIMs can be subdivided in single-sided single UIMs, as in STAM1, and in single-sided tandem UIMs, as in the proteasome subunit S5a [58] (Figure 5A). The tandem UIMs in S5a provide a model for the recognition of polyubiquitin chains [59]. In contrast, a double-sided single UIM in the hepatocyte growth factor-regulated tyrosine kinase substrate (HRS) allows for efficient binding of multiple monoubiquitinated receptors in the process of endosomal protein sorting [58]. Comparison with these known UIMs suggests that the motif in DNMT1 belongs to the group of single-sided single UIMs, which would be compatible with the recognition of single ubiquitinated histone tails.

In summary, the functional analysis of UHRF1 domains and the identification of a UIM in DNMT1 challenge traditional views of maintenance DNA methylation as a simple copying mechanism. Instead, DNA methylation by DNMT1 requires reading of H3R2, H3K9me3 and hemimethylated DNA by UHRF1 and subsequent ubiquitination of H3K18 by its RING domain thereby integrating signals from different epigenetic pathways. These multiple layers controlling DNMT1 activity suggest that overall methylation densities in chromatin domains are maintained rather than specific methylation patterns precisely copied. The functional characterization of the UIM further raises the possibility that other ubiquitin E3 ligases like RING1A/1B of PRC1 might direct DNMT1 activity to repressive chromatin domains beyond simple maintenance.

Materials and Methods

Expression constructs and antibodies

Fusion constructs were generated using enhanced GFP, monomeric RFP or monomeric Ch. The expression constructs for GFP, RFP-DNMT1, GFP-DNMT1 wt, GFP-DNMT1 Δ 458-500, GFP-DNMT1 309-628 (GFP-TS) and UHRF1-His have been described previously [9, 29, 33, 60, 61]. GFP-TS Δ 458-500, GFP-DNMT1 Δ 356-404 and GFP-DNMT1 point mutant (D381A-E382A-S392A and D381A-E382A-M385A-S392A-D395A) expression constructs as well as UHRF1-GFP H346G and H730A were derived from the corresponding wt constructs by overlap extension PCR [62]. The GFP-UHRF1 single-domain construct for the ubiquitin-like domain (Ubl) was generated by PCR using the corresponding wt full-length construct. Ch-UHRF1 and GFP-UHRF1 expression constructs have been described previously [22, 63]. Expression constructs for GFP-H3 R2A, K18A, K23A as well as K18A-K23A were obtained by overlap extension PCR on the corresponding wt construct. The construct for LacI-GBP has been reported before [36, 64, 65]. All constructs were verified by DNA sequencing (MWG Biotech).

For immunofluorescence staining of heterochromatin, a mouse anti-H3K9me3 and an anti-H4K20me3 antibody were used (Active

Motif). Endogenous DNMT1 was stained with the rat monoclonal antibody 5A10 [4] and PCNA with the rat monoclonal antibody 16D10 [66]. As secondary antibodies an anti-mouse Alexa Fluor 594 and anti-rat Alexa Fluor 647 antibody were applied, respectively (Invitrogen).

For detection of GFP fusion proteins by western blot, a mouse anti-GFP (Roche) or a rat anti-GFP (Chromotek) antibody was used. RFP or Ch fusion proteins were detected by the rat anti-red antibody 5F8 [67]. UHRF1 was visualized by a rabbit anti-UHRF1 antibody [24] and HA-ubiquitin by the mouse monoclonal anti-HA antibody 12CA5. Equal loading of cell lysates was assessed by a mouse anti- β -Actin antibody (Sigma-Aldrich). The rabbit anti-H3 antibody was purchased from Abcam and the anti-H2AK119ub from New England Biolabs. Depending on the expected intensity of the signals, secondary antibodies either conjugated to horseradish peroxidase (anti-rabbit (Biorad), anti-rat and anti-mouse (Dianova)) or conjugated to fluorescent dyes (anti-mouse and anti-rat Alexa Fluor 647 as well as anti-rat Alexa Fluor 488 (Invitrogen)) were applied. For detection of HRP-conjugated antibodies, an ECL Plus reagent (GE Healthcare, Thermo Scientific) was used.

Cell culture, transfection and immunofluorescence staining

HEK 293T and BHK cells were cultured in DMEM supplemented with 10% fetal calf serum and 50 μ g/ml gentamycin (PAA). MEF cells were cultured in DMEM supplemented with 15% fetal calf serum, 0.1 mM β -mercaptoethanol (Invitrogen), 2 mM l-glutamine, 1 \times MEM non-essential amino acids, 100 U/ml penicillin and 100 g/ml streptomycin (PAA). ESCs including J1 wt, *Dnmt1*^{-/-}, E14 wt and *Uhrf1*^{-/-} were cultured without feeder cells in gelatinized flasks as described [33]. Culture medium was supplemented with 1 000 U/ml recombinant leukemia inhibitory factor (Millipore). The *Dnmt1*^{-/-} ESCs used in this study are homozygous for the c allele [68]. Mouse E14 wt and *Uhrf1*^{-/-} cells have been reported before [61]. Mouse ESCs and MEF cells were transfected with FuGENE HD (Roche), Lipofectamine[®] 2 000 or 3 000 reagent (Invitrogen) according to the manufacturer's instructions. HEK 293T cells and BHK cells were transfected using polyethylenimine as transfection reagent (Sigma) according to the manufacturer's instructions. Cell fixation and microscopy were carried out as described [35].

Generation of stable ESC lines and DNA methylation analyses

Forty-eight hours after expression of GFP-tagged constructs in *Dnmt1*^{-/-} or *Uhrf1*^{-/-} ESCs, GFP-positive mouse ESCs were separated using a fluorescence-activated cell sorting (FACS) Aria II instrument (Becton Dickinson). Stably expressing cells were expanded in selection medium containing 10 μ g/ml blasticidin (GFP-DNMT1 wt and GFP-DNMT1 Δ 458-500) or 500 ng/ml puromycin (UHRF1-GFP wt, H346G and H730A) and GFP-positive cells were FACS sorted a second time. Furthermore, the UHRF1-GFP wt, H346G and H730A cell lines were single-cell sorted. Single clones of GFP-DNMT1 Δ 458-500 and corresponding wt [29] were picked manually. For all cell lines, clones with low expression levels were chosen for further analyses. The level and the accuracy of the expressed GFP fusion constructs were checked by western blot analyses (Figure 3A and Supplementary information, Figures S1B and S3D). For functional analyses of GFP-DNMT1 wt and GFP-DNMT1 UIM mutants (Δ 356-404, D381A-E382A-S392A and D381A-E382A-M385A-S392A-D395A) as well as UHRF1-

GFP wt or UHRF1-GFP point mutants (H346G and H730A) by transient rescue assays, 48 h after expression of these proteins in *Dnmt1*^{-/-} or *Uhrf1*^{-/-} ESCs, respectively, GFP-positive cells were collected with FACS. Genomic DNA isolation, bisulfite conversion and PCR conditions were described before [6, 60, 69]. Primer sets used for amplification of minor satellites, major satellites, *skeletal α-actin* and the *Dnmt1o* promoter are listed in Supplementary information, Table S1. All PCR products were analyzed by pyrosequencing (Varionostic), which results in a quantitative data set for individual CpG sites [70].

Co-immunoprecipitation and western blotting

For co-immunoprecipitation assays, the GFP and RFP, Ch or His fusion constructs were co-expressed in HEK 293T cells and protein extracts were normalized to the same GFP or RFP concentration prior to co-immunoprecipitation with the GFP-Trap or RFP-Trap (Chromotek). Bound fractions were first detected by fluorescence intensity measurements and second by western blot analyses.

Acid extraction and TCA precipitation of histones

Histones were isolated by acid extraction as reported previously [71]. In brief, 10⁷ mouse ESCs or HEK 293T cells were treated in hypotonic buffer (10 mM Tris-HCl pH 8, 10 mM KCl, 1.5 mM MgCl₂, 1 mM DTT and 1× Protease Inhibitor, 2 mM PMSF) for 30 min and centrifuged at 1 000×g at 4 °C to get the intact nuclei. After washing steps, nuclei were resuspended in 0.4 N H₂SO₄ and incubated on a rotator at 4 °C overnight. After centrifugation, histones in the supernatant were transferred into a fresh reaction tube and precipitated using 33% trichloroacetic acid (TCA). After washing twice with cold acetone, histones were dissolved in H₂O. Histone concentrations were measured using the PierceTM 660 nm protein assay kit (Thermo Scientific).

Ubiquitinated histone binding experiment

For ubiquitinated histone binding experiment, acid extracted histones from HEK 293T cells were used. GFP-DNMT1 and its mutants were immobilized on the GFP-Trap (Chromotek) and incubated with equal amounts of acid extracted histones for 30 min at 4 °C. After washing steps, the bound fractions were analyzed by western blot.

Due to unspecific binding of histones to the eppendorf tubes, we used eppendorf tubes with low binding affinity during mass spectrometry sample preparation.

Immunoprecipitation of ubiquitinated GFP-H3

GFP-H3 wt and R2A mutant constructs were co-expressed in HEK 293T cells with UHRF1-His and harvested after treatment with 2 mM N-ethylmaleimide (NEM, AppliChem) for 5 min. Lysates were prepared by firstly isolating nuclei in hypotonic buffer (10 mM HEPES pH 7.9, 10 mM KCl, 0.1 mM MgCl₂, 10% glycerol, 0.1 mM EDTA, 0.1 mM DTT, 1× protease inhibitor, 2 mM PMSF, 0.1% NP-40, 0.625 mg/ml NEM) and secondly by lysis of the nuclei in hypertonic buffer (20 mM HEPES pH 7.9, 150 mM KCl, 1.5 mM MgCl₂, 10% glycerol, 0.1 mM EDTA, 1 mM DTT, 1× protease inhibitor, 2 mM PMSF, 1 mg/ml DNase1 (AppliChem), 0.625 mg/ml NEM). Prior to immunoprecipitation, the GFP concentration was equalized using lysates from UHRF1-His transfected HEK 293T cells for dilution. After immunoprecipitation of GFP-H3 with the GFP-Trap (Chromotek) and washing (20 mM

HEPES pH 7.9, 300 mM KCl, 10% glycerol, 0.1% Triton X-100), the bound fraction was analyzed by western blot.

For semiquantitative analysis of the GFP-H3 wt or K18A, K23A, K18A-K23A and R2A ubiquitination, the GFP fusion constructs were co-expressed with HA-ubiquitin in HEK 293T cells and 2 days after transfection, the cells were harvested as described above and further processed as reported previously [29].

F3H assay and trapping assay

The F3H assay was performed as described previously [65]. In the trapping assay, mouse ESCs stably expressing GFP-DNMT1 wt or Δ458-500 were cultured in Ibidi chambers and incubated with 10 μM of the cytosine analogue 5-aza-2'-deoxycytidine (Sigma). Images were acquired with a UltraVIEW VoX spinning disc microscope (PerkinElmer) assembled to an Axio Observer D1 inverted stand (Zeiss) and using a 63×/1.4 NA Plan-Apochromat oil immersion objective.

In vitro peptide pull-down assay

The peptide pull-down assay from nuclear cell extracts of HEK 293T cells expressing UHRF1-GFP fusion constructs was performed as described [72] with the following modifications. C-terminally biotinylated histone peptides were purchased from PSL and are listed in Supplementary information, Table S2. Streptactin beads (Iba) were used for the immobilization of biotinylated peptides in binding buffer (10 mM Tris-HCl, pH 7.5, 300 mM NaCl, 0.5 mM EDTA, 1 mM DTT). After the binding reaction, beads were washed four times with wash buffer (20 mM HEPES pH 7.9, 20% glycerol, 0.2 mM EDTA, 300 mM KCl, 0.1% Triton X-100). Bound fractions were eluted by boiling in 2× Laemmli sample buffer and analyzed by western blot.

Mass spectrometry

The gel was stained with Coomassie and H3 bands were manually excised, propionylated and digested with trypsin as described before [73] with minor modifications. For peptide extraction, gel slices were incubated twice with 50 μl of 50% acetonitrile 0.25% TFA and twice more with 50 μl of acetonitrile. The resulting liquid containing the digested peptides was totally evaporated, redissolved with 15 μl of 0.1% formic acid and stored at -20 °C until further processing.

Tryptic peptides were injected (5 μl) in an Ultimate 3 000 HPLC system (LC Packings Dionex). Samples were desalted online in a C18 microcolumn (300 m i.d. × 5 mm, packed with C18 PepMapTM, 5 μm, 100 Å by LC Packings), and peptides were separated with a gradient from 5% to 60% acetonitrile in 0.1% formic acid over 40 min at 300 nl/min on a C18 analytical column (75 μm i.d. × 15 cm, packed with C18 PepMapTM, 3 μm, 100 Å by LC Packings).

The effluent from the HPLC was directly electrosprayed into a linear trap quadrupole-Orbitrap XL mass spectrometer (Thermo Fisher Scientific). The MS instrument was operated in data-dependent mode. Survey full-scan MS spectra (from *m/z* 300–2 000) were acquired in the Orbitrap with resolution *R* = 60 000 at *m/z* 400 (after accumulation to a “target value” of 500 000 in the linear ion trap). The six most intense peptide ions with charge states between two and four were sequentially isolated to a target value of 10 000 and fragmented by collision-induced dissociation and recorded in the linear ion trap. For all measurements with the Orbitrap detector, three lock-mass ions were used for internal calibration [74].

Typical MS conditions were spray voltage, 1.5 kV; no sheath and auxiliary gas flow; heated capillary temperature, 200 °C; normalized collision-induced dissociation energy 35%; activation $q = 0.25$; and activation time = 30 ms.

Mascot 2.3.02 was used for protein identification with the following settings: Database: Swissprot 57.7; Taxonomy: *Homo sapiens* (human); MS tolerance: 10 ppm; MS/MS tolerance: 0.5 Da; peptide FDR: 0.1; protein FDR: 0.01; minimum peptide length: 5; and variable modifications: propionyl (K, N-term), GlyGly (K).

Quantification of modified H3 18-26 peptides was based on the intensities of the MS1 peaks. The spectra depicted in Figure 4A and 4B were used to determine the exact masses ($m/z \pm 10$ ppm) and used as a reference for further quantification.

Quantitative analysis of DNMT1 subnuclear localization

During late S phase, DNMT1 is enriched in replication foci at chromocenters. In order to quantify the subnuclear distribution of GFP-DNMT1 wt and defined UIM mutants the following procedure was used: confocal z-stacks (0.21 μ m interval) were acquired with identical scan settings in three color channels to visualize replication foci (anti-PCNA staining, 594 nm excitation), DNMT1 localization (GFP-DNMT1 fusions enhanced with GFP-booster (Chromotek), 488 nm excitation) and DNA counterstaining (DAPI, 405 nm excitation). For each color channel, maximum intensity projections were calculated and only GFP-expressing cells were analyzed. Segmentation of replication foci or whole nuclei was performed with the Weka segmentation plugin [75] in Fiji [76]. Training of the classifier was finalized until the result matched the visual impression (Figure 7A). Due to variations in ESC samples, replication foci were segmented using different classifiers for wt or the different UIM mutants. In contrast, for all somatic cells, one classifier was sufficient to segment replication foci. Whole nuclei were segmented by a classifier based on the DAPI signal. After Weka segmentation, the resulting binary masks were filtered using the particle analyzer of Fiji with a circularity value ≥ 0.25 . To select for cells in late S phase, only replication foci ≥ 150 pixel were further analyzed in the ESC samples. In MEF cell samples, only late S phase cells were imaged and analyzed without applying size exclusion for replication foci. Nuclear masks (size $\geq 3\,000$ pixel) were used to quantify the total amount of GFP fusion protein in a single nucleus. Nuclei were further subsegmented by replication foci masks. For each nucleus, the ratio between the mean GFP signals in replication foci relative to the mean GFP signal outside the foci was calculated. Raw data were corrected for background signals by subtracting the modal grey value. Ratios from all nuclei expressing GFP-DNMT1 wt or UIM mutants were visualized as box plots. Numerical calculations and statistical analysis were performed with R [77].

Statistical analysis

Results were expressed as mean values \pm SD or as mean values \pm SEM from the number of biological replicates indicated in the corresponding figure legend.

Acknowledgments

We thank Stefan Jentsch (Max Planck Institute of Biochemistry, Germany) for providing the HA-ubiquitin construct and Peter Becker (Adolf Butenandt Institute, Germany) for the 601 DNA

construct. We are grateful to the following colleagues for providing ESCs and somatic cells: Masahiro Muto and Haruhiko Koseki for mouse E14 wt and *Uhrf1*^{-/-} ESCs; En Li and T. Chen for mouse J1 wt and *Dnmt1*^{-/-}; Thomas Jenuwein for MEF cells; and L. David Spector for providing BHK cells containing a lac operator repeat array. We thank E.M. Baur (Ludwig Maximilians University, Germany) for technical help with the GFP-TS UIM point mutant plasmid constructs. This work was supported by grants from the Deutsche Forschungsgemeinschaft (DFG, SFB1064 A17 to HL and Z03 to AI), the Nanosystem Initiative Munich (NIM to HL) and the Epigenomics Flagship Project (EPIGEN-CNR -IT to IMB). KF and GP were supported by the International Max Planck Research School for Molecular and Cellular Life Sciences (IMPRS-LS). PW, NL and MS are fellows of the Graduate School Life Science Munich (LSM). MS is a fellow of the Integrated Research Training Group (IRTG) of the SFB1064. NL and WQ were also supported by the China Scholarship Council (CSC).

References

- 1 Bird A. DNA methylation patterns and epigenetic memory. *Genes Dev* 2002; **16**:6-21.
- 2 Leonhardt H, Page AW, Weier HU, Bestor TH. A targeting sequence directs DNA methyltransferase to sites of DNA replication in mammalian nuclei. *Cell* 1992; **71**:865-873.
- 3 Chuang LS, Ian HI, Koh TW, Ng HH, Xu G, Li BF. Human DNA-(cytosine-5) methyltransferase-PCNA complex as a target for p21WAF1. *Science* 1997; **277**:1996-2000.
- 4 Schneider K, Fuchs C, Dobay A, et al. Dissection of cell cycle-dependent dynamics of Dnmt1 by FRAP and diffusion-coupled modeling. *Nucleic Acids Res* 2013; **41**:4860-4876.
- 5 Easwaran HP, Schermelleh L, Leonhardt H, Cardoso MC. Replication-independent chromatin loading of Dnmt1 during G2 and M phases. *EMBO Rep* 2004; **5**:1181-1186.
- 6 Schermelleh L, Haemmer A, Spada F, et al. Dynamics of Dnmt1 interaction with the replication machinery and its role in postreplicative maintenance of DNA methylation. *Nucleic Acids Res* 2007; **35**:4301-4312.
- 7 Spada F, Haemmer A, Kuch D, et al. DNMT1 but not its interaction with the replication machinery is required for maintenance of DNA methylation in human cells. *J Cell Biol* 2007; **176**:565-571.
- 8 Margot JB, Aguirre-Arteta AM, Di Giacco BV, et al. Structure and function of the mouse DNA methyltransferase gene: Dnmt1 shows a tripartite structure. *J Mol Biol* 2000; **297**:293-300.
- 9 Fellinger K, Rothbauer U, Felle M, Langst G, Leonhardt H. Dimerization of DNA methyltransferase 1 is mediated by its regulatory domain. *J Cell Biochem* 2009; **106**:521-528.
- 10 Syeda F, Fagan RL, Wean M, et al. The replication focus targeting sequence (RFTS) domain is a DNA-competitive inhibitor of Dnmt1. *J Biol Chem* 2011; **286**:15344-15351.
- 11 Takeshita K, Suetake I, Yamashita E, et al. Structural insight into maintenance methylation by mouse DNA methyltransferase 1 (Dnmt1). *Proc Natl Acad Sci USA* 2011; **108**:9055-9059.
- 12 Achour M, Jacq X, Ronde P, et al. The interaction of the SRA domain of ICBP90 with a novel domain of DNMT1 is involved in the regulation of VEGF gene expression. *Oncogene*

2008; **27**:2187-2197.

13 Felle M, Joppien S, Nemeth A, *et al.* The USP7/Dnmt1 complex stimulates the DNA methylation activity of Dnmt1 and regulates the stability of UHRF1. *Nucleic Acids Res* 2011; **39**:8355-8365.

14 Berkysurek AC, Suetake I, Arita K, *et al.* The DNA Methyltransferase Dnmt1 directly interacts with the SET and RING finger associated (SRA) domain of the multifunctional protein Uhrf1 to facilitate accession of the catalytic center to hemi-methylated DNA. *J Biol Chem* 2013; **289**:379-386.

15 Zhang J, Gao Q, Li P, *et al.* S phase-dependent interaction with DNMT1 dictates the role of UHRF1 but not UHRF2 in DNA methylation maintenance. *Cell Res* 2011; **21**:1723-1739.

16 Bostick M, Kim JK, Esteve PO, Clark A, Pradhan S, Jacobsen SE. UHRF1 plays a role in maintaining DNA methylation in mammalian cells. *Science* 2007; **317**:1760-1764.

17 Sharif J, Muto M, Takebayashi S, *et al.* The SRA protein Np95 mediates epigenetic inheritance by recruiting Dnmt1 to methylated DNA. *Nature* 2007; **450**:908-912.

18 Li E, Bestor TH, Jaenisch R. Targeted mutation of the DNA methyltransferase gene results in embryonic lethality. *Cell* 1992; **69**:915-926.

19 Arita K, Ariyoshi M, Tochio H, Nakamura Y, Shirakawa M. Recognition of hemi-methylated DNA by the SRA protein UHRF1 by a base-flipping mechanism. *Nature* 2008; **455**:818-821.

20 Avvakumov GV, Walker JR, Xue S, *et al.* Structural basis for recognition of hemi-methylated DNA by the SRA domain of human UHRF1. *Nature* 2008; **455**:822-825.

21 Qian C, Li S, Jakoncic J, Zeng L, Walsh MJ, Zhou MM. Structure and hemimethylated CpG binding of the SRA domain from human UHRF1. *J Biol Chem* 2008; **283**:34490-34494.

22 Rottach A, Frauer C, Pichler G, Bonapace IM, Spada F, Leonhardt H. The multi-domain protein Np95 connects DNA methylation and histone modification. *Nucleic Acids Res* 2010; **38**:1796-1804.

23 Cheng J, Yang Y, Fang J, *et al.* Structural insight into coordinated recognition of trimethylated histone H3 lysine 9 (H3K9me3) by the plant homeodomain (PHD) and tandem tudor domain (TTD) of UHRF1 (ubiquitin-like, containing PHD and RING finger domains, 1) protein. *J Biol Chem* 2013; **288**:1329-1339.

24 Citterio E, Papait R, Nicassio F, *et al.* Np95 is a histone-binding protein endowed with ubiquitin ligase activity. *Mol Cell Biol* 2004; **24**:2526-2535.

25 Karagianni P, Amazit L, Qin J, Wong J. ICBP90, a novel methyl K9 H3 binding protein linking protein ubiquitination with heterochromatin formation. *Mol Cell Biol* 2008; **28**:705-717.

26 Xie S, Jakoncic J, Qian C. UHRF1 double tudor domain and the adjacent PHD finger act together to recognize K9me3-containing histone H3 tail. *J Mol Biol* 2012; **415**:318-328.

27 Papait R, Pistore C, Grazini U, *et al.* The PHD domain of Np95 (mUHRF1) is involved in large-scale reorganization of pericentromeric heterochromatin. *Mol Biol Cell* 2008; **19**:3554-3563.

28 Jenkins Y, Markovtsov V, Lang W, *et al.* Critical role of the ubiquitin ligase activity of UHRF1, a nuclear RING finger protein, in tumor cell growth. *Mol Biol Cell* 2005; **16**:5621-5629.

29 Qin W, Leonhardt H, Spada F. Usp7 and Uhrf1 control ubiquitination and stability of the maintenance DNA methyltransferase Dnmt1. *J Cell Biochem* 2011; **112**:439-444.

30 Du Z, Song J, Wang Y, *et al.* DNMT1 stability is regulated by proteins coordinating deubiquitination and acetylation-driven ubiquitination. *Sci Signal* 2010; **3**:ra80.

31 Mudbhary R, Hoshida Y, Chernyavskaya Y, *et al.* UHRF1 overexpression drives DNA hypomethylation and hepatocellular carcinoma. *Cancer Cell* 2014; **25**:196-209.

32 Nishiyama A, Yamaguchi L, Sharif J, *et al.* Uhrf1-dependent H3K23 ubiquitylation couples maintenance DNA methylation and replication. *Nature* 2013; **502**:249-253.

33 Schermelleh L, Spada F, Easwaran HP, *et al.* Trapped in action: direct visualization of DNA methyltransferase activity in living cells. *Nat Methods* 2005; **2**:751-756.

34 Liu X, Gao Q, Li P, *et al.* UHRF1 targets DNMT1 for DNA methylation through cooperative binding of hemi-methylated DNA and methylated H3K9. *Nat Commun* 2013; **4**:1563.

35 LDambacher S, Deng W, Hahn M, *et al.* CENP-C facilitates the recruitment of M18BP1 to centromeric chromatin. *Nucleus* 2012; **3**:101-110.

36 Zolghadr K, Mortusewicz O, Rothbauer U, *et al.* A fluorescent two-hybrid assay for direct visualization of protein interactions in living cells. *Mol Cell Proteomics* 2008; **7**:2279-2287.

37 Hu L, Li Z, Wang P, Lin Y, Xu Y. Crystal structure of PHD domain of UHRF1 and insights into recognition of unmodified histone H3 arginine residue 2. *Cell Res* 2011; **21**:1374-1378.

38 Rajakumara E, Wang Z, Ma H, *et al.* PHD finger recognition of unmodified histone H3R2 links UHRF1 to regulation of euchromatic gene expression. *Mol Cell* 2011; **43**:275-284.

39 Wang C, Shen J, Yang Z, *et al.* Structural basis for site-specific reading of unmodified R2 of histone H3 tail by UHRF1 PHD finger. *Cell Res* 2011; **21**:1379-1382.

40 Frauer C, Leonhardt H. A versatile non-radioactive assay for DNA methyltransferase activity and DNA binding. *Nucleic Acids Res* 2009; **37**:e22.

41 Bestor TH, Ingram VM. Two DNA methyltransferases from murine erythroleukemia cells: purification, sequence specificity, and mode of interaction with DNA. *Proc Natl Acad Sci USA* 1983; **80**:5559-5563.

42 Yoder JA, Soman NS, Verdine GL, Bestor TH. DNA (cytosine-5)-methyltransferases in mouse cells and tissues. Studies with a mechanism-based probe. *J Mol Biol* 1997; **270**:385-395.

43 Jeltsch A. On the enzymatic properties of Dnmt1: specificity, processivity, mechanism of linear diffusion and allosteric regulation of the enzyme. *Epigenetics* 2006; **1**:63-66.

44 Bashtrykov P, Jankevicius G, Jurkowska RZ, Ragozin S, Jeltsch A. The UHRF1 protein stimulates the activity and specificity of the maintenance DNA methyltransferase DNMT1 by an allosteric mechanism. *J Biol Chem* 2014; **289**:4106-4115.

45 Rothbart SB, Dickson BM, Ong MS, *et al.* Multivalent histone engagement by the linked tandem Tudor and PHD domains of UHRF1 is required for the epigenetic inheritance of DNA methylation. *Genes Dev* 2013; **27**:1288-1298.

46 Rothbart SB, Krajewski K, Nady N, *et al.* Association of UHRF1 with methylated H3K9 directs the maintenance of DNA methylation. *Nat Struct Mol Biol* 2012; **19**:1155-1160.

47 Song J, Rechkoblit O, Bestor TH, Patel DJ. Structure of DNMT1-DNA complex reveals a role for autoinhibition in main-

tenance DNA methylation. *Science* 2011; **331**:1036-1040.

48 Kalb R, Latwiel S, Baymaz HI, et al. Histone H2A monoubiquitination promotes histone H3 methylation in Polycomb repression. *Nat Struct Mol Biol* 2014; **21**:569-571.

49 Leeb M, Wutz A. RING1B is crucial for the regulation of developmental control genes and PRC1 proteins but not X inactivation in embryonic cells. *J Cell Biol* 2007; **178**:219-229.

50 Blackledge NP, Farcas AM, Kondo T, et al. Variant PRC1 complex-dependent H2A ubiquitylation drives PRC2 recruitment and polycomb domain formation. *Cell* 2014; **157**:1445-1459.

51 Vire E, Brenner C, Deplus R, et al. The Polycomb group protein EZH2 directly controls DNA methylation. *Nature* 2006; **439**:871-874.

52 Cooper S, Dienstbier M, Hassan R, et al. Targeting polycomb to pericentric heterochromatin in embryonic stem cells reveals a role for H2AK119u1 in PRC2 recruitment. *Cell Reports* 2014; **7**:1456-1470.

53 Kurdistani SK, Tavazoie S, Grunstein M. Mapping global histone acetylation patterns to gene expression. *Cell* 2004; **117**:721-733.

54 Tsai WW, Wang Z, Yiu TT, et al. TRIM24 links a non-canonical histone signature to breast cancer. *Nature* 2010; **468**:927-932.

55 Wang Z, Zang C, Rosenfeld JA, et al. Combinatorial patterns of histone acetylations and methylations in the human genome. *Nat Genet* 2008; **40**:897-903.

56 Raiborg C, Stenmark H. The ESCRT machinery in endosomal sorting of ubiquitylated membrane proteins. *Nature* 2009; **458**:445-452.

57 Lim J, Son WS, Park JK, Kim EE, Lee BJ, Ahn HC. Solution structure of UIM and interaction of tandem ubiquitin binding domains in STAM1 with ubiquitin. *Biochem Biophys Res Commun* 2011; **405**:24-30.

58 Hirano S, Kawasaki M, Ura H, et al. Double-sided ubiquitin binding of Hrs-UIM in endosomal protein sorting. *Nat Struct Mol Biol* 2006; **13**:272-277.

59 Wang Q, Young P, Walters KJ. Structure of S5a bound to monoubiquitin provides a model for polyubiquitin recognition. *J Mol Biol* 2005; **348**:727-739.

60 Frauer C, Rottach A, Meilinger D, et al. Different binding properties and function of CXXC zinc finger domains in Dnmt1 and Tet1. *PLoS One* 2011; **6**:e16627.

61 Meilinger D, Fellinger K, Bultmann S, et al. Np95 interacts with de novo DNA methyltransferases, Dnmt3a and Dnmt3b, and mediates epigenetic silencing of the viral CMV promoter in embryonic stem cells. *EMBO Rep* 2009; **10**:1259-1264.

62 Ho SN, Hunt HD, Horton RM, Pullen JK, Pease LR. Site-directed mutagenesis by overlap extension using the polymerase chain reaction. *Gene* 1989; **77**:51-59.

63 Pichler G, Wolf P, Schmidt CS, et al. Cooperative DNA and histone binding by Uhrf2 links the two major repressive epigenetic pathways. *J Cell Biochem* 2011; **112**:2585-2593.

64 Rothbauer U, Zolghadr K, Tillib S, et al. Targeting and tracing antigens in live cells with fluorescent nanobodies. *Nat Methods* 2006; **3**:887-889.

65 Herce HD, Deng W, Helma J, Leonhardt H, Cardoso MC. Visualization and targeted disruption of protein interactions in living cells. *Nat Commun* 2013; **4**:2660.

66 Rottach A, Kremmer E, Nowak D, et al. Generation and characterization of a rat monoclonal antibody specific for PCNA. *Hybridoma (Larchmt)* 2008; **27**:91-98.

67 Rottach A, Kremmer E, Nowak D, Leonhardt H, Cardoso MC. Generation and characterization of a rat monoclonal antibody specific for multiple red fluorescent proteins. *Hybridoma (Larchmt)* 2008; **27**:337-343.

68 Lei H, Oh SP, Okano M, et al. De novo DNA cytosine methyltransferase activities in mouse embryonic stem cells. *Development* 1996; **122**:3195-3205.

69 Tucker KL, Beard C, Dausmann J, et al. Germ-line passage is required for establishment of methylation and expression patterns of imprinted but not of nonimprinted genes. *Genes Dev* 1996; **10**:1008-1020.

70 Tost J, Gut IG. DNA methylation analysis by pyrosequencing. *Nat Protoc* 2007; **2**:2265-2275.

71 Shechter D, Dormann HL, Allis CD, Hake SB. Extraction, purification and analysis of histones. *Nat Protoc* 2007; **2**:1445-1457.

72 Wysocka J. Identifying novel proteins recognizing histone modifications using peptide pull-down assay. *Methods* 2006; **40**:339-343.

73 Villar-Garea A, Israel L, Imhof A. Analysis of histone modifications by mass spectrometry. *Curr Protoc Protein Sci* 2008; Chapter 14:Unit 14.10.

74 Olsen JV, de Godoy LM, Li G, et al. Parts per million mass accuracy on an Orbitrap mass spectrometer via lock mass injection into a C-trap. *Mol Cell Proteomics* 2005; **4**:2010-2021.

75 Mark Hall EF, Geoffrey Holmes, Bernhard Pfahringer, Peter Reutemann, Ian H. Witten. The WEKA data mining software: an update. *ACM SIGKDD Explorations Newsletter* 2009; **11**:10-18.

76 Schindelin J, Arganda-Carreras I, Frise E, et al. Fiji: an open-source platform for biological-image analysis. *Nat Methods* 2012; **9**:676-682.

77 R Core Team (2014). R: a language and environment for statistical computing. R Foundation for Statistical Computing, Vienna, Austria. URL <http://www.R-project.org/>.

78 Robert X, Gouet P. Deciphering key features in protein structures with the new ENDscript server. *Nucleic Acids Res* 2014; **42**:W320-W324.

(**Supplementary information** is linked to the online version of the paper on the *Cell Research* website.)



This work is licensed under the Creative Commons Attribution-NonCommercial-No Derivative Works 3.0 Unported License. To view a copy of this license, visit <http://creativecommons.org/licenses/by-nc-nd/3.0>

Supplementary information, Data S1

Materials and methods

Antibodies

For detection of (GFP-)DNMT1 by western blot, a mouse anti-DNMT1 antibody (pATH52 [1, 2]) was used. Equal loading was confirmed by immunoblotting with a specific anti-Lamin B1 (Abcam) or anti- β -Actin (Sigma) antibody. The rabbit anti-H2A antibody was purchased from Millipore.

In vitro DNA methylation assay

For analyses of *in vitro* DNA methylation activity, GFP-DNMT1 was purified by immunoprecipitation from HEK 293T extracts. The concentration of GFP-DNMT1 in the bound fractions was measured by fluorescent read out. In order to get enough unmodified DNA templates, the 601 DNA sequences were amplified with the primers: TGCATGTATTGAACAG (forward) and TGCACAGGATGTATATATC (reverse). 3 μ g of GFP-DNMT1 were incubated with 88 ng of DNA template in methylation buffer containing 160 μ M SAM and 100 ng/ μ l BSA at 37°C for 3 hours. After inactivation of the reaction at 65°C for 30 min, the DNA was isolated with a Nucleospin PCR cleaning kit (Macherey-Nagel) and bisulfite treated with EZ DNA Methylation-Gold Kit (Zymo research). Primer sequences for the 601 DNA were TGTATGTATTGAATAG (forward primer) and TACACAAATATATATATC (reverse primer). For amplification we used Qiagen Hot Start Polymerase in 1x Qiagen Hot Start Polymerase buffer supplemented with 0.2 mM dNTPs, 0.2 μ M forward primer, 0.2 μ M reverse primer, 1.3 mM Betaine (Sigma) and 60 mM Tetramethylammonium-chloride (TMAC, Sigma). Pyrosequencing reactions were carried out by Varionostic GmbH (Ulm).

Preparation of hemimethylated DNA substrates

To prepare the hemimethylated DNA, an efficient method for long heteroduplex DNA was used as described [3]. One pair of modified PCR primers were synthesized, which are labeled with phosphate at 5'-end, 5'-phosphorylated-TGCATGTATTGAACAG-3' and 5'-phosphorylated-TGCACAGGATGTATATATC-3'. To get single and upper strand DNA, the DNA was amplified with the reverse primer labeled with phosphate at the 5'-end, following a lambda-nuclease digestion (NEB). The same procedure is required for making lower strand DNA. To prepare the methylated lower strand DNA, one more step, *in vitro* methylation by bacterial methyltransferase M.SssI (NEB), is required before treatment with the lambda-nuclease. In the end, equal amounts of upper and lower strand DNA were mixed and incubated at 95°C for 5 min, followed by annealing. To get rid of contamination from double strand DNA after lambda-nuclease treatment, the hydroxyapatite chromatography was carried out. Hydroxyapatite column (Sigma) was packed according to the manufacturer's instructions and the single stranded DNA was eluted by elution buffer containing 150 mM sodium phosphate.

In vitro DNA binding assays

In vitro DNA binding assays were performed as described previously [4]. Briefly, two double stranded DNA oligonucleotides labeled with different ATTO fluorophores were used as substrates in direct competition. DNA oligonucleotide substrates with identical sequence contained an unmodified or hemimethylated cytosine at a single, central CpG site (UMB: unmethylated binding substrate, ATTO550; HMB: hemimethylated binding substrates, ATTO647N; Supplementary Table S3). GFP fusion proteins were expressed in HEK 293T cells and immunoprecipitated using the GFP-Trap (Chromotek). Immobilized UHRF1-GFP wt and mutants were washed three times before incubation with DNA substrates at a final concentration of 160 nM each. After removal of unbound substrates, protein amounts (GFP fluorescence) and bound DNA were measured with an Infinite M1000 plate reader (Tecan).

In vivo autoubiquitination assay

The *in vivo* autoubiquitination assay of UHRF1-GFP was performed as described before [5]. The resulting ubiquitination levels were detected with a specific mouse monoclonal anti-HA antibody (12CA5) and quantified using Image J and a statistical Student's t-test analysis. Equal amounts of (UHRF1-)GFP in the bound fraction were verified by immunoblotting with a specific anti-GFP antibody (Chromotek).

Slot blot analysis

To quantify global DNA methylation levels, the Bio-Rad slot blot system was used according to the manufacturer's instruction. Prior to loading on a Nitrocellulose membrane (Amersham), genomic DNA was denatured in 6x SSC buffer for 10 min at 95°C and incubated for 10 min on ice. The membrane was crosslinked, blocked with 5% milk and immunostained with specific rabbit anti-ssDNA (Eurogentec) and mouse anti-5mC (IBL) antibodies. Quantification was performed using the ImageJ gel analysis tool.

In vitro histone tail peptide binding assay

The *in vitro* histone tail peptide binding assay was performed as described before [6] with the following modification. GFP fusion proteins were equalized to a GFP concentration of 130 nM prior to immunoprecipitation with the GFP-Trap. The TAMRA-labeled H3 peptides used in this assay are listed in Supplementary Table S2.

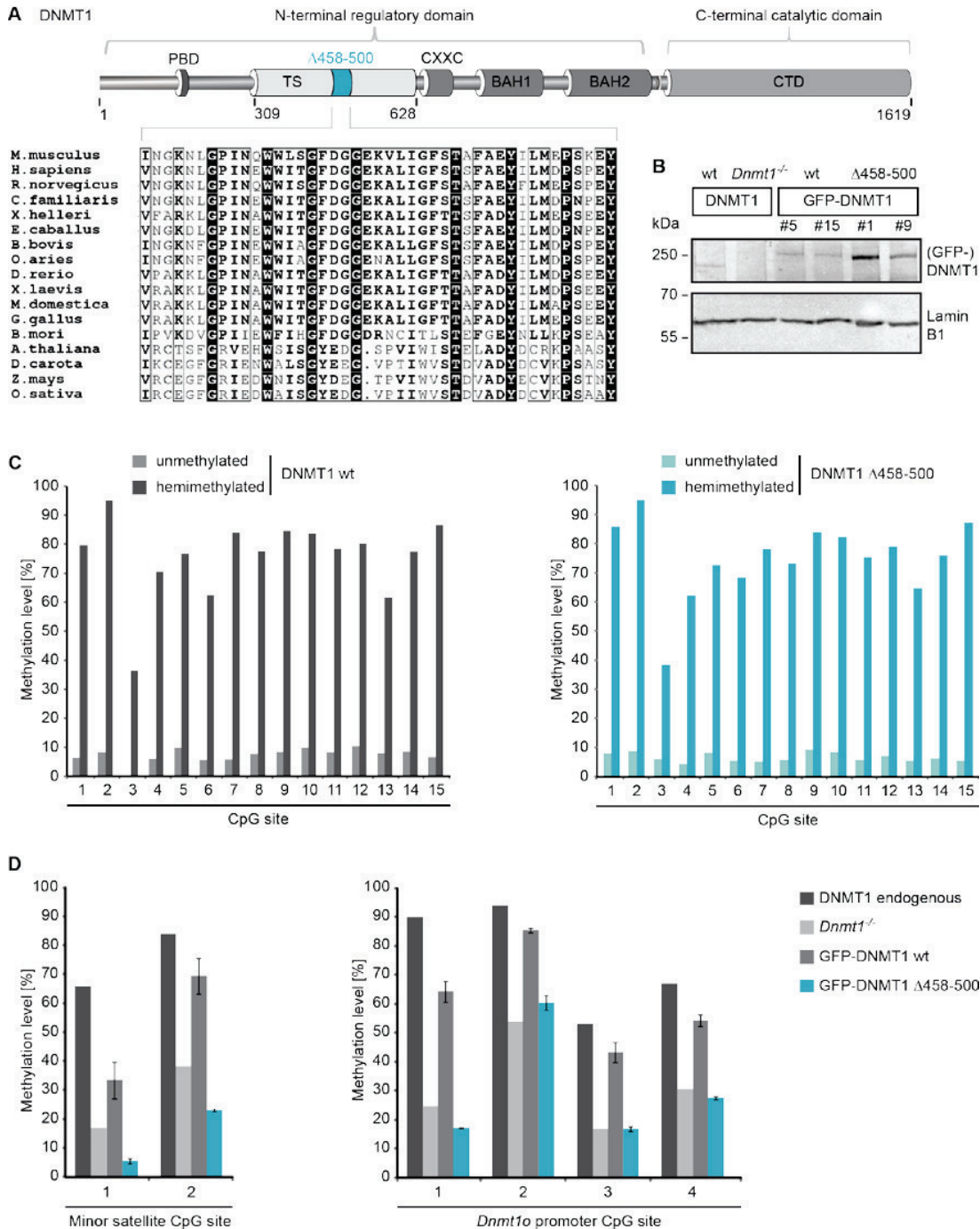
Ubiquitinated histone H3 binding experiment

For ubiquitinated H3 binding experiment, HEK 293T cells were incubated with 2 mM N-Ethylmaleimide (NEM, AppliChem) for 10 min before harvesting and were treated in hypotonic buffer (10 mM Tris-HCl pH 8, 10 mM KCl, 1.5 mM MgCl₂, 1 mM DTT and 1x Protease Inhibitor, 2 mM PMSF) for 10 min on ice to isolate the intact nuclei. Nuclei resuspended in MNase digestion buffer (10 mM Tris-HCl, pH 7.4, 10 mM NaCl, 3 mM CaCl₂, 0.1% NP-40, 1x Protease Inhibitor (Serva), 2 mM PMSF) were digested with 40 U/ml MNase at 37°C for 5 min to get mononucleosomes.

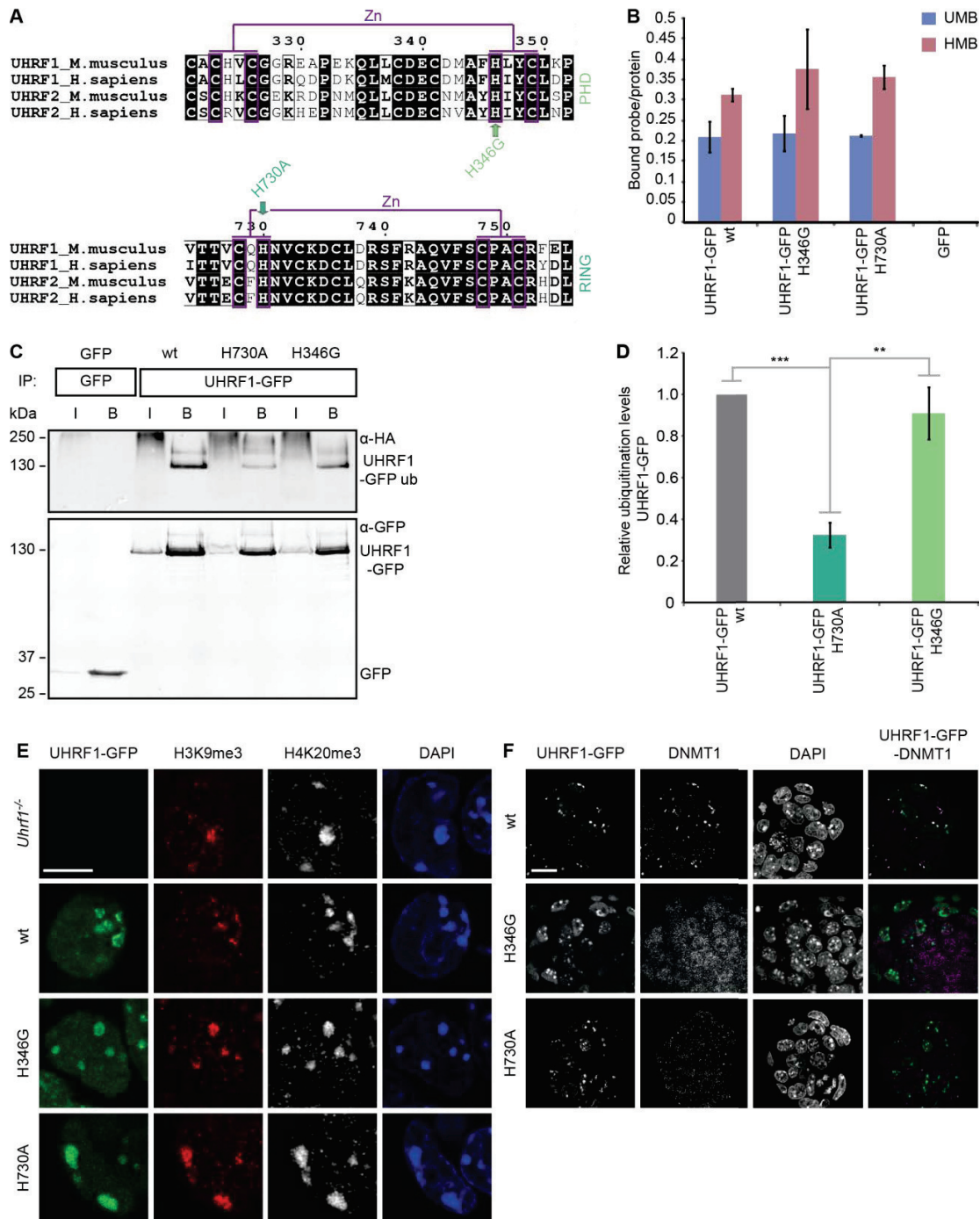
GFP-DNMT1 and its mutants were immobilized on the GFP-Trap and incubated with equal amount of mononucleosomes for 2 hours. After washing steps, the bound fractions were analyzed by western blot.

Supplementary references

- 1 Bestor TH. Activation of mammalian DNA methyltransferase by cleavage of a Zn binding regulatory domain. *EMBO J* 1992; **11**:2611-2617.
- 2 Li E, Bestor TH, Jaenisch R. Targeted mutation of the DNA methyltransferase gene results in embryonic lethality. *Cell* 1992; **69**:915-926.
- 3 Thomas E, Pingoud A, Friedhoff P. An efficient method for the preparation of long heteroduplex DNA as substrate for mismatch repair by the *Escherichia coli* MutHLS system. *Biol Chem* 2002; **383**:1459-1462.
- 4 Frauer C, Leonhardt H. A versatile non-radioactive assay for DNA methyltransferase activity and DNA binding. *Nucleic Acids Res* 2009; **37**:e22.
- 5 Qin W, Leonhardt H, Spada F. Usp7 and Uhrf1 control ubiquitination and stability of the maintenance DNA methyltransferase Dnmt1. *J Cell Biochem* 2011; **112**:439-444.
- 6 Pichler G, Wolf P, Schmidt CS et al. Cooperative DNA and histone binding by Uhrf2 links the two major repressive epigenetic pathways. *J Cell Biochem* 2011; **112**:2585-2593.
- 7 Robert X, Gouet P. Deciphering key features in protein structures with the new ENDscript server. *Nucleic Acids Res* 2014; **42**:W320-324.
- 8 Hirano S, Kawasaki M, Ura H et al. Double-sided ubiquitin binding of Hrs-UIM in endosomal protein sorting. *Nat Struct Mol Biol* 2006; **13**:272-277.

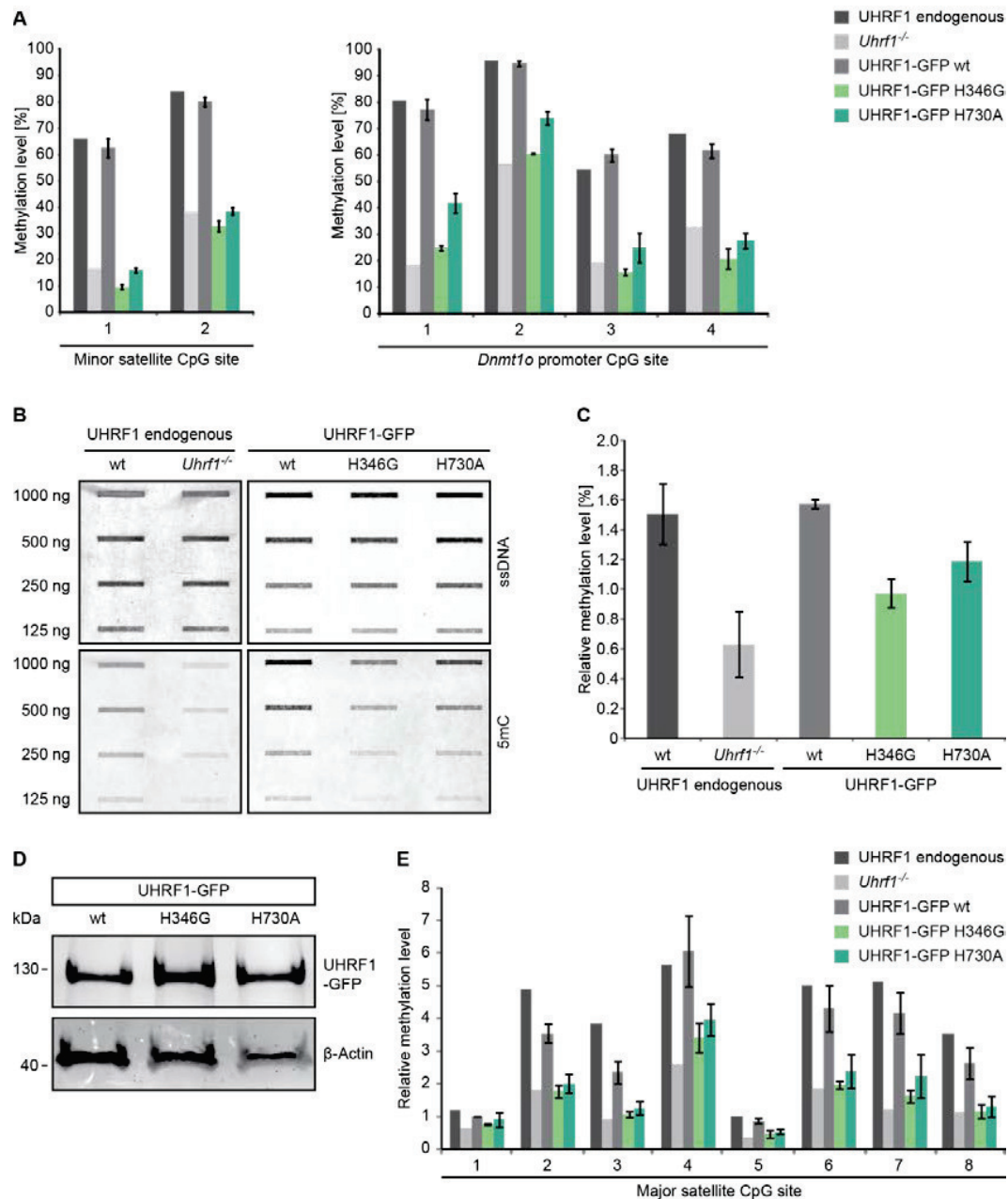


Supplementary information, Figure S1 GFP-DNMT1 carrying a deletion of amino acids 458-500 in the TS domain is still active *in vitro*, but inactive *in vivo*. **(A)** Schematic outline of DNMT1 domains and the TS domain deletion (Δ458-500). The deleted region comprises a conserved core of the TS domain showing high sequence similarities among higher eukaryotes. The alignment was generated using ESPript [7]. **(B)** Expression levels of GFP-DNMT1 wt (clones #5 and #15) and the TS domain deletion mutant (Δ458-500, clones #1 and #9) in stable ESC lines were compared to the endogenous DNMT1 level in J1 wt cells. Lamin B1 is shown as loading control. DNMT1 was detected with a specific anti-DNMT1 antibody. **(C)** *In vitro* methylation assay of GFP-DNMT1 wt and Δ458-500 mutant using unmodified or hemimethylated DNA as a substrate. **(D)** Local DNA methylation analyses at minor satellite repeats and the *Dnmt1o* promoter. CpG methylation levels of mouse J1 *Dnmt1*^{-/-} ESCs stably expressing GFP-DNMT1 wt or Δ458-500 mutant constructs were analyzed by bisulfite treatment of genomic DNA, PCR amplification and direct pyrosequencing. The methylation level of the J1 wt cell line (endogenous DNMT1) and untransfected J1 *Dnmt1*^{-/-} cells are shown for comparison. Displayed are mean values ± SD from two different clones.

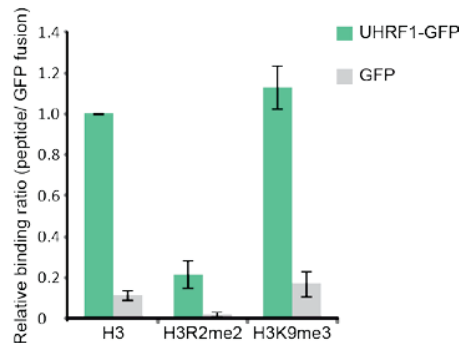


Supplementary information, Figure S2 The UHRF1-GFP PHD and RING domain mutants preserve their preference for hemimethylated DNA and their heterochromatin association, but cannot recruit endogenous DNMT1 to heterochromatin. **(A)** Primary sequence alignment of mouse and human UHRF1 and UHRF2 at regions of the PHD and RING domain, respectively. Note that the mutations affect conserved amino acids contributing to the coordination of zinc (Zn) ions. **(B)** *In vitro* DNA binding assay. The binding of immunoprecipitated UHRF1-GFP wt or PHD (H346G) and RING domain (H730A) mutants to either un- (UMB) or hemimethylated (HMB) fluorescently labeled double stranded oligonucleotide probes was tested in direct competition. Shown are mean fluorescence intensity ratios of bound probe over bound GFP fusion of three independent experiments \pm SD. GFP was used as negative control. **(C)** *In vivo* autoubiquitination assay of UHRF1-GFP. Wt or PHD and RING domain mutant constructs were transiently co-expressed with HA-ubiquitin in HEK 293T cells and UHRF1-GFP was immunoprecipitated using the GFP-Trap. Ubiquitination levels were detected by immunoblotting with an anti-HA antibody and bound fractions were verified with a specific anti-GFP antibody. GFP was used as negative control. I, input; B, bound. One representative blot of three independent replicates is depicted. **(D)** Quantification of the *in vivo* autoubiquitination activity of UHRF1-GFP wt or PHD and RING domain mutant

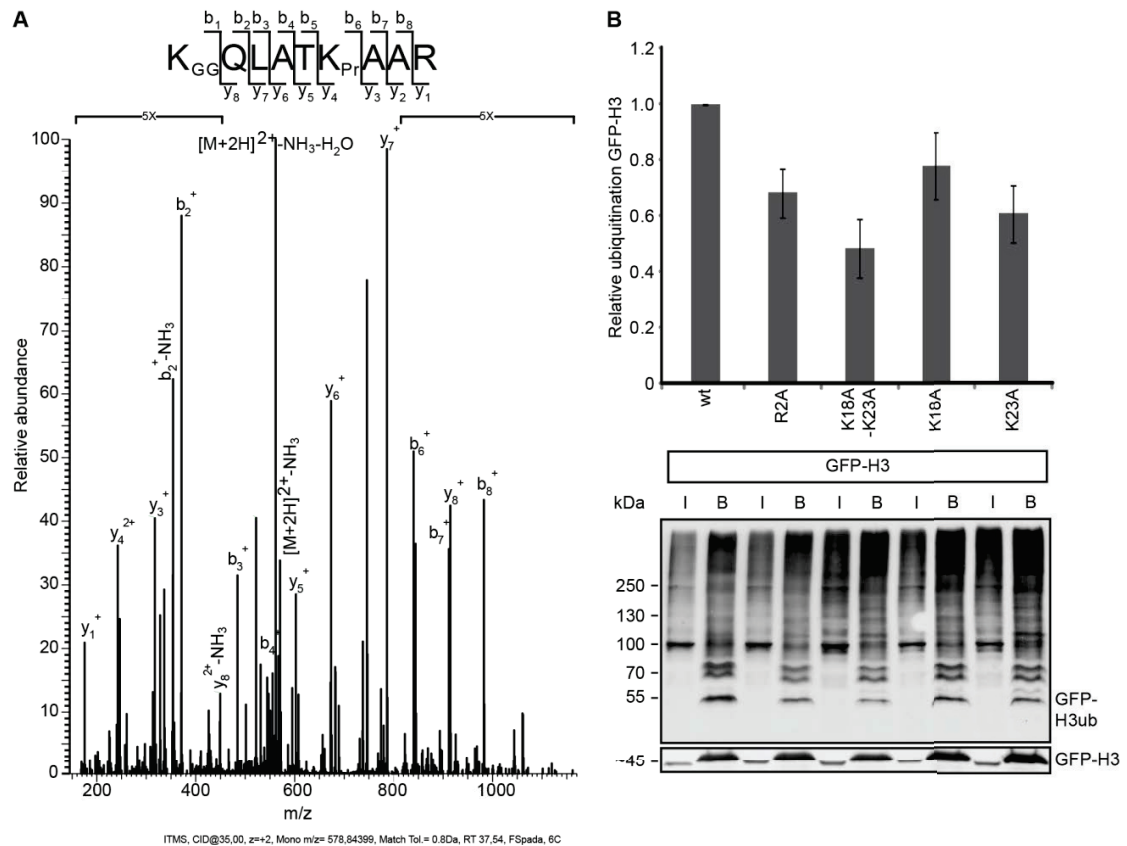
constructs depicted in (C). Shown are mean values \pm SD of three independent biological replicates analyzed using ImageJ and normalized to the ubiquitination level of the UHRF1-GFP wt construct. Differences between the UHRF1-GFP wt or PHD mutant and the RING domain mutant were analyzed using a Student's t-test and considered statistically significant for $P < 0.01$ (**) and highly significant for $P < 0.001$ (***) (E) and (F) Confocal mid sections of fixed E14 *Uhrf1*^{-/-} ESCs stably expressing UHRF1-GFP wt or PHD (H346G) and RING domain (H730A) mutant constructs. (E) H3K9me3 and H4K20me3 were stained with specific antibodies as markers for heterochromatin and DNA was counterstained with DAPI. Scale bar, 5 μ m. (F) Endogenous DNMT1 in ESCs stably expressing UHRF1-GFP wt or its PHD and RING domain mutants was stained by a specific antibody and DNA was counterstained with DAPI. Scale bar, 10 μ m.



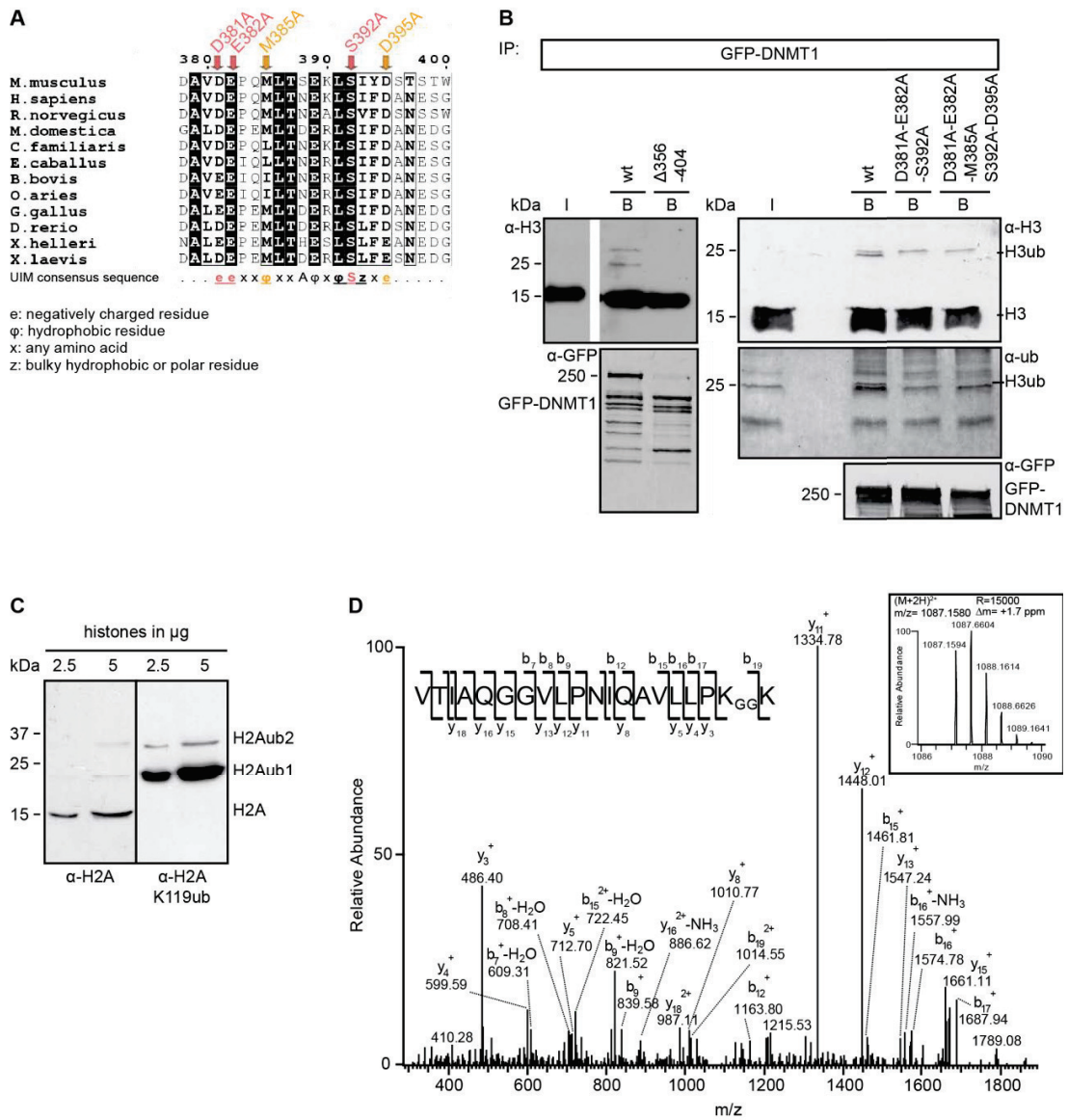
Supplementary information, Figure S3 The UHRF1-GFP PHD and RING domain mutants cannot mediate DNA remethylation in mouse E14 *Uhrf1*^{-/-} ESCs. **(A)** Local DNA methylation analyses at minor satellite repeats and the *Dnmt1o* promoter. CpG methylation levels of mouse E14 *Uhrf1*^{-/-} ESCs stably expressing UHRF1-GFP wt or PHD (H346G) and RING domain (H730A) mutant constructs were analyzed by bisulfite treatment of genomic DNA, PCR amplification and direct pyrosequencing. The methylation level of E14 wt ESCs (endogenous UHRF1) and untransfected E14 *Uhrf1*^{-/-} cells are shown for comparison. Mean values \pm SD from two different clones were calculated. **(B)** and **(C)** Global DNA methylation analysis of stable UHRF1-GFP wt or PHD and RING domain mutant cell lines compared to E14 wt ESCs expressing endogenous UHRF1 and E14 *Uhrf1*^{-/-} ESCs. **(B)** Slot blot analysis using a dilution series of genomic DNA and immunodetection with specific anti-single stranded (ss) DNA and anti-5-methylcytosine (5mC) antibodies. A representative slot blot of technical duplicates is shown. **(C)** The 5mC signals relative to the signals of ssDNA were quantified using the ImageJ gel analysis tool. Relative global DNA methylation levels are indicated as mean values \pm SD of technical duplicates. **(D)** Expression analysis of UHRF1-GFP wt or PHD and RING domain mutants after transient transfection in E14 *Uhrf1*^{-/-} ESCs and FACS sorting. Fusion proteins were detected with a specific anti-GFP antibody and β-Actin serves as a loading control. **(E)** Local DNA methylation analyses of E14 *Uhrf1*^{-/-} ESCs transiently expressing GFP-UHRF1 wt or PHD (H346G) and RING domain (H730A) mutant constructs. CpG methylation levels at the major satellite repeats were analyzed by bisulfite treatment of genomic DNA, PCR amplification and direct pyrosequencing. Shown are mean values \pm SD from three independent experiments normalized to the value of UHRF1-GFP wt at the first CpG site.



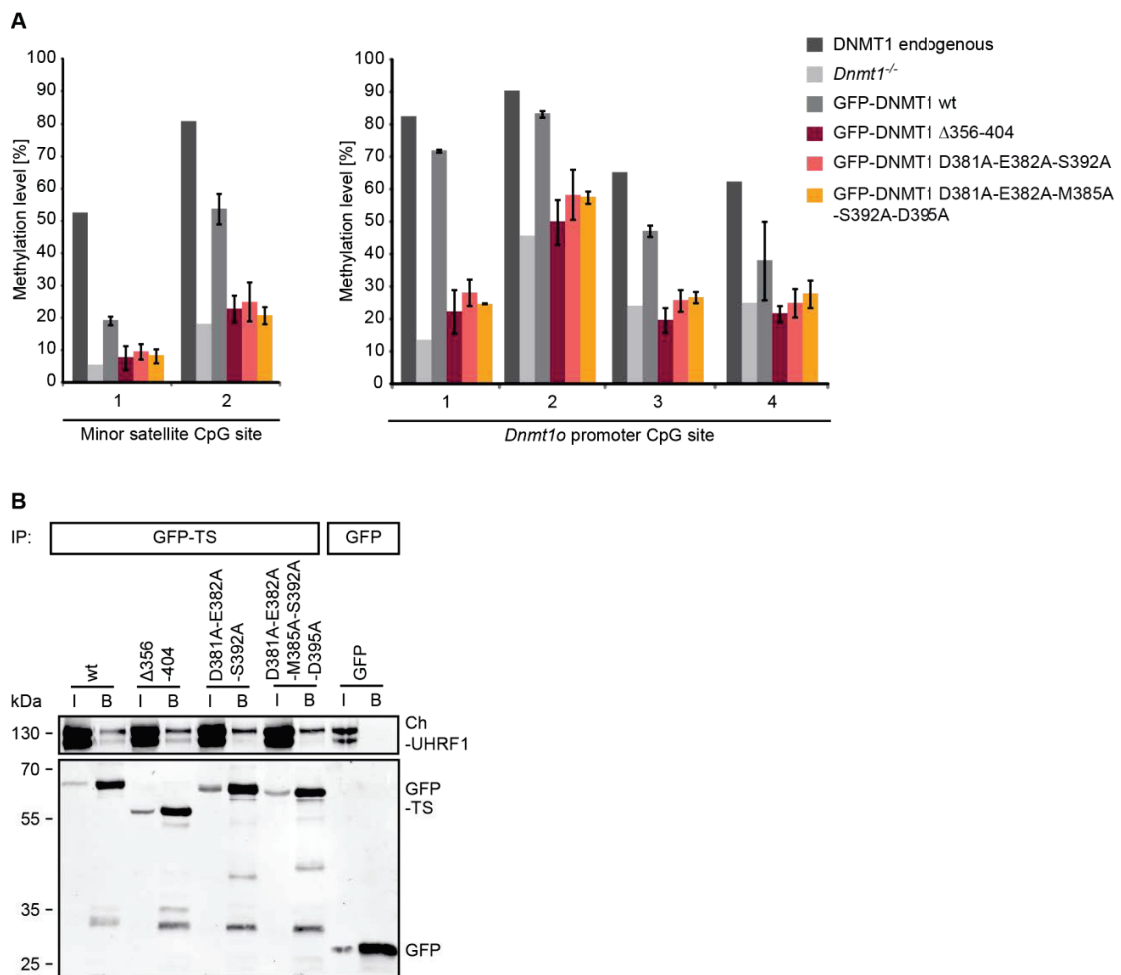
Supplementary information, Figure S4 Histone H3 binding by UHRF1-GFP is sensitive to R2 methylation. Fluorescent *in vitro* histone tail peptide binding assay of UHRF1-GFP using TAMRA labeled H3 tails carrying no modification (H3), an asymmetrically dimethylated arginine 2 (H3R2me2) or a trimethylated lysine 9 (H3K9me3). Shown are mean values of the relative binding ratio of histone tail peptides over GFP fusion proteins from five independent experiments \pm SEM. GFP was used as negative control.



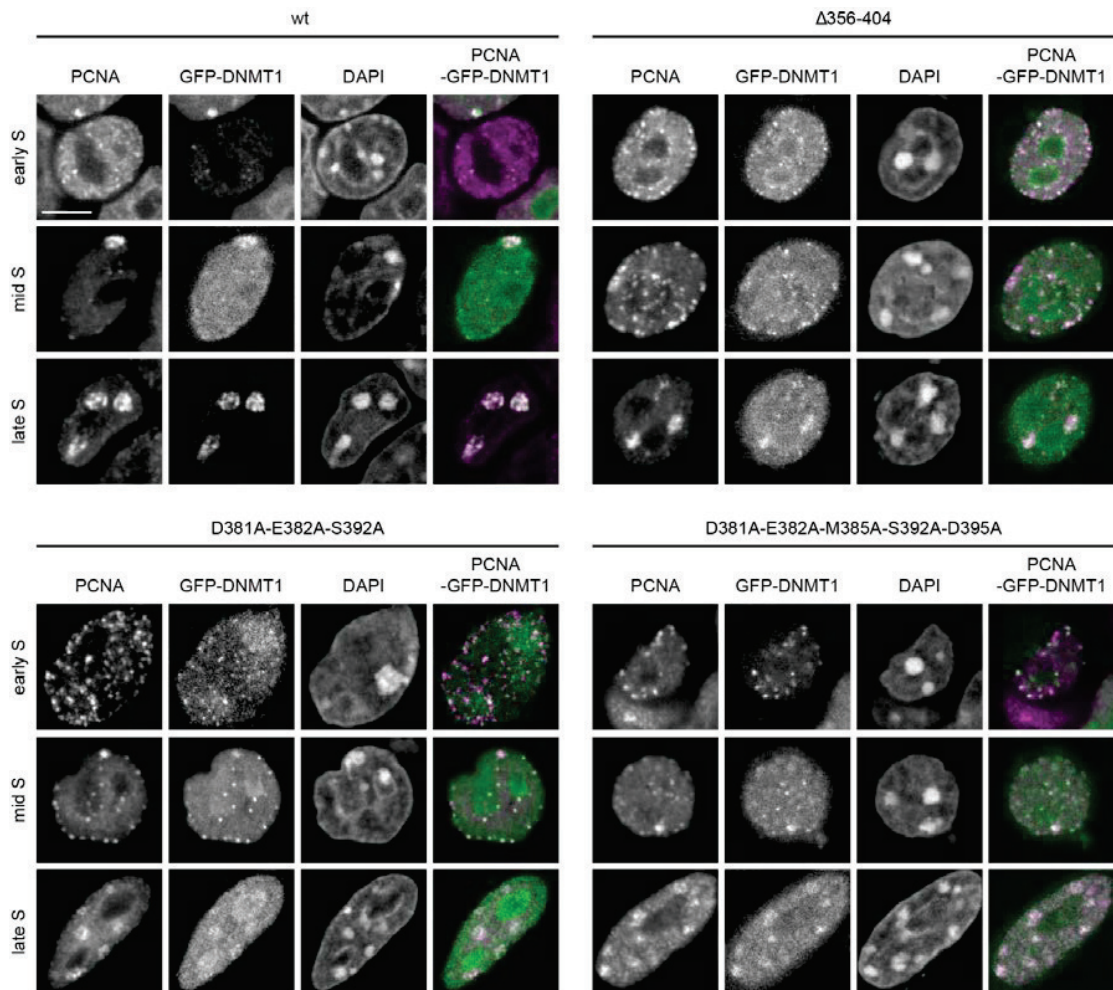
Supplementary information, Figure S5 H3 histone tail ubiquitination and dependence on R2. **(A)** After expression of UHRF1-GFP and HA-Ubiquitin in HEK 293T cells, acid extracted ubiquitinated histones were immunoprecipitated with an anti-HA antibody and analyzed by mass spectrometry. The Collision-induced dissociation (CID) MS/MS spectrum of the histone H3 18-26 peptide shows ubiquitination (GG) at the K18 residue and no modification (Pr) at the K23 residue. Detailed information is provided in the method section. **(B)** Mapping and quantification of UHRF1 ubiquitination target sites in H3 N-terminal tails and dependence of the ubiquitination on R2. GFP-H3 constructs carrying R2A, K18A, K23A or K18A-K23A mutations were transiently co-expressed in HEK 293T cells with HA-ubiquitin and after immunoprecipitation with the GFP-Trap, ubiquitinated GFP-H3 was detected by western blot with an anti-HA antibody. Equal loading of GFP-H3 is shown by the anti-GFP blot below. I, input; B, bound. Quantifications were performed with ImageJ. Shown are mean values \pm SEM of four to five independent experiments.



Supplementary information, Figure S6 DNMT1 UIM deletion and point mutants are defective in ubiquitinated H3 binding. **(A)** Primary sequence alignment of the ubiquitin interacting motif (UIM) in the TS domain of DNMT1 from different species. The consensus sequence for single-sided UIMs [8] and the UIM mutations used in this study (D381A-E382A-S392A, D381A-E382A-M385A-S392A-D395A) are indicated. **(B)** Ubiquitinated histone H3 binding assay. After extraction of mononucleosomes from HEK 293T cells, the extracts were incubated with GFP-DNMT1 wt or mutants immobilized on the GFP-Trap and the bound fractions were analyzed with specific anti-H3, anti-ubiquitin and anti-GFP antibodies. **(C)** Characterization of the anti-H2AK119ub antibody (New England Biolabs) in comparison to the antibody against non ubiquitinated H2A (Millipore) by immunoblotting. 2.5 or 5 μ g of acid extracted histones were loaded to analyze the specificity of the antibodies. H2Aub1, monoubiquitinated H2A; H2Aub2, diubiquitinated H2A. **(D)** Identification of the H2A 101-120 peptide carrying ubiquitination (GG) on K119 by LC-MS/MS. The sample was prepared by excision of a band from acid extracted histones corresponding to H2Aub1 in the immunoblot from (C). MS2 fragmentation spectrum of the precursor ion is shown in the inset. The displayed b and y ion series generated by CID fragmentation of the H2A 101-120 peptide modified with GG on K119 provided highly confident identification and post translational modification localization. Inset: mass, charge and measurement error determination of the H2A peptide of interest. Displayed is the isotopic distribution of the H2A peptide from which the mass-to-charge ratio (m/z) and the charge (2+) were obtained. Δm : difference between the expected and the measured masses, R : resolution of the MS measurement.



Supplementary information, Figure S7 DNMT1 UIM deletion and point mutants still interacting with UHRF1, affect maintenance DNA methylation. **(A)** Local DNA methylation analyses of *Dnmt1*^{-/-} ESCs transiently expressing GFP-DNMT1 wt or Δ356-404 and UIM point mutants (D381A-E382A-S392A, D381A-E382A-M385A-S392A-D395A). CpG methylation levels at the minor satellite repeats and the *Dnmt1o* promoter were analyzed by bisulfite treatment of genomic DNA, PCR amplification and direct pyrosequencing. Methylation levels of untransfected J1 *Dnmt1*^{-/-} cells are shown for comparison. Mean values ± SD of two to four independent experiments were calculated. **(B)** Co-immunoprecipitation assay of GFP-TS and Ch-UHRF1 *in vitro*. GFP-DNMT1 TS domain wt or UIM mutants were co-expressed with Ch-UHRF1 and after co-immunoprecipitation using the GFP-Trap, the bound fractions were detected by western blot with specific antibodies against GFP and Ch. GFP was used as negative control. I, input; B, bound.



Supplementary information, Figure S8 DNMT1 UIM mutants show only weak association with PCNA-stained replication sites especially in late S phase. Confocal mid sections of GFP-DNMT1 wt or Δ 356-404 and UIM point mutants (D381A-E382A-S392A, D381A-E382A-M385A-S392A-D395A) transiently expressed in J1 *Dnmt1*^{-/-} ESCs with respect to replicating DNA stained with a specific anti-PCNA antibody. Chromatin was counterstained with DAPI. Scale bar, 5 μ m.

Supplementary information, Table S1 PCR primers for bisulfite PCR and pyrosequencing.

Name	Sequence
F-major satellites	5' AAAATGAGAAATATTTATTTG 3'
R-major satellites biotinylated	5' GAGAAATATATACTTTAGGA 3'
F-outer <i>skeletal α-actin</i>	5' AGTTGGGGATATTTTATA 3'
R-outer <i>skeletal α-actin</i>	5' TGGGAAGGGTAGTAATATT 3'
F-inner <i>skeletal α-actin</i>	5' TTTTGGTTAGTGTAGGAGAT 3'
R-inner <i>skeletal α-actin</i> biotinylated	5' TGGGAAGGGTAGTAATATT 3'
F- <i>Dnmt1o</i> -2-1	5' GTTGTCCCCGGGGGGT 3'
R-outer <i>Dnmt1o</i> -2-2	5' CAACCTTAACAACACAACAAATA 3'
R-inner <i>Dnmt1o</i> -2-3 biotinylated	5' CAACTATACACTATCAAATAACCTA 3'
F-minor satellites	5' TAATGAGTTATAATGAGAAA 3'
R-minor satellites biotinylated	5' ATATACACTATTCTACAAAT 3'

Supplementary information, Table S2 Sequence of histone H3 1-20 peptides used for the histone peptide pull-down and histone peptide binding assays. X3, trimethylated lysine; Z, acetylated lysine; X2a, asymmetrically dimethylated arginine.

Name	Sequence	Label
H3	ARTKQTARKSTGGKAPRKQLK	
H3K9me3	ARTKQTARX3STGGKAPRKQLK	Biotin at C-terminus
H3K9ac	ARTKQTARZSTGGKAPRKQLK	
H3	ARTKQTARKSTGGKAPRKQLK	
H3K9me3	ARTKQTARX3STGGKAPRKQLK	TAMRA at C-terminus
H3R2me2	AX2aTKQTARKSTGGKAPRKQLK	

Supplementary information, Table S3 DNA oligonucleotides used for the preparation of double stranded probes for *in vitro* DNA binding assays with the primer extension reaction. M, 5-methylcytosine.

Oligo name	DNA sequence
CG-up	5' CTCAACAACTAACTACCATCCGGACCAGAAGAGTCATCATGG 3'
MG-up	5' CTCAACAACTAACTACCATCMGGACCAGAAGAGTCATCATGG 3'
Fill-In-550	5' ATTO550-CCATGATGACTCTTCTGGTC 3'
Fill-In-647N	5' ATTO647N-CCATGATGACTCTTCTGGTC 3'
Substrate	Combination of oligos in the primer extension reaction
UMB-550	CG-up + Fill-In-550
HMB-647N	MG-up + Fill-In-647N

2.7 Mutations of the DNMT1 TS domain found in HSAN-IE patients disrupt interaction with UHRF1, affect subnuclear targeting and lead to cell cycle-dependent destabilization

Mutations of the DNMT1 TS domain found in HSAN-IE patients disrupt interaction with UHRF1, affect subnuclear targeting and lead to cell cycle-dependent destabilization

Patricia Wolf¹, Katrin Schneider^{1,a}, Martha Smets¹, Stephanie Link¹, Veronika Solis^{1,2}, Karin Fellinger^{1,b}, Daniela Meilinger¹, Elisabeth Kremmer³, Weihua Qin¹ and Heinrich Leonhardt^{1*}

¹Department of Biology II and Center for Integrated Protein Science Munich (CIPSM), Ludwig Maximilian University of Munich, Großhaderner Str. 2, 82152 Planegg-Martinsried, Germany

²Max Planck Institute of Neurobiology, Am Klopferspitz 18, 82152 Martinsried, Germany

³Helmholtz Center Munich, German Research Center for Environmental Health (GmbH), Institute of Molecular Immunology, Marchioninistr. 25, 81377 Munich, Germany

Current addresses:

^aDefiniens AG, Bernhard-Wicki-Straße 5, 80636 München, Germany

^bIntervet International GmbH, Unterschleißheim, Germany

*Correspondence: Tel: +49 89 2180 74232; Fax: +49 89 2180 74236, h.leonhardt@lmu.de (H.L.)

ABSTRACT

Among the writers of epigenetic marks, DNMT1 is the key enzyme responsible for maintaining DNA methylation after replication. PCNA and UHRF1 are important binding partners of DNMT1 recruiting the enzyme to its substrate. Remarkably, the TS domain known to target DNMT1 to pericentromeric heterochromatin is affected by various mutations in HSAN-IE and ADCA-DN patients. The disease mechanisms and its molecular basis, however, remain elusive. We performed functional assays using two HSAN-IE associated DNMT1 TS mutants and found a reduced methylation activity in mouse ESCs. Importantly, the TS domain-mediated interaction with UHRF1 was diminished and mutant DNMT1 was not properly recruited to late replicating chromatin. Similarly, DNA methylation defects were observed, when the DNMT1 interacting domains in UHRF1, the Ubl and the SRA domain, were deleted. In addition, we found that HSAN-IE associated DNMT1 mutants showed faster protein kinetics and decreased protein stability, especially in late S and G2 phase. This study provides strong evidence for a central importance of the TS domain in regulating DNA methylation by DNMT1 and contributes to understanding the molecular basis for methylation defects observed in HSAN-IE patients.

INTRODUCTION

Epigenetic mechanisms are crucial for the regulation of gene expression during development and differentiation. Tissue-specific DNA methylation patterns established during development are faithfully propagated to future somatic cell generations by the action of the DNA methyltransferase 1 (DNMT1) (Bird 2002). After replication, DNMT1 copies DNA methylation marks in a CpG context from the mother strand to the daughter strand by catalytic activity of its C-terminal domain (CTD). The complex regulation of enzyme targeting and activation is, however, mediated by the N-terminal domain (NTD) harboring distinct subdomains. The association of DNMT1 with replication sites relies on binding of the proliferating cell nuclear antigen (PCNA) binding domain (PBD) to PCNA (Leonhardt et al. 1992; Chuang et al. 1997; Rountree et al. 2000). Accordingly, DNMT1 shows a cell cycle-dependent localization in mouse nuclei (Leonhardt et al. 1992). In late S phase, when constitutive heterochromatin like the major satellite repeats is replicated, DNMT1 is clearly enriched at chromocenters. Heterochromatin binding during G2 is mediated by the targeting sequence (TS) domain independently from DNA replication probably ensuring a thorough propagation of DNA methylation patterns to the progeny (Easwaran et al. 2004). DNMT1 interacts with ubiquitin-like, containing PHD and RING finger domains 1 (UHRF1, also known as 95-kDa mouse nuclear protein (Np95)), an important cofactor of maintenance DNA methylation that targets DNMT1 to its substrate consisting of hemimethylated CpG sites (Bostick et al. 2007). Interaction with DNMT1 has been reported to be mediated by the SET and RING-associated (SRA) domain of UHRF1 (Achour et al. 2008; Felle et al. 2011). UHRF1 also binds to hemimethylated DNA via its SRA domain (Bostick et al. 2007; Sharif et al. 2007; Arita et al. 2008; Avvakumov et al. 2008; Qian et al. 2008) and to methylated histone H3K9 via its tandem Tudor domain (TTD) and plant homeodomain (PHD) (Citterio et al. 2004; Karagianni et al. 2008; Rottach et al. 2010; Cheng et al. 2013). By collaborative readout of methylated histones and hemimethylated DNA, UHRF1 serves as a bridge between chromatin and DNMT1 in order to regulate methylation of the newly synthesized strand after replication (Liu et al. 2013). Besides recruitment of DNMT1 to its target sites by intermolecular protein-protein binding, also changes in intramolecular interactions serve as a prerequisite for DNMT1 enzymatic activity. Firstly, in complex with unmethylated DNA, the linker between the zinc finger (CXXC) domain and the bromo-adjacent homology domain 1 (BAH1) blocks the access of DNA to the catalytic center (Song et al. 2011b). Secondly, the crystal structure of a longer fragment of DNMT1 reveals that in absence of DNA the TS domain is anchored in the DNA binding pocket of the C-terminal domain (Takeshita et al. 2011). Thus, these two autoinhibitory mechanisms have to be overcome by structural changes resulting in the activation of the enzyme.

Besides enzyme targeting and activation, DNMT1 stability also contributes to the regulation of maintenance DNA methylation. Abundance of DNMT1 during the cell cycle is governed by coordinated action of its stabilizer ubiquitin-specific peptidase 7 (USP7, also known as herpes virus associated ubiquitin-specific protease (HAUSP)) and the destabilizer UHRF1. USP7 has been shown to deubiquitinate DNMT1 leading to protection from proteasomal degradation (Du et al. 2010; Qin et al. 2011). DNMT1 is further stabilized by deacetylation mediated by the histone deacetylase 1 (HDAC1) (Du et al. 2010). On the contrary, UHRF1 ubiquitinates DNMT1 thereby marking it for proteasomal degradation, a process that is driven by Tip60-mediated acetylation of DNMT1 (Du et al. 2010).

Although the role of maintenance DNA methylation is coupled to replication in mitotic cells, DNMT1 is highly expressed in embryonic and adult neurons, especially in the central nervous system (CNS) (Goto et

al. 1994). DNA methylation has been implicated in neurogenesis contributing to learning and memory formation (Yu et al. 2011). Recently, several studies have described the identification of *DNMT1* mutations in patients suffering from hereditary sensory and autonomic neuropathies with dementia and hearing loss (HSAN-IE) and autosomal dominant cerebellar ataxia deafness and narcolepsy (ADCA-DN) (Klein et al. 2011; Winkelmann et al. 2012; Gosal et al. 2013; Pedroso et al. 2013; Yuan et al. 2013; Moghadam et al. 2014a). The disease phenotypes are characterized by late-onset progressive neurologic disorders including the CNS and the peripheral nervous system (PNS) (Klein et al. 2013). Strikingly, solely the TS domain is affected by (neurodegenerative diseases associated) mutations indicating its important role in enzyme regulation. However, the molecular basis underlying the disease mechanism is far from being understood.

In this study, we elucidate the functional relevance of the TS domain for regulation of *DNMT1*. By use of functional complementation assays, we mapped distinct regions within the TS domain indispensable for *DNMT1* activity *in vivo*. In turn, we show that each single domain of the interaction partner UHRF1 is necessary for the regulation of maintenance DNA methylation by *DNMT1*. Importantly, we found that *DNMT1* TS point mutations previously identified in HSAN-IE patients (Klein et al. 2011) lead to defects in binding UHRF1 and restoring DNA methylation at heterochromatic sites. *DNMT1* TS point mutants failed to correctly associate with late replicating chromatin, displayed increased protein mobility and decreased protein stability in a cell cycle-dependent manner. In summary, our study reveals a fundamental role of the TS domain in *DNMT1* heterochromatin targeting by interaction with UHRF1, in maintenance DNA methylation and in cell cycle-dependent protein abundance. Our findings provide new insights in the molecular evidence accounting for changes in the methylome of HSAN-IE patients.

MATERIAL AND METHODS

Mammalian expression constructs and antibodies

Fusion constructs were generated using enhanced green fluorescent protein (GFP), monomeric red fluorescent protein (RFP) or monomeric cherry (Ch). The expression constructs for RFP-DNMT1, GFP-DNMT1 wt, GFP-DNMT1 Δ 458-500, GFP-NTD, Ch-TS, GFP-DNMT1 (1-308), GFP-TS, GFP-DNMT1 (629-1110), GFP-CTD and Ch-USP7 have been described previously (Easwaran et al. 2004; Schermelleh et al. 2005; Fellinger et al. 2009; Frauer et al. 2011; Qin et al. 2011). GFP-DNMT1 deletion and point mutant as well as UHRF1-GFP deletion expression constructs were derived from the corresponding wt constructs by overlap extension PCR (Ho et al. 1989). The GFP-UHRF1 single domain constructs for the Ubl and Ring have been reported before (De Vos et al. 2014b). UHRF1-His, UHRF1-GFP, Ch-UHRF1, GFP-UHRF1 TTD, PHD and SRA single domain expression constructs have been described previously (Meilinger et al. 2009; Rottach et al. 2010; Pichler et al. 2011). GFP, RFP and RFP-PCNA have been reported before (Easwaran et al. 2004; Sporbert et al. 2005; Qin et al. 2011; Becker et al. 2013). All constructs were verified by DNA sequencing.

The following monoclonal antibodies were used for immunoblotting: mouse anti-His (C-terminal, Invitrogen), rat anti-RFP (5F8, Chromotek) (Rottach et al. 2008), rat anti-GFP (3H9, Chromotek), and mouse anti β -actin (Sigma) and the newly generated anti-DNMT1 (14F6, Supplementary Figure S5C). For immunofluorescence staining of heterochromatin, a mouse anti-H3K9me3 antibody was used (Active Motif). For immunofluorescence staining of endogenous proteins we used the previously described specific monoclonal rat anti-DNMT1 antibody 5A10 (Schneider et al. 2013) and a specific polyclonal rabbit anti-UHRF1 antibody (Citterio et al. 2004). As secondary antibodies an anti-mouse or anti-rat Alexa Fluor 594 and an anti-rabbit Alexa Fluor 488 antibody were applied, respectively (Invitrogen). In dependence on the expected intensity of the signals, secondary antibodies either conjugated to horseradish peroxidase (anti-rabbit (Biorad), anti-rat and anti-mouse (Dianova)) or conjugated to fluorescent dyes (anti-mouse and anti-rat Alexa Fluor 488 (Invitrogen)) were applied. For detection of HRP-conjugated antibodies an ECL Plus reagent (GE Healthcare, Thermo Scientific) was used.

Cell culture, transfection and immunofluorescence staining

HEK293T cells were cultured in Dulbecco's modified Eagle medium supplemented with 10% fetal bovine serum and 50 μ g/ml gentamycine. HEK293T cells were transfected with polyethylenimine (Sigma). MEF cells were cultured in Dulbecco's modified Eagle medium supplemented with 15% fetal bovine serum, non essential amino acids, 2 mM L-glutamine, 0.1 mM β -mercaptoethanol (Gibco-BRL), 100 U/ml penicillin and 100 μ g/ml streptomycin (PAA Laboratories GmbH). Mouse ESCs were cultured as published (Schermelleh et al. 2007) with the exception that the medium was supplemented with 2i inhibitors (1 μ M MEK inhibitor PD and 3 μ M GSK-3 inhibitor CHIR) (2i, Axon Medchem) (Ying et al. 2008). To analyse the methylation level in stably expressing UHRF1-GFP ESC lines, we cultured the cell lines in the same medium supplemented with 1,000 U/ml recombinant mouse leukemia inhibitory factor LIF (Millipore). Mouse J1 *Dnmt1* $^{-/-}$ ESCs are homozygous for the c null allele and have been described before (Lei et al. 1996). Mouse E14 wt and *Uhrf1* $^{-/-}$ cells (M. Muto and H. Koseki) as well as J1 triple knockout cells (Masaki Okano) have been reported previously (Meilinger et al. 2009). Mouse ESCs and MEF cells were transfected with

Lipofectamin (Invitrogen). Fixation, DAPI counterstaining and image acquisition cells was performed as described before (Rottach et al. 2010).

Live cell microscopy and fluorescence after photobleaching analysis

Live cell imaging and FRAP analysis were performed as described previously (Schneider et al. 2013) with the following exceptions. Photobleaching was performed with the acousto-optical tunable filter (AOTF) of the 488 nm laser line set to 100% transmission. Typically, for each series 20 prebleach and 200 postbleach frames were recorded with time intervals of 150 ms, followed by 180 frames with a time interval of 0.5 s. Data correction, normalization and quantitative evaluations were performed by automated processing with Fiji/ImageJ (Schindelin et al. 2012; Schneider et al. 2012) using a set of self-developed macros followed by calculations in Excel and R (R-Core-Team 2013).

In long-term imaging experiments, a z-stack of 6 μ m with a step size of 1.5 μ m was recorded every 20 min for \sim 30 h. To avoid photodamage of the cells, the AOTF of the laser was set to a low transmission value of 6%.

Generation of stable ESC lines and DNA methylation analysis

48 h after transfection with GFP tagged constructs, GFP positive ESC cells were separated using a fluorescence activated cell sorting (FACS) Aria II instrument (Becton Dickinson) and the cells were subsequently grown in selective medium containing 10 μ g/ml blasticidin (GFP-DNMT1 cell lines) or normal medium (UHRF1-GFP cell lines). After expansion cells were again FACS sorted one or two more times until at least 90% of the population was GFP positive. Furthermore, the GFP-DNMT1 cell lines were single cell sorted and clones with low expression levels were chosen for further analysis. The GFP-DNMT1 ESC line has been reported before (Qin et al. 2011). Genomic DNA isolation, bisulfite conversion, Primer sets and PCR conditions were described before (Tucker et al. 1996; Frauer et al. 2011). All PCR products were analysed by pyrosequencing (Varionostic).

Preparation of protein extracts, protein-protein interaction assay and co-immunoprecipitation

GFP and RFP or Ch fusion constructs were expressed in HEK293T cells and two days after transfection cells were harvested in ice cold PBS. Cell pellets from one to two 100 cm dishes were lysed in 200 μ l lysis buffer and a protein-protein interaction assay in GFP-multiTrap plates (Chromotek) was performed as described (Pichler et al. 2012) with the following adaptations: GFP extracts were equalized to a concentration of 60 nM in immunoprecipitation buffer (20 mM Tris-HCl pH 7.5, 150 mM NaCl, 0.5 mM EDTA) prior to one step purification in blocked (3% milk) GFP-multiTrap plates. After stringent washing (wash buffer; 20 mM Tris-HCl pH 7.5, 300 mM NaCl, 0.5 mM EDTA) purified GFP fusion proteins were incubated with crude protein extracts of RFP or Ch fusion proteins at a concentration of 1.1 to 2.1 μ M diluted in IP buffer (excess of amount RFP or Ch fusion proteins in relation to GFP fusions: 18-35 times). Bound fractions were quantified by fluorescence intensity measurements with a Tecan Infinite M1000 plate reader (Tecan). For co-immunoprecipitation assays, the GFP and RFP or Ch fusion constructs were co-expressed in HEK293T cells, protein extracts were equalized and depending on the expression amounts of 5- 30 pmol GFP-fusion protein were applied for the co-immunoprecipitation with the GFP-Trap

(Chromotek). Note that the plasmid amount of GFP fusion construct and RFP fusion constructs used for transfection was adapted in a way to have at least a three-fold excess of the molar RFP or Ch fusion protein amount in relation to GFP fusions. Bound fractions were firstly detected by fluorescence intensity measurements and secondly by immunoblotting using specific antibodies.

Cycloheximide assay

Mouse ESCs were plated to equal densities one day before cycloheximide (Sigma-Aldrich) treatment at 0.03 mg/ml. Cells were collected and counted 0 and 5 h after drug addition. Cell pellets were lysed in appropriate volumes of lysis buffer (20 mM Tris-HCl pH 7.5, 150 mM NaCl, 2 mM MgCl₂, 0.5% NP40, 1mg/ml DNaseI (AppliChem), 2 mM PMSF, protease inhibitor cocktail (Roche) and protease inhibitor mix M (SERVA)). Protein levels were detected by immunoblotting with specific antibodies.

Statistical analysis

Results were depicted as mean values \pm the standard deviation or as mean values \pm the standard error of the mean from the number of biological replicates indicated in the corresponding figure legend. The difference between two mean values was analyzed by Student's t-test and was considered as statistically significant in case of $P<0.02$ (*) and highly significant for $P<0.001$ (protein-protein interaction assay) or $P<0.0002$ (methylation analysis) (**), respectively.

Sequence alignments

Alignments were prepared using ClustalW2 and ESPript.

RESULTS

Deletions and mutations of conserved amino acids within the TS domain found in HSAN-IE patients affect DNMT1 activity *in vivo*

Although the catalytic activity of DNMT1 is referred to its CTD, the NTD of the enzyme is indispensable for maintenance methylation (Fatemi et al. 2001). We were interested in how the TS domain influences the methylation activity of DNMT1 *in vivo*. Representing the largest domain of the NTD spanning from amino acid 309 to 628 in mouse isoform 2, the TS domain shows highly conserved regions among different species including mammals, birds, fish, amphibians and insects (Figure 1). To map the functional relevance of individual regions within the TS domain, we created a systematic set of deletion mutants. Notably, the regions intended for deletion were determined under consideration of secondary structure information to abate the risk of destroying the higher order protein structure. For functional tests, *Dnmt1*^{-/-} embryonic stem cells (ESCs) were transiently transfected with the set of GFP-DNMT1 TS domain deletion constructs and 48 h after expression, cells were sorted using a fluorescence activated cell sorting (FACS) instrument and genomic DNA was isolated. Pyrosequencing at major satellite repeats revealed that two regions between amino acid 356 to 404 as well as from 458 to 573 are functionally relevant for maintenance methylation at pericentromeric heterochromatin (Figure 2A, shown in dark blue). Whereas cells expressing the wild type (wt) GFP-DNMT1 construct showed average methylation levels of 39%, the methylation was reduced to levels as low as 16% (GFP-DNMT1 delta 528-541) when parts of the relevant regions were deleted. On the contrary, a truncated version of GFP-DNMT1 lacking the flexible N-terminal region of the TS domain (amino acid 309 to 355) that is less conserved, was able to fully restore methylation at major satellite repeats (Figure 2A, shown in light blue). The methylation activity of a construct carrying a deletion in the C-terminal region of the TS domain (amino acid 579 to 595) was also comparable to that of the wt fusion protein.

Interestingly, mutations of two highly conserved amino acids in the TS domain lead to a neurodegenerative disease described as HSAN-IE (Klein et al. 2011; Klein et al. 2013). Using the alignment shown in Figure 1B, we identified the corresponding amino acids in the mouse protein and cloned the single HSAN-IE associated mutations P496Y (human: D490E.P491Y) and Y500C (human: Y495C) in mammalian expression constructs. It has to be noted that the aspartate at position 490 in human DNMT1 was found to be mutated to glutamate in HSAN-IE patients, but in the mouse protein the corresponding position is taken by glutamate, anyway. As the HSAN-IE associated mutations are included in a functionally relevant region of the TS domain (Figure 2A, GFP-DNMT1 delta 458-500), we further investigated the ability of the single point mutants GFP-DNMT1 P496Y and GFP-DNMT1 Y500C as well as of the double point mutant GFP-DNMT1 P496Y.Y500C to restore methylation at major satellite repeats in *Dnmt1*^{-/-} ESCs (Figure 2B). Indeed, the HSAN-IE single point mutations significantly affected DNMT1 activity *in vivo* when compared to the GFP-DNMT1 wt protein. The combination of both mutations even showed a highly significant reduction in DNA methylation activity pointing towards an additive effect of the two HSAN-IE mutations. The same remethylation defect was observed at the *skeletal α-actin* promoter (Supplementary Figure S1A). Herein, the decrease in the DNA methylation level was even highly significant for the GFP-DNMT1 P496Y mutant. As a control, we determined the DNA methylation level of the imprinted and unmethylated *H19a* promoter (Tucker et al. 1996) and as expected, we did not observe any significant

changes between the wt and the HSAN-IE mutant constructs (Supplementary Figure S1B). Moreover, we generated ESC lines stably expressing the GFP-DNMT1 wt and the single as well as the double mutant proteins. Analyses of the methylation level at the major satellite repeats and the *skeletal α-actin* promoter by pyrosequencing revealed that none of the HSAN-IE mutants was able to restore DNA methylation at these loci when stably expressed (Figure 2C). In summary, we could show that the TS domain of DNMT1 is indispensable for maintenance DNA methylation. Deletions of the TS domain in the region between amino acid 356 to 404 and amino acid 458 to 573 as well as point mutations characterized in HSAN-IE patients lead to decreased methylation levels at pericentromeric heterochromatin.

The TS domain of DNMT1 mediates the interaction with UHRF1

UHRF1 was found to be required for maintaining DNA methylation patterns after replication by direct interaction with DNMT1 (Bostick et al. 2007). To get deeper insights into the mechanism of DNMT1 recruitment to replication sites, we mapped the domains contributing to the interaction with UHRF1 by co-immunoprecipitation assays. For this purpose, we used a systematic set of GFP tagged truncated constructs for the NTD as well as the CTD of DNMT1, and constructs for different single and combined domains of UHRF1, respectively (Figure 3A). UHRF1-His co-immunoprecipitated with the NTD, but not the CTD of DNMT1 (Figure 3B, bottom). Within the NTD, solely the TS domain of DNMT1 showed interaction with UHRF1. As a second line of evidence, the mapping results were also confirmed by a semi-quantitative fluorescence protein-protein interaction assay *in vitro* that revealed the same preference of the TS domain for UHRF1 binding (Figure 3B, top). Mapping studies on UHRF1 illustrate that among all domains only the SRA domain of UHRF1 could co-immunoprecipitate RFP-DNMT1 (Figure 3C). In line with previous findings (Achour et al. 2008; Felle et al. 2011; Berk'yurek et al. 2013), our systematic mapping studies demonstrate that by means of the TS domain DNMT1 interacts mainly with the SRA domain of UHRF1.

HSAN-IE associated mutations in the DNMT1 TS domain affect the interaction with UHRF1

Since the TS domain contains the binding site for UHRF1 and HSAN-IE associated point mutants could not restore DNA methylation in *Dnmt1*^{-/-} ESCs, we hypothesized that the interaction with UHRF1 might be lost. To investigate the effects on UHRF1 binding, we performed a co-immunoprecipitation assay using GFP-TS domain wt or P496Y, Y500C single and P496Y.Y500C double point mutants co-expressed with Ch-UHRF1 in HEK293T cells and detected the bound fractions by immunoblotting (Figure 4A). Ch-UHRF1 co-immunoprecipitated with GFP-TS wt, whereas it was only weakly detected in the bound fraction of the P496Y and Y500C single and double point GFP-TS mutants. Semiquantitative protein-protein interaction assays in a GFP-multiTrap plate (Pichler et al. 2012) confirmed these results (Figure 4B). The interaction of Ch-UHRF1 with the GFP-DNMT1 NTD was significantly reduced by both single and double point mutations and also by deletion of a region containing the mutated amino acids (GFP-DNMT1 NTD Δ458-500). In conclusion, our findings suggest that a central part within the TS domain is crucial for mediating the interaction of DNMT1 with UHRF1 and that this interaction is affected by the HSAN-IE associated mutations located in this region.

Strong heterochromatin association and slow protein kinetics of the TS domain are dependent on interaction with UHRF1 but not on DNA methylation

It was shown that UHRF1 targets DNMT1 to heterochromatin by cooperative binding to hemimethylated DNA and histone H3 tails (Rothbart et al. 2012; Liu et al. 2013). Accordingly, DNMT1 displays a diffuse nuclear pattern in *Uhrf1*^{-/-} ESCs (Supplementary Figure S2) (Bostick et al. 2007). We mapped the interacting region for UHRF1 with DNMT1 to the TS domain which strongly associated with heterochromatin in mouse embryonic fibroblast (MEF) cells throughout interphase and co-localized with Ch-UHRF1 at DAPI- dense regions (Supplementary Figure S3A and S3B). To figure out which mark or binding partner the heterochromatin association of the TS domain is dependent on, we further investigated the localization in ESCs with different genetic backgrounds. We found that the heterochromatic localization remains unchanged in cells with decreased (J1 *Dnmt1*^{-/-}) or almost no DNA methylation (triple knockout (TKO) cells devoid of DNMT1, 3A and 3B, Figure 5A, left panel). In ESCs devoid of UHRF1 (E14 *Uhrf1*^{-/-}), however, the foci of the TS domain at DAPI-dense regions were entirely abrogated and the signal was spread diffusely in the nucleus (Figure 5A, right panel). Consequently, strong heterochromatin association of the TS domain is dependent on UHRF1 but not on DNA methylation.

In addition, we expressed the GFP-TS wt and the GFP-TS mutant constructs Y500C and P496Y.Y500C deficient in UHRF1 binding in MEF cells and studied their protein kinetics as well as their subnuclear distribution after fixation and counterstaining with DAPI (Figure 5B and 5C). We could emphatically show that the GFP-TS wt domain displayed slow protein kinetics with a large immobile fraction (Figure 5C). Concordantly, GFP-TS localized at chromocenters intensely stained by DAPI (Figure 5B). In contrast to that, the HSAN-IE associated GFP-TS Y500C and P496Y.Y500C mutants were diffusely localized in the nucleus and even excluded from chromocenters supporting the fact that binding to UHRF1 was impaired. The GFP-TS P496Y.Y500C double point mutant was also found in the nucleoli and weakly in the cytoplasm. In line with the diffuse nuclear localization and the exclusion from DAPI-dense heterochromatic sites, the GFP-TS mutants revealed fast protein kinetics without an immobile fraction (Figure 5C). Accordingly to the results obtained in *Uhrf1*^{-/-} ESCs, the abolishment of local enrichment at chromocenters by the GFP-TS Y500C and P496Y.Y500C mutants underlines the significance of the interaction with UHRF1 for proper targeting of DNMT1 to densely compacted chromatin.

Each domain of UHRF1 is relevant for the regulation of DNMT1 methylation activity *in vivo*

In the previous experiments, we have shown that the interaction with UHRF1 is necessary for targeting and maintenance DNA methylation by DNMT1. Next, we set out to examine which domains of UHRF1 are functionally relevant for the regulation of DNMT1 maintenance methylation. To this end, we constructed single domain deletions of UHRF1 (Figure 6A) and investigated their role in mediating DNA methylation *in vivo*. We made use of E14 *Uhrf1*^{-/-} ESCs which have considerably decreased methylation levels when compared to the E14 wt strain (Figure 6B). As reported before, the UHRF1-GFP wt fusion protein is able to partially complement methylation at the major satellite repeats (Meilinger et al. 2009). However, all *Uhrf1*^{-/-} ESC lines stably expressing UHRF1-GFP single domain deletion mutants displayed low methylation levels comparable to the untransfected control (Figure 6B). Hence, UHRF1 Δ Ubl-GFP, UHRF1 Δ TTD-GFP,

UHRF1 Δ PHD-GFP as well as UHRF1 Δ SRA-GFP and UHRF1 Δ Ring-GFP are not sufficient as cofactors for DNA methylation by DNMT1.

Furthermore, we tested the interaction of Ch-TS with the UHRF1-GFP single domain deletion mutants by co-immunoprecipitation (Figure 6C). Whereas deletions of the TTD, the PHD and the Ring domain had no or only a weak effect on the interaction, deletions of the Ubl and the SRA domain reduced the binding of Ch-TS to UHRF1-GFP. Consequently, the TS domain of DNMT1 can interact with two domains of UHRF1, the Ubl and the SRA domain. To get further insights in DNMT1 targeting in dependence on single domains of UHRF1, we studied the subnuclear localization of the stably expressed UHRF1-GFP wt or single domain deletion mutants and endogenous DNMT1 by immunofluorescence staining (Supplementary Material, Figure S4). In the wt UHRF1-GFP cell line, DNMT1 showed late S phase-specific horse-shoe like pattern that were, however, completely abrogated in all single domain UHRF1-GFP deletion cell lines displaying diffuse nuclear localization of DNMT1. In conclusion, none of the UHRF1 domains is dispensable for targeting DNMT1 for maintenance methylation.

The stability of DNMT1 is dependent on interaction with UHRF1 and on proper chromatin targeting

During co-immunoprecipitation assays and localization studies it became evident that the HSAN-IE associated GFP-DNMT1 mutants were expressed much weaker than the wt protein and displayed more degradation bands when immunoblotting with a specific anti-GFP antibody was performed (Figure 4A). Therefore, we investigated the protein stability of stably expressed wt and mutant GFP-DNMT1 in *Dnmt1* $^{-/-}$ ESC lines by a cycloheximide assay (Figure 7A and 7B). Protein expression after 5 h of cycloheximide treatment was compared to the expression without treatment (0 h), detected by immunoblotting using the specific anti-DNMT1 antibody 14F6 (Supplementary Figure S5C) and followed by quantification of the resulting signals. Whereas the effect of translational inhibition on endogenous UHRF1 protein expression was equal in each cell line, the expression of GFP-DNMT1 was stronger affected in the mutant cell lines upon cycloheximide treatment when compared to the wt. Notably, immunofluorescence localization studies in these stable ESC lines indicated that the HSAN-IE associated mutants, especially GFP-DNMT1 P496Y and the GFP-DNMT1 P496Y.Y500C double point mutants, were only partially recruited to heterochromatic sites in comparison to the wt protein (Supplementary Figure S5A and S5B). Our previous findings on the UHRF1 binding deficiency of the TS mutants in combination with their mislocalization and faster protein kinetics provide evidence for the necessity of proper and tight DNMT1 chromatin binding mediated by UHRF1 to guarantee stability of the methyltransferase. Notably, the interaction of the GFP-DNMT1 mutants with the stabilizer USP7 was not affected (Supplementary Figure S5D), arguing for a normal DNMT1 deubiquitination process.

The destabilization of HSAN-IE associated GFP-DNMT1 TS mutants is cell cycle-dependent

Since the TS domain-mediated interaction of DNMT1 with UHRF1 might be essential for late S phase-specific localization and kinetics of DNMT1 (Schneider et al. 2013), our aim was to decipher the expression and stability of the GFP-DNMT1 TS mutants on the single cell level following the cell cycle. Therefore, we imaged living MEF cells transiently co-transfected with GFP-DNMT1 wt or the GFP-DNMT1 P496Y.Y500C double point mutant and RFP-PCNA as a cell cycle marker (Figure 7C and 7D). Comparison of relative

expression levels of GFP-DNMT1 wt versus the double point mutant points towards a cell cycle-dependent destabilization. Although the expression in early to mid S phase was comparable to the wt, the GFP signal of mutant DNMT1 gradually dropped when the cell entered late S phase. Interestingly, the signal of GFP-DNMT1 P496Y.Y500C recovered when the cell had passed mitosis and entered into G1 phase (Figure 7C). Furthermore, the double point mutant displayed only weak late S phase-specific association with chromocenters and was devoid of the prolonged heterochromatin binding in G2 that was observed for the wt protein (Figure 7D). Taken together, our results provide evidence for a cell cycle-dependent destabilization of GFP-DNMT1 P496Y.Y500C beginning in late S phase that is mirrored by insufficient targeting of the protein to late replicating heterochromatin.

DISCUSSION

Besides PCNA, UHRF1 is an important recruitment factor for DNMT1 that guides the enzyme to hemimethylated DNA, the substrate for maintenance methylation (Bostick et al. 2007; Sharif et al. 2007). Whereas the interaction with PCNA is dispensable for maintenance DNA methylation (Schermelleh et al. 2007; Spada et al. 2007), the interaction with UHRF1 seems to play a critical role in this process (Bostick et al. 2007). As the TS domain of DNMT1 mediates the interaction with UHRF1 (Figure 3), we performed a functional mapping using a systematic set of deletion mutants. Functional complementation assays showed that two regions in the TS domain (amino acid 356-404 and 458-573) are indispensable for regulating DNA methylation by DNMT1 *in vivo* (Figure 2A). In contrast, the very N-terminal region of the TS domain (amino acid 309-355) which is poorly conserved and consists of varying length among different species (Figure 1B), is dispensable for DNMT1 activity. Interestingly, this region has not been dissolved in the crystal structure of mouse DNMT1 comprising a fragment spanning from amino acid 291 to 1620 (Takeshita et al. 2011) pointing towards a disordered flexible region that may not contribute to the regulation of enzyme activity. However, this region was characterized as an intrinsically disordered domain contributing to DNA methylation during mouse embryonic development (Borowczyk et al. 2009).

Importantly, we found that GFP-DNMT1 P496Y, Y500C and P496Y.Y500C are defective in binding to UHRF1 (Figure 4). These HSAN-IE associated DNMT1 TS domain mutants were inactive *in vivo* (Figure 2, Supplementary Figure S1) suggesting that the interaction of DNMT1 with UHRF1 is indeed required for epigenetic inheritance of DNA methylation. Our findings on functional defects are consistent with the global methylation analysis of genomic DNA from HSAN-IE patients with the corresponding mutations (human DNMT1: D490E.P491Y and Y495C) revealing DNA hypomethylation when compared to an unaffected group (Klein et al. 2011).

Decreased methylation levels caused by HSAN-IE associated mutations might also be explained by the findings that UHRF1 functions as an allosteric activator of DNMT1 (Syeda et al. 2011; Takeshita et al. 2011; Berkyurek et al. 2013; Bashtrykov et al. 2014a; Bashtrykov et al. 2014f). Upon binding to the SRA domain of UHRF1, the TS domain is released from the CTD of DNMT1 enabling access of substrate DNA to the catalytic center DNMT1 (Berkyurek et al. 2013; Bashtrykov et al. 2014a). HSAN-IE mutations defective in binding to UHRF1, however, might impede the conformational change in DNMT1 and the UHRF1-mediated release mechanism, thereby preserving the autoinhibitory state of the TS domain blocking catalytic activity of the CTD.

In addition to its important role in mediating the interaction with UHRF1, the TS domain of DNMT1 contributes to heterochromatin association of DNMT1 (Leonhardt et al. 1992; Schneider et al. 2013) that persists in G2 phase (Easwaran et al. 2004; Schermelleh et al. 2007). In our study, chromocenter localization and high immobile protein fractions were characteristic for the wt GFP-TS domain. Given that these characteristics were completely abolished by the HSAN-IE associated mutations and absent in *Uhrf1*^{-/-} ESCs (Figure 5), we propose that the interaction of the TS domain with UHRF1 plays a central role for tight binding of DNMT1 to heterochromatin marked by densely methylated DNA and histone tails.

Binding of UHRF1 to methylated H3K9 via its TTD and PHD as well as to hemimethylated DNA via its SRA domain has been reported to serve as a prerequisite for directing DNMT1 for maintenance DNA methylation (Rothbart et al. 2012; Liu et al. 2013; Rothbart et al. 2013). Using functional complementation assays, we found that each domain of the multifunctional UHRF1 protein is required for the regulation of

DNA methylation by DNMT1 (Figure 6). We propose that besides the three chromatin binding domains in UHRF1 (TTD, PHD and SRA domain) and the DNMT1 interaction surface on the SRA domain, also the Ubl domain as well as the Ring domain of UHRF1 are essential for regulating maintenance DNA methylation. In agreement with the finding that the UHRF1 Δ Ubl-GFP and the UHRF1 Δ SRA-GFP mutants were not sufficient as cofactors for maintenance methylation, we mapped the DNMT1 interaction site to the Ubl and SRA domain (Figure 3C and 6C). Binding of DNMT1 to the UHRF1 SRA domain is consistent with previous findings (Achour et al. 2008; Felle et al. 2011). But in addition, we provide evidence, to our knowledge for the first time, for a second interaction site in the Ubl domain of UHRF1. Whether these two DNMT1 interaction sites on UHRF1 act independently or in a timely and spatially coordinated manner, remains to be elucidated. The regulatory function of the Ring domain might be explained by a recent study on *Xenopus* egg extracts illustrating that the E3 ubiquitin ligase properties of UHRF1 are required for ubiquitination of histone H3 on K23 that serves as a binding site for DNMT1 (Nishiyama et al. 2013).

In accordance with recent findings on human DNMT1 (Klein et al. 2011), we observed a destabilizing effect of the HSAN-IE associated mutations. In particular, our results suggest that although mutant DNMT1 still interacts with USP7, it shows decreased expression especially in late S and G2 phase that recovered during G1 phase (Figure 7, Supplementary Figure S5D). Analyses of the cell cycle-dependent subnuclear localization revealed a reduced heterochromatin enrichment of mutant DNMT1 in the destabilized state during late S and G2 phase (Figure 7D). Thus, we propose that destabilization of mutant DNMT1 might rely on the disrupted UHRF1 binding and the resulting weakened chromatin association. Similar to DNMT3A and DNMT3B that are stabilized on nucleosomes containing methylated DNA (Jeong et al. 2009; Stachulski et al. 2011), the stability of DNMT1 has recently been proposed to depend on indirect chromatin association via UHRF1 binding to methylated H3K9 that persists during mitosis (Rothbart et al. 2012). Taken together, free DNMT1 enzymes, which are not associated with chromatin either due to UHRF1 histone binding defects by TTD mutations or UHRF1 interaction deficiencies by DNMT1 HSAN-IE mutations, might be more likely to be degraded compared to correctly targeted chromatin bound enzymes. Whether degradation of non chromatin bound DNMT1 relies on UHRF1-dependent ubiquitination or on activity of another yet unknown E3 ubiquitin ligase specific for DNMT1 and whether this proteasomal pathway is initiated by DNMT1 acetylation or methylation, remains to be determined. We hypothesize that the observed stability regulating mechanism might prevent aberrant DNA methylation by inadequately targeted DNMT1.

In postmitotic neurons, DNMT1 has been reported to undergo rapid protein turnover (Fan et al. 2001). Therefore, the destabilizing effect of the TS domain mutations might be more pronounced in the nervous system in comparison to other tissues and might contribute to the nervous system restricted phenotype observed in HSAN-IE patients.

Given the important role of DNMT1 in maintenance DNA methylation after replication, one might assume that DNMT1 may play a subordinate role in postmitotic cells like neurons. However, DNMT1 is known to be involved in adult neurogenesis (Yu et al. 2011). Furthermore, DNMT1 deficiency in mitotic CNS precursor cells accompanied by DNA hypomethylation has been reported to affect cell survival in mice. Mutant CNS cells of mosaic animals are selectively eliminated during adulthood (Fan et al. 2001) arguing for an important role of DNMT1 for postnatal survival of CNS cells. Whether UHRF1 also regulates DNA methylation by DNMT1 in neuronal cells yet remains elusive.

In summary, our study provides new insights in the molecular basis of global DNA hypomethylation found in HSAN-IE patients. We show that DNMT1 HSAN-IE associated mutations result in UHRF1 binding defects, changes of subnuclear localization and in protein destabilization.

FUNDING

This work was supported by grants from the Deutsche Forschungsgemeinschaft [DFG SFB 646/B10, DFG SFB1064/A17 and Z05 to H.L, DFG SFB1064/Z02 to E.K.]. P.W. and M.S. are fellows of the Graduate School Life Science Munich (LSM). K.S. and K.F. were supported by the International Max Planck Research School for Molecular and Cellular Life Sciences (IMPRS-LS). S.L. was funded by an award of Lehre@LMU of the Ludwig-Maximilians University Munich. W.Q. was supported by the China Scholarship Council (CSC).

ACKNOWLEDGMENT

We are grateful to the following colleagues for providing ESCs and somatic cells: Masahiro Muto and Haruhiko Koseki for mouse wt E14 and *Uhrf1*^{-/-} ESCs; En Li and T. Chen for mouse J1 wt and *Dnmt1*^{-/-} ESCs; Masaki Okano for J1 TKO ESCs; Thomas Jenuwein for wt MEF cells.

REFERENCES

1. Bird, A. (2002) DNA methylation patterns and epigenetic memory. *Genes Dev*, **16**, 6-21.
2. Leonhardt, H., Page, A.W., Weier, H.U. and Bestor, T.H. (1992) A targeting sequence directs DNA methyltransferase to sites of DNA replication in mammalian nuclei. *Cell*, **71**, 865-873.
3. Chuang, L.S., Ian, H.I., Koh, T.W., Ng, H.H., Xu, G. and Li, B.F. (1997) Human DNA-(cytosine-5) methyltransferase-PCNA complex as a target for p21WAF1. *Science*, **277**, 1996-2000.
4. Rountree, M.R., Bachman, K.E. and Baylin, S.B. (2000) DNMT1 binds HDAC2 and a new co-repressor, DMAP1, to form a complex at replication foci. *Nat Genet*, **25**, 269-277.
5. Easwaran, H.P., Schermelleh, L., Leonhardt, H. and Cardoso, M.C. (2004) Replication-independent chromatin loading of Dnmt1 during G2 and M phases. *EMBO Rep*, **5**, 1181-1186.
6. Bostick, M., Kim, J.K., Esteve, P.O., Clark, A., Pradhan, S. and Jacobsen, S.E. (2007) UHRF1 plays a role in maintaining DNA methylation in mammalian cells. *Science*, **317**, 1760-1764.
7. Achour, M., Jacq, X., Ronde, P., Alhosin, M., Charlot, C., Chataigneau, T., Jeanblanc, M., Macaluso, M., Giordano, A., Hughes, A.D. *et al.* (2008) The interaction of the SRA domain of ICBP90 with a novel domain of DNMT1 is involved in the regulation of VEGF gene expression. *Oncogene*, **27**, 2187-2197.
8. Felle, M., Joppien, S., Nemeth, A., Diermeier, S., Thalhammer, V., Dobner, T., Kremmer, E., Kappler, R. and Langst, G. (2011) The USP7/Dnmt1 complex stimulates the DNA methylation activity of Dnmt1 and regulates the stability of UHRF1. *Nucleic Acids Res*, **39**, 8355-8365.
9. Sharif, J., Muto, M., Takebayashi, S., Suetake, I., Iwamatsu, A., Endo, T.A., Shinga, J., Mizutani-Koseki, Y., Toyoda, T., Okamura, K. *et al.* (2007) The SRA protein Np95 mediates epigenetic inheritance by recruiting Dnmt1 to methylated DNA. *Nature*, **450**, 908-912.
10. Arita, K., Ariyoshi, M., Tochio, H., Nakamura, Y. and Shirakawa, M. (2008) Recognition of hemi-methylated DNA by the SRA protein UHRF1 by a base-flipping mechanism. *Nature*, **455**, 818-821.
11. Avvakumov, G.V., Walker, J.R., Xue, S., Li, Y., Duan, S., Bronner, C., Arrowsmith, C.H. and Dhe-Paganon, S. (2008) Structural basis for recognition of hemi-methylated DNA by the SRA domain of human UHRF1. *Nature*, **455**, 822-825.
12. Qian, C., Li, S., Jakoncic, J., Zeng, L., Walsh, M.J. and Zhou, M.M. (2008) Structure and hemimethylated CpG binding of the SRA domain from human UHRF1. *J Biol Chem*, **283**, 34490-34494.
13. Citterio, E., Papait, R., Nicassio, F., Vecchi, M., Gomiero, P., Mantovani, R., Di Fiore, P.P. and Bonapace, I.M. (2004) Np95 is a histone-binding protein endowed with ubiquitin ligase activity. *Mol Cell Biol*, **24**, 2526-2535.
14. Karagianni, P., Amazit, L., Qin, J. and Wong, J. (2008) ICBP90, a novel methyl K9 H3 binding protein linking protein ubiquitination with heterochromatin formation. *Mol Cell Biol*, **28**, 705-717.
15. Rottach, A., Frauer, C., Pichler, G., Bonapace, I.M., Spada, F. and Leonhardt, H. (2010) The multi-domain protein Np95 connects DNA methylation and histone modification. *Nucleic Acids Res*, **38**, 1796-1804.
16. Cheng, J., Yang, Y., Fang, J., Xiao, J., Zhu, T., Chen, F., Wang, P., Li, Z., Yang, H. and Xu, Y. (2013) Structural insight into coordinated recognition of trimethylated histone H3 lysine 9 (H3K9me3) by the plant homeodomain (PHD) and tandem tudor domain (TTD) of UHRF1 (ubiquitin-like, containing PHD and RING finger domains, 1) protein. *J Biol Chem*, **288**, 1329-1339.
17. Liu, X., Gao, Q., Li, P., Zhao, Q., Zhang, J., Li, J., Koseki, H. and Wong, J. (2013) UHRF1 targets DNMT1 for DNA methylation through cooperative binding of hemi-methylated DNA and methylated H3K9. *Nat Commun*, **4**, 1563.
18. Song, J., Rechkoblit, O., Bestor, T.H. and Patel, D.J. (2011) Structure of DNMT1-DNA complex reveals a role for autoinhibition in maintenance DNA methylation. *Science*, **331**, 1036-1040.

19. Takeshita, K., Suetake, I., Yamashita, E., Suga, M., Narita, H., Nakagawa, A. and Tajima, S. (2011) Structural insight into maintenance methylation by mouse DNA methyltransferase 1 (Dnmt1). *Proc Natl Acad Sci U S A*, **108**, 9055-9059.
20. Qin, W., Leonhardt, H. and Spada, F. (2011) Usp7 and Uhrf1 control ubiquitination and stability of the maintenance DNA methyltransferase Dnmt1. *J Cell Biochem*, **112**, 439-444.
21. Du, Z., Song, J., Wang, Y., Zhao, Y., Guda, K., Yang, S., Kao, H.Y., Xu, Y., Willis, J., Markowitz, S.D. *et al.* (2010) DNMT1 stability is regulated by proteins coordinating deubiquitination and acetylation-driven ubiquitination. *Sci Signal*, **3**, ra80.
22. Goto, K., Numata, M., Komura, J.I., Ono, T., Bestor, T.H. and Kondo, H. (1994) Expression of DNA methyltransferase gene in mature and immature neurons as well as proliferating cells in mice. *Differentiation*, **56**, 39-44.
23. Yu, N.K., Baek, S.H. and Kaang, B.K. (2011) DNA methylation-mediated control of learning and memory. *Mol Brain*, **4**, 5.
24. Klein, C.J., Botuyan, M.V., Wu, Y., Ward, C.J., Nicholson, G.A., Hammans, S., Hojo, K., Yamanishi, H., Karpf, A.R., Wallace, D.C. *et al.* (2011) Mutations in DNMT1 cause hereditary sensory neuropathy with dementia and hearing loss. *Nat Genet*, **43**, 595-600.
25. Yuan, J., Higuchi, Y., Nagado, T., Nozuma, S., Nakamura, T., Matsuura, E., Hashiguchi, A., Sakiyama, Y., Yoshimura, A. and Takashima, H. (2013) Novel mutation in the replication focus targeting sequence domain of DNMT1 causes hereditary sensory and autonomic neuropathy IE. *J Peripher Nerv Syst*, **18**, 89-93.
26. Winkelmann, J., Lin, L., Schormair, B., Kornum, B.R., Faraco, J., Plazzi, G., Melberg, A., Cornelio, F., Urban, A.E., Pizza, F. *et al.* (2012) Mutations in DNMT1 cause autosomal dominant cerebellar ataxia, deafness and narcolepsy. *Hum Mol Genet*, **21**, 2205-2210.
27. Pedroso, J.L., Povoas Barsottini, O.G., Lin, L., Melberg, A., Oliveira, A.S. and Mignot, E. (2013) A novel de novo exon 21 DNMT1 mutation causes cerebellar ataxia, deafness, and narcolepsy in a Brazilian patient. *Sleep*, **36**, 1257-1259, 1259A.
28. Moghadam, K.K., Pizza, F., La Morgia, C., Franceschini, C., Tonon, C., Lodi, R., Barboni, P., Seri, M., Ferrari, S., Liguori, R. *et al.* (2014) Narcolepsy is a common phenotype in HSAN IE and ADCA-DN. *Brain*.
29. Gosal, D., J., E. and E., M. (2013) A mutation in the DNMT1 gene causing autosomal dominant ataxia with deafness and cataplexy. *J Neurol Neurosurg Psychiatry*.
30. Klein, C.J., Bird, T., Ertekin-Taner, N., Lincoln, S., Hjorth, R., Wu, Y., Kwok, J., Mer, G., Dyck, P.J. and Nicholson, G.A. (2013) DNMT1 mutation hot spot causes varied phenotypes of HSAN1 with dementia and hearing loss. *Neurology*, **80**, 824-828.
31. Schermelleh, L., Spada, F., Easwaran, H.P., Zolghadr, K., Margot, J.B., Cardoso, M.C. and Leonhardt, H. (2005) Trapped in action: direct visualization of DNA methyltransferase activity in living cells. *Nat Methods*, **2**, 751-756.
32. Fellinger, K., Rothbauer, U., Felle, M., Langst, G. and Leonhardt, H. (2009) Dimerization of DNA methyltransferase 1 is mediated by its regulatory domain. *J Cell Biochem*, **106**, 521-528.
33. Frauer, C., Rottach, A., Meilinger, D., Bultmann, S., Fellinger, K., Hasenoder, S., Wang, M., Qin, W., Soding, J., Spada, F. *et al.* (2011) Different binding properties and function of CXXC zinc finger domains in Dnmt1 and Tet1. *PLoS One*, **6**, e16627.
34. Ho, S.N., Hunt, H.D., Horton, R.M., Pullen, J.K. and Pease, L.R. (1989) Site-directed mutagenesis by overlap extension using the polymerase chain reaction. *Gene*, **77**, 51-59.
35. De Vos, M., El Ramy, R., Quenet, D., Wolf, P., Spada, F., Magroun, N., Babbio, F., Schreiber, V., Leonhardt, H., Bonapace, I.M. *et al.* (2014) Poly(ADP-ribose) polymerase 1 (PARP1) associates with E3 ubiquitin-protein ligase UHRF1 and modulates UHRF1 biological functions. *J Biol Chem*.
36. Pichler, G., Wolf, P., Schmidt, C.S., Meilinger, D., Schneider, K., Frauer, C., Fellinger, K., Rottach, A. and Leonhardt, H. (2011) Cooperative DNA and histone binding by Uhrf2 links the two major repressive epigenetic pathways. *J Cell Biochem*, **112**, 2585-2593.

37. Meilinger, D., Fellinger, K., Bultmann, S., Rothbauer, U., Bonapace, I.M., Klinkert, W.E., Spada, F. and Leonhardt, H. (2009) Np95 interacts with de novo DNA methyltransferases, Dnmt3a and Dnmt3b, and mediates epigenetic silencing of the viral CMV promoter in embryonic stem cells. *EMBO Rep*, **10**, 1259-1264.

38. Becker, A., Allmann, L., Hofstatter, M., Casa, V., Weber, P., Lehmkuhl, A., Herce, H.D. and Cardoso, M.C. (2013) Direct homo- and hetero-interactions of MeCP2 and MBD2. *PLoS One*, **8**, e53730.

39. Sporbert, A., Domaing, P., Leonhardt, H. and Cardoso, M.C. (2005) PCNA acts as a stationary loading platform for transiently interacting Okazaki fragment maturation proteins. *Nucleic Acids Res*, **33**, 3521-3528.

40. Rottach, A., Kremmer, E., Nowak, D., Leonhardt, H. and Cardoso, M.C. (2008) Generation and characterization of a rat monoclonal antibody specific for multiple red fluorescent proteins. *Hybridoma (Larchmt)*, **27**, 337-343.

41. Schneider, K., Fuchs, C., Dobay, A., Rottach, A., Qin, W., Wolf, P., Alvarez-Castro, J.M., Nalaskowski, M.M., Kremmer, E., Schmid, V. *et al.* (2013) Dissection of cell cycle-dependent dynamics of Dnmt1 by FRAP and diffusion-coupled modeling. *Nucleic Acids Res*, **41**, 4860-4876.

42. Schermelleh, L., Haemmer, A., Spada, F., Rosing, N., Meilinger, D., Rothbauer, U., Cardoso, M.C. and Leonhardt, H. (2007) Dynamics of Dnmt1 interaction with the replication machinery and its role in postreplicative maintenance of DNA methylation. *Nucleic Acids Res*, **35**, 4301-4312.

43. Ying, Q.L., Wray, J., Nichols, J., Batlle-Morera, L., Doble, B., Woodgett, J., Cohen, P. and Smith, A. (2008) The ground state of embryonic stem cell self-renewal. *Nature*, **453**, 519-523.

44. Lei, H., Oh, S.P., Okano, M., Juttermann, R., Goss, K.A., Jaenisch, R. and Li, E. (1996) De novo DNA cytosine methyltransferase activities in mouse embryonic stem cells. *Development*, **122**, 3195-3205.

45. Schneider, C.A., Rasband, W.S. and Eliceiri, K.W. (2012) NIH Image to ImageJ: 25 years of image analysis. *Nat Methods*, **9**, 671-675.

46. Schindelin, J., Arganda-Carreras, I., Frise, E., Kaynig, V., Longair, M., Pietzsch, T., Preibisch, S., Rueden, C., Saalfeld, S., Schmid, B. *et al.* (2012) Fiji: an open-source platform for biological-image analysis. *Nat Methods*, **9**, 676-682.

47. R-Core-Team. (2013). R Foundation for Statistical Computing, Vienna, Austria.

48. Tucker, K.L., Beard, C., Dausmann, J., Jackson-Grusby, L., Laird, P.W., Lei, H., Li, E. and Jaenisch, R. (1996) Germ-line passage is required for establishment of methylation and expression patterns of imprinted but not of nonimprinted genes. *Genes Dev*, **10**, 1008-1020.

49. Pichler, G., Jack, A., Wolf, P. and Hake, S.B. (2012) Versatile toolbox for high throughput biochemical and functional studies with fluorescent fusion proteins. *PLoS One*, **7**, e36967.

50. Fatemi, M., Hermann, A., Pradhan, S. and Jeltsch, A. (2001) The activity of the murine DNA methyltransferase Dnmt1 is controlled by interaction of the catalytic domain with the N-terminal part of the enzyme leading to an allosteric activation of the enzyme after binding to methylated DNA. *J Mol Biol*, **309**, 1189-1199.

51. Berkysrek, A.C., Suetake, I., Arita, K., Takeshita, K., Nakagawa, A., Shirakawa, M. and Tajiama, S. (2013) The DNA Methyltransferase Dnmt1 Directly Interacts with the SET and RING Finger Associated (SRA) Domain of the Multifunctional Protein Uhrf1 to Facilitate Accession of the Catalytic Center to Hemi-methylated DNA. *J Biol Chem*.

52. Rothbart, S.B., Krajewski, K., Nady, N., Tempel, W., Xue, S., Badeaux, A.I., Barsyte-Lovejoy, D., Martinez, J.Y., Bedford, M.T., Fuchs, S.M. *et al.* (2012) Association of UHRF1 with methylated H3K9 directs the maintenance of DNA methylation. *Nat Struct Mol Biol*, **19**, 1155-1160.

53. Spada, F., Haemmer, A., Kuch, D., Rothbauer, U., Schermelleh, L., Kremmer, E., Carell, T., Langst, G. and Leonhardt, H. (2007) DNMT1 but not its interaction with the replication

machinery is required for maintenance of DNA methylation in human cells. *J Cell Biol*, **176**, 565-571.

54. Borowczyk, E., Mohan, K.N., D'Aiuto, L., Cirio, M.C. and Chaillet, J.R. (2009) Identification of a region of the DNMT1 methyltransferase that regulates the maintenance of genomic imprints. *Proc Natl Acad Sci U S A*, **106**, 20806-20811.

55. Bashttrykov, P., Jankevicius, G., Jurkowska, R.Z., Ragozin, S. and Jeltsch, A. (2014) The UHRF1 Protein Stimulates the Activity and Specificity of the Maintenance DNA Methyltransferase DNMT1 by an Allosteric Mechanism. *J Biol Chem*, **289**, 4106-4115.

56. Syeda, F., Fagan, R.L., Wean, M., Avvakumov, G.V., Walker, J.R., Xue, S., Dhe-Paganon, S. and Brenner, C. (2011) The replication focus targeting sequence (RFTS) domain is a DNA-competitive inhibitor of Dnmt1. *J Biol Chem*, **286**, 15344-15351.

57. Bashttrykov, P., Rajavelu, A., Hackner, B., Ragozin, S., Carell, T. and Jeltsch, A. (2014) Targeted Mutagenesis Results in an Activation of DNA Methyltransferase 1 and Confirms an Autoinhibitory Role of its RFTS Domain. *Chembiochem*.

58. Rothbart, S.B., Dickson, B.M., Ong, M.S., Krajewski, K., Houlston, S., Kireev, D.B., Arrowsmith, C.H. and Strahl, B.D. (2013) Multivalent histone engagement by the linked tandem Tudor and PHD domains of UHRF1 is required for the epigenetic inheritance of DNA methylation. *Genes Dev*, **27**, 1288-1298.

59. Nishiyama, A., Yamaguchi, L., Sharif, J., Johmura, Y., Kawamura, T., Nakanishi, K., Shimamura, S., Arita, K., Kodama, T., Ishikawa, F. *et al.* (2013) Uhrf1-dependent H3K23 ubiquitylation couples maintenance DNA methylation and replication. *Nature*.

60. Jeong, S., Liang, G., Sharma, S., Lin, J.C., Choi, S.H., Han, H., Yoo, C.B., Egger, G., Yang, A.S. and Jones, P.A. (2009) Selective anchoring of DNA methyltransferases 3A and 3B to nucleosomes containing methylated DNA. *Mol Cell Biol*, **29**, 5366-5376.

61. Sharma, S., De Carvalho, D.D., Jeong, S., Jones, P.A. and Liang, G. (2011) Nucleosomes containing methylated DNA stabilize DNA methyltransferases 3A/3B and ensure faithful epigenetic inheritance. *PLoS Genet*, **7**, e1001286.

62. Fan, G., Beard, C., Chen, R.Z., Csankovszki, G., Sun, Y., Siniaia, M., Biniszkiewicz, D., Bates, B., Lee, P.P., Kuhn, R. *et al.* (2001) DNA hypomethylation perturbs the function and survival of CNS neurons in postnatal animals. *J Neurosci*, **21**, 788-797.

FIGURES AND LEGENDS

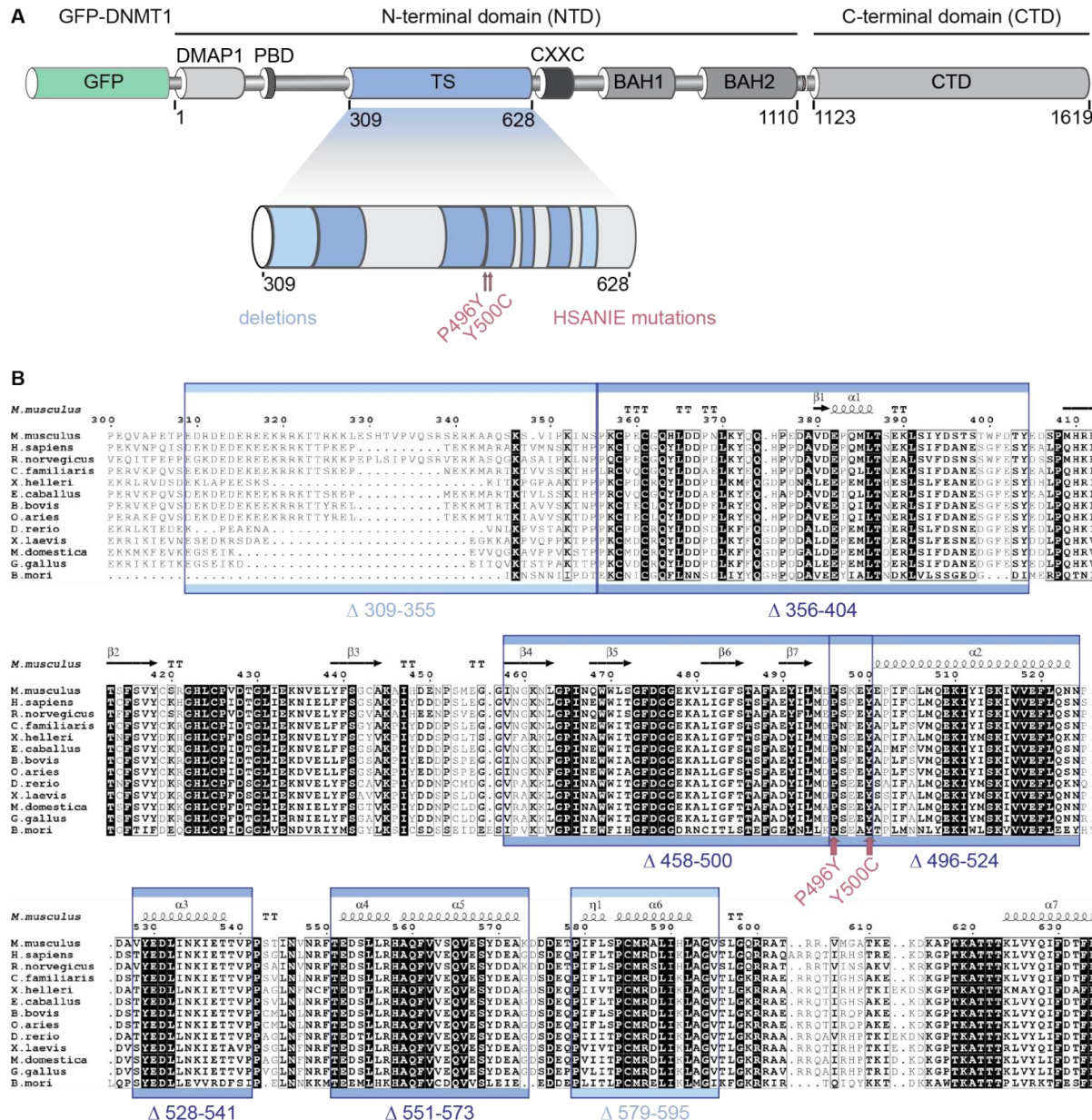


Figure 1. The DNMT1 TS domain is conserved among different species. (A) Domain structure of GFP-DNA methyltransferase 1 (DNMT1) with illustration of deletions and HSAN-IE associated point mutations used for functional characterization of the TS domain. The large regulatory N-terminal domain (NTD) of DNMT1 is comprised of a DNA methyltransferase associated protein 1 (DMAP1) -binding domain, a PCNA (proliferating cell nuclear antigen) -binding domain (PBD), a targeting sequence (TS) domain, a zinc finger (CXXC) domain, two bromo-adjacent homology (BAH1 and BAH2) domains and a C-terminal catalytic domain (CTD). (B) Primary sequence alignment of TS domains from different species. The secondary structure of the mouse TS domain is indicated (pdb: 3AV4). Highly conserved residues are black shaded. Deleted regions are indicated by blue rectangles and HSAN-IE associated point mutations by red arrows. Functionally relevant regions within the TS domain are depicted in dark blue. HSAN-IE: hereditary sensory and autonomic neuropathy type IE.

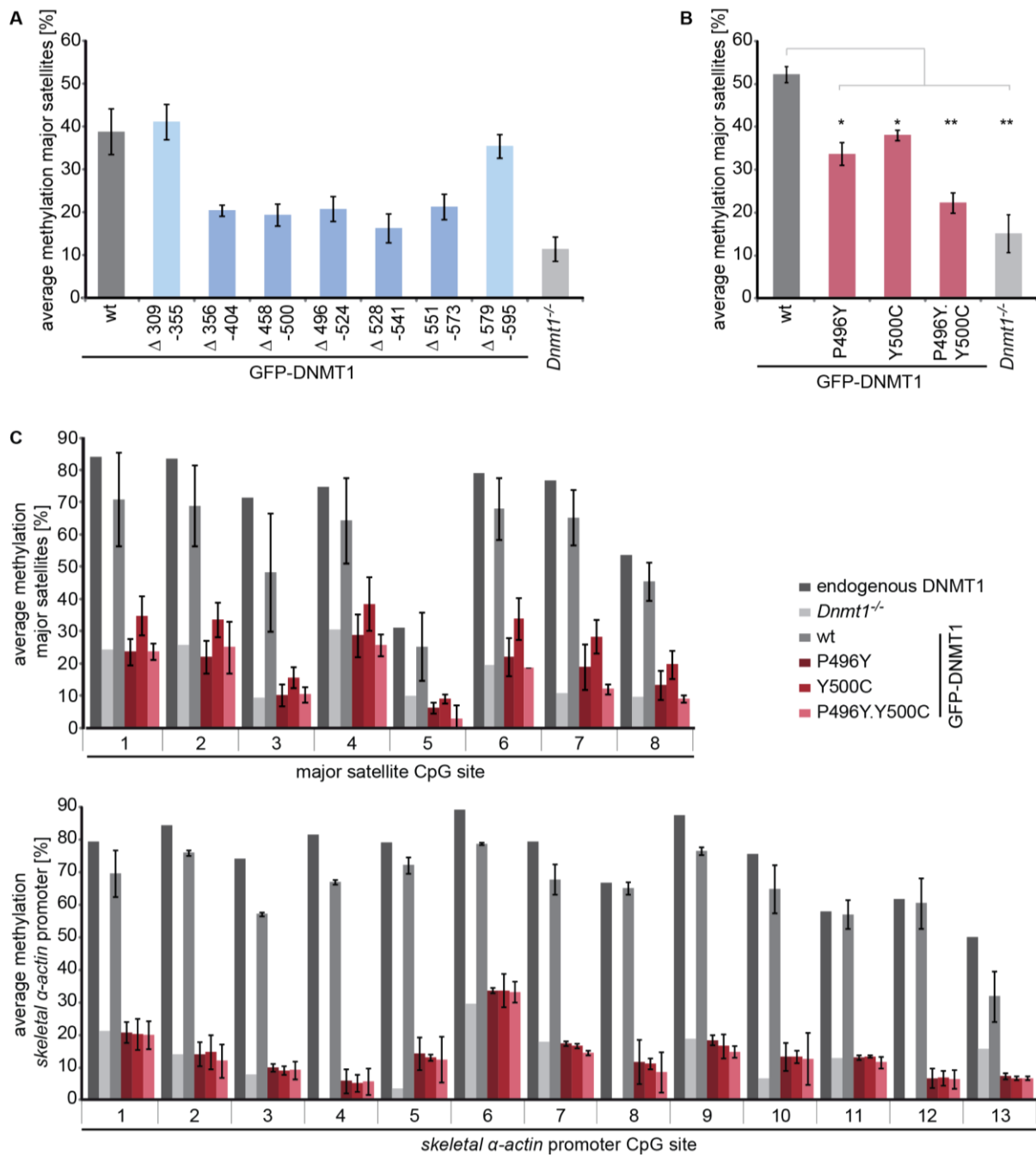


Figure 2. Deletions and HSAN-IE associated mutations in the TS domain of DNMT1 affect the methylation activity *in vivo*. (A) and (B) Local methylation analysis at major satellite repeats. Mouse *Dnmt1*^{-/-} ESCs were FACS-sorted 48 h after transient expression of GFP-DNMT1 wild type (wt) and deletion or HSAN-IE associated point mutant constructs and CpG methylation levels were analyzed by bisulfite treatment of genomic DNA, PCR amplification and direct pyrosequencing. Methylation levels of untransfected cells are displayed for comparison. Shown are mean values \pm s.d. from (A) two to six or (B) three independent biological replicates (average from eight CpG sites, respectively). (B) Two-sample t-tests were performed that assume equal variances. Asterisks represent statistically significant difference in regard to the wt: *P<0.02, **P<0.0002. (C) CpG methylation levels at the major satellite repeats and the skeletal α -actin promoter of mouse *Dnmt1*^{-/-} ESCs stably expressing GFP-DNMT1 wt or HSAN-IE associated point mutants were analyzed by bisulfite treatment, PCR amplification and direct pyrosequencing. Methylation levels of untransfected cells are displayed for comparison. Shown are mean values from two different single cell clones, respectively.

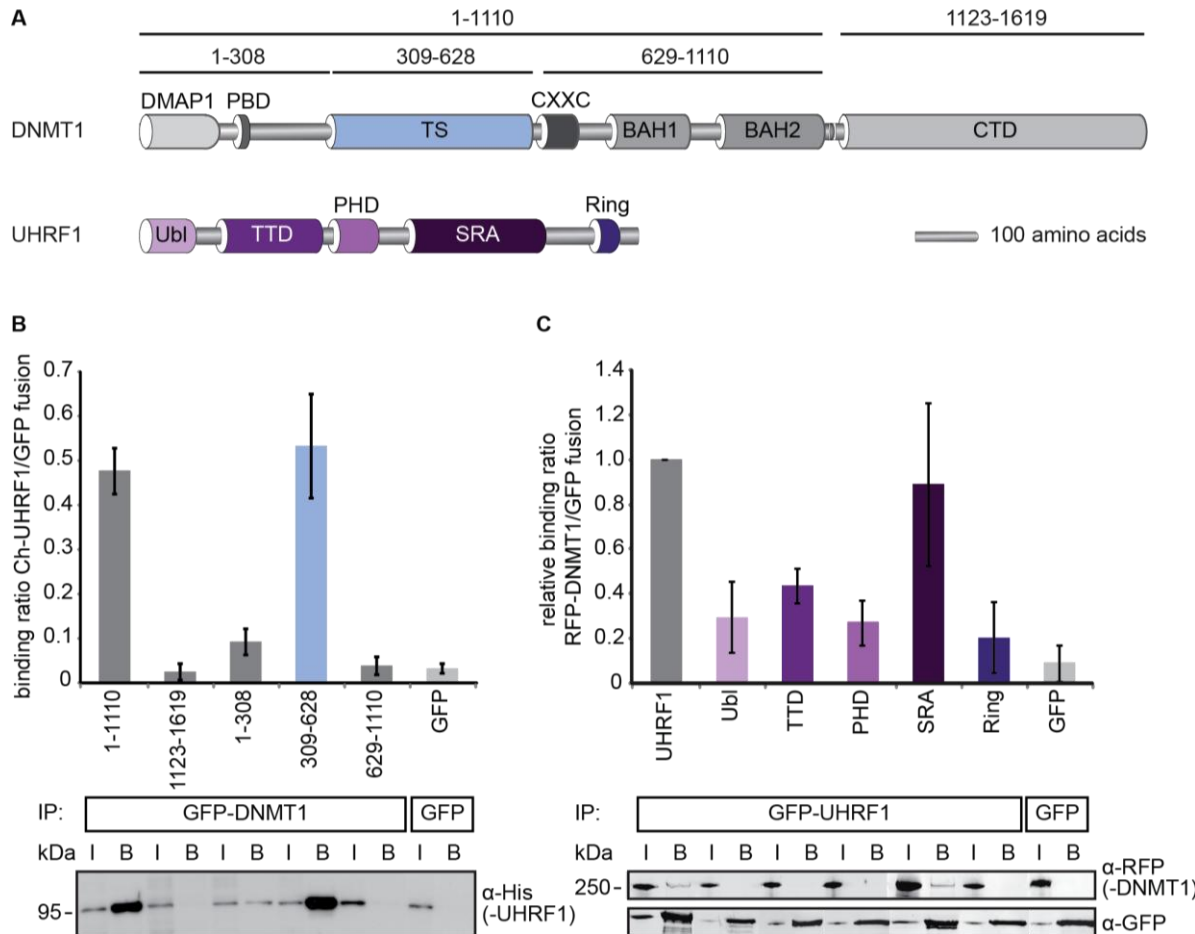


Figure 3. The interaction with UHRF1 is mediated by the TS domain of DNMT1. (A) Schematic outline of DNMT1 and the ubiquitin-like, containing PHD and RING finger domains 1 (UHRF1) expression constructs used for protein-protein interaction mapping studies. UHRF1 harbors an ubiquitin-like domain (Ubl) followed by a tandem Tudor domain (TTD), a plant homeodomain (PHD), a SET and RING associated (SRA) domain and a really interesting new gene (Ring) domain. (B) Top: Mapping and relative quantification of the interaction GFP-DNMT1 with Ch-UHRF1 by fluorescence protein-protein interaction assay *in vitro*. After immunoprecipitation, different GFP-DNMT1 expression constructs were incubated with protein extracts of Ch-UHRF1 and the bound fractions were detected by fluorescence read-out. Ratios of Ch-UHRF1 over GFP fusion proteins are shown as mean values \pm s.e.m. of three to six biological replicates. Bottom: Different DNMT1 expression constructs were co-expressed with UHRF1-His in HEK 293T cells and after immunoprecipitation using the GFP-Trap, UHRF1-His was detected by western blot with an anti-His antibody. GFP was used as negative control. (C) Top: Mapping and relative quantification of the interaction GFP-UHRF1 with RFP-DNMT1 by fluorescence protein-protein interaction assay *in vitro*. Ratios of RFP-DNMT1 over GFP fusion proteins are shown as mean values \pm s.e.m. of three biological replicates normalized to the binding ratio of the GFP-UHRF1 full length protein. Bottom: Bound fractions of one representative experiment were detected by western blot with specific antibodies against RFP and GFP. GFP was used as negative control. I = Input, B = Bound.

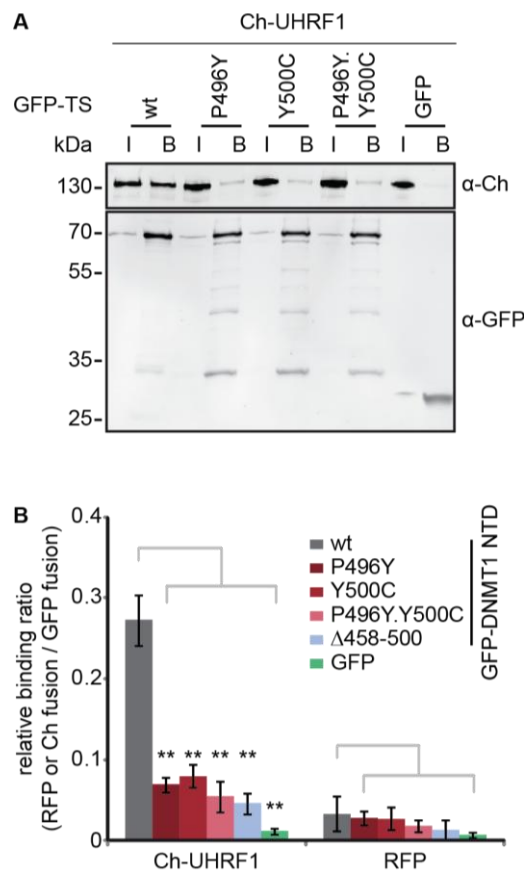


Figure 4. HSAN-IE associated point mutations and a central deletion in the TS domain of DNMT1 affect the interaction with UHRF1. (A) Co-immunoprecipitation of GFP-TS P496Y, Y500C single and the P496Y.Y500C double point mutants as well as the corresponding wt co-expressed with Ch-UHRF1 in HEK293T cells. Bound fractions were analyzed by immunoblotting with an anti-GFP and anti-Ch antibody, respectively. GFP was used as negative control. I = Input, B = Bound. **(B)** Fluorescence protein-protein interaction assay. After one-step purification of the GFP-DNMT1 NTD wt and mutant constructs in a GFP-multiTrap plate, the binding of Ch-UHRF1 expressed in HEK293T cells was determined by fluorescence readout. GFP and RFP were used as negative control, respectively. Shown are mean relative binding ratios \pm s.e.m of Ch-UHRF1 or RFP over GFP fusion proteins from four to six biological replicates. Two-sample t-tests were performed that assume equal variances. Statistical significance compared to the relative binding ratio of GFP-DNMT1 NTD wt is indicated: *P<0.02, **P<0.001.

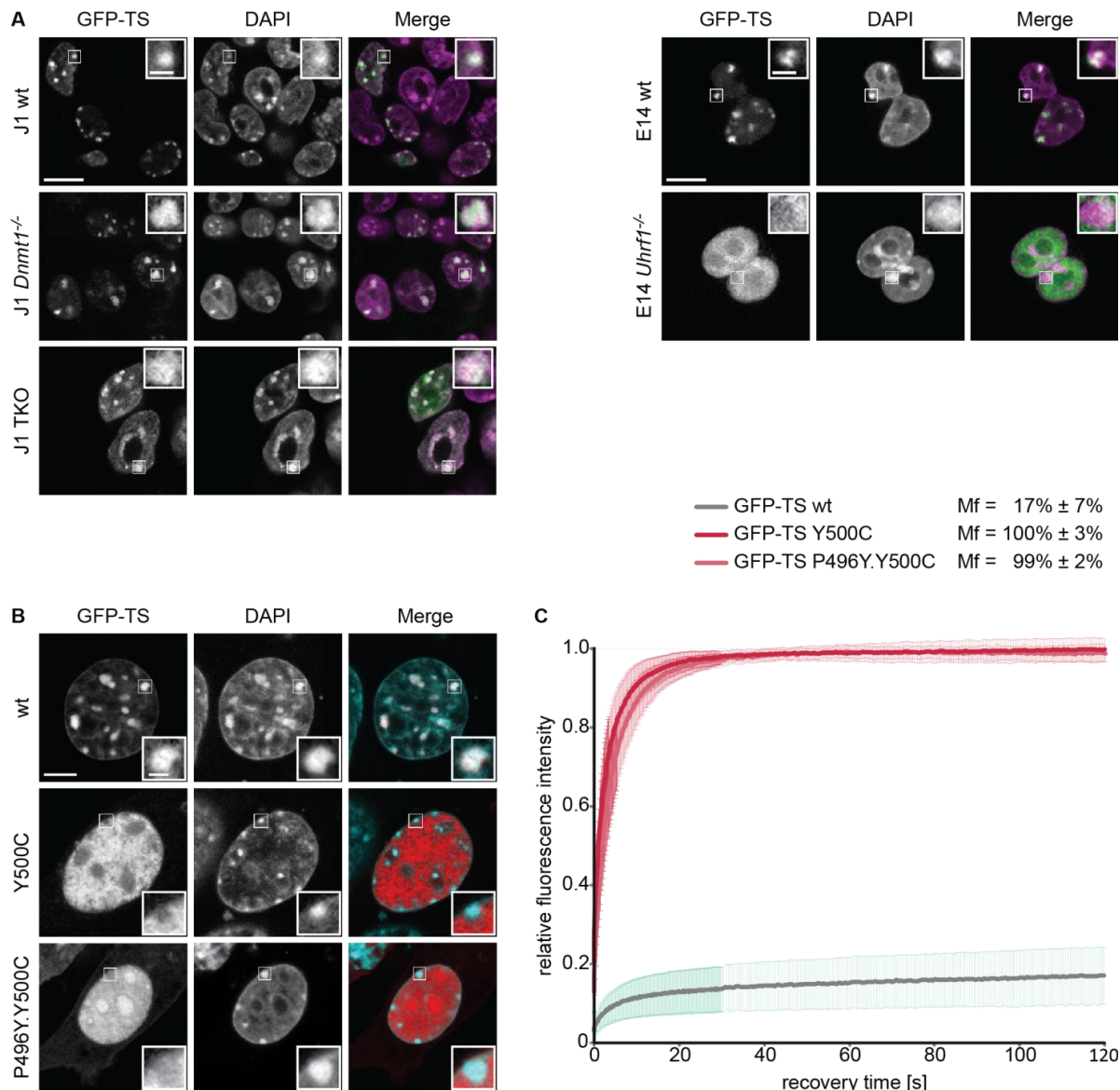


Figure 5. Mutations in the TS domain impede the strong heterochromatin association and the slow protein kinetics of the wt domain. (A) Confocal mid sections of fixed mouse ESCs (J1, E14) transiently expressing GFP-TS and counterstained with DAPI as a marker for heterochromatin. ESCs with different genetic backgrounds were used that are devoid of DNMT1 (J1 *Dnmt1*^{-/-}), all three DNA methyltransferases DNMT1, DNMT3A and DNMT3B (J1 triple knockout (TKO)) as well as cells devoid of UHRF1 (E14 *Uhrf1*^{-/-}). In the merged image, DAPI is depicted in magenta. Scale bar 10 μ m; enlargements: 3-times magnification, scale bar 2 μ m. (B) Confocal mid sections of fixed MEF cells transfected with GFP-TS wt or GFP-TS Y500C single and P496Y, Y500C double mutant constructs. In the merged image, GFP-TS is depicted in red and DAPI in magenta. Scale bar 5 μ m; enlargements: 3-times magnification, scale bar 1 μ m. (C) Protein kinetics of GFP-TS wt and HSAN-IE associated GFP-TS Y500C and P497Y.Y500C point mutants in living MEF cells determined by half nucleus fluorescent recovery after photobleaching (FRAP) analysis. Curves represent mean \pm s.e.m. of at least 13 nuclei. The mobile fraction (M_f) is indicated.

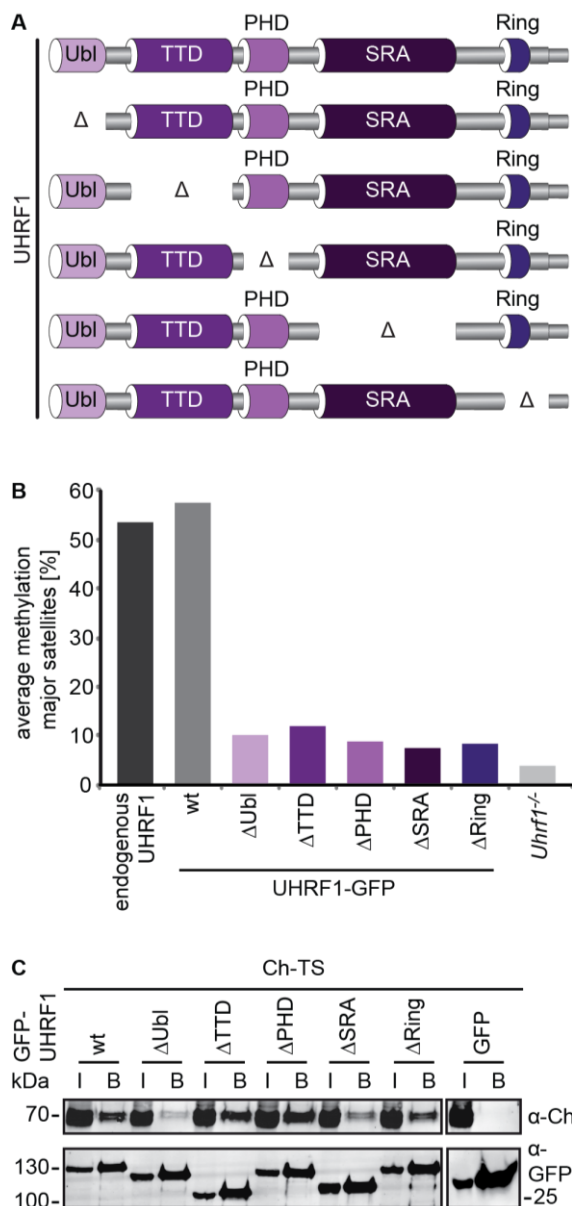


Figure 6. Each domain of UHRF1 is necessary for regulation of DNA methylation by DNMT1. (A) Schematic outline of different UHRF1-GFP single domain deletion (Δ) constructs used for rescue experiments. (B) Local methylation analysis at the of major satellite repeats. CpG methylation levels in E14 *Uhrtf1*^{-/-} ESCs stably expressing UHRF1-GFP wt or single domain deletions were analyzed by bisulfite treatment of genomic DNA, PCR amplification and direct pyrosequencing. Methylation levels of untransfected cells are shown for comparison. Values represent means from eight CpG sites, respectively. (C) Co-immunoprecipitation of UHRF1-GFP wt and single domain deletion mutants with Ch-TS after co-expression in HEK293T cells. Bound fractions were detected by immunoblotting with anti-GFP and anti-Ch antibodies, respectively. GFP was used as negative control. I = Input, B = Bound.

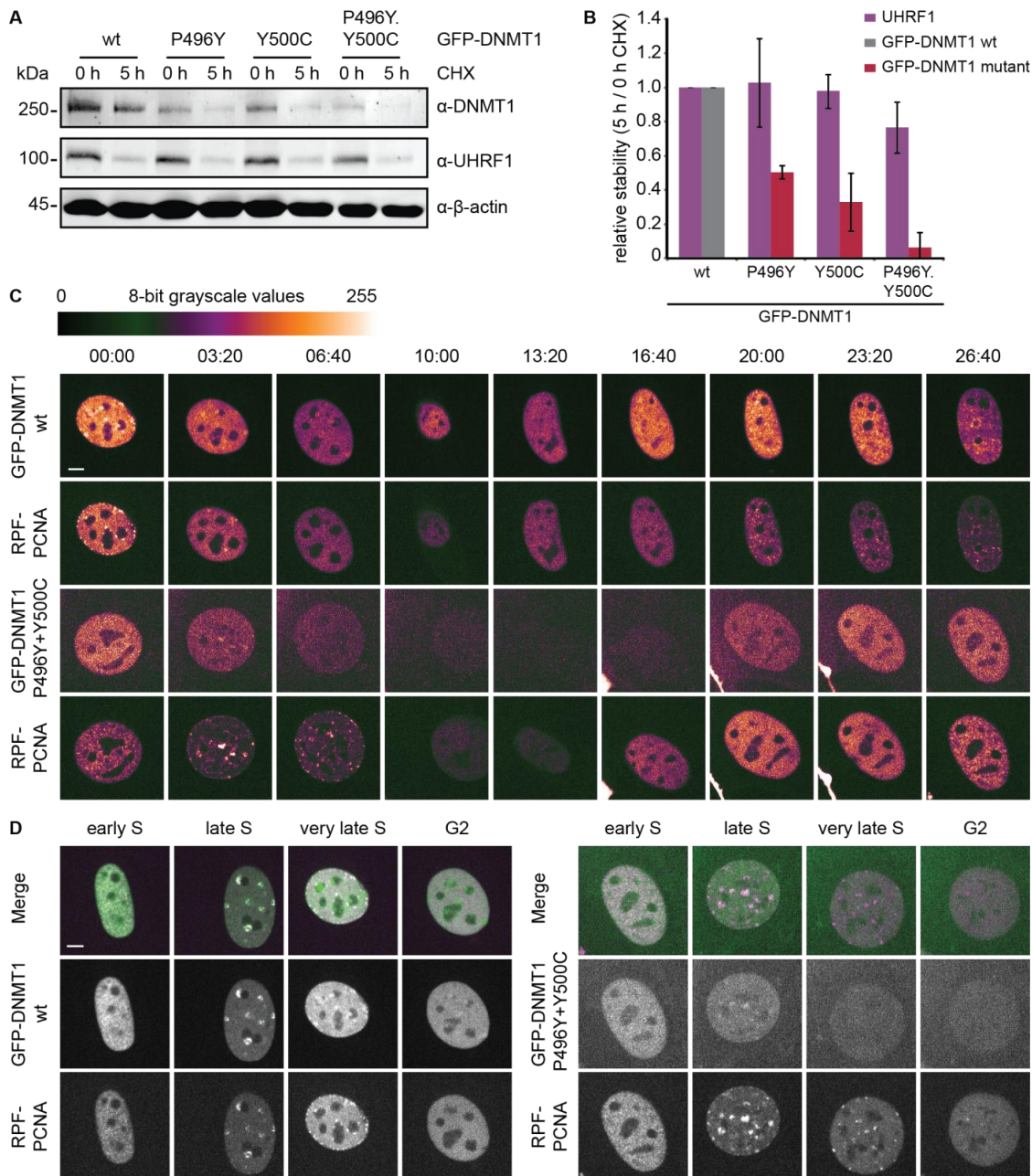


Figure 7. HSAN-IE associated mutations in the TS domain of DNMT1 decrease protein stability in a cell cycle-dependent manner. (A) and (B) Cycloheximide (CHX) assay in *Dnmt1*^{-/-} ESCs stably expressing GFP-DNMT1 wt or P496Y and Y500C single as well as P496Y.Y500C double point mutants. Cells were seeded to equal densities and treated with 0.03 mg/ml CHX for 0 and 5 h, respectively. After harvesting, expression levels of GFP-DNMT1 and endogenous UHRF1 were analyzed by immunoblotting with specific antibodies and by quantification of the resulting signals using Image J. Equal loading was confirmed by β -actin staining. (A) Shown is one representative blot of two independent experiments with lysates of approximately 360,000 cells loaded per lane. (B) Quantification of the protein expression 5 h after CHX treatment compared to the expression without treatment (0 h). Shown are mean values \pm s.d. of two biological replicates relative to the loading control and normalized to the expression of GFP-DNMT1 or UHRF1 in the wt cell line, respectively. (C) Live cell series of MEF cells transiently co-expressing GFP-DNMT1 wt or the P496Y.Y500C double point mutant and RFP-PCNA as a cell cycle marker. Starting from very late S phase (wt) or mid S phase (P496Y.Y500C) images were taken every 200 min. For better comparison, signals were adjusted according to expression levels of the different constructs. White represents the highest and black the lowest intensity. Scale bar 5 μ m. (D) Defined cell cycle stages of the live cell series depicted in (C). In the merged image, RFP-PCNA is depicted in magenta. Scale bar 5 μ m.

SUPPLEMENTARY FIGURES AND LEGENDS

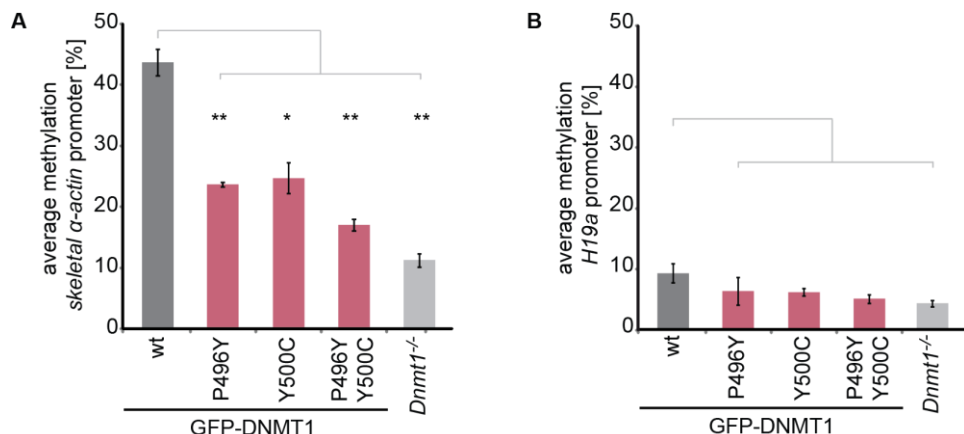


Figure S1. HSAN-IE associated DNMT1 TS mutants cannot restore the local methylation level at the skeletal α -actin promoter. (A) and (B) Mouse *Dnmt1*^{-/-} ESCs were FACS-sorted 48 h after transient transfection with GFP-DNMT1 wt or P496Y and Y500C single as well as P496Y.Y500C double mutant constructs and CpG methylation levels at (A) the skeletal α -actin and (B) the $H19a$ promoter were analyzed by bisulfite treatment, PCR amplification and direct pyrosequencing. Methylation levels of untransfected cells are displayed for comparison. Bar graphs represent mean values \pm s.d. from three biological replicates (average from 13 or 6 CpG sites, respectively) and two-sample t-tests were performed that assume equal variances. Statistical significance compared to the methylation level of GFP-DNMT1 wt is indicated: * $P<0.02$, ** $P<0.0002$.

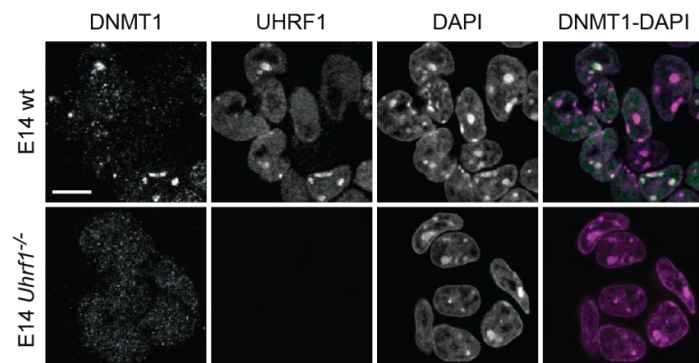


Figure S2. DNMT1 shows a diffuse nuclear pattern in *Uhrf1*^{-/-} ESCs. Confocal mid sections of fixed mouse E14 wt and *Uhrf1*^{-/-} ESCs. Endogenous DNMT1 and UHRF1 were immunostained with specific antibodies and chromatin was counterstained with DAPI. In the merged image, DAPI is depicted in magenta and DNMT1 in green. Scale bar 10 μ m.

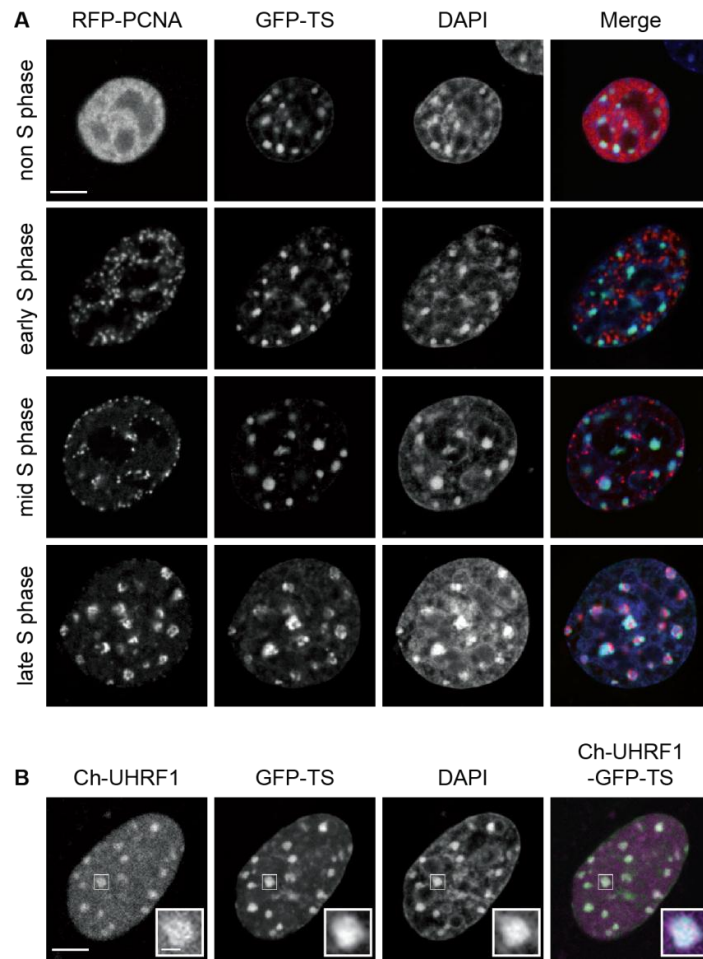


Figure S3. The TS domain of DNMT1 shows strong heterochromatin association that is independent of the cell cycle and co-localizes with UHRF1. (A) Confocal mid sections of fixed mouse embryonic fibroblast (MEF) cells co-expressing GFP-TS and the cell cycle marker RFP-PCNA. DAPI is used for chromatin counterstaining. Scale bar 5 μ m. **(B)** Confocal mid sections of fixed MEF cells co-expressing GFP-TS and Ch-UHRF1. DAPI is used for chromatin counterstaining. In the merged image, Ch-UHRF1 is depicted in magenta. Scale bar 5 μ m; enlargements: 3-times magnification, scale bar 1 μ m.

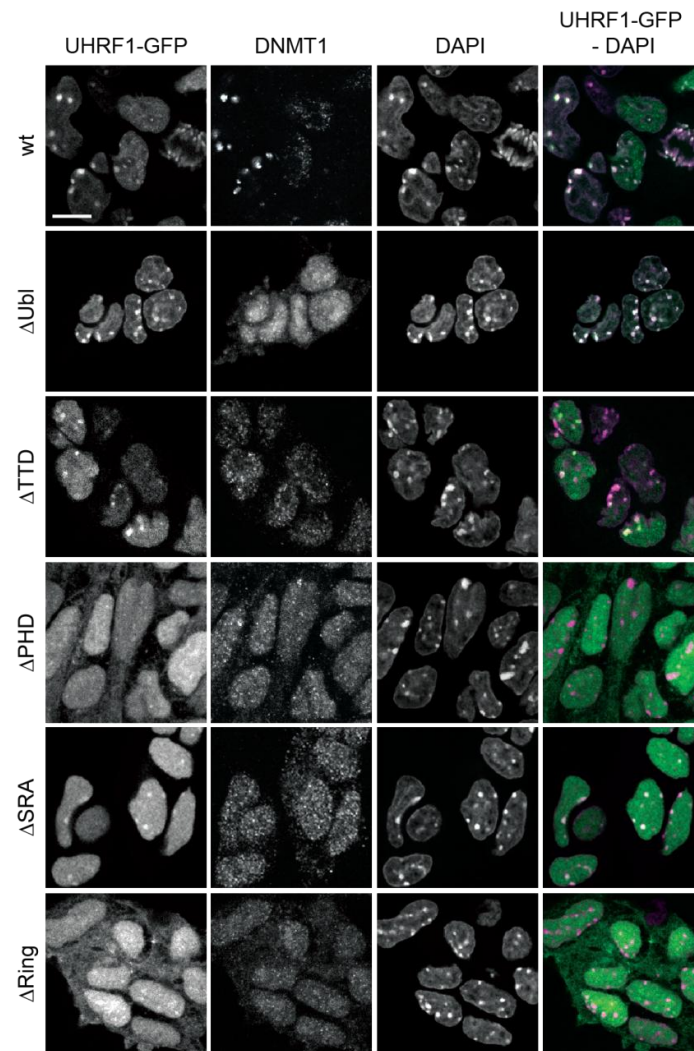


Figure S4. DNMT1 is mislocalized in *Uhrf1*^{-/-} ESCs stably expressing GFP-UHRF1 single domain deletion mutants. Confocal mid sections of fixed mouse E14 *Uhrf1*^{-/-} ESCs stably expressing UHRF1-GFP wt or single domain deletion mutant constructs. Endogenous DNMT1 was immunostained with a specific antibody and chromatin was counterstained with DAPI. In the merged image, DAPI is depicted in magenta. Scale bar 10 μ m.

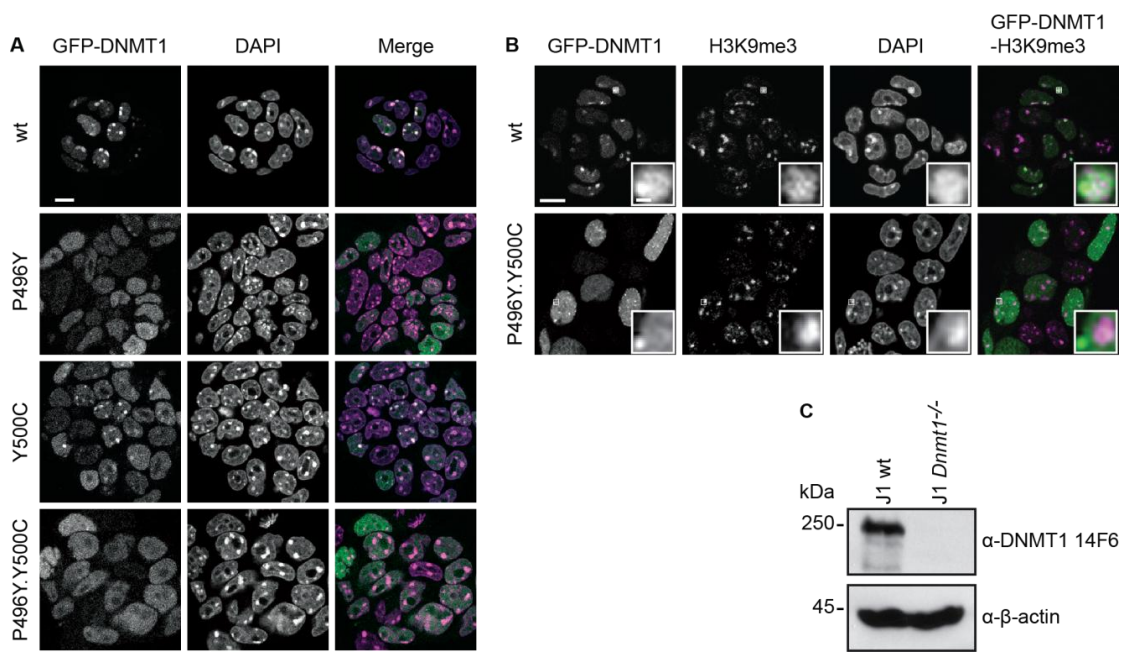


Figure S5. GFP-DNMT1 TS mutations lead to decreased association with heterochromatin. (A) and (B) Localization of GFP-DNMT1 wt and HSAN-IE associated mutants P496Y, Y500C and P496Y.Y500C stably expressed in J1 *Dnmt1*^{-/-}. DAPI was used for chromatin counterstaining. In the merged image, DAPI is depicted in magenta. Scale bar 5 μ m. (B) In stable cell lines from (A) heterochromatin was immunostained with a specific anti-H3K9me3 antibody. In the merged image, H3K9me3 is depicted in magenta. Scale bar 5 μ m; enlargements: 3-times magnification, scale bar 1 μ m. (C) Specificity of the monoclonal anti-DNMT1 antibody 14F6. Approximately 450,000 J1 wt and J1 *Dnmt1*^{-/-} mouse ESCs were loaded per lane and endogenous DNMT1 was detected using the anti-DNMT1 antibody 14F6; β -actin shows equal loading.

3. Discussion

The key regulator of maintenance DNA methylation, UHRF1, is known to directly interact with DNMT1. However, the protein domains mediating this interaction remain elusive. Therefore, we developed a semiquantitative assay in a 96-well format that allows for systematic mapping analyses of protein-protein interactions.

3.1 Potential and limitations of the developed protein-protein interaction assay

In the field of proteomics, the analysis of protein-protein interactions plays a fundamental role. Identification and characterization of new protein binding partners opens the possibility for a better understanding of the interconnection between different biological pathways, protein complex formation and protein regulation, for instance by allosteric activation or PTMs. Various methods for the study of protein-protein interactions have been developed. These include genetic assays like Yeast two-Hybrid, *in vitro* techniques like co-immunoprecipitation or *in vivo* molecule proximity based techniques like fluorescence resonance energy transfer (FRET) or bimolecular fluorescence complementation (BiFC) assays as well as protein co-localization.

Here we describe a versatile method based on the affinity purification of GFP fusion proteins in a 96-well micro plate coated with immobilized GFP-Trap (GFP-multiTrap) (Rothbauer et al. 2008; Pichler et al. 2012). Using GFP and RFP tagged fusion proteins and fluorescently labeled binding substrates carrying defined modifications, it is possible to quantify protein-protein and protein-substrate interactions in a semiquantitative manner (Figure 3.1). After one-step purification of GFP fusion proteins, the potential binding to RFP fusion proteins was analyzed. Relative protein-protein binding ratios were measured with a fluorescence intensity read-out system and relative molar binding ratios of RFP over GFP fusion proteins were calculated.

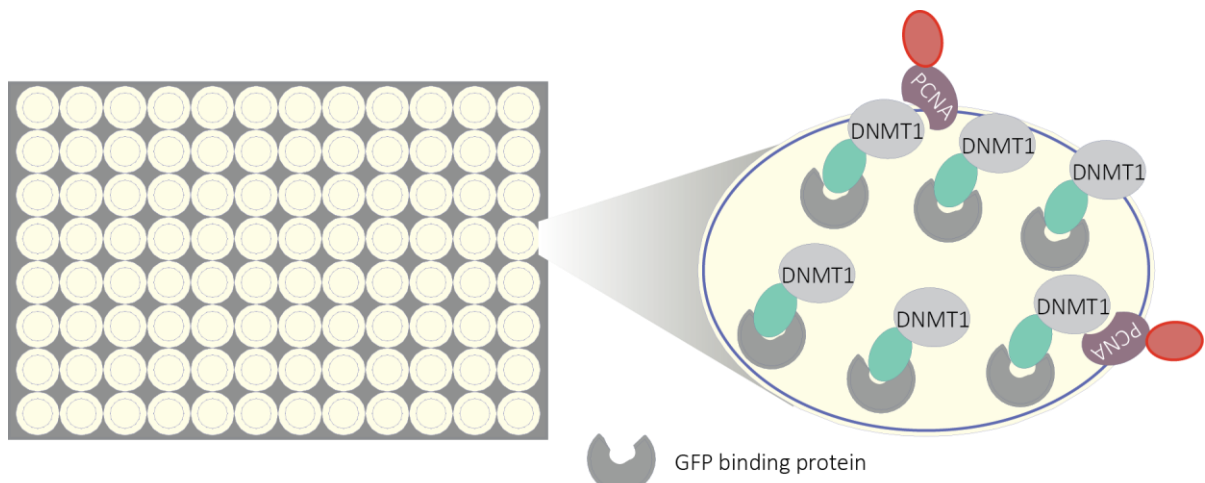


Figure 3.1: Scheme of the protein-protein interaction assay based on the GFP-multiTrap. Illustration of GFP-DNMT1 interacting with RFP-PCNA.

To test the suitability of the GFP-multiTrap format, we choose to investigate the interaction of the PBD in DNMT1 with the replication platform PCNA (Leonhardt et al. 1992; Chuang et al. 1997). In our experiments, the incubation of a constant amount of the GFP-PBD domain of DNMT1 with increasing concentrations of RFP-PCNA resulted in an increase of the binding ratio. For RFP input concentrations higher than 30 times the concentration of bound GFP-PBD, however, the binding ratio reached a plateau meaning that all binding sites on GFP-PBD were saturated. This experiment also demonstrated that no unspecific binding of RFP to GFP-PBD was detected independently of the input concentration. In general, this finding implicates that for each interacting protein partner, tests should be performed to determine the excess of RFP fusion protein needed in order to achieve saturation.

Fusion of the proteins of interest to fluorescent tags not only allows for the quantification of interactions *in vitro*, but also for their visualization in living cells. The developed protein-protein interaction assay offers several advantages when compared to conventional co-immunoprecipitation methods (Table 3.1). Firstly, performance of the interaction assay in GFP-multiTrap plates is less labor-intense and less time consuming. Compared to batch purification of GFP fusion proteins with GFP-Trap beads, the one-step purification with the GFP-multiTrap allows for fast and parallel immunoprecipitation of different proteins of interest. Essentially, centrifugation steps for the sedimentation of beads are substituted by fast and efficient washing steps. Secondly, the medium throughput manner enables testing of different interacting partners in parallel. By applying triplicates per interacting protein partners, obtained results become more reliable. Moreover, test experiments for optimization of the assay settings, like varying protein input concentrations and different binding and washing conditions can easily be performed in parallel. Thirdly, this fluorescence intensity based protein-protein interaction assay offers the possibility to calculate relative binding ratios between the interacting partners. Quantifying interactions can help to understand the impact of different domains in mediating this interaction (mapping experiments) or to estimate the nature of the interaction (transient or stable). Furthermore, the robustness of different interactions can be investigated by applying different subsequent washing conditions with intermediary fluorescence intensity measurements. Finally, as the assay is based on fluorescent fusion proteins, it is compatible with other methods for analysis of interactions like Western blotting, co-localization studies, our recently developed fluorescence three hybrid assay (F3H) (Zolghadr et al. 2008; Herce et al. 2013) or fluorescence recovery after photobleaching (FRAP).

During the development of the presented assay, we found that to achieve a semiquantitative readout, the amounts of GFP fusion proteins in the bound fraction have to be balanced prior to the incubation with the potential RFP fusion binding partners. Thus the potential interactors were expressed separately from the GFP fusions bearing the risk that interactions, which are for instance dependent on other cellular components, are not detectable.

In order to express the suitability of this protein-protein interaction assay for medium throughput approaches, we calculated the Z-factor ($Z = 1 - \frac{3x(\sigma_p + \sigma_n)}{|\mu_p - \mu_n|}$; σ is the standard deviation of the positive (σ_p) and the negative (σ_n) control; μ is the mean value for the molar binding ratio of the positive (μ_p) and negative (μ_n) controls) (Zhang et al. 1999). The binding ratio of RFP-PCNA to GFP-PBD was used as positive state (p) and the ratio of RFP to GFP-PBD as negative state (n). The Z-factor of 0.56 indicates that this approach allows for quantification of protein-protein interactions in a robust and reproducible manner.

In general, our assay is well suited for the semiquantitative analysis of robust protein-protein interactions in a multi-well format. An increase in the sensitivity was achieved by applying an enzyme-linked immunosorbent assay (ELISA) with specific antibodies for endogenous interaction partners of the bound GFP fusion proteins.

Table 3.1: Overview of advantages and disadvantages of the fluorescent protein-protein interaction assay in the GFP-multiTrap.

Properties	Advantage or disadvantage
Handling in general	Fast, less labor intense (compared to conventional co-immunoprecipitation methods)
Protein amounts	Low
Background	Low
Reproducibility	High
Manifoldness	High (protein-DNA, protein-histone tail peptide, protein-protein binding)
Sensitivity	Low (increased by ELISA)
Compatibility with other methods	High (e.g. ELISA, Western blot, co-localization, F3H, FRAP)

3.2 Regulation and abundance of DNMT1 during the cell cycle

3.2.1 UHRF1-mediated mechanisms regulating DNMT1 chromatin targeting

Precisely coordinated mechanisms regulating DNMT1 targeting to chromatin are essential for faithful propagation of DNA methylation during replication. Although DNMT1 was reported to have an intrinsic 30 to 40-fold preference for hemimethylated DNA and to bind the replication protein PCNA, the cofactor UHRF1 was found to be indispensable for recruitment of DNMT1 to its substrate (Ooi and Bestor 2008; Hashimoto et al. 2009).

Chromatin targeting of DNMT1 by direct interaction with UHRF1

First evidence of UHRF1 as an important recruitment factor for DNMT1 emerged from studies describing its preference for hemimethylated DNA resulting from the semiconservative replication mechanism and its direct interaction with DNMT1 (Bostick et al. 2007; Sharif et al. 2007; Arita et al. 2008; Avvakumov et al. 2008; Hashimoto et al. 2008) (Figure 3.3). *Uhrf1* knockout cells mimic the phenotype of *Dnmt1* knockout cells characterized by global DNA hypomethylation (Li et al. 1992; Bostick et al. 2007). Recently, the UHRF1 interacting domain has been mapped to the TS domain of DNMT1 (Achour et al. 2008; Felle et al. 2011; Berk'yurek et al. 2013; Bashtrykov et al. 2014a), but also to its catalytic CTD (Bostick et al. 2007). We further characterized the interaction by precise mapping studies on UHRF1 and DNMT1. Consistent with previous studies, we found that the TS domain is the interacting site in DNMT1 as shown by semiquantitative co-immunoprecipitation assays and *in vivo* localization studies. On the side of UHRF1, the DNMT1 interacting domain has been mostly assigned to the SRA domain (Felle et al. 2011; Berk'yurek et al. 2013; Bashtrykov et al. 2014a). Surprisingly, in our experiments, two domains in UHRF1 contributed to the interaction. Besides the SRA domain, we could show that the Ubl domain of UHRF1 is involved in the interaction with DNMT1. Whether the Ubl and the SRA domain act together or independently in specific cell cycle stages or different steps of the methylation mechanism, possibly depend on the structural conformation of DNMT1, requires further investigation. One might also speculate that one domain of UHRF1 is responsible for the recruitment of DNMT1 to its substrate, whereas the other interacting domain is necessary for DNMT1 binding prior to its ubiquitination by the UHRF1 RING domain (3.2.2). In any case, our findings suggest that the Ubl as well as the SRA domain are crucial for the regulation of maintenance DNA methylation.

UHRF1 as a reader and writer of histone PTMs

The role of UHRF1 in maintenance methylation exceeds its ability to interact with DNMT1 and to recognize the DNA methylation substrate. Growing evidence suggests that UHRF1 binds and sets distinct epigenetic marks on chromatin. Reading and writing of these marks by different UHRF1 domains and their implications in DNMT1 interaction, recruitment and regulation are summarized in Table 3.2.

Table 3.2: Role of different UHRF1 domains in H3 or DNA binding, heterochromatin localization, interactions with DNMT1 and maintenance DNA methylation. Each domain of UHRF1 has distinct roles in regulating maintenance methylation by DNMT1. - indicates no role, +/- a partial influence and + an important role. Properties of UHRF1 domains that remain unclear or need further investigations are marked by (?).

Role of UHRF1 domains	H3 N-terminal tail or DNA binding	H3 PTMs setting	PH localization	Interaction with DNMT1	Regulation of DNMT1 PH localization	Regulation of DNA methylation by DNMT1
Ubl	-	-	-	+	+ (?)	+ (?)
TTD	+ (H3K9me3)	-	+/-	-	+	+
PHD	+ (H3R2)	-	+/-	-	+	+
SRA	+ (hemi 5mC)	-	+/-	+	+	+
RING	-	+ (H3K18ub)	-	-	+	+

Besides the DNA binding SRA domain, UHRF1 contains two histone reader modules. Firstly, the TTD forms an aromatic cage to bind H3 tails di- and trimethylated at K9 (Citterio et al. 2004; Karagianni et al. 2008; Rottach et al. 2010). Secondly, the PHD has been proposed to contribute to binding of this repressive mark and to recognize unmodified H3R2 of the same histone tail (Wang et al. 2011; Arita et al. 2012; Xie et al. 2012a; Cheng et al. 2013). In this study, we could confirm that the UHRF1 PHD binds to H3R2 and that this binding is sensitive towards R2 dimethylation (Qin et al. 2015), consistent with previous studies (Rajakumara et al. 2011). Moreover, H3R2 recognition by the PHD was necessary for localization of DNMT1 at chromocenters and for maintenance DNA methylation. Consistently, H3K9me3 binding by the combined TTD and PHD was recently proposed to be essential for regulating maintenance methylation by DNMT1 (Rothbart et al. 2013).

It has been proposed that histone binding of the PHD plays an important role in targeting UHRF1 to euchromatic regions linked to active gene expression (Rajakumara et al. 2011). Whether the PHD is only required for association of UHRF1 with euchromatin or also contributes to TTD-mediated recognition of repressive H3K9me3, remains unclear. Notably, asymmetric dimethylation of H3R2 by the protein arginine methyltransferase 6 (PRMT6) has recently been found to antagonize the euchromatic mark H3K4me3 resulting in transcriptional repression (Hyllus et al. 2007). Given that PHD-mediated recognition of H3 is sensitive towards asymmetric dimethylation of R2 and is involved in DNMT1 targeting, this histone reader specificity of UHRF1 might indeed be important for DNA methylation in euchromatic regions.

Intriguingly, the nuclear lipid signaling molecule phosphatidylinositol 5-phosphate (PI5P) has been shown to coordinate histone binding specificity of UHRF1 (Gelato et al. 2014; Reynoard and Gozani 2014). In absence of PI5P the association of UHRF1 with chromatin is dominated by the PHD-mediated binding to the unmodified H3 N-terminal tail. In the presence of PI5P, however, the TTD is the driving force for UHRF1 binding to H3K9me3. This switch in histone binding preferences is based on a conformational change of the protein triggered by PI5P binding to a polybasic region (PBR) in the C-terminus of UHRF1. An intramolecular interaction between the TTD and the PBR blocks the histone binding ability of the TTD, which is released by allosteric activation of PI5P binding to the PBR. Interestingly, PI5P levels increase during S phase (Shah et al. 2013). This dynamic regulation might influence cell cycle-dependent differences of UHRF1 association with chromatin. Therefore, DNMT1 targeting to H3K9me3-rich heterochromatin by UHRF1 interaction might be favored in late S phase. The inhibitory function of the PBR within UHRF1 opens an additional level of regulation depending on the nuclear levels of PI5P.

Besides its important function in reading distinct epigenetic marks on DNA and histones, UHRF1 was recently reported to set histone PTMs that might help to recruit DNMT1 to its substrate (Nishiyama et al. 2013). The authors of this study illustrate that UHRF1 ubiquitinates histone H3 by means of its RING domain. Notably, whereas Nishiyama and colleagues found the residue K23 to be ubiquitinated by UHRF1 in *Xenopus* egg extracts and human cells (Nishiyama et al. 2013), our mass spectrometry data support ubiquitination at K18, but not K23 in mouse ESCs (Qin et al. 2015). Therefore, the ubiquitinated residue on H3 might vary among different species. S phase-dependent ubiquitination of H3 by UHRF1 was found to be dependent on binding of the SRA domain to hemimethylated DNA. Thus UHRF1 DNA binding might precede the process of setting the new histone mark (Nishiyama et al. 2013). We investigated the contribution of the PHD in UHRF1-dependent H3 ubiquitination. Interestingly, a PHD mutant defective in binding H3 peptides carrying an unmodified R2 residue also showed decreased ubiquitination activity towards H3. Therefore, we suggest that PHD-mediated H3R2 recognition might be one of the first steps in UHRF1 heterochromatin binding and might serve as a prerequisite for subsequent RING domain-mediated H3K18 ubiquitination.

Ubiquitin-dependent chromatin targeting of DNMT1

Recently, it was proposed that UHRF1-dependent ubiquitination of H3K23 is recognized by DNMT1 (Nishiyama et al. 2013). However, the mode of recognition remained elusive. We identified a ubiquitin interacting motif (UIM) within the TS domain of DNMT1 that mediates the recognition of ubiquitinated histone tails (Qin et al. 2015).

UIMs represent specific ubiquitin binding modules and were first described in the 26 S protease subunit 5a (S5a, Figure 3.2) (Young et al. 1998; Wang et al. 2005). According to several crystal structures, protein regions harboring a UIM form a short α -helix as part of a protein fold (Fisher et al. 2003; Lim et al. 2011), like the UIM in DNMT1. UIMs might potentially arrange into oligomers that could explain the presence of several successive UIMs in some ubiquitin binding proteins like in S5a (tandem UIMs) (Fisher et al. 2003; Hirano et al. 2006). Various biological functions are ascribed to proteins containing UIMs that are based on the recognition of mono- and polyubiquitin, or the interaction with ubiquitin-like modifiers (Schultz and Letunic 1998, 2012). The individual role of ubiquitin binding proteins in ubiquitin metabolism often depends on the UIM type and the mode of ubiquitin recognition. The structure of the double-sided single UIM in the hepatocyte growth factor regulated tyrosine kinase substrate (HRS), for instance, suggests that this protein can efficiently recognize multiply monoubiquitinated proteins prone for lysosomal degradation. The mode of ubiquitin recognition on double-sided single UIMs is based on the presence of two closely-spaced UIMs shifted by two amino acids only (Hirano et al. 2006). In contrast, the single-sided tandem UIMs in S5a enables recognition of polyubiquitinated proteins and their subsequent degradation by the proteasome (Wang et al. 2005).

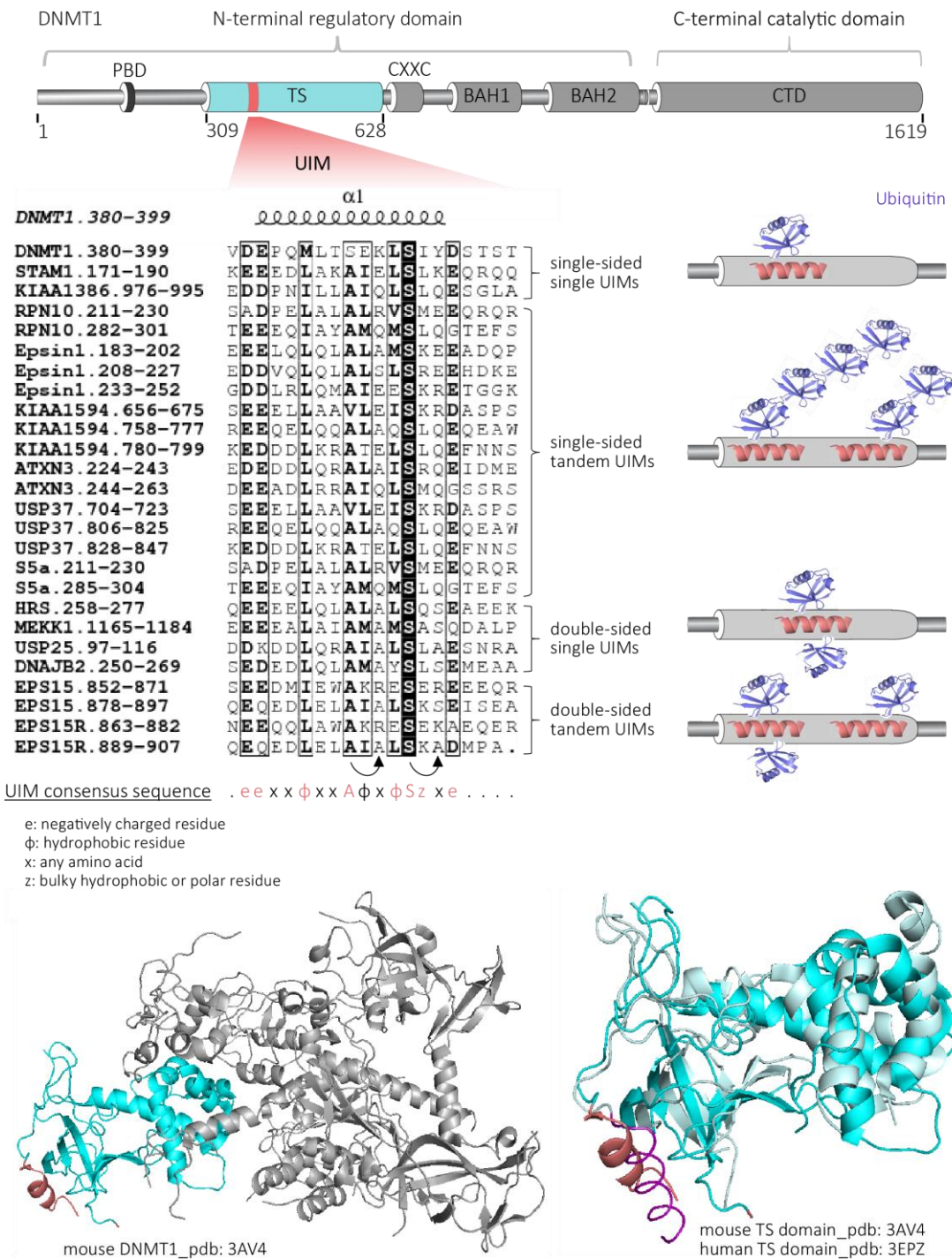


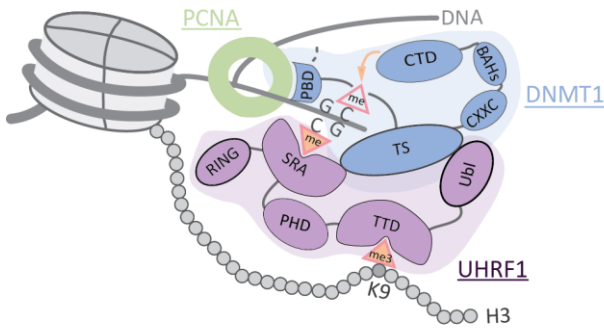
Figure 3.2: Primary sequence and secondary structure of the ubiquitin interacting motif (UIM) in DNMT1. Top: Domain structure of DNMT1 with illustration of the UIM in the TS domain. Center: Alignment of protein regions containing UIMs that were identified by use of the Expasy ScanProsite tool, except for DNMT1. The consensus sequence for single-sided UIMs is shown below (Hirano et al. 2006). The shift of the motif in double-sided UIMs by two amino acids (A x A x S x S/A) is indicated by arrowheads. The putative subtype of the UIM with its mode of ubiquitin recognition is exemplified on the right. The UIM in the TS domain of DNMT1 does not entirely match the published consensus sequence (Hirano et al. 2006), but it comprises important features like the negatively charged amino acids D381, E382 and D395, the hydrophobic M385 and the highly conserved S at position 395. Bottom left: Secondary structure of mouse DNMT1 (pdb: 3AV4, (Takeshita et al. 2011)) with representation of the UIM (salmon) in the TS domain (cyan). Bottom right: We used superimposition of the secondary structure of the mouse (cyan, pdb: 3AV4) and human (lightcyan, pdb: 3EPZ, (Syeda et al. 2011)) TS domain in Pymol to show that the UIM in DNMT1 forms an α -helix (depicted in salmon and purple, respectively).

A UIM module is composed of 20 residues carrying e-e-x-x- ϕ -x-x-A- ϕ -x- ϕ -S-z-x-e (Hirano et al. 2006), ϕ -x-x-A-x-x-S-x-x-e (Hofmann and Falquet 2001), x-e-e-e-x- ϕ -x-x-A-x-x-S-x-x-e-x-x-x (Miller et al. 2004) or x-e-e-e-e- ϕ -x-x-A-x-x-S-x-x-e-x-x-x (Fisher et al. 2003) as consensus sequence, where x is any amino acid, e is a negatively charged residue, ϕ is a hydrophobic residue and z is a bulky hydrophobic or polar residue. The UIM in the TS domain of DNMT1 does not completely match with these consensus sequences, but it contains important features of single-sided single UIMs (Figure 3.2). Crystallographic studies of the UIM in STAM1 indicate that the three central amino acids L176, A179 and S183, form a hydrophobic interface for ubiquitin binding (Lim et al. 2011). Like in STAM1, the UIM in DNMT1 also contains the central hydrophobic amino acid M385 and S392 flanked by negatively charged amino acids (D381, E382, D395). However, the UIM in DNMT1 does not harbor the central A, which is highly conserved in other ubiquitin binding proteins.

In vitro, we analyzed binding of specific DNMT1 UIM mutants to ubiquitinated H3 indicating that it is dependent on conserved amino acids in the motif. The negatively charged residues D381 and E382 in the N-terminal part of the motif and the highly conserved S395 were necessary for binding to ubiquitinated H3. By use of DNMT1 UIM mutants defective in binding ubiquitinated H3, we showed that the motif is essential for maintenance DNA methylation *in vivo*. Moreover, mutations in the UIM led to weaker association of DNMT1 with chromocenters in late S phase. In line with this, a deletion and a mutation in the RING domain of UHRF1 disrupting its E3 ubiquitin ligase activity resulted in diffuse nuclear localization of DNMT1. These findings suggest a recruitment of DNMT1 that is dependent on the RING domain-mediated writing of ubiquitinated histone H3K18. Therefore, the function of UHRF1 as a writer of a histone PTM initiates a ubiquitin-dependent targeting mechanism of DNMT1. This mechanism relies on binding of the UIM to ubiquitinated H3, but not on direct interaction with UHRF1 (Figure 3.3).

In general, ubiquitination of histones is most prevalent on H2A and H2B and has been linked to transcriptional repression and activation, respectively (Zhang 2003). Really interesting new gene 1A and B (RING1A/B), which are part of the Polycomb repressive complex 1 (PRC1), are examples for proteins containing a similar RING domain as UHRF1. In ESCs, RING1A/B are involved in repression of developmental regulatory genes by mono-ubiquitination of H2A at K119 (Wang et al. 2004; Stock et al. 2007; Endoh et al. 2008). Similar to ubiquitinated H2AK119, we show that the modification on H3 set by UHRF1 is linked to repressive DNA methylation. UHRF1 ubiquitinates H3 on K18 and thereby recruits DNMT1 for DNA methylation. Interestingly, we also found that DNMT1 binds to ubiquitinated H2AK119. In agreement with our finding, a recent study reported DNMT1 among ubiquitinated H2A binding proteins (Kalb et al. 2014). Given that DNMTs interact with EZH2 (Vire et al. 2006), a component of the PRC2 complex that sets the heterochromatic H3K27me3 mark, UIM-mediated binding of DNMT1 to ubiquitinated H2A might link DNA methylation to other polycomb-mediated repressive epigenetic pathways. These findings open new perspectives for a function of DNMT1 distinct from classic maintenance DNA methylation.

Targeting of DNMT1 by direct interaction with UHRF1



Ubiquitin-dependent targeting of DNMT1

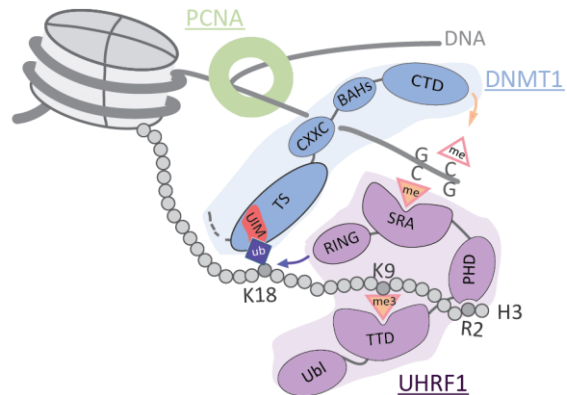


Figure 3.3: Schematic representation of DNMT1 chromatin targeting mechanisms. In both mechanisms, chromatin association of UHRF1 is achieved by TTD-mediated binding to H3K9me3 and SRA-mediated binding to hemimethylated DNA. left: Chromatin targeting of DNMT1 by direct interaction of its TS domain with the Ubl and the SRA domains of UHRF1. Interaction with the SRA domain leads to release of the autoinhibitory function of the TS domain and allows for catalytic activity of the CTD. Interaction of the PBD in DNMT1 with PCNA couples maintenance methylation with DNA replication. The impact of UHRF1 PHD-mediated binding to H3R2 remains elusive. right: Ubiquitin-dependent chromatin targeting of DNMT1 relies on UHRF1 RING domain-mediated ubiquitination of H3 at K18. Binding of the PHD to unmodified H3R2 might serve as a prerequisite for subsequent E3 ubiquitin ligase activity on H3. DNMT1 recognizes ubiquitinated H3K18 by its UIM and methylates target sites in the DNA. Whether this mechanism is coupled to replication and PBD-mediated PCNA binding remains unclear.

In summary, the TS domain has two important functions in UHRF1-mediated mechanisms regulating DNMT1 chromatin recruitment: Firstly, DNMT1 targeting by direct interaction with UHRF1 and secondly, DNMT1 targeting by UIM-mediated binding to ubiquitinated H3K18. To date, it remains elusive whether the two functions of the TS domain are connected or take place in different cell cycle phases. Given that in our studies defects in UHRF1 interaction as well as ubiquitinated H3 binding led to decreased DNMT1 activity in heterochromatic regions, we speculate that both targeting mechanisms are essential for the regulation of maintenance methylation. Future studies analyzing the necessity of different UHRF1 chromatin binding abilities for H3 ubiquitination and its dependencies on the cell cycle will expand our understanding about timing and precise regulation of DNMT1 targeting.

Mounting evidence indicates that the TS domain has to be released from the catalytic center of DNMT1 before the methylation reaction can take place (Syeda et al. 2011; Takeshita et al. 2011). In absence of DNA, the TS domain blocks the catalytic center in the CTD of DNMT1 and prohibits binding of the substrate. In this molecular conformation, the TS domain folds back on the CTD and forms an intramolecular interaction stabilized by several hydrogen bonds (Takeshita et al. 2011). However, this autoinhibitory mechanism is resolved when the TS domain interacts with the SRA domain in UHRF1 resulting in allosteric activation of DNMT1. Additionally, the interaction was reported to increase the specificity of DNMT1 towards hemimethylated target sites (Berk'yurek et al. 2013; Bashtrykov et al. 2014a). Consistent with the autoinhibitory role of intramolecular interactions, a DNMT1 TS domain mutant abolishing the hydrogen bonds with the CTD was shown to increase DNMT1 methylation activity without affecting its specificity for hemimethylated sites (Bashtrykov et al. 2014f). Consequently, release of the TS domain from the catalytic center of DNMT1 accompanied by a conformational change is a prerequisite for

enzyme activation. One might also speculate that TS domain-dependent binding of DNMT1 to ubiquitinated H3K18 might play a role in releasing autoinhibition.

Furthermore, the H3K23 ubiquitination mark was proposed to serve as a proofreader for the propagation of DNA methylation after replication (Nishiyama et al. 2013). DNMT1 binding to ubiquitinated H3 might be replication-independent and might facilitate faithful inheritance of DNA methylation patterns over many cell generations. Especially in densely methylated regions the speed of maintenance DNA methylation might not be able to cope with the progression of the replication fork making a replication-independent recruitment of DNMT1 to hemimethylated sites essential. In line with this, the TS domain of DNMT1 was previously proposed to mediate replication-independent chromatin loading of DNMT1 in G2 phase (Easwaran et al. 2004).

Interestingly, after depletion of DNMT1, H3K23 ubiquitination levels were highly increased in *Xenopus* egg extracts. Reintroduction of an inactive DNMT1 mutant in DNMT1-depleted cells did not alter H3 ubiquitination levels arguing for a catalytic activity-dependent effect (Nishiyama et al. 2013). Notably, release of DNMT1 from chromatin has been found to coincide with deubiquitination of H3K23. This observation might be explained by the presence of ubiquitin-specific peptidase 7 (USP7), a known interactor of DNMT1 (Du et al. 2010; Qin et al. 2011). USP7 functions as a deubiquitinase and might remove ubiquitination marks from H3 after catalytic activity of DNMT1 on the surrounding DNA (Nishiyama et al. 2013). One might speculate that deubiquitination of H3 removes DNMT1 from chromatin after completion of DNA methylation at the end of S phase or in early G2 phase. Studies on cell cycle-dependent DNMT1 conformation and complex composition especially with respect to modified DNA, histones, UHRF1 and USP7 will give us a much better understanding about the regulation of maintenance DNA methylation than we currently possess.

It should be noted that acetylation of H3 at K23 is abundant in mammalian cells (Marvin et al. 1990; Thomas et al. 2006). Remarkably, in *Arabidopsis* two H3K18 and K23 acetyltransferases, repressor of silencing 1 (ROS1) and increased DNA methylation 1 (IDM1), have been shown to suppress DNA methylation at promoter sequences (Li et al. 2012; Qian et al. 2012). Consequently, H3K18/K23 ubiquitination and acetylation might have competitive roles in the regulation of maintenance DNA methylation. Binding studies of DNMT1 at H3K18/K23 ubiquitinated versus acetylated promoter regions would be of great interest to enlarge our understanding about DNMT1 targeting. Moreover, analyses of the precise H3K18/K23 ubiquitination and acetylation timing will shed light on the cell cycle-dependent regulatory functions of these histone modifications.

Collectively, UHRF1 has a multifaceted role in directing DNA methylation by DNMT1 that involve its histone and DNA modification reader functions as well as its histone PTM writer domain. Intramolecular autoinhibitory mechanisms and the nuclear lipid signaling molecule PI5P add an additional level of complexity to UHRF1-mediated DNMT1 chromatin targeting. By elucidating the precise and coordinated role of different UHRF1 domains and by identification and functional characterization of the UIM in DNMT1, we have started to unveil a novel ubiquitin-dependent mechanism controlling DNA methylation.

3.2.2 Cell cycle-dependent modifications and interactions controlling DNMT1 abundance

DNMT1 protein levels are dynamically regulated during the cell cycle. Whereas lowest levels are found in G1 phase, they are increased during S phase and drop again in G2 phase (Du et al. 2010). DNMT1 abundance is regulated at the transcriptional and the protein level. Different PTMs on DNMT1 enhance stabilization of the protein or initiate its proteasomal degradation (Figure 3.4).

Acetylation driven ubiquitination of DNMT1 by UHRF1 leads to destabilization of the protein (Du et al. 2010). Interestingly, the trigger of this pathway, the acetyltransferase Tip60, has an increased expression in late S phase resulting in elevated levels of acetylated DNMT1 at the end of replication. The amino acids in DNMT1 targeted by Tip60 still remain unknown. UHRF1, in turn, ubiquitinates acetylated DNMT1 by means of its RING domain, thereby marking the protein for proteasomal degradation. Deubiquitination by USP7 (also known as herpesvirus-associated ubiquitin-specific protease (HAUSP)) leads to stabilization of DNMT1 (Du et al. 2010; Felle et al. 2011; Qin et al. 2011). Moreover, DNMT1 is stabilized by HDAC1-mediated deacetylation counteracting the activity of Tip60.

DNMT1 monomethylation by SET7 at K142 and K1096 in human and mouse cells, respectively, leads to destabilization of the protein (Esteve et al. 2009). Monomethylated DNMT1 is prone to subsequent ubiquitination and results in proteasomal degradation of the protein. Yet, it is not clear whether UHRF1 or another E3 ubiquitin ligase is involved in the methylation driven ubiquitination of DNMT1. Remarkably, a PTM on the adjacent S143 promotes stabilization of DNMT1 (Esteve et al. 2011). S143 phosphorylated DNMT1 is protected from K142 methylation and consequently cannot be marked for proteasomal degradation. During S phase, the phosphorylated form of DNMT1 is more prevalent, whereas the methylated form is mainly found in late S and G2 phase. This switch between two mutually exclusive PTMs controls the cell cycle-dependent regulation of DNMT1 protein abundance. In addition, lysine-specific demethylase 1A (LSD1) functions as a stabilizer by demethylating DNMT1 and thus counteracting the methyltransferase SET7 (Wang et al. 2009). However, regulatory effects of methylation of other lysine residues within DNMT1 than K142 or K1096 cannot be ruled out.

DNMT1 stability was found to be altered in human cancer cells, but evidence about the mode of deregulation remains contradictory. In healthy tissues, activated ataxia telangiectasia mutated (ATM) interacts with DNMT1 and coordinates its acetylation by Tip60. This leads to UHRF1-mediated ubiquitination and destabilization of DNMT1. In contrast, retinoblastoma protein (pRB) stabilizes DNMT1 by antagonizing ATM and enabling HDAC1-mediated deacetylation of DNMT1. On the one hand, in tumor cells lacking functional pRB, the ATM-Tip60 driven destabilization pathway is favored. Consequently, low DNMT1 protein levels might lead to decreased promoter methylation and aberrant gene expression related to malignant progression (Shamma et al. 2013). On the other hand, upregulation of the stabilizer LSD1 might lead to increased DNMT1 protein levels in many types of cancer (Agoston et al. 2005; Metzger et al. 2005; Sun et al. 2007).

The regulation of DNMT1 protein stability has been suggested to rely on its very N-terminal region. This hypothesis was addressed by a study using engineered mice heterozygous for the somatic and the oocyte-specific isoform of DNMT1 (Howell et al. 2001), both driven by the somatic endogenous promoter to ensure equal transcription (Ding and Chaillet 2002). In late embryonic stages, protein levels of the somatic longer isoform were five times reduced compared to the shorter oocyte-specific isoform indicating that the first 118 amino acids contribute to the control of DNMT1 stability.

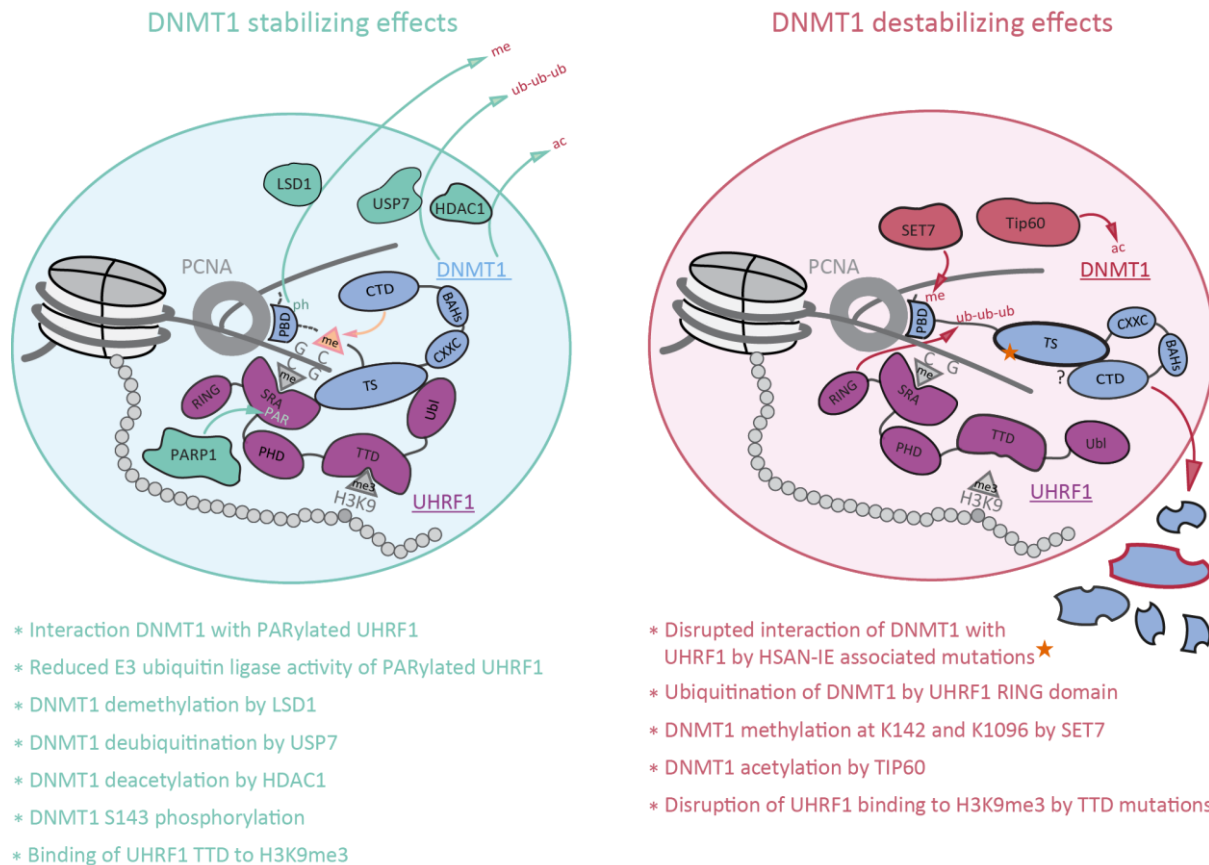


Figure 3.4: Overview of DNMT1 stabilizing and destabilizing effects with indication of proteins writing and erasing PTMs. DNMT1 is stabilized by interaction with PARylated UHRF1, which possesses a reduced E3 ubiquitin ligase activity. Ubiquitination on DNMT1 is removed by USP7 and ubiquitination driving PTMs like methylation and acetylation are erased by the action of LSD1 and HDAC1, respectively. Moreover, S143 phosphorylation prevents K142 methylation on DNMT1 and subsequent ubiquitination. Chromatin targeting of DNMT1 is ensured by binding of the UHRF1 TTD to H3K9me3. In contrast, DNMT1 is destabilized by disruption of the interaction with UHRF1 due to HSAN-IE associated mutations. The release of the TS domain from the CTD of DNMT1 might be blocked if it is not allosterically activated by interaction with the SRA domain of UHRF1. DNMT1 methylation by SET7 and its acetylation by TIP60 trigger DNMT1 ubiquitination thereby marking it for proteasomal degradation. Furthermore, disruption of UHRF1 TTD histone binding leads to destabilization of DNMT1.

Poly(ADP-)ribosylation (PARylation) has also been shown to serve as a trigger for E3 ubiquitin ligase activity (Zhang et al. 2011; Kalisch et al. 2012). To address the question whether poly-(ADP-ribose) polymerase 1 (PARP1)-mediated PARylation of UHRF1 has an influence on its E3 ubiquitin ligase activity, we analyzed DNMT1 ubiquitination and abundance in the presence or absence of PARP1 (De Vos et al. 2014a). Notably, we found an enhanced interaction of PARylated UHRF1 with DNMT1. In the presence of PARP1, the E3 ubiquitin ligase activity of UHRF1 towards DNMT1, however, was decreased suggesting an inhibitory effect of UHRF1 PARylation on DNMT1 destabilizing mechanisms. Remarkably, the stabilizing effect of PARP1 was most evident in late S and G2 phase. One model could envision that tighter binding of DNMT1 to PARylated UHRF1 does not increase DNMT1 ubiquitination but rather its robust binding to heterochromatin associated with increased protein stability.

Interestingly, we and others found DNMT1 to be prone for proteasomal degradation in *Uhrf1* knockout and knockdown cells (Rothbart et al. 2012), indicating that the integrity of the complex DNA-UHRF1-DNMT1 is important for protein stabilization. Consistently, we observed the same protein destabilization

for DNMT1 mutants defective in binding to UHRF1 (see 3.3.1). HSAN-IE associated mutations disrupted the interaction with UHRF1 and resulted in cell cycle-dependent protein degradation. Live cell analyses revealed that GFP-DNMT1 P496Y.Y500C was expressed at similar levels as the wt protein in early S phase, whereas expression levels dropped when the cell entered mid and late S phase. The lowest expression was found in G2, but was recovered in G1 phase. The cell cycle-dependent degradation of mutated proteins might argue for an important role of UHRF1 binding in DNMT1 stabilization at chromatin especially at the end of DNA replication. As stated above, former studies have demonstrated that the TS domain may be responsible for prolonged association of DNMT1 with chromatin during late S and G2 phase in part by interaction with heterochromatin bound UHRF1 (Easwaran et al. 2004; Schneider et al. 2013). Given that DNMT1 is more prone for proteasomal degradation in late S and G2 phase due to SET7-mediated methylation, non-chromatin associated DNMT1 molecules might preferentially be ubiquitinated. Moreover, TTD-mediated chromatin targeting of UHRF1 has been shown to be required for DNMT1 stability in mitosis (Rothbart et al. 2012).

Based on these results we hypothesize that DNMT1 molecules, which are not targeted to chromatin, are more likely to be degraded. It is tempting to speculate that this degradation pathway might ensure that only correctly targeted DNMT1 has a lifetime allowing for catalytic activity on DNA. Another possibility is that DNMT1 enzymes, which are not actively engaged in maintenance DNA methylation and are thus excessive, could preferentially be marked for proteasomal degradation. Compatible with this hypothesis, the *de novo* methyltransferases DNMT3A and DNMT3B have recently been demonstrated to be stabilized by binding to nucleosomes containing methylated DNA (Jeong et al. 2009; Stachulski et al. 2011). Another study supporting this hypothesis reports induction of free non-chromatin bound DNMT1 degradation after treatment of the cells with 5-aza-deoxycytidine (5-aza-dC) (Patel et al. 2010). An earlier study claims that this destabilizing effect is independent of the catalytic activity of DNMT1, but dependent on the nuclear localization signal (NLS) and the BAH domains (Ghoshal et al. 2005). By deletion of the NLS or the BAH domains, degradation of DNMT1 was prevented. As both deletion mutants localized mostly in the cytoplasm, spatial separation from degradation inducing factors can, however, not be ruled out. Physiological turnover of DNMT1 as well as the 5-aza-dC induced degradation was mediated by a component of the anaphase promoting complex (APC), CDH1, exerting E3 ubiquitin ligase activity on DNMT1. CDH1 is known to be activated after dephosphorylation in anaphase and telophase of mitosis (Peters 2002) for subsequent ubiquitination of substrates harboring a KEN motif (Pfleger and Kirschner 2000). Such a KEN box was found in the very N-terminal part of the DNMT1 CXXC domain and its mutation to AAA led to stabilization of the enzyme (Ghoshal et al. 2005). Given that the destabilization of DNMT1 observed in *Uhrf1*^{-/-} cells is decoupled from ubiquitination by UHRF1, a yet unknown E3 ubiquitin ligase might mark non-chromatin bound free DNMT1 molecules for proteasomal degradation, possibly CDH1. Elucidating whether this destabilizing mechanism is promoted by DNMT1 methylation or acetylation and which proteins are involved with respect to the cell cycle would shed light on the underlying degradation pathway.

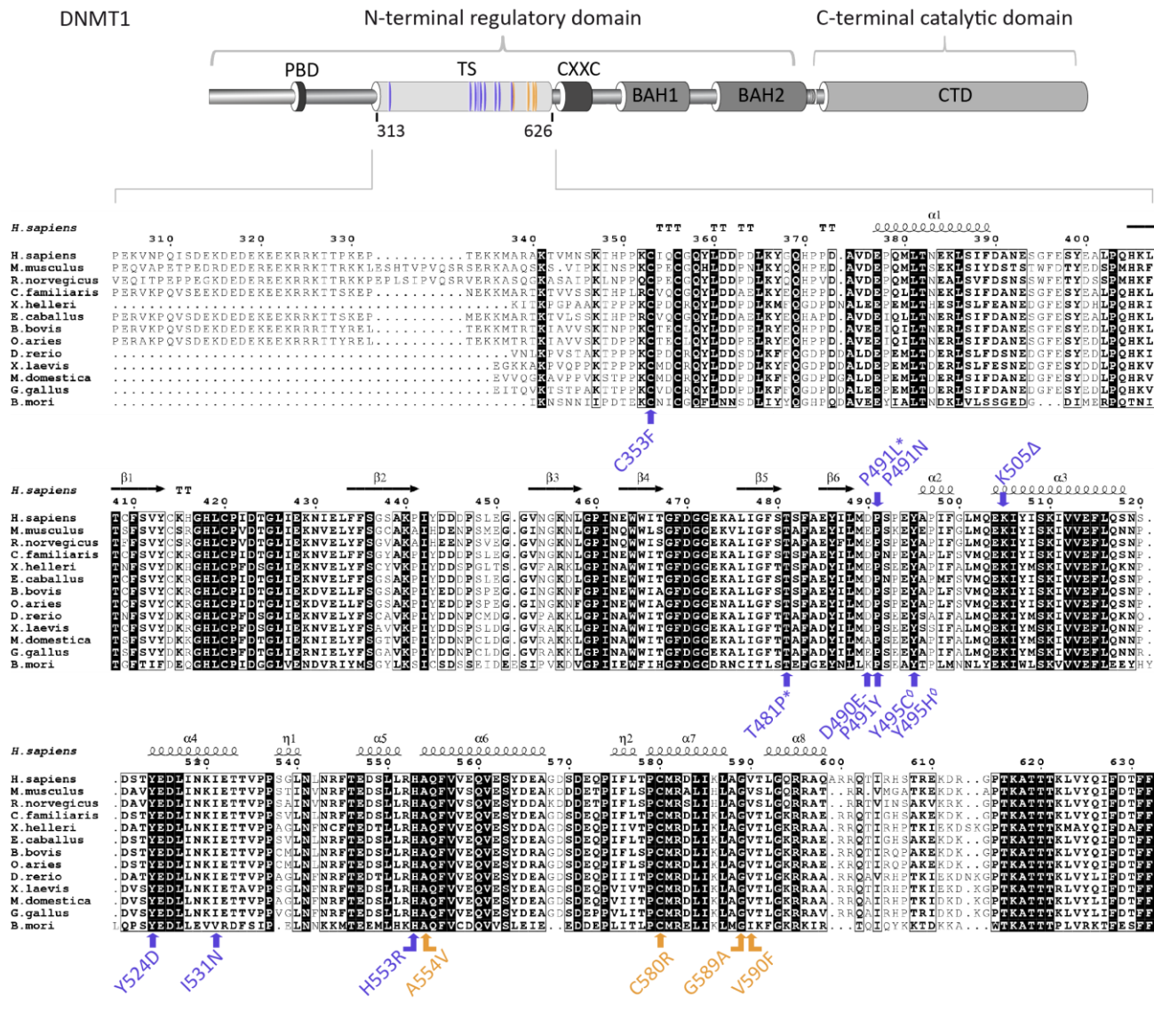
Taken together, DNA methylation is not only controlled by mechanisms coordinating DNMT1 chromatin targeting, but also by cell cycle-dependent regulation of DNMT1 protein abundance. Future research should focus on further elucidating the interplay between differential DNMT1-protein complex composition and associated PTMs, conformational changes, intra- and intermolecular interactions as well

as histone and DNA modifications to clarify the regulatory role of different DNMT1 targeting mechanisms in time and space.

3.3 Hereditary sensory and autonomic neuropathy type I with mutations in *DNMT1*

3.3.1 The TS domain as hotspot for HSAN-IE and ADAC-DN associated mutations in *DNMT1*

Among thirteen other proteins, *DNMT1* is associated with the neurodegenerative disease HSAN. Within the subgroup HSAN-I and CMT2B, mutations in six genes have been described so far. However, the ever growing number of affected genes, for instance, by the recent identification of *Atlastin 3* (*ATL3*) (Fischer et al. 2014; Kornak et al. 2014), suggests that even more genes might be involved in this disease. To date, 14 different *DNMT1* point mutations and one deletion mutation have been characterized, which are causative for HSAN-IE and ADCA-DN. Strikingly, all point and deletion mutations are located within the TS domain in the NTD of *DNMT1* (Figure 3.5, see Table 1.1). No mutations were found in the weakly conserved very N-terminal part of the TS domain (amino acid 313-340) and only one mutation is located in the subsequent region (C353F). HSAN-IE associated mutations cluster in the central part, whereas ADCA-DN associated mutations are located in the C-terminal part of the TS domain. All identified mutations affect highly conserved amino acids.



mutations associated with HSAN-IE
mutations associated with ADCA-DN

* de novo mutation

◊ mutation identified in >1 patient

Figure 3.5: Overview of DNMT1 TS domain mutations found in patients suffering from HSAN-IE or ADCA-DN. Top: Schematic outline of DNMT1 domains with indication of the 15 disease related mutations in the TS domain. bottom: Primary sequence alignment of the TS domain from different species with representation of disease associated mutations and the human TS domain secondary structure (pdb: 3EPZ). Note that the amino acid positions in the protein were adapted to the human DNMT1 isoform shown in the alignment (NP_001370.1).

In order to clarify regulatory defects of HSAN-IE associated TS domain mutations (Klein et al. 2011), we cloned mutant mouse DNMT1 constructs (DNMT1 P496Y and DNMT1 Y500C, corresponding to human DNMT1 D490E.P491Y and DNMT1 Y495Y) and performed biochemical and functional cell biological assays.

Since the TS domain has been described as mediator for the interaction with UHRF1 (Achour et al. 2008; Felle et al. 2011), we investigated the ability of the HSAN-IE associated TS domain mutants to

interact with UHRF1 and to restore DNA methylation in mouse *Dnmt1*^{-/-} ESCs. As described above (see 3.2.2), interaction of the mutants GFP-DNMT1 P496Y or GFP-DNMT1 Y500C as well as of the combination of both mutations with Cherry-UHRF1 was impaired. In support of the assumption that chromatin targeting of DNMT1 by direct interaction with UHRF1 is essential for the regulation of maintenance DNA methylation (see 3.2.1), we found that the HSAN-IE associated DNMT1 mutants were indeed inactive *in vivo*. In agreement with this observation, we could show that a TS domain deletion mutant (GFP-DNMT1 Δ458-500) covering the region of the point mutations was unable to restore DNA methylation levels in *Dnmt1*^{-/-} ESCs. Consistently, DNA samples of HSAN-IE patients were characterized by global DNA hypomethylation (Klein et al. 2011).

To elucidate the interplay between UHRF1 interaction and chromatin association *in vivo*, we analyzed DNMT1 subnuclear distribution and protein dynamics by FRAP. In line with defects in chromatin targeting via interaction with UHRF1, GFP-DNMT1 P496Y, GFP-DNMT1 Y500C and the combination of both mutations showed only weak association with late replicating heterochromatin. In contrast to cell cycle-specific localization patterns of full length DNMT1, the wildtype TS domain was constantly associated with heterochromatin in dependence on UHRF1, but not on methylated DNA. Consistent with strong chromocenter association, FRAP analyses revealed slow kinetics of GFP-TS wt with a high immobile fraction of ~75%. In contrast, the diffuse nuclear localization of the HSAN-IE associated TS domain mutants was reflected by considerably faster protein kinetics without an immobile fraction. These results suggest UHRF1-dependent localization patterns of DNMT1 and reinforce the link between TS domain-mediated UHRF1 binding and DNMT1 chromatin targeting.

Furthermore, we found a cell cycle-dependent destabilization of the mutant proteins (see 3.2.2). In agreement with these observations, HSAN-IE associated mutations in human DNMT1 have been shown to be less stable when compared to the wild type (Klein et al. 2011). Consistently, a recent study illustrates that HSAN-IE associated DNMT1 mutants are prone for aggresome induced autophagy resulting in altered protein homeostasis (Baets et al. 2015).

In summary, our study revealed that DNMT1 mutants defective in UHRF1 and late replicating chromatin binding lead to cell cycle-dependent destabilization and DNA hypomethylation. Understanding the detailed biological defects of the remaining DNMT1 disease associated mutants may shed light on the common disease mechanism in HSAN-IE and ADCA-DN.

3.3.2 Functionally relevant regions within the TS domain

The finding that the TS domain was responsible for UHRF1 interaction and strong heterochromatin association prompted us to seek for regions within the TS domain that are functionally relevant for enzymatic activity of DNMT1 *in vivo*. To this end we created a systematic set of GFP-DNMT1 TS domain deletion constructs (Figure 3.6) and analyzed their activity by a functional complementation assay.

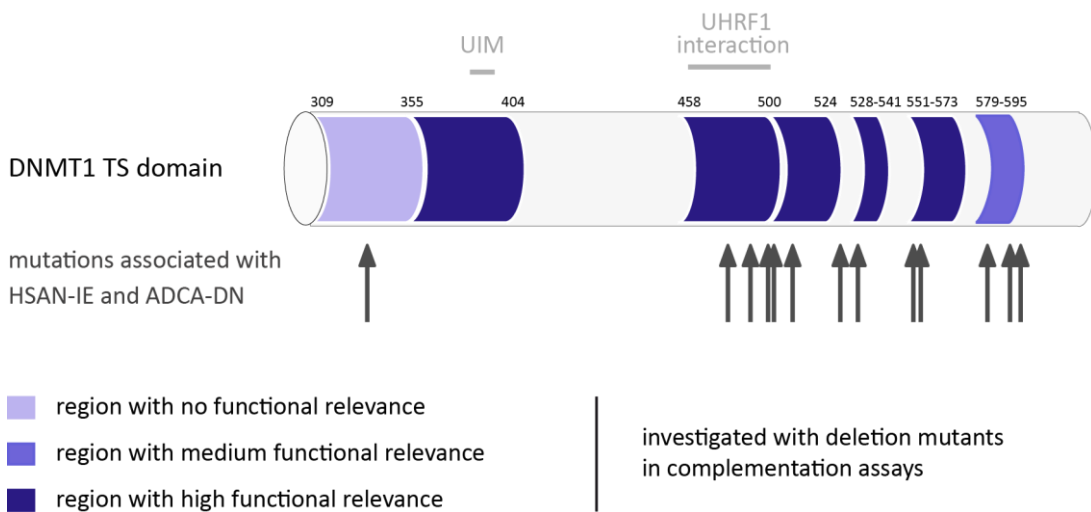


Figure 3.6: Outline of functionally relevant regions in the DNMT1 TS domain. Functionally important regions within the TS domain were mapped with deletion mutants and a complementation assay. For comparison the ubiquitin interacting motif (UIM), the UHRF1 interacting region and the neurodegenerative disease associated mutations are indicated.

Interestingly, the very N-terminal region of the TS domain, which shows only low conservation among different species (see Figure 3.5) and is only affected by one disease associated mutations, was dispensable for DNMT1 activity. In contrast, regions comprising amino acid 356 to 404 as well as 458 to 573 were important for the regulation of mouse DNMT1 enzymatic activity *in vivo* and their deletion resulted in inactivation of maintenance DNA methylation. According to the idea of different regulatory functions attributed to the TS domain, the inactivation of enzyme activity by deletion of amino acid 356 to 404 can be explained by the UIM located in this region (see 3.2.1). Using this deletion as well as defined point mutants, we could show that the UIM-mediated DNMT1 chromatin targeting via binding to ubiquitinated H3K18 is indispensable for maintenance DNA methylation. In agreement with our results, a deletion of the region encompassing amino acid 325 to 425 in mouse DNMT1 has been shown to be defective in binding to ubiquitinated H3 (Nishiyama et al. 2013). Moreover, we assume that GFP-DNMT1 Δ 458-500 is inactive as a consequence of deleting the region responsible for interaction with UHRF1. In the C-terminal part of the TS domain, the amino acids E530, D531, D553 and L592 are known to contribute to DNMT1 autoinhibition by interaction with the CTD via four hydrogen bonds (Song et al. 2011b; Berk'yurek et al. 2013). However, whether this part of the TS domain has further distinct regulatory functions remains elusive.

Given the multifunctional regulatory role of the TS domain in mediating DNMT1 chromatin targeting and enzymatic activity, we propose that disease associated TS domain mutants might have defects in different regulatory steps. These defects might, however, all lead to decreased DNA methylation activity of DNMT1.

3.3.3 Unraveling HSAN disease mechanisms

Although several studies on disease-associated mutations in important epigenetic factors like *MeCP2*, *DNMT3A* and *DNMT1* exemplify the involvement of decreased or increased DNA methylation in neurodegeneration, the biological processes linking these epigenetic changes to neuronal cell death

remain to be determined. Nonetheless, studying the function of wildtype proteins and comparing them to disease associated mutated proteins is a prerequisite for the identification of suitable drug targets. Apparently, the treatment of HSANs, for instance, is limited due to the lack of basic knowledge about common disease mechanisms, of relevant drug targets and certainly due to the unprofitable market of these rarely occurring diseases for pharmaceutical companies.

To gain insight into the biological pathways underlying the PNS degeneration, future studies should focus on finding common pathways involved in the regulation of axonal survival and on modeling of neuronal pathogenesis. Firstly, mouse models can help to understand the biological background of the disease phenotype and offer the possibility of testing potential drugs. Secondly, the use of human induced pluripotent stem cells (iPSCs) from patients, though it still remains challenging, is an elegant tool to model disease mechanisms under physiological conditions without overexpression and off target effects due to different genetic backgrounds of mouse strains (Lee et al. 2009). In a recent study, Lee and colleagues have derived human iPSCs from HSAN-III (also known as familial dyautonomia) patients carrying point mutations in the *IKBKAP* gene. After differentiation into peripheral neurons, defects in protein-specific functions like mis-splicing were found. Reversion of these defects has been tested by potential candidate drugs offering new insights into the disease mechanism and treatment of familial dyautonomia. Patient derived human iPSCs have also helped to validate the phenotypes of other neurodegenerative disease such as Alzheimer's disease, Parkinson's disease, Huntington's disease, amyotrophic lateral sclerosis and spinal muscular atrophy (Jung et al. 2012).

Given the genetic and clinical heterogeneity of HSANs, a common molecular pathway leading to pathogenesis has not yet been completely elucidated. Whereas proteins like the nerve growth factor receptor Trk-A mutated in HSAN-IV have directly been implicated in neuronal development, growth and survival (Rotthier et al. 2012), the role of DNA methylation by DNMT1 for neurogenesis is only partially understood.

The role of DNMT1 in neurogenesis has been studied with conditional gene deletions in mouse models (Fan et al. 2001). By use of conditional knockout mice that allowed for specific *Dnmt1* deletion in different developmental stages, effects of DNMT1 deficiency in embryonic CNS precursor cells and adult postmitotic CNS neurons have been investigated. *In vitro*, postmitotic cerebellar neurons survived and developed healthy and did not show global changes in DNA methylation levels after DNMT1 depletion. *In vivo*, conditional *Dnmt1* gene deletion in postmitotic CNS neurons did derange neither animal viability nor long-term neuronal survival and did not change DNA methylation levels. In contrast, *Dnmt1* gene deletions in CNS precursor cells at embryonic day E9 to E10 resulted in DNA hypomethylation in the brain and in perinatal lethality (one hour after birth) of mutant mice due to defects in neuronal respiratory control and ensuing respiratory failure. DNMT1 was undetectable at embryonic day E15.5 arguing for a rapid protein turnover, however, with no influence on the differentiation process into neurons. Interestingly, studies on a mosaic mutant containing only 30% *Dnmt1* deleted neurons suggest that DNMT1-deficient hypomethylated neurons were selectively eliminated from the postnatal brain. Thus, DNMT1 seems to be crucial for maintenance DNA methylation in CNS precursor cells and for cell viability and function of postmitotic CNS neurons. In summary, this study provides strong evidence for an essential role of DNMT1 and DNA methylation in neuronal precursors and for deleterious effect of DNMT1 depletion on neuronal survival (Fan et al. 2001).

Dnmt1 gene deletion in mouse NPCs results in elevated Signal Transducers and Activators of Transcription (STAT) activity as well as enhanced and precipitate differentiation into astrocytes. These findings indicate that DNA methylation has an inhibitory effect on Januskinase (JAK) -STAT signaling and regulates the timing of astrogliogenesis (Fan et al. 2005). In mouse retinal NPCs, *Dnmt1* gene deletion does not alter cell proliferation, but hinders maturation and survival of postmitotic neurons. Mutant mice showed fast postnatal retinal degeneration suggesting that maintenance DNA methylation is required for mammalian retinal development (Rhee et al. 2012).

DNA methylation patterns in the brain are not immutable after birth, but they underlie dynamic changes triggered by external stimuli allowing for behavioral plasticity, memory formation and maintenance. One might speculate about the existence of specific regulatory mechanisms selectively changing DNA modification states in neuronal cells, whereas the modification patterns in other cell types are faithfully maintained (Yu et al. 2011). It is puzzling, that patients carrying mutation in *DNMT1* show a PNS-restricted phenotype. However, given that DNA methylation patterns might be selectively modulated in neurons, DNMT1 might have additional replication-uncoupled roles in the nervous system distinct from its classical role as a maintenance enzyme in dividing somatic cells. Considering the important role and high expression of DNMT1 in the nervous system, and potential replication-independent DNA methylation by DNMT1, it is better understandable that the heterozygous mutations of HSAN-IE and ADCA-DN patients have a more pronounced effect on the CNS and PNS compared to other tissues. DNMT1 protein abundance is diminished by the destabilizing effects of the HSAN-IE mutations (see 3.3.1) and might be further compromised by fast protein turnover (Fan et al. 2001).

Taken together, DNMT1 is known to play a crucial role in the function of CNS neurons in postnatal animals, but the defined molecular disease mechanisms of *DNMT1* mutations leading to the nervous system-restricted and late-onset phenotype observed in HSAN-IE and ADCA-DN patients remain to be elucidated.

4. Annex

4.1 References

Abcam BBa. 2014. p. <http://www.abcam.com/index.html?pageconfig=resource&rid=13076&source=page trap>.

Abdel-Wahab O, Mullally A, Hedvat C, Garcia-Manero G, Patel J, Wadleigh M, Malinge S, Yao J, Kilpivaara O, Bhat R et al. 2009. Genetic characterization of TET1, TET2, and TET3 alterations in myeloid malignancies. *Blood* **114**: 144-147.

Abu-Farha M, Lambert JP, Al-Madhoun AS, Elisma F, Skerjanc IS, Figeys D. 2008. The tale of two domains: proteomics and genomics analysis of SMYD2, a new histone methyltransferase. *Molecular & cellular proteomics : MCP* **7**: 560-572.

Achour M, Jacq X, Ronde P, Alhosin M, Charlot C, Chataigneau T, Jeanblanc M, Macaluso M, Giordano A, Hughes AD et al. 2008. The interaction of the SRA domain of ICBP90 with a novel domain of DNMT1 is involved in the regulation of VEGF gene expression. *Oncogene* **27**: 2187-2197.

Agoston AT, Argani P, Yegnasubramanian S, De Marzo AM, Ansari-Lari MA, Hicks JL, Davidson NE, Nelson WG. 2005. Increased protein stability causes DNA methyltransferase 1 dysregulation in breast cancer. *The Journal of biological chemistry* **280**: 18302-18310.

Al-Mahdawi S, Pinto RM, Ismail O, Varshney D, Lymeri S, Sandi C, Trabzuni D, Pook M. 2008. The Friedreich ataxia GAA repeat expansion mutation induces comparable epigenetic changes in human and transgenic mouse brain and heart tissues. *Hum Mol Genet* **17**: 735-746.

Anderson SL, Qiu J, Rubin BY. 2003. EGCG corrects aberrant splicing of IKAP mRNA in cells from patients with familial dysautonomia. *Biochemical and biophysical research communications* **310**: 627-633.

Anderson SL, Rubin BY. 2005. Tocotrienols reverse IKAP and monoamine oxidase deficiencies in familial dysautonomia. *Biochemical and biophysical research communications* **336**: 150-156.

Anselmo AN, Earnest S, Chen W, Juang YC, Kim SC, Zhao Y, Cobb MH. 2006. WNK1 and OSR1 regulate the Na⁺, K⁺, 2Cl⁻ cotransporter in HeLa cells. *Proc Natl Acad Sci U S A* **103**: 10883-10888.

Arita K, Ariyoshi M, Tochio H, Nakamura Y, Shirakawa M. 2008. Recognition of hemi-methylated DNA by the SRA protein UHRF1 by a base-flipping mechanism. *Nature* **455**: 818-821.

Arita K, Isogai S, Oda T, Unoki M, Sugita K, Sekiyama N, Kuwata K, Hamamoto R, Tochio H, Sato M et al. 2012. Recognition of modification status on a histone H3 tail by linked histone reader modules of the epigenetic regulator UHRF1. *Proc Natl Acad Sci U S A* **109**: 12950-12955.

Avvakumov GV, Walker JR, Xue S, Li Y, Duan S, Bronner C, Arrowsmith CH, Dhe-Paganon S. 2008. Structural basis for recognition of hemi-methylated DNA by the SRA domain of human UHRF1. *Nature* **455**: 822-825.

Baets J, Duan X, Wu Y, Smith G, Seeley WW, Mademan I, McGrath NM, Beadell NC, Khouri J, Botuyan MV et al. 2015. Defects of mutant DNMT1 are linked to a spectrum of neurological disorders. *Brain : a journal of neurology*.

Bannister AJ, Zegerman P, Partridge JF, Miska EA, Thomas JO, Allshire RC, Kouzarides T. 2001. Selective recognition of methylated lysine 9 on histone H3 by the HP1 chromo domain. *Nature* **410**: 120-124.

Barker PA, Lomen-Hoerth C, Gensch EM, Meakin SO, Glass DJ, Shooter EM. 1993. Tissue-specific alternative splicing generates two isoforms of the trkA receptor. *The Journal of biological chemistry* **268**: 15150-15157.

Barski A, Cuddapah S, Cui K, Roh TY, Schones DE, Wang Z, Wei G, Chepelev I, Zhao K. 2007. High-resolution profiling of histone methylations in the human genome. *Cell* **129**: 823-837.

Bashtarykov P, Jankevicius G, Jurkowska RZ, Ragozin S, Jeltsch A. 2014a. The UHRF1 protein stimulates the activity and specificity of the maintenance DNA methyltransferase DNMT1 by an allosteric mechanism. *The Journal of biological chemistry* **289**: 4106-4115.

Bashtrykov P, Rajavelu A, Hackner B, Ragozin S, Carell T, Jeltsch A. 2014f. Targeted Mutagenesis Results in an Activation of DNA Methyltransferase 1 and Confirms an Autoinhibitory Role of its RFTS Domain. *Chembiochem*.

Becker A, Allmann L, Hofstatter M, Casa V, Weber P, Lehmkuhl A, Herce HD, Cardoso MC. 2013. Direct homo- and hetero-interactions of MeCP2 and MBD2. *PLoS One* **8**: e53730.

Berezney R, Dubey DD, Huberman JA. 2000. Heterogeneity of eukaryotic replicons, replicon clusters, and replication foci. *Chromosoma* **108**: 471-484.

Berk'yurek AC, Suetake I, Arita K, Takeshita K, Nakagawa A, Shirakawa M, Tajima S. 2013. The DNA Methyltransferase Dnmt1 Directly Interacts with the SET and RING Finger Associated (SRA) Domain of the Multifunctional Protein Uhrf1 to Facilitate Accession of the Catalytic Center to Hemi-methylated DNA. *The Journal of biological chemistry*.

Bernstein BE, Kamal M, Lindblad-Toh K, Bekiranov S, Bailey DK, Huebert DJ, McMahon S, Karlsson EK, Kulkosky EJ, 3rd, Gingeras TR et al. 2005. Genomic maps and comparative analysis of histone modifications in human and mouse. *Cell* **120**: 169-181.

Bestor TH. 2000. The DNA methyltransferases of mammals. *Hum Mol Genet* **9**: 2395-2402.

Bestor TH, Verdine GL. 1994. DNA methyltransferases. *Current opinion in cell biology* **6**: 380-389.

Biennu T, Chelly J. 2006. Molecular genetics of Rett syndrome: when DNA methylation goes unrecognized. *Nature reviews Genetics* **7**: 415-426.

Binda O, LeRoy G, Bua DJ, Garcia BA, Gozani O, Richard S. 2010. Trimethylation of histone H3 lysine 4 impairs methylation of histone H3 lysine 9: regulation of lysine methyltransferases by physical interaction with their substrates. *Epigenetics : official journal of the DNA Methylation Society* **5**: 767-775.

Bird A. 2002. DNA methylation patterns and epigenetic memory. *Genes & development* **16**: 6-21.

Bird A, Tweedie S. 1995. Transcriptional noise and the evolution of gene number. *Philosophical transactions of the Royal Society of London Series B, Biological sciences* **349**: 249-253.

Bird AP, Taggart MH, Nicholls RD, Higgs DR. 1987. Non-methylated CpG-rich islands at the human alpha-globin locus: implications for evolution of the alpha-globin pseudogene. *The EMBO journal* **6**: 999-1004.

Bonapace IM, Latella L, Papait R, Nicassio F, Sacco A, Muto M, Crescenzi M, Di Fiore PP. 2002. Np95 is regulated by E1A during mitotic reactivation of terminally differentiated cells and is essential for S phase entry. *The Journal of cell biology* **157**: 909-914.

Borowczyk E, Mohan KN, D'Aiuto L, Cirio MC, Chaillet JR. 2009. Identification of a region of the DNMT1 methyltransferase that regulates the maintenance of genomic imprints. *Proc Natl Acad Sci U S A* **106**: 20806-20811.

Bostick M, Kim JK, Esteve PO, Clark A, Pradhan S, Jacobsen SE. 2007. UHRF1 plays a role in maintaining DNA methylation in mammalian cells. *Science* **317**: 1760-1764.

Botuyan MV, Lee J, Ward IM, Kim JE, Thompson JR, Chen J, Mer G. 2006. Structural basis for the methylation state-specific recognition of histone H4-K20 by 53BP1 and Crb2 in DNA repair. *Cell* **127**: 1361-1373.

Bourc'his D, Bestor TH. 2004. Meiotic catastrophe and retrotransposon reactivation in male germ cells lacking Dnmt3L. *Nature* **431**: 96-99.

Bourc'his D, Xu GL, Lin CS, Bollman B, Bestor TH. 2001. Dnmt3L and the establishment of maternal genomic imprints. *Science* **294**: 2536-2539.

Brandeis M, Frank D, Keshet I, Siegfried Z, Mendelsohn M, Nemes A, Temper V, Razin A, Cedar H. 1994. Sp1 elements protect a CpG island from de novo methylation. *Nature* **371**: 435-438.

Braun SM, Jessberger S. 2014. Adult neurogenesis and its role in neuropsychiatric disease, brain repair and normal brain function. *Neuropathology and applied neurobiology* **40**: 3-12.

Bronner C, Achour M, Arima Y, Chataigneau T, Saya H, Schini-Kerth VB. 2007. The UHRF family: oncogenes that are drugable targets for cancer therapy in the near future? *Pharmacology & therapeutics* **115**: 419-434.

Brooks PJ, Marietta C, Goldman D. 1996. DNA mismatch repair and DNA methylation in adult brain neurons. *The Journal of neuroscience : the official journal of the Society for Neuroscience* **16**: 939-945.

Buck-Kohntop BA, Defossez PA. 2013. On how mammalian transcription factors recognize methylated DNA. *Epigenetics : official journal of the DNA Methylation Society* **8**: 131-137.

Buck-Kohntop BA, Stanfield RL, Ekiert DC, Martinez-Yamout MA, Dyson HJ, Wilson IA, Wright PE. 2012. Molecular basis for recognition of methylated and specific DNA sequences by the zinc finger protein Kaiso. *Proc Natl Acad Sci U S A* **109**: 15229-15234.

Cao R, Wang L, Wang H, Xia L, Erdjument-Bromage H, Tempst P, Jones RS, Zhang Y. 2002. Role of histone H3 lysine 27 methylation in Polycomb-group silencing. *Science* **298**: 1039-1043.

Cardoso MC, Leonhardt H. 1999. DNA methyltransferase is actively retained in the cytoplasm during early development. *The Journal of cell biology* **147**: 25-32.

Carlson LL, Page AW, Bestor TH. 1992. Properties and localization of DNA methyltransferase in preimplantation mouse embryos: implications for genomic imprinting. *Genes & development* **6**: 2536-2541.

Carrozza MJ, Utley RT, Workman JL, Cote J. 2003. The diverse functions of histone acetyltransferase complexes. *Trends in genetics : TIG* **19**: 321-329.

Casas-Delucchi CS, Brero A, Rahn HP, Solovei I, Wutz A, Cremer T, Leonhardt H, Cardoso MC. 2011. Histone acetylation controls the inactive X chromosome replication dynamics. *Nature communications* **2**: 222.

Chen CC, Wang KY, Shen CK. 2012. The mammalian de novo DNA methyltransferases DNMT3A and DNMT3B are also DNA 5-hydroxymethylcytosine dehydroxymethylases. *The Journal of biological chemistry* **287**: 33116-33121.

Chen T, Tsujimoto N, Li E. 2004. The PWW domain of Dnmt3a and Dnmt3b is required for directing DNA methylation to the major satellite repeats at pericentric heterochromatin. *Molecular and cellular biology* **24**: 9048-9058.

Cheng J, Yang Y, Fang J, Xiao J, Zhu T, Chen F, Wang P, Li Z, Yang H, Xu Y. 2013. Structural insight into coordinated recognition of trimethylated histone H3 lysine 9 (H3K9me3) by the plant homeodomain (PHD) and tandem tudor domain (TTD) of UHRF1 (ubiquitin-like, containing PHD and RING finger domains, 1) protein. *The Journal of biological chemistry* **288**: 1329-1339.

Chestnut BA, Chang Q, Price A, Lesuisse C, Wong M, Martin LJ. 2011. Epigenetic regulation of motor neuron cell death through DNA methylation. *The Journal of neuroscience : the official journal of the Society for Neuroscience* **31**: 16619-16636.

Cho HJ, Kim BJ, Suh YL, An JY, Ki CS. 2006. Novel mutation in the HSN2 gene in a Korean patient with hereditary sensory and autonomic neuropathy type 2. *Journal of human genetics* **51**: 905-908.

Cho YW, Hong T, Hong S, Guo H, Yu H, Kim D, Guszczynski T, Dressler GR, Copeland TD, Kalkum M et al. 2007. PTIP associates with MLL3- and MLL4-containing histone H3 lysine 4 methyltransferase complex. *The Journal of biological chemistry* **282**: 20395-20406.

Choi JD, Lee JS. 2013. Interplay between Epigenetics and Genetics in Cancer. *Genomics & informatics* **11**: 164-173.

Chuang LS, Ian HI, Koh TW, Ng HH, Xu G, Li BF. 1997. Human DNA-(cytosine-5) methyltransferase-PCNA complex as a target for p21WAF1. *Science* **277**: 1996-2000.

Citterio E, Papait R, Nicassio F, Vecchi M, Gomiero P, Mantovani R, Di Fiore PP, Bonapace IM. 2004. Np95 is a histone-binding protein endowed with ubiquitin ligase activity. *Molecular and cellular biology* **24**: 2526-2535.

Clouaire T, Stancheva I. 2008. Methyl-CpG binding proteins: specialized transcriptional repressors or structural components of chromatin? *Cellular and molecular life sciences : CMLS* **65**: 1509-1522.

Coen K, Pareyson D, Auer-Grumbach M, Buyse G, Goemans N, Claeys KG, Verpoorten N, Laura M, Scaiola V, Salmhofer W et al. 2006. Novel mutations in the HSN2 gene causing hereditary sensory and autonomic neuropathy type II. *Neurology* **66**: 748-751.

Coffee B, Zhang F, Warren ST, Reines D. 1999. Acetylated histones are associated with FMR1 in normal but not fragile X-syndrome cells. *Nat Genet* **22**: 98-101.

Creppe C, Malinouskaya L, Volvert ML, Gillard M, Close P, Malaise O, Laguesse S, Cornez I, Rahmouni S, Ormenese S et al. 2009. Elongator controls the migration and differentiation of cortical neurons through acetylation of alpha-tubulin. *Cell* **136**: 551-564.

Crick F. 1984. Memory and molecular turnover. *Nature* **312**: 101.

Daniel JM, Spring CM, Crawford HC, Reynolds AB, Baig A. 2002. The p120(ctn)-binding partner Kaiso is a bimodal DNA-binding protein that recognizes both a sequence-specific consensus and methylated CpG dinucleotides. *Nucleic acids research* **30**: 2911-2919.

De Vos M, El Ramy R, Quenet D, Wolf P, Spada F, Magroun N, Babio F, Schreiber V, Leonhardt H, Bonapace IM et al. 2014a. Poly(ADP-ribose) polymerase 1 (PARP1) associates with E3 ubiquitin-protein ligase UHRF1 and modulates UHRF1 biological functions. *The Journal of biological chemistry* **289**: 16223-16238.

De Vos. 2014b. Poly(ADP-ribose) polymerase 1 (PARP1) associates with E3 ubiquitine-protein ligase UHRF1 and modulates UHRF1 biological functions. *J Biol Chem*.

Deaton AM, Bird A. 2011. CpG islands and the regulation of transcription. *Genes & development* **25**: 1010-1022.

Delhommeau F, Dupont S, Della Valle V, James C, Trannoy S, Masse A, Kosmider O, Le Couedic JP, Robert F, Alberdi A et al. 2009. Mutation in TET2 in myeloid cancers. *The New England journal of medicine* **360**: 2289-2301.

Dhayalan A, Rajavelu A, Rathert P, Tamas R, Jurkowska RZ, Ragozin S, Jeltsch A. 2010. The Dnmt3a PWWP domain reads histone 3 lysine 36 trimethylation and guides DNA methylation. *The Journal of biological chemistry* **285**: 26114-26120.

Ding F, Chaillet JR. 2002. In vivo stabilization of the Dnmt1 (cytosine-5)- methyltransferase protein. *Proc Natl Acad Sci U S A* **99**: 14861-14866.

Dou Y, Milne TA, Tackett AJ, Smith ER, Fukuda A, Wysocka J, Allis CD, Chait BT, Hess JL, Roeder RG. 2005. Physical association and coordinate function of the H3 K4 methyltransferase MLL1 and the H4 K16 acetyltransferase MOF. *Cell* **121**: 873-885.

Du Z, Song J, Wang Y, Zhao Y, Guda K, Yang S, Kao HY, Xu Y, Willis J, Markowitz SD et al. 2010. DNMT1 stability is regulated by proteins coordinating deubiquitination and acetylation-driven ubiquitination. *Science signaling* **3**: ra80.

Duan Q, Chen H, Costa M, Dai W. 2008. Phosphorylation of H3S10 blocks the access of H3K9 by specific antibodies and histone methyltransferase. Implication in regulating chromatin dynamics and epigenetic inheritance during mitosis. *The Journal of biological chemistry* **283**: 33585-33590.

Dyck P. 1993. Neuronal atrophy and degeneration predominantly affecting peripheral sensory and autonomic neurons. *Peripheral neuropathy* **2**.

Easwaran HP, Schermelleh L, Leonhardt H, Cardoso MC. 2004. Replication-independent chromatin loading of Dnmt1 during G2 and M phases. *EMBO reports* **5**: 1181-1186.

Ehrlich M, Gama-Sosa MA, Huang LH, Midgett RM, Kuo KC, McCune RA, Gehrke C. 1982. Amount and distribution of 5-methylcytosine in human DNA from different types of tissues of cells. *Nucleic acids research* **10**: 2709-2721.

Endoh M, Endo TA, Endoh T, Fujimura Y, Ohara O, Toyoda T, Otte AP, Okano M, Brockdorff N, Vidal M et al. 2008. Polycomb group proteins Ring1A/B are functionally linked to the core transcriptional regulatory circuitry to maintain ES cell identity. *Development* **135**: 1513-1524.

Ernsberger U. 2009. Role of neurotrophin signalling in the differentiation of neurons from dorsal root ganglia and sympathetic ganglia. *Cell Tissue Res* **336**: 349-384.

Esteve PO, Chang Y, Samaranayake M, Upadhyay AK, Horton JR, Feehery GR, Cheng X, Pradhan S. 2011. A methylation and phosphorylation switch between an adjacent lysine and serine determines human DNMT1 stability. *Nat Struct Mol Biol* **18**: 42-48.

Esteve PO, Chin HG, Benner J, Feehery GR, Samaranayake M, Horwitz GA, Jacobsen SE, Pradhan S. 2009. Regulation of DNMT1 stability through SET7-mediated lysine methylation in mammalian cells. *Proc Natl Acad Sci U S A* **106**: 5076-5081.

Fan G, Beard C, Chen RZ, Csankovszki G, Sun Y, Siniaia M, Biniszkiewicz D, Bates B, Lee PP, Kuhn R et al. 2001. DNA hypomethylation perturbs the function and survival of CNS neurons in postnatal animals. *The Journal of neuroscience : the official journal of the Society for Neuroscience* **21**: 788-797.

Fan G, Martinowich K, Chin MH, He F, Fouse SD, Hutnick L, Hattori D, Ge W, Shen Y, Wu H et al. 2005. DNA methylation controls the timing of astrogliogenesis through regulation of JAK-STAT signaling. *Development* **132**: 3345-3356.

Fatemi M, Hermann A, Pradhan S, Jeltsch A. 2001. The activity of the murine DNA methyltransferase Dnmt1 is controlled by interaction of the catalytic domain with the N-terminal part of the enzyme leading to an allosteric activation of the enzyme after binding to methylated DNA. *Journal of molecular biology* **309**: 1189-1199.

Feldman N, Gerson A, Fang J, Li E, Zhang Y, Shinkai Y, Cedar H, Bergman Y. 2006. G9a-mediated irreversible epigenetic inactivation of Oct-3/4 during early embryogenesis. *Nature cell biology* **8**: 188-194.

Felle M, Joppien S, Nemeth A, Diermeier S, Thalhammer V, Dobner T, Kremmer E, Kappler R, Langst G. 2011. The USP7/Dnmt1 complex stimulates the DNA methylation activity of Dnmt1 and regulates the stability of UHRF1. *Nucleic acids research* **39**: 8355-8365.

Fellinger K, Rothbauer U, Felle M, Langst G, Leonhardt H. 2009. Dimerization of DNA methyltransferase 1 is mediated by its regulatory domain. *Journal of cellular biochemistry* **106**: 521-528.

Feng J, Chang H, Li E, Fan G. 2005. Dynamic expression of de novo DNA methyltransferases Dnmt3a and Dnmt3b in the central nervous system. *Journal of neuroscience research* **79**: 734-746.

Ficz G, Branco MR, Seisenberger S, Santos F, Krueger F, Hore TA, Marques CJ, Andrews S, Reik W. 2011. Dynamic regulation of 5-hydroxymethylcytosine in mouse ES cells and during differentiation. *Nature* **473**: 398-402.

Fischer D, Schabhatt M, Wieland T, Windhager R, Strom TM, Auer-Grumbach M. 2014. A novel missense mutation confirms ATL3 as a gene for hereditary sensory neuropathy type 1. *Brain : a journal of neurology* **137**: e286.

Fischle W, Tseng BS, Dormann HL, Ueberheide BM, Garcia BA, Shabanowitz J, Hunt DF, Funabiki H, Allis CD. 2005. Regulation of HP1-chromatin binding by histone H3 methylation and phosphorylation. *Nature* **438**: 1116-1122.

Fisher RD, Wang B, Alam SL, Higginson DS, Robinson H, Sundquist WI, Hill CP. 2003. Structure and ubiquitin binding of the ubiquitin-interacting motif. *The Journal of biological chemistry* **278**: 28976-28984.

Flynn J, Azzam R, Reich N. 1998. DNA binding discrimination of the murine DNA cytosine-C5 methyltransferase. *Journal of molecular biology* **279**: 101-116.

Franceschini P, Martino S, Ciocchini M, Ciuti E, Vardeu MP, Guala A, Signorile F, Camerano P, Franceschini D, Tovo PA. 1995. Variability of clinical and immunological phenotype in immunodeficiency-centromeric instability-facial anomalies syndrome. Report of two new patients and review of the literature. *European journal of pediatrics* **154**: 840-846.

Frauer C, Rottach A, Meilinger D, Bultmann S, Fellinger K, Hasenoder S, Wang M, Qin W, Soding J, Spada F et al. 2011. Different binding properties and function of CXXC zinc finger domains in Dnmt1 and Tet1. *PLoS One* **6**: e16627.

Fritsch L, Robin P, Mathieu JR, Souidi M, Hinaux H, Rougeulle C, Harel-Bellan A, Ameyar-Zazoua M, Ait-Si-Ali S. 2010. A subset of the histone H3 lysine 9 methyltransferases Suv39h1, G9a, GLP, and SETDB1 participate in a multimeric complex. *Molecular cell* **37**: 46-56.

Fujimori A, Matsuda Y, Takemoto Y, Hashimoto Y, Kubo E, Araki R, Fukumura R, Mita K, Tatsumi K, Muto M. 1998. Cloning and mapping of Np95 gene which encodes a novel nuclear protein associated with cell proliferation. *Mamm Genome* **9**: 1032-1035.

Fuks F, Burgers WA, Brehm A, Hughes-Davies L, Kouzarides T. 2000. DNA methyltransferase Dnmt1 associates with histone deacetylase activity. *Nat Genet* **24**: 88-91.

Fuks F, Hurd PJ, Deplus R, Kouzarides T. 2003. The DNA methyltransferases associate with HP1 and the SUV39H1 histone methyltransferase. *Nucleic acids research* **31**: 2305-2312.

Gaudet F, Rideout WM, 3rd, Meissner A, Dausman J, Leonhardt H, Jaenisch R. 2004. Dnmt1 expression in pre- and postimplantation embryogenesis and the maintenance of IAP silencing. *Molecular and cellular biology* **24**: 1640-1648.

Ge YZ, Pu MT, Gowher H, Wu HP, Ding JP, Jeltsch A, Xu GL. 2004. Chromatin targeting of de novo DNA methyltransferases by the PWWP domain. *The Journal of biological chemistry* **279**: 25447-25454.

Gelato KA, Tauber M, Ong MS, Winter S, Hiragami-Hamada K, Sindlinger J, Lemak A, Bultsma Y, Houlston S, Schwarzer D et al. 2014. Accessibility of different histone H3-binding domains of UHRF1 is allosterically regulated by phosphatidylinositol 5-phosphate. *Molecular cell* **54**: 905-919.

Ghoshal K, Datta J, Majumder S, Bai S, Kutay H, Motiwala T, Jacob ST. 2005. 5-Aza-deoxycytidine induces selective degradation of DNA methyltransferase 1 by a proteasomal pathway that requires the

KEN box, bromo-adjacent homology domain, and nuclear localization signal. *Molecular and cellular biology* **25**: 4727-4741.

Gilbert N, Boyle S, Fiegler H, Woodfine K, Carter NP, Bickmore WA. 2004. Chromatin architecture of the human genome: gene-rich domains are enriched in open chromatin fibers. *Cell* **118**: 555-566.

Gjerset RA, Martin DW, Jr. 1982. Presence of a DNA demethylating activity in the nucleus of murine erythroleukemic cells. *The Journal of biological chemistry* **257**: 8581-8583.

Globisch D, Munzel M, Muller M, Michalakis S, Wagner M, Koch S, Bruckl T, Biel M, Carell T. 2010. Tissue distribution of 5-hydroxymethylcytosine and search for active demethylation intermediates. *PLoS One* **5**: e15367.

Gold-von Simson G, Goldberg JD, Rolnitzky LM, Mull J, Leyne M, Voustianouk A, Slaugenhaus SA, Axelrod FB. 2009. Kinetin in familial dysautonomia carriers: implications for a new therapeutic strategy targeting mRNA splicing. *Pediatr Res* **65**: 341-346.

Goll MG, Bestor TH. 2005. Eukaryotic cytosine methyltransferases. *Annual review of biochemistry* **74**: 481-514.

Goll MG, Kirpekar F, Maggert KA, Yoder JA, Hsieh CL, Zhang X, Golic KG, Jacobsen SE, Bestor TH. 2006. Methylation of tRNAAsp by the DNA methyltransferase homolog Dnmt2. *Science* **311**: 395-398.

Gosal D, Ealing, J., Mignot, E. 2013. A mutation in the DNMT1 gene causing autosomal dominant ataxia with deafness and cataplexy. *J Neurol Neurosurg Psychiatry*.

Gosal D, J. E, E. M. 2013. A mutation in the DNMT1 gene causing autosomal dominant ataxia with deafness and cataplexy. *J Neurol Neurosurg Psychiatry*.

Goto K, Numata M, Komura JI, Ono T, Bestor TH, Kondo H. 1994. Expression of DNA methyltransferase gene in mature and immature neurons as well as proliferating cells in mice. *Differentiation; research in biological diversity* **56**: 39-44.

Greeson NT, Sengupta R, Arida AR, Jenuwein T, Sanders SL. 2008. Di-methyl H4 lysine 20 targets the checkpoint protein Crb2 to sites of DNA damage. *The Journal of biological chemistry* **283**: 33168-33174.

Gregory GD, Vakoc CR, Rozovskaia T, Zheng X, Patel S, Nakamura T, Canaani E, Blobel GA. 2007. Mammalian ASH1L is a histone methyltransferase that occupies the transcribed region of active genes. *Molecular and cellular biology* **27**: 8466-8479.

Griffith JS, Mahler HR. 1969. DNA ticketing theory of memory. *Nature* **223**: 580-582.

Gu TP, Guo F, Yang H, Wu HP, Xu GF, Liu W, Xie ZG, Shi L, He X, Jin SG et al. 2011. The role of Tet3 DNA dioxygenase in epigenetic reprogramming by oocytes. *Nature* **477**: 606-610.

Guccione E, Bassi C, Casadio F, Martinato F, Cesaroni M, Schuchlautz H, Luscher B, Amati B. 2007. Methylation of histone H3R2 by PRMT6 and H3K4 by an MLL complex are mutually exclusive. *Nature* **449**: 933-937.

Guo JU, Su Y, Zhong C, Ming GL, Song H. 2011. Hydroxylation of 5-methylcytosine by TET1 promotes active DNA demethylation in the adult brain. *Cell* **145**: 423-434.

Hackett JA, Sengupta R, Zyllicz JJ, Murakami K, Lee C, Down TA, Surani MA. 2013. Germline DNA demethylation dynamics and imprint erasure through 5-hydroxymethylcytosine. *Science* **339**: 448-452.

Hahn MA, Qiu R, Wu X, Li AX, Zhang H, Wang J, Jui J, Jin SG, Jiang Y, Pfeifer GP et al. 2013. Dynamics of 5-hydroxymethylcytosine and chromatin marks in Mammalian neurogenesis. *Cell reports* **3**: 291-300.

Hajkova P, Jeffries SJ, Lee C, Miller N, Jackson SP, Surani MA. 2010. Genome-wide reprogramming in the mouse germ line entails the base excision repair pathway. *Science* **329**: 78-82.

Hanada K. 2003. Serine palmitoyltransferase, a key enzyme of sphingolipid metabolism. *Biochimica et biophysica acta* **1632**: 16-30.

Hansen RS, Stoger R, Wijmenga C, Stanek AM, Canfield TK, Luo P, Matarazzo MR, D'Esposito M, Feil R, Gimelli G et al. 2000. Escape from gene silencing in ICF syndrome: evidence for advanced replication time as a major determinant. *Hum Mol Genet* **9**: 2575-2587.

Hashimoto H, Horton JR, Zhang X, Bostick M, Jacobsen SE, Cheng X. 2008. The SRA domain of UHRF1 flips 5-methylcytosine out of the DNA helix. *Nature* **455**: 826-829.

Hashimoto H, Horton JR, Zhang X, Cheng X. 2009. UHRF1, a modular multi-domain protein, regulates replication-coupled crosstalk between DNA methylation and histone modifications. *Epigenetics : official journal of the DNA Methylation Society* **4**: 8-14.

Hashimoto H, Liu Y, Upadhyay AK, Chang Y, Howerton SB, Vertino PM, Zhang X, Cheng X. 2012. Recognition and potential mechanisms for replication and erasure of cytosine hydroxymethylation. *Nucleic acids research* **40**: 4841-4849.

Hata K, Okano M, Lei H, Li E. 2002. Dnmt3L cooperates with the Dnmt3 family of de novo DNA methyltransferases to establish maternal imprints in mice. *Development* **129**: 1983-1993.

Hattori N, Nishino K, Ko YG, Hattori N, Ohgane J, Tanaka S, Shiota K. 2004. Epigenetic control of mouse Oct-4 gene expression in embryonic stem cells and trophoblast stem cells. *The Journal of biological chemistry* **279**: 17063-17069.

Hauke J, Riessland M, Lunke S, Eyupoglu IY, Blumcke I, El-Osta A, Wirth B, Hahn E. 2009. Survival motor neuron gene 2 silencing by DNA methylation correlates with spinal muscular atrophy disease severity and can be bypassed by histone deacetylase inhibition. *Hum Mol Genet* **18**: 304-317.

He YF, Li BZ, Li Z, Liu P, Wang Y, Tang Q, Ding J, Jia Y, Chen Z, Li L et al. 2011. Tet-mediated formation of 5-carboxylcytosine and its excision by TDG in mammalian DNA. *Science* **333**: 1303-1307.

Heintzman ND, Stuart RK, Hon G, Fu Y, Ching CW, Hawkins RD, Barrera LO, Van Calcar S, Qu C, Ching KA et al. 2007. Distinct and predictive chromatin signatures of transcriptional promoters and enhancers in the human genome. *Nat Genet* **39**: 311-318.

Hendzel MJ, Wei Y, Mancini MA, Van Hooser A, Ranalli T, Brinkley BR, Bazett-Jones DP, Allis CD. 1997. Mitosis-specific phosphorylation of histone H3 initiates primarily within pericentromeric heterochromatin during G2 and spreads in an ordered fashion coincident with mitotic chromosome condensation. *Chromosoma* **106**: 348-360.

Henikoff S, Shilatifard A. 2011. Histone modification: cause or cog? *Trends in genetics : TIG* **27**: 389-396.

Herce HD, Deng W, Helma J, Leonhardt H, Cardoso MC. 2013. Visualization and targeted disruption of protein interactions in living cells. *Nature communications* **4**: 2660.

Hirano S, Kawasaki M, Ura H, Kato R, Raiborg C, Stenmark H, Wakatsuki S. 2006. Double-sided ubiquitin binding of Hrs-UIM in endosomal protein sorting. *Nat Struct Mol Biol* **13**: 272-277.

Ho SN, Hunt HD, Horton RM, Pullen JK, Pease LR. 1989. Site-directed mutagenesis by overlap extension using the polymerase chain reaction. *Gene* **77**: 51-59.

Hofmann K, Falquet L. 2001. A ubiquitin-interacting motif conserved in components of the proteasomal and lysosomal protein degradation systems. *Trends in biochemical sciences* **26**: 347-350.

Holtzman DM, Kilbridge J, Li Y, Cunningham ET, Jr., Lenn NJ, Clary DO, Reichardt LF, Mobley WC. 1995. TrkB expression in the CNS: evidence for the existence of several novel NGF-responsive CNS neurons. *The Journal of neuroscience : the official journal of the Society for Neuroscience* **15**: 1567-1576.

Hon GC, Hawkins RD, Ren B. 2009. Predictive chromatin signatures in the mammalian genome. *Hum Mol Genet* **18**: R195-201.

Hopfner R, Mousli M, Jeltsch JM, Voulgaris A, Lutz Y, Marin C, Bellocq JP, Oudet P, Bronner C. 2000. ICBP90, a novel human CCAAT binding protein, involved in the regulation of topoisomerase IIalpha expression. *Cancer Res* **60**: 121-128.

Hotchkiss RD. 1948. The quantitative separation of purines, pyrimidines, and nucleosides by paper chromatography. *The Journal of biological chemistry* **175**: 315-332.

Howell CY, Bestor TH, Ding F, Latham KE, Mertineit C, Trasler JM, Chaillet JR. 2001. Genomic imprinting disrupted by a maternal effect mutation in the Dnmt1 gene. *Cell* **104**: 829-838.

Howlett SK, Reik W. 1991. Methylation levels of maternal and paternal genomes during preimplantation development. *Development* **113**: 119-127.

Hsu JY, Sun ZW, Li X, Reuben M, Tatchell K, Bishop DK, Grushcow JM, Brame CJ, Caldwell JA, Hunt DF et al. 2000. Mitotic phosphorylation of histone H3 is governed by Ipl1/aurora kinase and Glc7/PP1 phosphatase in budding yeast and nematodes. *Cell* **102**: 279-291.

Hu YG, Hirasawa R, Hu JL, Hata K, Li CL, Jin Y, Chen T, Li E, Rigolet M, Viegas-Pequignot E et al. 2008. Regulation of DNA methylation activity through Dnmt3L promoter methylation by Dnmt3 enzymes in embryonic development. *Hum Mol Genet* **17**: 2654-2664.

Hunnicutt BJ, Chaverra M, George L, Lefcort F. 2012. IKAP/Elp1 is required in vivo for neurogenesis and neuronal survival, but not for neural crest migration. *PLoS One* **7**: e32050.

Hutagalung AH, Novick PJ. 2011. Role of Rab GTPases in membrane traffic and cell physiology. *Physiol Rev* **91**: 119-149.

Hyllus D, Stein C, Schnabel K, Schiltz E, Imhof A, Dou Y, Hsieh J, Bauer UM. 2007. PRMT6-mediated methylation of R2 in histone H3 antagonizes H3 K4 trimethylation. *Genes & development* **21**: 3369-3380.

Inano K, Suetake I, Ueda T, Miyake Y, Nakamura M, Okada M, Tajima S. 2000. Maintenance-type DNA methyltransferase is highly expressed in post-mitotic neurons and localized in the cytoplasmic compartment. *Journal of biochemistry* **128**: 315-321.

Indo Y. 2002. Genetics of congenital insensitivity to pain with anhidrosis (CIPA) or hereditary sensory and autonomic neuropathy type IV. Clinical, biological and molecular aspects of mutations in TRKA(NTRK1) gene encoding the receptor tyrosine kinase for nerve growth factor. *Clin Auton Res* **12 Suppl 1**: i20-32.

Inoue A, Shen L, Dai Q, He C, Zhang Y. 2011. Generation and replication-dependent dilution of 5fC and 5caC during mouse preimplantation development. *Cell research* **21**: 1670-1676.

Inoue A, Zhang Y. 2011. Replication-dependent loss of 5-hydroxymethylcytosine in mouse preimplantation embryos. *Science* **334**: 194.

Iqbal K, Jin SG, Pfeifer GP, Szabo PE. 2011. Reprogramming of the paternal genome upon fertilization involves genome-wide oxidation of 5-methylcytosine. *Proc Natl Acad Sci U S A* **108**: 3642-3647.

Iskandar BJ, Rizk E, Meier B, Hariharan N, Bottiglieri T, Finnell RH, Jarrard DF, Banerjee RV, Skene JH, Nelson A et al. 2010. Folate regulation of axonal regeneration in the rodent central nervous system through DNA methylation. *The Journal of clinical investigation* **120**: 1603-1616.

Ito S, D'Alessio AC, Taranova OV, Hong K, Sowers LC, Zhang Y. 2010. Role of Tet proteins in 5mC to 5hmC conversion, ES-cell self-renewal and inner cell mass specification. *Nature* **466**: 1129-1133.

Ito S, Shen L, Dai Q, Wu SC, Collins LB, Swenberg JA, He C, Zhang Y. 2011. Tet proteins can convert 5-methylcytosine to 5-formylcytosine and 5-carboxylcytosine. *Science* **333**: 1300-1303.

Iwata A, Nagashima Y, Matsumoto L, Suzuki T, Yamanaka T, Date H, Deoka K, Nukina N, Tsuji S. 2009. Intracellular degradation of polyglutamine aggregates by the ubiquitin-proteasome system. *The Journal of biological chemistry* **284**: 9796-9803.

Jacobs SA, Khorasanizadeh S. 2002. Structure of HP1 chromodomain bound to a lysine 9-methylated histone H3 tail. *Science* **295**: 2080-2083.

Jankowska AM, Szpurka H, Tiu RV, Makishima H, Afable M, Huh J, O'Keefe CL, Ganetzky R, McDevitt MA, Maciejewski JP. 2009. Loss of heterozygosity 4q24 and TET2 mutations associated with myelodysplastic/myeloproliferative neoplasms. *Blood* **113**: 6403-6410.

Jeanpierre M, Turleau C, Aurias A, Prieur M, Ledeist F, Fischer A, Viegas-Pequignot E. 1993. An embryonic-like methylation pattern of classical satellite DNA is observed in ICF syndrome. *Hum Mol Genet* **2**: 731-735.

Jenkins Y, Markovtsov V, Lang W, Sharma P, Pearsall D, Warner J, Franci C, Huang B, Huang J, Yam GC et al. 2005. Critical role of the ubiquitin ligase activity of UHRF1, a nuclear RING finger protein, in tumor cell growth. *Mol Biol Cell* **16**: 5621-5629.

Jenuwein T, Allis CD. 2001. Translating the histone code. *Science* **293**: 1074-1080.

Jeong S, Liang G, Sharma S, Lin JC, Choi SH, Han H, Yoo CB, Egger G, Yang AS, Jones PA. 2009. Selective anchoring of DNA methyltransferases 3A and 3B to nucleosomes containing methylated DNA. *Molecular and cellular biology* **29**: 5366-5376.

Jin Q, Yu LR, Wang L, Zhang Z, Kasper LH, Lee JE, Wang C, Brindle PK, Dent SY, Ge K. 2011. Distinct roles of GCN5/PCAF-mediated H3K9ac and CBP/p300-mediated H3K18/27ac in nuclear receptor transactivation. *The EMBO journal* **30**: 249-262.

Jin SG, Kadam S, Pfeifer GP. 2010. Examination of the specificity of DNA methylation profiling techniques towards 5-methylcytosine and 5-hydroxymethylcytosine. *Nucleic acids research* **38**: e125.

Jorgensen S, Schotta G, Sorensen CS. 2013. Histone H4 lysine 20 methylation: key player in epigenetic regulation of genomic integrity. *Nucleic acids research* **41**: 2797-2806.

Jung YW, Hysolli E, Kim KY, Tanaka Y, Park IH. 2012. Human induced pluripotent stem cells and neurodegenerative disease: prospects for novel therapies. *Current opinion in neurology* **25**: 125-130.

Jurkowski TP, Meusburger M, Phalke S, Helm M, Nellen W, Reuter G, Jeltsch A. 2008. Human DNMT2 methylates tRNA(Asp) molecules using a DNA methyltransferase-like catalytic mechanism. *Rna* **14**: 1663-1670.

Kagiwada S, Kurimoto K, Hirota T, Yamaji M, Saitou M. 2013. Replication-coupled passive DNA demethylation for the erasure of genome imprints in mice. *The EMBO journal* **32**: 340-353.

Kalb R, Latwiel S, Baymaz HI, Jansen PW, Muller CW, Vermeulen M, Muller J. 2014. Histone H2A monoubiquitination promotes histone H3 methylation in Polycomb repression. *Nat Struct Mol Biol* **21**: 569-571.

Kalisch T, Ame JC, Dantzer F, Schreiber V. 2012. New readers and interpretations of poly(ADP-ribosylation). *Trends in biochemical sciences* **37**: 381-390.

Kaneda M, Okano M, Hata K, Sado T, Tsujimoto N, Li E, Sasaki H. 2004. Essential role for de novo DNA methyltransferase Dnmt3a in paternal and maternal imprinting. *Nature* **429**: 900-903.

Kaplan DR, Martin-Zanca D, Parada LF. 1991. Tyrosine phosphorylation and tyrosine kinase activity of the trk proto-oncogene product induced by NGF. *Nature* **350**: 158-160.

Karagianni P, Amazit L, Qin J, Wong J. 2008. ICBP90, a novel methyl K9 H3 binding protein linking protein ubiquitination with heterochromatin formation. *Molecular and cellular biology* **28**: 705-717.

Keren H, Donyo M, Zeevi D, Maayan C, Pupko T, Ast G. 2010. Phosphatidylserine increases IKBKAP levels in familial dysautonomia cells. *PLoS One* **5**: e15884.

Kim JH, Lane WS, Reinberg D. 2002. Human Elongator facilitates RNA polymerase II transcription through chromatin. *Proc Natl Acad Sci U S A* **99**: 1241-1246.

Kim JK, Esteve PO, Jacobsen SE, Pradhan S. 2009. UHRF1 binds G9a and participates in p21 transcriptional regulation in mammalian cells. *Nucleic acids research* **37**: 493-505.

Kimura H, Tada M, Nakatsuji N, Tada T. 2004. Histone code modifications on pluripotential nuclei of reprogrammed somatic cells. *Molecular and cellular biology* **24**: 5710-5720.

Kishikawa S, Murata T, Ugai H, Yamazaki T, Yokoyama KK. 2003. Control elements of Dnmt1 gene are regulated in cell-cycle dependent manner. *Nucleic acids research Supplement*: 307-308.

Kizer KO, Phatnani HP, Shibata Y, Hall H, Greenleaf AL, Strahl BD. 2005. A novel domain in Set2 mediates RNA polymerase II interaction and couples histone H3 K36 methylation with transcript elongation. *Molecular and cellular biology* **25**: 3305-3316.

Klein CJ, ed. 2012. *DNMT1-related dementia, deafness, and sensory neuropathy*.

Klein CJ, Bird T, Ertekin-Taner N, Lincoln S, Hjorth R, Wu Y, Kwok J, Mer G, Dyck PJ, Nicholson GA. 2013. DNMT1 mutation hot spot causes varied phenotypes of HSAN1 with dementia and hearing loss. *Neurology* **80**: 824-828.

Klein CJ, Botuyan MV, Wu Y, Ward CJ, Nicholson GA, Hammans S, Hojo K, Yamanishi H, Karpf AR, Wallace DC et al. 2011. Mutations in DNMT1 cause hereditary sensory neuropathy with dementia and hearing loss. *Nat Genet* **43**: 595-600.

Klose RJ, Bird AP. 2006. Genomic DNA methylation: the mark and its mediators. *Trends in biochemical sciences* **31**: 89-97.

Kohli RM, Zhang Y. 2013. TET enzymes, TDG and the dynamics of DNA demethylation. *Nature* **502**: 472-479.

Kondo T, Bobek MP, Kuick R, Lamb B, Zhu X, Narayan A, Bourc'his D, Viegas-Pequignot E, Ehrlich M, Hanash SM. 2000. Whole-genome methylation scan in ICF syndrome: hypomethylation of non-satellite DNA repeats D4Z4 and NBL2. *Hum Mol Genet* **9**: 597-604.

Konstandin N, Bultmann S, Szwagierczak A, Dufour A, Ksienzyk B, Schneider F, Herold T, Mulaw M, Kakadia PM, Schneider S et al. 2011. Genomic 5-hydroxymethylcytosine levels correlate with TET2 mutations and a distinct global gene expression pattern in secondary acute myeloid leukemia. *Leukemia* **25**: 1649-1652.

Kornak U, Mademan I, Schinke M, Voigt M, Krawitz P, Hecht J, Barvencik F, Schinke T, Giesselmann S, Beil FT et al. 2014. Sensory neuropathy with bone destruction due to a mutation in the membrane-shaping atlastin GTPase 3. *Brain : a journal of neurology* **137**: 683-692.

Kosmider O, Gelsi-Boyer V, Cheok M, Grabar S, Della-Valle V, Picard F, Viguie F, Quesnel B, Beyne-Rauzy O, Solary E et al. 2009. TET2 mutation is an independent favorable prognostic factor in myelodysplastic syndromes (MDSs). *Blood* **114**: 3285-3291.

Kouzarides T. 2007. Chromatin modifications and their function. *Cell* **128**: 693-705.

Kriaucionis S, Heintz N. 2009. The nuclear DNA base 5-hydroxymethylcytosine is present in Purkinje neurons and the brain. *Science* **324**: 929-930.

Kubota H, Yokota S, Yanagi H, Yura T. 1999. Structures and co-regulated expression of the genes encoding mouse cytosolic chaperonin CCT subunits. *European journal of biochemistry / FEBS* **262**: 492-500.

Kunert N, Marhold J, Stanke J, Stach D, Lyko F. 2003. A Dnmt2-like protein mediates DNA methylation in *Drosophila*. *Development* **130**: 5083-5090.

Kurth I, Pamminger T, Hennings JC, Soehendra D, Huebner AK, Rotthier A, Baets J, Senderek J, Topaloglu H, Farrell SA et al. 2009. Mutations in FAM134B, encoding a newly identified Golgi protein, cause severe sensory and autonomic neuropathy. *Nat Genet* **41**: 1179-1181.

Lachner M, O'Carroll D, Rea S, Mechtler K, Jenuwein T. 2001. Methylation of histone H3 lysine 9 creates a binding site for HP1 proteins. *Nature* **410**: 116-120.

Lafreniere RG, MacDonald ML, Dube MP, MacFarlane J, O'Driscoll M, Brais B, Meilleur S, Brinkman RR, Dadivas O, Pape T et al. 2004. Identification of a novel gene (HSN2) causing hereditary sensory and autonomic neuropathy type II through the Study of Canadian Genetic Isolates. *American journal of human genetics* **74**: 1064-1073.

Lane N, Dean W, Erhardt S, Hajkova P, Surani A, Walter J, Reik W. 2003. Resistance of IAPs to methylation reprogramming may provide a mechanism for epigenetic inheritance in the mouse. *Genesis* **35**: 88-93.

Langemeijer SM, Kuiper RP, Berends M, Knops R, Aslanyan MG, Massop M, Stevens-Linders E, van Hoogen P, van Kessel AG, Raymakers RA et al. 2009. Acquired mutations in TET2 are common in myelodysplastic syndromes. *Nat Genet* **41**: 838-842.

Law JA, Jacobsen SE. 2010. Establishing, maintaining and modifying DNA methylation patterns in plants and animals. *Nature reviews Genetics* **11**: 204-220.

Lee G, Papapetrou EP, Kim H, Chambers SM, Tomishima MJ, Fasano CA, Ganat YM, Menon J, Shimizu F, Viale A et al. 2009. Modelling pathogenesis and treatment of familial dysautonomia using patient-specific iPSCs. *Nature* **461**: 402-406.

Lee JH, Skalnik DG. 2005. CpG-binding protein (CXXC finger protein 1) is a component of the mammalian Set1 histone H3-Lys4 methyltransferase complex, the analogue of the yeast Set1/COMPASS complex. *The Journal of biological chemistry* **280**: 41725-41731.

Lee JH, Tate CM, You JS, Skalnik DG. 2007. Identification and characterization of the human Set1B histone H3-Lys4 methyltransferase complex. *The Journal of biological chemistry* **282**: 13419-13428.

Lee JS, Smith E, Shilatifard A. 2010. The language of histone crosstalk. *Cell* **142**: 682-685.

Lehertz B, Ueda Y, Derijck AA, Braunschweig U, Perez-Burgos L, Kubicek S, Chen T, Li E, Jenuwein T, Peters AH. 2003. Suv39h-mediated histone H3 lysine 9 methylation directs DNA methylation to major satellite repeats at pericentric heterochromatin. *Current biology : CB* **13**: 1192-1200.

Lei H, Oh SP, Okano M, Juttermann R, Goss KA, Jaenisch R, Li E. 1996. De novo DNA cytosine methyltransferase activities in mouse embryonic stem cells. *Development* **122**: 3195-3205.

Leonhardt H, Page AW, Weier HU, Bestor TH. 1992. A targeting sequence directs DNA methyltransferase to sites of DNA replication in mammalian nuclei. *Cell* **71**: 865-873.

Leonhardt H, Rahn HP, Weinzierl P, Sporbert A, Cremer T, Zink D, Cardoso MC. 2000. Dynamics of DNA replication factories in living cells. *The Journal of cell biology* **149**: 271-280.

Levenson JM, Roth TL, Lubin FD, Miller CA, Huang IC, Desai P, Malone LM, Sweatt JD. 2006. Evidence that DNA (cytosine-5) methyltransferase regulates synaptic plasticity in the hippocampus. *The Journal of biological chemistry* **281**: 15763-15773.

Levi-Montalcini R, Skaper SD, Dal Toso R, Petrelli L, Leon A. 1996. Nerve growth factor: from neurotrophin to neurokine. *Trends Neurosci* **19**: 514-520.

Li B, Carey M, Workman JL. 2007a. The role of chromatin during transcription. *Cell* **128**: 707-719.

Li E, Bestor TH, Jaenisch R. 1992. Targeted mutation of the DNA methyltransferase gene results in embryonic lethality. *Cell* **69**: 915-926.

Li JY, Pu MT, Hirasawa R, Li BZ, Huang YN, Zeng R, Jing NH, Chen T, Li E, Sasaki H et al. 2007b. Synergistic function of DNA methyltransferases Dnmt3a and Dnmt3b in the methylation of Oct4 and Nanog. *Molecular and cellular biology* **27**: 8748-8759.

Li X, Qian W, Zhao Y, Wang C, Shen J, Zhu JK, Gong Z. 2012. Antisilencing role of the RNA-directed DNA methylation pathway and a histone acetyltransferase in Arabidopsis. *Proc Natl Acad Sci U S A* **109**: 11425-11430.

Li X, Wei W, Zhao QY, Widagdo J, Baker-Andresen D, Flavell CR, D'Alessio A, Zhang Y, Bredy TW. 2014. Neocortical Tet3-mediated accumulation of 5-hydroxymethylcytosine promotes rapid behavioral adaptation. *Proc Natl Acad Sci U S A* **111**: 7120-7125.

Li Y, Mori T, Hata H, Homma Y, Kochi H. 2004. NIRF induces G1 arrest and associates with Cdk2. *Biochemical and biophysical research communications* **319**: 464-468.

Lim J, Son WS, Park JK, Kim EE, Lee BJ, Ahn HC. 2011. Solution structure of UIM and interaction of tandem ubiquitin binding domains in STAM1 with ubiquitin. *Biochemical and biophysical research communications* **405**: 24-30.

Lister R, Mukamel EA, Nery JR, Urich M, Puddifoot CA, Johnson ND, Lucero J, Huang Y, Dwork AJ, Schultz MD et al. 2013. Global epigenomic reconfiguration during mammalian brain development. *Science* **341**: 1237905.

Lister R, Pelizzola M, Down RH, Hawkins RD, Hon G, Tonti-Filippini J, Nery JR, Lee L, Ye Z, Ngo QM et al. 2009. Human DNA methylomes at base resolution show widespread epigenomic differences. *Nature* **462**: 315-322.

Liu X, Gao Q, Li P, Zhao Q, Zhang J, Li J, Koseki H, Wong J. 2013. UHRF1 targets DNMT1 for DNA methylation through cooperative binding of hemi-methylated DNA and methylated H3K9. *Nature communications* **4**: 1563.

Liutkeviciute Z, Lukinavicius G, Masevicius V, Daujotyte D, Klimasauskas S. 2009. Cytosine-5-methyltransferases add aldehydes to DNA. *Nature chemical biology* **5**: 400-402.

Lo WS, Trievel RC, Rojas JR, Duggan L, Hsu JY, Allis CD, Marmorstein R, Berger SL. 2000. Phosphorylation of serine 10 in histone H3 is functionally linked in vitro and in vivo to Gcn5-mediated acetylation at lysine 14. *Molecular cell* **5**: 917-926.

Lubin FD, Roth TL, Sweatt JD. 2008. Epigenetic regulation of BDNF gene transcription in the consolidation of fear memory. *The Journal of neuroscience : the official journal of the Society for Neuroscience* **28**: 10576-10586.

Lunn MR, Wang CH. 2008. Spinal muscular atrophy. *Lancet* **371**: 2120-2133.

Ma DK, Jang MH, Guo JU, Kitabatake Y, Chang ML, Pow-Anpongkul N, Flavell RA, Lu B, Ming GL, Song H. 2009. Neuronal activity-induced Gadd45b promotes epigenetic DNA demethylation and adult neurogenesis. *Science* **323**: 1074-1077.

Macleod D, Charlton J, Mullins J, Bird AP. 1994. Sp1 sites in the mouse aprt gene promoter are required to prevent methylation of the CpG island. *Genes & development* **8**: 2282-2292.

Maga G, Hubscher U. 2003. Proliferating cell nuclear antigen (PCNA): a dancer with many partners. *Journal of cell science* **116**: 3051-3060.

Maiti A, Drohat AC. 2011. Thymine DNA glycosylase can rapidly excise 5-formylcytosine and 5-carboxylcytosine: potential implications for active demethylation of CpG sites. *The Journal of biological chemistry* **286**: 35334-35338.

Margot JB, Ehrenhofer-Murray AE, Leonhardt H. 2003. Interactions within the mammalian DNA methyltransferase family. *BMC molecular biology* **4**: 7.

Marr RA, Thomas RM, Peterson DA. 2010. Insights into neurogenesis and aging: potential therapy for degenerative disease? *Future neurology* **5**: 527-541.

Martinowich K, Hattori D, Wu H, Fouse S, He F, Hu Y, Fan G, Sun YE. 2003. DNA methylation-related chromatin remodeling in activity-dependent BDNF gene regulation. *Science* **302**: 890-893.

Martins-Taylor K, Schroeder DI, LaSalle JM, Lalande M, Xu RH. 2012. Role of DNMT3B in the regulation of early neural and neural crest specifiers. *Epigenetics : official journal of the DNA Methylation Society* **7**: 71-82.

Marvin KW, Yau P, Bradbury EM. 1990. Isolation and characterization of acetylated histones H3 and H4 and their assembly into nucleosomes. *The Journal of biological chemistry* **265**: 19839-19847.

Mattson MP. 2003. Methylation and acetylation in nervous system development and neurodegenerative disorders. *Ageing research reviews* **2**: 329-342.

Mayer W, Niveleau A, Walter J, Fundele R, Haaf T. 2000. Demethylation of the zygotic paternal genome. *Nature* **403**: 501-502.

Meilinger D, Fellinger K, Bultmann S, Rothbauer U, Bonapace IM, Klinkert WE, Spada F, Leonhardt H. 2009. Np95 interacts with de novo DNA methyltransferases, Dnmt3a and Dnmt3b, and mediates epigenetic silencing of the viral CMV promoter in embryonic stem cells. *EMBO reports* **10**: 1259-1264.

Mellen M, Ayata P, Dewell S, Kriaucionis S, Heintz N. 2012. MeCP2 binds to 5hmC enriched within active genes and accessible chromatin in the nervous system. *Cell* **151**: 1417-1430.

Mersfelder EL, Parthun MR. 2006. The tale beyond the tail: histone core domain modifications and the regulation of chromatin structure. *Nucleic acids research* **34**: 2653-2662.

Metzger E, Wissmann M, Yin N, Muller JM, Schneider R, Peters AH, Gunther T, Buettner R, Schule R. 2005. LSD1 demethylates repressive histone marks to promote androgen-receptor-dependent transcription. *Nature* **437**: 436-439.

Miller CA, Gavin CF, White JA, Parrish RR, Honasoge A, Yancey CR, Rivera IM, Rubio MD, Rumbaugh G, Sweatt JD. 2010. Cortical DNA methylation maintains remote memory. *Nature neuroscience* **13**: 664-666.

Miller CA, Sweatt JD. 2007. Covalent modification of DNA regulates memory formation. *Neuron* **53**: 857-869.

Miller SL, Malotky E, O'Bryan JP. 2004. Analysis of the role of ubiquitin-interacting motifs in ubiquitin binding and ubiquitylation. *The Journal of biological chemistry* **279**: 33528-33537.

Miniou P, Jeanpierre M, Blanquet V, Sibella V, Bonneau D, Herbelin C, Fischer A, Niveleau A, Viegas-Pequignot E. 1994. Abnormal methylation pattern in constitutive and facultative (X inactive chromosome) heterochromatin of ICF patients. *Hum Mol Genet* **3**: 2093-2102.

Moghadam KK, Pizza F, La Morgia C, Franceschini C, Tonon C, Lodi R, Barboni P, Seri M, Ferrari S, Liguori R et al. 2014a. Narcolepsy is a common phenotype in HSAN IE and ADCA-DN. *Brain : a journal of neurology*.

Moghadam KK, Pizza F, Tonon C, Lodi R, Carelli V, Poli F, Franceschini C, Barboni P, Seri M, Ferrari S et al. 2014e. Polysomnographic and neurometabolic features may mark preclinical autosomal dominant cerebellar ataxia, deafness, and narcolepsy due to a mutation in the DNA (cytosine-5)-methyltransferase gene, DNMT1. *Sleep medicine*.

Mohamedali AM, Smith AE, Gaken J, Lea NC, Mian SA, Westwood NB, Strupp C, Gattermann N, Germing U, Mufti GJ. 2009. Novel TET2 mutations associated with UPD4q24 in myelodysplastic syndrome. *Journal of clinical oncology : official journal of the American Society of Clinical Oncology* **27**: 4002-4006.

Monk M, Boubelik M, Lehnert S. 1987. Temporal and regional changes in DNA methylation in the embryonic, extraembryonic and germ cell lineages during mouse embryo development. *Development* **99**: 371-382.

Mori T, Li Y, Hata H, Kochi H. 2004. NIRF is a ubiquitin ligase that is capable of ubiquitinating PCNP, a PEST-containing nuclear protein. *FEBS letters* **557**: 209-214.

Mori T, Li Y, Hata H, Ono K, Kochi H. 2002. NIRF, a novel RING finger protein, is involved in cell-cycle regulation. *Biochemical and biophysical research communications* **296**: 530-536.

Mortusewicz O, Schermelleh L, Walter J, Cardoso MC, Leonhardt H. 2005. Recruitment of DNA methyltransferase I to DNA repair sites. *Proc Natl Acad Sci U S A* **102**: 8905-8909.

Müller U, Bauer C, Siegl M, Rottach A, Leonhardt H. 2014. TET-mediated oxidation of methylcytosine causes TDG or NEIL glycosylase dependent gene reactivation. *Nucleic acids research* **42**: 8592-8604.

Munzel M, Globisch D, Bruckl T, Wagner M, Welzmiller V, Michalakis S, Muller M, Biel M, Carell T. 2010. Quantification of the sixth DNA base hydroxymethylcytosine in the brain. *Angewandte Chemie* **49**: 5375-5377.

Muto M, Kanari Y, Kubo E, Takabe T, Kurihara T, Fujimori A, Tatsumi K. 2002. Targeted disruption of Np95 gene renders murine embryonic stem cells hypersensitive to DNA damaging agents and DNA replication blocks. *The Journal of biological chemistry* **277**: 34549-34555.

Namekawa M, Muriel MP, Janer A, Latouche M, Dauphin A, Debeir T, Martin E, Duyckaerts C, Prigent A, Depienne C et al. 2007. Mutations in the SPG3A gene encoding the GTPase atlastin interfere with vesicle trafficking in the ER/Golgi interface and Golgi morphogenesis. *Molecular and cellular neurosciences* **35**: 1-13.

Nan X, Campoy FJ, Bird A. 1997. MeCP2 is a transcriptional repressor with abundant binding sites in genomic chromatin. *Cell* **88**: 471-481.

Nelson ED, Kavalali ET, Monteggia LM. 2008. Activity-dependent suppression of miniature neurotransmission through the regulation of DNA methylation. *The Journal of neuroscience : the official journal of the Society for Neuroscience* **28**: 395-406.

Nguyen S, Meletis K, Fu D, Jhaveri S, Jaenisch R. 2007. Ablation of de novo DNA methyltransferase Dnmt3a in the nervous system leads to neuromuscular defects and shortened lifespan. *Developmental dynamics : an official publication of the American Association of Anatomists* **236**: 1663-1676.

Nicol GD, Vasko MR. 2007. Unraveling the story of NGF-mediated sensitization of nociceptive sensory neurons: ON or OFF the Trks? *Molecular interventions* **7**: 26-41.

Nielsen PR, Nietlispach D, Mott HR, Callaghan J, Bannister A, Kouzarides T, Murzin AG, Murzina NV, Laue ED. 2002. Structure of the HP1 chromodomain bound to histone H3 methylated at lysine 9. *Nature* **416**: 103-107.

Nishioka K, Chuikov S, Sarma K, Erdjument-Bromage H, Allis CD, Tempst P, Reinberg D. 2002a. Set9, a novel histone H3 methyltransferase that facilitates transcription by precluding histone tail modifications required for heterochromatin formation. *Genes & development* **16**: 479-489.

Nishioka K, Rice JC, Sarma K, Erdjument-Bromage H, Werner J, Wang Y, Chuikov S, Valenzuela P, Tempst P, Steward R et al. 2002b. PR-Set7 is a nucleosome-specific methyltransferase that modifies lysine 20 of histone H4 and is associated with silent chromatin. *Molecular cell* **9**: 1201-1213.

Nishiyama A, Yamaguchi L, Sharif J, Johmura Y, Kawamura T, Nakanishi K, Shimamura S, Arita K, Kodama T, Ishikawa F et al. 2013. Uhrf1-dependent H3K23 ubiquitylation couples maintenance DNA methylation and replication. *Nature*.

Niu Y, Otasek D, Jurisica I. 2010. Evaluation of linguistic features useful in extraction of interactions from PubMed; application to annotating known, high-throughput and predicted interactions in I2D. *Bioinformatics* **26**: 111-119.

Nolte F, Hofmann WK. 2008. Myelodysplastic syndromes: molecular pathogenesis and genomic changes. *Annals of hematology* **87**: 777-795.

Okada Y, Yamagata K, Hong K, Wakayama T, Zhang Y. 2010. A role for the elongator complex in zygotic paternal genome demethylation. *Nature* **463**: 554-558.

Okada Y, Yamazaki H, Sekine-Aizawa Y, Hirokawa N. 1995. The neuron-specific kinesin superfamily protein KIF1A is a unique monomeric motor for anterograde axonal transport of synaptic vesicle precursors. *Cell* **81**: 769-780.

Okano M, Bell DW, Haber DA, Li E. 1999. DNA methyltransferases Dnmt3a and Dnmt3b are essential for de novo methylation and mammalian development. *Cell* **99**: 247-257.

Okano M, Xie S, Li E. 1998a. Cloning and characterization of a family of novel mammalian DNA (cytosine-5) methyltransferases. *Nat Genet* **19**: 219-220.

Okano. 1998b. Dnmt2 is not required for de novo and maintenance methylation of viral DNA in embryonic stem cells. *Nucleic acids research* **26**: 2536-2540.

Okuse K, Mizuno N, Matsuoka I, Kurihara K. 1993. Induction of cholinergic and adrenergic differentiation in N-18 cells by differentiation agents and DNA demethylating agents. *Brain research* **626**: 225-233.

Olek A, Walter J. 1997. The pre-implantation ontogeny of the H19 methylation imprint. *Nat Genet* **17**: 275-276.

Ooi SK, Bestor TH. 2008. Cytosine methylation: remaining faithful. *Current biology : CB* **18**: R174-176.

Ooi SK, Qiu C, Bernstein E, Li K, Jia D, Yang Z, Erdjument-Bromage H, Tempst P, Lin SP, Allis CD et al. 2007. DNMT3L connects unmethylated lysine 4 of histone H3 to de novo methylation of DNA. *Nature* **448**: 714-717.

Otani J, Kimura H, Sharif J, Endo TA, Mishima Y, Kawakami T, Koseki H, Shirakawa M, Suetake I, Tajima S. 2013. Cell cycle-dependent turnover of 5-hydroxymethyl cytosine in mouse embryonic stem cells. *PLoS One* **8**: e82961.

Otani J, Nankumo T, Arita K, Inamoto S, Ariyoshi M, Shirakawa M. 2009. Structural basis for recognition of H3K4 methylation status by the DNA methyltransferase 3A ATRX-DNMT3-DNMT3L domain. *EMBO reports* **10**: 1235-1241.

Otero G, Fellows J, Li Y, de Bizemont T, Dirac AM, Gustafsson CM, Erdjument-Bromage H, Tempst P, Svejstrup JQ. 1999. Elongator, a multisubunit component of a novel RNA polymerase II holoenzyme for transcriptional elongation. *Molecular cell* **3**: 109-118.

Papait R, Pistore C, Grazini U, Babbio F, Cogliati S, Pecoraro D, Brino L, Morand AL, Dechampesme AM, Spada F et al. 2008. The PHD domain of Np95 (mUHRF1) is involved in large-scale reorganization of pericentromeric heterochromatin. *Mol Biol Cell* **19**: 3554-3563.

Patel K, Dickson J, Din S, Macleod K, Jodrell D, Ramsahoye B. 2010. Targeting of 5-aza-2'-deoxycytidine residues by chromatin-associated DNMT1 induces proteasomal degradation of the free enzyme. *Nucleic acids research* **38**: 4313-4324.

Pedroso JL, Povoas Barsottini OG, Lin L, Melberg A, Oliveira AS, Mignot E. 2013. A novel de novo exon 21 DNMT1 mutation causes cerebellar ataxia, deafness, and narcolepsy in a Brazilian patient. *Sleep* **36**: 1257-1259, 1259A.

Peters AH, Kubicek S, Mechteder K, O'Sullivan RJ, Derijck AA, Perez-Burgos L, Kohlmaier A, Opravil S, Tachibana M, Shinkai Y et al. 2003. Partitioning and plasticity of repressive histone methylation states in mammalian chromatin. *Molecular cell* **12**: 1577-1589.

Peters JM. 2002. The anaphase-promoting complex: proteolysis in mitosis and beyond. *Molecular cell* **9**: 931-943.

Pfaffeneder T, Hackner B, Truss M, Munzel M, Muller M, Deiml CA, Hagemeier C, Carell T. 2011. The discovery of 5-formylcytosine in embryonic stem cell DNA. *Angewandte Chemie* **50**: 7008-7012.

Pfleger CM, Kirschner MW. 2000. The KEN box: an APC recognition signal distinct from the D box targeted by Cdh1. *Genes & development* **14**: 655-665.

Pichler G, Jack A, Wolf P, Hake SB. 2012. Versatile toolbox for high throughput biochemical and functional studies with fluorescent fusion proteins. *PLoS One* **7**: e36967.

Pichler G, Wolf P, Schmidt CS, Meilinger D, Schneider K, Frauer C, Fellinger K, Rottach A, Leonhardt H. 2011. Cooperative DNA and histone binding by Uhrf2 links the two major repressive epigenetic pathways. *Journal of cellular biochemistry* **112**: 2585-2593.

Pieper HC, Evert BO, Kaut O, Riederer PF, Waha A, Wullner U. 2008. Different methylation of the TNF-alpha promoter in cortex and substantia nigra: Implications for selective neuronal vulnerability. *Neurobiology of disease* **32**: 521-527.

Plath K, Fang J, Mlynarczyk-Evans SK, Cao R, Worringer KA, Wang H, de la Cruz CC, Otte AP, Panning B, Zhang Y. 2003. Role of histone H3 lysine 27 methylation in X inactivation. *Science* **300**: 131-135.

Pogribny IP, Beland FA. 2009. DNA hypomethylation in the origin and pathogenesis of human diseases. *Cellular and molecular life sciences : CMLS* **66**: 2249-2261.

Pradhan S, Bacolla A, Wells RD, Roberts RJ. 1999. Recombinant human DNA (cytosine-5) methyltransferase. I. Expression, purification, and comparison of de novo and maintenance methylation. *The Journal of biological chemistry* **274**: 33002-33010.

Prokhorchuk AV, Aitkhozhina DS, Sablina AA, Ruzov AS, Prokhorchuk EB. 2001. [KAISO--a new member of the BTB/POZ family specifically bindsto methylated DNA sequences]. *Genetika* **37**: 737-744.

Prokhortchouk A, Hendrich B, Jorgensen H, Ruzov A, Wilm M, Georgiev G, Bird A, Prokhortchouk E. 2001. The p120 catenin partner Kaiso is a DNA methylation-dependent transcriptional repressor. *Genes & development* **15**: 1613-1618.

Qian C, Li S, Jakoncic J, Zeng L, Walsh MJ, Zhou MM. 2008. Structure and hemimethylated CpG binding of the SRA domain from human UHRF1. *The Journal of biological chemistry* **283**: 34490-34494.

Qian W, Miki D, Zhang H, Liu Y, Zhang X, Tang K, Kan Y, La H, Li X, Li S et al. 2012. A histone acetyltransferase regulates active DNA demethylation in Arabidopsis. *Science* **336**: 1445-1448.

Qin W, Leonhardt H, Spada F. 2011. Usp7 and Uhrf1 control ubiquitination and stability of the maintenance DNA methyltransferase Dnmt1. *Journal of cellular biochemistry* **112**: 439-444.

Qin W, Wolf P, Liu N, Link S, Smets M, Mastra F, Forne I, Pichler G, Horl D, Fellinger K et al. 2015. DNA methylation requires a DNMT1 ubiquitin interacting motif (UIM) and histone ubiquitination. *Cell research*.

R-Core-Team. 2013. A Language and Environment for Statistical Computing. R Foundation for Statistical Computing, Vienna, Austria.

Rai K, Chidester S, Zavala CV, Manos EJ, James SR, Karpf AR, Jones DA, Cairns BR. 2007. Dnmt2 functions in the cytoplasm to promote liver, brain, and retina development in zebrafish. *Genes & development* **21**: 261-266.

Rajakumara E, Wang Z, Ma H, Hu L, Chen H, Lin Y, Guo R, Wu F, Li H, Lan F et al. 2011. PHD finger recognition of unmodified histone H3R2 links UHRF1 to regulation of euchromatic gene expression. *Molecular cell* **43**: 275-284.

Ramsahoye BH, Biniszkiewicz D, Lyko F, Clark V, Bird AP, Jaenisch R. 2000. Non-CpG methylation is prevalent in embryonic stem cells and may be mediated by DNA methyltransferase 3a. *Proc Natl Acad Sci U S A* **97**: 5237-5242.

Rea S, Eisenhaber F, O'Carroll D, Strahl BD, Sun ZW, Schmid M, Opravil S, Mechtler K, Ponting CP, Allis CD et al. 2000. Regulation of chromatin structure by site-specific histone H3 methyltransferases. *Nature* **406**: 593-599.

Reik W, Walter J. 2001. Genomic imprinting: parental influence on the genome. *Nature reviews Genetics* **2**: 21-32.

Reynoird N, Gozani O. 2014. Nuclear PI5P, Uhrf1, and the Road Not Taken. *Molecular cell* **54**: 901-903.

Rhee KD, Yu J, Zhao CY, Fan G, Yang XJ. 2012. Dnmt1-dependent DNA methylation is essential for photoreceptor terminal differentiation and retinal neuron survival. *Cell death & disease* **3**: e427.

Rice JC, Nishioka K, Sarma K, Steward R, Reinberg D, Allis CD. 2002. Mitotic-specific methylation of histone H4 Lys 20 follows increased PR-Set7 expression and its localization to mitotic chromosomes. *Genes & development* **16**: 2225-2230.

Riviere JB, Ramalingam S, Lavastre V, Shekarabi M, Holbert S, Lafontaine J, Srour M, Merner N, Rochefort D, Hince P et al. 2011. KIF1A, an axonal transporter of synaptic vesicles, is mutated in hereditary sensory and autonomic neuropathy type 2. *American journal of human genetics* **89**: 219-230.

Riviere JB, Verlaan DJ, Shekarabi M, Lafreniere RG, Benard M, Der Kaloustian VM, Shbaklo Z, Rouleau GA. 2004. A mutation in the HSN2 gene causes sensory neuropathy type II in a Lebanese family. *Annals of neurology* **56**: 572-575.

Robertson KD, Wolffe AP. 2000. DNA methylation in health and disease. *Nature reviews Genetics* **1**: 11-19.

Roddier K, Thomas T, Marleau G, Gagnon AM, Dicaire MJ, St-Denis A, Gosselin I, Sarrazin AM, Larbrisseau A, Lambert M et al. 2005. Two mutations in the HSN2 gene explain the high prevalence of HSAN2 in French Canadians. *Neurology* **64**: 1762-1767.

Rothbart SB, Dickson BM, Ong MS, Krajewski K, Houlston S, Kireev DB, Arrowsmith CH, Strahl BD. 2013. Multivalent histone engagement by the linked tandem Tudor and PHD domains of UHRF1 is required for the epigenetic inheritance of DNA methylation. *Genes & development* **27**: 1288-1298.

Rothbart SB, Krajewski K, Nady N, Tempel W, Xue S, Badeaux AI, Barsyte-Lovejoy D, Martinez JY, Bedford MT, Fuchs SM et al. 2012. Association of UHRF1 with methylated H3K9 directs the maintenance of DNA methylation. *Nat Struct Mol Biol* **19**: 1155-1160.

Rothbauer U, Zolghadr K, Muyldermans S, Schepers A, Cardoso MC, Leonhardt H. 2008. A versatile nanotrap for biochemical and functional studies with fluorescent fusion proteins. *Molecular & cellular proteomics : MCP* **7**: 282-289.

Rottach A, Frauer C, Pichler G, Bonapace IM, Spada F, Leonhardt H. 2010. The multi-domain protein Np95 connects DNA methylation and histone modification. *Nucleic acids research* **38**: 1796-1804.

Rottach A, Kremmer E, Nowak D, Leonhardt H, Cardoso MC. 2008. Generation and characterization of a rat monoclonal antibody specific for multiple red fluorescent proteins. *Hybridoma (Larchmt)* **27**: 337-343.

Rottach A, Leonhardt H, Spada F. 2009. DNA methylation-mediated epigenetic control. *Journal of cellular biochemistry* **108**: 43-51.

Rotthier A, Baets J, De Vriendt E, Jacobs A, Auer-Grumbach M, Levy N, Bonello-Palot N, Kilic SS, Weis J, Nascimento A et al. 2009. Genes for hereditary sensory and autonomic neuropathies: a genotype-phenotype correlation. *Brain : a journal of neurology* **132**: 2699-2711.

Rotthier A, Baets J, Timmerman V, Janssens K. 2012. Mechanisms of disease in hereditary sensory and autonomic neuropathies. *Nature reviews Neurology* **8**: 73-85.

Rougier N, Bourc'his D, Gomes DM, Niveleau A, Plachot M, Paldi A, Viegas-Pequignot E. 1998. Chromosome methylation patterns during mammalian preimplantation development. *Genes & development* **12**: 2108-2113.

Rountree MR, Bachman KE, Baylin SB. 2000. DNMT1 binds HDAC2 and a new co-repressor, DMAP1, to form a complex at replication foci. *Nat Genet* **25**: 269-277.

Saint-Martin C, Leroy G, Delhommeau F, Panelatti G, Dupont S, James C, Plo I, Bordessoule D, Chomienne C, Delannoy A et al. 2009. Analysis of the ten-eleven translocation 2 (TET2) gene in familial myeloproliferative neoplasms. *Blood* **114**: 1628-1632.

Santos-Reboucas CB, Pimentel MM. 2007. Implication of abnormal epigenetic patterns for human diseases. *European journal of human genetics : EJHG* **15**: 10-17.

Schermelleh L, Haemmer A, Spada F, Rosing N, Meilinger D, Rothbauer U, Cardoso MC, Leonhardt H. 2007. Dynamics of Dnmt1 interaction with the replication machinery and its role in postreplicative maintenance of DNA methylation. *Nucleic acids research* **35**: 4301-4312.

Schermelleh L, Spada F, Easwaran HP, Zolghadr K, Margot JB, Cardoso MC, Leonhardt H. 2005. Trapped in action: direct visualization of DNA methyltransferase activity in living cells. *Nat Methods* **2**: 751-756.

Schiesser S, Hackner B, Pfaffeneder T, Muller M, Hagemeier C, Truss M, Carell T. 2012. Mechanism and stem-cell activity of 5-carboxycytosine decarboxylation determined by isotope tracing. *Angewandte Chemie* **51**: 6516-6520.

Schindelin J, Arganda-Carreras I, Frise E, Kaynig V, Longair M, Pietzsch T, Preibisch S, Rueden C, Saalfeld S, Schmid B et al. 2012. Fiji: an open-source platform for biological-image analysis. *Nat Methods* **9**: 676-682.

Schneider CA, Rasband WS, Eliceiri KW. 2012. NIH Image to ImageJ: 25 years of image analysis. *Nat Methods* **9**: 671-675.

Schneider K, Fuchs C, Dobay A, Rottach A, Qin W, Wolf P, Alvarez-Castro JM, Nalaskowski MM, Kremmer E, Schmid V et al. 2013. Dissection of cell cycle-dependent dynamics of Dnmt1 by FRAP and diffusion-coupled modeling. *Nucleic acids research* **41**: 4860-4876.

Schotta G, Lachner M, Sarma K, Ebert A, Sengupta R, Reuter G, Reinberg D, Jenuwein T. 2004. A silencing pathway to induce H3-K9 and H4-K20 trimethylation at constitutive heterochromatin. *Genes & development* **18**: 1251-1262.

Schultz DC, Ayyanathan K, Negorev D, Maul GG, Rauscher FJ, 3rd. 2002. SETDB1: a novel KAP-1-associated histone H3, lysine 9-specific methyltransferase that contributes to HP1-mediated silencing of euchromatic genes by KRAB zinc-finger proteins. *Genes & development* **16**: 919-932.

Schultz DC, Letunic. 1998, 2012. http://smart.embl.de/smart/do_annotation.pl?DOMAIN=UIM. , Proc. Natl. Acad. Sci. USA Nucleic Acids Res.

Seisenberger S, Peat JR, Reik W. 2013. Conceptual links between DNA methylation reprogramming in the early embryo and primordial germ cells. *Current opinion in cell biology* **25**: 281-288.

Shah ZH, Jones DR, Sommer L, Foulger R, Bultsma Y, D'Santos C, Divecha N. 2013. Nuclear phosphoinositides and their impact on nuclear functions. *FEBS J* **280**: 6295-6310.

Shamma A, Suzuki M, Hayashi N, Kobayashi M, Sasaki N, Nishiuchi T, Doki Y, Okamoto T, Kohno S, Muranaka H et al. 2013. ATM mediates pRB function to control DNMT1 protein stability and DNA methylation. *Molecular and cellular biology* **33**: 3113-3124.

Sharif J, Muto M, Takebayashi S, Suetake I, Iwamatsu A, Endo TA, Shinga J, Mizutani-Koseki Y, Toyoda T, Okamura K et al. 2007. The SRA protein Np95 mediates epigenetic inheritance by recruiting Dnmt1 to methylated DNA. *Nature* **450**: 908-912.

Shearstone JR, Pop R, Bock C, Boyle P, Meissner A, Socolovsky M. 2011. Global DNA demethylation during mouse erythropoiesis in vivo. *Science* **334**: 799-802.

Sheikh MA, Malik YS, Yu H, Lai M, Wang X, Zhu X. 2013. Epigenetic regulation of Dpp6 expression by Dnmt3b and its novel role in the inhibition of RA induced neuronal differentiation of P19 cells. *PLoS One* **8**: e55826.

Shekarabi M, Girard N, Riviere JB, Dion P, Houle M, Toulouse A, Lafreniere RG, Vercauteran F, Hince P, Laganiere J et al. 2008. Mutations in the nervous system-specific HSN2 exon of WNK1 cause hereditary sensory neuropathy type II. *The Journal of clinical investigation* **118**: 2496-2505.

Shirane K, Toh H, Kobayashi H, Miura F, Chiba H, Ito T, Kono T, Sasaki H. 2013. Mouse oocyte methylomes at base resolution reveal genome-wide accumulation of non-CpG methylation and role of DNA methyltransferases. *PLoS genetics* **9**: e1003439.

Shogren-Knaak M, Ishii H, Sun JM, Pazin MJ, Davie JR, Peterson CL. 2006. Histone H4-K16 acetylation controls chromatin structure and protein interactions. *Science* **311**: 844-847.

Silva J, Mak W, Zvetkova I, Appanah R, Nesterova TB, Webster Z, Peters AH, Jenuwein T, Otte AP, Brockdorff N. 2003. Establishment of histone h3 methylation on the inactive X chromosome requires transient recruitment of Eed-Enx1 polycomb group complexes. *Developmental cell* **4**: 481-495.

Sims RJ, 3rd, Reinberg D. 2008. Is there a code embedded in proteins that is based on post-translational modifications? *Nature reviews Molecular cell biology* **9**: 815-820.

Slaugenhoupt SA, Blumenfeld A, Gill SP, Leyne M, Mull J, Cuajungco MP, Liebert CB, Chadwick B, Idelson M, Reznik L et al. 2001. Tissue-specific expression of a splicing mutation in the IKBKAP gene causes familial dysautonomia. *American journal of human genetics* **68**: 598-605.

Smith ZD, Meissner A. 2013. DNA methylation: roles in mammalian development. *Nature reviews Genetics* **14**: 204-220.

Song CX, Szulwach KE, Fu Y, Dai Q, Yi C, Li X, Li Y, Chen CH, Zhang W, Jian X et al. 2011a. Selective chemical labeling reveals the genome-wide distribution of 5-hydroxymethylcytosine. *Nature biotechnology* **29**: 68-72.

Song J, Rechko O, Bestor TH, Patel DJ. 2011b. Structure of DNMT1-DNA complex reveals a role for autoinhibition in maintenance DNA methylation. *Science* **331**: 1036-1040.

Southall SM, Cronin NB, Wilson JR. 2014. A novel route to product specificity in the Suv4-20 family of histone H4K20 methyltransferases. *Nucleic acids research* **42**: 661-671.

Southall SM, Wong PS, Odozo Z, Roe SM, Wilson JR. 2009. Structural basis for the requirement of additional factors for MLL1 SET domain activity and recognition of epigenetic marks. *Molecular cell* **33**: 181-191.

Spada F, Haemmer A, Kuch D, Rothbauer U, Schermelleh L, Kremmer E, Carell T, Langst G, Leonhardt H. 2007. DNMT1 but not its interaction with the replication machinery is required for maintenance of DNA methylation in human cells. *The Journal of cell biology* **176**: 565-571.

Sporbert A, Domaing P, Leonhardt H, Cardoso MC. 2005. PCNA acts as a stationary loading platform for transiently interacting Okazaki fragment maturation proteins. *Nucleic acids research* **33**: 3521-3528.

Sproul D, Meehan RR. 2013. Genomic insights into cancer-associated aberrant CpG island hypermethylation. *Briefings in functional genomics* **12**: 174-190.

Spruijt CG, Gnerlich F, Smits AH, Pfaffeneder T, Jansen PW, Bauer C, Munzel M, Wagner M, Muller M, Khan F et al. 2013. Dynamic readers for 5-(hydroxy)methylcytosine and its oxidized derivatives. *Cell* **152**: 1146-1159.

Squazzo SL, O'Geen H, Komashko VM, Krig SR, Jin VX, Jang SW, Margueron R, Reinberg D, Green R, Farnham PJ. 2006. Suz12 binds to silenced regions of the genome in a cell-type-specific manner. *Genome research* **16**: 890-900.

Stachulski AV, Pidathala C, Row EC, Sharma R, Berry NG, Iqbal M, Bentley J, Allman SA, Edwards G, Helm A et al. 2011. Thiazolidines as novel antiviral agents. 1. Inhibition of hepatitis B virus replication. *Journal of medicinal chemistry* **54**: 4119-4132.

Stern DE, Berger SL. 2000. Acetylation of histones and transcription-related factors. *Microbiology and molecular biology reviews : MMBR* **64**: 435-459.

Stock JK, Giadrossi S, Casanova M, Brookes E, Vidal M, Koseki H, Brockdorff N, Fisher AG, Pombo A. 2007. Ring1-mediated ubiquitination of H2A restrains poised RNA polymerase II at bivalent genes in mouse ES cells. *Nature cell biology* **9**: 1428-1435.

Strahl BD, Allis CD. 2000. The language of covalent histone modifications. *Nature* **403**: 41-45.

Suetake I, Shinozaki F, Miyagawa J, Takeshima H, Tajima S. 2004. DNMT3L stimulates the DNA methylation activity of Dnmt3a and Dnmt3b through a direct interaction. *The Journal of biological chemistry* **279**: 27816-27823.

Sun L, Zhao H, Xu Z, Liu Q, Liang Y, Wang L, Cai X, Zhang L, Hu L, Wang G et al. 2007. Phosphatidylinositol 3-kinase/protein kinase B pathway stabilizes DNA methyltransferase I protein and maintains DNA methylation. *Cellular signalling* **19**: 2255-2263.

Syeda F, Fagan RL, Wean M, Avvakumov GV, Walker JR, Xue S, Dhe-Paganon S, Brenner C. 2011. The replication focus targeting sequence (RFTS) domain is a DNA-competitive inhibitor of Dnmt1. *The Journal of biological chemistry* **286**: 15344-15351.

Szulwach KE, Li X, Li Y, Song CX, Wu H, Dai Q, Irler H, Upadhyay AK, Gearing M, Levey AI et al. 2011. 5-hmC-mediated epigenetic dynamics during postnatal neurodevelopment and aging. *Nature neuroscience* **14**: 1607-1616.

Szwagierczak A, Bultmann S, Schmidt CS, Spada F, Leonhardt H. 2010. Sensitive enzymatic quantification of 5-hydroxymethylcytosine in genomic DNA. *Nucleic acids research* **38**: e181.

Tachibana M, Sugimoto K, Fukushima T, Shinkai Y. 2001. Set domain-containing protein, G9a, is a novel lysine-preferring mammalian histone methyltransferase with hyperactivity and specific selectivity to lysines 9 and 27 of histone H3. *The Journal of biological chemistry* **276**: 25309-25317.

Tachibana M, Sugimoto K, Nozaki M, Ueda J, Ohta T, Ohki M, Fukuda M, Takeda N, Niida H, Kato H et al. 2002. G9a histone methyltransferase plays a dominant role in euchromatic histone H3 lysine 9 methylation and is essential for early embryogenesis. *Genes & development* **16**: 1779-1791.

Tagarro I, Fernandez-Peralta AM, Gonzalez-Aguilera JJ. 1994. Chromosomal localization of human satellites 2 and 3 by a FISH method using oligonucleotides as probes. *Human genetics* **93**: 383-388.

Tahiliani M, Koh KP, Shen Y, Pastor WA, Bandukwala H, Brudno Y, Agarwal S, Iyer LM, Liu DR, Aravind L et al. 2009. Conversion of 5-methylcytosine to 5-hydroxymethylcytosine in mammalian DNA by MLL partner TET1. *Science* **324**: 930-935.

Takagi M, Ozawa T, Hara K, Naruse S, Ishihara T, Shimbo J, Igarashi S, Tanaka K, Onodera O, Nishizawa M. 2006. New HSN2 mutation in Japanese patient with hereditary sensory and autonomic neuropathy type 2. *Neurology* **66**: 1251-1252.

Takeshima H, Suetake I, Tajima S. 2008. Mouse Dnmt3a preferentially methylates linker DNA and is inhibited by histone H1. *Journal of molecular biology* **383**: 810-821.

Takeshita K, Suetake I, Yamashita E, Suga M, Narita H, Nakagawa A, Tajima S. 2011. Structural insight into maintenance methylation by mouse DNA methyltransferase 1 (Dnmt1). *Proc Natl Acad Sci U S A* **108**: 9055-9059.

Taverna SD, Li H, Ruthenburg AJ, Allis CD, Patel DJ. 2007. How chromatin-binding modules interpret histone modifications: lessons from professional pocket pickers. *Nat Struct Mol Biol* **14**: 1025-1040.

Tawa R, Ono T, Kurishita A, Okada S, Hirose S. 1990. Changes of DNA methylation level during pre- and postnatal periods in mice. *Differentiation; research in biological diversity* **45**: 44-48.

Tefferi A, Lim KH, Abdel-Wahab O, Lasho TL, Patel J, Patnaik MM, Hanson CA, Pardanani A, Gilliland DG, Levine RL. 2009. Detection of mutant TET2 in myeloid malignancies other than myeloproliferative neoplasms: CMML, MDS, MDS/MPN and AML. *Leukemia* **23**: 1343-1345.

Thoma F, Koller T, Klug A. 1979. Involvement of histone H1 in the organization of the nucleosome and of the salt-dependent superstructures of chromatin. *The Journal of cell biology* **83**: 403-427.

Thomas CE, Kelleher NL, Mizzen CA. 2006. Mass spectrometric characterization of human histone H3: a bird's eye view. *Journal of proteome research* **5**: 240-247.

Trasler JM, Trasler DG, Bestor TH, Li E, Ghibu F. 1996. DNA methyltransferase in normal and Dnmt/Dnmt mouse embryos. *Developmental dynamics : an official publication of the American Association of Anatomists* **206**: 239-247.

Tsumura A, Hayakawa T, Kumaki Y, Takebayashi S, Sakaue M, Matsuoka C, Shimotohno K, Ishikawa F, Li E, Ueda HR et al. 2006. Maintenance of self-renewal ability of mouse embryonic stem cells in the absence of DNA methyltransferases Dnmt1, Dnmt3a and Dnmt3b. *Genes to cells : devoted to molecular & cellular mechanisms* **11**: 805-814.

Tucker KL, Beard C, Dausmann J, Jackson-Grusby L, Laird PW, Lei H, Li E, Jaenisch R. 1996. Germ-line passage is required for establishment of methylation and expression patterns of imprinted but not of nonimprinted genes. *Genes & development* **10**: 1008-1020.

Uemura T, Kubo E, Kanari Y, Ikemura T, Tatsumi K, Muto M. 2000. Temporal and spatial localization of novel nuclear protein NP95 in mitotic and meiotic cells. *Cell structure and function* **25**: 149-159.

Unoki M, Nishidate T, Nakamura Y. 2004. ICBP90, an E2F-1 target, recruits HDAC1 and binds to methyl-CpG through its SRA domain. *Oncogene* **23**: 7601-7610.

Urdinguio RG, Sanchez-Mut JV, Esteller M. 2009. Epigenetic mechanisms in neurological diseases: genes, syndromes, and therapies. *Lancet neurology* **8**: 1056-1072.

Valinluck V, Tsai HH, Rogstad DK, Burdzy A, Bird A, Sowers LC. 2004. Oxidative damage to methyl-CpG sequences inhibits the binding of the methyl-CpG binding domain (MBD) of methyl-CpG binding protein 2 (MeCP2). *Nucleic acids research* **32**: 4100-4108.

Vaquero A, Loyola A, Reinberg D. 2003. The constantly changing face of chromatin. *Science of aging knowledge environment : SAGE KE* **2003**: RE4.

Vaquero A, Sternglanz R, Reinberg D. 2007. NAD⁺-dependent deacetylation of H4 lysine 16 by class III HDACs. *Oncogene* **26**: 5505-5520.

Veldic M, Caruncho HJ, Liu WS, Davis J, Satta R, Grayson DR, Guidotti A, Costa E. 2004. DNA-methyltransferase 1 mRNA is selectively overexpressed in telencephalic GABAergic interneurons of schizophrenia brains. *Proc Natl Acad Sci U S A* **101**: 348-353.

Vermeulen M, Mulder KW, Denissov S, Pijnappel WW, van Schaik FM, Varier RA, Baltissen MP, Stunnenberg HG, Mann M, Timmers HT. 2007. Selective anchoring of TFIID to nucleosomes by trimethylation of histone H3 lysine 4. *Cell* **131**: 58-69.

Vire E, Brenner C, Deplus R, Blanchon L, Fraga M, Didelot C, Morey L, Van Eynde A, Bernard D, Vanderwinden JM et al. 2006. The Polycomb group protein EZH2 directly controls DNA methylation. *Nature* **439**: 871-874.

Wagner EJ, Carpenter PB. 2012. Understanding the language of Lys36 methylation at histone H3. *Nature reviews Molecular cell biology* **13**: 115-126.

Walsh CP, Chaillet JR, Bestor TH. 1998. Transcription of IAP endogenous retroviruses is constrained by cytosine methylation. *Nat Genet* **20**: 116-117.

Wang C, Shen J, Yang Z, Chen P, Zhao B, Hu W, Lan W, Tong X, Wu H, Li G et al. 2011. Structural basis for site-specific reading of unmodified R2 of histone H3 tail by UHRF1 PHD finger. *Cell research* **21**: 1379-1382.

Wang F, Zhang P, Ma Y, Yang J, Moyer MP, Shi C, Peng J, Qin H. 2012. NIRF is frequently upregulated in colorectal cancer and its oncogenicity can be suppressed by let-7a microRNA. *Cancer letters* **314**: 223-231.

Wang H, An W, Cao R, Xia L, Erdjument-Bromage H, Chatton B, Tempst P, Roeder RG, Zhang Y. 2003. mAM facilitates conversion by ESET of dimethyl to trimethyl lysine 9 of histone H3 to cause transcriptional repression. *Molecular cell* **12**: 475-487.

Wang H, Cao R, Xia L, Erdjument-Bromage H, Borchers C, Tempst P, Zhang Y. 2001. Purification and functional characterization of a histone H3-lysine 4-specific methyltransferase. *Molecular cell* **8**: 1207-1217.

Wang H, Wang L, Erdjument-Bromage H, Vidal M, Tempst P, Jones RS, Zhang Y. 2004. Role of histone H2A ubiquitination in Polycomb silencing. *Nature* **431**: 873-878.

Wang J, Hevi S, Kurash JK, Lei H, Gay F, Bajko J, Su H, Sun W, Chang H, Xu G et al. 2009. The lysine demethylase LSD1 (KDM1) is required for maintenance of global DNA methylation. *Nat Genet* **41**: 125-129.

Wang Q, Young P, Walters KJ. 2005. Structure of S5a bound to monoubiquitin provides a model for polyubiquitin recognition. *Journal of molecular biology* **348**: 727-739.

Wang Z, Zang C, Rosenfeld JA, Schones DE, Barski A, Cuddapah S, Cui K, Roh TY, Peng W, Zhang MQ et al. 2008. Combinatorial patterns of histone acetylations and methylations in the human genome. *Nat Genet* **40**: 897-903.

Watanabe D, Suetake I, Tada T, Tajima S. 2002. Stage- and cell-specific expression of Dnmt3a and Dnmt3b during embryogenesis. *Mechanisms of development* **118**: 187-190.

Watanabe D, Suetake I, Tajima S, Hanaoka K. 2004. Expression of Dnmt3b in mouse hematopoietic progenitor cells and spermatogonia at specific stages. *Gene expression patterns : GEP* **5**: 43-49.

Watanabe D, Uchiyama K, Hanaoka K. 2006. Transition of mouse de novo methyltransferases expression from Dnmt3b to Dnmt3a during neural progenitor cell development. *Neuroscience* **142**: 727-737.

Weaver IC. 2007. Epigenetic programming by maternal behavior and pharmacological intervention. Nature versus nurture: let's call the whole thing off. *Epigenetics : official journal of the DNA Methylation Society* **2**: 22-28.

Weaver IC, Cervoni N, Champagne FA, D'Alessio AC, Sharma S, Seckl JR, Dymov S, Szyf M, Meaney MJ. 2004. Epigenetic programming by maternal behavior. *Nature neuroscience* **7**: 847-854.

Wei Y, Yu L, Bowen J, Gorovsky MA, Allis CD. 1999. Phosphorylation of histone H3 is required for proper chromosome condensation and segregation. *Cell* **97**: 99-109.

Wen L, Li X, Yan L, Tan Y, Li R, Zhao Y, Wang Y, Xie J, Zhang Y, Song C et al. 2014. Whole-genome analysis of 5-hydroxymethylcytosine and 5-methylcytosine at base resolution in the human brain. *Genome biology* **15**: R49.

Winkelmann J, Lin L, Schormair B, Kornum BR, Faraco J, Plazzi G, Melberg A, Cornelio F, Urban AE, Pizza F et al. 2012. Mutations in DNMT1 cause autosomal dominant cerebellar ataxia, deafness and narcolepsy. *Hum Mol Genet* **21**: 2205-2210.

Woodcock CL, Ghosh RP. 2010. Chromatin higher-order structure and dynamics. *Cold Spring Harbor perspectives in biology* **2**: a000596.

Woodfine K, Fiegler H, Beare DM, Collins JE, McCann OT, Young BD, Debernardi S, Mott R, Dunham I, Carter NP. 2004. Replication timing of the human genome. *Hum Mol Genet* **13**: 191-202.

Wossidlo M, Nakamura T, Lepikhov K, Marques CJ, Zakhartchenko V, Boiani M, Arand J, Nakano T, Reik W, Walter J. 2011. 5-Hydroxymethylcytosine in the mammalian zygote is linked with epigenetic reprogramming. *Nature communications* **2**: 241.

Wu H, Coskun V, Tao J, Xie W, Ge W, Yoshikawa K, Li E, Zhang Y, Sun YE. 2010. Dnmt3a-dependent nonpromoter DNA methylation facilitates transcription of neurogenic genes. *Science* **329**: 444-448.

Wu H, D'Alessio AC, Ito S, Wang Z, Cui K, Zhao K, Sun YE, Zhang Y. 2011a. Genome-wide analysis of 5-hydroxymethylcytosine distribution reveals its dual function in transcriptional regulation in mouse embryonic stem cells. *Genes & development* **25**: 679-684.

Wu H, D'Alessio AC, Ito S, Xia K, Wang Z, Cui K, Zhao K, Sun YE, Zhang Y. 2011b. Dual functions of Tet1 in transcriptional regulation in mouse embryonic stem cells. *Nature* **473**: 389-393.

Wu H, Siarheyeva A, Zeng H, Lam R, Dong A, Wu XH, Li Y, Schapira M, Vedadi M, Min J. 2013. Crystal structures of the human histone H4K20 methyltransferases SUV420H1 and SUV420H2. *FEBS letters* **587**: 3859-3868.

Wu H, Zhang Y. 2014. Reversing DNA methylation: mechanisms, genomics, and biological functions. *Cell* **156**: 45-68.

Wu J, Liu S, Liu G, Dombkowski A, Abrams J, Martin-Trevino R, Wicha MS, Ethier SP, Yang ZQ. 2012a. Identification and functional analysis of 9p24 amplified genes in human breast cancer. *Oncogene* **31**: 333-341.

Wu JC, Santi DV. 1987. Kinetic and catalytic mechanism of Hhal methyltransferase. *The Journal of biological chemistry* **262**: 4778-4786.

Wu SC, Zhang Y. 2010. Active DNA demethylation: many roads lead to Rome. *Nature reviews Molecular cell biology* **11**: 607-620.

Wu TF, Zhang W, Su ZP, Chen SS, Chen GL, Wei YX, Sun T, Xie XS, Li B, Zhou YX et al. 2012b. UHRF2 mRNA expression is low in malignant glioma but silencing inhibits the growth of U251 glioma cells in vitro. *Asian Pacific journal of cancer prevention : APJCP* **13**: 5137-5142.

Wu Z, Huang K, Yu J, Le T, Namihira M, Liu Y, Zhang J, Xue Z, Cheng L, Fan G. 2012c. Dnmt3a regulates both proliferation and differentiation of mouse neural stem cells. *Journal of neuroscience research* **90**: 1883-1891.

Wutz A. 2011. Gene silencing in X-chromosome inactivation: advances in understanding facultative heterochromatin formation. *Nature reviews Genetics* **12**: 542-553.

Xiao B, Jing C, Kelly G, Walker PA, Muskett FW, Frenkel TA, Martin SR, Sarma K, Reinberg D, Gamblin SJ et al. 2005. Specificity and mechanism of the histone methyltransferase Pr-Set7. *Genes & development* **19**: 1444-1454.

Xiao B, Jing C, Wilson JR, Walker PA, Vasisht N, Kelly G, Howell S, Taylor IA, Blackburn GM, Gamblin SJ. 2003. Structure and catalytic mechanism of the human histone methyltransferase SET7/9. *Nature* **421**: 652-656.

Xie S, Jakoncic J, Qian C. 2012a. UHRF1 double tudor domain and the adjacent PHD finger act together to recognize K9me3-containing histone H3 tail. *Journal of molecular biology* **415**: 318-328.

Xie W, Barr CL, Kim A, Yue F, Lee AY, Eubanks J, Dempster EL, Ren B. 2012b. Base-resolution analyses of sequence and parent-of-origin dependent DNA methylation in the mouse genome. *Cell* **148**: 816-831.

Xu GL, Bestor TH, Bourc'his D, Hsieh CL, Tommerup N, Bugge M, Hulten M, Qu X, Russo JJ, Viegas-Pequignot E. 1999. Chromosome instability and immunodeficiency syndrome caused by mutations in a DNA methyltransferase gene. *Nature* **402**: 187-191.

Yamaguchi S, Hong K, Liu R, Shen L, Inoue A, Diep D, Zhang K, Zhang Y. 2012. Tet1 controls meiosis by regulating meiotic gene expression. *Nature* **492**: 443-447.

Yamaguchi S, Shen L, Liu Y, Sendler D, Zhang Y. 2013. Role of Tet1 in erasure of genomic imprinting. *Nature* **504**: 460-464.

Yang H, Pesavento JJ, Starnes TW, Cryderman DE, Wallrath LL, Kelleher NL, Mizzen CA. 2008. Preferential dimethylation of histone H4 lysine 20 by Suv4-20. *The Journal of biological chemistry* **283**: 12085-12092.

Yao B, Jin P. 2014. Unlocking epigenetic codes in neurogenesis. *Genes & development* **28**: 1253-1271.

Yates PA, Burman RW, Mummaneni P, Krussel S, Turker MS. 1999. Tandem B1 elements located in a mouse methylation center provide a target for de novo DNA methylation. *The Journal of biological chemistry* **274**: 36357-36361.

Ying QL, Wray J, Nichols J, Batlle-Morera L, Doble B, Woodgett J, Cohen P, Smith A. 2008. The ground state of embryonic stem cell self-renewal. *Nature* **453**: 519-523.

Yokota S, Yanagi H, Yura T, Kubota H. 2001. Cytosolic chaperonin-containing t-complex polypeptide 1 changes the content of a particular subunit species concomitant with substrate binding and folding activities during the cell cycle. *European journal of biochemistry / FEBS* **268**: 4664-4673.

Young P, Deveraux Q, Beal RE, Pickart CM, Rechsteiner M. 1998. Characterization of two polyubiquitin binding sites in the 26 S protease subunit 5a. *The Journal of biological chemistry* **273**: 5461-5467.

Yu NK, Baek SH, Kaang BK. 2011. DNA methylation-mediated control of learning and memory. *Molecular brain* **4**: 5.

Yu Y, Song C, Zhang Q, DiMaggio PA, Garcia BA, York A, Carey MF, Grunstein M. 2012. Histone H3 lysine 56 methylation regulates DNA replication through its interaction with PCNA. *Molecular cell* **46**: 7-17.

Yuan CC, Matthews AG, Jin Y, Chen CF, Chapman BA, Ohsumi TK, Glass KC, Kutateladze TG, Borowsky ML, Struhl K et al. 2012. Histone H3R2 symmetric dimethylation and histone H3K4 trimethylation are tightly correlated in eukaryotic genomes. *Cell reports* **1**: 83-90.

Yuan J, Higuchi Y, Nagado T, Nozuma S, Nakamura T, Matsuura E, Hashiguchi A, Sakiyama Y, Yoshimura A, Takashima H. 2013. Novel mutation in the replication focus targeting sequence domain of DNMT1 causes hereditary sensory and autonomic neuropathy IE. *Journal of the peripheral nervous system : JPNS* **18**: 89-93.

Zhang JH, Chung TD, Oldenburg KR. 1999. A Simple Statistical Parameter for Use in Evaluation and Validation of High Throughput Screening Assays. *Journal of biomolecular screening* **4**: 67-73.

Zhang RR, Cui QY, Murai K, Lim YC, Smith ZD, Jin S, Ye P, Rosa L, Lee YK, Wu HP et al. 2013. Tet1 regulates adult hippocampal neurogenesis and cognition. *Cell Stem Cell* **13**: 237-245.

Zhang Y. 2003. Transcriptional regulation by histone ubiquitination and deubiquitination. *Genes & development* **17**: 2733-2740.

Zhang Y, Liu S, Mickanin C, Feng Y, Charlat O, Michaud GA, Schirle M, Shi X, Hild M, Bauer A et al. 2011. RNF146 is a poly(ADP-ribose)-directed E3 ligase that regulates axin degradation and Wnt signalling. *Nature cell biology* **13**: 623-629.

Zhu PP, Patterson A, Lavoie B, Stadler J, Shoeb M, Patel R, Blackstone C. 2003. Cellular localization, oligomerization, and membrane association of the hereditary spastic paraplegia 3A (SPG3A) protein atlastin. *The Journal of biological chemistry* **278**: 49063-49071.

Zolghadr K, Mortusewicz O, Rothbauer U, Kleinhans R, Goehler H, Wanker EE, Cardoso MC, Leonhardt H. 2008. A fluorescent two-hybrid assay for direct visualization of protein interactions in living cells. *Molecular & cellular proteomics : MCP* **7**: 2279-2287.

<http://biogps.org>.

4.2 Abbreviations

Abbreviation	Meaning
Δ	deletion
53BP1	p53 binding protein 1
5-aza-dC	5-aza-deoxycytidine
5caC	5-carboxycytosine
5fC	5-formylcytosine
5hmC	5-hydroxymethylcytosine
5mC	5-methylcytosine
ac	acetylated
ADCA-DN	autosomal dominant cerebellar ataxia, deafness and narcolepsy
ADD	ATRX–DNMT3–DNMT3L
ADP	adenosine diphosphate
AID	activation-induced deaminase
aIPC	astrocyte intermediate progenitor cell
AML	acute myeloid leukemia
AOTF	acousto-optical tunable filter
APC	anaphase promoting complex
APOBEC	apolipoprotein B mRNA-editing enzyme complex
<i>App</i>	<i>amyloid precursor protein</i>
ar	ADP ribosylated
ASH1L	Absent, small and homeotic discs 1-like
ATL3	<i>Atlastin 3</i>
ATM	ataxia telangiectasia mutated
BAH1/2	bromo-adjacent homology 1/2
<i>BDNF</i>	<i>brain derived neurotrophic factor</i>
BER	base excision repair
BiFC	bimolecular fluorescence complementation
CBP	CREB binding protein
CDK2	cyclin-dependent kinase 2
CF	cerebrospinal fluid
Ch	cherry
CIPA	congenital insensitivity to pain with anhidrosis
CNS	central nervous system
CTD	carboxy-terminal domain
CXXC	zinc finger
DG	dentate gyrus
<i>Dlx2</i>	<i>Distal-less homeobox 2</i>
DMAP1	DNA methyltransferase associated protein 1
DNMT1/2/3A/3B/3L	DNA methyltransferase 1/2/3A/3B/3L
DNMT1o	oocyte-specific isoform of DNMT1
ELP3	Elongator complex 3
ELSA	enzyme-linked immunosorbent assay

Abbreviation	Meaning
ESC	embryonic stem cell
EZH2	enhancer of zeste homolog 2
F3H	fluorescence three hybrid assay
FACS	fluorescence activated cell sorting
<i>Fgf1B</i>	<i>fibroblast growth factor 1</i>
<i>FMR1</i>	<i>fragile X mental retardation-1</i>
FRET	fluorescence resonance energy transfer
<i>FXN</i>	<i>frataxin</i>
GADD45B	growth arrest and DNA damage-inducible protein 45B
GCN5	general control nonderepressible 5
GCNF	germ cell nuclear receptor
GFP	green fluorescent protein
HAT	histone acetyltransferase
HAUSP	herpes virus associated ubiquitin-specific protease
HDAC	histone deacetylase
hiPSC	induced pluripotent stem cell
HMN	hereditary motor neuropathy
HMSN	hereditary motor and sensory neuropathy
HMT	histone methyltransferase
HP1	heterochromatin binding protein 1
HRS	hepatocyte growth factor regulated tyrosine kinase substrate
HSAN	hereditary sensory and autonomic neuropathy
<i>HSP</i>	<i>hereditary spastic paraplegia</i>
IAP	intracisternal A particle
ICBP90	inverted CCAAT binding protein of 90 kDa
ICF	Immunodeficiency, Centromeric region instability, Facial anomalies
IDM1	increased DNA methylation 1
JAK	januskinase
KG	lysine-glycine
<i>KIF-1A</i>	<i>kinesin family member 1A</i>
LINE	long interspersed nuclear elements
LSD1	lysine-specific demethylase 1A
LTRs	long terminal repeats
M phase	mitosis phase
MBD	methyl-CpG binding domain
MBP	5mC binding protein
MDS	myelodysplastic syndrome
me1	monomethylated
me2	dimethylated
me2a	assymmetrically dimethylated
me2s	symmetrically dimethylated
me3	trimethylated
MEF	mouse embryonic fibroblast

Abbreviation	Meaning
M _f	mobile fraction
ml	myoinositol
MPD	myeloproliferative disorder
MRI	magnetic resonance imaging
MSLT	multiple sleep latency test
nIPCs	neuronal intermediate progenitor cells
nIPCs	neuronal intermediate progenitor cell
NIRF	Np95/ICBP90-like RING finger
NLS	nuclear localization signal
NP95/97	Nuclear protein of 95/97 kDa
NPC	neuronal progenitor cell
NSC	neuronal stem cell
NSD1/2/3	nuclear receptor SET domain-containing 1/2/3
NTD	N-terminal domain
N-terminal	Amino-terminal
<i>oct4</i>	<i>octamer binding transcription factor 4</i>
oIPC	oligodendrocyte intermediate progenitor cell
PARP1	poly(ADP-ribose) polymerase 1
PARylation	poly(ADP-)ribosylation
PBD	PCNA binding domain
PBR	polybasic region
PCAF	p300/CBP-associated factor
PCNA	proliferating cell nuclear antigen
PCNP	PEST-containing nuclear protein
pdb	protein database
PGC	primordial germ cell
ph	phosphorylated
PH	pericentromeric heterochromatin
PHD	plant homeodomain
PI5P	phosphatidylinositol 5-phosphate
PNS	peripheral nervous system
pRB	retinoblastoma protein
PRC2	polycomb group repressor complex 2
PRMT6	protein arginine methyltransferase 6
<i>Ps1</i>	<i>presenilin 1</i>
PTM	Post translational modification
PWWP	proline-tryptophan-tryptophan-proline
RARE	RA receptor element
REM	rapid eye movement
RFP	red fluorescent protein
RGC	radial glial cell
RING	really interesting new gene
ROS1	repressor of silencing 1

Abbreviation	Meaning
RSWA	REM sleep without atonia
S phase	synthesis phase
SAM	S-Adenosyl-L-Methionine
SETD1A/1B/3	SET domain containing 1A/1B/3
SETDB1	SET domain, bifurcated 1
SETMAR	SET domain and mariner transposase fusion gene-containing
SGZ	subgranular zone
SINE	short interspersed nuclear element
<i>SMN1</i>	<i>survival of motor neuron 1</i>
SMYD2	SET and MYND domain-containing 2
SOMREMP	sleep-onset rapid eye movement period
SRA	SET and RING-associated
STAT	Signal Transducers and Activators of Transcription
su	sumoylated
SUV39H1/H2	suppressor of variegation 3-9 homolog 1 and 2
SUV4-20H1/2	suppressor of variegation 4-20 homolog 1/2
SVZ	subventricular zone
TDG	thymine DNA glycosylase
TET	ten eleven translocation
TIP60	Tat interacting protein of 60 kDa
TKO	triple knockout
<i>TNFα</i>	<i>tumor necrosis factor alpha</i>
TS	targeting sequence
TSA	Trichostatin A
TSS	transcriptional start site
TTD	tandem Tudor domain
ub	ubiquitinated
Ubl	ubiquitin-like
UHRF1	ubiquitin-like, containing PHD and RING finger domains 1
UIM	ubiquitin interacting motif
USP7	ubiquitin-specific processing protease 7
VZ	ventricular zone
WNK1	with-no-lysine(K)-1

4.3 List of genes and corresponding proteins associated with HSAN-I to V.

Genes and corresponding proteins are listed according to the HSAN type and the mode of inheritance with information about the expression pattern and biological functions. HSAN: hereditary sensory and autonomic neuropathy; ADCA-DN: autosomal dominant cerebellar ataxia, deafness and narcolepsy.

Gene name	Mutation	Type of HSAN	Inheritance	Protein name	Expression	Biological function
<i>SPTLC1</i>	Missense mutations	HSAN-I	Autosomal dominant	SPT1: Serine palmitoyltransferase subunit 1	Cells of immune system, brain	Catalysis of first step in <i>de novo</i> biosynthesis of sphingolipids (Hanada 2003)
<i>SPTLC2</i>	Missense mutations			SPT2: Serine palmitoyltransferase subunit 2	Cells of immune system	
<i>RAB7A</i>	Missense mutations	CMT2B: Charcot–Marie–Tooth disease type 2B		RAB7A: Ras-related protein RAB7A	Ubiquitously	Small RAB GTPase, formation and transport of intracellular vesicle; tethering and fusion of endosomal membranes (Hutagalung and Novick 2011)
<i>ATL1</i>	Missense mutations	HSAN-I, hereditary spastic paraparesis (HSP)	Autosomal dominant	ATLA1: Atlastin-1	Brain, hippocampus, pyramidal neurons (Zhu et al. 2003)	GTPase activity; role in intracellular membrane trafficking at the endoplasmic reticulum-to-Golgi interface (Zhu et al. 2003; Namekawa et al. 2007)
<i>ATL3</i>	Missense mutations	HSAN-I		ATLA3: Atlastin-3	CNS (Fischer et al. 2014)	endoplasmic reticulum-shaping GTPase, facilitates connection of ER tubules to networks by homotypic membrane fusion (Kornak et al. 2014)
<i>DNMT1</i>	Missense mutations	HSAN-I with subtype HSAN-IE and ADCA-DN		DNMT1: DNA methyltransferase 1	Ubiquitously, postmitotic neurons of adult CNS (Tawa et al. 1990), immune cells	Maintenance DNA methyltransferase; propagation of DNA methylation during after replication and repair (Bird 2002)
<i>WNK1</i>	Missense, nonsense mutations; insertions, deletions	HSAN-II	Autosomal recessive	WNK1: with-no-lysine(K)-1; only HSN2-containing nervous tissue-specific isoform of WNK1 affected (Shekarabi et al. 2008)	HSN2-containing isoform: CNS, PNS, dorsal root ganglia and sciatic nerves (Shekarabi et al. 2008)	Serine-threonine protein kinase; sodium, chloride and potassium homeostasis (Anselmo et al. 2006)
<i>FAM 134B</i>	Missense mutations			FAM134B: family with sequence similarity 134, member B	PNS (sensory and autonomic ganglia) (Kurth et al. 2009)	Component of the <i>cis</i> -Golgi matrix, shaping and tethering the membrane stacks (Kurth et al. 2009)

Gene name	Mutation	Type of HSAN	Inheritance	Protein name	Expression	Biological function
<i>KIF1A</i>	Frame-shift mutations mostly in nerve-specific exon (Riviere et al. 2011)	HSAN-II	Autosomal recessive	KIF1A: Kinesin family member 1A	Nerve-specific splice variant: dorsal root ganglia (Riviere et al. 2011)	Molecular motor protein; anterograde axonal transport of synaptic vesicle precursors (Okada et al. 1995); interacts with the domain of WNK1 encoded by the HSN2 exon (Riviere et al. 2011)
<i>IKBKP</i>	Splice-site and missense mutations	HSAN-III (also known as familial dysautonomia or Riley-Day syndrome)		ELP1: Elongator complex protein 1 (also known as I κ B kinase complex-associated protein)	Differentiating neurons of CNS and PNS (Hunnicutt et al. 2012)	Scaffold protein, assembly of RNA polymerase II elongator complex (Otero et al. 1999); acetylation of α -tubulin (Creppe et al. 2009)
<i>NTRK1</i>	> 40 missense, nonsense, frameshift and splice-site mutations (Greco et al., 1999)	HSAN-IV (also known as congenital insensitivity to pain with anhidrosis (CIPA))		Trk-A: tyrosin kinase A	Long isoform (Trk-AII) in neuronal tissues (Barker et al. 1993), CNS (Holtzman et al. 1995)	High-affinity nerve growth factor receptor; tyrosin kinase; neurotrophin signaling; β -NGF as binding ligand; development and survival of sympathetic ganglia and nociceptive sensory neurons in dorsal root ganglia, of cholinergic neurons of the basal forebrain (Indo 2002); activity of β -NGF-Trk-A pathway in immune and endocrine system (Levi-Montalcini et al. 1996)
<i>NGF</i>	Missense or frameshift mutations	HSAN-V		β -NGF: β -nerve growth factor	PNS, immune cells (Rotthier et al. 2012)	Neurotrophin family of proteins, regulation of neuronal survival; development and function; contribution to inflammatory and immune response (Nicol and Vasko 2007; Ernsberger 2009); binds to Trk-A (Kaplan et al. 1991; Indo 2002)
<i>CCT5</i>	Missense mutation	HSAN with spastic paraplegia		TCP-1 ϵ : T-complex protein 1 subunit ϵ	Ubiquitously (Kubota et al. 1999)	Cytosolic molecular chaperone, promotes ATP-dependent folding of actin and tubulin (Yokota et al. 2001)

4.4 Contributions

Declaration of contributions to “Generation and characterization of rat and mouse monoclonal antibodies specific for MeCP2 and their use in X-inactivation studies”

For this project, I preselected and characterized rat monoclonal anti-MeCP2 antibodies by epitope mapping experiments shown in Figure 3 and immunofluorescence stainings depicted in Figure 6a. Moreover, I proofread the manuscript.

Declaration of contributions to “Versatile toolbox for high throughput biochemical and functional studies with fluorescent fusion proteins”

For this project, I established and optimized the protein-protein interaction assay in the GFP-multiTrap plates and evaluated the data for the corresponding Figure 3. In addition, I provided the data for Supplementary Figure S1B and I proofread the manuscript.

Declaration of contributions to “Cooperative DNA and histone binding by Uhrf2 links the two major repressive epigenetic pathways”

To characterize the chromatin binding properties of UHRF2, I performed a histone tail peptide binding assay with the full length protein and its individual domains as well as a defined mutant. I evaluated the results and prepared the draft for the Figures 2A, 2B and 4A. With the help of Katrin Schneider I examined subnuclear localization and protein kinetics of UHRF2 and a histone binding mutant in MEF wildtype and *Suv39dn* cell lines. Katrin and me evaluated the FRAP data and prepared the Figures 3B and 3C as well as Supplementary Figure 4D and 4E.

Declaration of contributions to “Dissection of cell cycle-dependent dynamics of Dnmt1 by FRAP and diffusion-coupled modeling”

To raise an antibody specific for DNMT1, I analyzed binding specificities of the antibody 5A10 in western blot and immunofluorescence staining and prepared the corresponding Supplementary Figures S1A and S1B. I also helped with proofreading the manuscript.

Declaration of contributions to “Poly(ADP-ribose) polymerase 1 (PARP1) associates with E3 ubiquitin-protein ligase UHRF1 and modulates UHRF1 biological functions”

For this project, I performed the DNA methylation analysis in wt and *PARP*^{−/−} cells at the major satellite repeats shown in Figure 5E. Furthermore, I provided the information for the UHRF1 single domain and deletion constructs cloned in our lab and proofread the manuscript.

Declaration of contributions to “DNA methylation requires a DNMT1 ubiquitin interacting motif (UIM) and histone ubiquitination”

This project was conceived by Heinrich Leonhard, Weihua Qin and me. I performed biochemical and cell biological experiments for the following Figures: Figures 3c ,d; 6c (in collaboration with Stephanie Link), 7 (in collaboration with David Hörl and Hartmann Harz); Supplementary Figures S3b-e (in collaboration with Stephanie Link and Martha Smets), S4, S7 (in collaboration with Stephanie Link), S8. For the first draft of the manuscript, I wrote the sections corresponding to the experiments performed. I combined all results to design the final Figures, included all changes during the revisions and corrected the manuscript together with Heinrich Leonhardt. Moreover, I was responsible for the correspondence with collaboration partners and for project planning including the development of a timeline and the coordination of different subprojects.

Declaration of contributions to “Mutations of the DNMT1 TS domain found in HSAN-IE patients disrupt interaction with UHRF1, affect subnuclear targeting and lead to cell cycle-dependent destabilization”

This project was conceived by Heinrich Leonhard and me. I performed the experiments shown in the Figures 2 (in collaboration with Stephanie Link), 3 (in collaboration with Karin Fellinger), 4, 5 (in collaboration with Veronika Solis), 6 (in collaboration with Martha Smets), 7 (in collaboration with Katrin Schneider) and the experiments for all Supplementary Figures. I designed all figures and wrote the manuscript.

4.5 Declaration

Declaration according to the 'Promotionsordnung der LMU München für die Fakultät Biologie'.

Betreuung

Hiermit erkläre ich, dass die vorgelegte Arbeit an der LMU von Herrn Prof. Dr. Heinrich Leonhardt betreut wurde.

Anfertigung

Hiermit versichere ich an Eides statt, dass die Dissertation selbstständig und ohne unerlaubte Hilfsmittel angefertigt wurde. Über Beiträge, die im Rahmen der kumulativen Dissertation in Form von Manuskripten in der Dissertation enthalten sind, wurde im Kapitel 4.4 Rechenschaft abgelegt und die eigenen Leistungen wurden aufgelistet.

Prüfung

Hiermit erkläre ich, dass die Dissertation weder als ganzes noch in Teilen an einem anderen Ort einer Prüfungskommission vorgelegt wurde. Weiterhin habe ich weder an einem anderen Ort eine Promotion angestrebt noch angemeldet noch versucht eine Doktorprüfung abzulegen.

München, den 17.06.2015

Patricia Wolf

4.6 Acknowledgements

First of all, I would like to thank my supervisor and doctoral father Prof. Dr. Heinrich Leonhardt who conceived the projects I was working on. I am grateful that I had the opportunity to work in his technically well equipped lab and to benefit from his enormous knowledge and experience in the field of epigenetics. Scientific discussions, the development of hypothetical models and support during writing of manuscripts substantially contributed to the success of this PhD study.

Next, I would like to thank the members of my thesis advisory committee, PD Dr. Sandra Hake and Prof. Dr. Gunnar Schotta for their scientific support and conception of future directions during my PhD study.

I would like to thank Dr. Beate Mannschreck, Dr. Cornelia Kellermann and Francisca Rosa Mende, the coordinators of the Graduate School Life Science Munich, for organizing retreats and diverse soft skill courses. Being part of the LSM doctoral program enriched my time as a PhD student scientifically and personally.

A great thanks goes to Dr. Andrea Rottach and Dr. Garwin Pichler who supervised my Diploma Thesis and provided supported during the initial period of my PhD study. Garwin, thank you for the nice cooperation in the lab and for your good ideas as well as your realistic view of the world. Andrea, I really appreciate your support during the writing of this thesis, your comments and suggestions. It was a pleasure to have a colleague with such an empathic and motivating character.

Thanks also to Udo for correcting and commenting on my thesis in record time, and of course for the nice drawings on my cell culture plates ;-). I am grateful to Stephi for helping me a lot with the practical work in the lab and for always being confident about the impact of our studies.

I also would like to thank my 'roommates' and colleagues Dr. Katrin Schneider and Katharina Thanisch for interesting discussions about work-related and private topics. I am sure that the exchange of ideas about how to manage the life as a PhD student, about fears and tears, about partnerships and leisure activities has added several new aspects to my life. I very much appreciated the great time we had in the 'girls' office and also our activities outside university.

Anja Gahl and Susanne Breitsameter also contributed to this work. Thank you Anja for always being well organized, purposeful and providing practical as well as mental support for our favorite task- the plasmid database ☺. Thank you Susanne for your kind collaboration on plasmid requests.

I am grateful to all my colleagues in the Leonhardt group for generating a pleasant working environment in the lab and for being attentive listeners during lab seminars. Thank you for all the support and exchange about scientific and daily life problems.

I would also like to thank my family for their support during my studies. Thank you Mom and Dad for your trust in my walks of life! And thank you my great two sisters Anja and Heidi, for always having an open ear for my problems and giving suggestions how to solve them. Thank you Heidi for the 'epigenetic puzzle' idea that provided a substantial contribution to the promotion of the DNMT1 UIM manuscript.

Gwendolyn, Conny, Anna and Carina thank you for funny evenings with good food, party music and a lot of fun on the dancing floor! I had and will always have a great time with you making me believe that we never become older ☺.

Last but not least, I would like to thank my boyfriend Christian who always gave me a helping hand wherever and whenever needed. He stood behind me in any situation of my life and showed understanding in all personal or work-related ups and downs. Thank you Christian for being an insightful, empathic and helpful partner!